



UNIVERSITÄT
BAYREUTH

Diketopyrrolopyrrole Materials

Synthesis, Structure Formation, Charge Transport and Photovoltaics

Christian Müller, 2015



Diketopyrrolopyrrole Materials: Synthesis, Structure Formation, Charge Transport and Photovoltaics

DISSERTATION

zur Erlangung des akademischen Grades
eines Doktors der Naturwissenschaften (Dr. rer. nat.)
im Rahmen des Promotionsprogrammes
BayNAT Polymer Science der Universität Bayreuth

vorgelegt von
Christian Müller
geboren in Schrobenhausen, Deutschland

Bayreuth 2015

This doctoral thesis was prepared at the department of Macromolecular Chemistry 1 at the University of Bayreuth from February 2011 until October 2015 and was supervised by Prof. Dr. Mukundan Thelakkat.

This is a full reprint of the dissertation submitted to obtain the academic degree of Doctor of Natural Sciences (Dr. rer. nat.) and approved by the Bayreuth Graduate School of Mathematical and Natural Sciences (BayNAT) of the University of Bayreuth.

Date of submission: 19.10.2015

Date of defense: 21.04.2016

Acting director:

Prof. Dr. Stephan Kümmel

Doctoral committee:

Prof. Dr. Mukundan Thelakkat (1st Reviewer)

Prof. Dr. Andreas Greiner (2nd Reviewer)

Prof. Dr. Carlo Unverzagt (Chairman)

Prof. Dr. Georg Papastavrou

Prof. Dr. Patrick Théato (3rd Reviewer)

Für meine Familie

We are like tenant farmers chopping down the fence around our house for fuel when we should be using Nature's inexhaustible sources of energy — sun, wind and tide. ... I'd put my money on the sun and solar energy. What a source of power! I hope we don't have to wait until oil and coal run out before we tackle that.

(*Thomas Edison, 1931*)¹

¹In conversation with Henry Ford and Harvey Firestone (1931), as quoted in:

J. D. Newton, *Uncommon friends : life with Thomas Edison, Henry Ford, Harvey Firestone, Alexis Carrel & Charles Lindbergh*, 1st ed., Harcourt Brace Jovanovich, San Diego, Calif., **1987**, p. 31.

Table of Contents

Summary	11
Zusammenfassung	13
1 Introduction	17
2 Overview of the Thesis	61
Individual Contribution to Joint Publications.....	75
Graphical Table of Contents	79
3 High Bulk Electron Mobility Diketopyrrolopyrrole Copolymers with Perfluorothiophene.....	79
4 Influence of Fluorination in π -extended Backbone Polydiketopyrrolopyrroles on Charge Carrier Mobility and Depth-dependent Molecular Alignment	143
5 EDOT-Diketopyrrolopyrrole Copolymers for High Bulk Hole Mobility and Near Infrared Absorption.....	197
6 Universal Molecular Orientation Control in Polydiketopyrrolopyrroles.....	227
7 Diketopyrrolopyrroles with a Distinct Energy Level Cascade for Efficient Charge Carrier Generation in Organic Solar Cells.....	261
8 Azido-Functionalized Thiophene as a Versatile Building Block To Cross-Link Low-Bandgap Polymers	295
9 Influence of Electron Extracting Interface Layers in Organic Bulk- Heterojunction Solar Cells	351
10 List of Publications.....	373
11 List of Contributions.....	375
Danksagung – Acknowledgements	377
(Eidesstattliche) Versicherungen und Erklärungen.....	379

Summary

This thesis is concerned with original work on structure-property relationships in semiconducting polymers. The common theme throughout the thesis is the diketopyrrolo[3,4-*c*]pyrrole (DPP) moiety that has gained considerable interest over the last few years. This DPP unit consists of an annulated bicyclic core, the diketopyrrolo[3,4-*c*]pyrrole, which is decorated with an aromatic flanking unit (Ar) on both sides. The resulting structure is herein abbreviated as DPP[Ar]₂. All polymers presented are synthesized by polycondensations and rely on the donor-acceptor approach which is a well-known concept to obtain low-bandgap organic semiconductors, allowing the precise control over energy levels as well as structural properties such as crystallinity and planarity. The polycondensations employ two monomers, one of which is always a dibrominated DPP monomer and the other comonomer M_{co} is either a distannylated or a di(boronic acid ester) functionalized compound for Stille and Suzuki-Miyaura polycondensations, respectively.

In a systematic approach the aryl flanking unit Ar on the DPP[Ar]₂ unit is varied from thiophene (T) through phenyl (Ph) to pyridine (Py) in order to give monomers with distinctively different electron densities on the DPP moiety as well as providing a tool for optimizing the dihedral angle within the DPP motif, i.e. in order to improve planarization and delocalization. Furthermore the comonomer M_{co} is varied in a strategic manner. The polymeric DPPs (PDPPs) derived from these two building blocks DPP[Ar]₂ and M_{co} are denoted as PDPP[Ar]₂-M_{co} with the aryl flanking unit in brackets and the comonomer delimited by a dash. Plain thiophene units were chosen as comonomer M_{co} to build a reference set of three copolymers, denoted as PDPP[Ar]₂-T (Ar = T, Ph, Py). When the comonomer thiophene is exchanged with a difluorinated thiophene TF₂, this not only results in a more electron-deficient polymer but also provides so called non-covalent diffusive interactions between the fluorine atoms and the hydrogen atoms of adjacent aromatic units. These interactions can be exploited to lock the dihedral angles between aromatic rings at small values hence improving planarization of the backbone. Taking into account both of these effects, the electron deficiency and the improved planarization, it is shown in the first part of this thesis that these systems provide superior electron transport properties with a record electron mobility that was hitherto only observed in fullerenes and in N2200, a commercialized poly(naphthalene diimide) copolymer. Complementary to the fluorination approach, the alkoxyated thiophene 3,4-ethylenedioxythiophene (EDOT) was used as comonomer. Again two effects play an important role when discussing charge transport properties, with the π -electron density being one of them and the other being polymer backbone planarity and alignment. Accordingly, this time the alkoxylation of the comonomer leads to polymers with a very electron rich backbone. Furthermore, the alkoxy moieties can once more be exploited for their non-covalent diffusive

interactions, this time between the alkoxy oxygens and hydrogen atoms of adjacent aryl units, leading to improved planarization due to decreased dihedral angles within the backbone. As the backbone electron density is increased considerably, these materials are well suited for hole transport and indeed the bulk hole mobility is found to be two orders of magnitudes higher than values reported for this class of materials. To further elucidate the influence of fluorination, a π -extended comonomer comprising a thiophene-phenyl-thiophene structure is employed and the degree of fluorination on the central phenyl unit is varied from nonfunctionalized over difluorination to tetrafluorination. The impact of this gradual variation on intrinsic material properties and ultimately charge transport behavior in transistors is investigated. It is shown by employing depth-sensitive grazing incidence wide angle X-ray scattering (GIWAXS) that fluorination generally improves the alignment of the polymers in thin films.

The GIWAXS analyses directly introduce the second part of the thesis, which correlates the changes made on a molecular level to the impact on solid state packing of the polymers in thin films. This research is done using GIWAXS at the Australian Synchrotron. In brief it is found that by systematically varying the aryl flanking unit of the DPP core and simultaneous exploitation of diffusive non-covalent interactions hitherto unachieved control over both mode of orientation as well as degree of alignment can be gained.

The third part of the thesis covers the application of small molecule DPPs as well as PDPPs in organic solar cells. A set of small molecular weight DPPs is synthesized and the frontier orbital energy levels are precisely tuned by deliberate variation of the terminal aryl units. Different π -electron densities when going from phenyl- through *m*-pyridine to *p*-pyridine termini lead to lowered energy levels while the bandgap is kept at a constant value. This property is exploited in a vacuum processed planar heterojunction solar cell with C₆₀ as the acceptor. By subsequently evaporating two of the materials with an energy level offset of around 200 meV, an energy level cascade is established at the donor/acceptor interface that leads to enhanced charge carrier generation. The power conversion efficiency is improved by a factor of 2 compared to reference cells with only one of the DPP donors, thus lacking the cascade structure at the interface. Furthermore, a modular approach for the simple and efficient synthesis of crosslinkable low-bandgap polymers is introduced in this part. Following this concept, a variety of crosslinkable PDPPs is designed, synthesized and characterized for their potential application in solar cells comprising a stable morphology. Finally, a PDPP:PCBM donor-acceptor system is compared with a P3HT:PCBM system as a reference blend system to study the influence of different electron extraction layers by determining built in potentials in combination with different cathode materials.

Zusammenfassung

Die vorliegende Dissertation befasst sich mit Forschungsarbeiten zu Struktur-Eigenschafts-Beziehungen in halbleitenden Polymeren. Den roten Faden durch diese Dissertation stellt die Diketopyrrolo[3,4-*c*]pyrrol (DPP) Einheit dar, die innerhalb der letzten Jahre ein beachtliches Interesse im Bereich der organischen Halbleiter geweckt hat. Diese DPP-Einheit besteht aus einem annullierten bicyclischem Kern, dem Diketopyrrolo[3,4-*c*]pyrrol, welcher an beiden Seiten einen angrenzenden Aromaten (Ar) trägt. Die hieraus resultierende Struktur wird in dieser Arbeit als DPP[Ar]₂ abgekürzt. Alle Polymere im Rahmen dieser Arbeit wurden durch Polykondensation synthetisiert und basieren auf dem Donor-Akzeptor Ansatz, welcher ein bekanntes Konzept ist, um organische Halbleiter mit geringer Bandlücke zu erhalten. Der Ansatz erlaubt sowohl die präzise Kontrolle über die Energieniveaus als auch über die strukturellen Eigenschaften, wie die Kristallinität und Planarität. In Polykondensationen werden zwei Monomere eingesetzt, von denen eines immer ein dibromiertes DPP-Monomer ist. Das andere Monomer ist entweder eine Distannylverbindung oder ein Diboronsäureester, für Stille beziehungsweise für Suzuki-Miyaura Polykondensationen.

In einem systematischen Ansatz werden die angrenzenden Aromaten Ar in der DPP[Ar]₂ Einheit von Thiophen (T) über Phenyl (Ph) zu Pyridin (Py) geändert, um Monomere mit charakteristische Elektronendichten innerhalb der DPP-Einheit zu erhalten. Weiterhin stellt diese Variation eine Möglichkeit dar, den dihedralen Winkel innerhalb des DPP-Motivs zu optimieren. Folglich wird eine verbesserte Planarisierung sowie erhöhte Delokalisierung erreicht. Weiterhin wird das Comonomer M_{co} systematisch verändert. Die DPP-Polymere (PDPPs), die aus den beiden Bausteinen DPP[Ar]₂ und M_{co} hervorgehen, werden als PDPP[Ar]₂-M_{co} bezeichnet, mit den an den DPP-Kern angrenzenden Aromaten Ar in Klammern und dem Comonomer, das durch einen Bindestrich abgetrennt wird. Unfunktionalisiertes Thiophen (T) wurde zunächst als Comonomer ausgewählt, um eine Reihe von drei Referenzverbindungen zu erhalten, gekennzeichnet als PDPP[Ar]₂-T (Ar = T, Ph, Py). Wird das Comonomer Thiophen durch ein difluoriertes Thiophen TF₂ ersetzt, schlägt sich dies nicht nur in einem elektronenärmeren Polymer nieder, sondern ermöglicht weiterhin sogenannte nicht-kovalente, diffusive Wechselwirkungen zwischen den Fluor-Atomen und den Wasserstoff-Atomen angrenzender aromatischer Einheiten. Diese Wechselwirkungen können genutzt werden, um den dihedralen Winkel zwischen den aromatischen Einheiten zu verkleinern und somit eine Verbesserung der Planarität des Polymer-Rückgrats zu erreichen. Diese beiden Effekte – die Elektronenarmut sowie die verbesserte Planarität – berücksichtigend, wird im ersten Teil der Dissertation gezeigt, dass diese Systeme überragende Elektronentransport-Eigenschaften mit einer Rekord Elektronen-Mobilität zeigen, die bisher nur in Fullerenen und N2200, einem kommerzialisierten Poly(naphthalendiimid) Copolymer

beobachtet wurde. Den Fluorierungs-Ansatz ergänzend, wurde alkoxyliertes Thiophen, nämlich 3,4-ethylenedioxythiophene (EDOT) als Comonomer genutzt. Bezüglich des Ladungsträgertransportes spielen wiederum zwei Effekte eine Rolle: Einerseits die π -Elektronendichte und andererseits die Planarität des Polymer-Rückgrats und dessen Orientierung. Entsprechend führt die Alkoxylierung des Comonomers diesmal zu Polymeren mit einem elektronenreichen Rückgrat. Auch die Alkoxy-Gruppen können genutzt werden, um nicht-kovalente, diffusive Wechselwirkungen zu erzeugen, diesmal zwischen den Sauerstoff-Atomen der Alkoxy-Gruppen und den Wasserstoff-Atomen der angrenzenden Aromaten. Dies führt zu einer verbesserten Planarisierung aufgrund eines verkleinerten dihedralen Winkles im Rückgrat des Polymers. Durch die deutliche Erhöhung der Elektronendichte im Rückgrat sind diese Materialien besonders für den Lochtransport geeignet. In der Tat wurde eine Loch-Mobilität im Bulk gemessen, die zwei Größenordnungen über den Werten liegt, die in der Regel für diese Klasse von Materialien berichtet wird. Um den Einfluss der Fluorierung näher zu untersuchen, wurde ein Comonomer mit erweitertem π -System verwendet, das aus einer Thiophen-Phenyl-Thiophen Einheit besteht. Nun wurde der Fluorierungsgrad am zentralen Phenyl-Ring von unfunktionalisiertem über difluorierten hin zu tetrafluoriertem Phenyl geändert. Der Einfluss dieser graduellen Änderung wurde im Hinblick auf die intrinsischen Materialeigenschaften und letztendlich auf die Ladungstransport-Eigenschaften in Transistoren untersucht. Es konnte mithilfe von tiefensensitivem *grazing incidence wide angle X-ray scattering* (GIWAXS) gezeigt werden, dass die Fluorierung generell die Anordnung der Polymere in dünnen Filmen verbessert.

Die GIWAXS Analysen leiten in den zweiten Teil der Dissertation über, in dem die Variation der chemischen Struktur auf molekularer Ebene mit dem Festkörper-Packverhalten der Polymere in dünnen Filmen korreliert wird. Die GIWAXS Messungen wurden am Australian Synchrotron durchgeführt und kurzgefasst konnte gezeigt werden, dass die systematische Variierung der an den DPP-Kern angrenzenden Aromaten und die gleichzeitige Nutzung von diffusiven, nicht-kovalenten Wechselwirkungen bisher unerreichte Kontrolle ermöglicht. Diese Kontrolle erstreckt sich sowohl über die Art der Orientierung als auch über den Grad der Orientierung im Polymer-Film.

Der dritte Teil der Dissertation beinhaltet die Anwendung von niedermolekularen DPPs und polymeren PDPPs in organischen Solarzellen. Eine Reihe niedermolekularer DPP-Verbindungen wurde synthetisiert und die Energieniveaus der Grenzorbitale wurden präzise durch überlegte Änderung der terminalen Aromaten gesteuert. Die Variierung dieser terminalen Arylgruppen von Phenyl über *m*-Pyridyl hin zu *p*-Pyridyl führt zu verschiedenen π -Elektronendichten, die wiederum niedrigere Energieniveaus bei gleichbleibender Bandlücke zur Folge haben. Diese Eigenschaft wird in vakuum-prozessierten Solarzellen mit planaren Heteroübergängen und C₆₀ als Akzeptor genutzt. Durch die aufeinanderfolgende Verdampfung zweier Materialien mit einem Energieniveau-Versatz von ungefähr 200 meV, wird an der

Donor-Akzeptor-Grenzfläche eine Energie-Kaskade eingeführt, die zu erhöhter Ladungsträger-Erzeugung führt. Verglichen zu einer Referenzzelle mit nur einer DPP-Verbindung ohne die entsprechende Energie-Kaskade an der Donor-Akzeptor-Grenzfläche, konnte eine Verdopplung des Wirkungsgrades erreicht werden. Weiterhin wird in diesem Teil ein modulares Konzept für die einfache und effiziente Synthese von quervernetzbaaren Polymersystemen mit kleiner Bandlücke entwickelt. Eine Reihe verschiedener quervernetzbarer PDPPs wurde entworfen, synthetisiert und im Hinblick auf eine potenzielle Anwendung in Solarzellen mit thermisch und zeitlich stabiler Morphologie charakterisiert. Schließlich wurde ein PDPP:PCBM Donor-Akzeptor-System mit einem P3HT:PCBM System als Referenz-Blend verglichen, um den Einfluss von diversen Elektronen-Extraktionsschichten in Kombination mit verschiedenen Kathoden-Materialien durch nähere Betrachtung des *built-in* Potentials zu untersuchen.

1 Introduction

Progressing from a physical peculiarity in 1976 to a well-established technology with widespread applications and a billion dollar market, organic semiconductors have moved a long way. In 2000, Alan J. Heeger, Alan G. MacDiarmid and Hideki Shirakawa were awarded the Nobel prize in chemistry for their discovery and development of conductive polymers.^[1] When Heeger was asked about the importance of the discovery, he offered two basic answers: “First they did not (could not?) exist, and second, that they offer a unique combination of properties not available from any other known materials. The first expresses an intellectual challenge; the second expresses a promise for utility in a wide variety of applications.”^[2]

Reading these words almost 40 years later, the “promise for utility in a wide variety of applications”^[2] was indeed kept with organic light emitting diodes (OLEDs)^[3] being assembled into smartphones and other screens; emerging solid state lighting from OLEDs;^[4-5] printed integrated circuits (ICs)^[6] being mass produced for application in smart packaging and ultimately organic photovoltaics with power conversion efficiencies approaching those of second generation thin film solar cells such as amorphous silicon.^[7]

Whereas OLEDs, organic lighting and printed ICs have reached market maturity, organic photovoltaics (OPV) has just recently had its breakthrough with high power conversion efficiencies of about 10% and development in large scale processing and applications. This progress is nicely laid out in a 2014 review from Frederik Krebs entitled “Rise To Power – OPV-Based Solar Parks” demonstrating that grid electricity from OPV is within reach.^[8]

Some of the most striking advantages of organic semiconductors are their processability, light weight and their flexibility which in combination offer cheap and unique possibilities for application. Figure 1-1a shows a flexible OLED display and in Figure 1-1b an opaque solar cell manufactured on a flexible substrate is shown. Moreover, even paper has been demonstrated to work as a substrate for organic photovoltaics (Figure 1-1c). As organic semiconductors can be processed from solution, large scale roll-to-roll (R2R, see Figure 1-1d-f) fabrication has emerged as a valuable tool for fast and cost efficient production of organic electronics in general^[9] and organic photovoltaics in particular.^[10-11] Being a very powersaving production method, organic solar cells exhibit small energy payback times (EPBT) of around 90 days.^[8]

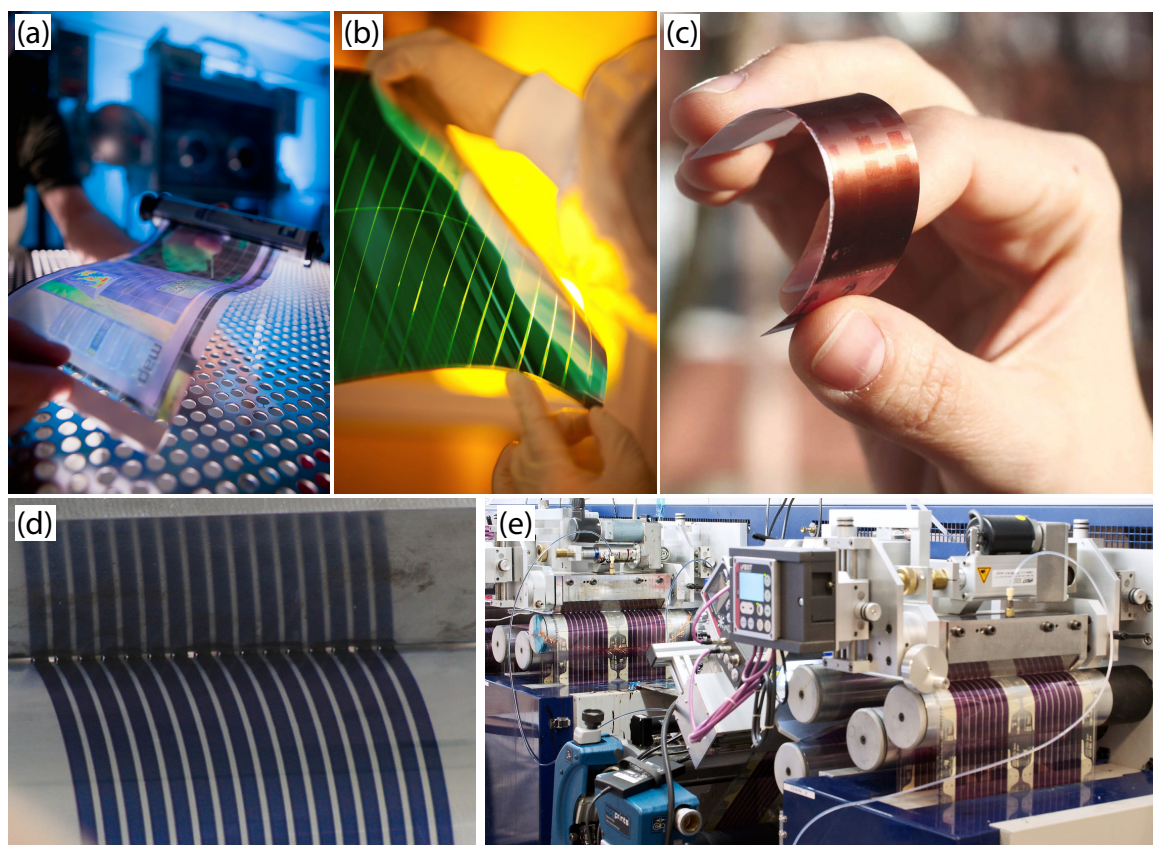


Figure 1-1. (a) Flexible display developed by the U.S. Army^[12] ; (b) Opaque organic solar cell by Heliateg^[13]; (c) Photograph of a printed photovoltaic cell on paper^[14] (reprinted with permission from Wiley & Sons, Inc.); (d) Active layer slot-die coating (reproduced from Søndergaard et al^[10] under the creative commons licence); (e) R2R slot-die coating of active layer polymers at Risø DTU (reproduced from Andersen et al^[15] with permission from The Royal Society of Chemistry).

1.1 Organic semiconductors

In fact, some early reports that date back to the late 19th century do mention colorful products upon electrolysis of the sulphate of aniline^[16] and the addition of concentrated sulfuric acid to thiophene.^[17] Whereas we know today, that here the electropolymerization of aniline to give polyaniline (PANI) and the polymerization of thiophene in strong acids to give polythiophene were described, the structure of the products obtained was considered to be a low molecular weight compound dye rather than a polymer.^[18] Figure 1-2 gives an overview of early semiconducting polymers that were discovered as a consequence of fundamental research triggered by the above findings.

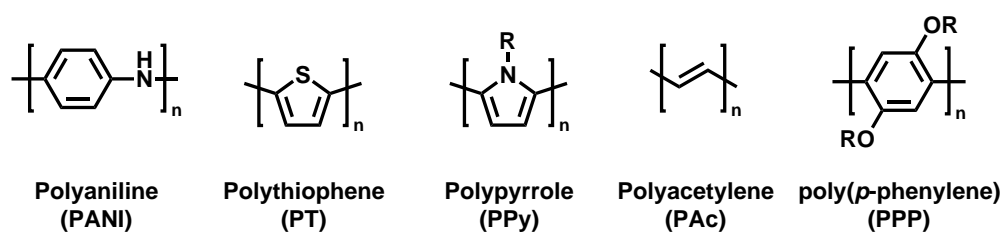


Figure 1-2. Early organic semiconductors.

A breakthrough in the design of organic semiconductors was reached, when long alkyl sidechains (R) were attached to the π -conjugated cores which rendered the resulting polymers soluble due to reduced aggregation. Two of the most prominent examples, a poly(*p*-phenylene vinylene) derivative (MEH-PPV) and poly(3-alkylthiophenes), in particular poly(3-hexylthiophene) (P3HT), are introduced in section 1.1.2.3.

This thesis reports the design and development of novel semiconducting polymers from the class of diketopyrrolopyrroles that are characterized by a small semiconductor bandgap and have gained recent interest in the research community due to their promising optical, structural and optoelectronic properties. In detail, the structure of those polymers is strategically changed by exploiting diffusive non-covalent interactions along the conjugated backbone. The impact on various polymer and semiconducting properties is investigated and as a result new polymers with record bulk charge carrier mobilities have been discovered.

1.1.1 Organic solar cells

Since the first successful demonstration of organic heterojunction solar cells by Tang,^[19] the power conversion efficiencies of organic solar cells have reached values comparable to their inorganic thin film analogs.^[7] The term organic solar cell covers a wide range of different devices,^[20-21] from all-polymer systems^[22-24] through polymer-small molecule blends^[25-27] to solar cells comprising only small molecules^[28-30] and even polymer/inorganic hybrid systems.^[31]

1.1.1.1 Architecture

A typical organic solar cell device is schematically shown in Figure 1-3a, comprising a glass substrate that is covered with a transparent indium tin oxide (ITO) front contact and poly(3,4-ethylenedioxythiophene) polystyrene sulfonate (PEDOT:PSS) as a hole extraction layer. The active layer consists of a distinct donor and an acceptor material which can be assembled in various ways (*vide infra*). The back contact is a metal electrode that is evaporated on top of the organic layer stack. Common materials include calcium, aluminium and silver depending on the desired work function. An interlayer may be added between the active layer and back contact in order to facilitate efficient electron extraction.

1.1.1.2 Working principle

The working principle is shown in Figure 1-3, where the inset of Figure 1-3a gives information about the local sites of the individual steps, Figure 1-3b gives information about the electronic levels of the individual materials in general and the electronic frontier orbital energies of donor and acceptor in particular. Figure 1-3c finally illustrates the state energies that can be observed from excitation to final charge separation. Organic solar cells are excitonic systems in which light is absorbed (*step 1*) and an electron of the absorbent material (usually the donor) is excited from the ground state (S_0) to the next excited state (S_1) which results in a strongly bound electron-hole pair,^[33] the frenkel exciton.^[34]

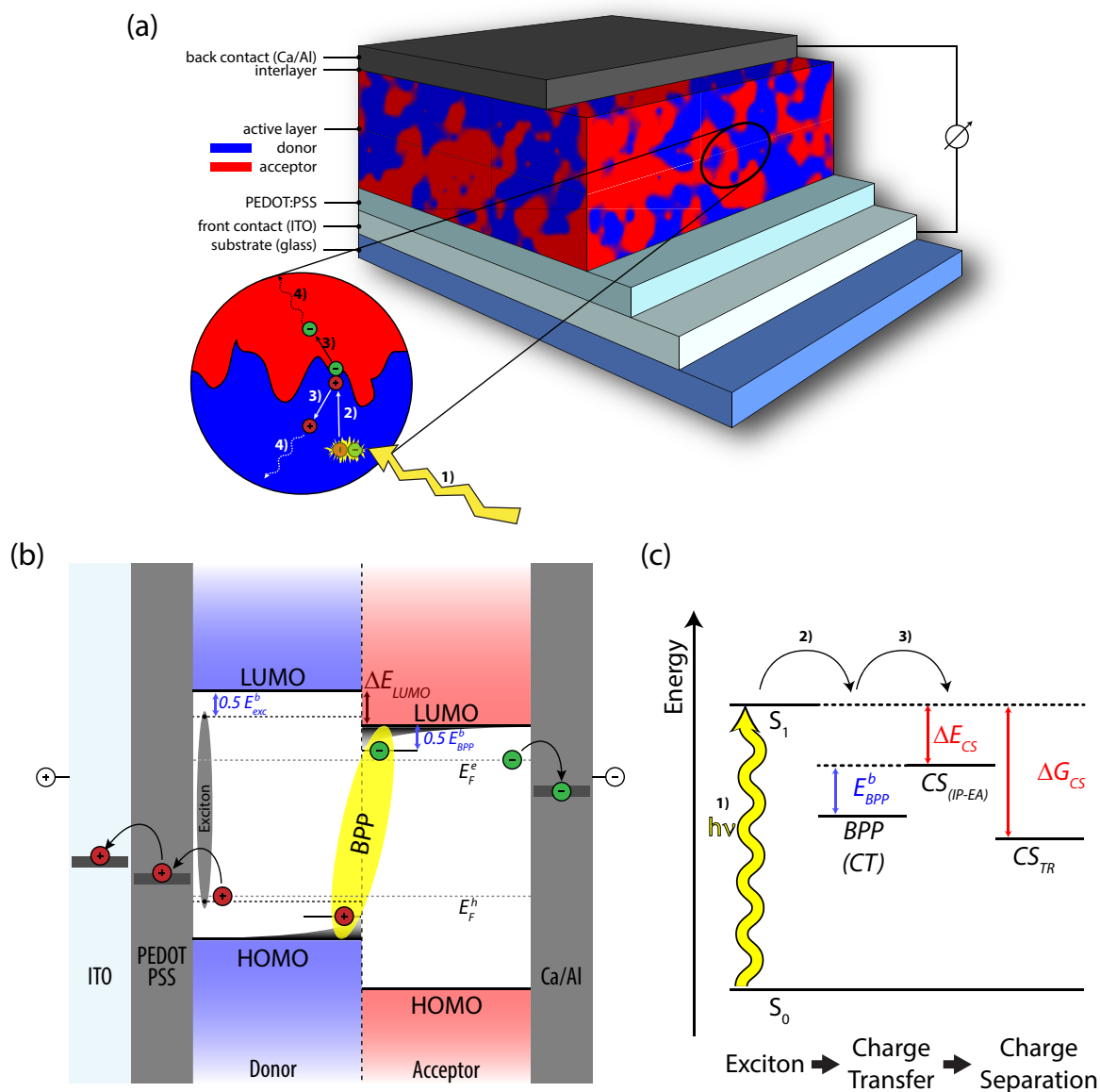


Figure 1-3. (a) Schematic architecture of an organic solar cell device comprising a bulk heterojunction as the active layer. An electron extracting interlayer may optionally be inserted between the active layer and the back contact. The inset depicts the working principle for excitonic solar cells; (b) Electronic scheme of an organic solar cell with energy levels of the individual materials, HOMO is the highest occupied molecular orbital and can be estimated the ionisation potential (IP), LUMO is the lowest unoccupied molecular orbital and can be estimated from the electron affinity (EA); (c) State energy diagram illustrating the ground state (S_0), state of the singlet exciton (S_1), the charge transfer state (CT), also referred to as coulombically bound polaron pair (BPP) and the charge separated states (CS), E_{exc}^b is the binding energy of the singlet exciton, E_{BPP}^b is the equivalent binding energy of the BPP states, ΔE_{CS} is the enthalpy difference driving charge separation and is defined as the difference in enthalpy between the singlet exciton energy (E_{S1}) and the enthalpy of the charge separated polarons at their respective material band edges (given by $IP - EA$), ΔG_{CS} is the total energy loss during the overall charge separation process; (b-c) Adapted from Dimitrov *et al.*^[32] Copyright 2014 American Chemical Society.

This exciton has diffusion lengths in the order of 10-20 nm^[35-37] in which it has to reach a donor-acceptor interface (*step 2*). At the interface a charge transfer state (CT) is generated, which is also referred to as coulombically bound polaron pair (BPP). Charge separation can

happen at the interface, if the energy available for charge separation is greater than the exciton binding energy ($\Delta E_{CS} > E_{exc}^b$). If this is the case, charges are separated (CS, *step 3*) leading to an electron in the acceptor and a hole in the donor material.^[38-39] The electron (E_F^e) and hole (E_F^h) quasi-Fermi levels that are found in donor-acceptor blend during device operation are different from the band edges of the neat materials and their splitting corresponds to the free energy of photogenerated charge carriers after thermal relaxation (CS_{TR} in Figure 1-3c). The charges are then transported (*step 4*) through the respective materials to the electrodes, i.e. the hole through the donor material to reach the ITO front contact and the electron through the acceptor material to come to the metal back contact. Electrode interlayers, such as the depicted conducting PEDOT:PSS at the front contact and for example lithium fluoride (LiF) or zirconium acetylacetonate (ZrAcac) at the back contact can be used to adjust the electrode work functions or the built-in potential in the device and thus facilitate the extraction of holes and electrons, respectively.

1.1.1.3 Active layer morphology

In order to obtain highly efficient solar cell devices, the morphology of the active layer must meet specific demands. First, donor and acceptor should be intermixed to a level that excitons can diffuse to a donor-acceptor interface within their lifetime, i.e. within their exciton diffusion length of 10-20 nm. Second, both the donor as well as the acceptor material have to form a interconnected network without the formation of isolated domains in order to avoid charge recombination and to allow efficient charge transport to the respective electrodes. Last, the morphology should be thermally and temporally stable in order to allow high temperature processing in large scale production (e.g. accelerated ink drying in inline ovens) and to achieve long device lifetimes.

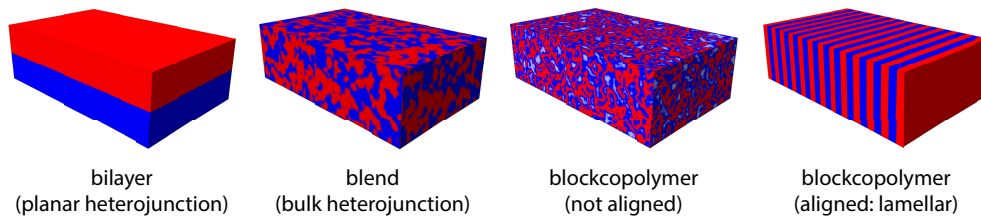


Figure 1-4. Active layer morphologies.

The active layer of the solar cell can be assembled in various ways and the most important ones are shown in Figure 1-4. Planar heterojunctions, i.e. bilayers, were used in the early days^[19] and are limited by the small exciton diffusion lengths for thick active layers and by inferior absorption in layers thin enough for efficient charge generation. However, this morphology also has advantages such as the easy processability of multilayer stacks (e.g. for energy level cascades^[40-41] or tandem and multijunction solar cells^[42-43]) and is, therefore, often used in industry. In particular for vacuum processable low molecular weight compounds, planar heterojunctions enable complex device stacks that in fact led to the latest certified power conversion efficiency record in OPV devices (12%, see section 1.1.2.4).^[44]

In 1995 the concept of bulk heterojunctions was first demonstrated,^[45-46] tremendously simplifying the preparation of efficient active layers by mixing donor and acceptor materials followed by solution processing of this blend. Depending on processing parameters such as concentrations, solvents, solvent additives as well as annealing, an ideal morphology of finely mixed donor and acceptor domains exhibiting interconnected networks can be obtained. This approach is not only feasible for blending polymers with small molecules, but also for blending different polymers.^[47] Due to the ease of processing, this system has become the most prominent morphology in academic OPV research, albeit severe limiting factors such as morphological instability at elevated temperatures: Even when the donor and acceptor domain sizes can exactly be tuned by processing, the resulting morphology is simply frozen upon evaporation of the solvent in thin film. This morphology is, however, not thermodynamically stable and thermal stress leads to a macrophase separation in the large majority of blends which leads to a vast deterioration of OPV device performance.^[48]

One approach to stabilize the bulk-heterojunction morphology of an active layer is crosslinking of the active layer, either by use of crosslinkable low-bandgap polymers or by addition of external crosslinkers.^[49-54] This solution is attractive especially for industry, as it does not unfavorably influence large scale processing and can be easily implemented in already available systems.^[55]

A more advanced path is offered by blockcopolymers,^[56-57] which cannot undergo macrophase separation as the donor and acceptor blocks are covalently linked. They are, however, known to microphase separate into well defined morphologies (e.g. lamellar, see Figure 1-4) at length scales that match the exciton diffusion length.^[58-62] Apart from representing the thermodynamic minimum, thus being thermally stable, these morphologies can offer close to perfect pathways for charge extraction.^[63-67] However, a desired orientation of domains needs to be achieved to realize highly efficient devices.

The importance of morphology control in donor-acceptor systems has been underrated for a long time in the pursuit of materials with optimal energy levels. More recently, research aimed at developing tailored morphologies, well-suited for charge generation and transport in organic solar cells, was proposed to be at least as fruitful.^[68-69]

1.1.1.4 Basic characterization

Organic solar cells are commonly characterized by their I - V characteristics (Figure 1-5a) and their external quantum efficiency (EQE, Figure 1-5b). During irradiation with light that matches the intensity and spectrum of AM1.5G sunlight, a counter voltage is applied to the photovoltage and the current is measured as a function of applied voltage.^[70]

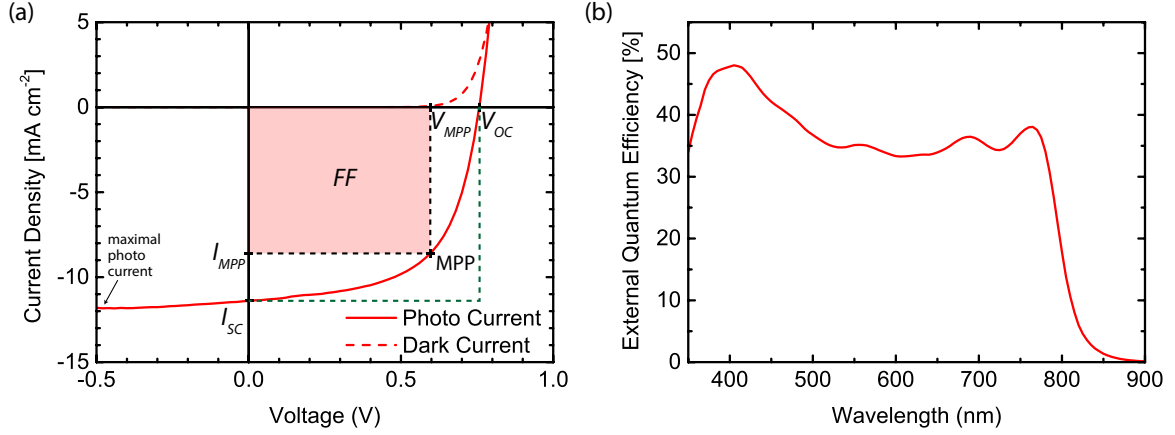


Figure 1-5. Typical characteristics of a solar cell: (a) I - V characterization with open circuit voltage V_{OC} , short circuit current I_{SC} , fill factor FF , maximum power point MPP and the voltage and current at the MPP V_{MPP} and I_{MPP} , respectively; (b) external quantum efficiency (EQE).

The electronic parameters used for characterization are the open-circuit voltage V_{OC} , the short-circuit current density I_{SC} and the fill factor FF . V_{OC} is mainly determined by the difference of the donor HOMO and the acceptor LUMO and is the maximum voltage that can be obtained. In most cases 0.6 eV loss is registered as energy requirement to create the charge separated state.^[71] I_{SC} is the maximum photocurrent density that is obtained under short-circuit conditions. The maximum power point MPP is defined as the point where the power output of the solar cell under continuous operation is highest. The fraction of the power obtained at this point (red shaded square) and the theoretically maximum calculated from the product of J_{SC} and V_{OC} (dashed green line) is defined as FF (see eq. 1), giving a measure of the quality of charge carrier extraction, which depends on different resistances and recombination effects.

$$FF = \frac{V_{MPP} I_{MPP}}{V_{OC} I_{SC}} \quad (1)$$

The power conversion efficiency η is defined as the ratio of power produced by the device (P_{out}) and the power of the incident light (P_{in}).

$$\eta = \frac{P_{out}}{P_{in}} = \frac{V_{OC} I_{SC} FF}{P_{in}} \quad (2)$$

The external quantum efficiency (EQE) is given by the number of electrons extracted from the device $N_{e^-,out}$ divided by the number of incident photons $N_{photons,in}$ (see eq. 3) and is usually measured in dependence of the incident wavelength (see spectrum in Figure 1-5b) which gives information about the photocurrent contribution at different wavelengths arising from different materials, such as the donor and the acceptor.

$$EQE = \frac{N_{e^-,out}}{N_{photons,in}} = \frac{I_{SC}}{P_{in}} \cdot \frac{\lambda}{hc} \quad (3)$$

1.1.2 Donor and acceptor materials

1.1.2.1 Demands for donor and acceptor materials

In order to allow exciton splitting into free charge carriers, the energy levels of both the donor and the acceptor material have to be well aligned (Figure 1-3, Figure 1-6).^[32] Both materials are characterized by their optical transitions, defining the optical gap $E_{g,opt}$ and by the energy levels of their frontier molecular orbitals, i.e. highest occupied molecular orbital (HOMO) and lowest unoccupied molecular orbital (LUMO). HOMO and LUMO levels can be estimated from the ionisation potentials and electron affinities, respectively. Those values are experimentally accessible *via* cyclic voltammetry. The difference of HOMO and LUMO is defined as fundamental gap or transport gap $E_{g,Donor}$ and $E_{g,Acceptor}$, respectively. In order to allow a charge separation, ΔE_{CS} has to be greater than the exciton binding energy E_{exc}^b (see section 1.1.1.2). As a rough guideline to facilitate this requirement, the offset in LUMO energies ΔE_{LUMO} should be at least 0.3 eV.^[32, 39, 71-73] The difference between the electron and hole quasi-Fermi levels E_F^e and E_F^h , respectively, represents the maximum open-circuit voltage that can theoretically be obtained (eV_{OC} in Figure 1-6b).

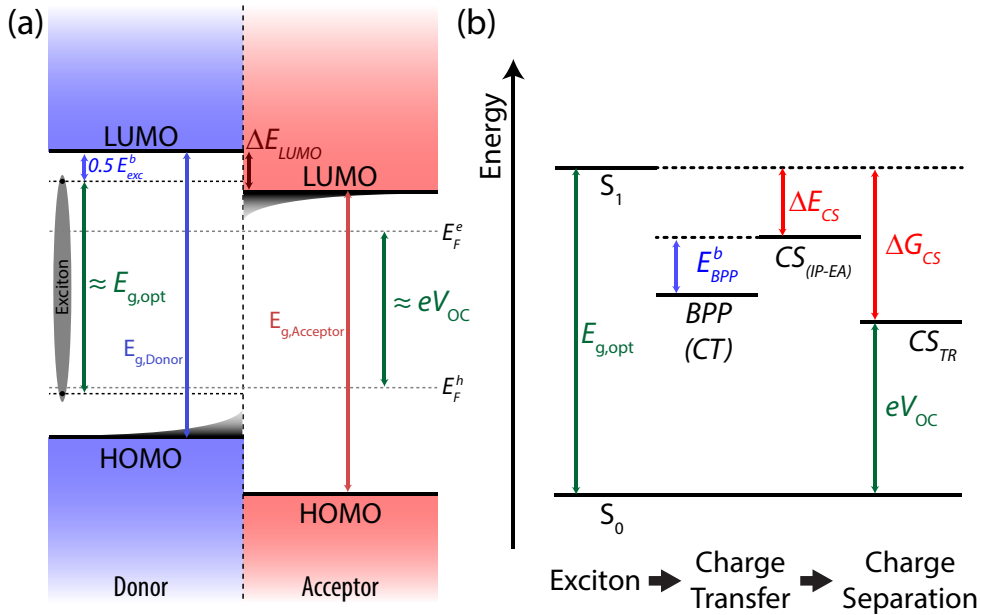


Figure 1-6. Donor and acceptor energy level alignment and the impact on the open-circuit voltage V_{OC} . (a) Electronic orbital energy diagram; (b) State energy diagram. See Figure 1-3 for a complete device stack and section 1.1.1.2 for the working principle of a solar cell device. Adapted with permission from Dimitrov *et al.*^[32] Copyright 2014 American Chemical Society.

1.1.2.2 Acceptor materials

An overview of widely used acceptor materials is given in Figure 1-7. In particular the fullerenes C_{60} and C_{70} or their soluble analogs PC₆₀BM and PC₇₀BM have become standard materials^[25, 27, 74] since the first report of photoinduced electron transfer from a conducting polymer to buckminsterfullerene.^[75] Fullerenes show only weak absorption due to symmetry forbidden optical transitions in the spherical C_{60} , which is partly avoided in the geometrically distorted

C₇₀. In order to harvest as much light as possible, an increased absorbance of the active layer is highly desirable. This can be achieved by using an acceptor material exhibiting strong absorption that ideally complements the donor absorption spectrum.^[26, 76] Large progress has recently been made and solar cells with helical perylene-3,4,9,10-tetracarboxylic diimide (PDI) exhibiting power conversion efficiencies over 6% have been demonstrated.^[77-78] Only few acceptor polymers with good electron transport properties have been developed, P(NDI2OD-T2) (commercially available as ActivInk N2200 from Polyera) being the most prominent one.^[79-81]

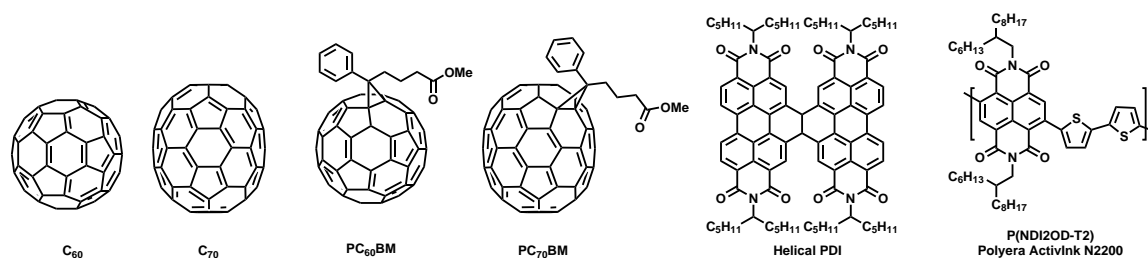


Figure 1-7. Chemical structures of various acceptor materials.

1.1.2.3 Donor polymers

A huge variety of donor materials has been synthesized over the last decade in pursuit of perfectly matched energy levels, enhanced absorption, charge transport properties and control over morphology. A small selection of donor materials is shown in Figure 1-8. This selection includes the long-known poly(3-hexylthiophene) P3HT^[82-84] as well as the poly(*p*-phenylene vinylene) derivative MEH-PPV, which dominated OPV research for most of the 1990s.^[85-86]

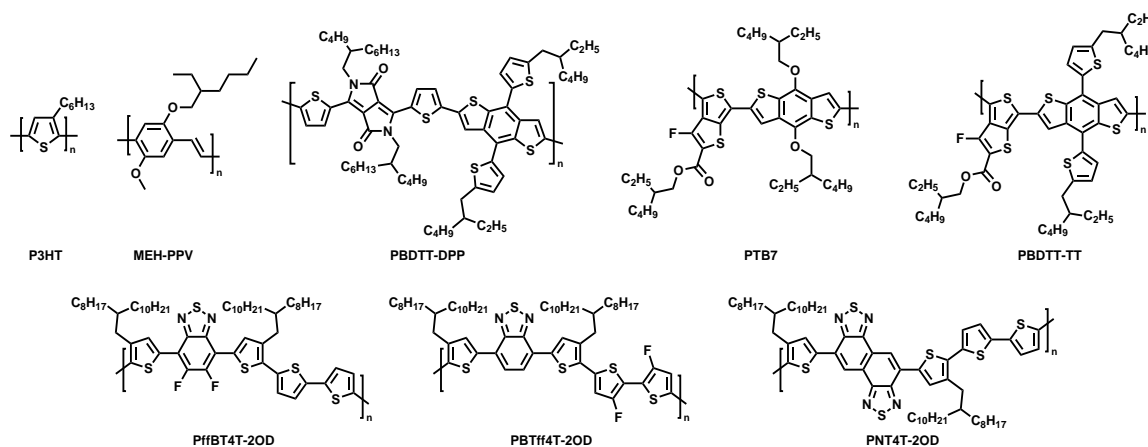


Figure 1-8. Overview of polymers used as donor materials in organic solar cells.

Recent development in low bandgap polymer research (see section 1.1.3 for low bandgap approach) led to the emergence of various high performing donor materials, such as PBDTT-DPP, which was used in a tandem junction organic solar cell to give a power conversion efficiency of 8.6%.^[87] The polymer PTB7^[88] gained popularity, when an efficiency of 9.2% was reported for a blend with PCBM in 2012.^[89] This polymer was further improved by exchanging the alkoxy sidechains of the benzodithiophene (BDT) core with thienyl-derivatives^[90] to give PBDTT-TT (various different names are used in literature for this polymer, including PBDTT-

FTTE,^[24] PBDTTT-EF-T^[91], PBDTT-TT-F^[92]). The additional thiophene units perpendicular to the polymer backbone resulted in a considerable decrease of the bandgap, yielding numerous efficiency records, e.g. 6.1% for a blend comprising a helical PDI acceptor,^[77] 5.7% in an all-polymer solar cell with N2200 as the acceptor,^[91] 6.7% for an all-polymer blend with fluorinated N2200,^[92] 7.7% when blended with the acceptor-polymer PNDIS-HD.^[24]

Three different donors (Figure 1-8, bottom row) were demonstrated to yield extremely high performance in organic solar cells when blended with PCBM *via* aggregation and morphology control. Following this approach, multiple cases of power conversion efficiencies greater than 10% have been reached, culminating in a PCE of 10.8% and fill factors up to 77%.^[69]

1.1.2.4 Low molecular weight donors

Beyond the acceptor materials described above, low molecular weight compounds also enjoy popularity as donor materials. Some of the benefits over the use of polymeric materials include their well defined structure (i.e. monodispersity), ease of synthesis, purification and reproducibility.^[29-30] Electronic and photophysical properties can be more precisely tuned in low molecular weight materials and the active layer morphologies obtained are reproducible to a large extent unlike in the case of polymers, which can vary from batch to batch in their molecular weight. Therefore, also the morphology of polymer:fullerene blends, which is influenced by the long range ordering of the polymer and the viscosity of the solution, is affected by batch to batch variations. Furthermore, small molecules allow for physical vapor deposition in order to obtain very well defined multilayer stacks and tandem cells.^[93-94]

In a recent report, a power conversion efficiency of 8.4% was reported for a solar cell comprising the low molecular weight compounds hexithiophene, boron subnaphthalocyanine chloride (subNC) and the homologue subPC.^[41] The power conversion efficiency world record for OPV is currently held by Heliatek with a certified efficiency of 12% in a solar cell prepared from low-molecular weight compounds by vacuum processing (see Figure 1-9).^[44]

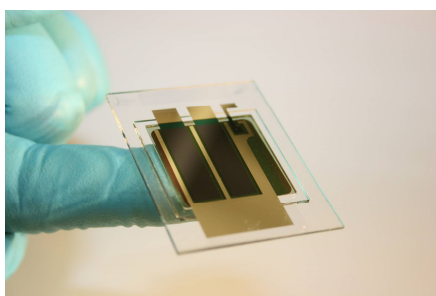


Figure 1-9. Organic Solar Cell by Heliatek with a 12% power conversion efficiency and an active area of 1.1 cm².^[13]

1.1.3 Low bandgap polymers

The bandgap of a conjugated polymer is influenced by several factors, such as aromaticity, bond-length alternation, stabilization of the quinoid structure (Figure 1-10a) and the average

π -conjugation length (Figure 1-10b).^[95-96] The π -conjugation length is not only defined by the length of the conjugated chain, but also by the π -conjugation that is possible in this system, which is determined by the effective π -orbital overlap and thus the coplanarity of the aryl units in the backbone as defined by the dihedral angles (see section 1.1.5). In particular, a concept called “donor-acceptor approach” has become an important tool as it allows synthetic fine-tuning of bandgap and energy levels by simply combining “donor” and “acceptor” units (Figure 1-10b, blue and red, respectively).^[96] Here, donor means aryl units with strong π -donor abilities or simply π -electron rich units and acceptor means aryl units with only weak π -donor abilities or simply π -electron deficient units.

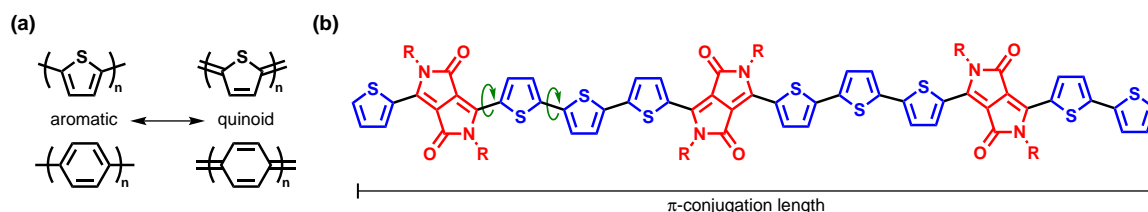


Figure 1-10. Strategies towards low bandgap polymers: (a) Quinoid approach; (b) Schematic illustration of the π -conjugation length, dihedral angles (green arrows) influencing polymer backbone planarity and units with differing π -electron densities (blue/red) allowing intramolecular charge transfers (ICT).

It should be emphasized here, that in literature often the terms „donor“ and „acceptor“ are used for both, donor and acceptor materials within an active layer (as described in section 1.1.1.2 and 1.1.2) on the one hand, and for electron-rich (donor) or electron-deficient (acceptor) *subunits* within a particular polymer structure (as described here), on the other hand. In order to avoid misunderstandings and confusion, albeit the common concept known as “donor-acceptor approach”, from here on this thesis uses the terms “electron-deficient” or “electron-rich” unit rather than donor or acceptor when building blocks of conjugated polymers are described.

One advantage of alternating electron-rich (ER) and -deficient (ED) units in the backbone is the increased double bond character between these units due to a push-pull mesomerism ($\text{ER-ED} \leftrightarrow {}^+\text{ER}=\text{ED}^-$) that effectively decreases the bond-length alternation within the polymer backbone and hence contributes to a decreased bandgap.^[96] Furthermore, the alternating occurrence of electron-rich and -deficient units allows intramolecular charge transfer states.^[97]

Aromatic units that are commonly used as electron-rich and electron-deficient units are shown in Figure 1-11a. When a specific single aromatic unit, such as thiophene (T) is polymerized, the molecular orbitals of the building blocks are combined by linear combination of molecular orbitals (LCMO). In a simplified way, a band-like structure is formed in the resulting polymer (e.g. P3HT) with a distinct HOMO and LUMO level (Figure 1-11b). Upon combination of units with distinctively different π -electron densities (Figure 1-11c), i.e. different HOMO and

LUMO levels, the orbital coupling leads to a considerably smaller bandgap E_g , as the resulting HOMO level is largely determined by the HOMO of the electron-rich unit and the resulting LUMO level is very similar to the LUMO of the electron-deficient unit.^[95] This approach is thus giving synthetic control over frontier orbital levels when designing new low bandgap polymers by choosing from a large variety of available building blocks. It has also been shown both theoretically and experimentally that a strict alternating arrangement is not required to achieve a lowering of the optical gap.^[98-99]

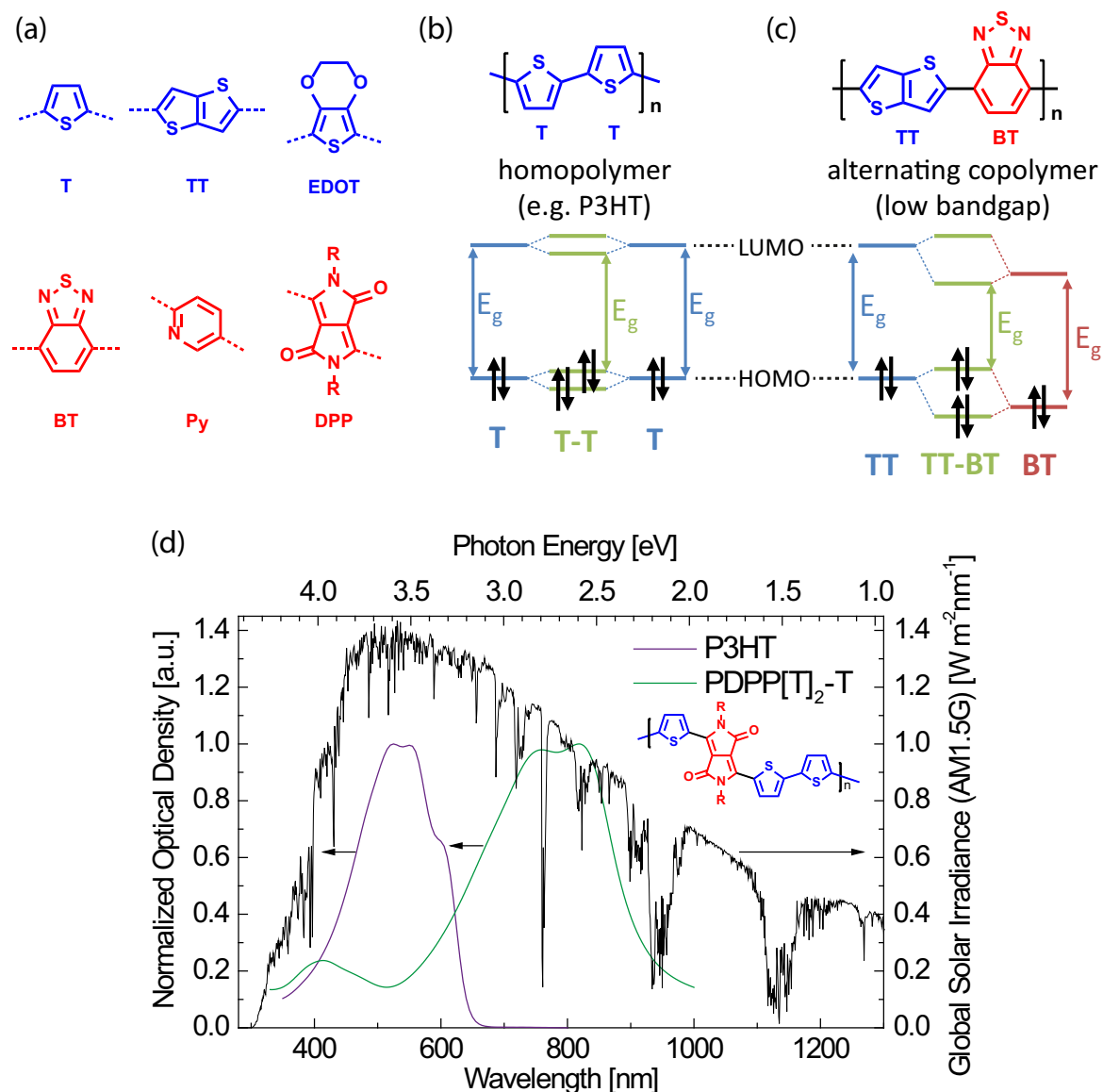


Figure 1-11. (a) Various electron rich (ER, blue) and electron deficient (ED, red) aromatic building blocks for conjugated polymers: Thiophene (T), thienothiophene (TT), 3,4-ethylenedioxythiophene (EDOT), benzothiadiazole (BT), Pyridine (Py), diketopyrrolopyrrole (DPP); (b) Chemical structure of homopolymers (alkyl sidechains are omitted for clarity) and the impact on the frontier molecular orbitals (HOMO/LUMO) upon linear combination of individual molecular orbitals; (c) Orbital coupling in alternating copolymers leads to a decreased bandgap and more control over resulting HOMO and LUMO energy levels; (d) Normalized absorption spectra of a common homopolymer (P3HT, purple) and a low bandgap polymer that is discussed later on in this thesis (PDPP[T]₂-T, green, chemical structure see inset) compared to the global solar irradiance.

Countless different electron-deficient and electron-rich materials have been synthesized and incorporated into low-bandgap systems, mostly in a try-and-error approach.^[22, 95, 100-106] Even bigger libraries have been compared on a theoretical basis with regard to the electron-richness or -deficiency of the individual building blocks and the polymers proposed from them.^[107-109]

The impact of a decreased optical gap on absorption is shown in Figure 1-11d, comparing a thiophene homopolymer (P3HT) with an optical gap of 1.85 eV (corresponding to an absorption onset of around 650 nm) to a low bandgap polymer with an optical gap of 1.3 eV and an absorption onset of 940 nm. When considering the global solar irradiance, low bandgap materials allow much more efficient harvesting of sunlight and thus enable higher short-circuit current densities due to the utilization of lower-energy radiation that is otherwise lost.

1.1.4 Synthetic methods

As the preparation of semiconducting all-conjugated polymers always involves the formation of C-C bonds, the tools allowing the synthesis of these materials are confined to a few methods. At the early stages of semiconducting polymer research, electropolymerization was a valuable tool due to its simplicity and the access to insoluble and conducting polymer films.^[110-114] This approach has now, however, been replaced almost completely by superior transition metal catalyzed C-C cross couplings^[115] that allow immense structural variability, control over the precise molecular structure and defined polymer geometries. These cross-couplings include Stille,^[116] Suzuki-Miyaura,^[117-118] Yamamoto,^[119] Negishi,^[120] Kumada-Tamao^[121-122] and Heck^[123] cross couplings as well as more recent methods such as direct arylation^[124-127] and direct catalytic cross-coupling of organolithium compounds.^[128] In recognition of the achievement of palladium catalyzed C-C cross coupling reactions the Nobel prize in chemistry was awarded to Suzuki, Negishi and Heck in 2010.^[129]

1.1.4.1 Transition metal catalyzed cross-couplings

In this thesis, the syntheses of both small molecules and polymers employ either Stille^[130] or Suzuki-Miyaura^[118, 131] cross-couplings, which are, therefore, discussed in greater detail. Stille pioneered the Pd⁽⁰⁾ catalyzed coupling reaction between an organostannane and an organic electrophile (e.g. a halide) to form a new C-C bond.^[116] Albeit the potentially toxic organotin compounds that are used as starting materials, the Stille cross-coupling is still very popular for the synthesis of functional conjugated polymers. This is primarily due to its tolerance against a wide variety of functional groups and the storage stability of the organotin compounds. One reason for this stability is its moisture and oxygen insensitivity. Furthermore, its almost quantitative yields are a crucial prerequisite for polycondensations in order to obtain high molecular weight polymers. The catalytic cycle for the Stille coupling is shown in Figure 1-12.^[132-137] One cycle comprises three distinct steps, i.e. oxidative addition, transmetalation and finally reductive elimination. The reaction is catalyzed by an active 14-electron Pd⁽⁰⁾

complex^[138] which can be generated *in situ* either by addition of a $\text{Pd}^{(0)}$ catalyst or a $\text{Pd}^{(\text{II})}$ catalyst, which is subsequently reduced to $\text{Pd}^{(0)}$ by organostannane homocoupling.^[139] Commonly used catalysts include $\text{Pd}(\text{PPh}_3)_4$, $\text{Pd}_2(\text{dba})_3$, $\text{Pd}(\text{OAc})_2$ which can be used with or without an additional ligand (L). After oxidative addition of an aryl halide (red) a $\text{Pd}^{(\text{II})}$ intermediate is formed. An organostannane subsequently transmetalates to the $\text{Pd}^{(\text{II})}$ intermediate in the rate determining step. Finally, the coupled product (red-blue) is formed by reductive elimination with the regeneration of the $\text{Pd}^{(0)}$ species. The reaction rate can be enhanced by choosing the correct substitution pattern for the two different aryl units, i.e. the electron-rich aryl unit should be stannylated whereas the more electron-deficient aryl unit should be halogenated.^[130]

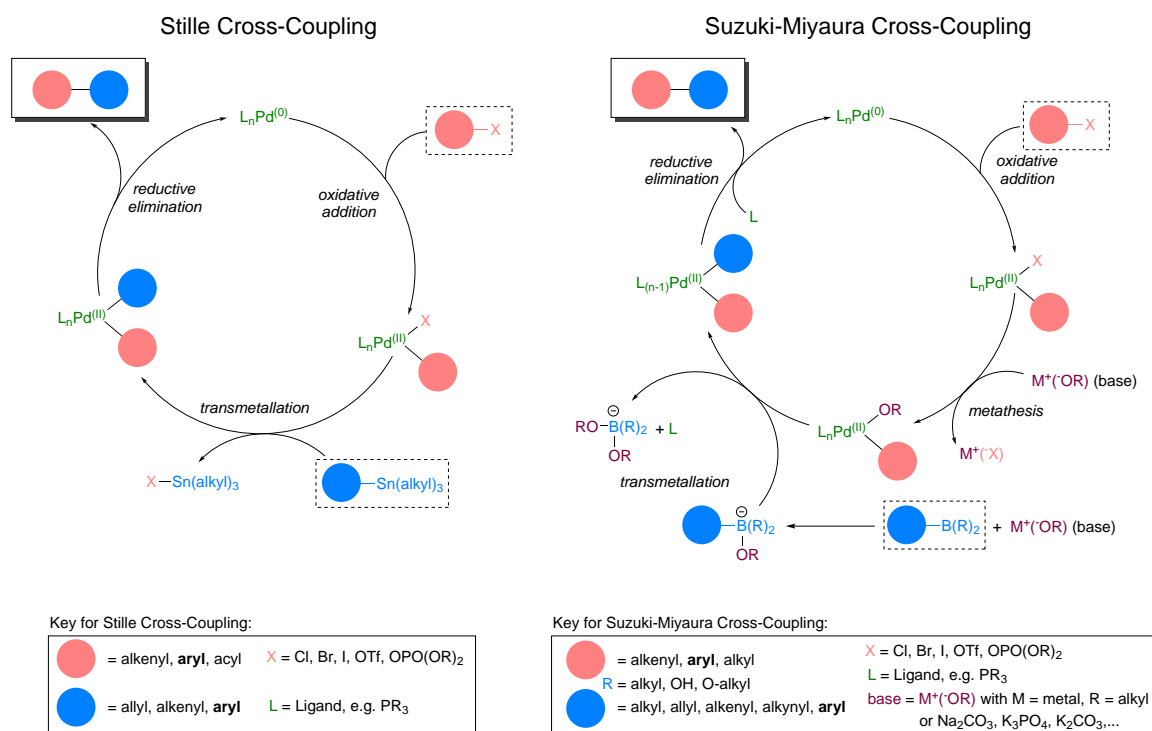


Figure 1-12. Mechanistic schemes (adapted from Kürti et al.^[137]) of the Stille and Suzuki-Miyaura cross-coupling reactions. Solid boxes represent the desired products, dashed boxes represent the employed starting materials. Whereas both reactions can also be used with a variety of substrates, such as alkenyl, acyl, allyl or even alkyl residues, commonly aryl compounds (bold) are used for the synthesis of all-conjugated polymers.

A widely used alternative to Stille cross-couplings was established by Suzuki and Miyaura, namely the Suzuki-Miyaura cross-coupling.^[117-118] In this reaction, an organoboron compound and an organic halide are coupled to form a new C-C sigma bond.^[137, 140-141] The advantage over the Stille cross-coupling is the safer and less toxic nature of the organoboron compounds, many of which are also commercially available. Furthermore, the reaction is insensitive to water and is in fact mostly performed in biphasic aqueous mixtures. Similar to the Stille cross-coupling the catalytic cycle (Figure 1-12) consists of an oxidative addition, a transmetalation and a reductive elimination which work identically. In the course of the additional metathesis in the Suzuki-Miyaura coupling, the anion attached to the palladium is exchanged for the anion of

the base. As the organoboron compounds are less reactive compared to their organostannane analogs, the addition of a base becomes necessary. The base leads to the quaternization of the boron atom, thus increasing the nucleophilicity of the attached aryl group leading to an accelerated transfer to the palladium in the transmetallation step.^[142]

1.1.4.2 AABB and AB type polycondensations

The stepwise polymerizations which are carried out using these transition metal catalyzed cross coupling reactions are also referred to as polycondensations because of the generation of low molecular weight byproducts from the former functional groups. The two distinct pathways leading to a polycondensation are shown in Figure 1-13. Both pathways involve the use of bifunctionalized monomers carrying two different functional groups, labelled A and B. In a Stille polycondensation for example these groups would be the stannane and a halide, respectively.

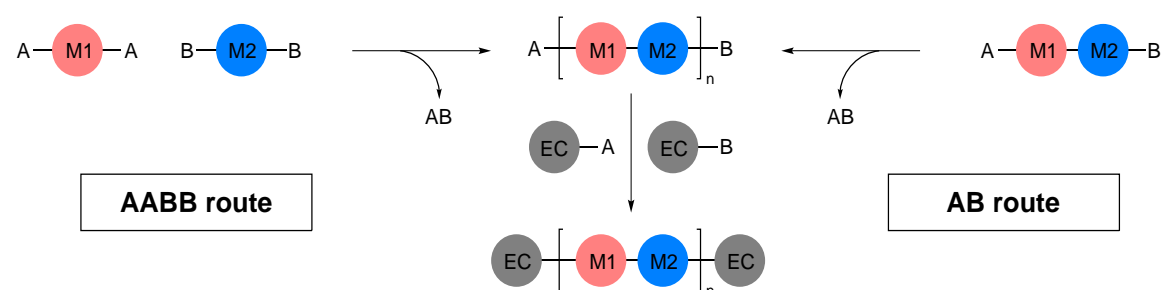


Figure 1-13. Two different polycondensation routes: AABB and AB approach to obtain a strictly alternating copolymer comprising the two comonomers M1 and M2. At the end of the polymerization the polymer is usually endcapped on both ends using an endcapping reagent EC.

In the ‘‘AABB route’’, two monomers M1 and M2 are used that both are bifunctionalized with either A or B groups. Catalytic cross-coupling of these two monomers leads to a step-growth polymerization. This AABB approach has various advantages, primarily the ease of monomer synthesis as all units show symmetric functionalization which greatly enhances yields and simplifies purification. Second, this modular approach allows the efficient synthesis of a polymer library, keeping one monomer constant whilst strategically varying the second one. Further, even ternary copolymers are easily accessible. A considerable drawback of this route is that the stoichiometry of both monomers has to be exactly kept at 1:1 in order to allow high degrees of polymerization and large molecular weights. The degree of polymerization (DP) can be described by Carothers equation (eq. 4) and is strongly dependent of the molar ratio r of AA-type (N_{AA}) and BB-type (N_{BB}) monomers with $r = N_{AA}/N_{BB}$.^[143]

$$DP = \frac{1 + r}{1 + r - 2rp} \quad (4)$$

Here, p is the conversion ranging from 0 to 1. For this reason, polymerizations with r deviating only by a small fraction from 1, only low molecular weight oligomers can be obtained, even at full conversion. Values for $r < 1$ can also originate from impurities contained in the monomer

or partial decomposition of one of the functional groups, making maximal monomer purity a crucial prerequisite for successful polymerization.^[131] The degree of polymerization is also limited if the conversion $p < 1$, e.g. caused by low catalyst turnover numbers or generally sluggish reactivity. Another problem for AABB polycondensation arises from the homocoupling (i.e. cross-coupling of an A functionality with another A functionality rather than A and B)^[144] that can be observed as a side reaction both in Stille and in Suzuki-Miyaura cross-couplings.^[137] Solvent-dissolved oxygen can be one possible origin for homocoupling.^[137]

The alternative “AB route” (Figure 1-13) employs only one monomer that carries both functional groups A and B. The monomer itself can either be a single aryl unit or comprise several moieties, e.g. M1-M2, inbetween the functional groups A and B. Whereas this route is usually much more laborious from a synthetic point of view due to asymmetric functionalization, the stoichiometry parameter r is eliminated from the Carother’s equation (eq. 5).

$$DP = \frac{1}{1-p} \quad (5)$$

As stoichiometry can only deviate from 1:1 by decomposing functional groups or imperfect functionalization in the first place, these systems are much more tolerant against weighing errors, making them ideal for small batches. Furthermore the AB route allows chain-growth polymerizations as will be discussed later on.

Following either route, after polymerization a strictly alternating $(M1-M2)_n$ copolymer chain is obtained which carries a functional group at either polymer end. These functional end groups can deteriorate the device performance in organic electronic devices^[145] and thus have to be scavenged by the addition of endcapping reagents (EC) at the end of the polymerization reaction. Two different endcapping reagents carrying exactly one of the two distinct functional groups have to be added subsequently and in excess to obtain the final endcapped polymer $EC-(M1-M2)_n-EC$. EC can be any aryl unit that is desired to be at the end of the polymer chain. The endcapping reagents can also carry additional orthogonal functionalities as a starting point for polymer analogous reactions (e.g. azides or alkynes for click reactions). In case of the AB route, the resulting copolymer carries two different functional groups A and B at the either end. These polymers can thus either be monofunctionalized or bifunctionalized orthogonally by choosing appropriate endcapping reagents.

1.1.4.3 Catalyst transfer polycondensation

Beyond the classical step-growth polycondensation, elegant catalyst design also allows chain-growth polycondensations of AB type monomers.^[146-148] This novel route was first discovered by McCullough *et al.* for the Kumada-Tamao coupling of Grignard reagents with aryl halides. The resulting living^[149] polycondensation is abbreviated as KTCTP (Kumada-Tamao Catalyst

Transfer Polycondensation).^[150-152] Furthermore, this approach has been adapted for Suzuki-Miyaura cross couplings by Yokozawa *et al.*, leading to SMCTP (Suzuki-Miyaura Catalyst Transfer Polycondensation).^[153-155] The mechanism is schematically shown in Figure 1-14a and is very similar for both types of reactions with the key step in the catalytic cycle being the oxidative addition. After the metal (M) complex has undergone a reductive elimination, diffusion of the catalyst from the polymer chain (leading to step-growth) competes against intramolecular migration of the catalyst along the π -conjugated polymer backbone over several metal-aryl π -coordination complexes (shaded orange). This migration is also referred to as ring walking and can occur along the polymer backbone over the order of even more than 10 nm.^[156-157] When the affinity of the catalyst to the polymer chain is high enough and the subsequent oxidative addition at the chain end is fast enough, this intramolecular catalyst transfer leads to a chain-growth polymerization. These chain-growth polymerizations can either be initiated *in-situ* by reduction of a metal(II) complex by two monomers or alternatively by use of an external initiator (RXL) which allows the synthesis of defined α -functionalized polymer chains (here with R) as shown in Figure 1-14a.^[155, 158-160]

When the blockcopolymer synthesis by sequential monomer addition to the living chain end was studied, it was found that the order of monomer addition has a large influence on the final blockcopolymer (see Figure 1-14b).^[161-162] When a polymer block comprising a weak π -donor monomer (red) is grown first, addition of second monomer with stronger π -donor ability (blue) results in the growth of a second block with excellent control and very low polydispersities. When, however, the block from the strong π -donor monomer is grown first, subsequent addition of the weaker π -donor does not lead to blockcopolymer formation.^[162-163] This was attributed to the higher affinity of the metal catalyst to the strong π -donor moieties than to the weak ones.^[164] Ring walking therefore occurs in the wrong direction and the catalyst will not reach the polymer chain end in order to undergo oxidative addition but rather dissociate from the polymer chain.^[163] At this point supposedly a step-growth mechanism takes over which results in bad control and high polydispersities.^[163]

This issue considerably limits the concept of chain-growth catalyst transfer polycondensation for the synthesis of low bandgap polymers which consist of aryl units with inherently different π -donor strengths (see section 1.1.3). In case of diketopyrrolopyrroles for example, a monomer unit consists of a weakly donating core (red) and strongly donating thiophene moieties (see Figure 1-14c). Upon initiation with an external Pd⁽⁰⁾ species, the catalyst will not be able to migrate to the chain end due to the central core with its electron deficient π -system. This prevention of migration by catalyst trapping has been experimentally proven for a thiophene-benzothiadiazole-thiophene (TBT) unit in the KTCTP system.^[165] This issue has still not completely been overcome, but catalyst systems have emerged that allow the chain-growth polycondensation of units with slightly different π -donating strengths, such as copolymerization of a fluorene-benzothiadiazole (F8BT) unit.^[166]

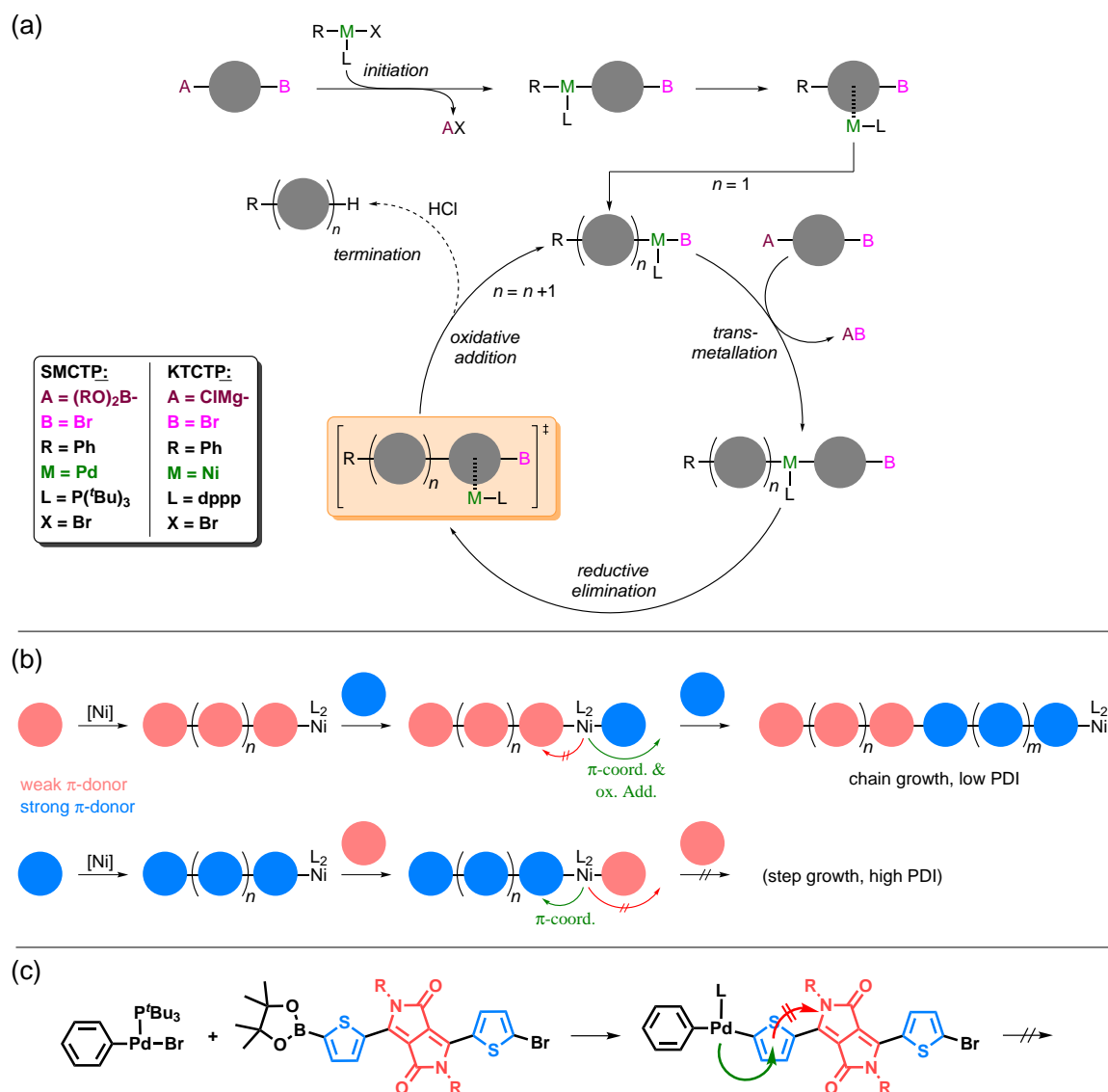


Figure 1-14. Catalyst transfer polycondensation concept: (a) Reaction mechanism for Suzuki-Miyaura Catalyst Transfer Polycondensation (SMCTP) and Kumada-Tamao Catalyst Transfer Polycondensation (KTCTP); (b) Blockcopolymer formation by sequential monomer addition for two monomers with different π -donor strengths – the success of the blockcopolymerization is depending on the order of monomer addition; (c) Problem of inherently different π -donor strengths in a low-bandgap building block.

1.1.5 Conformation locks *via* coordinative bonding

As discussed in section 1.1.3, the planarity of the conjugated backbone has a severe effect on its bandgap due to effective π -orbital overlap. Moreover, charge transport properties are also influenced by backbone planarity. Planar systems allow both efficient intrachain charge carrier transport along the conjugated backbone as well as efficient charge hopping between individual chains by decreased π - π stacking distances and improved π - π coupling of adjacent chains.^[167] It is, therefore, of large interest to minimize dihedral angles in conjugated polymers as much as possible.

It has recently been published and backed by a number of theoretical calculations that the planarity of backbones in a conjugated polymer can be increased via diffusive nonbonding heteroatom interactions.^[168-170] There are, however, several contradictory reports in the recent literature on the origin and the exact conformation that are caused by heteroatom interactions. Elaborate theoretical work by Ratner *et al.* based on quantum chemical calculations (Figure 1-15) mainly favours hydrogen-heteroatom interactions such as $\text{H}\cdots\text{F}$, $\text{H}\cdots\text{O}$, $\text{H}\cdots\text{S}$ etc., whereas interaction such as $\text{S}\cdots\text{F}$ and $\text{O}\cdots\text{F}$ are demonstrated to be nearly zero.^[168] Several other reports claim that $\text{S}\cdots\text{F}$ and $\text{O}\cdots\text{F}$ interactions influence the planarization of semiconducting polymer backbones, often without sufficient experimental proof.^[171-172]

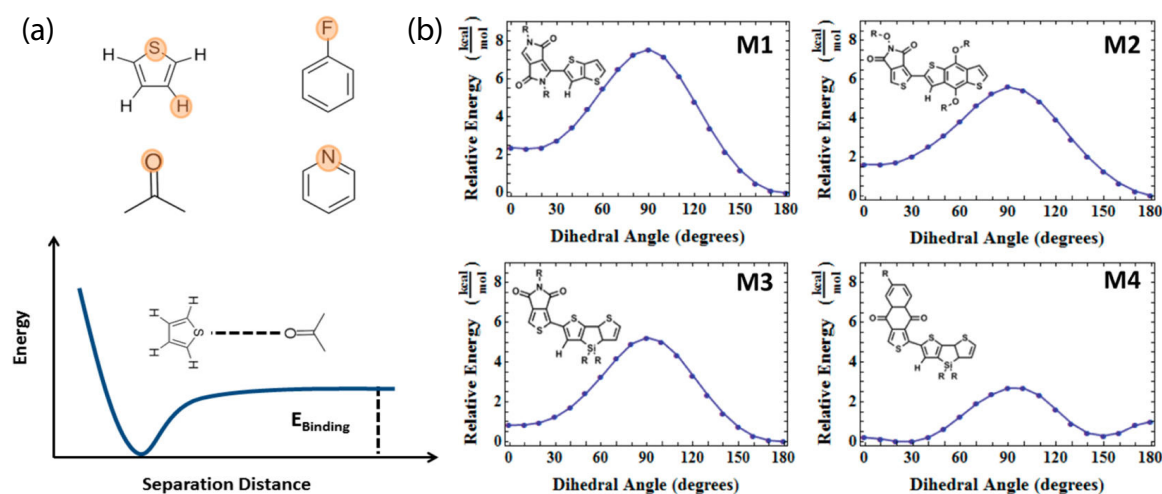


Figure 1-15. Reprinted with permission from Jackson *et al.*^[168] Copyright 2015 American Chemical Society. a) Representative molecules used to analyze the strength of nonbonding interactions. The plot represents a cartoon of an example calculation where the separation distance of the two atoms is varied and a potential energy curve is generated. The binding energy of that interaction is defined as the difference between the energy of the molecules at infinite separation and at the minimum of the potential well;^[168] (b) Torsional potentials for different low-bandgap donor-acceptor building blocks calculated at the RI-MP2/cc-pVTZ level. The molecular conformation shown in each plot is the 0° conformation. Rotation occurs around the inter-ring C-C bond connecting the donor and acceptor blocks.^[168]

Figure 1-15a shows the theoretical approach developed by Ratner *et al.* in order to analyze the strength of diffusive non-covalent interactions. The separation distance between two units of question is gradually decreased and the relative energy of the complete system is calculated. The binding energy E_{Binding} is then defined as the difference between the energy at infinite distance and the minimal energy at equilibrium distance. Binding energy values were obtained for $\text{CH}\cdots\text{N}$ (2.20 kcal/mol), $\text{CH}\cdots\text{O}$ (1.86 kcal/mol), $\text{CH}\cdots\text{F}$ (0.94 kcal/mol), $\text{CH}\cdots\text{S}$ (0.74 kcal/mol) and $\text{O}\cdots\text{S}$ (0.51 kcal/mol, see Figure 1-15a) among others.^[168]

The consequence of these interactions is illustrated in Figure 1-15b. Ratner *et al.* calculated the relative energy of various motifs (M1-M4) commonly found in organic semiconductors comprising two aryl moieties in dependence of the dihedral angle between those units.^[168] It was shown that the $\text{CH}\cdots\text{O}$ interaction which is stronger than the $\text{O}\cdots\text{S}$ interaction leads to a

conformation with the hydrogen atom of the thienothiophene ring pointing towards the oxygen of the ketogroup in diketopyrrolopyrrole (M1, Figure 1-15b), i.e. the relative energy exhibits a minimum at 180° with a benefit of approximately 2 kcal/mol over the depicted structure with the sulfur atom pointing towards the keto group. The same trend can be observed in other motifs (M2-M3). In M4 steric crowding caused by the large solubilizing side chains attached to the silicon leads to different situation with the energy minimum actually favoring a $S\cdots O$ coordination.^[168]

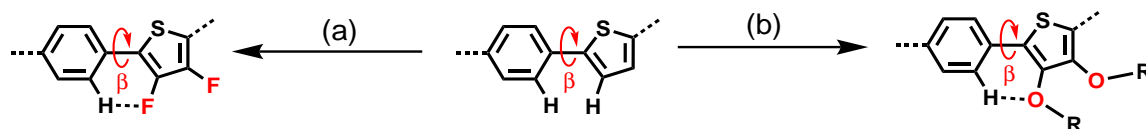


Figure 1-16. Introduction of moieties for diffusive non-covalent interactions between adjacent aryl units; (a) fluorination; (b) alkoxy groups.

Therefore, substitution of aromatic hydrogen atoms in the comonomer with fluorine gives rise to $CH\cdots F$ coordination sites (Figure 1-16a) and electron-deficient comonomers. This fluorination approach has been demonstrated using fluorinated units for the development of semiconducting polymers relevant to both OFET as well as OPV devices.^[171, 173-181] Alternatively $CH\cdots O$ interactions can be exploited to planarize the conjugated polymer backbones (Figure 1-16b). Also these $CH\cdots O$ interactions have recently been exploited pursuing the synthesis of planar polymers via intramolecular non-covalent interactions.^[171, 182]

Another approach to sterically lock-in conjugated systems is covalent bridging. This has been demonstrated in ladder-type comonomers with up to five multi-fused aromatic rings.^[183-186] However, even if these comonomers are very rigid for themselves, the dihedral angle to the adjacent comonomer cannot be minimized by this approach.

1.2 Charge transport in organic and polymeric materials

In general, charge transport in organic semiconductors differs from that in inorganic semiconductors. For example, whereas the charge carrier mobility in inorganic semiconductors is independent of charge carrier density, organic semiconductors are characterized by mobilities dependent on the charge carrier density.^[187-188] A brief overview regarding the basic principles of charge transport as well as two methods used in this thesis, i.e. space charge limited current (SCLC) measurements and organic field effect transistors (OFET), is given here and more detailed information can be found in literature.^[189] In particular, the reader is referred to a very comprehensive standard reference on electronic processes in organic semiconductors, just released by Köhler and Bäessler.^[190]

The key parameter that characterizes the motion of charge carriers in semiconductors is their mobility, which is defined as the drift velocity v divided by the electric field F (eq. 6).

$$\mu = \frac{v}{F} \quad (6)$$

Here, the drift velocity does not necessarily need to be proportional to the electric field and, *de facto*, μ often does depend on the electric field, as will be further discussed in the SCLC section. The current density flowing through an organic semiconductor in any device is given by the number N of charges e that flow per unit time t and unit area A ,

$$j = \frac{eN}{At} = \frac{eN}{At} \frac{l}{l} = env = en\mu F \quad (7)$$

where $n = N/Al$ is the number density of charges, l is a unit length and $l/t = v$. After applying Ohm's law,

$$j = \sigma_c F \quad (8)$$

where σ_c is the conductivity of the sample, we can establish the following correlation between the mobility and conductivity.

$$\sigma_c = en\mu \quad (9)$$

The mechanism of charge carrier transport in organic semiconductors can be described by different models, such as band transport, hopping transport, polaronic transport and disorder controlled transport for individual transport regimes. Detailed information discussing those can be found in literature.^[190]

1.2.1 Space Charge Limited Current (SCLC)

When charge carriers are injected into an organic semiconductor and the supply of charge carriers is not limited by injection, the current will eventually be limited by its own space charge which shields the electric field at the injection electrode. In a simple diode device comprising a semiconductor of thickness d sandwiched between two electrodes with an applied bias V , comparable to a capacitor, the capacitor charge per unit area is

$$q = CV = \epsilon_r \epsilon_0 \frac{V}{d} \quad (10)$$

If all capacitor charges migrate to the opposite electrode, the resulting current density is $J = q/\tau_{\text{transit}}$ with τ_{transit} being the time which the charge carriers need to pass through the thickness of the semiconductor film, i.e. the transit time is

$$\tau_{\text{transit}} = \frac{d}{\mu F} = \frac{d^2}{\mu V} \quad (11)$$

Assuming a spatially homogeneous electric field in the semiconductor, this leads to a maximum unipolar current that can flow through the device, given by

$$J = \epsilon_r \epsilon_0 \mu \frac{F^2}{d} \quad (12)$$

However, the electric field is not homogeneous within the semiconductor. Therefore, the simplified above expression turns out to be deviating from the correct expression, which is known as the Mott-Gurney equation (eq. 13).^[190-191]

$$J = \frac{9}{8} \epsilon_0 \epsilon_r \mu \frac{V^2}{L^3} \quad (13)$$

Here, ϵ_r is the relative permittivity of the material (~ 3.5), ϵ_0 the permittivity of vacuum, V the voltage across the active layer, and L the thickness of the polymer layer.

As mentioned above, the charge carrier mobility of organics is often dependent on the electrical field that is applied. This circumstance is described by the Poole-Frenkel relationship^[192]

$$\mu(F) = \mu_0 \exp\left(\gamma\sqrt{F}\right) \quad (14)$$

Here, μ_0 the charge carrier mobility at zero field, γ the field dependence parameter and F the average electric field across the active layer. In the Murgatroyd formula (eq. 15) two independent variables, namely the zero field mobility (μ_0) and the field dependence parameter (γ), are varied to fit a measured J - V curve. The usefulness of the Murgatroyd formula over the classical Mott-Gurney equation^[191] is that it is able to fit a broader range of I - V curves and also masks other effects, such as charge carrier-density dependent transport^[187] and trapping influence.^[193]

$$J = \frac{9}{8} \epsilon_r \epsilon_0 \mu_0 \exp\left(0.89\gamma\sqrt{F}\right) \frac{V^2}{L^3} \quad (15)$$

SCLC mobilities within this thesis are reported at a constant field which condenses the information of two independent parameters (μ_0 and γ) to a single parameter and allows a direct charge carrier mobility comparison across different materials.^[194]

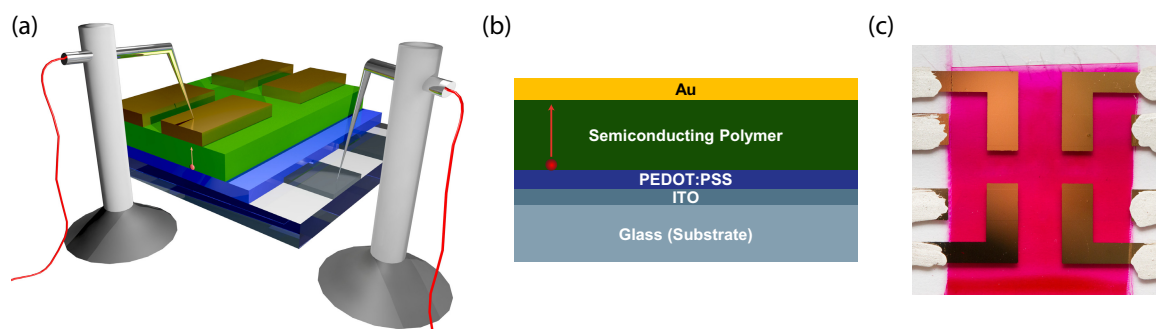


Figure 1-17. Space-charge carrier limited current measurement: (a) Schematic device architecture and set-up; (b) Layer stack for a hole-only SCLC device with charge carrier transport direction; (c) Top photograph of a glass substrate comprising four individual SCLC devices in a L-electrode configuration.

Practically, diode devices for measuring the unipolar space charge limited current comprise a semiconducting polymer layer in the range of several hundred nanometers which is sandwiched between an ohmic injection electrode and an exit electrode. Here, ohmic electrode means that the current flow is not limited by the charge injection at this electrode. A schematic illustration of such a device for hole-transport measurements is shown in Figure 1-17a. Determination of electron mobility requires adapted electrodes with work-functions fitting the frontier orbital energy levels (i.e. LUMO) of the semiconductor, rather than those of the HOMO for hole-transport. Figure 1-17b shows the layer stack for the diode with the charge carrier transport direction indicated by a red arrow. A real life device prepared by subsequent spin-coating of PEDOT:PSS and semiconducting polymer on a structured ITO substrate, followed by a top metal-electrode evaporation is shown in Figure 1-17c. One substrate comprises four individual diode devices for statistics. The electrodes are designed in a way that overlapping of top and bottom contact exactly defines the active area and thus avoids errors from misaligned contacts.

1.2.2 Organic Field Effect Transistors (OFET)

The generic structure and working principle of an OFET device differs from the diode geometry found in SCLC devices. A short summary is given here and a comprehensive review by Zaumseil can be found in literature.^[189]

OFET devices comprise three electrodes. The source and the drain electrode are separated by the organic semiconductor. The third electrode is the gate electrode, which is separated by an insulating dielectric layer from the semiconductor. An illustration of a bottom gate / bottom contact OFET device is shown in Figure 1-18. In principle, charge carriers can flow through the semiconductor from the source electrode to the drain electrode (Figure 1-18b). However, the length of that channel L is much larger than in SCLC devices, usually in the range of 10–100 μm . Therefore, charge carriers are only transported when a sufficiently high gate voltage V_g is applied in order to increase the charge carrier density. Thus in general, the charge carrier density in field effect transistors is higher than in the diode configuration and correspondingly the mean mobility is higher in OFET measurements.^[187-188]

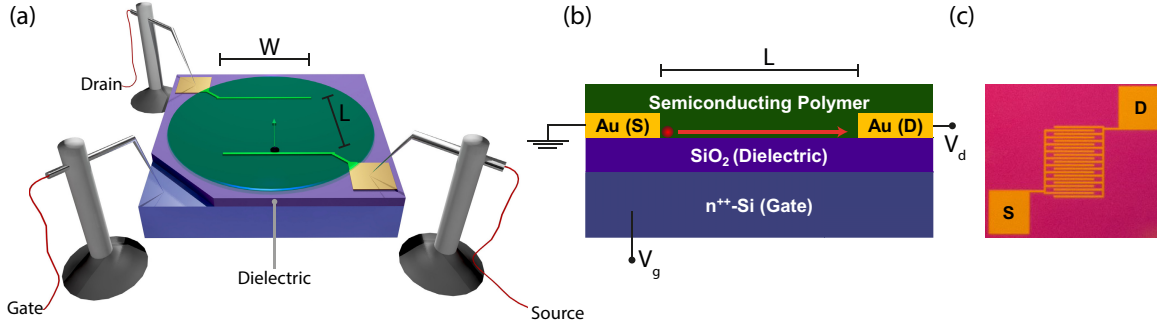


Figure 1-18. Organic field effect transistor device in a bottom gate / bottom contact configuration: (a) Schematic device architecture and experiment setup, illustrating the channel width (W) and channel length (L); (b) Side view of a layer stack with highly doped silicon as gate electrode and thermally grown silicon oxide as the dielectric, the red arrow indicates the charge carrier transport direction; (c) Photograph of an OFET device with an interdigitated electrode-structure and source (S) / drain (D) contact pads. Interdigitated electrodes increase the overall channel width and thus enhance the signal to noise ratio.

The working principle and different operation regimes of an organic field effect transistor are illustrated in Figure 1-19. When a gate voltage V_g higher than the threshold voltage V_{Th} is applied, charges accumulate at the dielectric-semiconductor interface due to the electrical field generated. The channel or accumulation layer is depicted in bright green. Depending on the gate voltage either electrons ($V_g > 0$ V) or holes ($V_g < 0$ V) will be induced. As the accumulation layer in an OFET is at most a few nanometers, charge transport and device operation are especially sensitive to properties of the semiconductor/dielectric interface,^[195] such as surface modification of the dielectric,^[189] or surface orientation and alignment of the semiconductor at the interface.^[196] Charges can now be transported from the source to the drain electrode by applying a drain voltage V_d . At small drain voltages, the transistor is operated in the linear regime (Figure 1-19a).

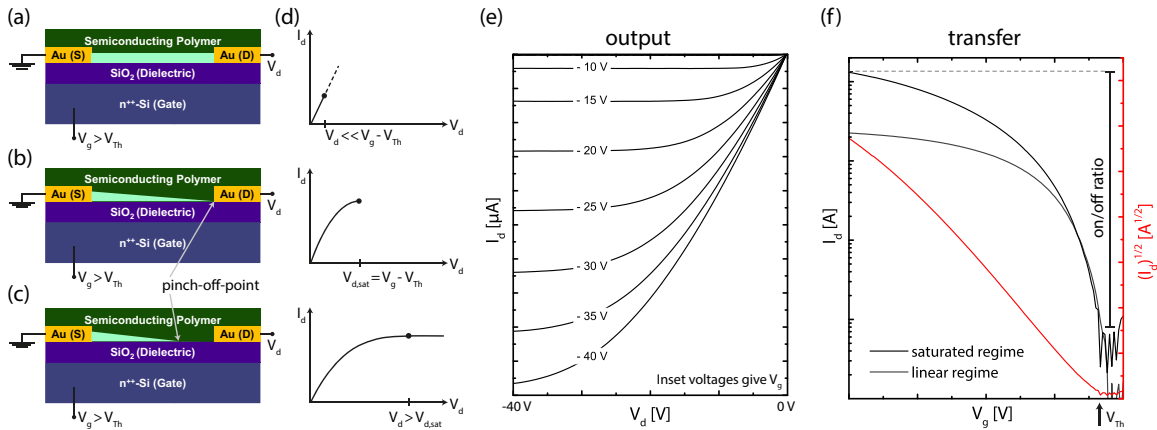


Figure 1-19. Operation regimes and characterisation of an organic field effect transistor (a-d adapted from Zaumseil et al).^[189] (a) Linear operation regime; (b) start of saturation regime at pinch-off-point; (c) saturation regime; (d) I - V characteristics for the corresponding operation regimes to the left; (e) output I - V characteristic at various gate voltages V_g ; (f) transfer I - V curve in linear and saturated regime (black curves on a log-plot, red curve on a square-root plot for mobility-evaluation using equation 16).^[197]

When V_d is increased the pinch-off-point is reached at which the distribution of induced charge carriers is characterized by a linear decrease from its maximum value at the source electrode to zero at the drain electrode (Figure 1-19b). A saturation current $I_{d,sat}$ flows across the channel at higher voltages V_d and the pinch-off-point shifts towards the source electrode generating a depletion zone close to the drain electrode. Figure 1-19e shows a typical output (i.e. drain current *versus* drain voltage) I - V curve for a p-channel device prepared in this thesis. The linear and saturated regimes are evident at low V_d and high V_d , respectively. A transfer I - V curve (i.e. drain current *versus* gate voltage) is shown in Figure 1-19f for operation in both linear and saturation regimes. The threshold voltage V_{Th} can be easily determined by the steep onset of current. Another important parameter for transistors is the on/off ratio $I_{on/off}$ which is the ratio of currents flowing in the on and off state, as illustrated in Figure 1-19f. The mobility can be calculated by equation 16 from the slope in the transfer $I_d^{0.5}$ - V_g -plot (red curve) when the transistor is operated in the saturation regime.^[189]

$$I_d \approx \frac{W}{2L} C_i \mu (V_g - V_{Th})^2 \quad (16)$$

A review of recent research and advances in the field of high-mobility organic semiconductor development for application in organic field effect transistors can be found in literature.^[198]

1.3 Solid state structure of semiconducting polymers in thin films

In addition to molecular properties such as absorption, frontier orbital energy levels and charge transport, the solid state structure of organic semiconductors has a crucial influence on the final device performance. The importance of supramolecular arrangement for functional devices is demonstrated throughout literature.^[199-205] The solid state structure of conjugated polymers is in the first place determined by intermolecular interactions, e.g. its crystallinity. When thin films of polymer semiconductors are prepared, the polymer chains typically exhibit distinct orientation with respect to the substrate.^[206-208] This orientation can either be edge-on with the solubilizing side chains oriented perpendicular to substrate or face-on with the planar π -face of the backbone being in plane with the substrate. Some polymers also show little to no preferential orientation while others show three dimensional crystallinity with order in all crystalline directions.^[209-210] The different main-orientations are illustrated in Figure 1-20a. Beyond the characteristic orientation, the solid state packing is defined by the stacking parameters, i.e. the spacing d in different crystalline directions. These directions are determined by lamellar (alkyl) stacking, π - π (face-to-face) stacking and backbone (repeating unit) stacking.

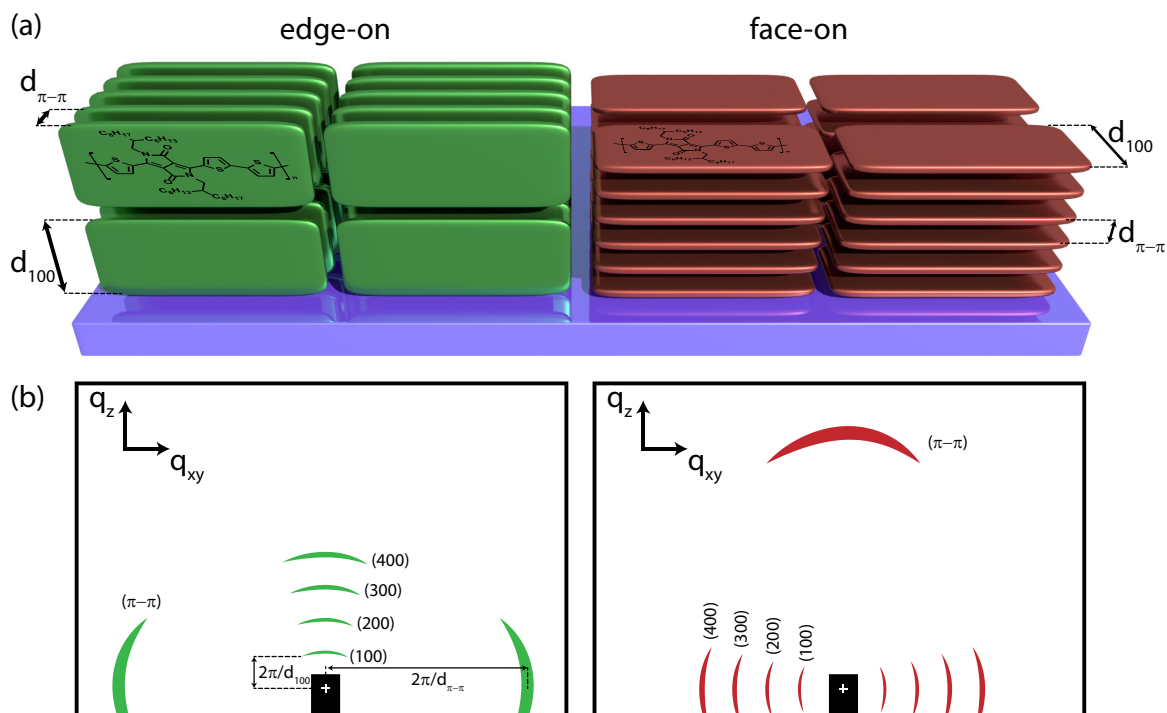


Figure 1-20. Orientation of liquid crystalline conjugated polymers in thin films with stacking parameters defining their solid state packing; (a) edge-on and face-on orientation; (b) GIWAXS scattering in corresponding directions.

The method of choice for elucidating the solid state packing of conjugated polymers in thin films is grazing incidence wide angle X-ray scattering (GIWAXS), which can be understood as wide angle X-ray scattering (WAXS) in a grazing incidence geometry.^[207] Representative scattering patterns for the thin film orientations discussed above are illustrated in Figure 1-20b and a typical experimental setup is schematically shown in Figure 1-21. A monochromatic X-ray beam is grazing the polymer sample at very low incident angles α (typically $\alpha < 1^\circ$) with respect to the sample surface and the scattered X-rays are detected in dependence of the scattering vectors in z (out-of-plane) and xy (in-plane) direction, respectively.

The obtained two-dimensional scatter patterns are reduced to one-dimensional datasets in the course of analysis, commonly for two polar angles $\chi = 0^\circ$ giving the out-of-plane scattering and for $\chi = 90^\circ$ to obtain the in-plane scattering. Occurrence of lamellar and π - π stacking peaks give rise to the orientation, i.e. in edge-on oriented films the lamellar stacking is observed out-of-plane and the π - π stacking is observed in-plane, whereas in face-on aligned samples the peaks appear in the opposite directions (Figure 1-20b).

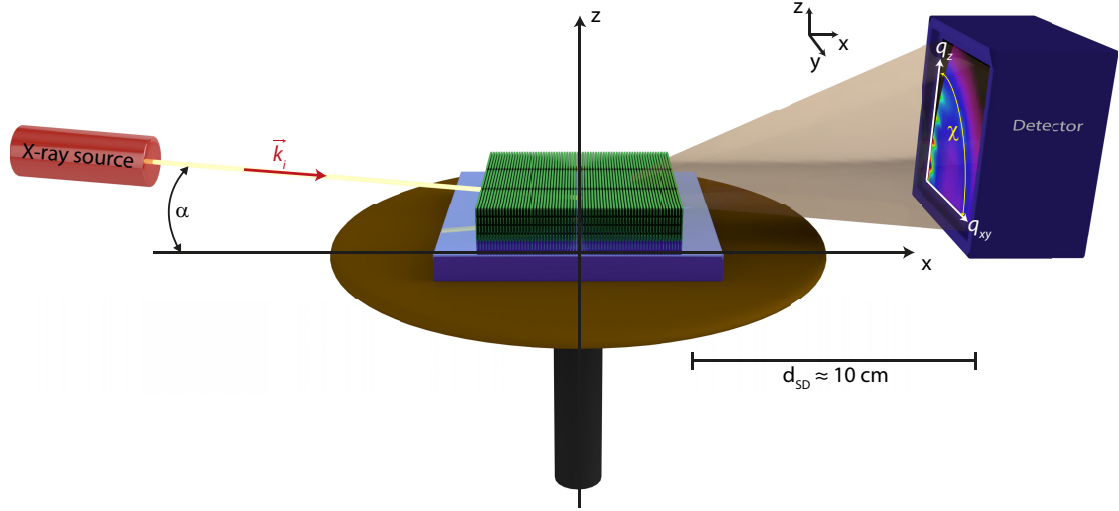


Figure 1-21. Schematic setup of a grazing incidence wide angle X-ray scattering (GIWAXS) experiment. A polymer thin film (green) on a silicon substrate is illuminated with a X-ray beam (commonly synchrotron radiation is used) that grazes the polymer film (green) at very low incident angles α . The scattering signal is detected by a 2D CCD detector in dependence of the scattering vectors in z and xy direction, q_z and q_{xy} , respectively. The polar angle χ denotes the direction of scattering from $\chi = 0^\circ$ (out-of-plane) to $\chi = 90^\circ$ (in-plane). The sample to detector distance d_{SD} is approximately 10 cm in wide angle scattering experiments.

The q values derived from the scattering signals give rise to spacing distances d , which are accompanied by the crystal coherence length ζ that is defined as follows.

$$\zeta = 2\pi / FWHM \quad (17)$$

Here $FWHM$ is the full width at half maximum of the respective scattering peak. The crystal coherence length gives information about the distance over which order is maintained. The concept of the coherence length is connected to the Scherrer equation, which connects the width of a peak to the crystal size.

In order to give a quantitative figure of the degree of orientation in a given sample, Herman's Orientation parameter S can be calculated.^[211] S is a measure of the degree of orientation of a given scattering reflection to a direction of interest and is defined as

$$S = \frac{1}{2} \left(3 \frac{\int_0^{\frac{\pi}{2}} I(\chi) \cos^2 \chi \sin \chi d\chi}{\int_0^{\frac{\pi}{2}} I(\chi) \sin \chi d\chi} - 1 \right) \quad (18)$$

where χ is the polar angle and I is the total scattering intensity of a peak. This results in S scaling from -0.5 when the scattering intensity of the peak is observed completely in-plane through 0, indicating no preferential scattering in-plane *vs* out-of-plane, to 1 when the scattering intensity of the peak is observed completely out-of-plane. In the case of alkyl lamella reflections, $S = 1$ indicates perfect edge-on stacking and $S = -0.5$ indicates perfect face-on stacking.

1.4 Diketopyrrolo[3,4-*c*]pyrroles

1.4.1 Discovery and early applications

A diketopyrrolo[3,4-*c*]pyrrolopyrrole (also referred to simply as diketopyrrolopyrrole or abbreviated as DPP) was first synthesized in small quantities 1974 by Farnum *et al* as the product of a failed Reformatsky reaction in the attempt to obtain 2-azetidinones.^[212] Since that first report, DPPs have come a long way and certainly became a hot topic as is obvious from the current publication numbers (see Figure 1-22).

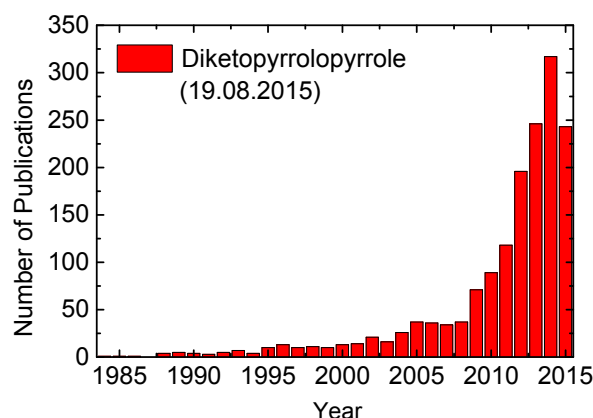
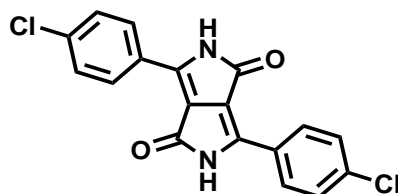


Figure 1-22. Literature hits for research topic "Diketopyrrolopyrrole" on SciFinder in August 2015.^[213]

The first reports about deliberate DPP synthesis and application are found from 1982 onwards in patents held by the Ciba-Geigy AG Switzerland, which recognized the suitability of DPPs as pigments.^[214-217] In particular the colorfast properties are highlighted,^[218] pigments from solid solutions,^[219] the development of new heterocyclic pigments,^[220] and generally DPP as novel class of heterocyclic pigments are reported in patent literature.^[221-222] These early patents also cover the so called C.I. Pigment Red 254 (see Figure 1-23) on which most of the Ferrari-red formulations are based. First reports of DPPs in scientific literature by Iqbal *et al* date back to 1988.^[223-224]



C.I. Pigment Red 254

Figure 1-23. Structure of an early reported DPP pigment that is most known for its application in Ferrari's automobile paints.

The DPP core is commonly synthesized following the succinate ester route, for which the mechanism is shown in Figure 1-24. Synthetic details as well as reactivity of the core towards

various reagents can be found in above mentioned patent literature as well as in many scientific contributions.^[225-227]

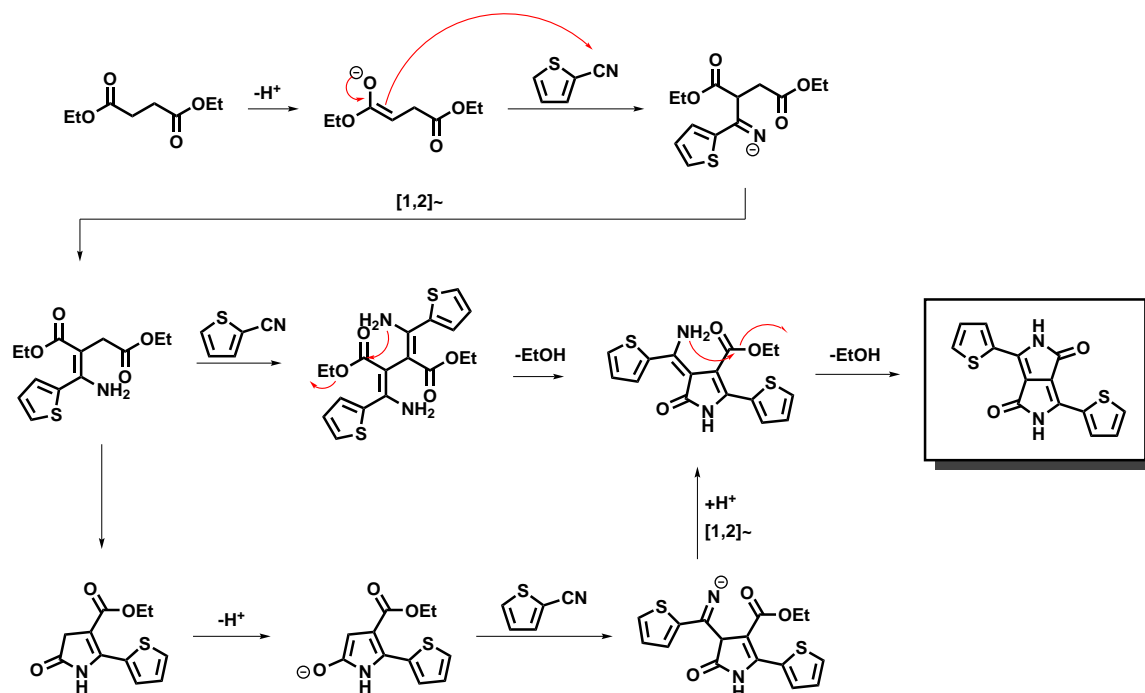


Figure 1-24. Proposed mechanism for the DPP core formation following the succinate route from diethyl succinate and thiophene-2-carbonitrile as starting materials.

1.4.2 Polymers and semiconducting materials based on DPPs

After the first report of an all-conjugated DPP polymer (PDPP) prepared by Stille polycondensation in 1993^[228] and another conjugated PDPP prepared by Suzuki coupling in 2000,^[229] the semiconducting nature of DPP compounds was ultimately recognized in 2005 when their application in electronic devices was patented by Tieke *et al.*^[230] Most of the academic research on PDPPs started around 2006 in the polymer research group of Bernd Tieke,^[231] where in particular the dissertation of Zhu deserves to be mentioned.^[232] These early PDPP semiconductors were mostly studied towards their emission properties that made them promising candidates for organic and polymer light emitting diodes (OLED/PLED), a polyfluorene-DPP copolymer being among the first examples.^[233] The synthetic methods employed for the preparation of these PDPP emitters involve Stille or Heck couplings,^[234] Suzuki cross-couplings^[235] as well as electropolymerization.^[232, 236-237]

The generic use of DPP polymers as organic semiconductors was then first patented by Turbiez *et al.* in 2008^[238] and high mobility organic field effect transistors have been published in the same year.^[239] Also the first use of PDPPs in solar cells was demonstrated in 2008 by Wienk *et al.*^[240]

Beyond PDPPs, also defined low molecular weight compounds based on DPP, hereafter referred to as small molecules, were used as organic semiconductors, first reported in 2008 by

the group of Thuc-Quyen Nguyen^[241] and at the same time applied as donor materials in solar cells.^[242] In 2009 this group demonstrated DPP based small molecule solar cells with nanoscale phase separation and high photovoltaic efficiencies with a report counting more than 500 citations, being the most cited DPP paper to date.^[28]

At this point, the group around René Janssen started to take interest in PDPPs and has since then contributed more to the progress in PDPP research than any other group. Diketopyrrolopyrroles have gained enormous interest in the design of semiconducting organic materials due to their extended absorption range,^[243] the excellent stability of the DPP core,^[218] their remarkable aggregation behavior^[244] and their superior performance in transistors,^[245-247] integrated circuits^[6] and solar cells.^[248] Over the past few years the performance boundaries of organic semiconductors were pushed over several orders of magnitude, not without the aid of DPPs. Charge carrier mobilities in organic field effect transistors for example have improved from about 0.1 cm²V⁻¹s⁻¹ in 2008^[239] to 12-18 cm²V⁻¹s⁻¹ for hole transport^[246, 249-250] and over 6 cm²V⁻¹s⁻¹ for electron transport.^[245, 251]

Likewise organic solar cell efficiencies have improved greatly over the last years and low molecular weight DPP compounds as well as DPP polymers have contributed significantly to this success.^[101-102] The careful optimization of the catalytic system for the polycondensations allowed to obtain polymers with very high molecular weights that exhibited improved power conversion efficiencies up to 8% in organic solar cells.^[252] Furthermore, side chains were optimized on different DPP systems in order to tailor material properties towards high performance in organic electronics.^[253-254] Within the DPP system, a huge variety of comonomers was screened and the obtained polymers were investigated in solar cells.^[255-256] DPPs proved to perform well not only as donors but also as acceptor materials,^[257] having a distinct advantage over fullerenes due to their good absorption properties. A blend of a thiazole-DPP with P3HT as the donor gave solar cells with efficiencies up to 2.6%, for example.^[243] Even solar cells comprising a DPP donor polymer and a complementary DPP acceptor polymer have been reported.^[248] The immense tunability of PDPPs also yielded ultra low bandgap polymers which can be combined with wide bandgap DPP polymers in tandem or multijunction solar cells in order to fully cover the solar irradiance spectrum.^[258]

1.5 Objective of this thesis

The aim of this thesis was the design and synthesis of novel semiconducting molecules and polymers based on DPP by systematic and rational change in chemical structure for application in organic electronics that are particularly suited for organic photovoltaics. The optical gap was, therefore, optimized to utilize as much of the solar irradiation as possible. Special attention was paid to the charge transport properties of these new materials in order to understand their suitability for different organic electronic devices rather than screening their performance in

solar cells in a hit-and-run approach. The charge carrier mobility is influenced by three major parameters which are individually addressed in this thesis (see Figure 1-25).

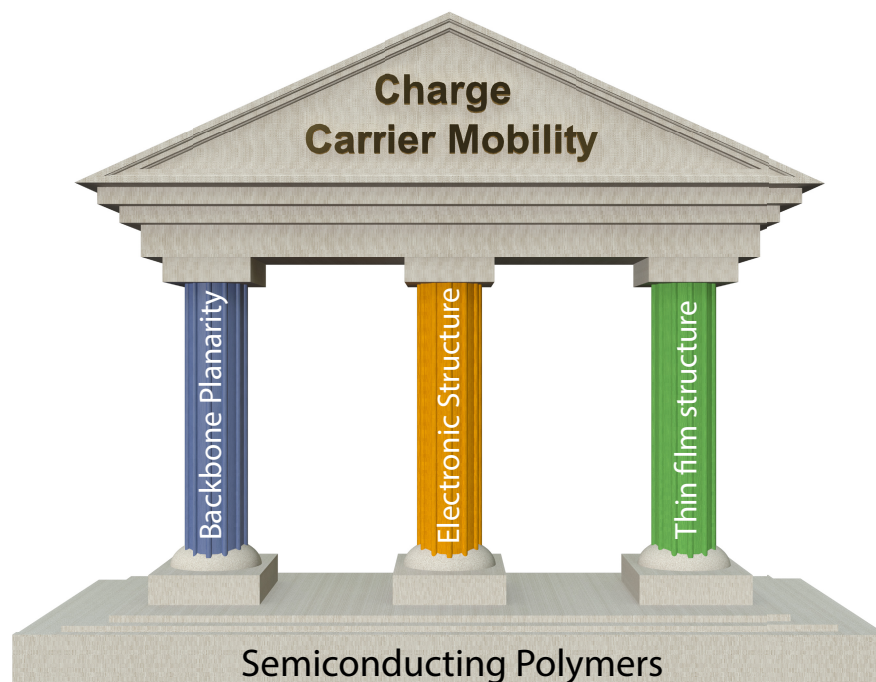


Figure 1-25. Parameters influencing the charge carrier mobility in organic semiconductors.

The first parameter is the backbone planarity of the all-conjugated polymer. High backbone planarity can be reached by minimizing all dihedral angles between the aromatic moieties along the backbone and it helps to improve charge transport as it increases π -delocalization and hence conjugation lengths. Furthermore, it facilitates smaller fundamental and optical gaps, enhancing its light harvesting capabilities. These issues are addressed by tuning different moieties in the backbone in order to gain control over all prevailing dihedral angles through steric demand and non-covalent, diffusive interactions. The second parameter that largely influences charge carrier transport is the electronic structure of the backbone. By attaching either electron withdrawing groups or electron donating groups, the frontier energy levels of the semiconductor can be tuned. Electron transport materials demand a high electron affinity which is accessible through increasing electron-deficiency in the backbone. Hole transport materials on the other hand demand a low ionisation potential that can be accessed by increasing electron-richness in the backbone. In order to obtain distinctive electron and hole transport materials as well as polymers with well-balanced ambipolar charge carrier transport, the influence of different electron withdrawing and donating groups is investigated. Finally, not only intrinsic material properties, but also the orientation and alignment of the polymer chains in the device have an impact on charge carrier transport. This alignment is determined by the relative orientation of the planar π -system to the substrate plane. In terms of charge transport two different device geometries are prevailing: organic field effect transistors exhibiting a horizontal charge transport within a very narrow channel along the

semiconductor/dielectric interface and diode geometry devices with vertical charge transport through the complete film thickness of several hundred nanometers. Depending on the device geometry, a different molecular polymer alignment may be beneficial. The objective here was to gain control over the mode of alignment as well as the degree of alignment and to correlate the supramolecular structure to the charge carrier mobilities in different device geometries. These objectives are possible only via a systematic structural variation.

References

- [1] "The Nobel Prize in Chemistry 2000". Nobelprize.org. Nobel Media AB 2014. Web. 13 Sep 2015. <http://www.nobelprize.org/nobel_prizes/chemistry/laureates/2000/>.
- [2] A. J. Heeger, *Angew. Chem. Int. Ed.* **2001**, *40*, 2591.
- [3] B. Geffroy, P. le Roy, C. Prat, *Polym. Int.* **2006**, *55*, 572.
- [4] F. So, J. Kido, P. Burrows, *MRS Bull.* **2011**, *33*, 663.
- [5] Y.-S. Tyan, *Journal of Photonics for Energy* **2011**, *1*, 011009.
- [6] K. J. Baeg, M. Caironi, Y. Y. Noh, *Adv. Mater.* **2013**, *25*, 4210.
- [7] M. A. Green, K. Emery, Y. Hishikawa, W. Warta, E. D. Dunlop, *Progress in Photovoltaics: Research and Applications* **2015**, *23*, 805.
- [8] F. C. Krebs, N. Espinosa, M. Hösel, R. R. Søndergaard, M. Jørgensen, *Adv. Mater.* **2014**, *26*, 29.
- [9] R. R. Søndergaard, M. Hösel, F. C. Krebs, *J. Polym. Sci., Part B: Polym. Phys.* **2013**, *51*, 16.
- [10] R. Søndergaard, M. Hösel, D. Angmo, T. T. Larsen-Olsen, F. C. Krebs, *Mater. Today* **2012**, *15*, 36.
- [11] M. Hösel, "Large-scale Roll-to-Roll Fabrication of Organic Solar Cells for Energy Production". PhD Thesis submitted to the *Department of Energy Conversion and Storage*, Technical University of Denmark, **2013**.
- [12] Photograph by Phillip Spears, 2006, CC License. <https://www.flickr.com/photos/rdecom/4146880795/>
- [13] Heliatek, <http://www.heliatek.com/de/presse/downloads>, 2015 (accessed 20.08.2015).
- [14] A. Hübler, B. Trnovec, T. Zillger, M. Ali, N. Wetzold, M. Mingebach, A. Wagenpfahl, C. Deibel, V. Dyakonov, *Advanced Energy Materials* **2011**, *1*, 1018.
- [15] T. R. Andersen, H. F. Dam, M. Hösel, M. Helgesen, J. E. Carlé, T. T. Larsen-Olsen, S. A. Gevorgyan, J. W. Andreasen, J. Adams, N. Li, F. Machui, G. D. Spyropoulos,

- T. Ameri, N. Lemaître, M. Legros, A. Scheel, D. Gaiser, K. Kreul, S. Berny, O. R. Lozman, S. Nordman, M. Välimäki, M. Vilkman, R. R. Søndergaard, M. Jørgensen, C. J. Brabec, F. C. Krebs, *Energy & Environmental Science* **2014**, 7, 2925.
- [16] H. Letheby, *J. Chem. Soc.* **1862**, 15, 161.
- [17] V. Meyer, *Berichte der deutschen chemischen Gesellschaft* **1883**, 16, 1465.
- [18] T. Yasui, *Bull. Chem. Soc. Jpn.* **1935**, 10, 305.
- [19] C. W. Tang, *Appl. Phys. Lett.* **1986**, 48, 183.
- [20] G. Li, R. Zhu, Y. Yang, *Nat Photon* **2012**, 6, 153.
- [21] J. D. Servaites, M. A. Ratner, T. J. Marks, *Energy Environ. Sci.* **2011**, 4, 4410.
- [22] A. Facchetti, *Chem. Mater.* **2011**, 23, 733.
- [23] A. Facchetti, *Mater. Today* **2013**, 16, 123.
- [24] Y. J. Hwang, B. A. Courtright, A. S. Ferreira, S. H. Tolbert, S. A. Jenekhe, *Adv. Mater.* **2015**.
- [25] B. C. Thompson, J. M. J. Fréchet, *Angew. Chem. Int. Ed.* **2008**, 47, 58.
- [26] J. E. Anthony, *Chem. Mater.* **2011**, 23, 583.
- [27] G. Dennler, M. C. Scharber, C. J. Brabec, *Adv. Mater.* **2009**, 21, 1323.
- [28] B. Walker, A. B. Tamayo, X.-D. Dang, P. Zalar, J. H. Seo, A. Garcia, M. Tantiwiwat, T.-Q. Nguyen, *Adv. Funct. Mater.* **2009**, 19, 3063.
- [29] B. Walker, C. Kim, T.-Q. Nguyen, *Chem. Mater.* **2011**, 23, 470.
- [30] J. Roncali, P. Leriche, P. Blanchard, *Adv. Mater.* **2014**, 26, 3821.
- [31] S. Günes, N. S. Sariciftci, *Inorg. Chim. Acta* **2008**, 361, 581.
- [32] S. D. Dimitrov, J. R. Durrant, *Chem. Mater.* **2014**, 26, 616.
- [33] M. Knupfer, *Applied Physics A: Materials Science & Processing* **2003**, 77, 623.
- [34] B. A. Gregg, M. C. Hanna, *J. Appl. Phys.* **2003**, 93, 3605.
- [35] J. J. M. Halls, K. Pichler, R. H. Friend, S. C. Moratti, A. B. Holmes, *Appl. Phys. Lett.* **1996**, 68, 3120.
- [36] D. E. Markov, E. Amsterdam, P. W. Blom, A. B. Sieval, J. C. Hummelen, *J. Phys. Chem. A* **2005**, 109, 5266.
- [37] D. E. Markov, C. Tanase, P. W. M. Blom, J. Wildeman, *Physical Review B* **2005**, 72.
- [38] T. M. Clarke, J. R. Durrant, *Chem. Rev.* **2010**, 110, 6736.

- [39] X. Y. Zhu, Q. Yang, M. Muntwiler, *Acc. Chem. Res.* **2009**, *42*, 1779.
- [40] Z.-K. Tan, K. Johnson, Y. Vaynzof, A. A. Bakulin, L.-L. Chua, P. K. H. Ho, R. H. Friend, *Adv. Mater.* **2013**, *25*, 4131.
- [41] K. Cnops, B. P. Rand, D. Cheyns, B. Verreert, M. A. Empl, P. Heremans, *Nat Commun* **2014**, *5*, 3406.
- [42] X. Xiao, K. Lee, S. R. Forrest, *Appl. Phys. Lett.* **2015**, *107*, 033901.
- [43] X. Xiao, K. Lee, S. R. Forrest, *Appl. Phys. Lett.* **2015**, *106*, 213301.
- [44] Heliatek, Press Release: "Neuer Weltrekord für organische Solarzellen: Heliatek behauptet sich mit 12 % Zelleffizienz als Technologieführer", **16.01.2013**, Dresden.
- [45] J. J. M. Halls, C. A. Walsh, N. Greenham, C. E. A. Marseglia, R. Friend, H. S. C. Moratti, A. Holmes, B, *Nature* **1995**, *376*, 498.
- [46] G. Yu, J. Gao, J. C. Hummelen, F. Wudl, A. J. Heeger, *Science* **1995**, *270*, 1789.
- [47] C. R. McNeill, *Energy Environ. Sci.* **2012**, *5*, 5653.
- [48] M. Jørgensen, K. Norrman, S. A. Gevorgyan, T. Tromholt, B. Andreasen, F. C. Krebs, *Adv. Mater.* **2012**, *24*, 580.
- [49] J. W. Rumer, I. McCulloch, *Mater. Today* **2015**.
- [50] J. E. Carle, B. Andreasen, T. Tromholt, M. V. Madsen, K. Norrman, M. Jorgensen, F. C. Krebs, *J. Mater. Chem.* **2012**, *22*, 24417.
- [51] G. Wantz, L. Derue, O. Dautel, A. Rivaton, P. Hudhomme, C. Dagron-Lartigau, *Polym. Int.* **2014**, *63*, 1346.
- [52] B. Liu, R. Q. Png, L. H. Zhao, L. L. Chua, R. H. Friend, P. K. Ho, *Nat Commun* **2012**, *3*, 1321.
- [53] R. Q. Png, P. J. Chia, J. C. Tang, B. Liu, S. Sivaramakrishnan, M. Zhou, S. H. Khong, H. S. Chan, J. H. Burroughes, L. L. Chua, R. H. Friend, P. K. Ho, *Nat Mater* **2010**, *9*, 152.
- [54] G. Griffini, J. D. Douglas, C. Piliago, T. W. Holcombe, S. Turri, J. M. Frechet, J. L. Mynar, *Adv. Mater.* **2011**, *23*, 1660.
- [55] M.-R. Chen, C.-C. Fan, T. R. Andersen, H. F. Dam, W.-F. Fu, Y.-Z. Lin, E. Bundgaard, F. C. Krebs, X.-W. Zhan, H.-Z. Chen, *Synth. Met.* **2014**, *195*, 299.
- [56] M. Sommer, S. Hüttner, M. Thelakkat, *J. Mater. Chem.* **2010**, *20*, 10788.
- [57] M. Sommer, S. Huettnner, M. Thelakkat, in *Complex Macromolecular Systems II*, Vol. 228 (Eds: A. H. E. Müller, H.-W. Schmidt), Springer Berlin / Heidelberg, **2010**, 123.

-
- [58] Y. Zhang, K. Tajima, K. Hirota, K. Hashimoto, *J. Am. Chem. Soc.* **2008**, *130*, 7812.
- [59] Y.-C. Tseng, S. B. Darling, *Polymers* **2010**, *2*, 470.
- [60] P. D. Topham, A. J. Parnell, R. C. Hiorns, *J. Polym. Sci., Part B: Polym. Phys.* **2011**, *49*, 1131.
- [61] J. T. Chen, E. L. Thomas, C. K. Ober, G. p. Mao, *Science* **1996**, *273*, 343.
- [62] F. S. Bates, *Annu. Rev. Phys. Chem.* **1990**, *41*, 525.
- [63] D. Gao, J. Hollinger, D. S. Seferos, *ACS Nano* **2012**, *6*, 7114.
- [64] R. Verduzco, I. Botiz, D. L. Pickel, S. M. Kilbey, K. Hong, E. Dimasi, S. B. Darling, *Macromolecules* **2011**, *44*, 530.
- [65] S. Huettnner, M. Sommer, J. Hodgkiss, P. Kohn, T. Thurn-Albrecht, R. H. Friend, U. Steiner, M. Thelakkat, *ACS Nano* **2011**, *5*, 3506.
- [66] V. Ho, B. W. Boudouris, B. L. McCulloch, C. G. Shuttle, M. Burkhardt, M. L. Chabinyc, R. A. Segalman, *J. Am. Chem. Soc.* **2011**, *133*, 9270.
- [67] M. Sommer, A. S. Lang, M. Thelakkat, *Angew. Chem. Int. Ed.* **2008**, *47*, 7901.
- [68] N. E. Jackson, B. M. Savoie, T. J. Marks, L. X. Chen, M. A. Ratner, *The Journal of Physical Chemistry Letters* **2015**, *6*, 77.
- [69] Y. Liu, J. Zhao, Z. Li, C. Mu, W. Ma, H. Hu, K. Jiang, H. Lin, H. Ade, H. Yan, *Nat Commun* **2014**, *5*, 5293.
- [70] H. Snaith, *Nature Photonics* **2012**, *6*, 337.
- [71] D. Veldman, S. C. J. Meskers, R. a. J. Janssen, *Adv. Funct. Mater.* **2009**, *19*, 1939.
- [72] J. L. Bredas, D. Beljonne, V. Coropceanu, J. Cornil, *Chem. Rev.* **2004**, *104*, 4971.
- [73] A. A. Bakulin, A. Rao, V. G. Pavelyev, P. H. M. van Loosdrecht, M. S. Pshenichnikov, D. Niedzialek, J. r. m. Cornil, D. Beljonne, R. H. Friend, *Science* **2012**, *335*, 1340.
- [74] C. J. Brabec, S. Gowrisanker, J. J. M. Halls, D. Laird, S. Jia, S. P. Williams, *Adv. Mater.* **2010**, *22*, 3839.
- [75] N. S. Sariciftci, L. Smilowitz, A. J. Heeger, F. Wudl, *Science* **1992**, *258*, 1474.
- [76] P. Sonar, J. P. Fong Lim, K. L. Chan, *Energy Environ. Sci.* **2011**, *4*, 1558.
- [77] Y. Zhong, M. T. Trinh, R. Chen, W. Wang, P. P. Khlyabich, B. Kumar, Q. Xu, C. Y. Nam, M. Y. Sfeir, C. Black, M. L. Steigerwald, Y. L. Loo, S. Xiao, F. Ng, X. Y. Zhu, C. Nuckolls, *J. Am. Chem. Soc.* **2014**, *136*, 15215.

- [78] P. E. Hartnett, A. Timalisina, H. S. Matte, N. Zhou, X. Guo, W. Zhao, A. Facchetti, R. P. Chang, M. C. Hersam, M. R. Wasielewski, T. J. Marks, *J. Am. Chem. Soc.* **2014**, *136*, 16345.
- [79] H. Yan, Z. Chen, Y. Zheng, C. Newman, J. R. Quinn, F. Dotz, M. Kastler, A. Facchetti, *Nature* **2009**, *457*, 679.
- [80] Z. Chen, Y. Zheng, H. Yan, A. Facchetti, *J. Am. Chem. Soc.* **2009**, *131*, 8.
- [81] R. Matsidik, H. Komber, A. Luzio, M. Caironi, M. Sommer, *J. Am. Chem. Soc.* **2015**, *137*, 6705.
- [82] R. D. McCullough, R. D. Lowe, M. Jayaraman, D. L. Anderson, *The Journal of Organic Chemistry* **1993**, *58*, 904.
- [83] P. Schilinsky, C. Waldauf, C. J. Brabec, *Appl. Phys. Lett.* **2002**, *81*, 3885.
- [84] T. A. Chen, R. D. Rieke, *J. Am. Chem. Soc.* **1992**, *114*, 10087.
- [85] C. Brabec, U. Scherf, V. Dyakonov, *Organic Photovoltaics*, Wiley-VCH, Weinheim **2014**.
- [86] A. Moliton, R. C. Hiorns, *Polym. Int.* **2004**, *53*, 1397.
- [87] L. Dou, J. You, J. Yang, C.-C. Chen, Y. He, S. Murase, T. Moriarty, K. Emery, G. Li, Y. Yang, *Nat Photon* **2012**, *6*, 180.
- [88] L. Lu, L. Yu, *Adv. Mater.* **2014**, *26*, 4413.
- [89] Z. He, C. Zhong, S. Su, M. Xu, H. Wu, Y. Cao, *Nature Photonics* **2012**, *6*, 593.
- [90] L. Huo, S. Zhang, X. Guo, F. Xu, Y. Li, J. Hou, *Angew. Chem. Int. Ed. Engl.* **2011**, *50*, 9697.
- [91] D. Mori, H. Benten, I. Okada, H. Ohkita, S. Ito, *Energy & Environmental Science* **2014**, *7*, 2939.
- [92] J. W. Jung, J. W. Jo, C. C. Chueh, F. Liu, W. H. Jo, T. P. Russell, A. K. Jen, *Adv. Mater.* **2015**, *27*, 3310.
- [93] M. Riede, C. Uhrich, J. Widmer, R. Timmreck, D. Wynands, G. Schwartz, W.-M. Gnehr, D. Hildebrandt, A. Weiss, J. Hwang, S. Sundarraj, P. Erk, M. Pfeiffer, K. Leo, *Adv. Funct. Mater.* **2011**, *21*, 3019.
- [94] J. Meiss, T. Menke, K. Leo, C. Uhrich, W.-M. Gnehr, S. Sonntag, M. Pfeiffer, M. Riede, *Appl. Phys. Lett.* **2011**, *99*, 043301.
- [95] Z.-G. Zhang, J. Wang, *J. Mater. Chem.* **2012**, *22*, 4178.
- [96] H. van Mullekom, *Materials Science and Engineering: R: Reports* **2001**, *32*, 1.

-
- [97] B. S. Rolczynski, J. M. Szarko, H. J. Son, Y. Liang, L. Yu, L. X. Chen, *J. Am. Chem. Soc.* **2012**, *134*, 4142.
- [98] A. Karolewski, A. Neubig, M. Thelakkat, S. Kummel, *Phys. Chem. Chem. Phys.* **2013**, *15*, 20016.
- [99] A. Neubig, M. Thelakkat, *Polymer* **2014**, *55*, 2621.
- [100] E. Bundgaard, F. C. Krebs, *Sol. Energy Mater. Sol. Cells* **2007**, *91*, 954.
- [101] D. Gendron, M. Leclerc, *Energy Environ. Sci.* **2011**, *4*, 1225.
- [102] S. Qu, H. Tian, *Chem. Commun.* **2012**, *48*, 3039.
- [103] G. L. Gibson, T. M. McCormick, D. S. Seferos, *J. Am. Chem. Soc.* **2012**, *134*, 539.
- [104] T. Xu, L. Yu, *Mater. Today* **2014**, *17*, 11.
- [105] J. D. Yuen, J. Fan, J. Seifter, B. Lim, R. Hufschmid, A. J. Heeger, F. Wudl, *J. Am. Chem. Soc.* **2011**, *133*, 20799.
- [106] P.-L. T. Boudreault, A. Najari, M. Leclerc, *Chem. Mater.* **2011**, *23*, 456.
- [107] M. C. Scharber, D. Mühlbacher, M. Koppe, P. Denk, C. Waldauf, A. J. Heeger, C. J. Brabec, *Adv. Mater.* **2006**, *18*, 789.
- [108] E. Bundgaard, F. Livi, O. Hagemann, J. E. Carlé, M. Helgesen, I. M. Heckler, N. K. Zawacka, D. Angmo, T. T. Larsen-Olsen, G. A. dos Reis Benatto, B. Roth, M. V. Madsen, M. R. Andersson, M. Jørgensen, R. R. Søndergaard, F. C. Krebs, *Advanced Energy Materials* **2015**, *5*, n/a.
- [109] J. Hachmann, R. Olivares-Amaya, S. Atahan-Evrenk, C. Amador-Bedolla, R. S. Sánchez-Carrera, A. Gold-Parker, L. Vogt, A. M. Brockway, A. n. Aspuru-Guzik, *The Journal of Physical Chemistry Letters* **2011**, *2*, 2241.
- [110] R. J. Waltman, J. Bargon, *Can. J. Chem.* **1986**, *64*, 76.
- [111] M. Zhou, J. Heinze, *Electrochim. Acta* **1999**, *44*, 1733.
- [112] G. Troch-Nagels, R. Winand, A. Weymeersch, L. Renard, *J. Appl. Electrochem.* **1992**, *22*, 756.
- [113] A. Lima, P. Schottland, S. Sadki, C. Chevrot, *Synth. Met.* **1998**, *93*, 33.
- [114] D. Sazou, C. Georgolios, *J. Electroanal. Chem.* **1997**, *429*, 81.
- [115] C. Liu, H. Zhang, W. Shi, A. Lei, *Chem. Rev.* **2011**, *111*, 1780.
- [116] J. K. Stille, *Angew. Chem.* **1986**, *98*, 504.
- [117] N. Miyaoura, A. Suzuki, *J. Chem. Soc., Chem. Commun.* **1979**, 866.

- [118] A. Suzuki, *Angew. Chem. Int. Ed.* **2011**, *50*, 6722.
- [119] T. Yamamoto, A. Morita, Y. Miyazaki, T. Maruyama, H. Wakayama, Z. H. Zhou, Y. Nakamura, T. Kanbara, S. Sasaki, K. Kubota, *Macromolecules* **1992**, *25*, 1214.
- [120] E. Negishi, *Acc. Chem. Res.* **1982**, *15*, 340.
- [121] K. Tamao, K. Sumitani, M. Kumada, *J. Am. Chem. Soc.* **1972**, *94*, 4374.
- [122] K. Tamao, S. Kodama, I. Nakajima, M. Kumada, A. Minato, K. Suzuki, *Tetrahedron* **1982**, *38*, 3347.
- [123] R. F. Heck, in *Organic Reactions*, John Wiley & Sons, Inc., **2004**.
- [124] L. Ackermann, R. Vicente, A. R. Kapdi, *Angew. Chem. Int. Ed. Engl.* **2009**, *48*, 9792.
- [125] D. Alberico, M. E. Scott, M. Lautens, *Chem. Rev.* **2007**, *107*, 174.
- [126] A. Facchetti, L. Vaccaro, A. Marrocchi, *Angew. Chem. Int. Ed.* **2012**, *51*, 3520.
- [127] D. J. Schipper, K. Fagnou, *Chem. Mater.* **2011**, *23*, 1594.
- [128] M. Giannerini, M. Fañanás-Mastral, B. L. Feringa, *Nat Chem* **2013**, *5*, 667.
- [129] "The Nobel Prize in Chemistry 2010". Nobelprize.org. Nobel Media AB 2014. Web. 16 Oct 2015. <http://www.nobelprize.org/nobel_prizes/chemistry/laureates/2010/>.
- [130] B. Carsten, F. He, H. J. Son, T. Xu, L. Yu, *Chem. Rev.* **2011**, *111*, 1493.
- [131] J. Sakamoto, M. Rehahn, G. Wegner, a. D. Schlüter, *Macromol. Rapid Commun.* **2009**, *30*, 653.
- [132] D. Milstein, J. K. Stille, *J. Am. Chem. Soc.* **1979**, *101*, 4981.
- [133] D. Milstein, J. K. Stille, *J. Am. Chem. Soc.* **1979**, *101*, 4992.
- [134] A. L. Casado, P. Espinet, *J. Am. Chem. Soc.* **1998**, *120*, 8978.
- [135] A. L. Casado, P. Espinet, A. M. Gallego, *J. Am. Chem. Soc.* **2000**, *122*, 11771.
- [136] A. L. Casado, P. Espinet, A. M. Gallego, J. M. Martínez-Ilarduya, *Chem. Commun.* **2001**, 339.
- [137] L. Kürti, B. Czako, *Strategic Applications of Named Reactions in Organic Synthesis*, Elsevier Academic Press, Amsterdam; Boston **2005**.
- [138] J. A. Casares, P. Espinet, G. Salas, *Chemistry - A European Journal* **2002**, *8*, 4843.
- [139] E. Shirakawa, T. Hiyama, *J. Organomet. Chem.* **1999**, *576*, 169.
- [140] G. B. Smith, G. C. Dezeny, D. L. Hughes, A. O. King, T. R. Verhoeven, *The Journal of Organic Chemistry* **1994**, *59*, 8151.
- [141] A. F. Littke, C. Dai, G. C. Fu, *J. Am. Chem. Soc.* **2000**, *122*, 4020.

-
- [142] N. Miyaoura, *J. Organomet. Chem.* **2002**, *653*, 54.
- [143] J. M. G. Cowie, V. Arrighi, *Polymers: Chemistry and Physics of Modern Materials*, CRC Press, Boca Raton, FL **2008**.
- [144] K. H. Hendriks, W. Li, G. H. Heintges, G. W. van Pruissen, M. M. Wienk, R. A. Janssen, *J. Am. Chem. Soc.* **2014**, *136*, 11128.
- [145] Y. Kim, S. Cook, J. Kirkpatrick, J. Nelson, J. R. Durrant, D. D. C. Bradley, M. Giles, M. Heeney, R. Hamilton, I. McCulloch, *J. Phys. Chem. C* **2007**, *111*, 8137.
- [146] R. Miyakoshi, A. Yokoyama, T. Yokozawa, *J. Polym. Sci. Part A: Polym. Chem.* **2008**, *46*, 753.
- [147] T. Yokozawa, A. Yokoyama, *Chem. Rev.* **2009**, *109*, 5595.
- [148] Z. J. Bryan, A. J. McNeil, *Macromolecules* **2013**, *46*, 8395.
- [149] M. C. Iovu, E. E. Sheina, R. R. Gil, R. D. McCullough, *Macromolecules* **2005**, *38*, 8649.
- [150] E. E. Sheina, J. Liu, M. C. Iovu, D. W. Laird, R. D. McCullough, *Macromolecules* **2004**, *37*, 3526.
- [151] R. Miyakoshi, A. Yokoyama, T. Yokozawa, *J. Am. Chem. Soc.* **2005**, *127*, 17542.
- [152] M. C. Stefan, A. E. Javier, I. Osaka, R. D. McCullough, *Macromolecules* **2009**, *42*, 30.
- [153] T. Yokozawa, H. Kohno, Y. Ohta, A. Yokoyama, *Macromolecules* **2010**, *43*, 7095.
- [154] T. Beryozkina, K. Boyko, N. Khanduyeva, V. Senkovskyy, M. Horecha, U. Oertel, F. Simon, M. Stamm, A. Kiriy, *Angew. Chem.* **2009**, *121*, 2733.
- [155] A. Yokoyama, H. Suzuki, Y. Kubota, K. Ohuchi, H. Higashimura, T. Yokozawa, *J. Am. Chem. Soc.* **2007**, *129*, 7236.
- [156] T. Beryozkina, V. Senkovskyy, E. Kaul, A. Kiriy, *Macromolecules* **2008**, *41*, 7817.
- [157] R. Tkachov, V. Senkovskyy, H. Komber, J.-U. Sommer, A. Kiriy, *J. Am. Chem. Soc.* **2010**, *132*, 7803.
- [158] A. Smeets, K. Van den Bergh, J. De Winter, P. Gerbaux, T. Verbiest, G. Koeckelberghs, *Macromolecules* **2009**, *42*, 7638.
- [159] N. Doubina, A. Ho, A. K. Y. Jen, C. K. Luscombe, *Macromolecules* **2009**, *42*, 7670.
- [160] H. A. Bronstein, C. K. Luscombe, *J. Am. Chem. Soc.* **2009**, *131*, 12894.
- [161] R. Miyakoshi, A. Yokoyama, T. Yokozawa, *Chem. Lett.* **2008**, *37*, 1022.
- [162] S. Wu, L. Bu, L. Huang, X. Yu, Y. Han, Y. Geng, F. Wang, *Polymer* **2009**, *50*, 6245.

- [163] P. Willot, S. Govaerts, G. Koeckelberghs, *Macromolecules* **2013**, *46*, 8888.
- [164] A. Yokoyama, A. Kato, R. Miyakoshi, T. Yokozawa, *Macromolecules* **2008**, *41*, 7271.
- [165] H. Komber, V. Senkovskyy, R. Tkachov, K. Johnson, A. Kiriy, W. T. S. Huck, M. Sommer, *Macromolecules* **2011**, *44*, 9164.
- [166] E. Elmalem, A. Kiriy, W. T. S. Huck, *Macromolecules* **2011**, *44*, 9057.
- [167] K. Neumann, C. Schwarz, A. Köhler, M. Thelakkat, *J. Phys. Chem. C* **2014**, *118*, 27.
- [168] N. E. Jackson, B. M. Savoie, K. L. Kohlstedt, M. Olvera de la Cruz, G. C. Schatz, L. X. Chen, M. A. Ratner, *J. Am. Chem. Soc.* **2013**, *135*, 10475.
- [169] H. J. Spencer, P. J. Skabara, M. Giles, I. McCulloch, S. J. Coles, M. B. Hursthouse, *J. Mater. Chem.* **2005**, *15*, 4783.
- [170] H. Do, A. Troisi, *Phys. Chem. Chem. Phys.* **2015**, in print.
- [171] H. G. Kim, B. Kang, H. Ko, J. Lee, J. Shin, K. Cho, *Chem. Mater.* **2015**, *27*, 829.
- [172] C. B. Nielsen, M. Turbiez, I. McCulloch, *Adv. Mater.* **2012**, *25*, 1859.
- [173] L. Dou, C.-C. Chen, K. Yoshimura, K. Ohya, W.-H. Chang, J. Gao, Y. Liu, E. Richard, Y. Yang, *Macromolecules* **2013**, *46*, 3384.
- [174] J. H. Park, E. H. Jung, J. W. Jung, W. H. Jo, *Adv. Mater.* **2013**, *25*, 2583.
- [175] J. W. Jo, S. Bae, F. Liu, T. P. Russell, W. H. Jo, *Adv. Funct. Mater.* **2015**, *25*, 120.
- [176] Z. Fei, M. Shahid, N. Yaacobi-Gross, S. Rossbauer, H. Zhong, S. E. Watkins, T. D. Anthopoulos, M. Heeney, *Chem. Commun.* **2012**, *48*, 11130.
- [177] J. W. Jo, J. W. Jung, H.-W. Wang, P. Kim, T. P. Russell, W. H. Jo, *Chem. Mater.* **2014**, *26*, 4214.
- [178] Z. Fei, P. Boufflet, S. Wood, J. Wade, J. Moriarty, E. Gann, E. L. Ratcliff, C. R. McNeill, H. Sirringhaus, J. S. Kim, M. Heeney, *J. Am. Chem. Soc.* **2015**, *137*, 6866.
- [179] T. Lei, X. Xia, J. Y. Wang, C. J. Liu, J. Pei, *J. Am. Chem. Soc.* **2014**, *136*, 2135.
- [180] P. M. Sonar, J. Chang, Z. Shi, J. Wu, J. Li, *J. Mater. Chem. C* **2015**, *3*, 2080.
- [181] D. Sainova, S. Janietz, U. Asawapirom, L. Romaner, E. Zojer, N. Koch, A. Vollmer, *Chem. Mater.* **2007**, *19*, 1472.
- [182] T. Lei, J. H. Dou, X. Y. Cao, J. Y. Wang, J. Pei, *J. Am. Chem. Soc.* **2013**, *135*, 12168.
- [183] C.-H. Chen, Y.-J. Cheng, C.-Y. Chang, C.-S. Hsu, *Macromolecules* **2011**, *44*, 8415.
- [184] Y.-J. Cheng, C.-H. Chen, Y.-S. Lin, C.-Y. Chang, C.-S. Hsu, *Chem. Mater.* **2011**, *23*, 5068.

-
- [185] Y. X. Xu, C. C. Chueh, H. L. Yip, F. Z. Ding, Y. X. Li, C. Z. Li, X. Li, W. C. Chen, A. K. Jen, *Adv. Mater.* **2012**, *24*, 6356.
- [186] C.-Y. Chang, Y.-J. Cheng, S.-H. Hung, J.-S. Wu, W.-S. Kao, C.-H. Lee, C.-S. Hsu, *Adv. Mater.* **2011**, *24*, 549.
- [187] C. Tanase, P. Blom, D. de Leeuw, *Physical Review B* **2004**, *70*, 193202.
- [188] C. Tanase, E. J. Meijer, P. W. M. Blom, D. M. de Leeuw, *Phys. Rev. Lett.* **2003**, *91*, 216601.
- [189] J. Zaumseil, H. Sirringhaus, *Chem. Rev.* **2007**, *107*, 1296.
- [190] A. Köhler, H. Bässler, *Electronic Processes in Organic Semiconductors, An Introduction*, Wiley-VCH Verlag GmbH & Co. KGaA, Weinheim **2015**.
- [191] N. F. Mott, R. W. Gurney, *Electronic Processes in Ionic Crystals*, The Clarendon Press: Oxford, UK, **1940**.
- [192] J. Frenkel, *Physical Review* **1938**, *54*, 647.
- [193] Z. Chiguvare, V. Dyakonov, *Physical Review B* **2004**, *70*, 235207.
- [194] J. C. Blakesley, F. A. Castro, W. Kylberg, G. F. A. Dibb, C. Arantes, R. Valaski, M. Cremona, J. S. Kim, J.-S. Kim, *Org. Electron.* **2014**, *15*, 1263.
- [195] L. L. Chua, J. Zaumseil, J. F. Chang, E. C. Ou, P. K. Ho, H. Sirringhaus, R. H. Friend, *Nature* **2005**, *434*, 194.
- [196] H. Sirringhaus, P. J. Brown, R. H. Friend, M. M. Nielsen, K. Bechgaard, B. M. W. Langeveld-Voss, A. J. H. Spiering, R. A. J. Janssen, E. W. Meijer, P. Herwig, D. M. de Leeuw, *Nature* **1999**, *401*, 685.
- [197] C. J. Mueller, C. R. Singh, M. Thelakkat, **2015**.
- [198] S. Holliday, J. E. Donaghey, I. McCulloch, *Chem. Mater.* **2014**, *26*, 647.
- [199] Z. B. Henson, K. Mullen, G. C. Bazan, *Nature Chemistry* **2012**, *4*, 699.
- [200] W. Chen, M. P. Nikiforov, S. B. Darling, *Energy Environ. Sci.* **2012**, *5*, 8045.
- [201] J. Rivnay, R. Steyrleuthner, L. H. Jimison, A. Casadei, Z. Chen, M. F. Toney, A. Facchetti, D. Neher, A. Salleo, *Macromolecules* **2011**, *44*, 5246.
- [202] H. Dong, X. Fu, J. Liu, Z. Wang, W. Hu, *Adv. Mater.* **2013**, *25*, 6158.
- [203] L. H. Jimison, M. F. Toney, I. McCulloch, M. Heeney, A. Salleo, *Adv. Mater.* **2009**, *21*, 1568.
- [204] A. M. Hiszpanski, Y.-L. Loo, *Energy Environ. Sci.* **2014**, *7*, 592.

- [205] I. McCulloch, M. Heeney, C. Bailey, K. Genevicius, I. Macdonald, M. Shkunov, D. Sparrowe, S. Tierney, R. Wagner, W. Zhang, M. L. Chabinye, R. J. Kline, M. D. McGehee, M. F. Toney, *Nat Mater* **2006**, *5*, 328.
- [206] M. A. Ruderer, P. Muller-Buschbaum, *Soft Matter* **2011**, *7*, 5482.
- [207] P. Muller-Buschbaum, *Adv. Mater.* **2014**, *26*, 7692.
- [208] P. M. Beaujuge, J. M. J. Fréchet, *J. Am. Chem. Soc.* **2011**, *133*, 20009.
- [209] Z. Zheng, K. H. Yim, M. S. Saifullah, M. E. Welland, R. H. Friend, J. S. Kim, W. T. Huck, *Nano Lett.* **2007**, *7*, 987.
- [210] L. Hartmann, K. Tremel, S. Uttiya, E. Crossland, S. Ludwigs, N. Kayunkid, C. Vergnat, M. Brinkmann, *Adv. Funct. Mater.* **2011**, *21*, 4047.
- [211] L. A. Perez, P. Zalar, L. Ying, K. Schmidt, M. F. Toney, T.-Q. Nguyen, G. C. Bazan, E. J. Kramer, *Macromolecules* **2014**, *47*, 1403.
- [212] D. G. Farnum, G. Mehta, G. G. I. Moore, F. P. Siegal, *Tetrahedron Lett.* **1974**, *15*, 2549.
- [213] SciFinder, Copyright by the American Chemical Society, <https://scifinder.cas.org>.
- [214] A. Iqbal, L. Cassar, *EP61426A1*, **1982**.
- [215] A. C. Rochat, L. Cassar, A. Iqbal, *9 4911*, **1983**.
- [216] L. Cassar, A. Iqbal, A. C. Rochat, *EP98808A2*, **1984**.
- [217] M. Jost, A. Iqbal, A. C. Rochat, *EP133156A2*, **1985**.
- [218] F. Baebler, *EP190999A2*, **1986**.
- [219] E. E. Jaffe, F. Baebler, *EP277914A2*, **1988**.
- [220] A. Iqbal, L. Cassar, A. C. Rochat, J. Pfenninger, O. Wallquist, *J. Coat. Technol.* **1988**, *60*, 37.
- [221] R. Kirchmayr, A. Iqbal, J. Pfenninger, A. Rochat, O. Wallquist, *Polym. Paint Colour J.* **1989**, *179*, 370.
- [222] R. Kirchmayr, A. Iqbal, J. Pfenninger, A. Rochat, O. Wallquist, *Polym. Paint Colour J.* **1989**, *179*, 457.
- [223] A. Iqbal, M. Jost, R. Kirchmayr, J. Pfenninger, A. Rochat, O. Wallquist, *Bull. Soc. Chim. Belg.* **1988**, *97*, 615.
- [224] Z. Hao, A. Iqbal, *Chem. Soc. Rev.* **1997**, *26*, 203.
- [225] C. J. H. Morton, R. Gilmour, D. M. Smith, P. Lightfoot, A. M. Z. Slawin, E. J. MacLean, *Tetrahedron* **2002**, *58*, 5547.

-
- [226] C. J. H. Morton, R. L. Riggs, D. M. Smith, N. J. Westwood, P. Lightfoot, A. M. Z. Slawin, *Tetrahedron* **2005**, *61*, 727.
- [227] R. L. Riggs, C. J. H. Morton, A. M. Z. Slawin, D. M. Smith, N. J. Westwood, W. S. D. Austen, K. E. Stuart, *Tetrahedron* **2005**, *61*, 11230.
- [228] W. K. Chan, Y. Chen, Z. Peng, L. Yu, *J. Am. Chem. Soc.* **1993**, *115*, 11735.
- [229] T. Beyerlein, B. Tieke, *Macromol. Rapid Commun.* **2000**, *21*, 182.
- [230] I. Heim, B. Tieke, R. Lenz, B. Schmidhalter, A. R. Rabindranath, M. Dueggeli, *WO2005049695A1*, **2005**.
- [231] B. Tieke, A. R. Rabindranath, K. Zhang, Y. Zhu, *Beilstein J Org Chem* **2010**, *6*, 830.
- [232] Y. Zhu, "New Diketopyrrolopyrrole(DPP)-Based Conjugated Polymers Prepared upon Palladium Catalyzed Polymerization and Electropolymerization Reactions". submitted to the Universität Köln, **2006**.
- [233] D. Cao, Q. Liu, W. Zeng, S. Han, J. Peng, S. Liu, *Macromolecules* **2006**, *39*, 8347.
- [234] Y. Zhu, I. Heim, B. Tieke, *Macromol. Chem. Phys.* **2006**, *207*, 2206.
- [235] A. R. Rabindranath, Y. Zhu, I. Heim, B. Tieke, *Macromolecules* **2006**, *39*, 8250.
- [236] Y. Zhu, K. Zhang, B. Tieke, *Macromol. Chem. Phys.* **2009**, *210*, 431.
- [237] K. Zhang, B. Tieke, J. C. Forgie, P. J. Skabara, *Macromol. Rapid Commun.* **2009**, *30*, 1834.
- [238] M. G. R. Turbiez, R. A. J. Janssen, e. al, *WO2008/000664A1*, **2008**.
- [239] L. Bürgi, M. Turbiez, R. Pfeiffer, F. Bienewald, H. J. Kirner, C. Winnewisser, *Adv. Mater.* **2008**, *20*, 2217.
- [240] M. M. Wienk, M. Turbiez, J. Gilot, R. A. J. Janssen, *Adv. Mater.* **2008**, *20*, 2556.
- [241] A. B. Tamayo, M. Tantiwivat, B. Walker, T.-Q. Nguyen, *J. Phys. Chem. C* **2008**, *112*, 15543.
- [242] A. B. Tamayo, B. Walker, T.-Q. Nguyen, *J. Phys. Chem. C* **2008**, *112*, 11545.
- [243] W. Li, Y. An, M. M. Wienk, R. A. J. Janssen, *J. Mater. Chem. A* **2015**.
- [244] X. Zhang, L. J. Richter, D. M. DeLongchamp, R. J. Kline, M. R. Hammond, I. McCulloch, M. Heeney, R. S. Ashraf, J. N. Smith, T. D. Anthopoulos, B. Schroeder, Y. H. Geerts, D. A. Fischer, M. F. Toney, *J. Am. Chem. Soc.* **2011**, *133*, 15073.
- [245] H. J. Yun, S. J. Kang, Y. Xu, S. O. Kim, Y. H. Kim, Y. Y. Noh, S. K. Kwon, *Adv. Mater.* **2014**, *26*, 7300.

- [246] I. Kang, H. J. Yun, D. S. Chung, S. K. Kwon, Y. H. Kim, *J. Am. Chem. Soc.* **2013**, *135*, 14896.
- [247] Z. Yi, S. Wang, Y. Liu, *Adv. Mater.* **2015**, *27*, 3589.
- [248] W. Li, W. S. Roelofs, M. Turbiez, M. M. Wienk, R. A. Janssen, *Adv. Mater.* **2014**, *26*, 3304.
- [249] A. R. Han, G. K. Dutta, J. Lee, H. R. Lee, S. M. Lee, H. Ahn, T. J. Shin, J. H. Oh, C. Yang, *Adv. Funct. Mater.* **2015**, *25*, 247.
- [250] J. Y. Back, H. Yu, I. Song, I. Kang, H. Ahn, T. J. Shin, S.-K. Kwon, J. H. Oh, Y.-H. Kim, *Chem. Mater.* **2015**, *27*, 1732.
- [251] B. Sun, W. Hong, Z. Yan, H. Aziz, Y. Li, *Adv. Mater.* **2014**, *26*, 2636.
- [252] K. H. Hendriks, G. H. Heintges, V. S. Gevaerts, M. M. Wienk, R. A. Janssen, *Angew. Chem. Int. Ed. Engl.* **2013**, *52*, 8341.
- [253] K. H. Hendriks, W. Li, M. M. Wienk, R. A. J. Janssen, *Advanced Energy Materials* **2013**, *3*, 674.
- [254] W. Li, K. H. Hendriks, A. Furlan, W. S. Roelofs, S. C. Meskers, M. M. Wienk, R. A. Janssen, *Adv. Mater.* **2014**, *26*, 1565.
- [255] W. Li, W. S. C. Roelofs, M. M. Wienk, R. A. J. Janssen, *J. Am. Chem. Soc.* **2012**, *134*, 13787.
- [256] W. Li, K. H. Hendriks, A. Furlan, M. M. Wienk, R. A. Janssen, *J. Am. Chem. Soc.* **2015**, *137*, 2231.
- [257] Y. Kim, C. E. Song, E.-J. Ko, D. Kim, S.-J. Moon, E. Lim, *RSC Adv.* **2014**, *5*, 4811.
- [258] W. Li, A. Furlan, K. H. Hendriks, M. M. Wienk, R. A. Janssen, *J. Am. Chem. Soc.* **2013**, *135*, 5529.

2 Overview of the Thesis

This thesis focusses on the design and development of new semiconducting polymers based on the structural core diketopyrrolo[3,4-*c*]pyrrole (DPP, see Figure 2-1) by systematic structural variation. These materials have recently gained huge interest due to their high photostability, high performance in various organic electronic devices, such as solar cells, transistors and integrated circuits. Herein, seven individual contributions are presented in the form of manuscripts. Six of them are published in peer-reviewed journals and one is prepared for submission.

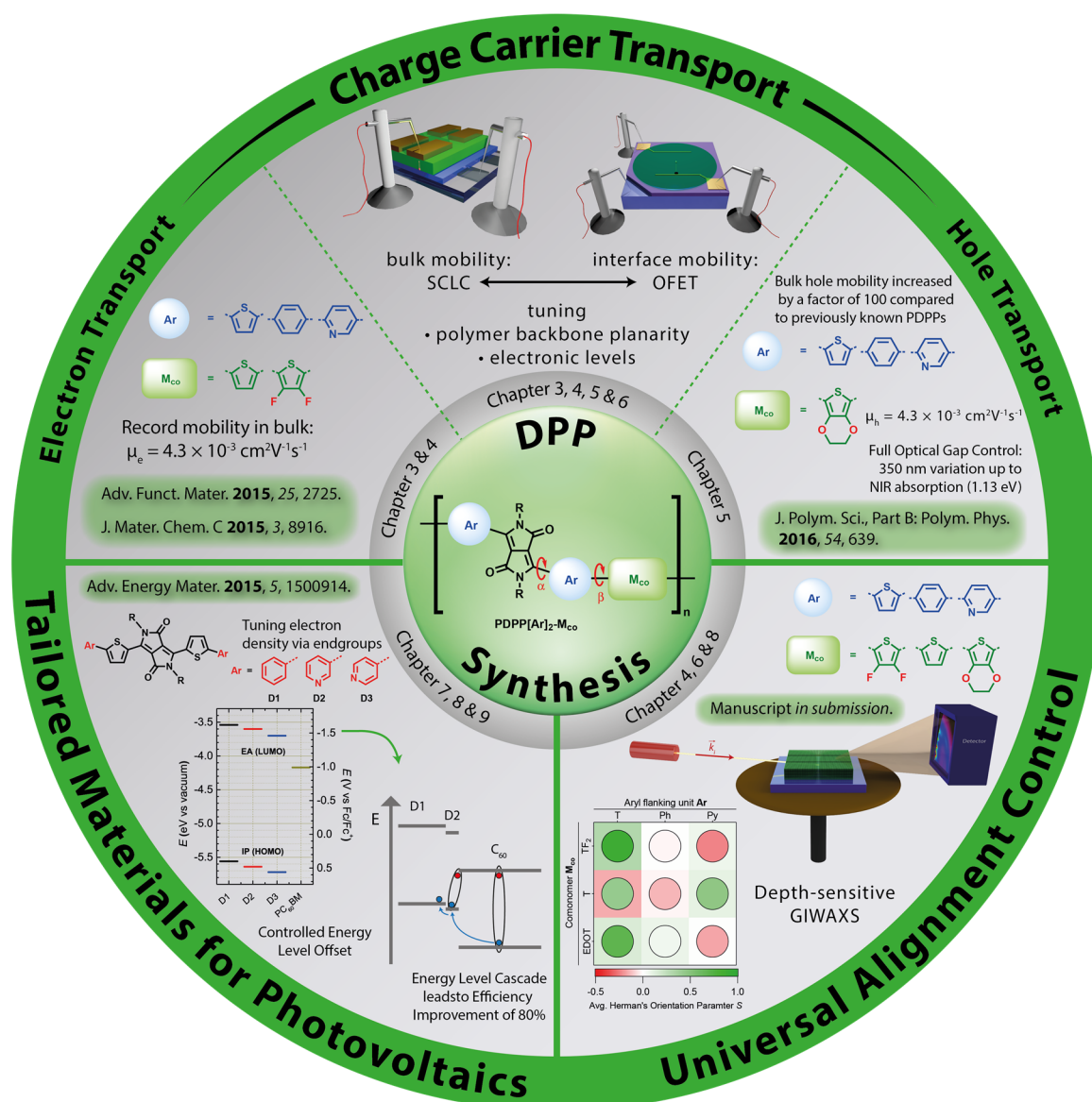


Figure 2-1. A variety of DPP materials, both polymeric as well as low molecular weight compounds, have systematically been designed and synthesized in order to suit specific demands in different devices.

Diketopyrrolo[3,4-*c*]pyrroles exhibit a bicyclic aromatic core which is flanked by two aromatic units (Ar). Alkyl sidechains (R) are added to improve solubility and two terminal bromine groups allow transition metal catalyzed cross-couplings with either mono-functional starting materials to give low molecular weight compounds (chapter 8) or with bi-functional comonomers (M_{co}) to obtain polymeric diketopyrrolopyrroles (PDPP, all other chapters). In this thesis dibromo-DPPs are copolymerized in palladium catalyzed cross-couplings with either bis(boronic acid esters) in Suzuki-Miyaura-polycondensations or with bistannylenes in Stille-polycondensations (see Figure 2-2).

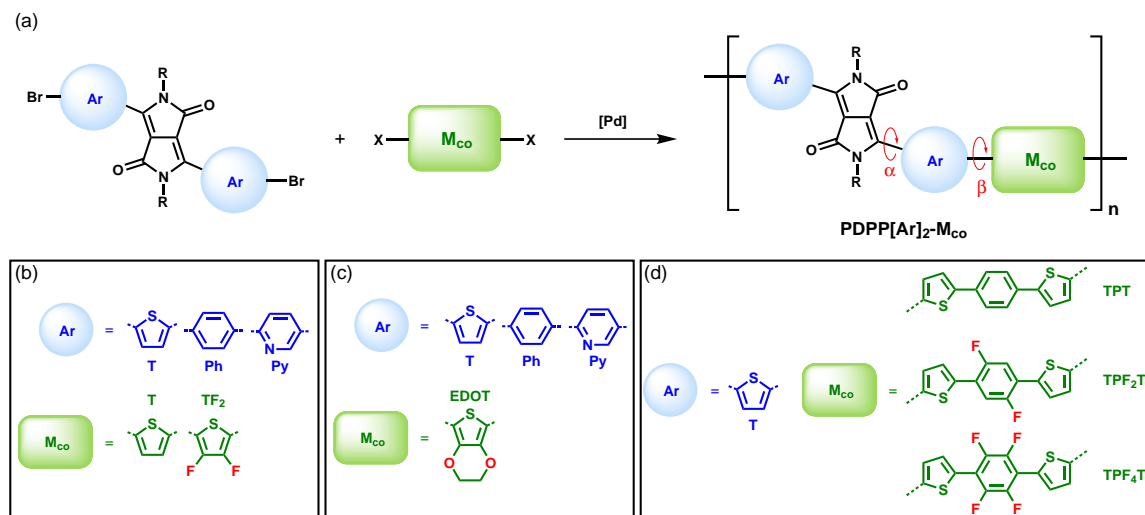


Figure 2-2. (a) Generic synthesis scheme for the copolymerization of a DPP monomer with a comonomer M_{co} to obtain PDPP[Ar]₂- M_{co} (Ar: aryl flanking unit, R: alkyl side chains, M_{co} : comonomer, X = -SnMe₃ for Stille-polycondensations, X = -B(OR)₂ for Suzuki-polycondensations). The two distinct dihedral angles α and β dictating the polymer backbone planarity are shown in the polymer structure; (b-d) Aryl flanking units Ar and comonomers M_{co} : Overview of the most important material sets covered in this thesis, each subfigure represents individual chapters.

The variety of DPP copolymers is named in the following way: The aryl flanking units (Ar) adjacent to the core are put in square brackets as [Ar] followed by the comonomer M_{co} divided by a dash to give the generic name PDPP[Ar]₂- M_{co} (see Figure 2-2). As polymer properties are never compared between compounds with different alkyl side chains (R), i.e. all polymers within the individual chapters have identical side chains, the R is omitted from the acronym for simplicity.

In the course of the thesis, three parameters influencing charge carrier mobility, i.e. polymer backbone planarity, electronic structure and thin film structure, are evaluated for the synthesized PDPPs and fundamental structure-property relationships are established. Finally, the performance of the materials in sandwich diodes, organic field effect transistors and solar cells is investigated.

This thesis can be roughly divided into three parts (see Figure 2-1). The first part is concerned with the systematical synthesis of PDPPs carrying varying aryl flanking units and fluorinated

or alkoxyated comonomers (Figure 2-2b-d) in order to obtain new semiconducting polymers with excellent electron or hole transport properties. The polymers are characterized in detail regarding their molecular weights, optical properties, electrochemical properties, solid state structure and most importantly their charge transport properties in space charge limited current devices and OFETs. To be more specific, electron transport polymers with electron withdrawing aryl flanking units and fluorinated comonomers (Figure 2-2b,c) are reported in the chapters 3 and 4, whereas the incorporation of electron rich EDOT monomers (Figure 2-2d) gave excellent hole transport polymers which are described in chapter 5.

The second part then focusses on the solid state structure of the synthesized hole and electron transport polymers in thin films. The depth-sensitive molecular alignment of the films is investigated under different conditions by angle-dependent grazing incidence wide angle scattering (GIWAXS) in the chapters 4 and 6.

Finally, the third part of the thesis covers the application of those DPP materials in organic solar cell devices. The synthesis, characterization and application of low molecular weight DPP compounds with a tailored energy level cascade in planar heterojunction solar cells is reported in chapter 7. A modular concept for the synthesis of crosslinkable low bandgap polymers, in particular different PDPP systems, is shown in chapter 8. A PDPP polymer as reference material has been used in a bulk heterojunction solar cell with PCBM as the acceptor to enable opto-electrical investigations of different electron extracting interface layers in combination with different cathodes in chapter 9.

2.1 Enhancing charge transport properties in PDPPs

As discussed in the introduction, three parameters have a large influence on the charge carrier mobility of a semiconducting polymer. These are the polymer backbone planarity, its electronic structure as well as the structure and alignment in thin films. In this part of the thesis the focus will be on the backbone planarity and the electronic structure.

2.1.1 Electron transport

When this work was started, almost all known DPP polymers exhibited hole transport properties and were used solely as donor materials in solar cells. Due to their high performance in solar cells and in transistors, it seemed tempting to design new materials based on the DPP core that provide good electron transport rather than hole transport properties. In order to induce electron transport with high charge carrier mobilities in this class of semiconducting polymers, two concepts have been pursued. First, to promote the electron transporting properties over the previously reported hole transport, electron withdrawing groups have been introduced to the polymer. Second, moieties that allow for non-covalent diffusive interactions between adjacent aryl units within the polymer backbone were introduced to obtain a highly

planar backbone with a strong inclination to aggregate. When keeping the DPP core as a constant motif in the polymer, two units can be systematically varied. These are the aryl flanking units (Ar) and the comonomers (M_{co}). In order to increase the electron deficiency, the aryl flanking unit was varied from the electron rich thiophene over phenyl to the electron deficient pyridine (see Figure 2-3).

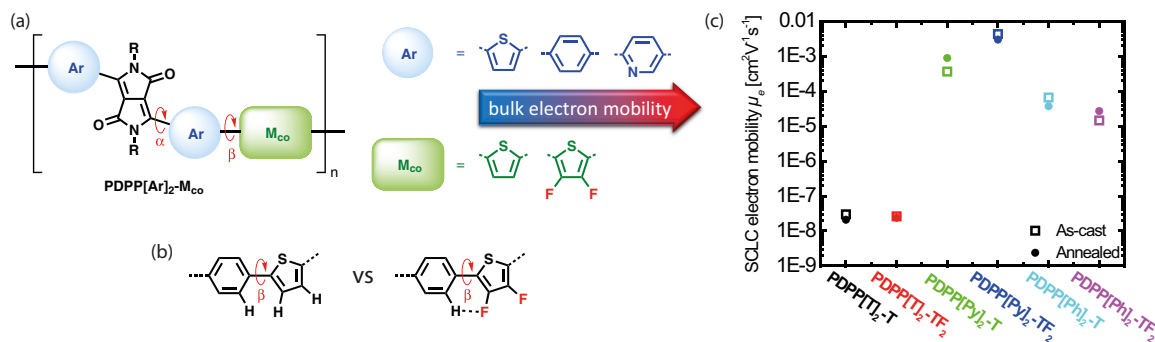


Figure 2-3. (a) Generic structure of the copolymers synthesized in chapter 3 with varying aryl flanking units Ar and comonomers M_{co} ; (b) Dihedral angle β between the comonomer and adjacent aryl flanking units with and without non-covalent diffusive H-F interactions; (c) Bulk electron mobility determined by SCLC.

Electron deficiency on the thiophene comonomer was increased by introduction of highly electronegative fluorine groups. These fluorine groups are not only contributing to an electron deficient backbone, but additionally provide non-covalent diffusive interactions (H-F) with hydrogen atoms from the adjacent aryl units. This allows to control and decrease the dihedral angle β as shown in Figure 2-3b. In a similar manner α can be controlled by carefully choosing the aryl flanking unit. The electron rich thiophene-DPPs usually show very small dihedral angles as seen in many structures derived from single crystal analysis. The phenyl-DPPs on the other hand exhibit a large dihedral twist of more than 20° and hence limited conjugation lengths in the resulting polymer chain. This twist represented by the dihedral angle α is mainly attributed to steric crowding as the keto group of the DPP core sterically interacts with the hydrogen atoms on the phenyl ring. Pyridine is therefore not only suitable in this system due to its inherent electron deficiency, but also because it lacks one hydrogen atom in the 2-position and therefore allows a co-planar polymer backbone as it avoids steric crowding. Indeed, the elegant synthetic strategy of combining pyridyl flanking units with difluorothiophene as the comonomer culminates in a record bulk electron mobility of $4.3 \times 10^{-3} \text{ cm}^2\text{V}^{-1}\text{s}^{-1}$, which is among the highest that have been reported for polymers. Hence, the mobility lies in the same range as the fullerene derivative PCBM that is commonly used as the acceptor material in solar cells. Due to the excellent bulk electron mobility this material is a promising acceptor candidate to be used in solar cells.

Apart from SCLC bulk mobilities, mobilities have also been investigated in organic field effect transistor devices. As the presented library of six polymers with varying aryl flanking units and comonomers (Figure 2-3a) exhibits a gradual change in electron deficiency in the polymer

backbone, the mode of charge transport in transistors can finely be tuned (see Figure 2-4). The electron rich PDPP[T]₂-T with thiophenes as flanking units as well as comonomer exclusively shows p-type behavior with excellent hole mobilities (OFET) around $0.6 \text{ cm}^2\text{V}^{-1}\text{s}^{-1}$. Upon fluorination of the comonomer in PDPP[T]₂-TF₂, electron transport is introduced and a highly ambipolar transistor is obtained. Upon further increase of the electron deficiency in the polymer by introduction of pyridine as the aryl flanking unit in PDPP[Py]₂-TF₂, the transistor is ultimately switched to exclusive n-type behavior, allowing only electron transport. Again excellent OFET electron mobilities have been achieved in the range of $0.2\text{-}0.6 \text{ cm}^2\text{V}^{-1}\text{s}^{-1}$.

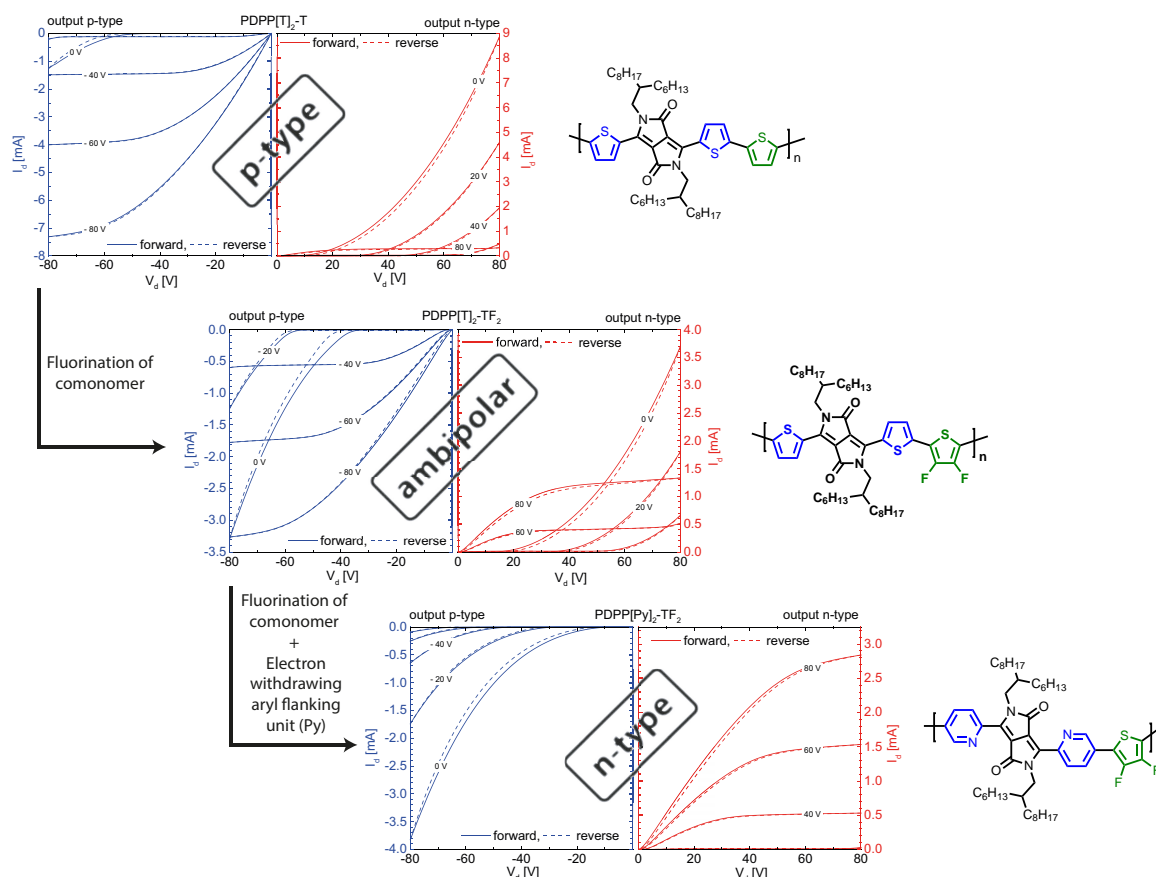


Figure 2-4. Output I - V characteristics for the OFETs fabricated from the polymers in chapter 3. The semiconducting nature can be tuned from exclusive p-type operation over ambipolarity to exclusive n-type operation by changing the aryl flanking unit and comonomer and thus controlling the electron deficiency in the backbone.

To get deeper insights how fluorination affects the charge transport in PDPPs, three different polymers with an π -extended backbone and a varying degree of fluorination were synthesized in chapter 4. The comonomer consists of a thiophene-(n -fluoro)phenyl-thiophene (TPF_{*n*}T) moiety ($n = 0,2,4$) without any alkyl substituents in order to allow for efficient aggregation and hence high mobilities (see Figure 2-5). The polymers have closely been studied regarding their optical properties, their electrochemistry and their solid state packing. Finally, the charge transport is studied in OFET devices. When the non-fluorinated TPT is used as a comonomer to obtain the polymer PDPP[T]₂-TPT, an exclusive p-type behavior can be observed. Again,

upon fluorination the material starts to show ambipolarity. This effect increases with the degree of fluorination. The output I - V characteristics are shown for the nonfluorinated polymer as well as for the tetrafluorinated derivative PDPP[T]₂-TPF₄T in Figure 2-5. The overall electron-deficiency in this polymer system was not enough to obtain n-type materials, which is reasonable when considering the amount of electron-rich thiophene units in the backbone. Nevertheless fluorination has been shown to be an effective method for increasing the electron transport properties in semiconducting polymers and introduce ambipolarity in otherwise exclusively p-type materials.

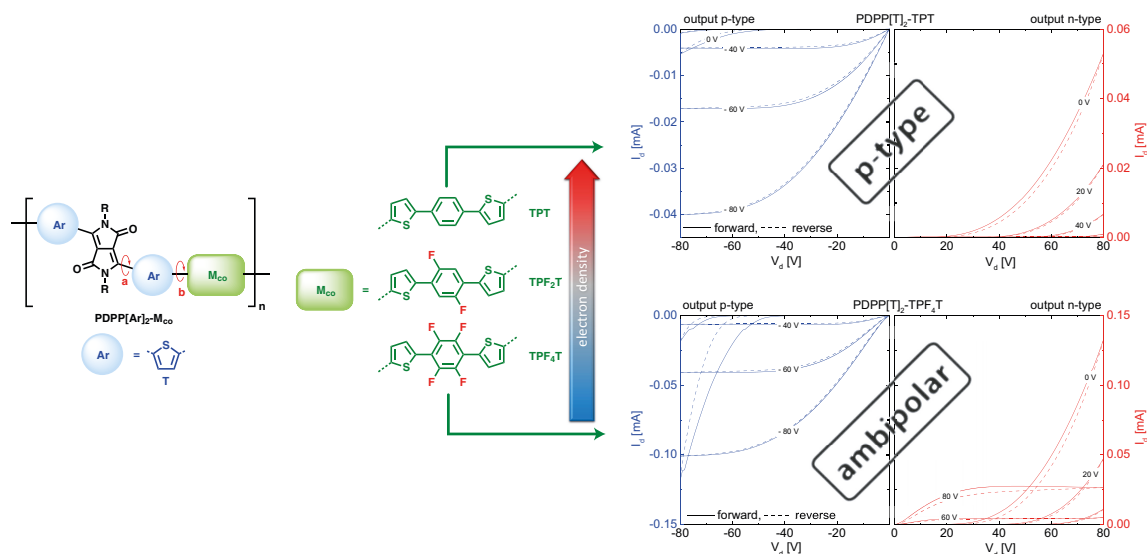


Figure 2-5. Structure of the π -extended backbone DPP copolymers as synthesized in chapter 4 with a varying degree of fluorination on the central phenyl-moiety of the TPT motif. OFET devices fabricated from the polymers can be tuned towards ambipolarity by increasing the degree of fluorination.

2.1.2 Hole transport

After successfully applying electron density tuning and controlling the polymer backbone planarity to obtain PDPPs with high electron mobilities, this approach was transferred to hole transport materials in order to access novel PDPPs with hitherto unprecedented hole mobilities for application as donor materials in solar cells. Again, the aryl flanking units on the DPP core were varied from thiophene over phenyl to pyridine. The comonomer thiophene however was this time substituted with 3,4-ethylenedioxythiophene (EDOT). The alkoxylation leads to a drastic increase in electron density in the backbone. Instead of H-F interaction in fluorinated PDPPs, EDOT offers two oxygen atoms that can contribute to non-covalent diffusive bondings with adjacent aryl units as shown in Figure 2-6a.

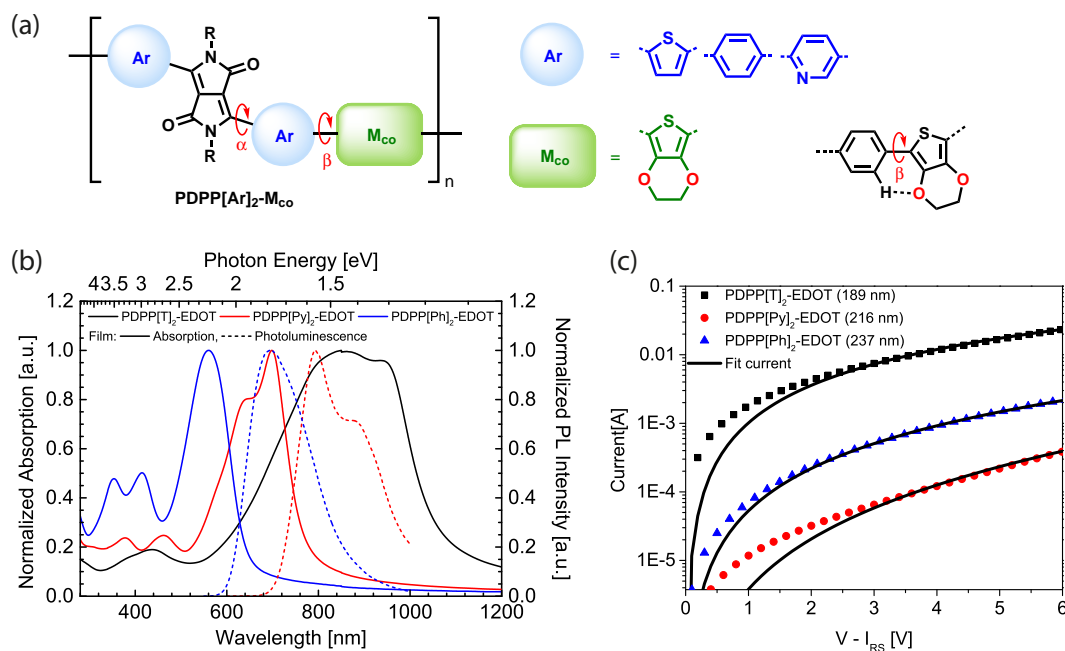


Figure 2-6. (a) Generic structure of the PDPP copolymers incorporating EDOT as the comonomer as synthesized in chapter 5. The dihedral angle β can be tuned by non-covalent diffusive H-O interactions between the comonomer and adjacent aryl flanking units; (b) Normalized absorption (solid lines) and photoluminescence (dashed lines) of thin films comparing the polymers with different aryl flanking units; (c) I - V characteristics for hole-only SCLC devices fabricated from the polymers.

Upon carefully characterizing the three polymers in Figure 2-7a the thiophene-flanked PDPP[T]₂-EDOT exhibits an outstandingly low optical gap with an absorption onset of 1100 nm in thin films corresponding to 1.13 eV which resembles the band gap of crystalline silicon (Figure 2-6b). The charge carrier mobility of the EDOT-copolymers was studied in both OFET devices and SCLC devices. The bulk hole mobility increased by one order of magnitude when going from pyridine to phenyl flanking units and by another order of magnitude when going from phenyl to thiophene flanking units (Figure 2-6c). This specific bulk value is of high importance when applying the materials in solar cell devices. In PDPP[T]₂-EDOT a bulk hole mobility of $2.9 \times 10^{-4} \text{ cm}^2\text{V}^{-1}\text{s}^{-1}$ could be obtained, which is higher by two orders of magnitude than previously reported SCLC mobilities in PDPPs. Considering the high bulk hole mobility of PDPP[T]₂-EDOT together with its extremely low optical gap of only 1.13 eV renders this polymer an exciting donor material to be applied in polymer solar cells.

2.2 Structural elucidation of polymer thin films

Complementing the results from the first part of the thesis, the solid state structure and alignment of the polymers in thin films is elucidated herein. The results shed further light on the charge transport behaviour observed in the previous chapters. Furthermore, it is shown that the mode of alignment (i.e. edge-on or face-on) on the one hand and the degree of

alignment on the other hand can be precisely tuned by controlling the nature of the aryl flanking units and comonomers.

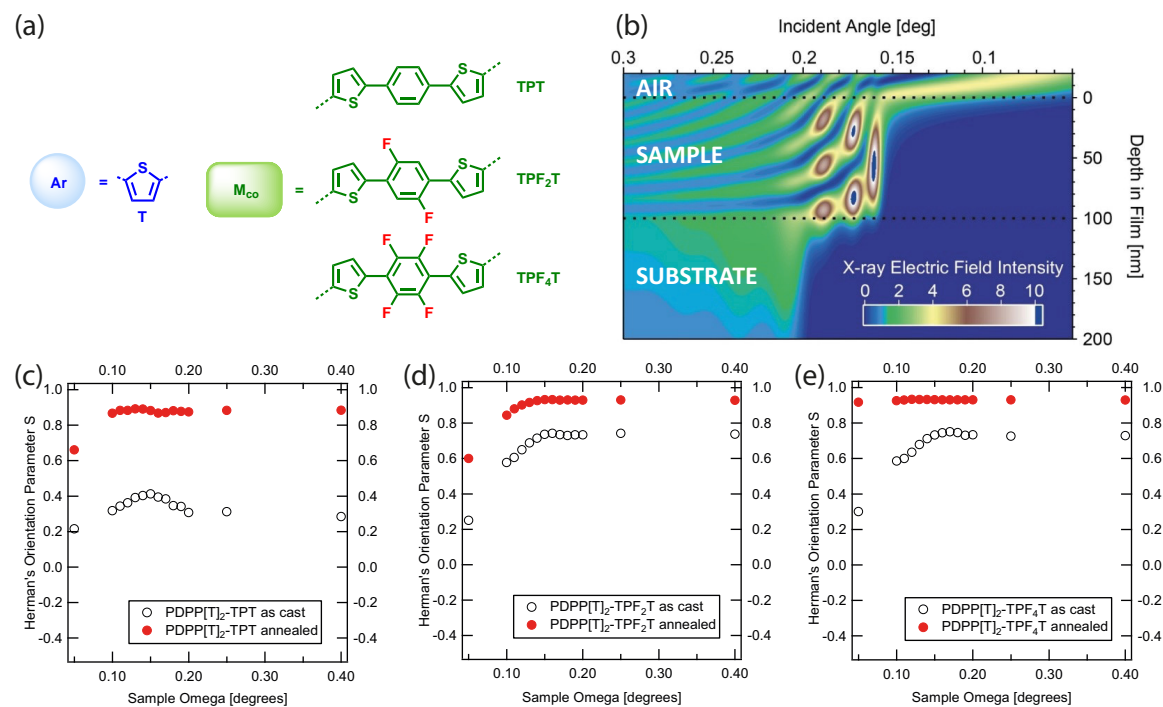


Figure 2-7. (a) Aryl flanking unit Ar and comonomers M_{co} for the three polymers under investigation (also see Figure 2-5) (b) X-ray Electric Field Intensity distribution over different thicknesses of the film at various X-ray incident angles; (c-e) Herman's Orientation Parameter S in dependence of the X-ray incident angle ω for the nonfluorinated PDPP[T]₂-TPT (c) and the n -fluorinated derivatives PDPP[T]₂-TPF₂T (d) and PDPP[T]₂-TPF₄T (e).

The π -extended backbone copolymers (Figure 2-5, Figure 2-7a) were also investigated regarding their solid state structure in thin films using depth-sensitive grazing incidence X-ray scattering (GIWAXS). Scattering patterns were recorded and evaluated for different X-ray incident angles, revealing information about the alignment in different depths of the film as the X-ray electrical field intensity (EFI) distribution varies when this angle is varied (see Figure 2-7b), i.e. scattering at incident angles below the critical angle exclusively originates from the upper ~ 10 nm of the film, while between the critical angle of the polymer film (~ 0.15 - 0.17°) and the critical angle of the silicon substrate ($\sim 0.2^\circ$) the location and intensity of scattering originates from deeper regions within the film (up to 100 nm). Finally, above the critical angle of the substrate, the EFI becomes much more even throughout the entire system, averaging out to an intensity of 1 at higher angles. Herman's Orientation Parameter S was then calculated for different incident angles as a measure for the alignment of the polymers in thin film, where a value of -0.5 corresponds to exclusive face-on alignment and a value of +1.0 corresponds to exclusive edge-on alignment. It was found that fluorination considerably improves the alignment towards an edge-on orientation in as-cast films compared to the nonfluorinated reference polymer. This edge-on alignment can generally be improved upon thermal annealing. From the incident angle-dependant S -Parameter plots however it became obvious, that

although the polymer shows an almost perfect edge-on alignment near the critical angle, the upper part of the film is not well aligned (Figure 2-7c,d). After tetrafluorination in PDPP[T]₂-TPF₄T however, a perfect edge-on alignment can be obtained throughout the complete film depth with an S-Parameter of ~ 1.0 at all incident angles (Figure 2-7e). A thorough investigation of the solid state packing in thin films for a library of 9 PDPPs (Figure 2-8a) is discussed in chapter 6. The polymers vary in their aryl flanking unit of the DPP core as well as the comonomer and have been introduced in section 2.1 regarding synthesis, chemical, physical and electronic characterization. The intrinsic parameters of semiconducting polymers such as the energy levels of the frontier molecular orbitals, the optical gap, extended optical absorption and emission as well as viscosity and solubility can be readily tuned by tailoring the molecular structure. Solid state packing, however, is mostly out of control and cannot even be predicted for most low-bandgap systems. It is shown here, how a comprehensive and universal control can be gained over both the mode and degree of alignment in thin film: The mode of alignment can be controlled by varying the aryl flanking unit of the DPP core and it is possible to even lock-in and increase the degree of the particular alignment by introducing moieties for diffusive non-covalent interactions in the monomers. The overall alignment averaged over all depths of the film is shown in Figure 2-8b as *S* parameter, where the square backgrounds in the matrix visualize the as-cast films and the filled circles represent the films after annealing. Again -0.5 (red) stands for face-on alignment whereas +1.0 (green) is related to edge-on alignment. The phenyl-flanked PDPPs show little to no alignment whereas the thiophene-flanked polymers show almost exclusive edge-on alignment, in particular after annealing. This alignment can be driven to perfection by the introduction of either alkoxy- or fluorine-groups that allow for diffusive non-covalent interaction with adjacent aryl rings along the polymer backbone. The same trend can be observed for the pyridine-flanked PDPPs, however here the alignment is switched to face-on. Again, after annealing especially the polymers with additional moieties for diffusive interactions show a good control over the alignment. The crystalline spacing in alkyl (lamellar) and π - π direction is compared in Figure 2-8c. The very small lamellar spacing of the phenyl flanked PDPPs is indicating a non-planar backbone structure due to the large dihedral twist in the sterically crowded DPP core. In contrast, both the thiophene-flanked PDPP[T]₂ and the pyridine-flanked PDPP[Py]₂ system show a largely increased lamellar spacing which points towards a planar and rigid polymer backbone. The same trend can be observed in the π - π stacking with the difference that the trend is inverted: The small π - π stacking distances in the PDPP[T]₂ and PDPP[Py]₂ polymers indicate aggregation and a tight face-to-face stacking with efficient π -orbital overlap. This structural characteristic is crucial for good charge transport as it allows interchain charge hopping and thus explains the high charge carrier mobilities found in these materials in the first part of the thesis. In contrast, the phenyl-flanked PDPPs exhibit rather large π - π distances that are again caused by the large dihedral twist in this polymer system, explaining the consistently low charge carrier mobilities found in PDPP[Ph]₂ polymers. The impact of the individual comonomers on π - π stacking is best shown

in the planar PDPP[T]₂ system: The already small spacing can be further decreased upon introduction of moieties allowing for diffusive non-covalent interactions, e.g. by fluorination in TF₂ or by alkoxylation in EDOT.

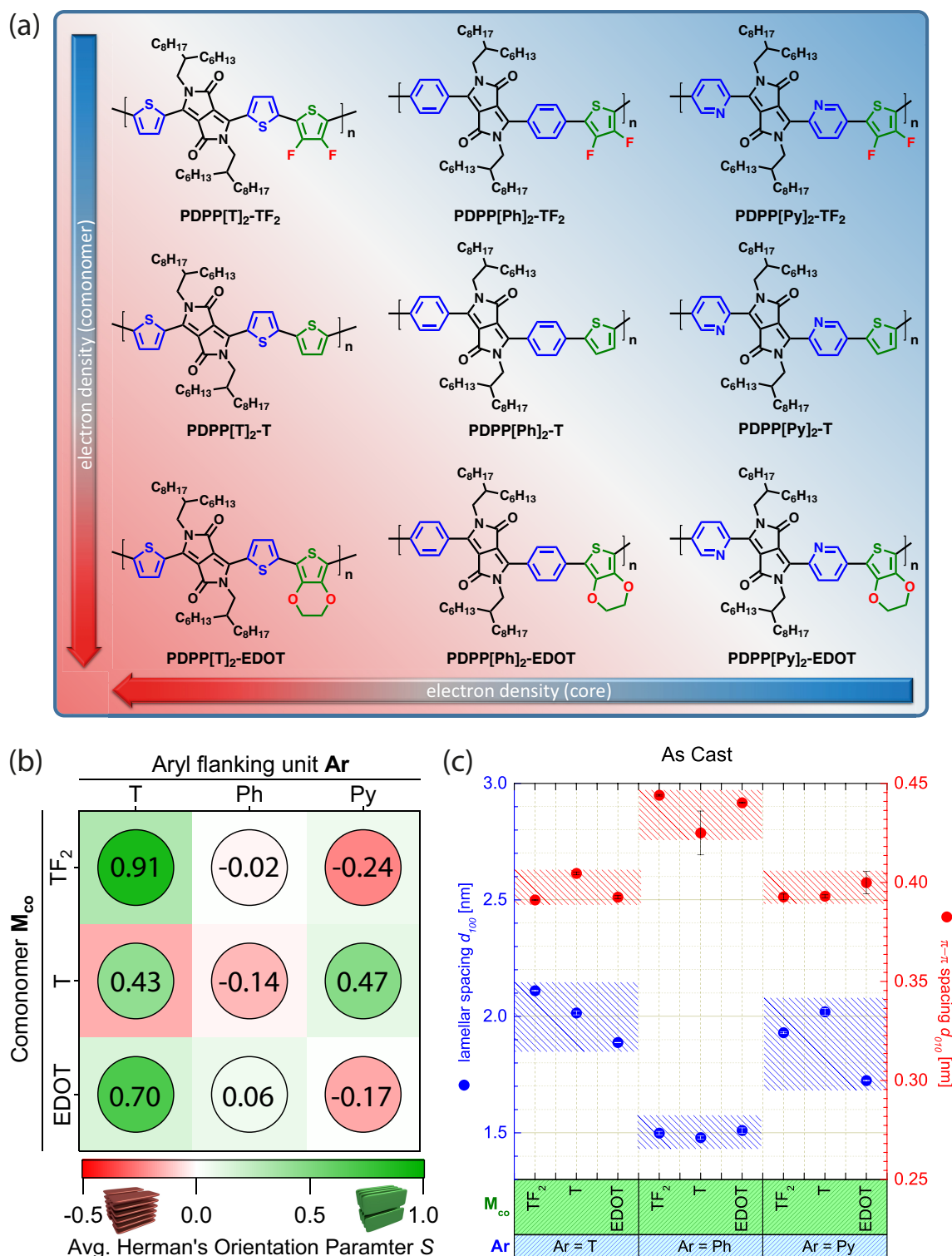


Figure 2-8. (a) PDPP polymer library with variation of the aryl flanking unit (right to left) and the comonomer (top to bottom); (b) Herman's Orientation Parameter S for thin films prepared from the 9 polymers as cast (square backgrounds) and after annealing (filled circles with numerical values); (c) first order lamellar stacking distances (blue) and π - π spacing (red) for the set of 9 polymers depending on aryl flanking unit and comonomer.

2.3 Tailored materials for photovoltaics

2.3.1 Energy level cascades in solar cells by tailoring small molecule donors

Low molecular weight donor materials based on a thiophene-flanked DPP core were synthesized by Suzuki cross-coupling and characterized in chapter 7. Three different terminal aryl units were employed, featuring a phenyl unit as reference, a *meta*-pyridine and a *para*-pyridine to obtain the three DPP compounds D1-D3 (see Figure 2-9a). The idea here was to fine tune the energy levels on the one hand and to increase any interaction between pyridyl units and fullerenes at the interfaces, on the other hand.

It was found that the optical properties of the materials in solution are absolutely identical, whereas considerable differences were observed in the solid state spectra of thin films, suggesting different solid state packing. Furthermore, cyclic voltammetry revealed that the fundamental band gap is identical for all three compounds. However, the particular energy levels are gradually shifted by about 80 meV each towards lower values when going from phenyl- over *m*-pyridine to *p*-pyridine terminal units (Figure 2-9b). As pyridines are more electron deficient aromatics than phenyl, the energy levels are correspondingly lower. When comparing the substitution pattern, the *ortho* and *para* positions in pyridine exhibit a lower electron density than the *meta* position which causes the lower energy levels in the *para*-substituted D3. This distinct energy level cascade was then exploited in organic solar cell devices that were prepared by vacuum deposition in the research group of Jens Pflaum at the University of Würzburg comprising a planar-heterojunction active layer with D1 as the donor material, D3 as a thin interface layer and fullerene C₆₀ as the acceptor (Figure 2-9c). The incorporation of D3 as an interface layer led to the formation of a distinct energy level cascade at the donor/acceptor interface which drastically improved charge carrier generation (Figure 2-9d). External quantum efficiency (EQE) measurements revealed that in particular the fullerene contribution to the photocurrent was enhanced in this device structure. This effect was attributed to the destabilization of bound charge transfer (CT) states at the D3/C₆₀ interface. By and large, the power conversion efficiency (PCE) could be doubled in this cascade D1/D3/C₆₀ device with small interlayer thicknesses when compared to a D1/C₆₀ reference bilayer device (Figure 2-9e).

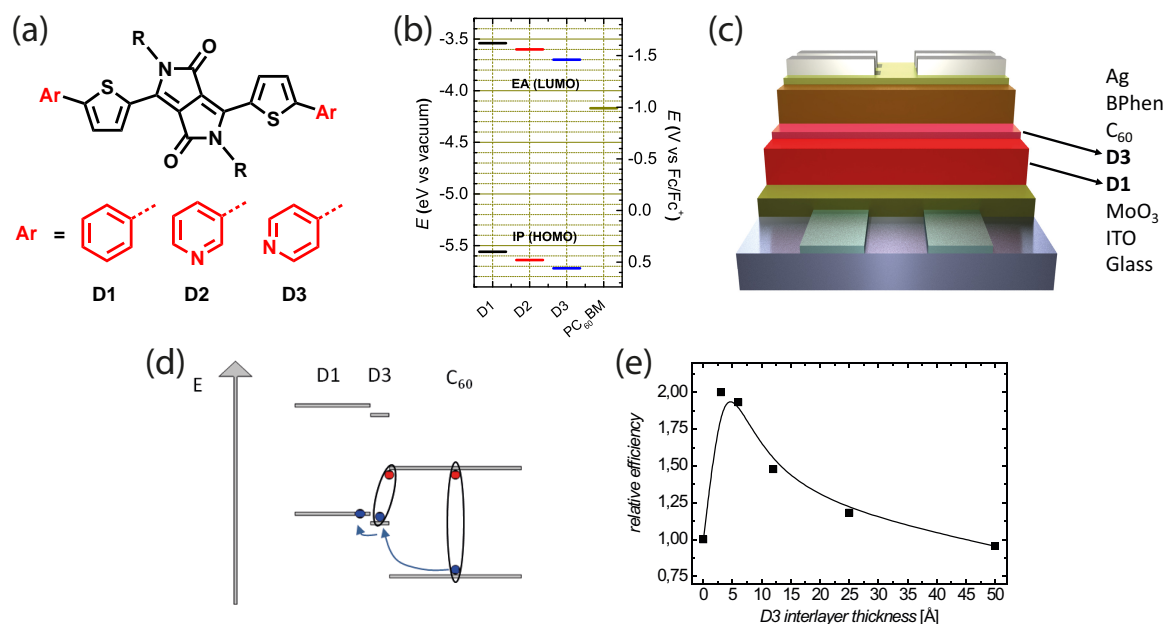


Figure 2-9. (a) Structure of three low molecular weight DPP compounds D1-D3 with varying terminal aryl units as reported in chapter 7; (b) Frontier orbital energy levels of D1-D3 as determined by cyclic voltammetry; (c) Schematics of a planar heterojunction organic solar cell device stack with a D1/D3/C₆₀ active layer as prepared by vacuum deposition; (d) Schematic drawing of the energy level alignment in a cascade cell with a thin interfacial D3 layer (red dots represent electrons, blue dot represent holes); (e) normalized power conversion efficiency of a D1/D3/C₆₀ cascade solar cell with respect to a D1/C₆₀ bilayer cell as a function of intermediate layer thickness.

2.3.2 Photocrosslinkable low bandgap polymers

When designing polymer solar cells based on bulk heterojunctions rather than defined bilayers, the morphological stability of the blend becomes important for longlasting solar cell modules and even for production. Largescale roll-to-roll (R2R) processing with high throughput at appreciable speeds demands for quick drying of active layer inks which is commonly done at elevated temperatures. At these temperatures blends tend to demix into macrophases and thus deteriorate the interconnected donor/acceptor-network. In order to provide stable blend morphologies, the crosslinking of active layers after spincoating has emerged as a suitable approach. This, however, involves the addition of a crosslinker without any or even with adverse electronic properties. The alternative approach involves the laborious modification of the monomers in the particular polymer system of question. In chapter 8 a new crosslinking concept is unveiled which relies on a modular tercopolymerization with small amounts of an azido-functionalized thiophene as the third comonomer. This approach is attractive due to its low synthetic effort and its general validity. 3-(6-Azidohexyl)thiophene as depicted in Figure 2-10a is used as a comonomer in the synthesis of a variety of low-bandgap copolymers using different polymerization techniques such as Suzuki-Miyaura cross-coupling and Stille cross-coupling (Figure 2-10a). When only a small amount of azide groups is introduced into the polymers, the impact on optical (see Figure 2-10b) and electrochemical properties is negligible. The small

amount of azide functionality is however enough to obtain polymers that can easily be crosslinked by UV illumination. Thermal stability of the solid state packing and alignment is studied in neat polymer thin films as well as in blends with [6,6]-phenyl C₇₁ butyric acid methyl ester (PCBM) as a relevant model system for organic photovoltaics. Solvent resistivity of these polymer films is investigated by absorption and photoluminescence measurements after crosslinking and rinsing (see Figure 2-10c). It is finally shown in organic field effect transistors that the introduction of the functionalized monomer does not considerably influence charge transport properties.

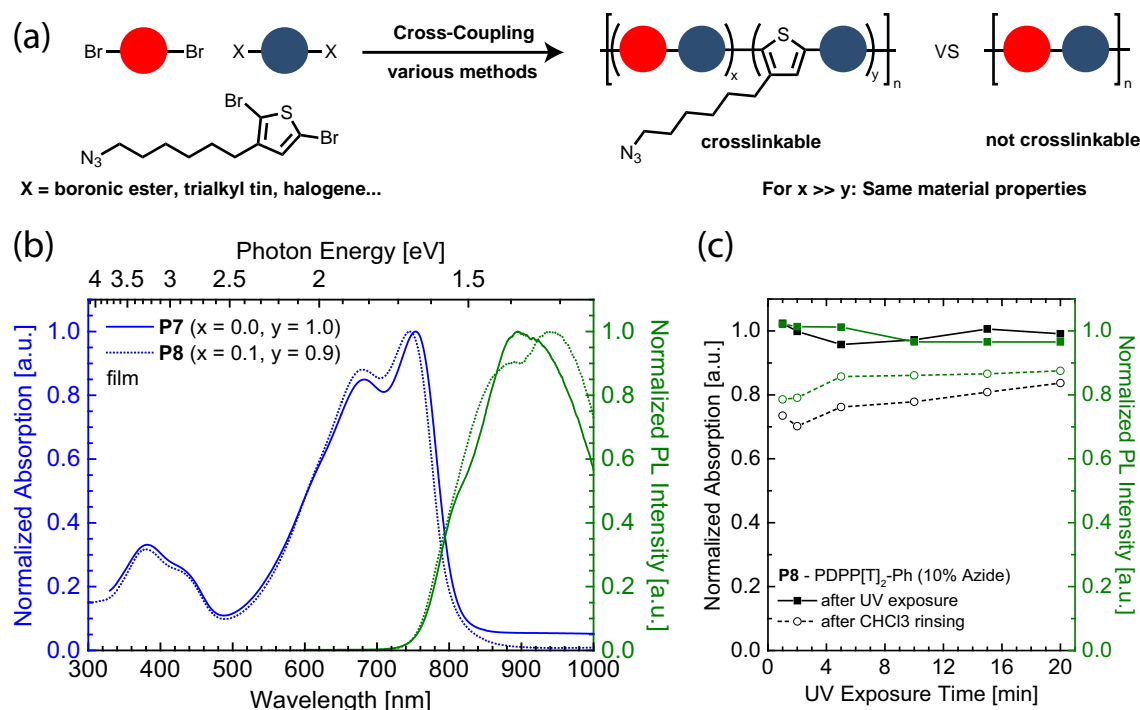


Figure 2-10. (a) Generic synthesis scheme for an azide-functionalized tercopolymer by AA/BB polycondensation using small amounts of a azide-functionalized dibromothiophene monomer (the non-crosslinkable strictly alternating copolymer is shown for comparison); (b) Comparison of absorption and photoluminescence in film for a functionalized tercopolymer P8 and its reference copolymer P7; (c) absorption and photoluminescence of P8 after crosslinking *via* UV exposure and after chloroform rinsing.

2.3.3 Charge collection interface layers in a PDPP:PCBM system

When designing organic solar cell devices, interface layers for charge extraction play a crucial role. In chapter 9 a PDPP[T]₂-Ph / PC₇₀BM blend (Figure 2-11a) is used as a photoactive layer for the investigation of various electron extraction layers in solar cell devices using various electrode combinations. Calcium (Ca), zirconium acetylacetonate (ZrAcac) and a polyfluorene derivative (PFN) are compared to a reference aluminium (Al) electrode (see Figure 2-11b) with respect to their work functions. The device architecture is depicted in Figure 2-11c and the *I*-*V* characteristics of solar cells employing the different interface layers are shown in Figure 2-11d. The use of a PFN interlayer and an aluminium electrode yields a power conversion efficiency of 4.7%. Further, electroabsorption measurements for the built-in voltage

determination and transfer matrix simulations for the determination of parasitic absorption in the interface layers have been performed. It is found that PFN based devices with a small parasitic absorption, small leakage currents and a relatively high built-in voltage perform best. This chapter highlights the importance of choosing suitable interlayers in organic solar cells and clearly demonstrates that it is not only the low work function of an electron extracting interlayer, but also its optical properties and charge selectivity that significantly influence the overall solar cell performance.

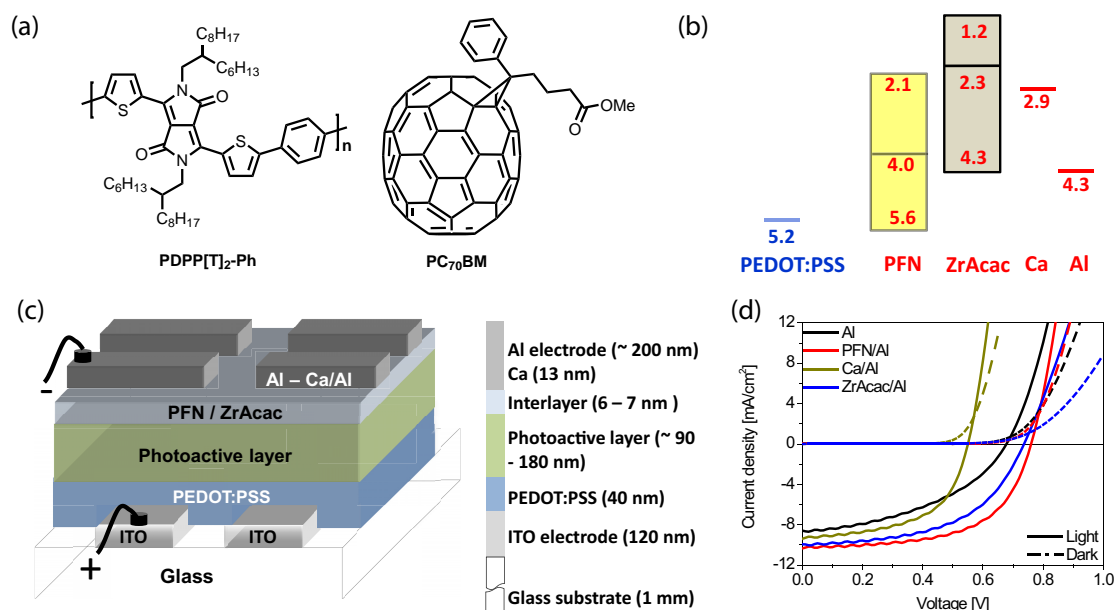


Figure 2-11. (a) Polymer PDPP[T]₂-Ph and PC₇₀BM used a model system in bulk heterojunction solar cells; (b) Comparative energy levels determined by UPS experiments of electron extracting interface layers used in this chapter; (c) Schematic device stack of organic solar cells prepared in this study. The photoactive layer is a bulk heterojunction of PDPP[T]₂-Ph and PC₇₀BM; (d) *I-V* curve for a PDPP[T]₂-Ph:PC₇₀BM solar cell under illumination, comparing different interface layers for electron extraction.

Individual Contribution to Joint Publications

The results of this thesis were obtained in cooperation with other groups and are published or prepared as manuscripts for submission as denoted below. In the following the individual contributions of all authors are summarized and specified.

Chapter 3

This chapter was published as a full paper in *Adv. Funct. Mater.* **2015**, *25*, 2725 under the title:

“High Bulk Electron Mobility Diketopyrrolopyrrole Copolymers with Perfluorothiophene”

by Christian J. Mueller, Chetan R. Singh, Martina Fried, Sven Huettner and Mukundan Thelakkat.

I designed the materials, planned the experiments, developed the synthesis of all unpublished compounds and synthesized the monomers as well as polymers. Furthermore, I characterized all materials, prepared, optimized and analyzed all transistor devices and wrote the manuscript.

Chetan R. Singh prepared and analyzed the SCLC devices and wrote the SCLC section of the manuscript.

Martina Fried (laboratory assistant, CTA) helped with the synthesis of some monomers under my guidance.

Sven Huettner performed the bulk XRD measurements during his beamtime at the Australian Synchrotron.

Mukundan Thelakkat supervised the project and corrected the manuscript.

Chapter 4

This chapter was published as a full paper in *J. Mater. Chem. C*, **2015**, *3*, 8916 under the title:

“Influence of Fluorination in π -extended Backbone Polydiketopyrrolopyrroles on Charge Carrier Mobility and Depth-Dependent Molecular Alignment”

by Christian J. Mueller, Eliot Gann, Christopher R. McNeill and Mukundan Thelakkat.

I designed the materials, planned the experiments, synthesized and characterized all monomers and polymers. I prepared, measured, analyzed and prepared the Graphs for all GIWAXS samples. Furthermore I prepared and analyzed all transistor devices and wrote the manuscript.

Eliot Gann organized the beamtime, helped with the analysis of the GIWAXS data, wrote the GIWAXS section of the manuscript and was involved in scientific discussion.

Christopher R. McNeill and Mukundan Thelakkat supervised the project and corrected the manuscript.

Chapter 5

This chapter was published as a full paper in the *Journal of Polymer Science Part B: Polymer Physics* **2016**, *54*, 639 under the title:

“EDOT-Diketopyrrolopyrrole Copolymers for High Bulk Hole Mobility and Near Infrared Absorption”

by Christian J. Mueller, Chetan R. Singh and Mukundan Thelakkat

I designed the polymers, planned the experiments and synthesized as well as characterized all monomers and polymers. Furthermore I prepared and analyzed all transistor devices as well as wrote the manuscript.

Chetan R. Singh prepared and analyzed all SCLC devices and wrote the SCLC paragraph of the manuscript.

Mukundan Thelakkat supervised the project and corrected the manuscript.

Chapter 6

This chapter is prepared for submission as a full paper under the title:

“Universal Molecular Orientation Control in Polydiketopyrrolopyrroles”

by Christian J. Mueller, Eliot Gann, Chetan R. Singh, Christopher R. McNeill and Mukundan Thelakkat.

I synthesized all polymers, prepared and measured the GIWAXS samples, analyzed the GIWAXS data and wrote the manuscript.

Eliot Gann organized and supervised the beamtime, helped with the analysis of the GIWAXS data, was involved in the scientific discussion and corrected the manuscript.

Chetan R. Singh measured the SCLC mobilities of the three EDOT copolymers.

Mukundan Thelakkat and Christopher R. McNeill supervised the project and corrected the manuscript.

Chapter 7

This chapter was published as a full paper in *Adv. Energy. Mater.* **2015**, *5*, 1500914 under the title:

“Diketopyrrolopyrroles with a Distinct Energy Level Cascade for Efficient Charge Carrier Generation in Organic Solar Cells”

by Christian J. Mueller, Michael Brendel, Pia Ruckdeschel, Jens Pflaum and Mukundan Thelakkat.

I planned the experiments, designed and synthesized all compounds and their precursors as well as characterized the materials and wrote the manuscript except for the device part. I furthermore conducted and analyzed the computational experiments.

Michael Brendel prepared and characterized the solar cell devices, wrote the device part of the manuscript, contributed to introduction and conclusion, was involved in the scientific discussion and corrected the manuscript.

Pia Ruckdeschel helped with the synthesis of the three compounds D1-D3 during her three week internship under my guidance.

Jens Pflaum and Mukundan Thelakkat supervised the project and corrected the manuscript.

Chapter 8

This chapter was published as a full paper in *Macromolecules* **2016**, *49*, 3749 under the title:

“Azido-Functionalized Thiophene as a Versatile Building Block To Cross-Link Low-Bandgap Polymers”

by Christian J. Mueller, Tobias Klein, Eliot Gann, Christopher R. McNeill and Mukundan Thelakkat.

I designed the materials and experiments, developed the synthesis and synthesized as well as characterized all of the materials except those stated below and **P9**. I planned, conducted and analyzed the GIWAXS experiments and furthermore wrote the manuscript.

Tobias Klein synthesized the azido-functionalized thiophene monomer **5** and the polymers **P1-P4** during his bachelor thesis under my supervision.

Eliot Gann organized and supervised the beamtime, was involved in the scientific discussion and corrected the manuscript.

Christopher McNeill was involved in the scientific discussion and corrected the manuscript.

Mukundan Thelakkat supervised the project and corrected the manuscript.

Chapter 9

This chapter was published as a full paper in *Advanced Materials Interfaces* **2016**, *3*, 1500422 under the title:

“Influence of Electron Extracting Interface Layers in Organic Bulk-Heterojunction Solar Cells”

by Chetan R. Singh, Cheng Li, Christian J. Mueller, Sven Hüttner and Mukundan Thelakkat

Chetan R. Singh planned the experiments, fabricated and characterized the solar cell devices, performed the electroabsorption spectroscopy and wrote the manuscript except of synthesis part.

Cheng Li established the electroabsorption spectroscopy set-up, was involved in the scientific discussion and corrected the manuscript.

I synthesized and characterized the PDPP polymer. I wrote parts of the manuscript concerning details on the synthesis of PDPP and its properties. Furthermore I was involved in the scientific discussion.

Sven Hüttner measured the optical constants of interlayers.

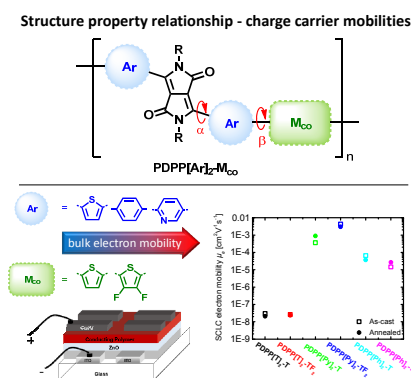
Mukundan Thelakkat supervised the project and corrected the manuscript.

Graphical Table of Contents

High Bulk Electron Mobility Diketopyrrolopyrrole Copolymers with Perfluorothiophene

Christian J. Mueller, Chetan R. Singh, Martina Fried, Sven Huettner and Mukundan Thelakkat

An excellent bulk electron mobility of $4.3 \times \text{cm}^2\text{V}^{-1}\text{s}^{-1}$ was obtained for diketopyrrolo[3,4-*c*]pyrrole copolymers by systematically tuning the diffusive non-bonding heteroatom interactions and dihedral angles between the aryl flanking units, DPP core and comonomer. Differences in crystalline packing, absorption, energy levels and charge carrier properties are comparatively studied in a series of copolymers.

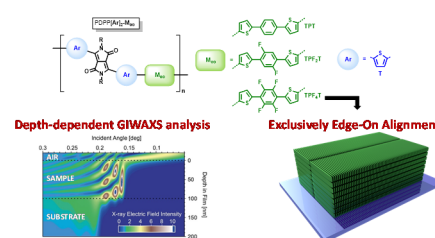


Page 83

Influence of fluorination in π -extended backbone polydiketo-pyrrolo[3,4-*c*]pyrroles on charge carrier mobility and depth-dependent molecular alignment

Christian J. Mueller, Eliot Gann, Christopher R. McNeill and Mukundan Thelakkat

The degree of fluorination in π -extended polydiketopyrrolopyrroles is correlated with semiconductor properties in transistors and an improved molecular alignment in thin films using depth-dependent grazing incidence X-ray scattering.

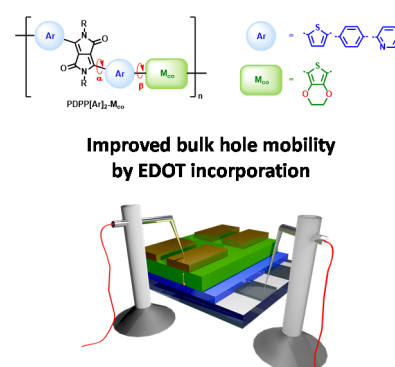


Page 143

EDOT-Diketopyrrolopyrrole Copolymers for High Bulk Hole Mobility and Near Infrared Absorption

Christian J. Mueller, Chetan R. Singh and M. Thelakkat

An excellent bulk hole mobility of $2.9 \times 10^{-4} \text{ cm}^2\text{V}^{-1}\text{s}^{-1}$ and extended absorption in the near-infrared was achieved in diketopyrrolopyrrole (DPP) copolymers by incorporation of 3,4-ethylenedioxythiophene (EDOT) as an extremely electron rich moiety. By tailoring energy levels, the band gap of crystalline silicon combined with excellent bulk hole transport properties can be achieved.

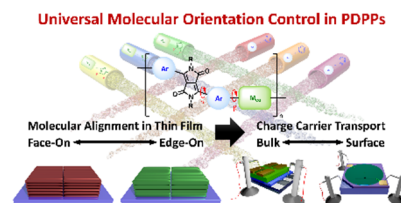


Page 197

Universal Molecular Orientation Control

Christian J. Mueller, Eliot Gann, Chetan R. Singh, Christopher R. McNeill and Mukundan Thelakkat

We show that full control over the mode and degree of orientation in semiconducting low-bandgap polymers is accessible by incorporation and exploitation of diffusive non-covalent interactions between adjacent aryl units in the polymer backbone. Using polydiketopyrrolopyrroles as a model system we find that the mode of orientation can be controlled *via* the aryl flanking unit of the diketopyrrolopyrrole core and the degree of orientation can be driven to perfection by incorporation of moieties which allow for non-covalent diffusive interactions into the comonomers.

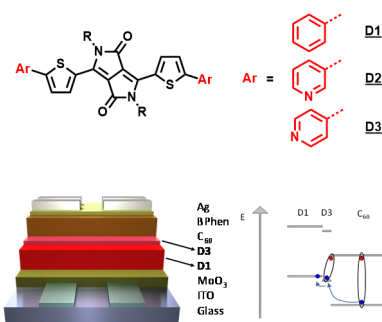


Page 227

Diketopyrrolopyrroles with a Distinct Energy Level Cascade for Efficient Charge Carrier Generation in Organic Solar Cells

Christian J. Mueller, Michael Brendel, Pia Ruckdeschel, Jens Pflaum and Mukundan Thelakkat

Tailored low molecular weight diketopyrrolopyrrole compounds with a precise energy level offset are synthesized by tuning the electron deficiency on the terminal aryl unit. Application of these compounds in cascade solar cells in combination with C₆₀ leads to drastically increased short circuit current densities and power conversion efficiencies.

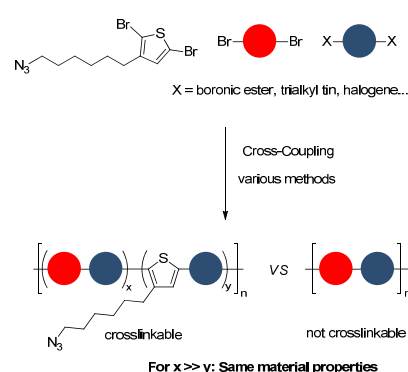


Page 261

Azido-Functionalized Thiophene as a Versatile Building Block To Cross-Link Low-Bandgap polymers

Christian J. Mueller, Tobias Klein, Eliot Gann, Christopher R. McNeill, Mukundan Thelakkat

We unveil a concept for the design of crosslinkable semiconducting polymers that is based on a modular tercopolymerization and stands out by its low synthetic effort, easy accessibility and its broad range of applications. It is shown that thermally stable blend morphologies and solvent resistant films can be obtained with low degrees of functionalization.

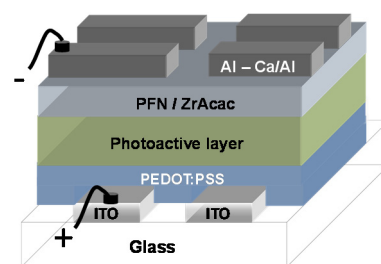


Page 295

Influence of Electron Extracting Interface Layers in Organic Bulk-Heterojunction Solar Cells

Chetan R. Singh, Cheng Li, Christian J. Mueller, Sven Hüttner and Mukundan Thelakkat

The influence of different electron extracting interlayers including Ca, ZrAcac, and PFN is investigated in normal organic solar cell geometry using electroabsorption measurements and transfer matrix simulations. It is shown that the solar cell performance is influenced by different parameters such as diode turn-on voltage, leakage currents, built-in voltages and parasitic absorption.



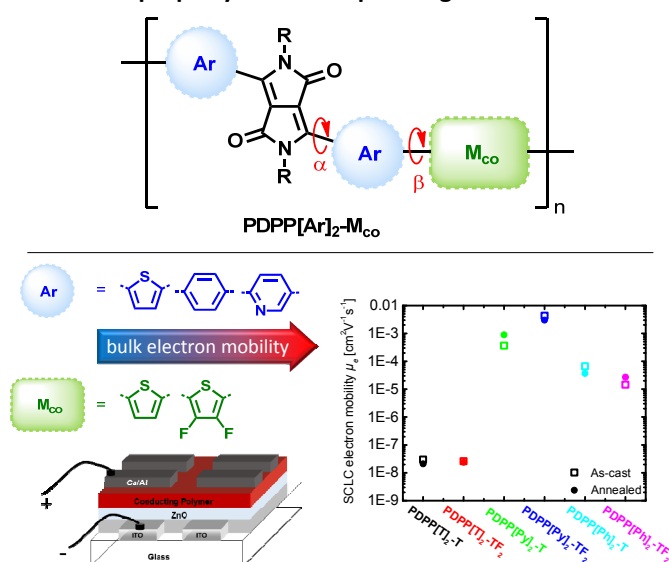
Page 351

3 High Bulk Electron Mobility Diketopyrrolopyrrole Copolymers with Perfluorothiophene

Christian J. Mueller, Chetan R. Singh, Martina Fried,
Sven Huettner and Mukundan Thelakkat*

Applied Functional Polymers – Macromolecular Chemistry I, University of Bayreuth, 95440
Bayreuth, Germany

Structure property relationship - charge carrier mobilities



Published in *Advanced Functional Materials*, **2015**, *25*, 2527-2736.

Reproduced with permission from Wiley VCH.

Abstract

We address the question of designing high electron mobility polymers by increasing the planarization using diffusive non-bonding heteroatom interactions in diketopyrrolopyrrole polymers. For this, three different diketopyrrolo[3,4-*c*]pyrrole (DPP) derivatives with thienyl-, 2-pyridinyl- and phenyl-flanked cores were copolymerized with an electron-rich thiophene unit as well as an electron-deficient 3,4-difluorothiophene unit as comonomer to obtain diverse polymeric DPPs which vary systematically in their structures. The crystallinity differs significantly with clear trends on varying both flanking unit and comonomer. The optical gap and energy levels depend more on the nature of the flanking aryl units rather than on fluorination. Additionally, we compare the charge transport properties, using different methods to differentiate between interface or orientation effects and bulk charge carrier transport. In OFET devices with very high electron as well as hole mobilities (up to $0.6 \text{ cm}^2\text{V}^{-1}\text{s}^{-1}$) were obtained and fluorination led to a more pronounced n-type nature in all polymers, resulting in ambipolar behavior in otherwise p-type materials. In contrast, SCLC measurements showed a strong influence of the flanking units only on electron mobilities. Especially, the elegant synthetic strategy of combining pyridyl flanking units with difluorothiophene as the comonomer culminated in a record bulk electron mobility of $4.3 \times 10^{-3} \text{ cm}^2\text{V}^{-1}\text{s}^{-1}$ in polymers.

3.1 Introduction

Diketopyrrolopyrrole (DPP) based polymer materials are promising candidates for organic field effect transistors (OFET) as well as organic photovoltaics (OPV) due to their high ambipolar charge carrier mobilities, low optical gap and high absorption coefficient.^[1-4] Most reports focus on DPP polymers (PDPP) as donor materials in OPV, which show high power conversion efficiencies (PCE) when blended with a C₆₀ or C₇₀ fullerene derivative (PCBM).^[1, 5] Usually, the bicyclic DPP core is flanked on both sides with aryl units, such as thiophene, phenyl or pyridine groups. This diaryl-DPP is usually copolymerized using a variety of comonomers containing phenyl, thiophene, or thienothiophene moieties.^[3, 6-8] The copolymers are synthesized using either Suzuki or Stille polycondensation. Among the vast variety of DPP copolymers, PDPP3T having thiophene as both flanking aryl units and comonomer is widely studied in a variety of devices.^[6, 9-10]

The charge carrier mobility of different PDPPs has been usually investigated in organic field effect transistor (OFET) devices. Hole and electron mobilities, in some of these materials are

high in the range of about 10^{-2} to 10^1 $\text{cm}^2\text{V}^{-1}\text{s}^{-1}$, especially after thermal treatment of the thin films.^[4, 11] This is mainly due to the high crystallinity of these tested PDPPs which favors ordered packing with possible orientation effects on annealing. It has been reported, that thermal annealing in some PDPPs leads to the formation of a preferentially edge-on orientation at the semiconductor-dielectric interface, causing these high mobilities.^[12] Thus, OFET mobilities give more insight into orientation effects at the interface, as charge carriers are transported within a narrow channel of 5-10 nm of the semiconducting layer. Even though this is very relevant for charge injection or collection at the electrode interface, it is very necessary to evaluate and understand the bulk charge carrier mobility of PDPPs as measured in a diode configuration. Here, charge carriers are transported vertically through the active layer over more than 100 nm, which is similar to thicknesses in solar cells. Moreover, there is a considerable difference in the charge-carrier density present in the OFET and diode configurations.^[13] For PDPPs space-charge limited current (SCLC) measurements in diode geometry are mainly reported in PDPP:PCBM blends. For determination of the hole-mobility (μ_h) of PDPP this is an acceptable experimental simplification since the contribution of fullerene to μ_h is negligible. Electron mobilities (μ_e), however, cannot be assessed in the blended material, since fullerenes contribute considerably to the electron transport.

One of the main questions of concern is the design and development of efficient electron transport polymer materials. In the case of DPP derivatives new heteroaromatic units have recently been attached to the DPP core to improve the acceptor nature of these materials. For example, Janssen et. al employed thiazole flanking units to provide n-type polymers that have successfully been used in all-polymer OPV as an acceptor material.^[14] Another general approach is to use fluorinated moieties to tune energy levels to obtain suitable donor or acceptor materials.^[12, 15-17]

Both absorption and charge carrier mobility of polymers are dependent on the degree of delocalization and hence planarity of the conjugated polymer backbone.^[18] Recently, it has been published and backed by a number of theoretical calculations that the planarity of backbones in conjugated polymer can be increased via diffusive nonbonding heteroatom interactions.^[19-20] In addition to the classical S-O interactions, most importantly CH-N, CH-O, CH-F and CH-S interactions of adjacent aryl units can contribute to a rigidification of the polymer chain. For PDPPs there are two options for modification of the backbone in order to increase the planarity. The aryl units Ar adjacent to the diketopyrrolo[3,4-*c*]pyrrole core can be altered in order to modify both of the dihedral angles α and β (see Scheme 3-1). Generally, PDPPs employing phenyl flanking units show only modest charge carrier mobilities in OFET devices and poor power conversion efficiencies in OPVs when blended with fullerene acceptors.^[21-22] This poor performance is mostly ascribed to the large dihedral angle between the bicyclic DPP core and the phenyl groups as flanking aromatic units.^[23] In contrast, most of the thienyl-

flanked PDPPs exhibit high charge carrier mobilities as well as high PCEs in OPV devices. This is not only due to a more favourable, coplanar structure but also due to effective orbital overlap that profits from a push-pull-effect of the DPP core and thiophene flanking units, which lowers the optical gap of the material. When 2-pyridine, which lacks the hydrogen atom at 2-position, is used instead of the phenyl-unit, the steric hindrance between the keto-group in the DPP core and the 2-hydrogen-position (vacant) of the adjacent aryl ring as well as any steric interaction between the 6-hydrogen pyridine and N-CH₂ of the alkyl chain can be avoided in appropriate conformations. Whereas thiophene is a very electron rich unit, pyridine is comparatively electron deficient, allowing for the design of electron-transporting materials. For example, the copolymer, which consists of pyridine flanked DPP and 2,2'-bithiophene as comonomers showed extremely high electron mobility in the range of 6 cm² V⁻¹ s⁻¹ in OFET devices.^[24]

The second option is the modification of the comonomer M_{co} in order to optimize the dihedral angle β . A versatile way of fixing this dihedral angle between the diaryl-DPP and the comonomer is the exploitation of the aforementioned diffusive interactions. Substitution of aromatic hydrogen atoms in the comonomer with fluorine gives rise to CH-F coordination sites and electron-deficient comonomers. This fluorination approach has been demonstrated using fluorinated units for the development of semiconducting polymers relevant to both OFET as well as OPV devices.^[12, 25-27] Ladder-type comonomers with up to five multi-fused aromatic rings sterically locked by covalent bridging have also been employed.^[28-30] However, even if these comonomers are very rigid for themselves, the dihedral angle β cannot be minimized by this approach.

Complex applications such as photovoltaics demand a combination of optimum absorption, crystallinity and bulk charge carrier transport at the same time. In order to achieve all these simultaneously a comprehensive picture of how structural variation affects the individual properties is required. This can be obtained only by a gradual structural variation and by comparatively studying its influences on diverse properties.

In this contribution, we therefore compare the influence of different aryl flanking units as well as the influence of fluorination of the comonomer on the charge carrier mobility, optical properties and crystallinity. The systematic variation of the structural units allows us to elucidate the influence of dihedral angles suggested in literature on moving from a) thiophene over pyridine to phenyl as the aryl flanking unit in PDPP and b) thiophene to difluorothiophene as comonomer. This interactive study is very essential to understand the positive as well as negative influences on optical properties and crystallinity when structural design is planned with an aim to improve electron transport. For this purpose, we synthesized a set of six DPP copolymers varying their flanking units and degree of fluorination in the comonomer.

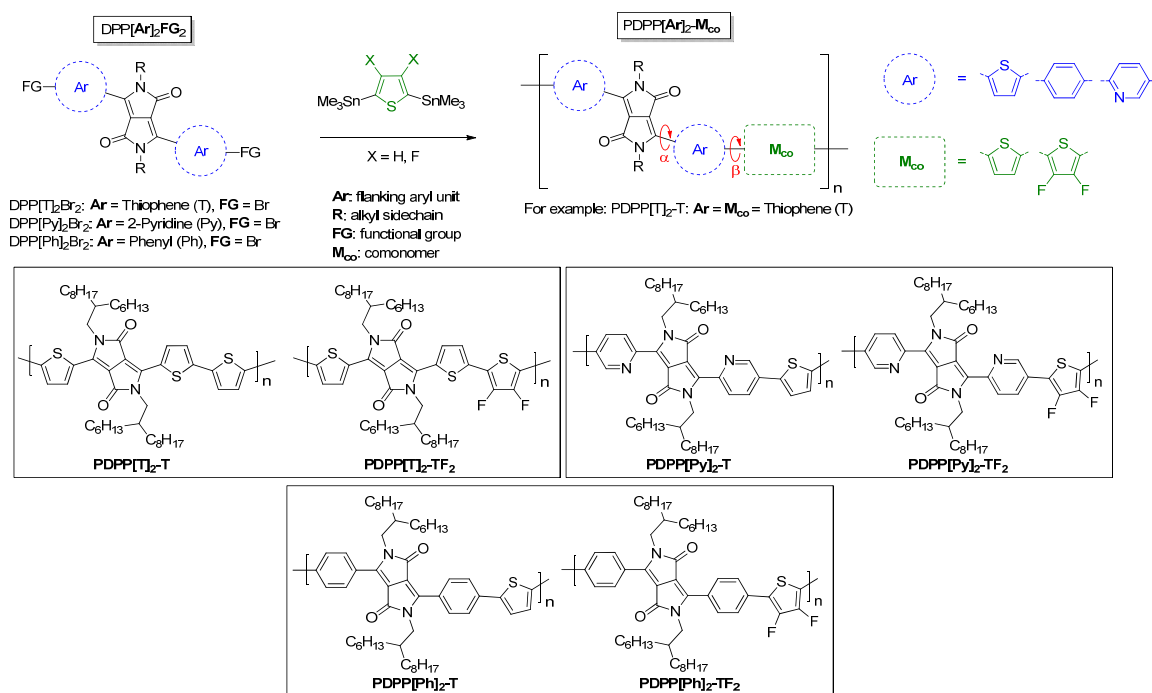
Two of these copolymers (herein denoted as PDPP[T]₂-T and PDPP[Ph]₂-T) having thiophene or phenyl flanking units along with thiophene as a comonomer are known in literature as PDPP3T^[6, 9] and PB^[31], respectively. To enable a comprehensive comparison of the newly synthesized systems with these known polymers, all the six copolymers were prepared using Stille polycondensation under similar synthetic conditions. This helps the evaluation of all the studied copolymers under the same conditions of measurement and device geometry in order to elucidate a structure-property relationship. The influence of structural variation on crystallinity was studied using Flash-DSC, XRD and polarization microscopy. In order to differentiate between any possible orientation effects as well as the influence of crystallinity on charge carrier mobility, all materials are measured under similar conditions, both in OFET and diode configuration (SCLC). Additionally, the influence of fluorination of the comonomer on charge carrier mobility is examined. This systematic and fundamental comparison gives valuable information for the further design of both donor and acceptor-type PDPP materials to suit the necessity of application.

Thus, in the design of electron transport DPP copolymers, we make use of two synthetic strategies based on the effects mentioned above: a) less steric hindrance between the DPP core and flanking aryl units by selecting a pyridyl group and b) perfluorinated thiophene as a comonomer. In this way a synergetic effect caused by both flanking units and comonomer may be expected and the resulting properties can be explained in terms of structural changes.

3.2 Results and discussion

3.2.1 Nomenclature

Different approaches for naming diketopyrrolopyrrole derivatives are used in literature. Most of them are based on a non-systematic use of alphabets leading to an arbitrary name, which does not help to understand the chemical structure from the name. Therefore, we suggest to use a modular acronym approach (see Scheme 3-1) in this paper as per the following guidelines. The thiophene-DPP structures are shown in a conformation in accordance with the crystal structures of model compounds, in which the CO \cdots HC interactions arising from the DPP and the flanking thiophene units are predominating over the S \cdots O interactions. In this nomenclature one can determine the molecular structure of the compound directly from the acronym without any additional aids.



Scheme 3-1. Synthesis of the PDPP copolymers using Pd₂(dba)₃ / P(*o*-Tol)₃ in chlorobenzene at 180 °C in a microwave reactor. All polymers were endcapped with 2-tributyltinthiophene and 2-bromothiophene. The modular nomenclature approach for DPP monomers and polymers is shown with the two dihedral angles of interest α and β depicted in the polymer structure.

Low molecular weight diketopyrrolopyrrole derivatives consist of a) the bicyclic DPP core, b) flanking aromatic units (Ar) adjacent to the core, c) solubilizing groups / side chains (R) and eventually d) terminal functional groups (FG). When comparing a series with identical side chains or when the side chains are negligible for discussion, the side chain may be omitted from the acronym for clarity. The flanking aryl units are put in square brackets as [Ar] followed by functional groups. For polymers, the comonomer M_{co} is given instead of the functional groups and delimited by a dash. For example, the dibromo-DPP monomer containing thiophene as flanking aromatic units can be represented as DPP[T]₂Br₂ and its copolymer using thiophene or phenyl as a comonomer as PDPP[T]₂-T and PDPP[T]₂-Ph, respectively. These two represent the polymers hitherto known in literature as PDPP3T^[9] and PDPPPTPT^[3, 5].

3.2.2 Synthesis

The dibrominated thienyl-DPP DPP[T]₂Br₂,^[32] pyridinyl-DPP DPP[Py]₂Br₂^[33] and phenyl-DPP DPP[Ph]₂Br₂^[34-35] monomers were synthesized following modified literature procedures. 2,5-bis(trimethylstannyl)-3,4-difluorothiophene was synthesized according to literature protocols.^[36-37] Detailed procedures are given in the supporting information. For the synthesis of the non-fluorinated polymers, the dibromo-DPPs were coupled with the distannylthiophene. However, for the fluorinated polymers, it should be noted that bromo-functionalization of the electron-deficient difluoro-thiophene unit and stannyl-functionalization of the relatively more

electron-rich DPP unit would be preferable for Stille-polycondensation.^[38] But in terms of monomer purification, 2,5-dibromo-3,4-difluorothiophene as a liquid compound is difficult to purify on a small scale to an extent that is necessary for polycondensation. On the other hand, 2,5-bis(trimethylstannyl)-3,4-difluorothiophene can be obtained in high purity via recrystallization. Therefore we found it much more practical to use the functionalization in the reverse order as shown in Scheme 3-1. In order to obtain high degrees of polymerization, the purity and stoichiometry of the monomers in polycondensation is highly relevant. Polymerizations were carried out in chlorobenzene at 180 °C under microwave conditions in pressurized and sealed vials.^[39-40] All polymers were endcapped with thiophene on both ends.

3.2.3 Characterization

3.2.3.1 Gel permeation chromatography

The polymers were obtained with number average molecular weights (M_n) in the range of 10 700 – 40 800 g mol⁻¹ and polydispersities (D) between 1.6 and 4.0 (Table 3-1) in good yields. GPC traces (supporting information Figure S3-1 – Figure S3-6) show a monomodal distribution for all polymers except PDPP[T]₂-TF₂, which exhibits a shoulder. The GPC traces of PDPP[T]₂-T and PDPP[T]₂-TF₂ exhibit very high peak molecular weights in the range of 10⁵ g mol⁻¹ unlike the others having peak molecular weights (M_p) less than 40 kg mol⁻¹. Since all polymerizations were carried out under comparable conditions of temperature, time, monomer purity and concentration, the very high molecular weight values might be attributed to aggregation of the highly crystalline thienyl-derivatives under the GPC measurement conditions. Accordingly, the number average degree of polymerization (DP_n) shows differences for the distinct PDPPs. The PDPP[T]₂ polymers were obtained with a DP_n of 41 and 47 whereas the PDPP[Py]₂ and PDPP[Ph]₂ polymers show a DP_n of 13-24. The flanking aryl units on the DPP core also have a severe effect on solubility. The PDPP[T]₂ polymers are only soluble in chloroform at room temperature and *o*-dichlorobenzene or 1,2,4-trichlorobenzene at elevated temperatures. PDPP[Py]₂ and PDPP[Ph]₂ polymers are much more soluble (e.g. in hexane or THF). It should be noted that the fluorinated polymer PDPP[Py]₂-TF₂ is insoluble in hexane although its molecular weight is considerably smaller than that of the non-fluorinated reference polymer PDPP[Py]₂-T, which is soluble in hexane. This is attributed to a rigidification of the backbone and hence a higher tendency for aggregation for the fluorinated derivatives.

Table 3-1. GPC and thermal data of the synthesized PDPPs.

Polymer	M_n ^{a)}	M_w ^{a)}	M_p ^{a)}	\bar{D} ^{b)}	DP_n ^{c)}	Yield	T_m ^{d)}
	[kg mol ⁻¹]	[kg mol ⁻¹]	[kg mol ⁻¹]				[°C]
PDPP[T] ₂ -T	34.2	107.7	81.7	3.1	41	79%	290
PDPP[T] ₂ -TF ₂	40.8	161.9	137.0	4.0	47	81%	331
PDPP[Py] ₂ -T	19.6	54.0	37.4	2.8	24	74%	294
PDPP[Py] ₂ -TF ₂	12.0	29.2	24.2	2.3	14	69%	333
PDPP[Ph] ₂ -T	10.7	25.3	21.5	2.4	13	87%	-
PDPP[Ph] ₂ -TF ₂	14.4	22.8	16.4	1.6	17	58%	-

^{a)} Determined by GPC at 150 °C using 1,2,4-trichlorobenzene as the eluent; ^{b)} Polydispersity; ^{c)} Degree of Polymerization calculated from M_n ; ^{d)} melting peak values from Flash-DSC.

3.2.3.2 Thermal properties

In general, PDPPs exhibit very high melting points almost near their respective degradation temperatures depending on the backbone rigidity and nature of the alkyl chains. Therefore we adopted Flash-DSC (flash dynamic scanning calorimetry) measurements to avoid any degradation and to obtain comparative transition temperatures with a single method. Melting points of the PDPPs as measured on a Flash-DSC with heating rates from 50 K/s to 1000 K/s are summarized in Table 3-1. All the DSC curves can be found in the supporting information (Figure S3-7). With regard to the flanking aryl units, the PDPP[T]₂ and PDPP[Py]₂ systems exhibit a melting point in Flash-DSC measurements. Further, the fluorination via comonomer increases the melting point drastically by about 40 °C. Thus, the non-fluorinated polymers PDPP[T]₂-T and PDPP[Py]₂-T show a similar melting point of 290 °C, whereas the fluorinated derivatives PDPP[T]₂-TF₂ and PDPP[Py]₂-TF₂ have melting points of 331 °C and 333 °C, respectively. Both of the PDPP[Ph]₂ polymers show neither a melting point nor a glass transition temperature in the DSC curves up to 400 °C, which indicates negligible crystallinity. To further explore the presence of any low-enthalpic transition, such as liquid-crystalline clearing which can be overseen in a flash-DSC measurement, PDPP[Ph]₂-T and PDPP[Ph]₂-TF₂ were examined using a polarization microscope. The polarization micrographs are given in the supporting information (Figure S3-8). It is evident that both of these polymers show liquid crystalline behavior in the range of 140 °C to 270 °C. Under crossed polarizers the shearable, birefringent textures observed in this range disappear on clearing, which can be reversibly observed on cooling.

3.2.3.3 Optical properties

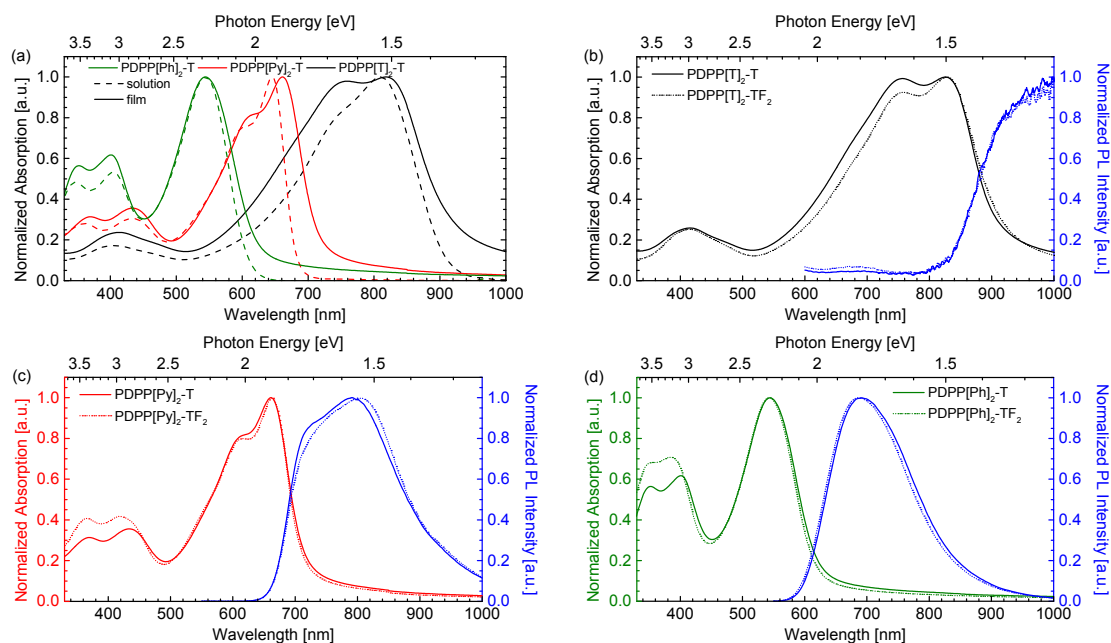


Figure 3-1. Absorption and photoluminescence (PL) spectra comparing the influence of (a) the flanking aryl unit in film and solution for the non-fluorinated copolymers and (b-d) fluorination of the comonomer in solid state for each pair. For solution spectra see supporting information (Figure S3-9).

The optical absorption and photoluminescence (PL) spectra of all the polymers in solid state are shown in Figure 3-1. Additional spectra in solution can be found in the supporting information (Figure S3-9). For all comparable pairs (fluorinated vs non-fluorinated), the absorption onsets in solid state compared to those in solution exhibit a red shift of about 50 nm due to aggregation as expected for these semi-crystalline polymers (Figure 3-1a); the smallest shift being observed for the less-ordered PDPP[Ph]₂ system. The flanking aryl units show pronounced influence on both spectral nature and onset. Thus, the spectral signatures change drastically from PDPP[Ph]₂-T to PDPP[T]₂-T; the broad structureless spectra transform to well-structured spectra having vibronic bands. This indicates, that the aggregation due to crystallization increases from phenyl- to thienyl-flanked DPPs. The optical gaps were calculated from the absorption onset in thin film *via* tangential fitting. Thus, the flanking aryl unit next to the DPP core shows a considerable influence on the absorption onset as well. The optical gaps for PDPP[T]₂-T, PDPP[Py]₂-T and PDPP[Ph]₂-T are 1.3 eV, 1.7 eV and 2.0 eV, respectively (Figure 3-1). The fluorination of the comonomer in all the three types of copolymers does not have any considerable influence either on spectral nature or on absorption onset in thin films (see Figure 3-1b,c,d). However, there are small changes in the absorption peak in solution spectra (supporting information Figure S3-9) for some of the fluorinated derivatives. For example, PDPP[T]₂-T in solution peaks at 821 nm whereas the peak of PDPP[T]₂-TF₂ is 15 nm red-shifted to 836 nm. Similarly, for the PDPP[Ph]₂

derivatives also a red-shift in absorption occurs only in solution. In the PDPP[Py]₂ system the absorption is not red-shifting upon fluorination.

The photoluminescence intensity for phenyl- is larger than for pyridyl-substituted PDPPs, whereas the thiophene-derivatives exhibit only negligible PL. Both the PDPP[T]₂ polymers exhibiting the smallest optical gaps with absorption in the NIR range show photoluminescence beyond our detection limit of 1000 nm. Generally speaking, fluorination seems to have only little effect on the photoluminescence of the investigated polymers as is the case for absorption.

The change in absorption onset upon variation of the flanking aryl unit can be explained with the help of planarization / delocalization effects. To give a quantitative assessment, we make use of published single crystal data available in the CCDC (Cambridge Crystallographic Data Centre) library. When discussing the backbone planarity of these three systems, PDPP[T]₂-M_{co}, PDPP[Py]₂-M_{co}, PDPP[Ph]₂-M_{co}, experimental crystal structures from the corresponding low molecular weight diaryl-DPP compounds are used in the following. For the well-known DPP[T]₂ system several crystal structures are published. The dihedral angle α is ranging from 3° to 9° (see supporting information Table S3-1). The phenyl-DPP motif shows drastically larger dihedral angles of 26-28°. For pyridinyl-DPP no applicable reference systems are available and therefore no estimation regarding the dihedral angle in our DPP[Py]₂ system can be made.

Regarding the dihedral angle β only few crystal structures with the motifs used in this study are published. Accordingly, the β -values could be comparatively estimated only for the polymers PDPP[T]₂-T and PDPP[T]₂-TF₂. Thus, angles in non-fluorinated oligothiophene (2-6°, see supporting information Table S3-2) are only slightly larger than angles in perfluorinated oligothiophenes (0-3°). Crystal structures of pyridine or phenyl rings adjacent to 3,4-difluorothiophene are not published to the best of our knowledge. Based on crystallinity data, it can be concluded that the phenyl flanking units lead to a considerable backbone twist which is not present in the thiophene system. For the 2-pyridyl system, which lacks the H-atom at 2-position no steric hindrance and, therefore, no considerable backbone twist is expected.

3.2.3.4 Cyclic voltammetry

The electrochemical behavior of all the polymers were studied with respect to reversibility as well as redox potentials. The individual cyclic voltammograms are given in the supporting information, Figure S3-10 and the comparison of the energy levels is shown in Figure 3-2. The energy levels of the PDPPs were calculated from the redox potentials calibrated against ferrocene using a published procedure taking into account solvent effects.^[41-42] All the redox-potential values were obtained by cyclic voltammetry on polymer thin films with ITO (indium tin oxide) as the working electrode. For values obtained from cyclic voltammetry, it is

recommended to use ionization potential (IP) and electron affinity (EA) rather than HOMO and LUMO, respectively.^[43] All the six polymers show typical reversible oxidation and reduction waves as known for other PDPPs in literature.^[44] The variation of the flanking aryl units from thiophene to pyridyl and phenyl shifts both IP and EA resulting in the broadest electrochemical gap E_{CV} for the PDPP[Ph]₂ polymers. The smallest electrochemical gap observed for PDPP[T]₂-T is similar to the observations in the optical gap measurements discussed above.

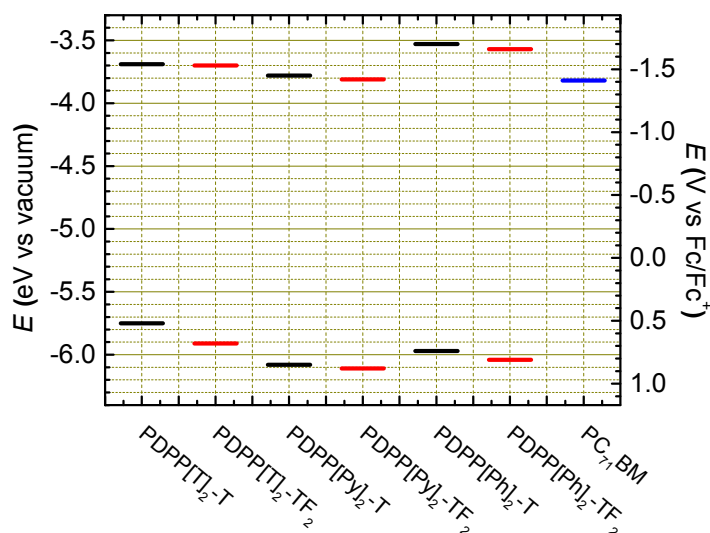


Figure 3-2. Energy level comparison for the synthesized polymers determined by cyclic voltammetry in thin film. The solid state reduction potential of PC₇₁BM (-1.41 eV) corresponding to an EA of -3.82 eV is shown for comparison.

Table 3-2. Solid state electrochemical and structural properties of the PDPPs.

Polymer	Cyclic Voltammetry				XRD			
	IP^a	EA^b	E_{cv}^c	E_{opt}^d	d_{lam}^e	d_{amorph}^f	$d_{\pi-\pi}^g$	ζ_{lam}^h
	[eV]	[eV]	[eV]	[eV]	[Å]	[Å]	[Å]	[nm]
PDPP[T] ₂ -T	-5.75	-3.69	2.06	1.32	19.16	4.52	3.86	6.9
PDPP[T] ₂ -TF ₂	-5.91	-3.70	2.21	1.33	19.83	4.40	3.65	8.8
PDPP[Py] ₂ -T	-6.08	-3.78	2.30	1.72	19.05	4.56	3.91	3.9
PDPP[Py] ₂ -TF ₂	-6.11	-3.81	2.30	1.73	18.63	4.48	3.90	4.1
PDPP[Ph] ₂ -T	-5.97	-3.53	2.44	1.98	14.94	4.04	-	2.7
PDPP[Ph] ₂ -TF ₂	-6.04	-3.57	2.47	2.03	14.62	3.90	-	2.1

^{a)} CV based ionisation potential, ^{b)} CV based electron affinity and ^{c)} electrochemical gap determined by CV in thin film; ^{d)} optical gap determined from absorption onset in film; ^{e)} lamellar spacing, ^{f)} amorphous peak ^{g)} π - π spacing, ^{h)} crystal correlation length $\zeta = 2\pi/\text{FWHM}$ of the lamellar peak.

The effect of fluorination is pronounced on the oxidation potential of PDPP[T]₂-TF₂. Otherwise, the influence is almost negligible on both IP and EA for the other derivatives. For example, the ionization potential is increased from 5.75 eV for PDPP[T]₂-T by 0.16 eV to

5.91 eV for PDPP[T]₂-TF₂. On the other hand the electron affinity is not affected by fluorination giving a value of 3.70 eV for both PDPP[T]₂-T and PDPP[T]₂-TF₂. Thus, the electrochemical gap increases in the PDPP[T]₂ system whereas no influence is observed for the PDPP[Py]₂ and PDPP[Ph]₂ systems upon fluorination. Comparing the differently flanked DPP units the PDPP[T]₂ polymers show the smallest, whereas the PDPP[Ph]₂ polymers show the highest electrochemical gap, which is in accordance with previous considerations on the degree of delocalization and the strength of the inherent D-A-D push/pull systems. The EA value for PDPP[Py]₂-TF₂ is -3.81 eV and it is comparable to the EA of the commonly used acceptor PC₇₁BM (Figure 3-2).

The approximate electron-hole pair binding energy (E_B) can be assessed from the difference between the optical (E_{opt}) and electrochemical gap (E_{CV}). This difference in optical and electrochemical gap varies considerably from the PDPP[T]₂ over PDPP[Py]₂ to PDPP[Ph]₂ polymers (Table 3-2). The influence of fluorination is again pronounced only in the PDPP[T]₂ system. Thus, the highest binding energy E_B is observed for PDPP[T]₂-TF₂ (0.88 eV) whereas the lowest value of 0.44 eV is obtained for PDPP[Ph]₂-TF₂.

3.2.3.5 Solid state structure

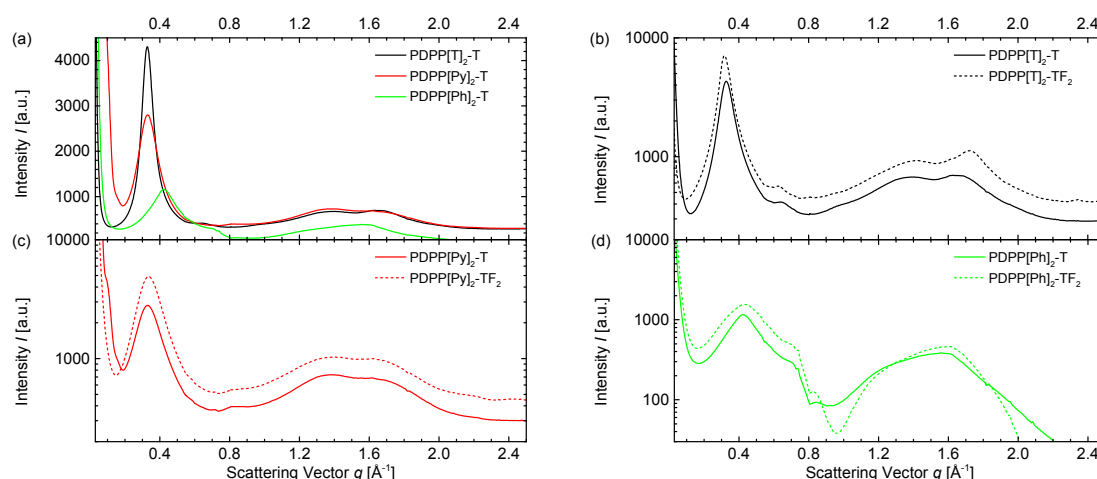


Figure 3-3. Bulk SAXS/WAXS measurements of the PDPPs: (a) comparison of different flanking units, (b-d) Comparison of fluorinated with non-fluorinated derivatives.

Comparative crystallinity and lamellar spacing was estimated from transmission powder xray diffraction (XRD) measurements in the small and wide angle xray scattering (SAXS/WAXS) region ($q = 0.016 - 2.86 \text{ \AA}^{-1}$) of free standing bulk samples without any thermal treatment. The sharp peaks with small FWHM (full width at half maximum) values reach a correlation length up to 8.8 nm and are centered at $q \approx 0.3 \text{ \AA}^{-1}$ indicating the lamellar spacing d_{lam} , whereas the broad peaks in the WAXS region represent the π - π distances $d_{\pi-\pi}$.^[45] An overview of the periodic distances d_{lam} and $d_{\pi-\pi}$ as well as the correlation lengths ζ are given in Table 3-2 and the individual diffractograms are shown in Figure 3-3. Qualitatively, the intensity of the d_{lam} peaks is higher for the fluorinated polymers for all the three DPP derivatives (comparing

normalized intensities) suggesting a higher crystallinity. On comparison of the influence of flanking aryl units, the PDPP[T]₂ polymers show the highest degree of crystallinity followed by the PDPP[Py]₂ polymers (Figure 3-3a). The PDPP[Ph]₂ polymers give the weakest d_{lam} signals showing only a small difference between non-fluorinated and fluorinated derivative. This is in accordance with the observations from DSC measurements. In general, the diffraction peaks at $q \approx 0.3 \text{ \AA}^{-1}$, corresponding to a inter-lamellar distance of around 19 \AA , are hardly influenced by fluorination. The second order can be found for the PDPP[T]₂ and for the PDPP[Py]₂ polymers, indicating a good lamellar organization. On the other hand, the π - π stacking distances decrease upon fluorination of the thiophene comonomer by about 0.1 \AA suggesting a stronger π - π interaction for the fluorinated derivatives. Furthermore, in the thienyl- and pyridinyl-DPP polymers the FWHM of the lamellar stacking peak is smaller for the fluorinated derivatives, which is indicating longer coherence lengths and may suggest larger crystals. This is also in agreement with the observed increase in melting points for those fluorinated derivatives.

3.2.4 Charge transport properties

In order to obtain a comprehensive picture regarding the influence of structural variation on charge carrier transport, we measured both OFET and SCLC mobilities for all the copolymers under as-cast as well as annealed conditions. In general, the charge carrier density in field effect transistors is higher than in the diode configuration and correspondingly the mean mobility is lower in SCLC measurements.^[13] The former are also influenced by orientation effects at the semiconductor-dielectric interface whereas in the latter information regarding isotropic bulk charge carrier mobilities irrespective of interfacial orientation effects is obtained.

3.2.4.1 OFET

The OFET mobilities were obtained in thin films using a bottom gate / bottom contact (BGBC) configuration and are summarized in Table 3-3. For each data point, a minimum of four devices was measured. As a typical example, transfer and output curves of PDPP[T]₂-T and PDPP[T]₂-TF₂ are shown in Figure 3-4. The curves of the PDPP[Py]₂ and PDPP[Ph]₂ polymers are given in the supporting information (Figure S3-11). All devices exhibit very high on/off ratios ($I_{on/off}$: 10^5 - 10^8) unless operated at very high drain voltages. In this case ($V_d = 80 \text{ V}$), the on/off ratio decreases to about 10^2 due to the ambipolar nature of the material. Detailed influence of the drain voltage on transfer characteristics is shown in the supporting information (Figure S3-12). All on/off ratios for different modes of operation are also given in supporting information (Table S3-3). Most of the samples were either p-type or n-type in the as-cast films. Only PDPP[T]₂-TF₂ exhibits ambipolar characteristics with high mobility values ($\mu_h = \mu_e = 0.2 \text{ cm}^2\text{V}^{-1}\text{s}^{-1}$).

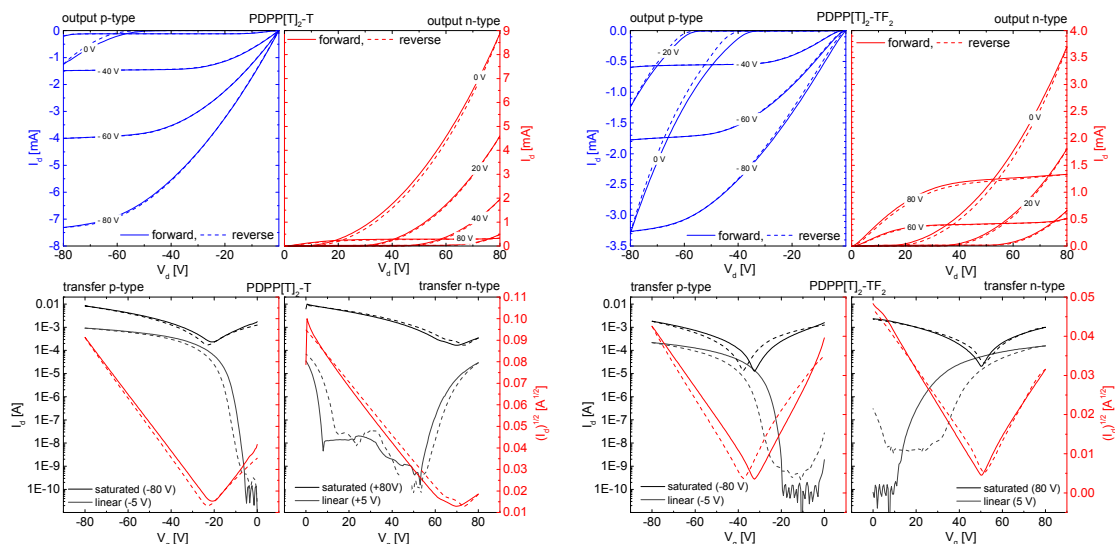


Figure 3-4. Representative OFET I - V curves in p-channel (blue output) and n-channel operation (red output) for PDPP[T]₂-T (left) and PDPP[T]₂-TF₂ (right). Solid lines represent forward scans, dashed lines the reverse scans in all graphs. In transfer curves (bottom), the black and grey plots indicate the transfer characteristics in the saturation and linear operation regime, respectively. I - V curves for the PDPP[Py]₂ and PDPP[Ph]₂ polymers can be found in supporting information Figure S3-12.

Table 3-3. Average OFET-Mobilities of the different PDPPs in a bottom gate / bottom contact configuration in as cast and annealed films.

Polymer	as cast		annealed ^{a)}	
	μ_h^b [cm ² V ⁻¹ s ⁻¹]	μ_e^b [cm ² V ⁻¹ s ⁻¹]	μ_h^b [cm ² V ⁻¹ s ⁻¹]	μ_e^b [cm ² V ⁻¹ s ⁻¹]
PDPP[T] ₂ -T	0.094 ± 0.02	-	0.53 ± 0.07 ^{c)}	-
PDPP[T] ₂ -TF ₂	0.10 ± 0.02	0.06 ± 0.01	0.22 ± 0.03 ^{d)}	0.19 ± 0.03 ^{d)}
PDPP[Py] ₂ -T	-	0.03 ± 0.003	-	0.55 ± 0.08 ^{c)}
PDPP[Py] ₂ -TF ₂	-	0.11 ± 0.02	-	0.13 ± 0.02 ^{c)}
PDPP[Ph] ₂ -T	(6 ± 3) × 10 ⁻⁴	-	(6 ± 2) × 10 ^{-4 e)}	-
PDPP[Ph] ₂ -TF ₂	(9 ± 0.4) × 10 ⁻⁵	(2 ± 0.2) × 10 ⁻⁴	(1 ± 0.5) × 10 ^{-4 e)}	(2 ± 0.3) × 10 ^{-4 e)}

^{a)}Annealing conditions as described in footnote, ^{b)} μ_h : hole mobility, μ_e : electron mobility, determined by linear fitting of $I_{ds}^{0.5}$ -Plot in saturated regime, values are averaged over a minimum of 4 to 8 devices for each measurement, ^{c)}250 °C 30 min, ^{d)}200 °C 15 min, ^{e)}100 °C 15 min.

Among the whole series, the PDPP[T]₂ system shows three orders of magnitude higher hole mobilities ($\mu_h = 10^{-1}$ cm²V⁻¹s⁻¹) than PDPP[Ph]₂ copolymers, which show the lowest values ($\mu_h = 10^{-4}$ cm²V⁻¹s⁻¹). In the case of pyridyl-flanked PDPPs no hole mobility could be measured even at high gate voltages. However, the highest electron mobility was observed for PDPP[Py]₂-TF₂ ($\mu_e = 10^{-1}$ cm²V⁻¹s⁻¹). Thus, the flanking aryl units have a very pronounced influence on the type of charge carrier transport, as well as charge carrier mobility values; thienyl being

highly suitable for hole transport, whereas pyridyl for electron transport. In all the copolymers the fluorination of the comonomer improves the electron transport considerably in as cast films. In addition, a threshold voltage shift towards more negative voltages was observed for the fluorinated derivatives. Generally, all devices showed increased charge carrier mobilities upon thermal annealing. In order to exploit the improved crystalline packing during annealing, all the samples were annealed at the highest possible temperatures in the range of 200-250 °C, if the samples were not dewetting or showing decreased performance in this range. In the case of PDPP[Ph]₂ copolymers 100 °C was chosen due to dewetting issues in the liquid crystalline phase above this temperature. After annealing, the observed influence of the flanking aryl units remains. Additionally, the crystalline PDPP[T]₂ and PDPP[Py]₂ copolymers exhibit maximum influence of annealing on both hole and electron mobilities. Thus, the highest hole mobility was obtained for PDPP[T]₂-T (average: 0.53 cm²V⁻¹s⁻¹, best: 0.64 cm²V⁻¹s⁻¹) and the highest electron mobility for PDPP[Py]₂-T (average: 0.55 cm²V⁻¹s⁻¹, best: 0.67 cm²V⁻¹s⁻¹). These are very high charge carrier mobility values obtained for PDPPs using SiO₂ as the gate dielectric. For example, a one order of magnitude lower hole mobility (0.05 cm²V⁻¹s⁻¹) was reported for the reference copolymer PDPP[T]₂-T.^[9] The liquid crystalline PDPP[Ph]₂ copolymers do not exhibit any change in either hole or electron mobility on thermal treatment. The observed charge carrier properties can be summarized as follows: The highly crystalline copolymers exhibit the highest charge carrier mobilities whereas the liquid crystalline copolymers show three orders of magnitude lower values. On annealing, the mobility is improved only for the crystalline samples. With respect to flanking aryl units, both thiophene and pyridyl with the smallest dihedral angles favor high mobilities which can be understood as due to improved planarization and interchain packing. Additionally, no detectable hole mobility and the highest electron mobility in the whole series was observed for the pyridyl-flanked PDPPs. The effect of fluorination is also pronounced in the electron mobility values. The exact contribution of orientation effects in these samples, especially in the crystalline ones, cannot be elucidated without additional experimental techniques, such as near edge xray absorption fine-structure spectroscopy (NEXAFS) or grazing incidence wide angle xray scattering (GIWAXS).

3.2.4.2 SCLC

To study the influence of electron-rich and electron-deficient moieties as aryl-flanking units and comonomers on bulk charge transport properties, both hole and electron mobilities were determined by fitting measured *I-V* characteristics using the empirical Murgatroyd formula (Equation 1)^[46] in single carrier SCLC devices.

$$J = \frac{9}{8} \epsilon_r \epsilon_0 \mu_0 \exp\left(0.89 \gamma \sqrt{F}\right) \frac{V^2}{L^3} \quad (1)$$

Here *J* is the current density, ϵ_s the relative permittivity of the material (~ 3.5), ϵ_0 the permittivity of vacuum, μ_0 the charge carrier mobility at zero field, γ the field dependence

parameter, F the average electric field across the active layer, V the voltage across the active layer, and L the thickness of the polymer layer. In the Murgatroyd formula two independent variables, namely the zero field mobility (μ_0) and the field dependence parameter (γ), are varied to fit the measured I - V curve. The usefulness of the Murgatroyd formula over the classical Mott-Gurney equation^[47] is that it is able to fit a broader range of I - V curves and also masks other effects, such as charge carrier-density dependent transport^[48] and trapping influence.^[49] However, γ is generally very sensitive to disorder and to the electrodes of the device. It is therefore hard to determine in a consistent way for different devices.^[50] To compare the bulk charge transport properties of a series of materials in a simple and consistent way, an effective charge carrier mobility was determined from all devices at a same field, $F = 1.5 \times 10^7 \text{ V m}^{-1}$, using the Poole-Frenkel relationship (Equation 2).

$$\mu(F) = \mu_0 \exp\left(\gamma\sqrt{F}\right) \quad (2)$$

The reporting of charge mobility at a constant field summarizes the information of two independent parameters (μ_0 and γ) in a single parameter and allows a straightforward charge mobility comparison across different materials.^[51] The field value, $F = 1.5 \times 10^7 \text{ V m}^{-1}$, was chosen as it represents a typical field at short circuit condition in thin film solar cell devices and also the SCLC fits were good around this field value for all the I - V curves reported in this article.

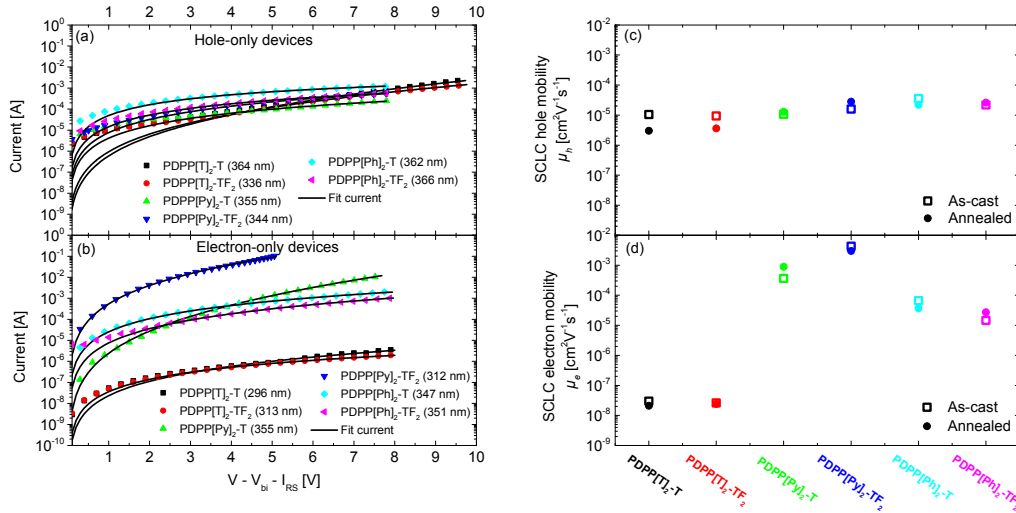


Figure 3-5. The I - V characteristics of as-cast PDDP films measured at room temperature in (a) hole-only and (b) electron-only device configuration. The solid lines represent the SCLC fit with field dependent mobility. The corresponding film thicknesses are mentioned within the parentheses. The I - V characteristics were corrected for the built-in voltage (V_{bi}) and the voltage drop (IR) over the contacts. Log-log plots of (a) and (b) are given in Figure S3-14. The effective SCLC charge carrier mobility of holes (c) and electrons (d) at an electric field of $1.5 \times 10^7 \text{ V/m}$ in different PDDP films. The mobility in as-cast films is depicted as un-filled squares while that in annealed films as filled circles. Each as-cast data point represents the average of 3 sets of devices produced for varying film thicknesses in the range of 200–600 nm.

The charge mobility value in every as-cast film was checked for reproducibility and consistency by repeating the experiment for different active layer thicknesses (supporting information Figure S3-13). Representative I - V curves of different PDPPs for as-cast films in hole-only and electron-only devices are shown in Figure 3-5(a) and (b), respectively. The effective hole and electron mobilities averaged over different film thickness devices are depicted in Figure 3-5(c) and (d).

Table 3-4. The average effective SCLC charge carrier mobility of holes (μ_h) and electrons (μ_e) in PDPP as-cast films for varying film thicknesses. The charge mobility in annealed films for single film thickness (around 350 nm) is also mentioned. The thienyl- and pyridinyl- films were annealed at 200 °C for 15 min. The phenyl- films were annealed at 100 °C for 15 min.

Polymer	As Cast		Annealed	
	μ_h	μ_e	μ_h	μ_e
	[cm ² V ⁻¹ s ⁻¹]	[cm ² V ⁻¹ s ⁻¹]	[cm ² V ⁻¹ s ⁻¹]	[cm ² V ⁻¹ s ⁻¹]
PDPP[T] ₂ -T	$(1.0 \pm 0.5) \times 10^{-5}$	$(3.0 \pm 0.9) \times 10^{-8}$	3.0×10^{-6}	2.1×10^{-8}
PDPP[T] ₂ -TF ₂	$(9.4 \pm 3.3) \times 10^{-6}$	$(2.6 \pm 1.5) \times 10^{-8}$	3.6×10^{-6}	2.4×10^{-8}
PDPP[Py] ₂ -T	$(1.1 \pm 0.9) \times 10^{-5}$	$(3.7 \pm 2.5) \times 10^{-4}$	1.3×10^{-5}	8.9×10^{-4}
PDPP[Py] ₂ -TF ₂	$(1.6 \pm 0.7) \times 10^{-5}$	$(4.3 \pm 0.1) \times 10^{-3}$	2.8×10^{-5}	3.0×10^{-3}
PDPP[Ph] ₂ -T	$(3.6 \pm 0.2) \times 10^{-5}$	$(6.6 \pm 3.1) \times 10^{-5}$	2.2×10^{-5}	3.7×10^{-5}
PDPP[Ph] ₂ -TF ₂	$(2.2 \pm 0.1) \times 10^{-5}$	$(1.5 \pm 0.6) \times 10^{-5}$	2.6×10^{-5}	2.7×10^{-5}

Table 3-4 summarizes the charge carrier mobilities of holes and electrons in PDPP films averaged over different thicknesses. A complete table listing film thicknesses and fitting parameters for all the devices can be found in the supporting information (Table S3-4 and Table S3-5). Furthermore, the charge carrier mobilities from the annealed films are also depicted in Figure 3-5(c) and (d) and the mobility values are mentioned in Table 3-4. As shown in Figure 3-5(c), the SCLC hole mobility does not vary significantly for the investigated set of materials. The hole mobility in all cases was in the order of 10^{-5} cm²V⁻¹s⁻¹ and seemed not to be affected by fluorination either. It is interesting to note that the hole mobility measured in OFETs was in the order of 10^{-1} cm²V⁻¹s⁻¹ for all polymers except the PDPP[Ph]₂ system. In contrast to the hole transport, the electron mobility was severely influenced by the aryl flanking unit. Both PDPP[T]₂-T and PDPP[T]₂-TF₂ showed the lowest bulk electron mobilities in the order of 10^{-8} cm²V⁻¹s⁻¹. In comparison, the PDPP[Py]₂-T shows up to 4 orders of magnitude better electron mobility ($\mu_e = 3.7 \times 10^{-4}$ cm²V⁻¹s⁻¹). The electron transport in the PDPP[Ph]₂ polymers was in between thienyl- and pyridinyl-PDPPs with mobilities in the range of $\mu_e = 3 \times 10^{-5}$ cm²V⁻¹s⁻¹. Upon fluorination, PDPP[Py]₂-TF₂, exhibits a considerable improvement of an order of magnitude in electron mobility resulting in a maximum bulk electron mobility of 4.3×10^{-3} cm²V⁻¹s⁻¹. To the best of our knowledge, this is among the

highest bulk electron mobilities reported for polymers^[52] and it is comparable to electron mobilities reported for fullerene derivatives.^[53] Annealing does not seem to influence either of the hole or electron mobility values suggesting that the expected crystallization effects in annealed films do not overcome grain-boundary effects in a bulk sample which do not have any orientation preferences. This is in contrast to the observed advantages of annealing in an interface-device, such as OFET, where orientation effects can play a big role. In short, the electron mobility results demonstrate that the flanking aromatic units (Ar) adjacent to the bicyclic DPP core have a more significant influence on the bulk electron transport than the fluorination in the class of DPP polymers. Moreover, the synthetic strategy to combine a pyridyl-flanking unit with a difluorothiophene comonomer proved to be highly efficient for electron transport.

3.3 Conclusion

Six polymers based on diketopyrrolo[3,4-*c*]pyrrole having varying flanking aryl units and thiophene or 3,4-difluorothiophene as the comonomer have been synthesized in order to elucidate the influence of structural variation on optical, thermal and electronic properties. This is the first comprehensive and comparative study of interdependence of diverse properties obtained via a change in chemical structure. On a comparison of flanking units, namely thiophene, pyridine and phenyl, profound influence on structural order, optical gap and charge carrier properties could be ascertained. For example, thienyl or pyridyl flanking units causing low dihedral angles favor planarization of the chains and interchain packing in solid state resulting in low optical gap, high structural order and very high charge carrier mobilities. On the other hand, the phenyl flanking unit, which leads to large torsional angles in the polymer backbone, causes a 2D liquid crystalline order and also shows the lowest charge carrier mobilities. In addition to the flanking aryl units the physical properties could also be tuned by using suitable comonomers varying in their electron deficiency. Thus, 3,4-difluorothiophene comonomer in combination with the electron withdrawing pyridyl flanking unit delivers one of the best electron transport polymer materials with a comparable bulk electron mobility to PCBM ($\mu_e = 4 \times 10^{-3} \text{ cm}^2\text{V}^{-1}\text{s}^{-1}$). An additional effect of fluorination is the increased crystallinity irrespective of the nature of flanking aryl units. This can be understood as due to decreased polymer chain-mobility in the fluorinated copolymers induced by a higher rigidity of the backbone and stronger π - π interactions. Such a detailed fundamental study regarding the influence of structural variation on semiconductor polymer properties allows a rational design of low-bandgap polymers in order to tune one or the other physical properties relevant for applications. Thus, the absorption can be extended up to the NIR region by shifting the absorption onset to $> 1000 \text{ nm}$ by changing the flanking unit from phenyl to thiophene. On the other hand, the incorporation of pyridyl units without any steric hindrance with the DPP

core maintains the crystallinity resulting in very good electron transport materials. A comparison of OFET and SCLC measurements gives a clear picture regarding the different contributions towards charge transport properties in thin film and bulk which are relevant for organic electronics and OPV applications. For example, the pyridinyl-flanked DPP copolymers show exclusively n-type behavior in OFET configuration whereas good ambipolar transport is observed in bulk SCLC measurements. Interestingly, the bulk hole mobility is completely independent of the nature of flanking units as well as fluorination of the comonomer. On the contrary, the electron transport is strongly influenced by these structural variations.

3.4 Experimental Section

3.4.1 Materials and methods

All commercial reagents were used without further purification unless otherwise noted. Microwave reactions were conducted in sealed containers using a Biotage Initiator Eight+ microwave. ^1H NMR (300 MHz) spectra were recorded on a Bruker AC 300 spectrometer and calibrated according to the respective solvent resonance signal. Gel permeation chromatography (GPC) analysis was carried out on an Agilent (Polymer Laboratories Ltd.) PL-GPC 220 high temperature chromatographic unit equipped with DP (differential pressure), RI (refractive index) and LS (light scattering at 15° and 90°) detectors and three linear mixed bed columns of PLgel 13 μm (Olexis) with a linear MW operating range: 500 - 15,000,000 g mol^{-1} . GPC analysis was performed at 150°C using 1,2,4-trichlorobenzene as the mobile phase. The samples were prepared by dissolving the polymer (0.1 wt-%) in the mobile phase solvent in an external oven and the solutions were run without filtration. The molecular weights of the samples were referenced to linear polystyrene ($M_w = 162 - 6,000,000 \text{ g mol}^{-1}$, $K = 12.100$ and $\text{Alpha} = 0.707$) and were not corrected with K and Alpha values for the measured sample. Cyclic voltammetry was performed under moisture- and oxygen-free conditions using a 0.1 M tetra-*n*-butylammonium hexafluorophosphate in acetonitrile electrolyte solution. A standard three-electrode assembly connected to a potentiostat (model 263A, EG&G Princeton Applied Research) was used at a scanning rate of 100 mV s^{-1} . The working electrode was a $10 \text{ }\Omega/\square$ ITO coated glass substrate. The polymers were spincoated onto the ITO substrates from chloroform at 3 mg/mL and 1500 rpm to obtain thicknesses of $10\text{-}20 \text{ nm}$. A platinum wire in acetonitrile was used as counter electrode and the quasi-reference electrode consisted of an Ag wire in an $\text{AgNO}_3/\text{acetonitrile}$ solution (0.1 M). The measurements were calibrated with an external ferrocene/ferrocenium standard, IP and EA values were calculated considering the solvent effects as per a published procedure^[41] using Equation 3 and 4 where the workfunction of Fc/Fc^+

is taken to be -5.23 eV. The reduction half-step potential $E_{1/2}^{\text{red}}$ (vs Fc/Fc⁺) is negative whereas the oxidation half-step potential $E_{1/2}^{\text{ox}}$ (vs Fc/Fc⁺) is positive.

$$EA \approx -5.23\text{eV} - E_{1/2}^{\text{red}}(\text{vs Fc/Fc}^+) \quad (3)$$

$$IP \approx -5.23\text{eV} - E_{1/2}^{\text{ox}}(\text{vs Fc/Fc}^+) \quad (4)$$

Absorption measurements were carried out on a JASCO V-670 spectrophotometer. Photoluminescence measurements were carried out on a JASCO FP-8600 spectrofluorometer. Optical properties in solution were measured in chloroform at a concentration of 0.01 mg/mL, films were spincoated on glass slides from a 7 mg/mL chloroform solution. Combined SAXS and WAXS measurements of the bulk material were carried out at the SAXS beamline of the Australian Synchrotron using a Pilatus 1M and a Pilatus 200k detector. The beam energy and detector distances were chosen in such a way, that there was a small overlap between the SAXS and WAXS signal, so that the resulting curves could be stitched together at $q = 0.81$.

3.4.2 Device preparation and characterization

Organic thin film transistors substrates in bottom gate / bottom contact configuration were bought from Fraunhofer IPMS (OFET Gen. 4). Heavily n-doped silicon (doping at wafer surface: $n \sim 3 \times 10^{17} \text{ cm}^{-3}$) was used as substrate and gate electrode. Thermally grown silicon oxide ($230 \text{ nm} \pm 10 \text{ nm}$) was used as the gate dielectric. Gold electrodes (30 nm on 10 nm ITO as adhesion layer) were used as source and drain contacts. The channel width was 10 mm for all devices and the channel length varied from 5 μm to 20 μm . The substrates were cleaned subsequently in acetone and 2-propanol in an ultrasonic bath for 10 minutes each. Treatment in an ozone oven at 50 °C for 20 min was followed by immersion in a 1 wt-% solution of octadecyltrichlorosilane in toluene at 60 °C for 60 min. After rinsing with toluene and 2-propanol the substrates were dried and the polymer was spincoated from a 4 mg/mL chloroform solution at 5000 rpm under ambient conditions. Devices were measured in a nitrogen atmosphere using an Agilent B1500 Semiconductor Parameter Analyzer. The devices were annealed in a nitrogen atmosphere at a maximum of 0.9 ppm O₂ at the temperatures given in the main text. Mobilities were calculated from the slopes in the $(I_d)^{0.5}$ - V_g plots in the saturation regime using Equation 5 where I_d is the drain current, W the channel width, L the channel length, C_i the capacitance, V_g the gate voltage and V_T the threshold voltage, respectively.

$$I_d \approx \frac{W}{2L} C_i \mu (V_g - V_T)^2 \quad (5)$$

Single carrier space-charge-limited-current (SCLC) devices in diode configuration were prepared for charge carrier mobility determination of holes and electrons within the layer stack of glass/ITO/PEDOT:PSS/Polymer/Au and glass/ITO/PEDOT:PSS/Polymer/Ca/Al, respectively. For hole only devices, a hole-injecting layer of PEDOT:PSS (HTL solar (40 nm) from CleviosTM) was spin coated onto cleaned patterned ITO glass substrates. For electron-only devices, a 40 nm thick layer of Zinc oxide (ZnO) was spin coated onto the patterned substrates using Sol-gel method. After depositing the bottom layers, polymer solutions (12-25 mg/mL in chloroform) were doctor bladed on top under inert conditions resulting in film thicknesses in the range of 200 to 600 nm. A set of films were also annealed in an inert atmosphere for 15 min at the temperatures given in the main text. Subsequently, the top electrodes (Au and Ca/Al) were thermally evaporated onto the polymer layers in respective devices under high vacuum. The devices had an active area of 9 mm² which is determined by the overlap of the ITO and the evaporated top electrode. Dark current-voltage I - V measurements were made under inert environment at room temperature with a Keithley 2400 source measure unit. Before these I - V measurements, the electron-only devices were exposed to 100 mW/cm² illumination for 3 min from an AM 1.5 class A solar simulator to improve the conductivity of the ZnO layer.^[54] After the light treatment, the I - V from the electron-only devices were nearly symmetric around 0 V. For mobility evaluation, forward bias voltages, i.e. hole injection from PEDOT:PSS, and reverse bias voltages, i.e. electron injection from ZnO were considered in hole-only and electron-only devices, respectively. The charge carrier mobilities were evaluated by fitting measured I - V characteristics in a voltage range from 2 to 7 V using the Murgatroyd formula.^[46] Prior to fitting, the measured I - V characteristics were corrected for the built in voltage (V_{bi}) and the voltage drop (IR) across contacts. The contact resistance was determined from a reference device without polymer layer and was found to be 27 Ω for both kind of devices. Considering the work function of the electrons and the Fermi-level pinning^[55] at contacts, the V_{bi} of 0.2 V and 0.0 V was assumed for hole-only and electron-only devices, respectively.

3.5 Acknowledgements

We acknowledge financial support from the Bavarian State Ministry of Education, Science and the Arts (Solar technologies go hybrid). C.J.M. thanks the Fonds der Chemischen Industrie for funding the PhD with a Kekulé scholarship and the German National Academic Foundation for other support during the PhD. Support from the Elitenetzwerk Bayern (ENB), Macromolecular Science is also kindly acknowledged. This research was undertaken on the SAXS beamline at the Australian Synchrotron, Victoria, Australia.

3.6 References

- [1] S. Qu, H. Tian, *Chem. Commun.* **2012**, 48, 3039.
- [2] C. B. Nielsen, M. Turbiez, I. McCulloch, *Adv. Mater.* **2012**, 25, 1859.
- [3] J. C. Bijleveld, V. S. Gevaerts, D. Di Nuzzo, M. Turbiez, S. G. J. Mathijssen, D. M. de Leeuw, M. M. Wienk, R. A. J. Janssen, *Adv. Mater.* **2010**, 22, E242.
- [4] S. Holliday, J. E. Donaghey, I. McCulloch, *Chem. Mater.* **2014**, 26, 647.
- [5] W. Li, K. H. Hendriks, A. Furlan, W. S. Roelofs, S. C. Meskers, M. M. Wienk, R. A. Janssen, *Adv. Mater.* **2014**, 26, 1565.
- [6] J. C. Bijleveld, R. A. M. Verstrijden, M. M. Wienk, R. A. J. Janssen, *J. Mater. Chem.* **2011**, 21, 9224.
- [7] W. Li, K. H. Hendriks, A. Furlan, W. S. C. Roelofs, M. M. Wienk, R. A. J. Janssen, *J. Am. Chem. Soc.* **2013**, 135, 18942.
- [8] H. Bronstein, E. Collado-Fregoso, A. Hadipour, Y. W. Soon, Z. Huang, S. D. Dimitrov, R. S. Ashraf, B. P. Rand, S. E. Watkins, P. S. Tuladhar, I. Meager, J. R. Durrant, I. McCulloch, *Adv. Funct. Mater.* **2013**, 23, 5647.
- [9] J. C. Bijleveld, A. P. Zoombelt, S. G. J. Mathijssen, M. M. Wienk, M. Turbiez, D. M. de Leeuw, R. A. J. Janssen, *J. Am. Chem. Soc.* **2009**, 131, 16616.
- [10] S. Venkatesan, N. Adhikari, J. Chen, E. C. Ngo, A. Dubey, D. W. Galipeau, Q. Qiao, *Nanoscale* **2014**, 6, 1011.
- [11] S. Cho, J. Lee, M. Tong, J. H. Seo, C. Yang, *Adv. Funct. Mater.* **2011**, 21, 1910.
- [12] J. H. Park, E. H. Jung, J. W. Jung, W. H. Jo, *Adv. Mater.* **2013**, 25, 2583.
- [13] C. Tanase, E. J. Meijer, P. W. M. Blom, D. M. de Leeuw, *Phys. Rev. Lett.* **2003**, 91, 216601.
- [14] W. Li, W. S. Roelofs, M. Turbiez, M. M. Wienk, R. A. Janssen, *Adv. Mater.* **2014**, 26, 3304.
- [15] J. Lee, M. Jang, S. M. Lee, D. Yoo, T. J. Shin, J. H. Oh, C. Yang, *ACS Appl Mater Interfaces* **2014**, 6, 20390.
- [16] H. Zhou, L. Yang, A. C. Stuart, S. C. Price, S. Liu, W. You, *Angew. Chem.* **2011**, 123, 3051.
- [17] D. J. Crouch, D. Sparrowe, M. Heeney, I. McCulloch, P. J. Skabara, *Macromol. Chem. Phys.* **2010**, 211, 2642.

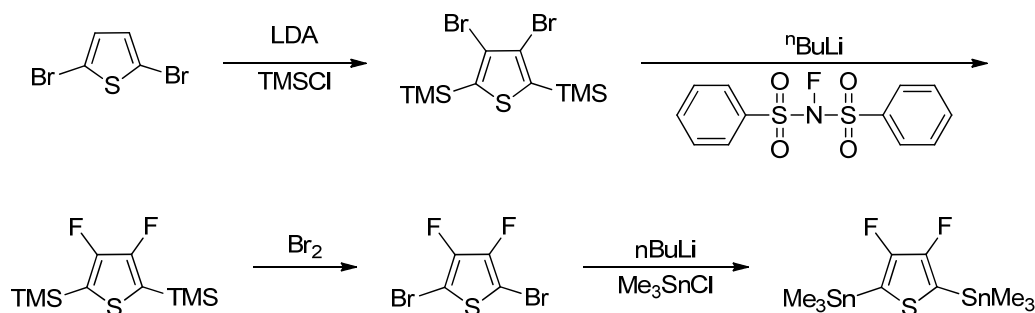
- [18] K. Neumann, C. Schwarz, A. Köhler, M. Thelakkat, *J. Phys. Chem. C* **2014**, *118*, 27.
- [19] N. E. Jackson, B. M. Savoie, K. L. Kohlstedt, M. Olvera de la Cruz, G. C. Schatz, L. X. Chen, M. A. Ratner, *J. Am. Chem. Soc.* **2013**, *135*, 10475.
- [20] H. J. Spencer, P. J. Skabara, M. Giles, I. McCulloch, S. J. Coles, M. B. Hursthouse, *J. Mater. Chem.* **2005**, *15*, 4783.
- [21] L. Chen, D. Deng, Y. Nan, M. Shi, P. K. L. Chan, H. Chen, *J. Phys. Chem. C* **2011**, *115*, 11282.
- [22] S.-Y. Liu, H.-Y. Li, M.-M. Shi, H. Jiang, X.-L. Hu, W.-Q. Li, L. Fu, H.-Z. Chen, *Macromolecules* **2012**, *45*, 9004.
- [23] C. Kanimozhi, M. Naik, N. Yaacobi-Gross, E. K. Burnett, A. L. Briseno, T. D. Anthopoulos, S. Patil, *J. Phys. Chem. C* **2014**, *118*, 11536.
- [24] B. Sun, W. Hong, Z. Yan, H. Aziz, Y. Li, *Adv. Mater.* **2014**, *26*, 2636.
- [25] J. W. Jo, S. Bae, F. Liu, T. P. Russell, W. H. Jo, *Adv. Funct. Mater.* **2015**, *25*, 120.
- [26] Z. Fei, M. Shahid, N. Yaacobi-Gross, S. Rossbauer, H. Zhong, S. E. Watkins, T. D. Anthopoulos, M. Heeney, *Chem Commun (Camb)* **2012**, *48*, 11130.
- [27] J. W. Jo, J. W. Jung, H.-W. Wang, P. Kim, T. P. Russell, W. H. Jo, *Chem. Mater.* **2014**, *26*, 4214.
- [28] C.-H. Chen, Y.-J. Cheng, C.-Y. Chang, C.-S. Hsu, *Macromolecules* **2011**, *44*, 8415.
- [29] Y.-J. Cheng, C.-H. Chen, Y.-S. Lin, C.-Y. Chang, C.-S. Hsu, *Chem. Mater.* **2011**, *23*, 5068.
- [30] Y. X. Xu, C. C. Chueh, H. L. Yip, F. Z. Ding, Y. X. Li, C. Z. Li, X. Li, W. C. Chen, A. K. Jen, *Adv. Mater.* **2012**, *24*, 6356.
- [31] M.-F. Falzon, A. P. Zoombelt, M. M. Wienk, R. A. J. Janssen, *Phys. Chem. Chem. Phys.* **2011**, *13*, 8931.
- [32] A. K. Palai, S. P. Mishra, A. Kumar, R. Srivastava, M. N. Kamalasanan, M. Patri, *Macromol. Chem. Phys.* **2010**, *211*, 1043.
- [33] A. C. Rochat, L. Cassar, A. Iqbal, *J. Chem. Soc. Chem. Commun.* **1983**, 94911.
- [34] M. Vala, J. Vyňuchal, P. Toman, M. Weiter, S. Luňák Jr, *Dyes and Pigments* **2010**, *84*, 176.
- [35] M. Vala, M. Weiter, J. Vyňuchal, P. Toman, S. Luňák, *J. Fluoresc.* **2008**, *18*, 1181.
- [36] R. M. Osuna, R. P. Ortiz, M. C. Ruiz Delgado, Y. Sakamoto, T. Suzuki, V. Hernández, J. T. López Navarrete, *J. Phys. Chem. B* **2005**, *109*, 20737.

- [37] Y. Sakamoto, S. Komatsu, T. Suzuki, *J. Am. Chem. Soc.* **2001**, *123*, 4643.
- [38] B. Carsten, F. He, H. J. Son, T. Xu, L. Yu, *Chem. Rev.* **2011**, *111*, 1493.
- [39] B. S. Nehls, U. Asawapirom, S. Földner, E. Preis, T. Farrell, U. Scherf, *Adv. Funct. Mater.* **2004**, *14*, 352.
- [40] H. Bronstein, Z. Chen, R. S. Ashraf, W. Zhang, J. Du, J. R. Durrant, P. Shakya Tuladhar, K. Song, S. E. Watkins, Y. Geerts, M. M. Wienk, R. A. J. Janssen, T. Anthopoulos, H. Sirringhaus, M. Heeney, I. McCulloch, *J. Am. Chem. Soc.* **2011**, *133*, 3272.
- [41] K. Gräf, M. A. Rahim, S. Das, M. Thelakkat, *Dyes and Pigments* **2013**, *99*, 1101.
- [42] C. M. Cardona, W. Li, A. E. Kaifer, D. Stockdale, G. C. Bazan, *Adv. Mater.* **2011**, *23*, 2367.
- [43] J.-L. Bredas, *Materials Horizons* **2014**, *1*, 17.
- [44] K. H. Hendriks, W. Li, M. M. Wienk, R. A. Janssen, *J. Am. Chem. Soc.* **2014**, *136*, 12130.
- [45] F. Liu, C. Wang, J. K. Baral, L. Zhang, J. J. Watkins, A. L. Briseno, T. P. Russell, *J. Am. Chem. Soc.* **2013**, *135*, 19248.
- [46] P. N. Murgatroyd, *Journal of Physics D - Applied Physics* **1970**, *3*, 151.
- [47] N. F. Mott, R. W. Gurney, *Electronic Processes in Ionic Crystals*, The Clarendon Press: Oxford, UK, **1940**.
- [48] C. Tanase, P. Blom, D. de Leeuw, *Physical Review B* **2004**, *70*, 193202.
- [49] Z. Chiguvare, V. Dyakonov, *Physical Review B* **2004**, *70*, 235207.
- [50] L. J. A. Koster, *Physical Review B* **2010**, *81*, 205318.
- [51] J. C. Blakesley, F. A. Castro, W. Kylberg, G. F. A. Dibb, C. Arantes, R. Valaski, M. Cremona, J. S. Kim, J.-S. Kim, *Org. Electron.* **2014**, *15*, 1263.
- [52] R. Steyrleuthner, M. Schubert, F. Jaiser, J. C. Blakesley, Z. Chen, A. Facchetti, D. Neher, *Adv. Mater.* **2010**, *22*, 2799.
- [53] M. A. Muth, W. Mitchell, S. Tierney, T. A. Lada, X. Xue, H. Richter, M. Carrasco-Orozco, M. Thelakkat, *Nanotechnology* **2013**, *24*, 484001.
- [54] M. R. Lilliedal, A. J. Medford, M. V. Madsen, K. Norrman, F. C. Krebs, *Sol. Energy Mater. Sol. Cells* **2010**, *94*, 2018.
- [55] S. Braun, W. R. Salaneck, M. Fahlman, *Adv. Mater.* **2009**, *21*, 1450.

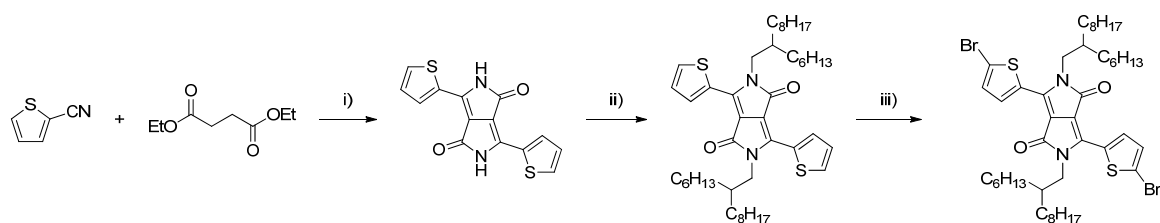
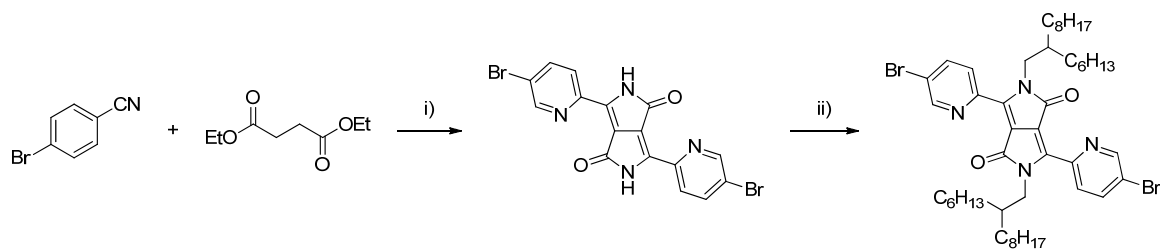
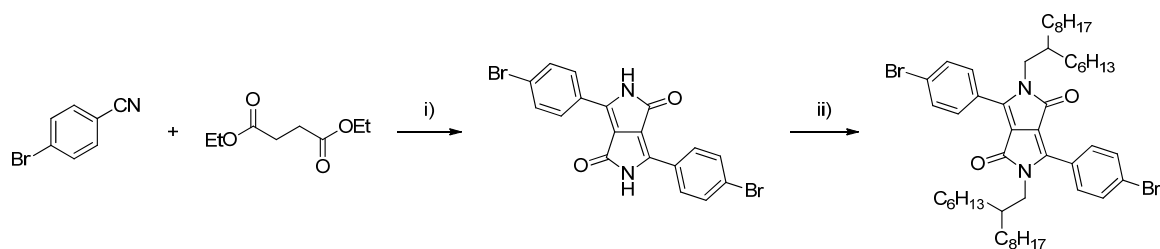
Supporting Information

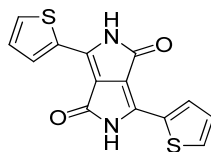
Monomer Syntheses	108
DPP[T] ₂ monomer.....	109
DPP[Py] ₂ monomer.....	110
DPP[Ph] ₂ monomer.....	111
3,4-Difluoro-2,5-bis(trimethylstannyl)-thiophene monomer.....	112
Monomer Characterization	115
Polymer Syntheses.....	124
Polymer Characterization	127
GPC (Gel permeation chromatography)	127
Flash-DSC.....	130
Polarization Micrographs	131
Absorption and Photoluminescence.....	132
Cyclic Voltammetry	133
CCDC library analysis	134
Devices.....	135
OFET IV curves	135
Additional SCLC data	138
Supporting References	141

Monomer Syntheses

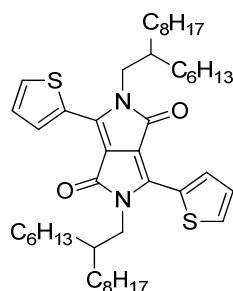


Scheme S3-1. Synthesis of the 3,4-difluorothiophene monomer.

Scheme S3-2. Synthesis of the dithienyl-DPP monomer DPP[T]₂{2HD}₂Br₂.Scheme S3-3. Synthesis of the dipyridinyl-DPP monomer DPP[Py]₂{2HD}₂Br₂.Scheme S3-4. Synthesis of the diphenyl-DPP monomer DPP[Ph]₂{2HD}₂Br₂.

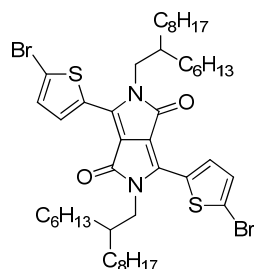
DPP[T]₂ monomer.

DPP[T]₂. Sodium 2-methylbutan-2-olate (8.85 g, 80 mmol) were provided in 34 mL 2-methylbutan-2-ol to give a white suspension. The mixture was heated to 100 °C until the base was completely dissolved. Thiophene-2-carbonitrile (5 mL, 53.6 mmol) was added and diethyl succinate (4.5 mL, 26.8 mmol) was added dropwise at a rate of 2.5 mL/h using a syringe pump. The deeply red reaction mixture was stirred for another 2 h at 100 °C thereafter. The mixture was cooled to 65 °C, 100 mL methanol were added and the solution was neutralized with acetic acid (5 mL, 88 mmol) to precipitate the product. The resulting suspension was refluxed for 2 min and filtrated while still warm. The red precipitate was washed with methanol and water several times until the filtrate remained colourless. Drying at high vacuum yielded 5.37 g 3,6-di(thiophen-2-yl)pyrrolo[3,4-c]pyrrole-1,4(2H,5H)-dione (17.88 mmol, 67%) as a red powder.



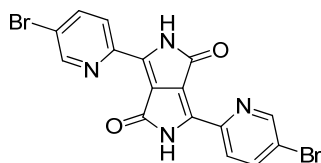
DPP[T]₂{2HD}₂. In a 250 mL three necked flask DPP[T]₂ (10 g, 33.3 mmol), potassium carbonate (18.41 g, 133 mmol) and 18-crown-6 (0.616 g, 2.33 mmol) were suspended in 110 mL anhydrous DMF. The solution was stirred at 130 °C for 1 h before 1-bromo-2-hexyldecane (25.4 g, 83.0 mmol) was added within 5 min. The reaction mixture was then stirred for 42 h at 100 °C. After cooling to room temperature and addition of 100 mL water the solution was stirred for 30 min. Another 100 mL water were added and the mixture was extracted with chloroform (4 x 100 mL). The combined organic phases were washed with 200 mL water and dried over magnesium sulfate. Solvents were removed under reduced pressure and the crude product was redissolved in 300 mL 1,4-dioxane. 1.4 mL concentrated hydrochloric was added and the mixture was stirred at 130 °C for 2 h. After cooling to room temperature the solution was filtrated over a plug of basic aluminium oxide. Flash chromatography (silica gel) using hexane:dichloromethane 1:1 as eluent and subsequent

recrystallization of the product from ethanol yielded 10.060 g DPP[T]₂{2HD}₂ (13.43 mmol, 40%) as a red fibrous solid.

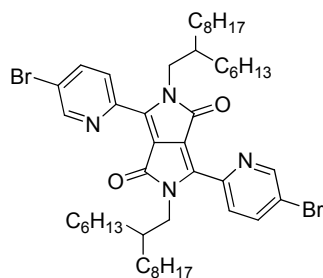


DPP[T]₂{2HD}₂Br₂. DPP[T]₂{2HD}₂ (4.608 g, 6.15 mmol) and *N*-bromosuccinimide (2.408 g, 13.53 mmol) were dissolved in 62 mL chloroform. The solution was purged with argon for 5 min. After stirring at room temperature for 70 h in the dark, the mixture was poured into 200 mL methanol and filtered. The residue was washed with excess hot methanol twice and subsequently recrystallized from ethanol to yield 3.729 g DPP[T]₂{2HD}₂Br₂ (4.11 mmol, 67%) as a metallic red solid.

DPP[Py]₂ monomer.

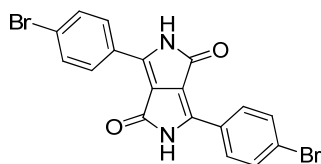


DPP[Py]₂Br₂. In a 250 mL three-necked flask sodium-2-methylbutan-2-olate (5.42 g, 49.2 mmol) was provided in 50 mL 2-methylbutan-2-ol to give a white suspension. The mixture was stirred at 100 °C until the base was dissolved. 5-Bromopicolinonitrile (9 g, 49.2 mmol) was added in one portion and diethyl succinate (4.09 mL, 24.6 mmol) was added dropwise within 5 min via syringe. The resulting black-purple suspension was stirred for another 2 h at 100 °C. After cooling to 40 °C 10 mL methanol were added carefully and the solution was acidified with 30 mL acetic acid to precipitate the product. The suspension was poured into 50 mL water and stirred at room temperature for 30 min. It was then filtrated and washed with excess water and methanol until the filtrate remained colourless. Drying under high vacuum yielded 5.068 g DPP[Py]₂Br₂ (11.3 mmol, 46%) as a red powder.

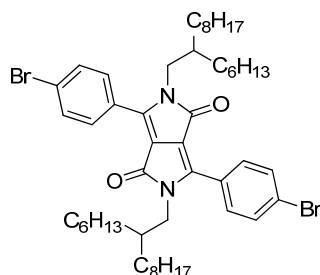


DPP[Py]₂{2HD}₂Br₂. In a 500 mL three-necked flask potassium carbonate (3.08 g, 22.3 mmol) and DPP[Py]₂Br₂ (2.50 g, 5.58 mmol) were suspended in 112 mL anhydrous DMF. The mixture was heated to 130 °C for 30 min to dissolve all starting materials and deprotonate the DPP. 1-Bromo-2-hexyldecane (6.81 g, 22.3 mmol) was then added dropwise via canula within 5 min. After complete addition the reaction was stirred at 130 °C for 2 h before it was cooled to room temperature. DMF was removed under reduced pressure and the residue was dried under high vacuum before it was redissolved in 60 mL chloroform and washed with 120 mL water once. The aqueous phase was extracted with chloroform (3 x 30 mL) and the combined organic layers were dried over magnesium sulfate. The solvent was removed under reduced pressure and the crude product was recrystallized from ethanol to yield 2.959 g DPP[Py]₂{2HD}₂Br₂ (3.30 mmol, 59%) as a red solid.

DPP[Ph]₂ monomer.

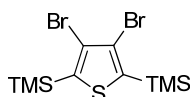


DPP[Ph]₂Br₂. In a 250 mL three-necked flask sodium 2-methylbutan-2-olate (6.05 g, 54.9 mmol) was provided in 55 mL anhydrous 2-methylbutan-2-ol to give a white suspension. The mixture was heated to 100 °C, where the base was dissolved whilst stirring. 4-Bromobenzonitrile (10.0 g, 54.9 mmol) was added in one portion and diethyl succinate (4.57 mL, 27.5 mmol) was added dropwise within 5 minutes via syringe. The solution turned into a black-purple suspension and the reaction mixture was stirred for another 2 h at 100°C. Methanol (50 mL) was added carefully after cooling to 65 °C and the solution was acidified with acetic acid (31.5 mL, 549 mmol) to precipitate the product. The suspension was poured into 200 mL water and stirred slowly at room temperature for 15 min. It was then filtrated. The red precipitate was washed with water and methanol until the filtrate remained colourless. The product was dried at HV overnight to yield 2.597 g DPP[Ph]₂Br₂ (5.82 mmol, 21%) as a red powder.

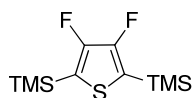


DPP[Ph]₂{2HD}₂Br₂. In a dry 250 mL schlenk flask DPP[Ph]₂Br₂ (3.00 g, 6.73 mmol) and potassium *tert*-butoxide (1.66 g, 14.8 mmol) were suspended in 60 mL anhydrous *N*-methyl-2-pyrrolidone and the mixture was stirred at 80 °C for 30 min before 1-bromo-2-hexyldecane (6.16 g, 20.2 mmol) was added via syringe pump within 60 min. The mixture was then stirred at 80 °C for 20 h. After cooling to room temperature 120 mL toluene were added, the solution was washed with water and finally brine. The organic phase was dried over magnesium sulfate, solvents were removed under reduced pressure. The crude solid was subjected to flash chromatography (silica gel) using a hexane / ethyl acetate gradient (1:1 → 1:5) as mobile phase. The solvent was removed from the product fractions and the product was finally recrystallized from ethanol to afford 802 mg DPP[Ph]₂{2HD}₂Br₂ (896 μmol, 13%) as red crystals.

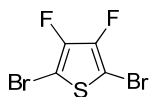
3,4-Difluoro-2,5-bis(trimethylstannyl)-thiophene monomer.



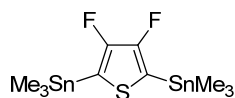
3,4-Dibromo-2,5-bis(trimethylsilyl)-thiophene. In a 1 L three-necked flask diisopropylamine (78 mL, 546 mmol) were dissolved in 250 mL anhydrous THF. The solution was cooled to -78 °C and *n*BuLi (2.5 M in hexane) (218 mL, 546 mmol) were added slowly. Subsequently 2,5-dibromothiophene (27.9 mL, 248 mmol) was added and the solution stirred for 2 h at -78 °C. Chlorotrimethylsilane (76 mL, 595 mmol) was added within 1 h to the yellow solution, the mixture was allowed to warm to room temperature and stirred overnight. The reaction solution was divided in parts of maximal 300 mL. Each part was diluted with 200 mL diethylether and 200 mL water. The phases were separated and the aqueous layer was extracted with diethylether (2 x 100 mL). The combined organic phases were dried over sodium sulfate, filtrated and concentrated under reduced pressure. Vacuum distillation at 10⁻² mbar yielded 90.55 g of 3,4-dibromo-2,5-bis(trimethylsilyl)-thiophene (215 mmol, 92%) as a colourless oil.



3,4-Difluoro-2,5-bis(trimethylsilyl)-thiophene. 3,4-dibromo-2,5-bis(trimethylsilyl)-thiophene (13.626 g, 35.3 mmol) was dissolved in 141 mL anhydrous tetrahydrofuran and cooled to $-78\text{ }^{\circ}\text{C}$. *n*BuLi (2.5 M in hexane) and *N*-fluoro-*N*-(phenylsulfonyl)benzenesulfonamide (abbreviated NFSI) were added at $-78\text{ }^{\circ}\text{C}$ alternately in the following portions: i) BuLi (14.73 mL, 36.83 mmol) within 15 min, stirred for 30 min. NFSI (11.613 g, 36.83 mmol), stirred for 30 min. ii) BuLi (7.34 mL, 18.34 mmol) within 15 min, stirred for 30 min. NFSI (5.784 g, 18.34 mmol), stirred for 30 min. iii) BuLi (3.67 mL, 9.17 mmol), stirred for 30 min. NFSI (2.7892 g, 9.17 mmol), stirred for 30 min. iv) BuLi (1.83 mL, 4.59 mmol), stirred for 30 min. NFSI (1.446 g, 4.586 mmol), stirred for 30 min. v) BuLi (1.83 mL, 4.59 mmol), stirred for 30 min. NFSI (2.225 g, 7.06 mmol), stirred for 30 min. The cooling bath was removed and the mixture was stirred at room temperature overnight. 200 mL 1 M HCl was added to the suspension. The organic layer was separated, washed with brine and dried over magnesium sulfate. After filtration the solution was concentrated under reduced pressure and filtrated over a silica gel plug using hexane as eluent. After removing the hexane under reduced pressure, vacuum distillation at 10 mbar yielded 5.599 g 3,4-difluoro-2,5-bis(trimethylsilyl)-thiophene (21.17 mmol, 60%) as a colourless oil.

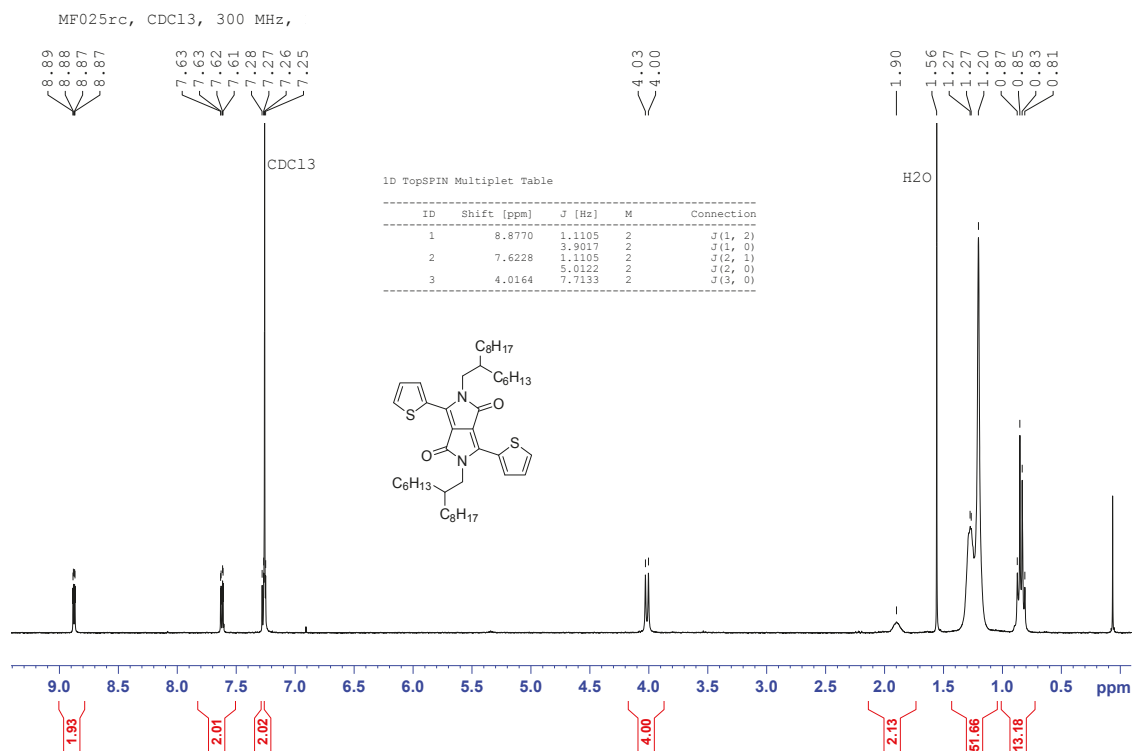
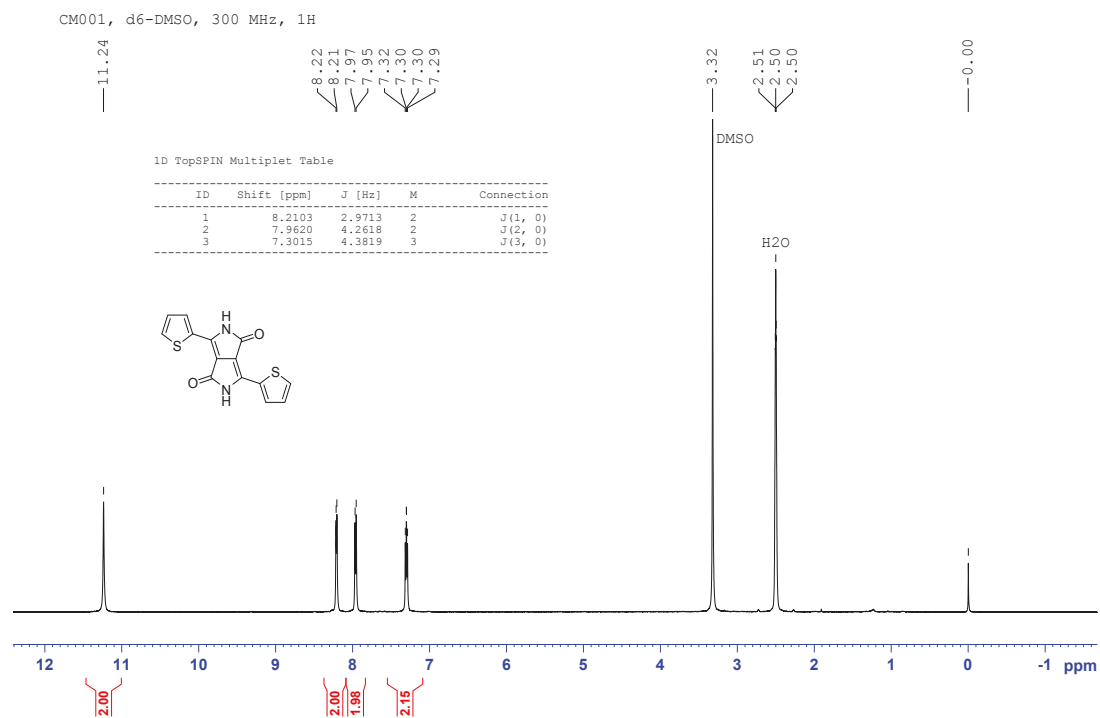


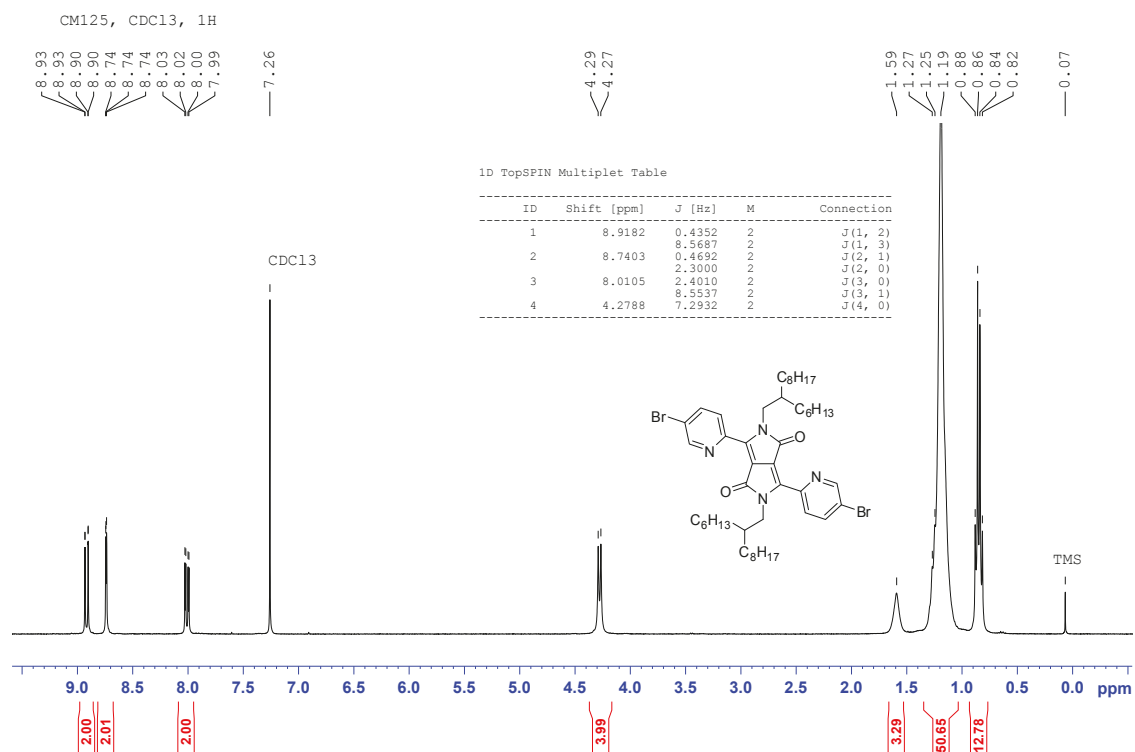
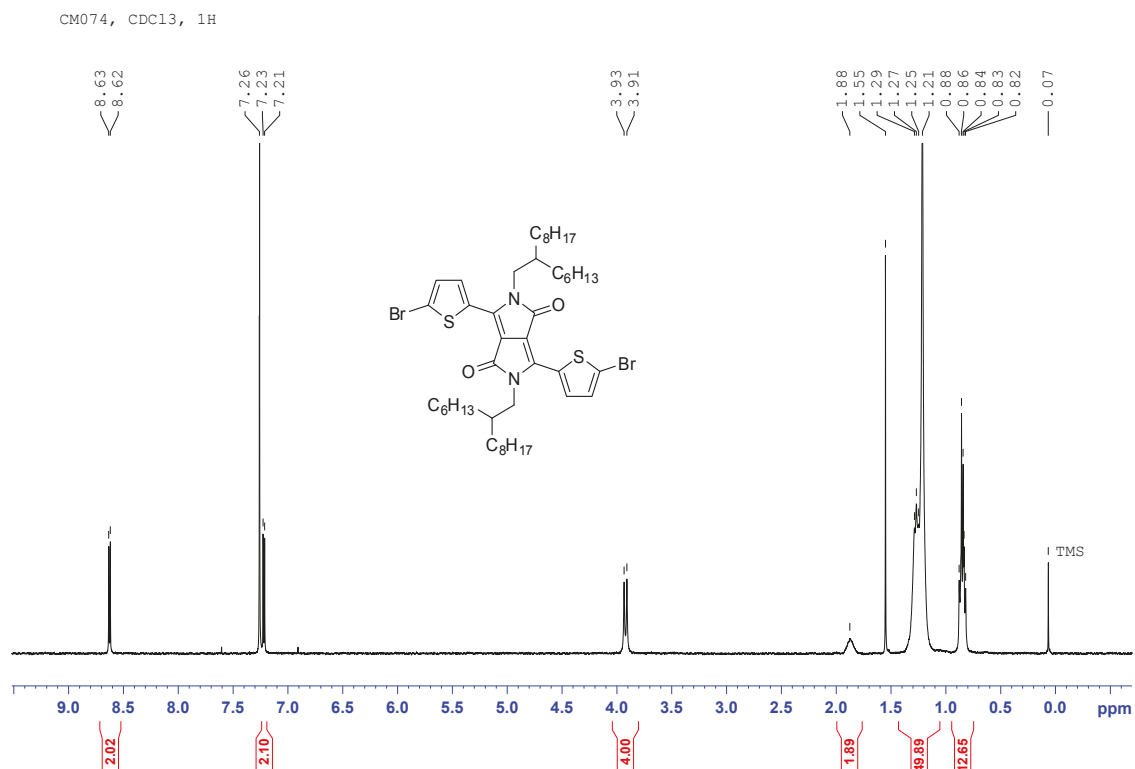
2,5-Dibromo-3,4-difluoro-thiophene. To a solution of 3,4-difluoro-2,5-bis(trimethylsilyl)-thiophene (5.103 g, 19.29 mmol) in 50 mL dichloromethane was added bromine (2.2 mL, 42.4 mmol) at a rate of 0.25 mL/min via syringe pump in order to maintain a gentle reflux. After complete addition the mixture was refluxed overnight at $50\text{ }^{\circ}\text{C}$. The solution was finally poured into 50 mL of a saturated aqueous sodium sulfite solution and extracted with dichloromethane (3 x 50 mL). The combined organic phases were washed with 400 mL 2 M sodium sulfite solution, 300 mL saturated sodium hydrogencarbonate solution and 300 mL brine. The combined organic layers were dried over magnesium sulfate, concentrated under reduced pressure and finally distilled at 10 mbar to yield 4.060 g 2,5-dibromo-3,4-difluoro-thiophene (14.61 mmol, 76%) as a colourless oil.

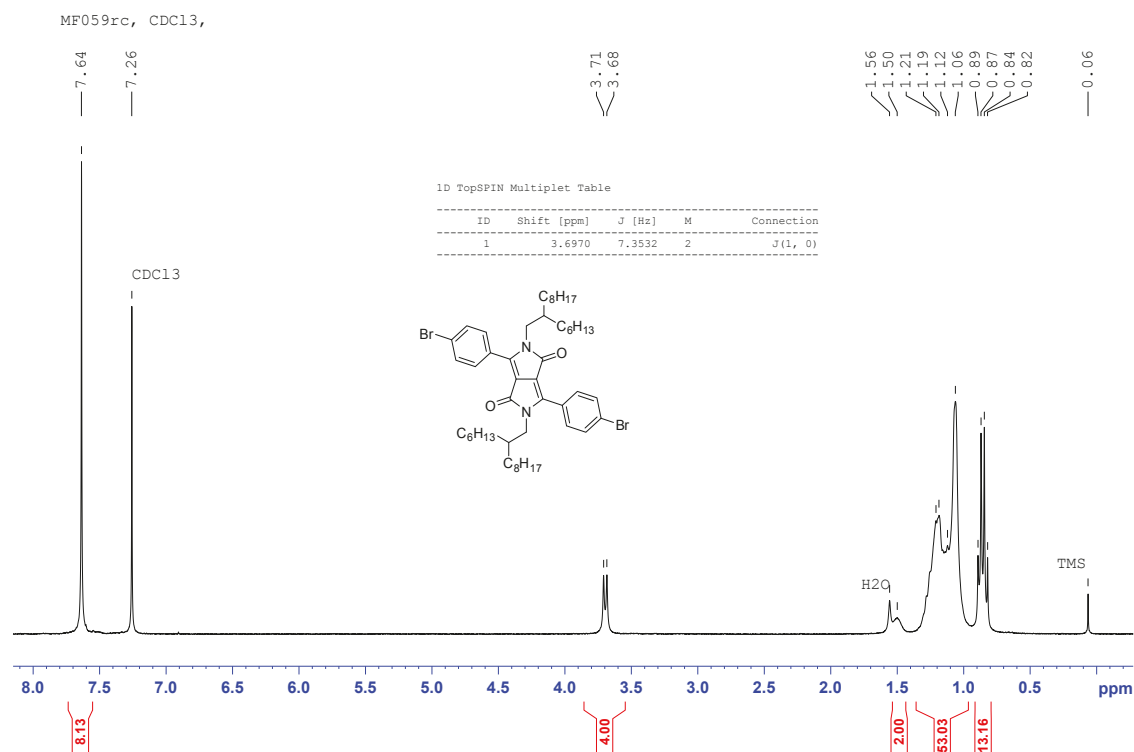
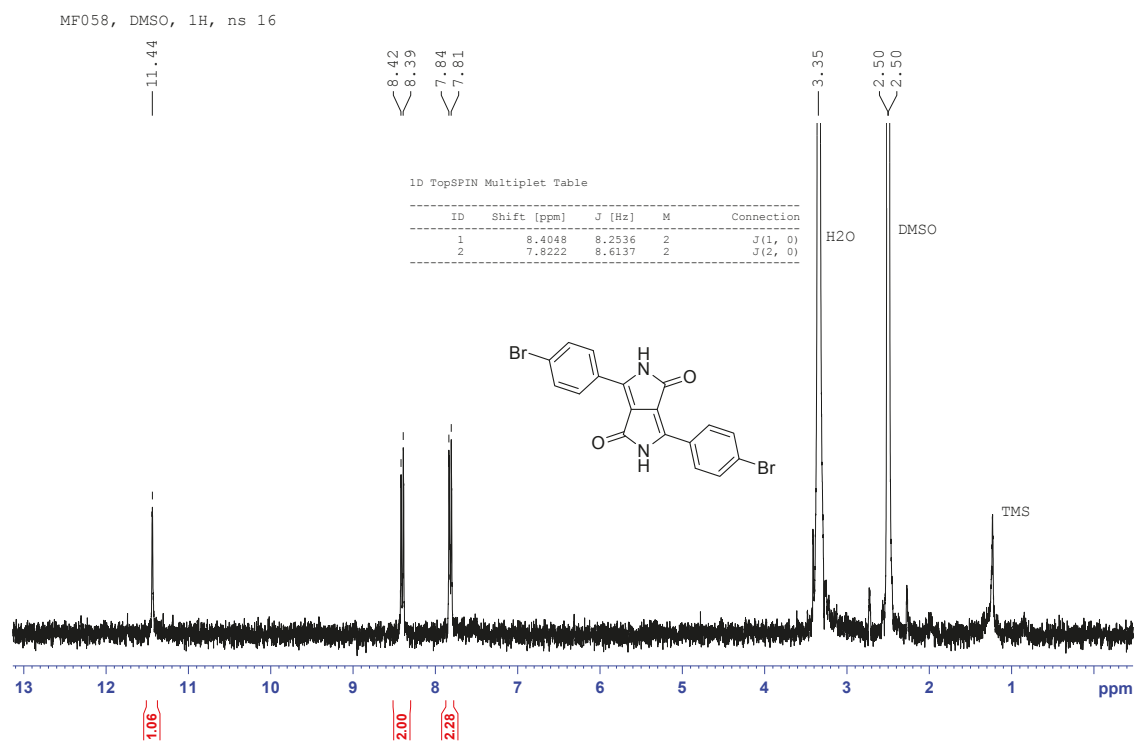


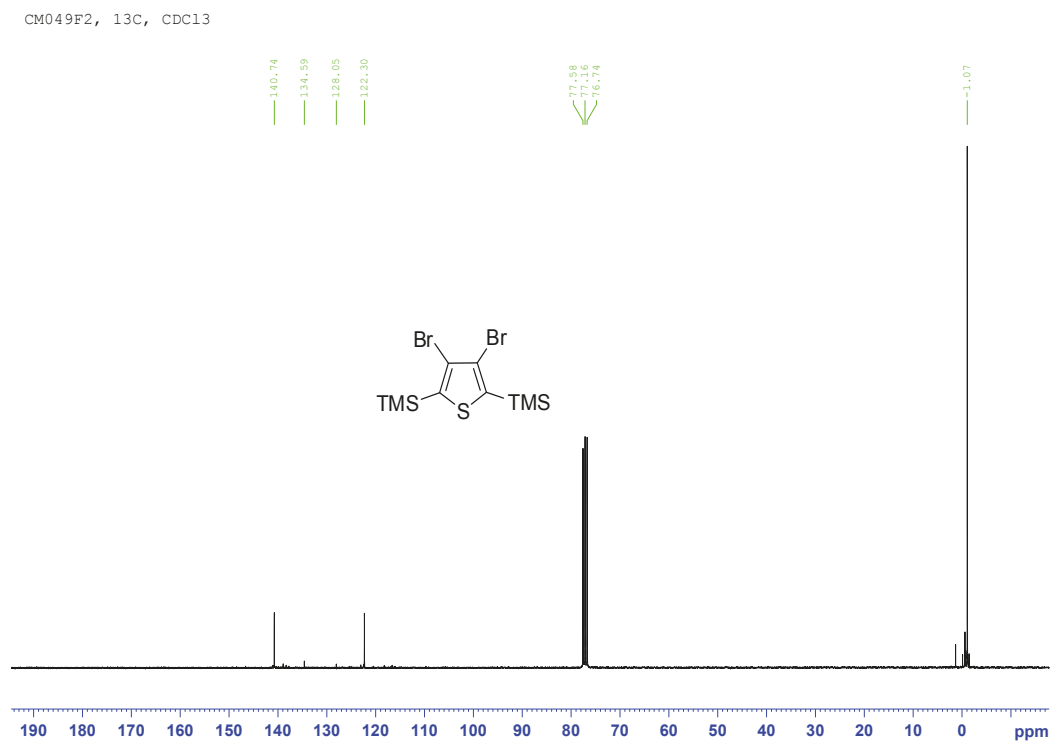
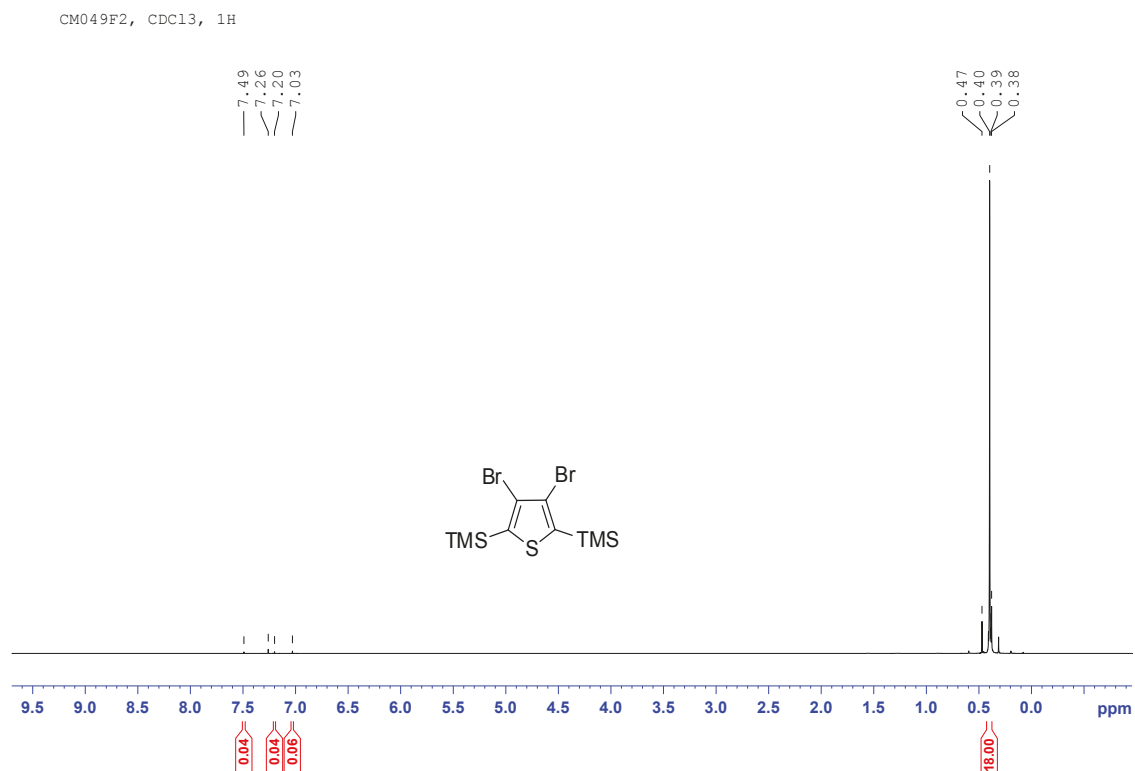
3,4-Difluoro-2,5-bis(trimethylstannyl)-thiophene. To a solution of 2,5-dibromo-3,4-difluorothiophene (2.715 g, 9.77 mmol) in THF (39,1 ml) was added *n*BuLi (2.5 M in hexane) (8.21 ml, 20.52 mmol) at -78 °C under argon. The resulting mixture was stirred at -78 °C for 30 min. A freshly prepared 1 M trimethyltin chloride stock solution in THF (22.4 mL; corresponds to 4.48 g, 22.47 mmol) was then added dropwise and the solution stirred at -78 °C for 1 h before it was allowed to warm to room temperature (within 1 h). Water (30 mL) was added and the mixture extracted with diethyl ether (3 x 50 mL). The organic layer was washed with brine (1 x 100 mL) and dried over magnesium sulfate. Solvents were removed under reduced pressure to obtain 3.972 g of a bright yellow crystalline solid (8.91 mmol, 91%) which was stored without further purification. Samples for use as monomer in Stille-polymerizations and for NMR spectroscopy were recrystallized freshly from hexane (reflux to room temperature to 4 °C) to obtain the product as large white crystals.

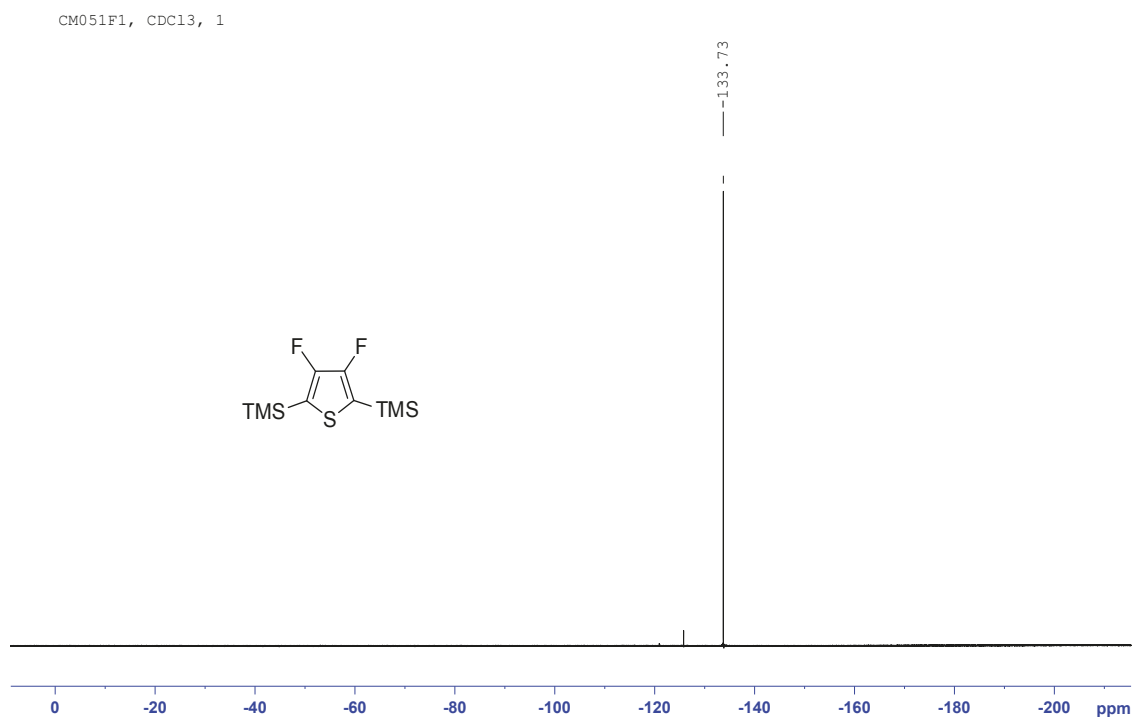
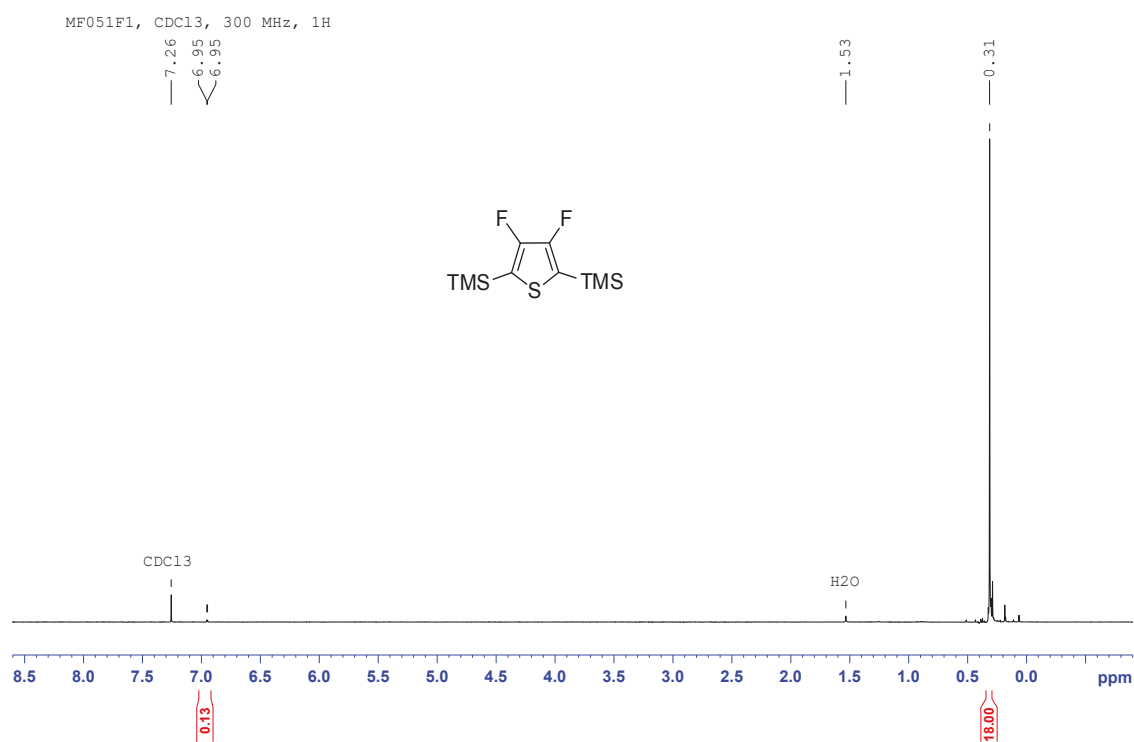
Monomer Characterization

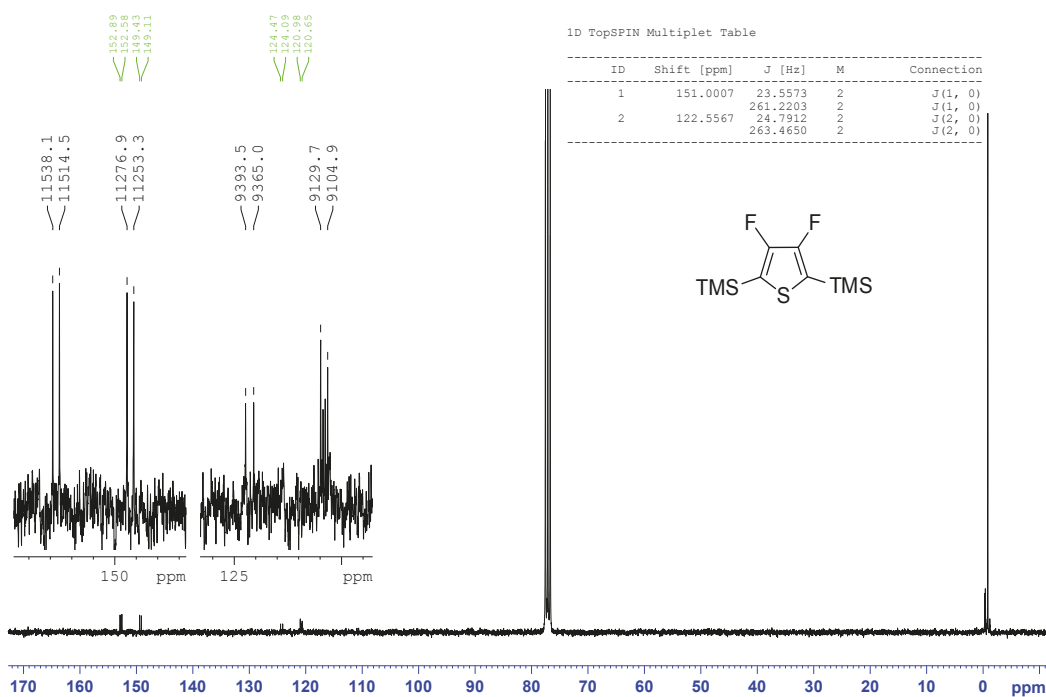
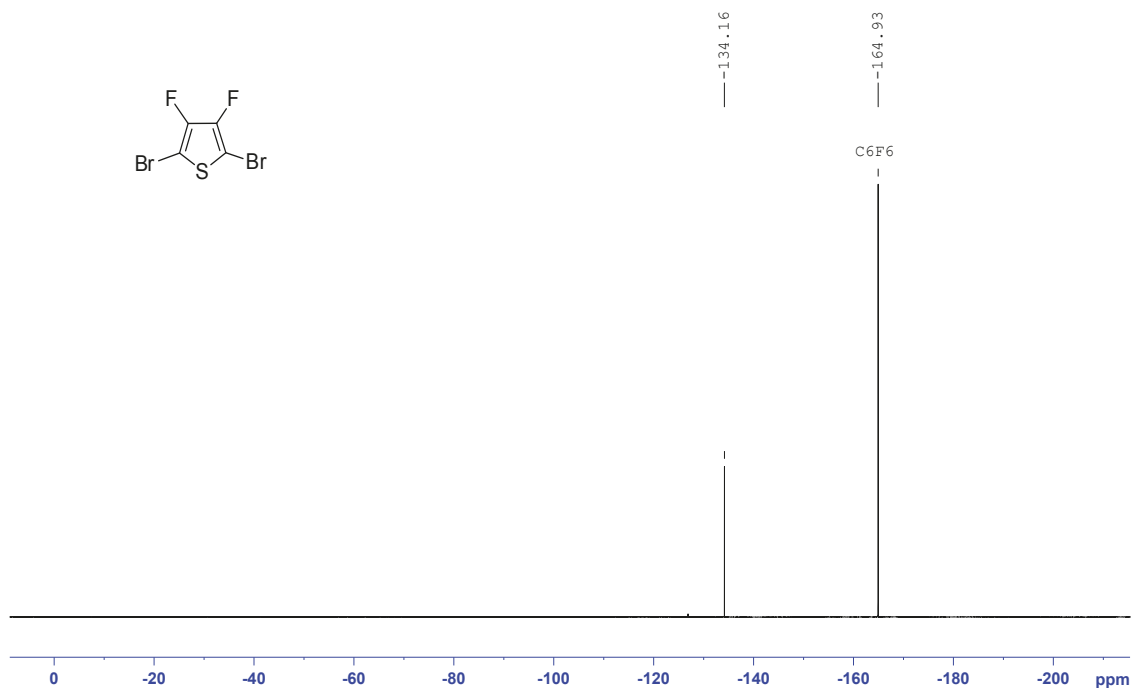


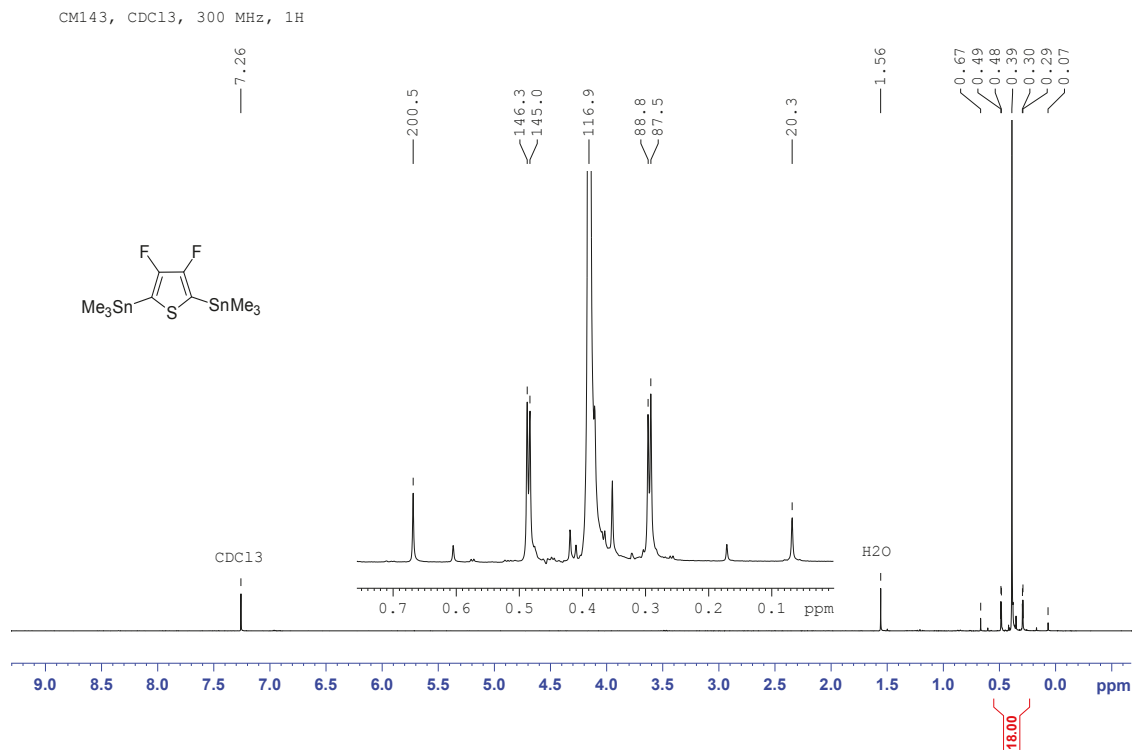
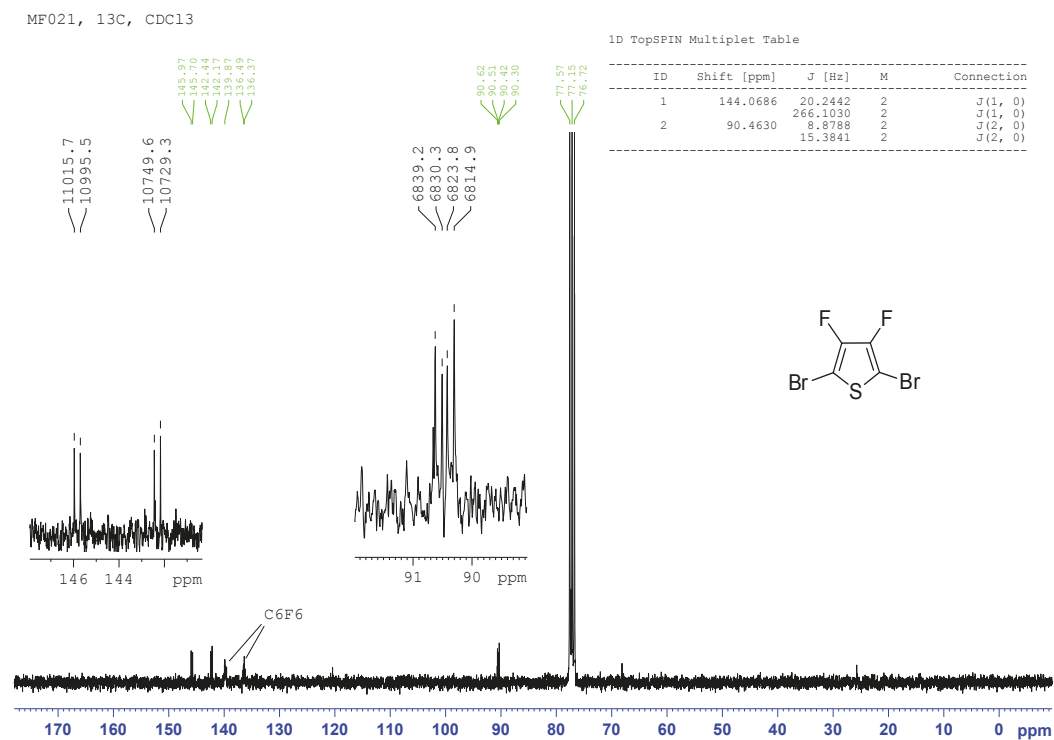




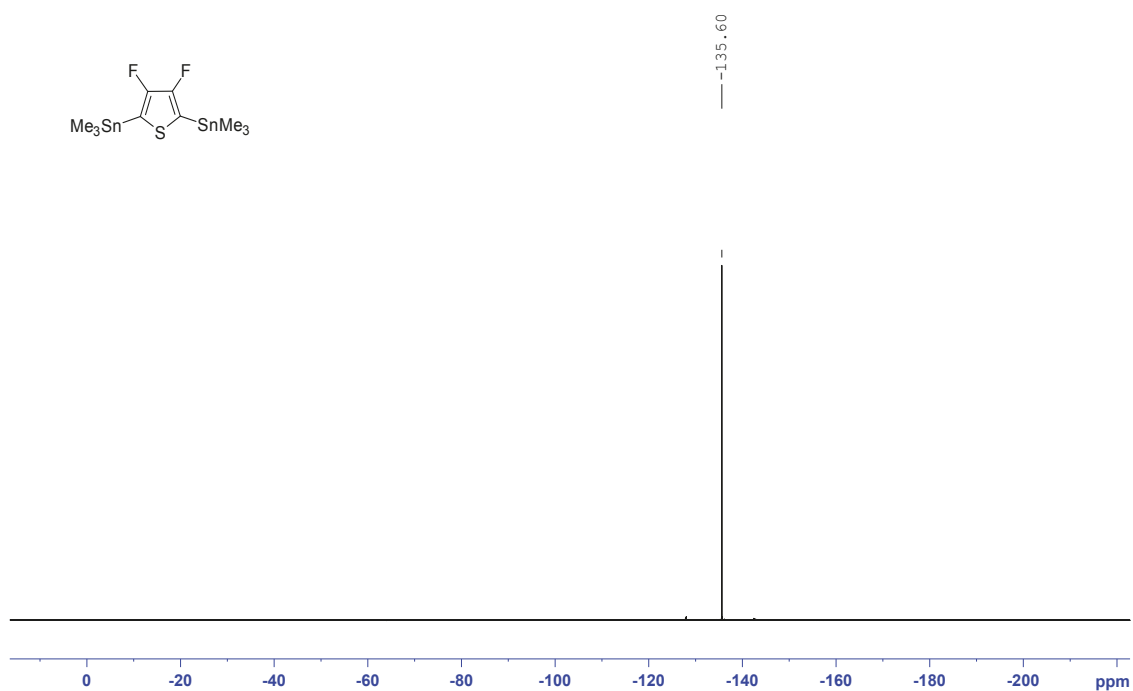
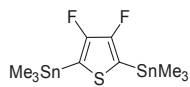




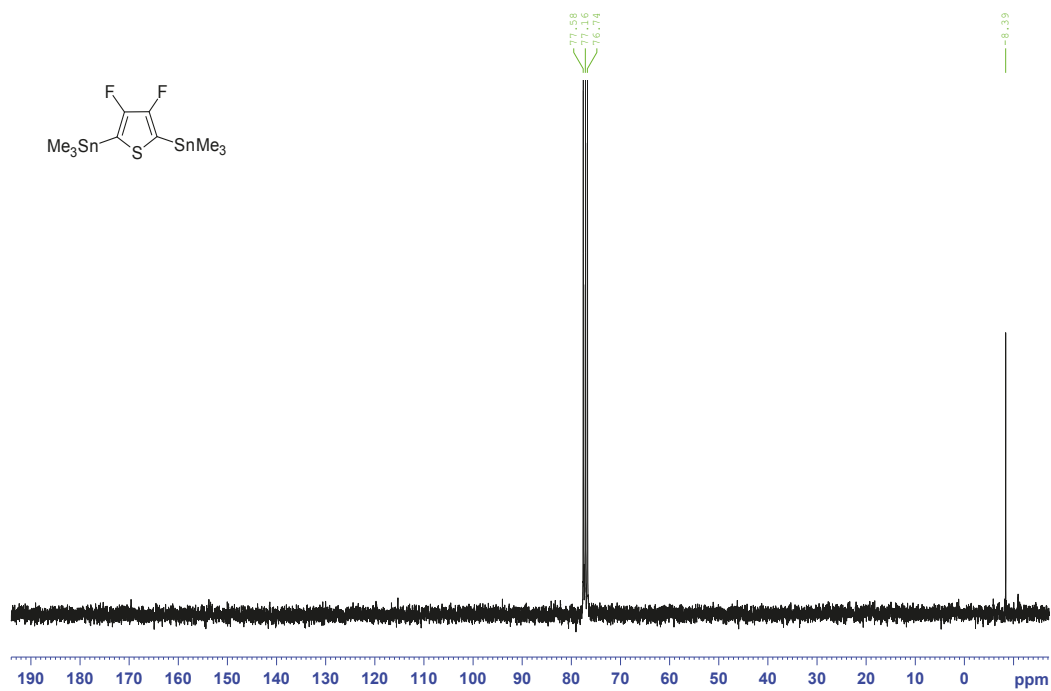
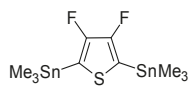
CM051, ^{13}C , CDCl_3

MF021, ^{19}F , CDCl_3


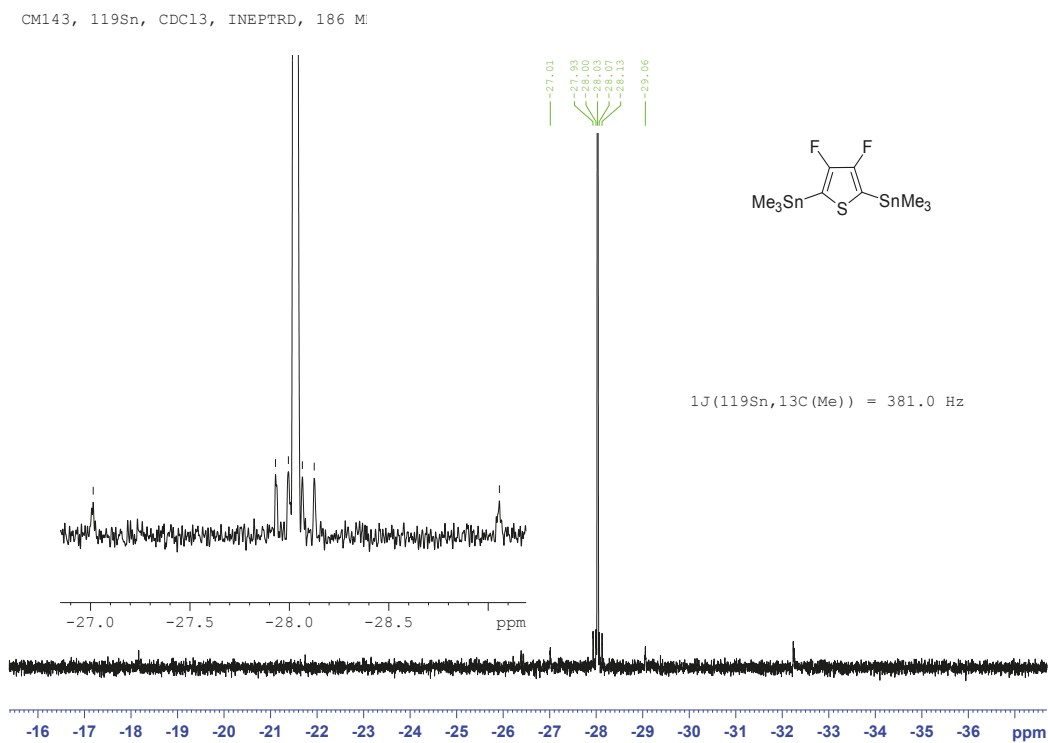
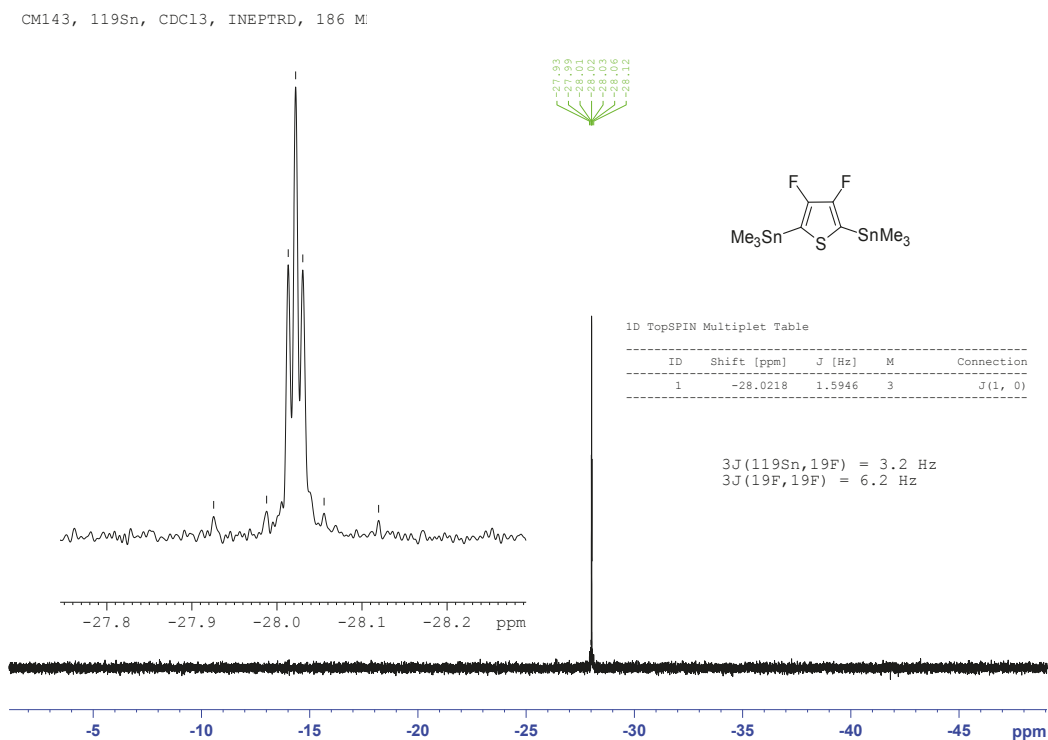


CM143, CDC13, 19F



CM143, 13C, CDC13 (10mg, 1024 scan:





Polymer Syntheses

Monomers were recrystallized freshly before polymerization. All reactions were conducted under argon using a double manifold schlenk line or sealed microwave vials. Glasware was severely dried under high vacuum. Solvents were degassed by three freeze-pump-thaw cycles.

PDPP[T]₂-T. An oven dried microwave vial was loaded with DPP[T]₂{2HD}₂Br₂ (100.93 mg, 0.111 mmol), 2,5-bis(trimethylstannyl)thiophene (45.6 mg, 0.111 mmol), tri-*o*-tolylphosphine (4.06 mg, 13.3 μmol) and finally tris(dibenzylideneacetone)dipalladium(0) (3.29 mg, 3.59 μmol). Dry and degassed chlorobenzene (2.5 mL) was added, the vial was sealed with a septum cap and subsequently purged with argon for 15 min. The mixture was stirred for 30 min at 180 °C in the microwave. After cooling to 50 °C 2-tributyltinthiophene (25 μL, 79 μmol) was added to the viscous green solution using a microliter syringe. The mixture was again heated at 180 °C for 5 min in the microwave, cooled to 50 °C and finally 2-bromothiophene (30 μL, 308 μmol) was added. The mixture was heated to 180 °C for 5 min in the microwave. After cooling to room temperature the polymer was precipitated in 150 mL methanol, filtrated over a 0.45 μm PTFE filter and dried in high vacuum. The crude polymer was subjected to soxhlet extraction using acetone, hexane and chloroform. The chloroform fraction was concentrated to 5 mL under reduced pressure and precipitated in 150 mL methanol. The precipitate was filtrated over a 0.45 μm PTFE filter and dried in high vacuum to obtain PDPP[T]₂-T as a dark purple solid (88 mg, 79%).

PDPP[T]₂-TF₂. An oven dried microwave vial was loaded with DPP[T]₂{2HD}₂Br₂ (152.25 mg, 0.168 mmol), 3,4-difluoro-2,5-bis(trimethylstannyl)thiophene (74.90 mg, 0.168 mmol), tri-*o*-tolylphosphine (6.61 mg, 22 μmol) and finally tris(dibenzylideneacetone)-dipalladium(0) (5.00 mg, 5.5 μmol). Dry and degassed chlorobenzene (3.7 mL) was added, the vial was sealed with a septum cap and subsequently purged with argon for 15 min. The mixture was stirred for 30 min at 180 °C in the microwave. After cooling to 50 °C 2-tributyltinthiophene (25 μL, 79 μmol) was added to the viscous green solution using a microliter syringe. The mixture was again heated at 180 °C for 5 min in the microwave, cooled to 50 °C and finally 2-bromothiophene (30 μL, 308 μmol) was added. The mixture was heated to 180 °C for 5 min in the microwave. After cooling to room temperature the polymer was precipitated in 150 mL methanol, filtrated over a 0.45 μm PTFE filter and dried in high vacuum. The crude polymer was subjected to soxhlet extraction using acetone, hexane, dichloromethane and chloroform. The chloroform fraction was concentrated to 5 mL under reduced pressure and precipitated in 150 mL methanol. The precipitate was filtrated over a 0.45 μm PTFE filter and dried in high vacuum to obtain PDPP[T]₂-TF₂ as a dark purple solid (128 mg, 88%).

PDPP[Py]₂-T. An oven dried microwave vial was loaded with DPP[Py]₂{2HD}₂Br₂ (101.13 mg, 0.113 mmol), 2,5-bis(trimethylstannyl)thiophene (46.22 mg, 0.113 mmol), tri-*o*-tolylphosphine (4.29 mg, 14 μmol) and finally tris(dibenzylideneacetone)dipalladium(0) (3.40 mg, 3.71 μmol). Dry and degassed chlorobenzene (2.5 mL) was added, the vial was sealed with a septum cap and subsequently purged with argon for 15 min. The mixture was stirred for 30 min at 180 °C in the microwave. After cooling to 50 °C 2-tributyltinthiophene (25 μL, 79 μmol) was added to the viscous blue solution using a microliter syringe. The mixture was again heated at 180 °C for 5 min in the microwave, cooled to 50 °C and finally 2-bromothiophene (30 μL, 308 μmol) was added. The mixture was heated to 180 °C for 5 min in the microwave. After cooling to room temperature the polymer was precipitated in 150 mL methanol, filtrated over a 0.45 μm PTFE filter and dried in high vacuum. The crude polymer was subjected to soxhlet extraction using acetone, hexane and chloroform. The hexane fraction was concentrated to dryness under reduced pressure, redissolved in a minimal amount of chloroform and precipitated in 150 mL methanol. The precipitate was filtrated over a 0.45 μm PTFE filter and dried in high vacuum to obtain PDPP[Py]₂-T as a dark purple solid (82 mg, 74%).

PDPP[Py]₂-TF₂. An oven dried microwave vial was loaded with DPP[Py]₂{2HD}₂Br₂ (162.75 mg, 0.181 mmol), 3,4-difluoro-2,5-bis(trimethylstannyl)thiophene (81.04 mg, 0.182 mmol), tri-*o*-tolylphosphine (6.81 mg, 22 μmol) and finally tris(dibenzylideneacetone)-dipalladium(0) (5.04 mg, 5.5 μmol). Dry and degassed chlorobenzene (4.0 mL) was added, the vial was sealed with a septum cap and subsequently purged with argon for 15 min. The mixture was stirred for 2 h at 180 °C in the microwave. After cooling to 50 °C 2-tributyltinthiophene (25 μL, 79 μmol) was added to the viscous blue solution using a microliter syringe. The mixture was again heated at 180 °C for 10 min in the microwave, cooled to 50 °C and finally 2-bromothiophene (30 μL, 308 μmol) was added. The mixture was heated to 180 °C for 10 min in the microwave. After cooling to room temperature the polymer was precipitated in 150 mL methanol, filtrated over a 0.45 μm PTFE filter and dried in high vacuum. The crude polymer was subjected to soxhlet extraction using methanol, acetone, hexane, and chloroform. The chloroform fraction was concentrated to 5 mL under reduced pressure and precipitated in 150 mL methanol. The precipitate was filtrated over a 0.45 μm PTFE filter and dried in high vacuum to obtain PDPP[Py]₂-TF₂ as a dark purple solid (128 mg, 69%).

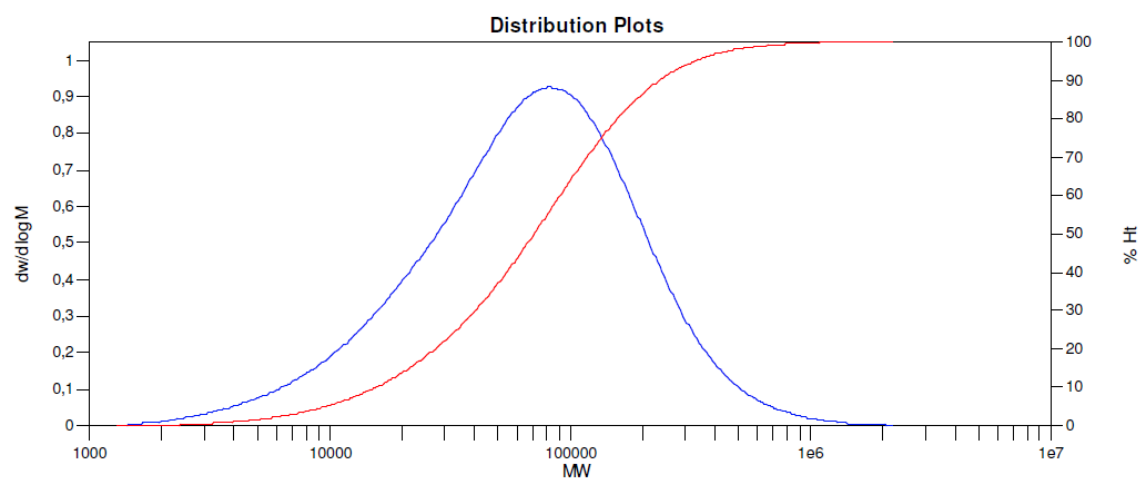
PDPP[Ph]₂-T. An oven dried microwave vial was loaded with DPP[Ph]₂{2HD}₂Br₂ (117.73 mg, 0.132 mmol), 2,5-bis(trimethylstannyl)thiophene (53.09 mg, 0.132 mmol), tri-*o*-tolylphosphine (4.80 mg, 16 μmol) and finally tris(dibenzylideneacetone)dipalladium(0) (3.61 mg, 3.6 μmol). Dry and degassed chlorobenzene (3.6 mL) was added, the vial was sealed with a septum cap and subsequently purged with argon for 15 min. The mixture was stirred

for 40 min at 180 °C in the microwave. After cooling to 50 °C 2-tributyltinthiophene (25 μ L, 79 μ mol) was added to the red solution using a microliter syringe. The mixture was again heated at 180 °C for 5 min in the microwave, cooled to 50 °C and finally 2-bromothiophene (50 μ L, 516 μ mol) was added. The mixture was heated to 180 °C for 10 min in the microwave. After cooling to room temperature the polymer was precipitated in 250 mL methanol and filtrated into a soxhlet thimble. The crude polymer was subjected to soxhlet extraction using methanol, acetone and hexane. The solvent was removed from the hexane fraction under reduced pressure, the solid remains were redissolved in a minimal amount of chloroform and precipitated in 250 mL methanol. The precipitate was filtrated over a 0.45 μ m PTFE filter and dried in high vacuum to obtain PDPP[Ph]₂-T as a dark red solid (94 mg, 87%).

PDPP[Ph]₂-TF₂. An oven dried microwave vial was loaded with DPP[Ph]₂{2HD}₂Br₂ (120.77 mg, 0.135 mmol), 3,4-difluoro-2,5-bis(trimethylstannyl)thiophene (60.15 mg, 0.135 mmol), tri-*o*-tolylphosphine (5.01 mg, 16 μ mol) and finally tris(dibenzylideneacetone)–dipalladium(0) (3.81 mg, 4.2 μ mol). Dry and degassed chlorobenzene (4.0 mL) was added, the vial was sealed with a septum cap and subsequently purged with argon for 15 min. The mixture was stirred for 40 min at 180 °C in the microwave. After cooling to 50 °C 2-tributyltinthiophene (25 μ L, 79 μ mol) was added to the red solution using a microliter syringe. The mixture was again heated at 180 °C for 5 min in the microwave, cooled to 50 °C and finally 2-bromothiophene (50 μ L, 516 μ mol) was added. The mixture was heated to 180 °C for 10 min in the microwave. After cooling to room temperature the polymer was precipitated in 250 mL methanol and filtrated into a soxhlet thimble. The crude polymer was subjected to soxhlet extraction using methanol, acetone and hexane. The solvent was removed from the hexane fraction under reduced pressure, the solid remains were redissolved in a minimal amount of chloroform and precipitated in 250 mL methanol. The precipitate was filtrated over a 0.45 μ m PTFE filter and dried in high vacuum to obtain PDPP[Ph]₂-TF₂ as a dark red solid (67 mg, 58%).

Polymer Characterization

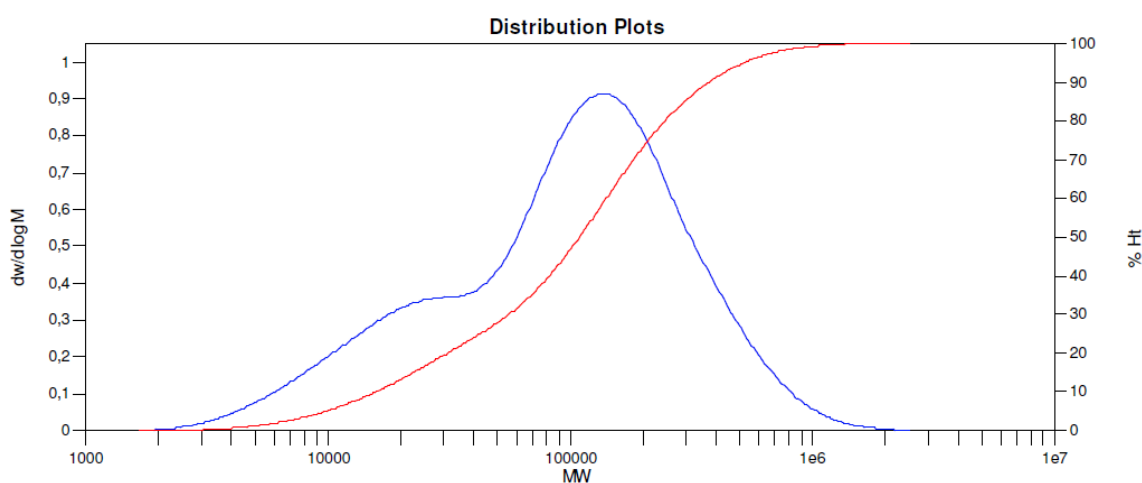
GPC (Gel permeation chromatography)



MW Averages

Peak No	Mp	Mn	Mw	Mz	Mz+1	Mv	PD
1	81671	34258	107696	262060	549724	93604	3.14367

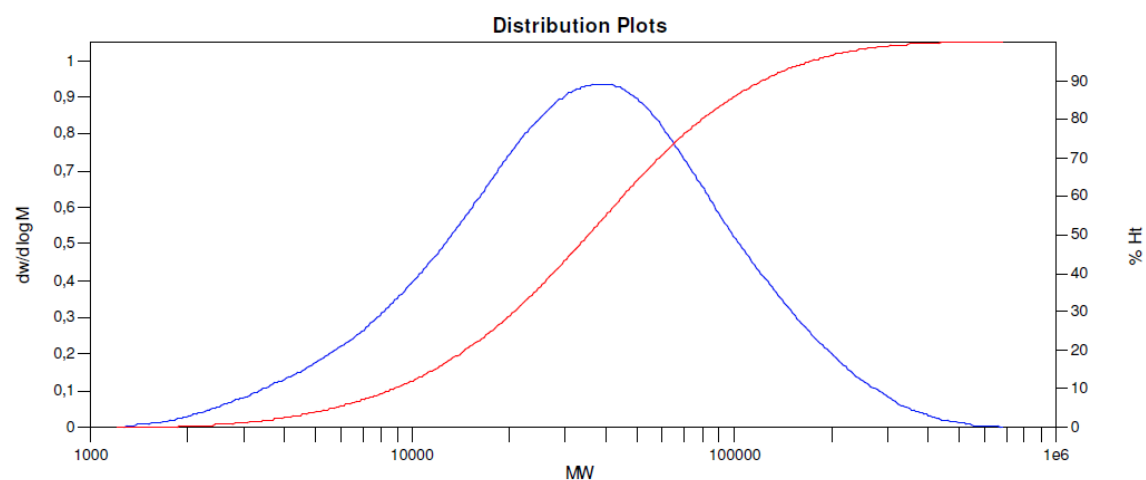
Figure S3-1. PDPP[T]₂-T molecular weight distribution.



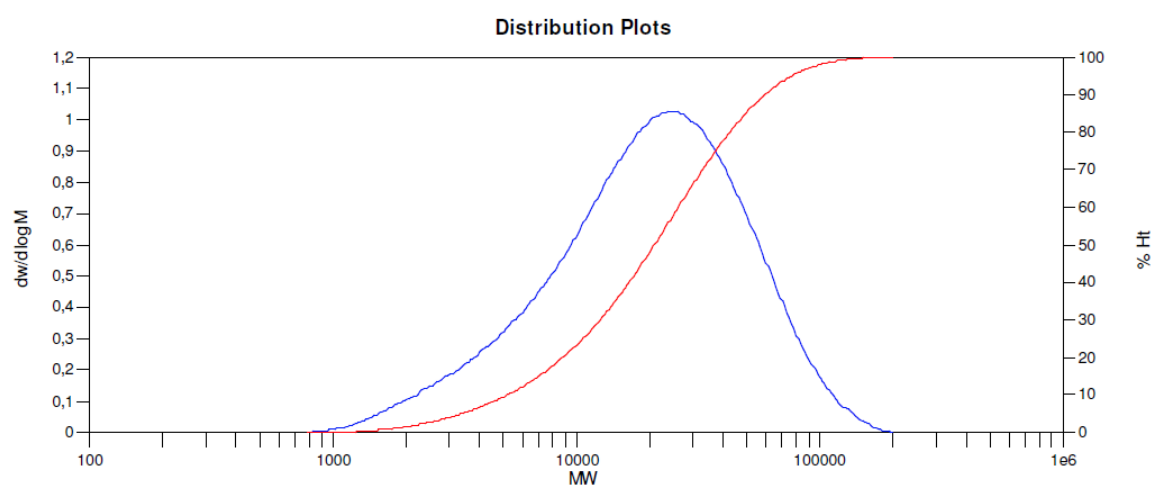
MW Averages

Peak No	Mp	Mn	Mw	Mz	Mz+1	Mv	PD
1	136954	40813	161900	370265	643778	139649	3.96687

Figure S3-2. PDPP[T]₂-TF₂ molecular weight distribution.

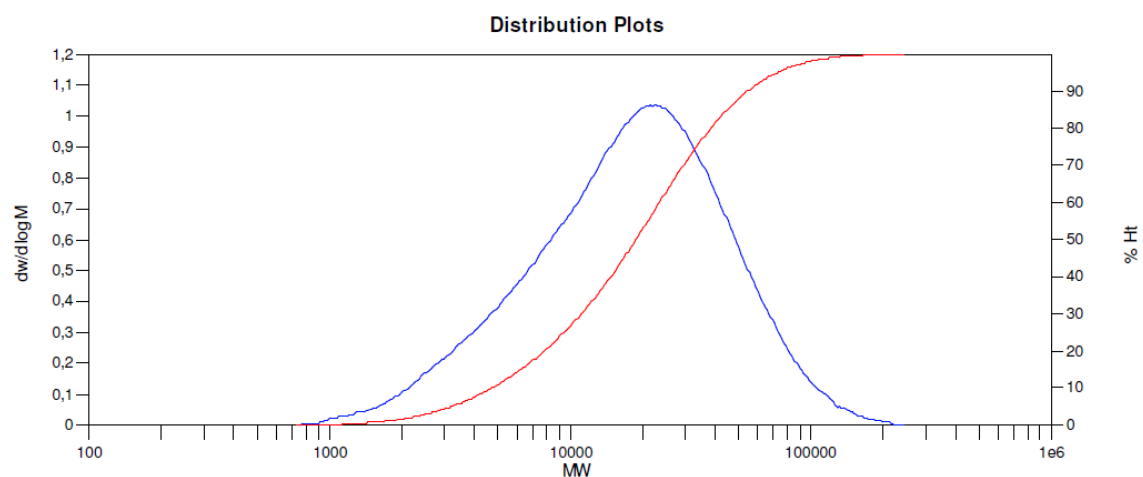
**MW Averages**

Peak No	Mp	Mn	Mw	Mz	Mz+1	Mv	PD
1	37383	19571	54028	119771	208161	47352	2.76062

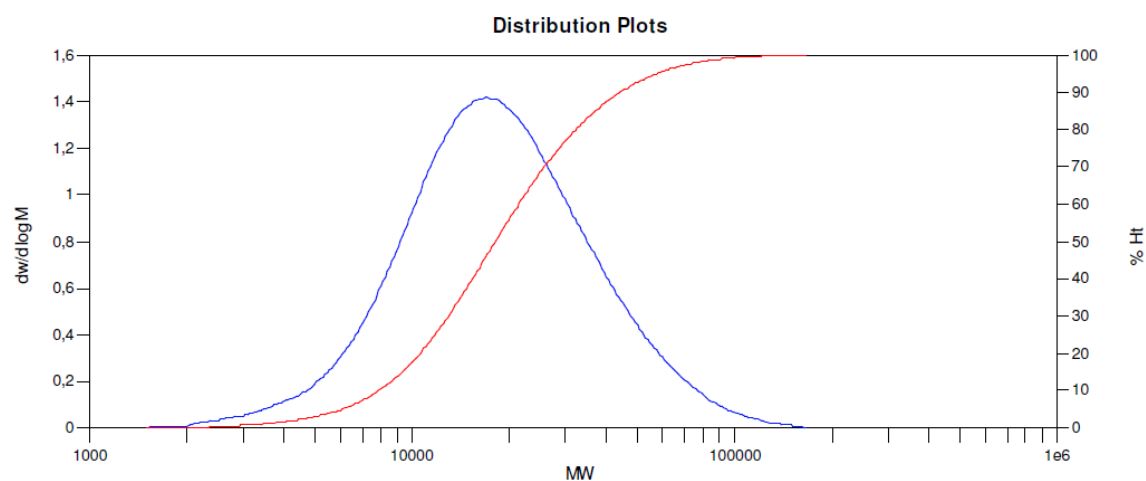
Figure S3-3. PDPP[Py]₂-T molecular weight distribution.**MW Averages**

Peak No	Mp	Mn	Mw	Mz	Mz+1	Mv	PD
1	24607	11665	27560	48472	70272	24960	2.36262

Figure S3-4. PDPP[Py]₂-TF₂ molecular weight distribution.

**MW Averages**

Peak No	Mp	Mn	Mw	Mz	Mz+1	Mv	PD
1	21456	10677	25334	47401	74370	22794	2.37276

Figure S3-5. PDPP[Ph]₂-T molecular weight distribution.**MW Averages**

Peak No	Mp	Mn	Mw	Mz	Mz+1	Mv	PD
1	16377	14391	22842	35798	53346	21361	1.58724

Figure S3-6. PDPP[Ph]₂-TF₂ molecular weight distribution.

Flash-DSC

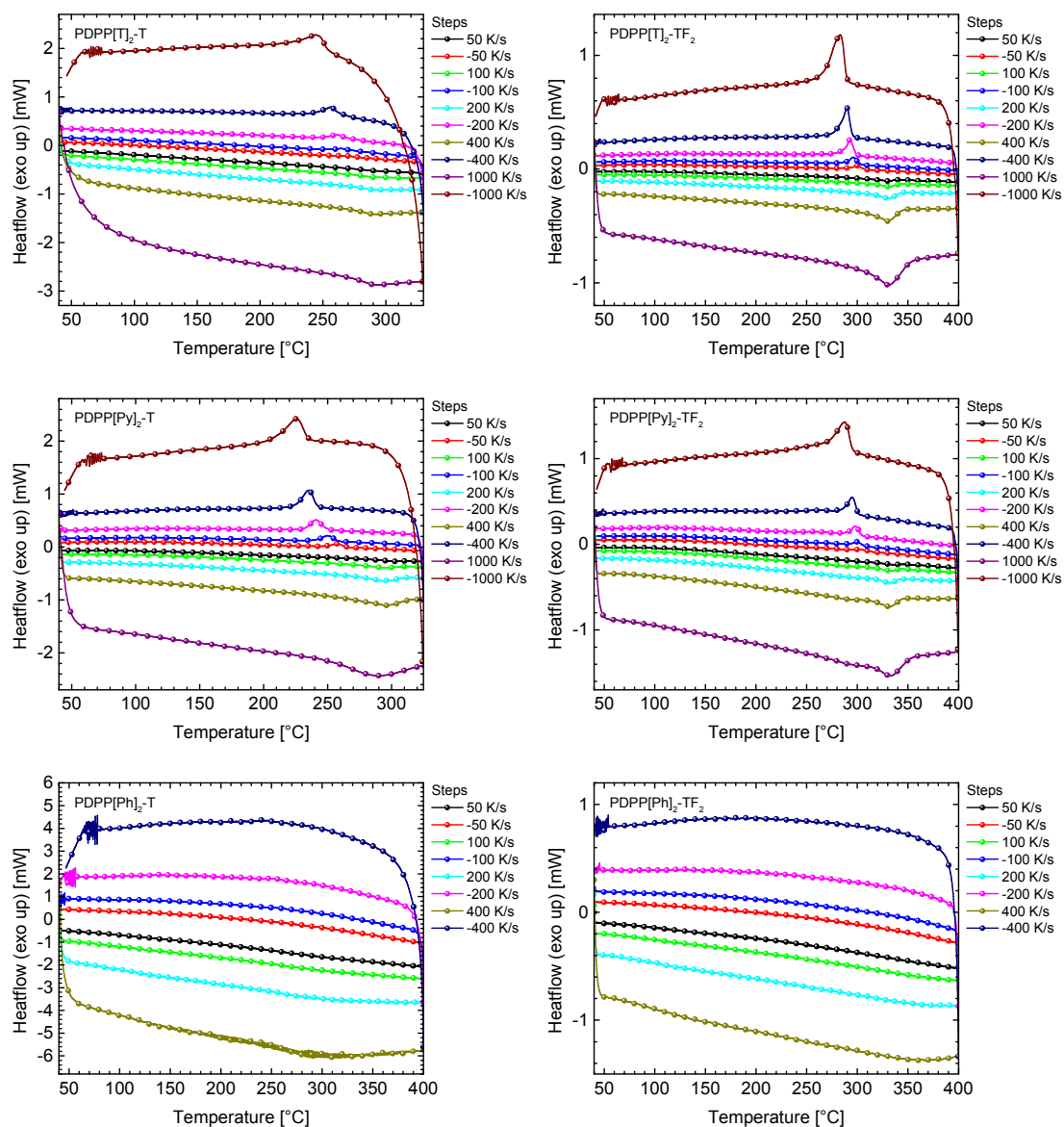


Figure S3-7. Flash-DSC measurements for all six polymers.

Polarization Micrographs

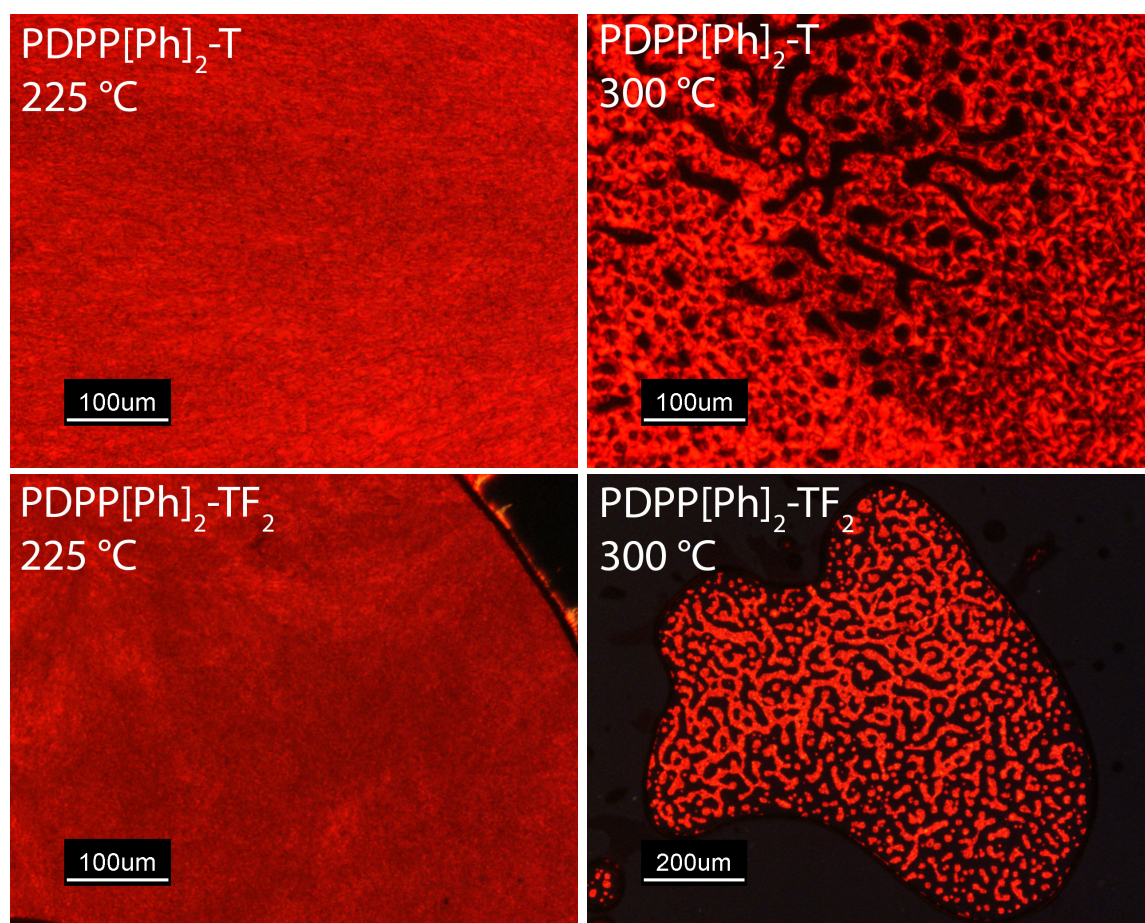


Figure S3-8. Optical micrographs for the PDPP[Ph]₂ polymers recorded with double-crossed polarizers. Liquid crystalline phase at 225 °C, process of clearing to isotropic phase at 300 °C.

Absorption and Photoluminescence

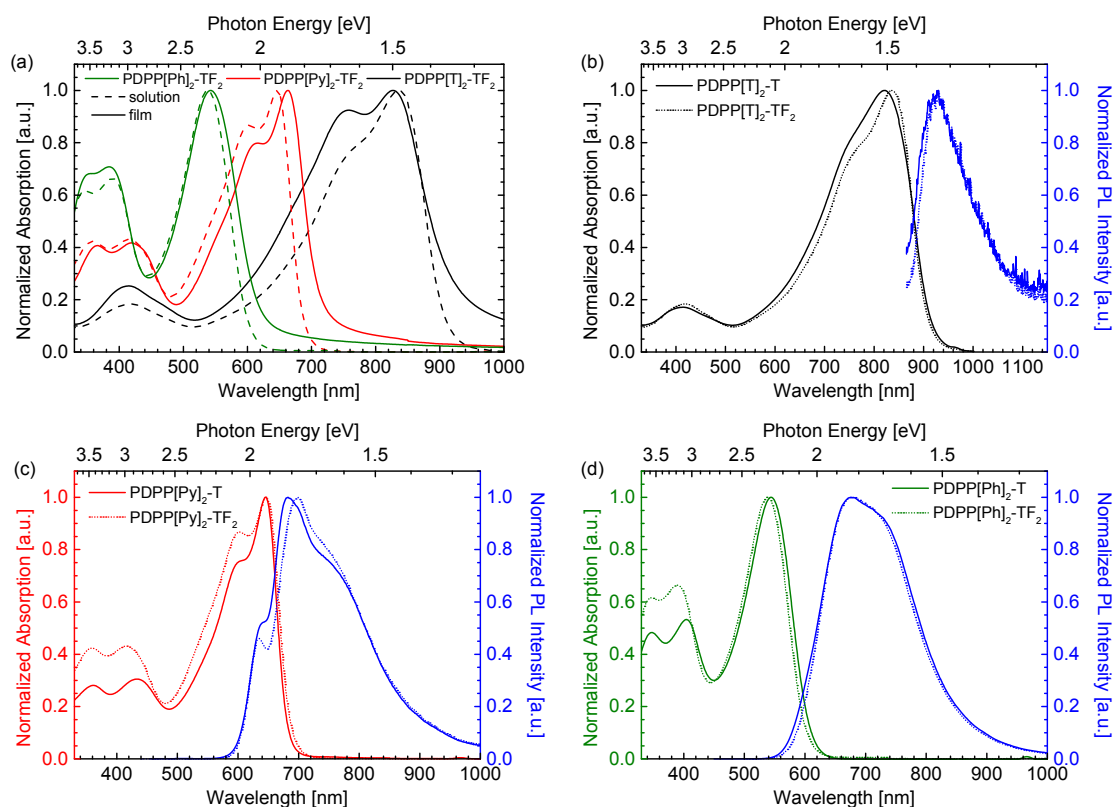


Figure S3-9. Absorption / Photoluminescence spectra. (a) Influence of the aryl flanking unit with difluorothiophene as the comonomer, comparison solution and film; (b-d) influence of fluorination (solution spectra).

Cyclic Voltammetry

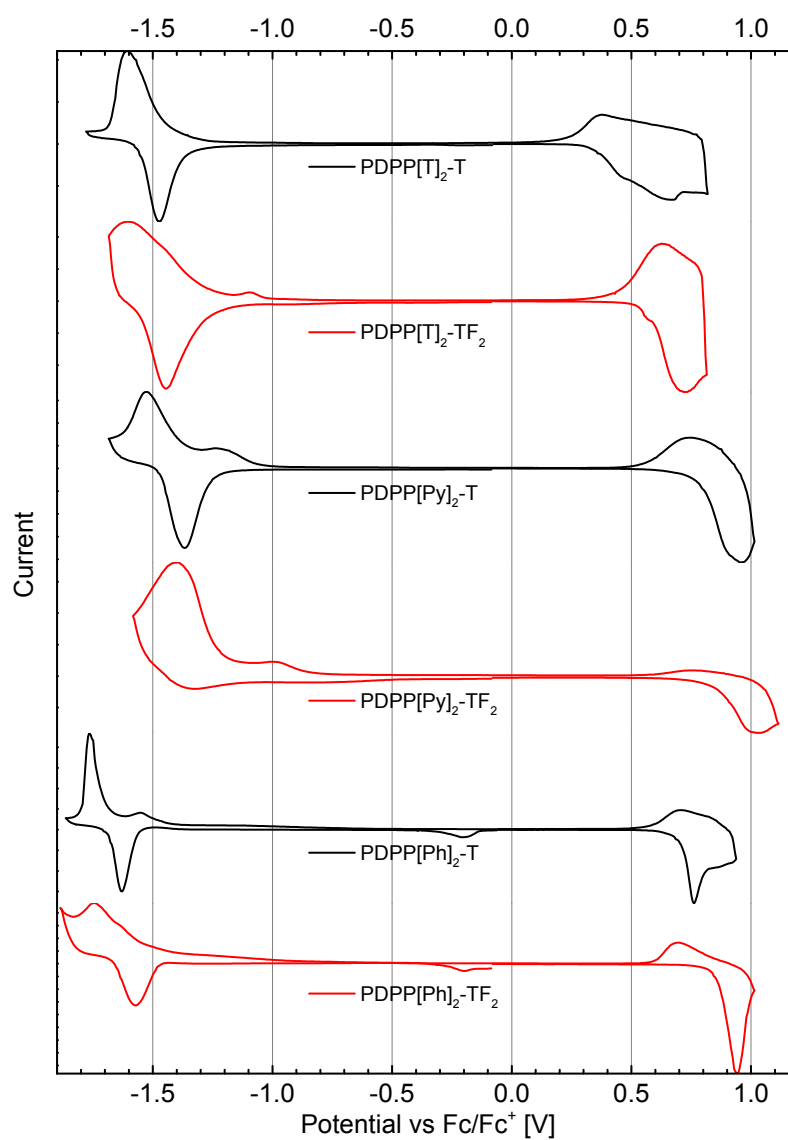


Figure S3-10. Cyclic voltammetry curves for the polymers measured in thin film. Potential against Fc/Fc⁺.

CCDC library analysis

Dihedral angles for low molecular model systems of the structural motifs used in the polymers in this study were evaluated by choosing appropriate datasets from the Cambridge Crystallographic Datacenter (CCDC). The Datasets, the respective dihedral angle α between the diketopyrrolopyrrole-core and the adjacent aryl unit are given in Table 3-1 and Table 3-2.

Table S3-1. Dihedral angles α in low molecular weight DPP compounds. Yellow entries deviate significantly from the average or are not applicable (no alkyl chain). Chemical structure inset highlights (bold) the definition of the dihedral angles α_1 and α_2 .

CCDC dataset	compound	dihedral angle α_1	dihedral angle α_2	reference
BIBDIB	DPP[T]2{nHex}2	-9.15	-9.15	[1]
CEYREF	DPP[T]2{3-OEG}2	-5.233	-5.233	[1]
KEMDEN	DPP[T]2{2EH}2Ar2	-14.444	-14.444	[2]
KEMDIR	DPP[T]2{2EH}2Ar2	-8.774	-8.774	[2]
LEJCOU	DPP[T]2{2DDd}2Per2	-5.799	-5.799	[3]
VOKBAA	DPP[T]2{nHex}2Br2	-6.007	-6.007	[4]
ZOHHAH	DPP[T]2{nHeptPyr+}2	-2.84	-2.84	[5]
FOGSEA	DPP[Py]2{H}2	8.722	8.722	[6]
FOGSEA	DPP[Py]2{H}2	1.015	1.015	[6]
GEGHUX	DPP[Ph]2{nHex}2T	-26.233	-26.233	[7]
GEGJOT	DPP[Ph]2{nHex}2T2	-27.611	-27.611	[7]

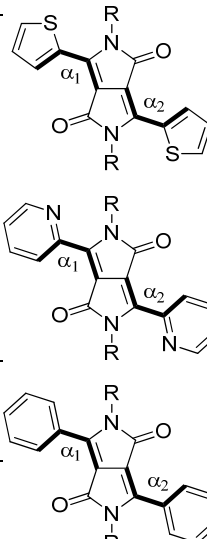


Table S3-2. Dihedral angles β in oligoaromatic units incorporating thiophene / 3,4-difluorothiophene.

CCDC dataset	compound	dihedral angle 1	dihedral angle 2	dihedral angle 3	reference
EYUXEB	T-T-T	174.276	177.995		[8]
EYUXEB	T-T-T	177.126	175.236		[8]
QOWFIR	F3T-TF2-TF2-TF2-TF2-TF3	177.126	175.236	180	[9]
<no-entry>	2Py-T-2Py	N/A	N/A		
<no-entry>	2Py-TF2-2Py	N/A	N/A		
SUSNEZ	Ph-T-Ph	174.847	176.828		[10]
<no-entry>	Ph-TF2-Ph	N/A	N/A		

Devices

OFET IV curves

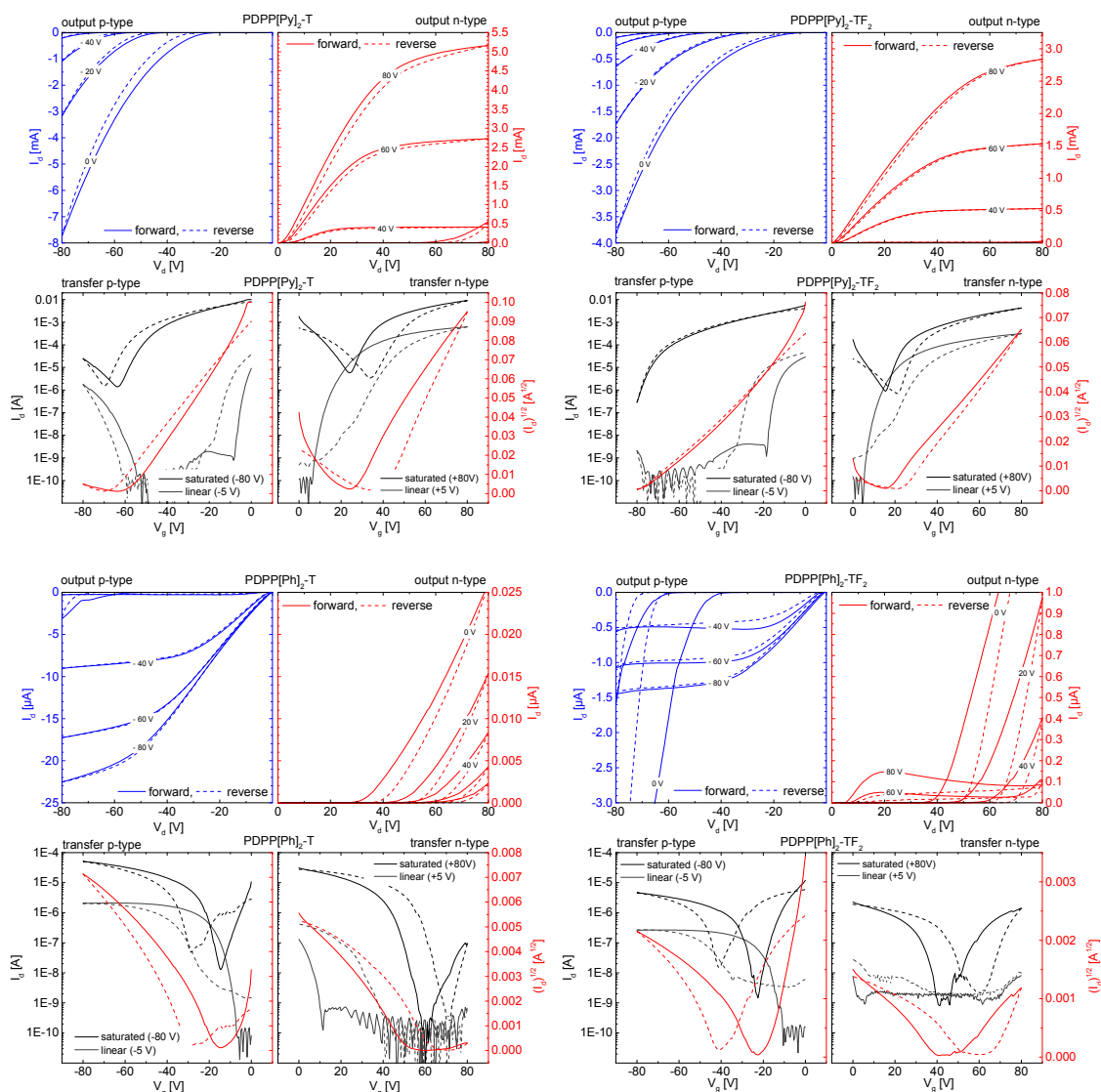


Figure S3-11. OFET I - V for the PDPP[Py]₂ (top) and PDPP[Ph]₂ polymers (bottom) using thiophene (left) and 3,4-difluorothiophene (right) as a comonomer. Output characteristics in p-channel (blue) and n-channel (red) operation.

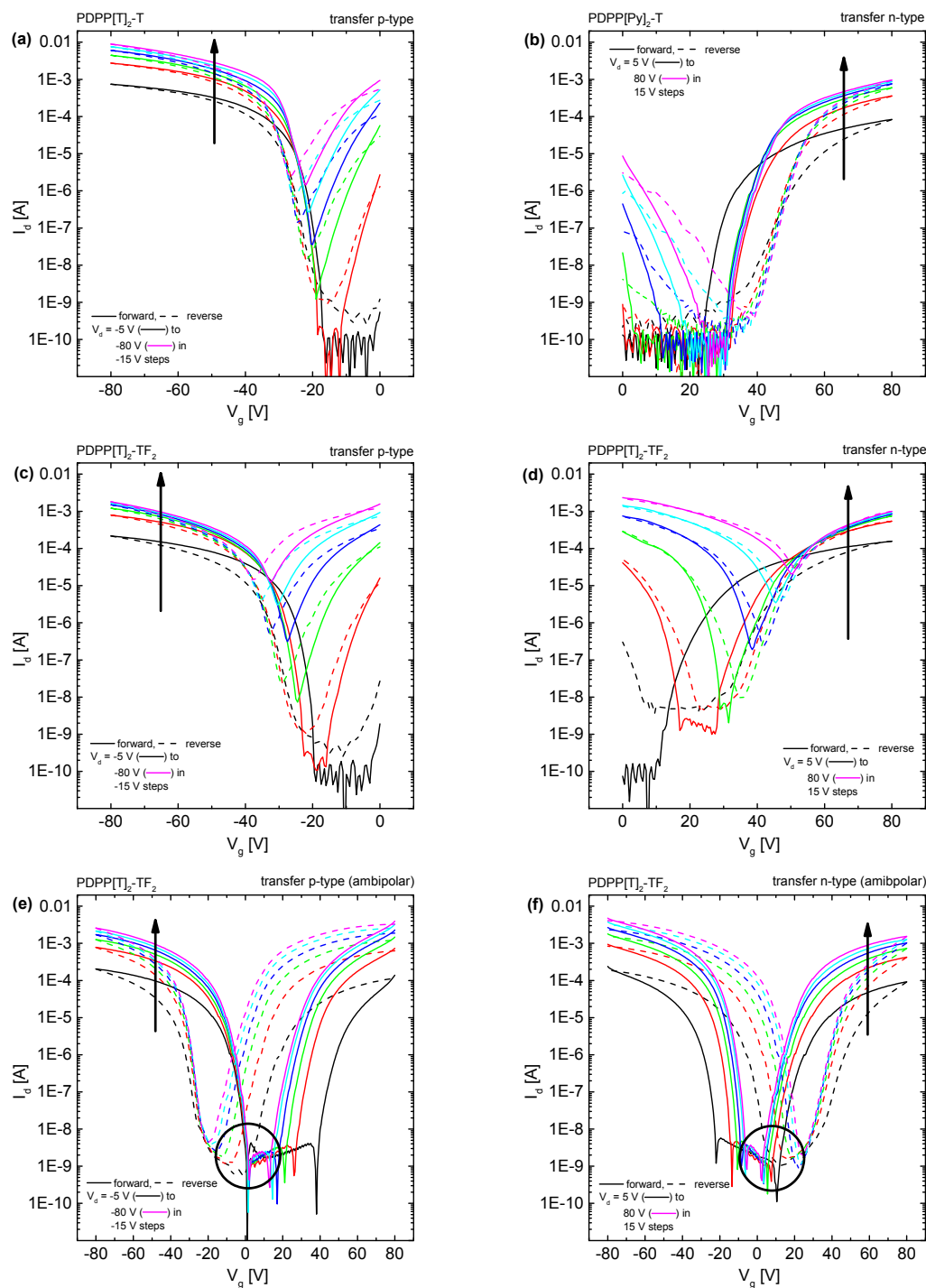


Figure S3-12. Transfer behavior at increasing drain-source voltages V_d . (a) For the ambipolar PDPP[T]₂-T the on/off ratio decreases significantly for operation in the saturation regime; (b) for non-ambipolar materials such as the exclusively n-type PDPP[Py]₂-T the on/off-ratio is barely influenced; (c) in the ambipolar PDPP[T]₂-TF₂ the on/off ratio is decreased when operated in p-channel mode, which can be avoided (e) when the measurement is conducted in an ambipolar range; (d) also in n-channel operation this effect can be observed as well as (f) avoided by choosing an ambipolar measurement range.

Table S3-3. OFET on/off ratios in different operation regimes. For ambipolar materials, the on/off ratio decreases in the saturation regime when high drain voltages are applied. Also see Figure S12.

	as cast				annealed			
	$I_{\text{on/off}}$	$I_{\text{on/off}}$	$I_{\text{on/off}}$	$I_{\text{on/off}}$	$I_{\text{on/off}}$	$I_{\text{on/off}}$	$I_{\text{on/off}}$	$I_{\text{on/off}}$
	p-type	p-type	n-type	n-type	p-type	p-type	n-type	n-type
	lin.	sat.	lin.	sat.	lin.	sat.	lin.	sat.
PDPP[T] ₂ -T	$>10^6$	$>10^2$	-	-	$>10^6$	$>10^2$	$>10^6$	2
PDPP[T] ₂ -TF ₂	$>10^6$	$>10^2$	$>10^6$	$>10^2$	$>10^6$	$>10^2$	$>10^6$	$>10^2$
PDPP[Py] ₂ -T	-	-	$>10^6$	$>10^6$	-	-	$>10^8$	$>10^3$
PDPP[Py] ₂ -TF ₂	-	-	$>10^5$	$>10^5$	-	-	$>10^8$	$>10^4$
PDPP[Ph] ₂ -T	$>10^5$	$>10^6$	-	-	$>10^5$	$>10^6$	-	-
PDPP[Ph] ₂ -TF ₂	$>10^4$	$>10^5$	$>10^2$	$>10^5$	$>10^5$	$>10^4$	$>10^4$	$>10^5$

Additional SCLC data

Table S3-4. Listing of film thicknesses and fitting parameters for all the hole-only devices.

Active layer	Thickness	Fitted mobility	Fitted gamma	Mobility at 1.5×10^7 V/m
	[nm]	[$\text{cm}^2\text{V}^{-1}\text{s}^{-1}$]	[$\text{V}^{-0.5}\text{m}^{0.5}$]	[$\text{cm}^2\text{V}^{-1}\text{s}^{-1}$]
PDPP[T] ₂ -T	332	2.7×10^{-8}	1.5×10^{-3}	7.5×10^{-6}
PDPP[T] ₂ -T	364	1.6×10^{-7}	1.2×10^{-3}	1.6×10^{-5}
PDPP[T] ₂ -T	398	1.3×10^{-7}	1.1×10^{-3}	7.8×10^{-6}
PDPP[T] ₂ -T + anneal	338	5.8×10^{-6}	-1.6×10^{-4}	3.0×10^{-6}
PDPP[T] ₂ -TF ₂	288	6.2×10^{-7}	7.8×10^{-4}	1.3×10^{-5}
PDPP[T] ₂ -TF ₂	336	3.0×10^{-7}	8.6×10^{-4}	8.4×10^{-6}
PDPP[T] ₂ -TF ₂	462	1.8×10^{-7}	9.4×10^{-4}	6.7×10^{-6}
PDPP[T] ₂ -TF ₂ + anneal	291	3.7×10^{-6}	-1.2×10^{-5}	3.6×10^{-6}
PDPP[Py] ₂ -T	355	6.1×10^{-6}	-2.4×10^{-5}	5.6×10^{-6}
PDPP[Py] ₂ -T	578	6.0×10^{-6}	-2.9×10^{-5}	5.4×10^{-6}
PDPP[Py] ₂ -T	596	1.9×10^{-5}	2.3×10^{-5}	2.1×10^{-5}
PDPP[Py] ₂ -T + anneal	479	1.3×10^{-5}	-7.7×10^{-6}	1.3×10^{-5}
PDPP[Py] ₂ -TF ₂	236	1.1×10^{-5}	2.3×10^{-5}	1.2×10^{-5}
PDPP[Py] ₂ -TF ₂	344	8.7×10^{-6}	8.2×10^{-5}	1.2×10^{-5}
PDPP[Py] ₂ -TF ₂	618	3.5×10^{-5}	-1.0×10^{-4}	2.4×10^{-5}
PDPP[Py] ₂ -TF ₂ + anneal	235	2.6×10^{-5}	2.6×10^{-5}	2.8×10^{-5}
PDPP[Ph] ₂ -T	313	1.1×10^{-4}	-2.7×10^{-4}	3.8×10^{-5}
PDPP[Ph] ₂ -T	362	1.2×10^{-4}	-3.4×10^{-4}	3.3×10^{-5}
PDPP[Ph] ₂ -T	497	1.5×10^{-4}	-3.7×10^{-4}	3.6×10^{-5}
PDPP[Ph] ₂ -T + anneal	380	2.5×10^{-5}	-3.9×10^{-5}	2.2×10^{-5}
PDPP[Ph] ₂ -TF ₂	366	2.9×10^{-5}	-1.7×10^{-4}	1.5×10^{-5}
PDPP[Ph] ₂ -TF ₂	532	9.0×10^{-5}	-2.2×10^{-4}	3.8×10^{-5}
PDPP[Ph] ₂ -TF ₂	580	3.3×10^{-5}	-2.7×10^{-4}	1.2×10^{-5}
PDPP[Ph] ₂ -TF ₂ + anneal	298	2.7×10^{-5}	-1.7×10^{-5}	2.6×10^{-5}

Table S3-5. Listing of film thicknesses and fitting parameters for all the electron-only devices.

Active layer	Thickness	Fitted mobility	Fitted gamma	Mobility at 1.5×10^7 V/m
	[nm]	[$\text{cm}^2\text{V}^{-1}\text{s}^{-1}$]	[$\text{V}^{-0.5}\text{m}^{0.5}$]	[$\text{cm}^2\text{V}^{-1}\text{s}^{-1}$]
PDPP[T] ₂ -T	246	4.9×10^{-9}	3.7×10^{-4}	2.0×10^{-8}
PDPP[T] ₂ -T	293	2.4×10^{-8}	9.1×10^{-5}	3.5×10^{-8}
PDPP[T] ₂ -T	296	1.2×10^{-8}	2.7×10^{-4}	3.5×10^{-8}
PDPP[T] ₂ -T + anneal	274	2.3×10^{-10}	1.2×10^{-3}	2.1×10^{-8}
PDPP[T] ₂ -TF ₂	186	6.0×10^{-8}	-1.2×10^{-4}	3.8×10^{-8}
PDPP[T] ₂ -TF ₂	313	3.9×10^{-8}	-6.3×10^{-5}	3.1×10^{-8}
PDPP[T] ₂ -TF ₂	396	1.9×10^{-8}	-1.7×10^{-4}	9.8×10^{-9}
PDPP[T] ₂ -TF ₂ + anneal	423	2.2×10^{-8}	2.5×10^{-5}	2.4×10^{-8}
PDPP[Py] ₂ -T	197	2.7×10^{-6}	1.4×10^{-3}	5.4×10^{-4}
PDPP[Py] ₂ -T	355	2.8×10^{-7}	1.7×10^{-3}	1.9×10^{-4}
PDPP[Py] ₂ -T + anneal	391	5.1×10^{-6}	1.3×10^{-3}	8.9×10^{-4}
PDPP[Py] ₂ -TF ₂	210	4.8×10^{-4}	4.9×10^{-4}	3.2×10^{-3}
PDPP[Py] ₂ -TF ₂	312	1.1×10^{-4}	9.5×10^{-4}	4.6×10^{-3}
PDPP[Py] ₂ -TF ₂	520	7.1×10^{-5}	1.1×10^{-3}	5.1×10^{-3}
PDPP[Py] ₂ -TF ₂ + anneal	219	1.8×10^{-4}	4.9×10^{-4}	3.2×10^{-3}
PDPP[Ph] ₂ -T	347	3.0×10^{-5}	7.5×10^{-5}	4.0×10^{-5}
PDPP[Ph] ₂ -T	491	3.2×10^{-5}	1.6×10^{-4}	5.8×10^{-5}
PDPP[Ph] ₂ -T	578	9.6×10^{-5}	2.1×10^{-5}	1.0×10^{-4}
PDPP[Ph] ₂ -T + anneal	279	3.0×10^{-4}	5.6×10^{-5}	3.7×10^{-5}
PDPP[Ph] ₂ -TF ₂	351	6.6×10^{-6}	2.8×10^{-4}	2.0×10^{-5}
PDPP[Ph] ₂ -TF ₂	357	2.8×10^{-6}	4.3×10^{-4}	1.5×10^{-5}
PDPP[Ph] ₂ -TF ₂	505	4.3×10^{-6}	1.8×10^{-4}	8.7×10^{-6}
PDPP[Ph] ₂ -TF ₂ + anneal	264	1.1×10^{-5}	2.4×10^{-4}	2.7×10^{-5}

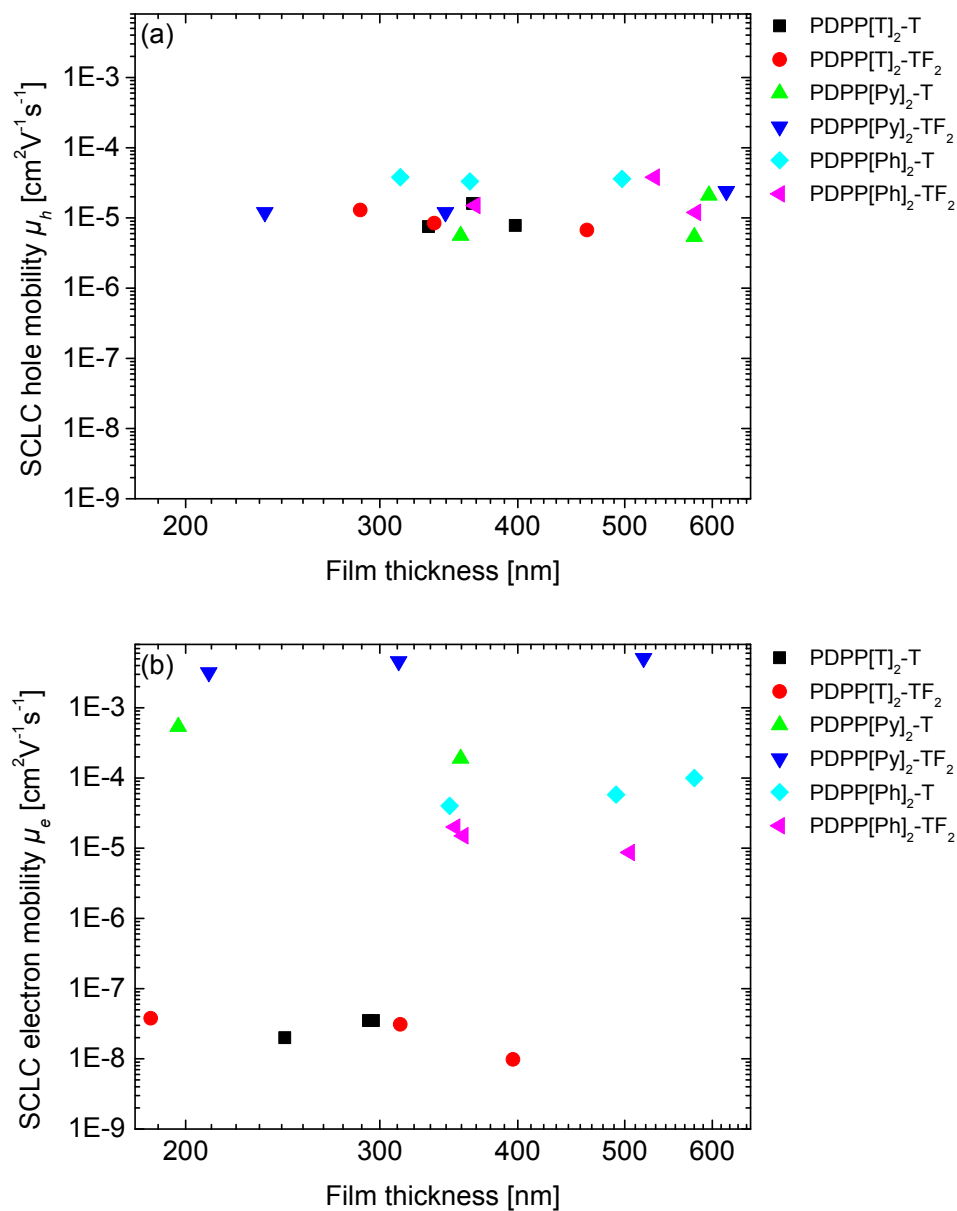


Figure S3-13. The effective SCLC charge carrier mobility of holes (a) and electrons (b) in as-cast different thickness PDPP films at an electric field of $1.5 \times 10^7 \text{ V m}^{-1}$. The independence of extracted mobility values on the film thicknesses suggests that the current response in the reported SCLC devices was not contact-limited but rather determined by the polymer films.

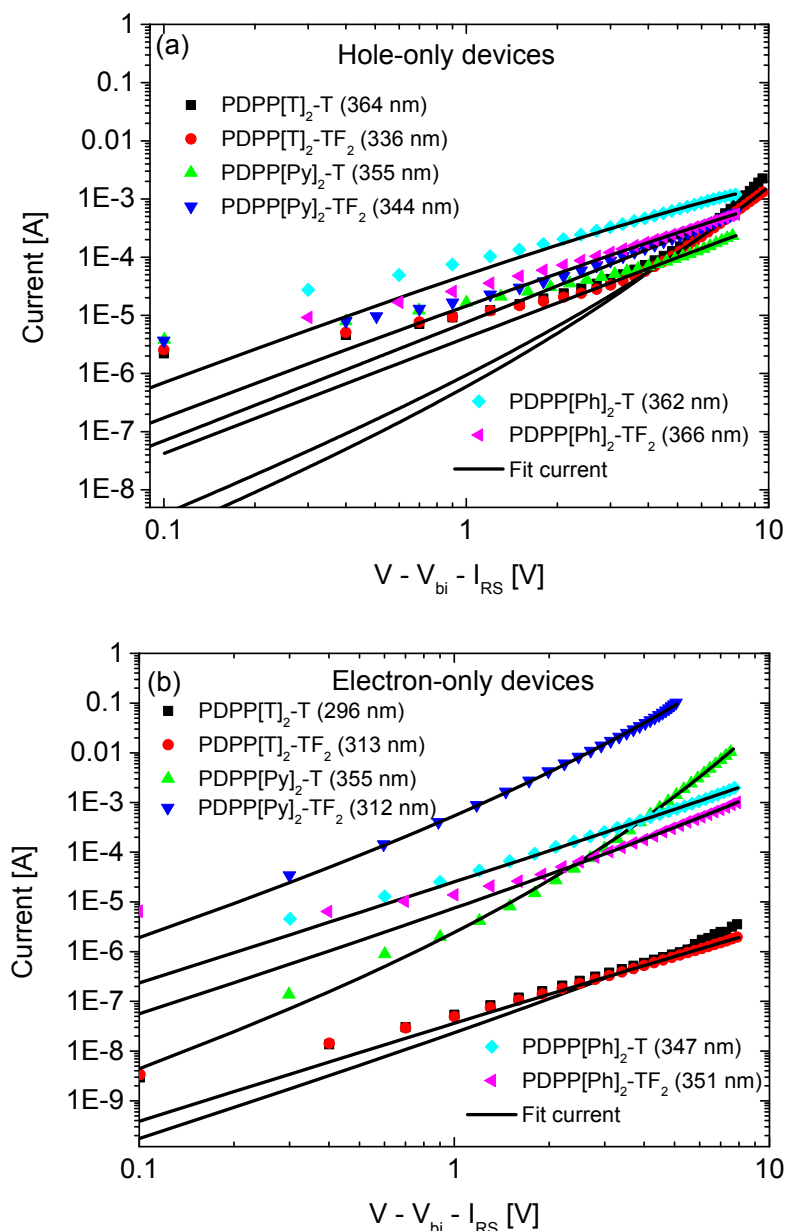


Figure S3-14. Double logarithmic plots of the SCLC I - V characteristics. The solid lines represent the SCLC fit with field dependent mobility. The corresponding film thicknesses are mentioned within the parentheses. The I - V characteristics were corrected for the built-in voltage (V_{bi}) and the voltage drop (IR) over the contacts.

Supporting References

- [1] M. A. Naik, N. Venkatramaiah, C. Kanimozhi, S. Patil, *J. Phys. Chem. C* **2012**, *116*, 26128.
- [2] J. Liu, B. Walker, A. Tamayo, Y. Zhang, T.-Q. Nguyen, *Adv. Funct. Mater.* **2013**, *23*, 47.

- [3] O. P. Lee, A. T. Yiu, P. M. Beaujuge, C. H. Woo, T. W. Holcombe, J. E. Millstone, J. D. Douglas, M. S. Chen, J. M. J. Fréchet, *Adv. Mater.* **2011**, *23*, 5359.
- [4] J. M. W. J. Roth-Barton, Cambridge Crystallographic Data Centre
Cambridge Crystallographic Data Centre 2014.
- [5] G. Wu, J. Thomas, M. Smet, Z. Wang, X. Zhang, *Chemical Science* **2014**, *5*, 3267.
- [6] T. Imoda, T. Hirota, H. Takahashi, J. Mizuguchi, *Acta Crystallographica Section E Structure Reports Online* **2005**, *61*, o616.
- [7] C. Kim, J. Liu, J. Lin, A. B. Tamayo, B. Walker, G. Wu, T.-Q. Nguyen, *Chem. Mater.* **2012**, *24*, 1699.
- [8] F. Van Bolhuis, H. Wynberg, E. E. Havinga, E. W. Meijer, E. G. J. Staring, *Synth. Met.* **1989**, *30*, 381.
- [9] Y. Sakamoto, S. Komatsu, T. Suzuki, *J. Am. Chem. Soc.* **2001**, *123*, 4643.
- [10] P. Pouzet, I. Erdelmeier, D. Ginderow, P. M. Dansette, D. Mansuy, J.-P. Mornon, *J. Heterocycl. Chem.* **1997**, *34*, 1567.

4 Influence of Fluorination in π -extended Backbone Polydiketopyrrolopyrroles on Charge Carrier Mobility and Depth-dependent Molecular Alignment

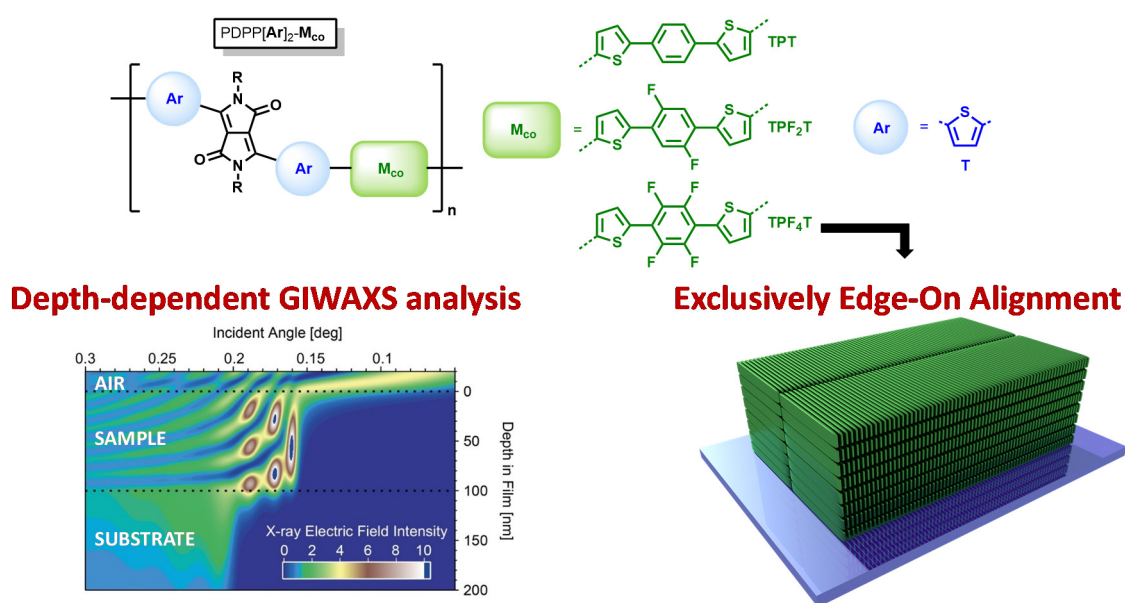
Christian J. Mueller,^a Eliot Gann,^{b,c}

Christopher R. McNeill^c and Mukundan Thelakkat^{*,a}

^a Applied Functional Polymers, Macromolecular Chemistry I, University of Bayreuth, 95440 Bayreuth, Germany.

^b Australian Synchrotron, 800 Blackburn Road, Clayton, VIC, 3168, Australia.

^c Department of Material Science and Engineering, Monash University, Wellington Road, Clayton VIC, 3800, Australia.



Published in *Journal of Materials Chemistry C*, **2015**, *3*, 8916-8925.

Reproduced with permission from The Royal Society of Chemistry.

Abstract

A series of π -extended polydiketopyrrolo[3,4-*c*]pyrroles with a varying degree of fluorination on the thiophene-phenyl-thiophene comonomer was synthesized by Stille polycondensation. The influence of the degree of fluorination was studied with regard to the polymer properties, such as absorption, electrochemical redox potentials, the solid state structure as well as depth-dependent molecular alignment in thin films. Additionally, their performance in organic field effect transistors was evaluated. Whereas fluorination slightly increases the alkyl lamella and shrinks the π - π spacings, the coherence lengths were found to improve significantly in both directions. All polymers were found to be p-type materials when employed in organic field effect transistors (OFET). These devices can be tuned towards ambipolarity in the case of the tetrafluorinated copolymer upon thermal annealing.

4.1 Introduction

Diketopyrrolopyrrole (DPP) based materials are promising candidates for organic electronics due to their high ambipolar charge carrier mobilities, low optical gap and high absorption coefficient. Especially their use in organic field effect transistors (OFETs) has received considerable attention over the last few years. This is mainly due to their remarkable structural order^[1] leading to high planarity of the DPP moieties arising from strong intermolecular π - π interactions which promote charge transport.^[2-3]

The π - π interactions in DPP copolymers can be increased by side chain engineering^[4-5] or by incorporating planarizing aromatic units as comonomers into the backbone.^[6] Examples are long non-alkylated oligoaromatic units such as hexa- or heptathiophenes,^[7] vinylene-bridged bithiophenes or biselenophenes,^[4] as well as highly π -extended donating units consisting of thiophene, selenophene and phenyl moieties.^[8]

Very recently it has been shown that comonomers with the thiophene-phenyl-thiophene (TPT) motif are especially promising candidates to facilitate highly planar, crystalline and aggregating DPP copolymers.^[8-10] In order to further promote the planarization of semiconducting polymers the exploitation of diffusive nonbonding heteroatom interactions has been employed.^[11] Two of those interactions are the hydrogen-fluorine and the hydrogen-oxygen interactions that help lock the conformation of the polymer backbone into a more planarized state. In low bandgap polymers, the influence of fluorination on regioselectivity of the resulting copolymer structure has also been reported.^[12] Not only fluorinated phenylene units have been shown to be valuable building blocks for semiconducting copolymers,^[13] but recently it has been shown that for the

TPT motif, bifluorination or bialkoxylation of the central phenyl unit facilitates charge transport and leads to either preferred edge-on alignment in the case of fluorination or face-on alignment in the case of alkoxylation.^[9] On the other hand, a tetrafluorinated TPT derivative has been employed in oligomers^[14-15] as well as in DPP copolymers carrying furanyl flanking units by Sonar et al.^[16] and has been found to provide ambipolarity in OFET devices. It is hitherto unknown whether this ambipolarity is caused by the furanyl-flanking units or the tetrafluorination of the TPT. Therefore it is interesting, to study the effect of fluorination in the conventional DPP copolymers with thienyl flanking units. The impact of tetrafluorination in a TPT moiety on the rotational barrier has been studied by computational methods.^[17]

In this contribution we report the synthesis of a series of three extended π -conjugated PDPPs by using a non-alkylated thiophene-*n*-fluorophenylene-thiophene ($n = 0, 2, 4$) unit as the comonomer. The crystalline depth-dependant alignment in thin films and the charge transport properties in OFET devices is studied with respect to the degree of fluorination in order to gain insight into the structure-property relationship of these π -extended systems and to evaluate the utility of fluorination in semiconducting polymers as a measure for improving semiconducting material properties. We also evaluate the various non-covalent interactions possible in these derivatives based on experimental crystallographic data of the building blocks.

4.2 Results and Discussion

4.2.1 Synthesis

The synthesis of the stannylated TPT-comonomers is summarized in Figure 4-1. For the nonfluorinated TPT unit **4a** a synthesis route which has been published for the bis(tributyltin)-analogs^[18-19] was adapted. For the difluorinated compound **4b** as well as the tetrafluorinated **4c**, a direct lithiation from **2b** and **2c**, respectively, has been reported.^[16, 20] We found that monostannylated compounds that are obtained as byproducts from direct lithiation of **2a-c** are difficult to separate even by multiple recrystallizations and sublimations. Therefore we adopted a different synthetic route involving first bromination followed by lithiation and stannylation to obtain **4b** and **4c**. The almost quantitative conversion achieved in this bromination route employed here results in high monomer purities. Therefore, this bromination route was employed for all the three stannylated DPP derivatives. In detail, starting from the 1,4-dibrominated phenylene compounds **1a-c** a Stille coupling was employed to obtain the TPT blocks **2a-c**. Subsequent bromination with NBS in DMF yielded the dibrominated TPT blocks **3a-c** in good yields, especially for the fluorinated derivatives where the yield was 80-95%. Lithiation of **3a-c** in THF at -78 °C followed by quenching with trimethyltin chloride gave the desired monomers **4a-c**. For the fluorinated compounds **4b** and **4c** the stannylation

was quantitative. For all three monomers it should be noted that purification is feasible by crystallization due to the high crystallinity of the obtained compounds.

The thienyl-DPP monomer **5** was synthesized following a literature procedure,^[21] which was adapted to increase the yield and purity. Polymerizations were carried out in chlorobenzene at 180 °C under microwave conditions using Pd₂(dba)₃ with P(*o*-Tol)₃ as the catalytic system.^[22] The resulting polymers are named after their respective DPP aryl flanking units (Ar) and comonomer (M_{co}) as shown in Figure 4-2.^[23] All polymers were endcapped with thiophene on both ends. Detailed procedures are given in the experimental section. All polymers were obtained in high number average molecular weights (*M_n*) in the range of 20 400 – 38 100 kg mol⁻¹ and dispersities (*D*) between 1.9 and 2.3 (Table 4-1). The individual GPC traces are given in the Supporting Information (Figures S4-1 to S4-3) and show a monomodal distribution for every polymer. All polymerizations were carried out using similar conditions regarding concentrations, degree of monomer purities, temperatures and catalytic system. All compounds were polymerized to the precipitation limit in chlorobenzene at 180 °C.

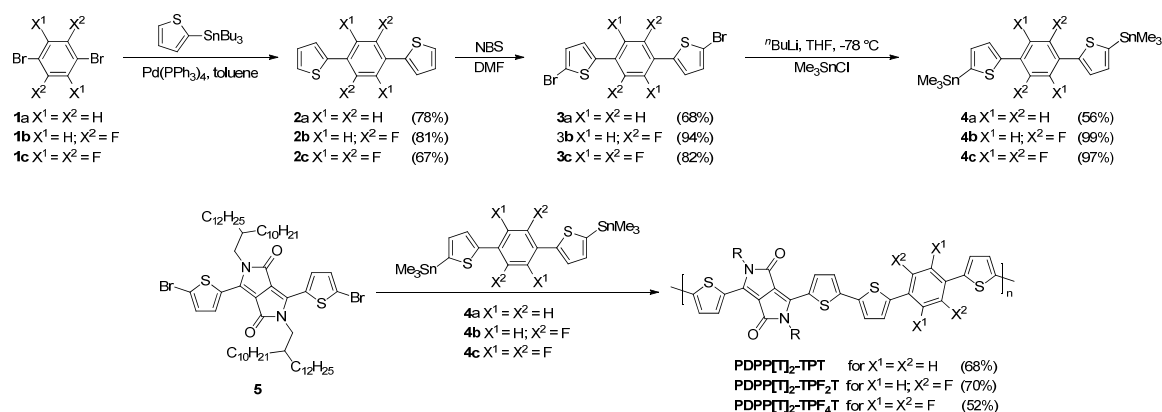


Figure 4-1. Syntheses of the thiophene-phenyl-thiophene monomers with different degrees of fluorination. Experimental details are given in the Supporting Information. Synthesis of the extended PDPP-TPF_nT copolymers by Stille-polycondensation. All yields are given in parentheses.

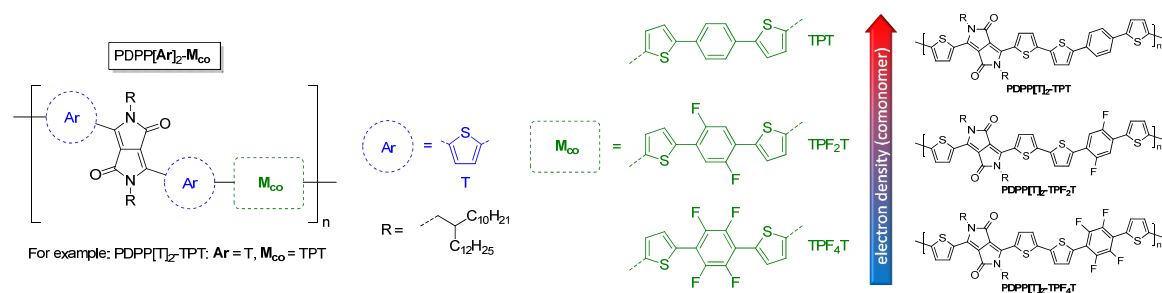


Figure 4-2. Structures of the new extended PDPP[T]₂-TPF_nT polymers in order of the overall electron density. R = 2-Decyltetradecyl (C₁₀/C₁₄). The systematic nomenclature of the DPP copolymers is adopted from our earlier publication.^[23]

Table 4-1. Intrinsic properties of the synthesized DPP polymers.

Polymer	M_n^a [kg mol ⁻¹]	M_w^a [kg mol ⁻¹]	\bar{D}^b	DP_n^c	$T_{5\%}^d$ [°C]	T_m^e [°C]	T_c^e [°C]	IP^f [eV]	EA^g [eV]	E_{CV}^h [eV]	E_{opt}^i [eV]
PDPP[T] ₂ -TPT	38.1	71.4	1.9	31	389	307	253	-5.69	-3.61	2.08	1.51
PDPP[T] ₂ -TPF ₂ T	24.5	53.1	2.2	20	406	337	289	-5.72	-3.60	2.12	1.46
PDPP[T] ₂ -TPF ₄ T	20.4	47.2	2.3	16	394	344	303	-5.89	-3.97	1.92	1.47

^aDetermined by GPC at 150 °C using 1,2,4-trichlorobenzene as the eluent; ^bdispersity; ^cDegree of Polymerization calculated from M_n ; ^ddecomposition onset (5%) determined by TGA; ^eaverage Flash-DSC peak melting temperature (T_m) and crystallization temperature (T_c) at -200 K s⁻¹; ^fIonisation potential (HOMO), ^gelectron affinity (LUMO) and ^hband-gap determined by cyclic voltammetry in thin film; ⁱoptical gap determined from absorption onset in film.

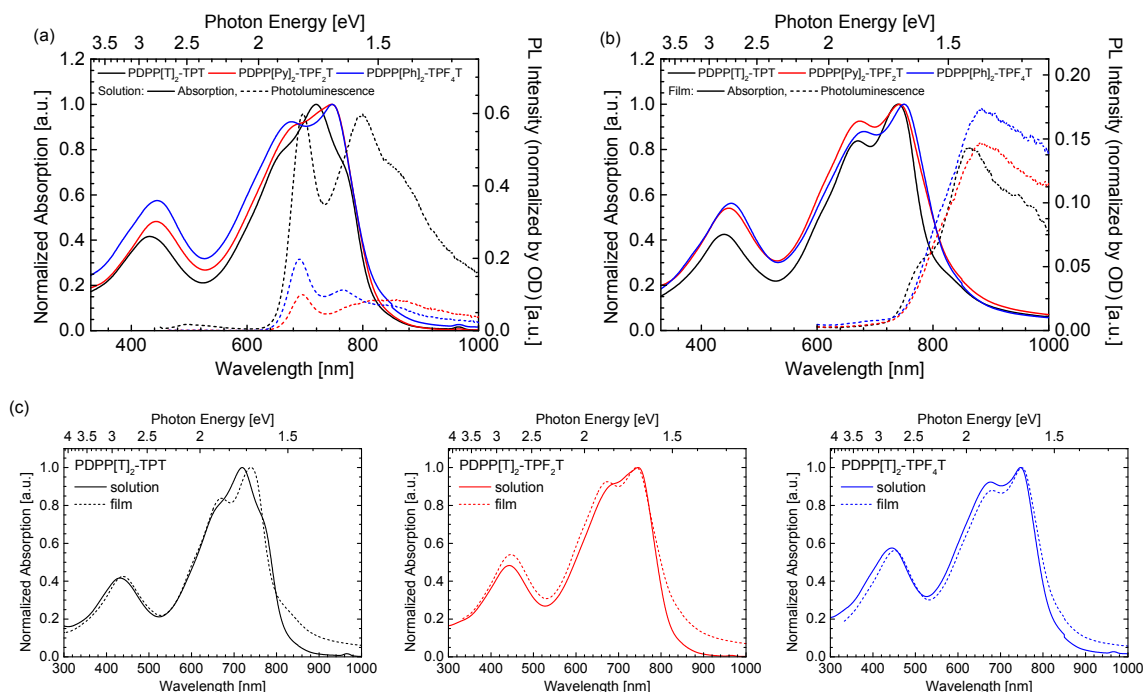


Figure 4-3. Absorption and photoluminescence data for the PDPP[T]₂-TPF_nT copolymers measured in (a) chloroform solution and in (b) film. A comparison of solution and film absorption spectra is shown in (c).

4.2.2 Characterization

The molecular weight of the fluorinated polymers is therefore smaller due to the lower solubility of these polymers upon introduction of fluorine groups. This behaviour has been reported before and is ascribed to the higher degree of aggregation occurring in fluorinated conjugated polymers.^[24] However, all three polymers are soluble and processable from chloroform. It has been shown earlier by Janssen et al. that the aggregation behaviour in PDPPs plays a significant role in determining alignment in thin film and the morphology of polymer/fullerene

blends. Furthermore it was shown that these effects can be influenced by either tuning the solubilizing alkyl sidechains^[5] or the aromatic units along the backbone.^[6]

Thermogravimetric analysis (see Supporting Information, Figure S4-6) shows very high decomposition onsets $T_{5\%}$ around 400 °C for all three derivatives, as is common for PDPPs.

The melting points of PDPPs are usually very high and close to their respective decomposition onsets which makes them difficult to observe using conventional dynamic scanning calorimetry (DSC). We therefore evaluated the thermal properties of these three polymers using a Flash-DSC setup with heating rates from 50 K s⁻¹ to 1000 K s⁻¹. The representative 200 Ks⁻¹ heating and cooling curves are shown in Figure 4-4b and the individual heating and cooling curves for all scan rates are shown in the Supporting Information (Figure S4-4). The respective melting points determined from the average peak value for the different ramping speeds are summarized in Table 4-1. The nonfluorinated PDPP[T]₂-TPT shows the lowest melting temperature (307 °C) whereas fluorination leads to increased melting temperatures of 337 °C and 344 °C for the di- and tetrafluorinated copolymers, respectively. This is in accordance with our previous reasoning on differences in molecular weight due to increased aggregation in the fluorinated polymers. Crystallization temperatures are rate-dependant due to the kinetic nature of crystallization. The crystallization temperatures derived from the -200 K s⁻¹ cooling curve given in Table 4-1 are exemplary and show the same trend as the melting temperatures (see Figure 4-4b).

The optical properties of the three polymers were investigated by absorption as well as photoluminescence measurements. The individual solution as well as solid-state spectra are shown in Figure 4-3.

All three polymers show similar absorption patterns and an almost identical optical gap of 1.5 eV (see Table 4-1). When comparing the individual solution spectra (Figure 4-3a), a slight shift in peak positions for the visible absorption band becomes observable, which is not apparent in the solid state spectra (Figure 4-3b). More specifically, when comparing the solution and film absorption spectra of the three individual compounds (Figure 4-3c), a notable change in absorption behaviour is observed only by the non-fluorinated PDPP[T]₂-TPT. Upon di-fluorination in PDPP[T]₂-TPF₂T, the solution and thin film spectra become much more similar. Finally, for the tetrafluorinated PDPP[T]₂-TPF₄T both absorption curves are more or less identical. We ascribe this behaviour to the strong aggregation of the fluorinated polymers and the presence of aggregates in the solutions that don't differ significantly from those finally formed in film. This finding is supported by the fact that the photoluminescence intensity for PDPP[T]₂-TPT in solution is stronger by a factor of about 3 than those from the fluorinated counterparts PDPP[T]₂-TPF₂T and PDPP[T]₂-TPF₄T. This photoluminescence quenching is again ascribed to the strong aggregation of the fluorinated polymers in solutions. In thin film,

when all the three polymers show the absorption spectrum of the aggregated species, the photoluminescence intensity is comparable for all three polymers.

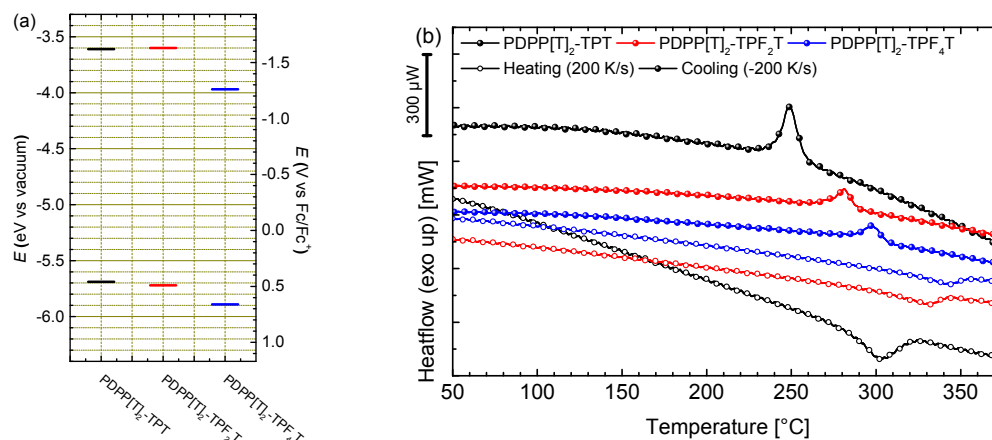


Figure 4-4. (a) Energy level comparison for the extended backbone DPP copolymers with a varying degree of fluorination. Values are determined by Cyclic voltammetry in thin film; (b) Flash-DSC curves for 200 Ks⁻¹ heating / cooling rates. See Supporting Information (Figure S4-5) for additional scan rates.

Oxidation and reduction potentials of the individual polymers were studied by cyclic voltammetry. The individual cyclic voltammograms are shown in Supporting Information (Figure S4-5). The energy levels of the polymers were calculated from the redox half step potentials calibrated against ferrocene in acetonitrile, for which a workfunction of -5.23 eV for the ferrocene/ferrocenium redox couple is taken from literature.^[25] All potentials were obtained using a standard three-electrode cyclic voltammetry setup. Polymers were spincoated onto ITO glass slides which were used as the working electrode and measurements were carried out in solutions containing a 0.1 M tetra-*n*-butylammonium hexafluorophosphate / acetonitrile electrolyte solution at a scan rate of 100 mV s⁻¹. The values for the ionization potential (IP), which closely resembles the highest occupied molecular orbital (HOMO) as well as the electron affinity (EA), which resembles the lowest unoccupied molecular orbital (LUMO) are summarized in Table 4-1 and comparatively shown in Figure 4-4.^[26] Interestingly, when compared to the nonfluorinated PDPP[T]₂-TPT (IP: -5.69 eV, EA: 3.61 eV), difluorination in PDPP[T]₂-TPF₂T only has a negligible effect on both, IP (-5.72 eV) and EA (-3.60 eV). The fundamental bandgap E_{cv} of 2.1 eV is therefore also identical for both polymers. Upon introduction of two more fluorine atoms yielding PDPP[T]₂-TPF₄T a clear shift of both energy levels towards lower values can be observed, resulting in an IP of -5.89 eV and an EA of -3.97 eV as well as a fundamental bandgap of 1.92 eV. Compared to the optical gap these values are significantly larger, which can be taken as an indicator for large a large exciton binding energy E_b in these polymers.^[26]

4.2.3 Influence of fluorination on backbone planarization: Weak non-covalent interactions.

There are several contradictory reports in the recent literature on the origin and the exact conformation that are caused by heteroatom interactions. Whereas elaborate theoretical work by Ratner et al. based on quantum chemical calculations mainly favours hydrogen-heteroatom interactions such as $\text{H}\cdots\text{F}$, $\text{H}\cdots\text{O}$, $\text{H}\cdots\text{S}$ etc., several reports claim that $\text{S}\cdots\text{F}$ and $\text{O}\cdots\text{F}$ interactions influence the planarization of semiconducting polymer backbones.^[9, 27] It has also been reported, that the interaction between heteroatoms such as $\text{S}\cdots\text{F}$ and $\text{O}\cdots\text{F}$ are nearly zero.^[11]

We like to emphasize, that for most of the motifs employed in these polymers, experimental structural data for building blocks is available from single crystal crystallography. We therefore analysed the Cambridge Crystallographic Database Centre (CCDC) library for the various low molecular weight TPT motifs with different degrees of fluorination on the central phenyl moiety. The experimental data supports the model that has been theoretically established by Ratner et al., i.e. for the difluorinated TPF_2T unit the fluorine atoms on the phenyl ring point towards the hydrogen atoms of the adjacent thiophene units.^[14] This experimental evidence does not support the proposed $\text{S}\cdots\text{F}$ interactions in TPF_2T , as reported in literature.^[9]

4.2.4 GIWAXS

Crystalline packing within the polymer thin films was investigated with Grazing Incidence Wide Angle X-ray Scattering (GIWAXS), see Figure 4-5. Exposures were taken at incident angles between 0.05 and 0.4 degrees at a resolution of 0.01 degrees near the critical angle ~ 0.17 degrees, to capture the highest intensity critical angle scattering, as well as some depth sensitive information (as shown in Figure 4-6).

All scattering patterns show clear alkyl lamella stacking, that is backbone to backbone across the alkyl side chains, and π - π stacking, from one molecular face to the next. All polymers exhibit liquid crystalline, semi-crystalline diffraction pattern, with little to no mixed index peaks (peaks away from purely out-of-plane or in-plane), indicating that the elements are largely stacking one dimensionally along different directions, and not forming three dimensional crystals. Additionally, all the polymers exhibit a generally edge-on orientation, with alkyl stacking largely out-of-plane and π - π stacking in-plane.

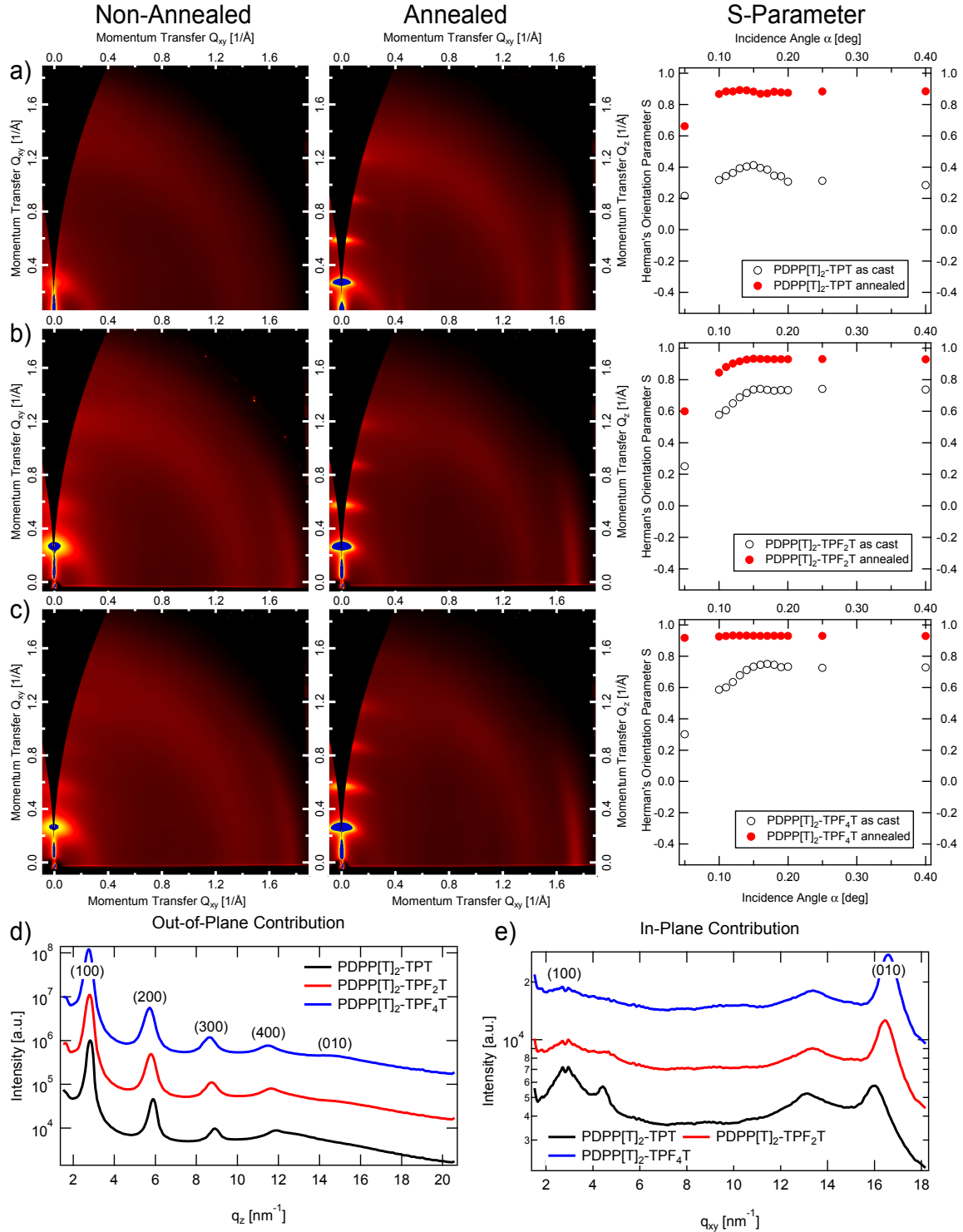


Figure 4-5. From left to right, the unannealed, and annealed 2D GIWAXS Patterns followed by the Herman's orientation parameter vs incident angle. From top to bottom: a) PDPP[T]₂-TPT, b) PDPP[T]₂-TPF₂T, and c) PDPP[T]₂-TPF₄T; d) Out-of-Plane contribution for the annealed polymers; e) In-plane contribution for the annealed polymers.

We can see that the effect of annealing in all cases is the intensification and sharpening of the peaks, with several orders of alkyl lamella stacking apparent, indicating increased crystallinity and larger crystalline domains present within the annealed films. The degree of orientational

alignment is quantified by the Herman's orientation parameter^[28] which runs from -0.5 (face-on orientation) to 1 (edge on orientation), of the first order alkyl stacking peak, plotted in the right most column of Figure 4-5(a-c). We can see at once that the unannealed films are less well oriented, however all films still have an average edge-on structure. Upon annealing, the orientation is strengthened in all cases towards almost perfect edge on orientation.

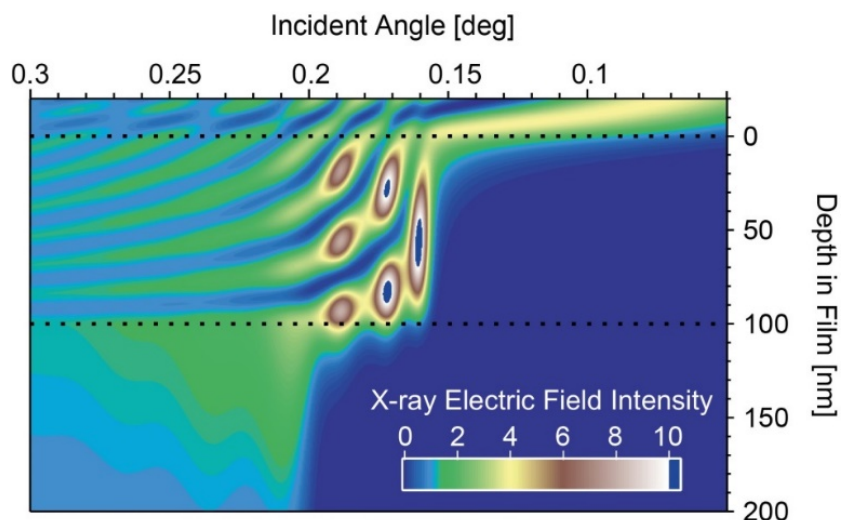


Figure 4-6. The calculated X-ray electric field intensity for a 100 nm thick film on Si. The area between the dotted black lines represents the polymer film. The critical angle at approximately 0.16-0.17 degrees is seen by the sudden large enhancement of electric field intensity within the polymer film. The critical angle of the lower Si substrate can be seen at ~ 0.2 degrees, at which point the X-ray electric field intensity becomes much more uniform throughout the film and substrate. At angles below the critical angle, the electric field intensity within the film is entirely at the surface, within the top ~ 10 nm.

To understand the angular dependence of the Hermans parameter vs angle, the electric field intensity of the X-ray beam is calculated vs angle and depth within a 100 nm thick polymer film as shown in Figure 4-6. Depths greater than 100 nm represent the Silicon substrate, while depths less than 0 represent the ambient environment. Scattering from any depth within the film is proportional to the X-ray electric field intensity at that depth. Thus, at incident angles less than the critical angle (~ 0.16 degrees in the simulation) X-rays scatter exclusively from the upper ~ 10 nm of the surface of the polymer film, while between the critical angle of the polymer film and the critical angle of the silicon substrate (~ 0.2 degrees) the location and intensity of scattering originates from deeper within the film. Finally, above the critical angle of the substrate, the electric field intensity becomes much more even throughout the entire system, averaging out to an intensity of 1 at very high angles. Thus looking at the angular dependence of the Herman's orientation parameter in Figure 4-5, we can conclude that for all of the unannealed films, as well as for the annealed PDPP[T]₂-TPT and PDPP[T]₂-TPF₂T films, the surface region of the samples are less well oriented than the bulk of the film. For PDPP[T]₂-TPF₄T, on the other hand, the exceptionally high degree of edge-on alignment extends all through the surface upon annealing. Sector averages of the out-of-plane (vertical,

Q_z) and in-plane (horizontal, Q_{xy}) directions of the annealed polymer films are shown in Figure 4-5d, and the results of fitting the alkyl stacking lamella peaks and π - π stacking peaks is shown in Table 4-2.

Table 4-2. Crystalline parameters found from the GIWAXS patterns. Uncertainties of the final digit are indicated in parentheses after the value.

Polymer	T ^a	d _{alkyl} ^b	ζ_{alkyl} ^{c,f}	d _{π-π} ^d	ζ_{π - $\pi}$ ^{e,f}
		[nm]	[nm]	[nm]	[nm]
PDPP[T] ₂ -TPT	as cast	2.3(1)	5.1(1)	0.395(3)	2.6(5)
PDPP[T] ₂ -TPT	250 °C	2.15(5)	22.3(1)	0.392(1)	5.2(1)
PDPP[T] ₂ -TPF ₂ T	as cast	2.2(1)	8.25(5)	0.375(1)	5.4(1)
PDPP[T] ₂ -TPF ₂ T	250 °C	2.2(1)	19.3(1)	0.381(1)	7.6(1)
PDPP[T] ₂ -TPF ₄ T	as cast	2.22(5)	7.82(3)	0.377(1)	5.3(1)
PDPP[T] ₂ -TPF ₄ T	250 °C	2.2(1)	18.9(1)	0.378(1)	8.1(1)

^a Annealing process; ^b alkyl spacing; ^c alkyl stacking coherence length; ^d π - π stacking spacing; ^e π - π stacking coherence length; ^f the crystal coherence length ζ gives information about the distance over which order is maintained and is defined as $\zeta = 2\pi/\text{FWHM}$, where FWHM is the full width at half maximum of the first order lamellar stacking or π - π stacking peak, respectively. It is related to the Scherrer equation, which connects the width of a peak to the crystal size.

We can see that the process of annealing increases the coherence lengths of both types of stacking, but particularly in the alkyl stacking direction, where the coherence length increases by a factor of 4 in the case of PDPP[T]₂-TPT, whereas the increase is only by a bit more than a factor of 2 for both fluorinated polymers. It is clear that the addition of fluorine to the backbone decreases the stacking distance, with the annealed PDPP[T]₂-TPF₄T film having the smallest of the annealed π - π stacking distances. In the case of the unannealed films, fluorination yields distinctly smaller π - π stacking values. With the alkyl lamella stacking stretching out at the same time upon fluorination, a general flattening of the unit cell can be deduced.

4.2.5 Charge Carrier Mobilities

To investigate the influence of the degree of fluorination on the charge carrier mobilities, the polymers were investigated in organic field effect transistor (OFET) devices using a bottom gate / bottom contact (BGBC) configuration. Details on the device preparation and charge carrier mobility determination are given in the experimental section.

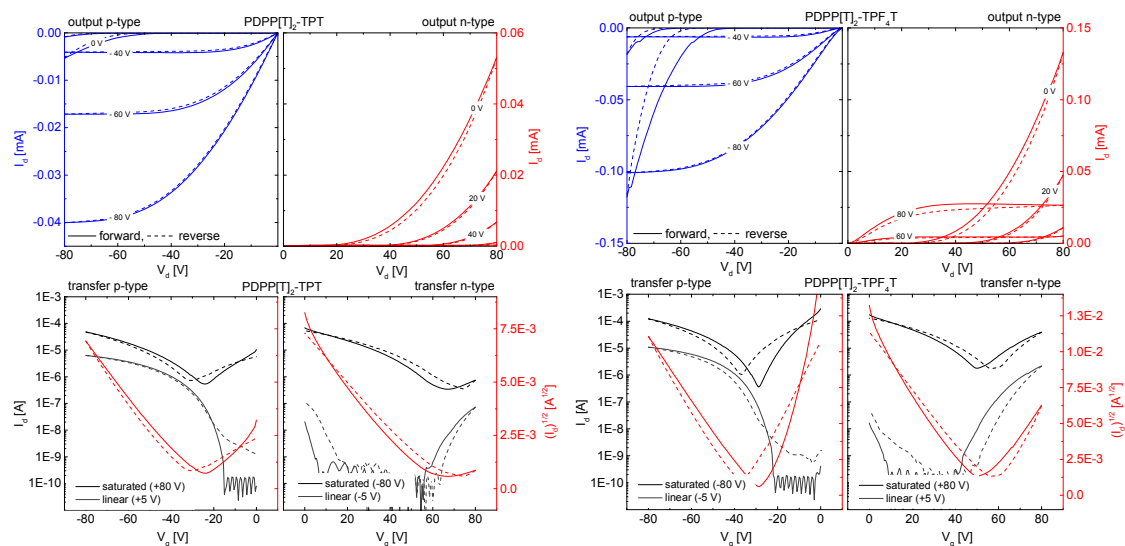


Figure 4-7. Representative OFET I - V curves in p-channel (blue output) and n-channel (red output) operation for the non-fluorinated PDPP[T]₂-TPT (left) and the tetrafluorinated PDPP[T]₂-TPF₄T (right) after annealing at 350 °C. Solid lines represent forward scans, dashed lines the reverse scans in all graphs. In transfer curves (bottom), the black and gray plots indicate the transfer characteristics in the saturation and linear operation regime, respectively. I - V curves for the difluorinated PDPP[T]₂-TPF₂T as well as a scaled comparison of the n-output characteristics for all three polymers are given in the Supporting Information (Figure S4-9, Figure S4-10).

Table 4-3. Average OFET-Mobilities of PDPP[Ar]₂-TPF_nT copolymers in a bottom gate / bottom contact configuration in as cast and annealed films.

Polymer	As Cast μ_h^a [cm ² V ⁻¹ s ⁻¹]	Annealed ^b 200 °C μ_h^a [cm ² V ⁻¹ s ⁻¹]	Annealed ^b 250 °C μ_h^a [cm ² V ⁻¹ s ⁻¹]	Annealed ^b 300 °C μ_h^a [cm ² V ⁻¹ s ⁻¹]	Annealed ^b 350 °C μ_h^a [cm ² V ⁻¹ s ⁻¹]	μ_e^a [cm ² V ⁻¹ s ⁻¹]
PDPP[T] ₂ -TPT	(2.3 ± 0.4) × 10 ⁻²	(4.1 ± 1.2) × 10 ⁻²	(2.6 ± 0.9) × 10 ⁻²	(5.8 ± 0.7) × 10 ⁻²	(3.7 ± 3.4) × 10 ⁻³	(2.0 ± 0.9) × 10 ⁻⁴
PDPP[T] ₂ -TPF ₂ T	(5.7 ± 0.9) × 10 ⁻³	(2.0 ± 0.4) × 10 ⁻²	(1.5 ± 0.5) × 10 ⁻²	(1.9 ± 0.8) × 10 ⁻²	(2.5 ± 0.9) × 10 ⁻²	(8.0 ± 3.4) × 10 ⁻³
PDPP[T] ₂ -TPF ₄ T	(2.6 ± 0.5) × 10 ⁻³	(1.3 ± 0.2) × 10 ⁻²	(1.1 ± 0.3) × 10 ⁻²	(1.4 ± 0.4) × 10 ⁻²	(1.5 ± 0.8) × 10 ⁻²	(1.3 ± 0.5) × 10 ⁻²

^aHole (μ_h) / electron (μ_e) mobilities determined from saturated operation regime. All values were averaged over a minimum of 10 devices; ^bAnnealing was performed for 15 min in a nitrogen atmosphere. See Supporting Information (Table S4-2) for threshold voltages and on/off ratios.

As typical examples, the I - V transfer as well as output curves for the non-fluorinated PDPP[T]₂-TPT and the tetrafluorinated PDPP[T]₂-TPF₄T are shown in Figure 4-7 and the mobility values are summarized for different annealing conditions in Table 4-3. The I - V curves for PDPP[T]₂-TPF₂T are given in the Supporting Information (Figure S4-9). A comparison of the output curves for all polymers in n-channel operation can also be found in the Supporting Information (Figure S4-10), giving an overview of the output currents in different scales. For

the as cast films as well as for annealed films up to 250 °C, no n-channel behavior was observable. For the p-type devices, the threshold voltage was 0 V for all devices and the non-fluorinated PDPP[T]₂-TPT shows the highest hole mobility ($\mu_h = 2.3 \times 10^{-2} \text{ cm}^2\text{V}^{-1}\text{s}^{-1}$). Difluorination leads to a fivefold decrease in hole mobility whereas tetrafluorination in PDPP[T]₂-TPF₄T results in a decrease of one order of magnitude in hole mobility ($2.6 \times 10^{-3} \text{ cm}^2\text{V}^{-1}\text{s}^{-1}$). This decrease in μ_h stands in contrast to the alignment of the as cast films which is much higher for the fluorinated derivatives as discussed in the GIWAXS section. Although surface alignment plays a crucial role in OFET devices, it is important to note that high hole mobilities are influenced by the electron-richness of the polymer as well as the quality of the dielectric-semiconductor interface. As already discussed, the S...F interaction in general is supposed to help planarization of the polymer backbone^[11] which is also in agreement with the structural data from single crystals of the incorporated oligomers.^[14-15, 29-31] In a series of fluorinated DPP copolymers, we have earlier shown that fluorination mainly improves the n-type character of semiconducting polymers or leads to ambipolarity in otherwise exclusively p-type materials.^[23]

Annealing leads to an increased hole mobility at the cost of higher threshold voltages around 30 V for the non-fluorinated PDPP[T]₂-TPT reaching a maximum of $5.8 \times 10^{-2} \text{ cm}^2\text{V}^{-1}\text{s}^{-1}$ after annealing at 300 °C. This increase can be explained by the higher degree of edge-on alignment as evidenced by the GIWAXS experiments and an S-Parameter close to 0.9 after annealing. In the fluorinated polymer films, the hole mobility is increased by one order of magnitude upon annealing at temperatures between 200 °C and 300 °C to give values in the range of $1\text{-}2 \times 10^{-2} \text{ cm}^2\text{V}^{-1}\text{s}^{-1}$.

Upon annealing at 350 °C, the non-fluorinated PDPP[T]₂-TPT shows an onset of a weak n-type character with a rather low electron mobility value of $2.0 \times 10^{-4} \text{ cm}^2\text{V}^{-1}\text{s}^{-1}$ and a high threshold voltage of 54 V, leading to barely visible output even when operated at a high gate voltage of 80 V. Even though it is a weak n-type behaviour, it clearly indicates the onset of ambipolar behaviour. On the other hand, for the fluorinated derivatives, annealing at 350 °C improves the n-channel performance considerably. Thus, electron mobilities of $8.0 \times 10^{-3} \text{ cm}^2\text{V}^{-1}\text{s}^{-1}$ for PDPP[T]₂-TPF₂T and $1.3 \times 10^{-2} \text{ cm}^2\text{V}^{-1}\text{s}^{-1}$ for PDPP[T]₂-TPF₄T respectively, could be obtained. The threshold voltage for n-channel operation is also decreased with respect to the non-fluorinated polymer and remains at around 50 V. Additionally, in these polymers, the hole-mobility is not negatively influenced by this high-temperature annealing step and remains in the range of $10^{-2} \text{ cm}^2\text{V}^{-1}\text{s}^{-1}$. The origin of the high threshold voltages could be related to electron trapping at the dielectric/polymer interface.^[32]

4.3 Experimental Section

4.3.1 Materials and methods

All reagents were used without further purification unless otherwise noted. Microwave reactions were conducted in sealed containers using a Biotage Initiator Eight+ microwave. All polymer ^1H and ^{19}F NMR spectra were recorded on a Varian INOVA 300 spectrometer at 393 K in 1,1,2,2-tetrachloroethane (TCE) as solvent. The ^1H spectra were referenced internally by using the residual solvent resonances. Deuterated solvents were obtained from Deutero. Gel permeation chromatography (GPC) analysis was carried out on an Agilent (Polymer Laboratories Ltd.) PL-GPC 220 high temperature chromatographic unit equipped with DP, RI and LS (15° and 90°) detectors and three linear mixed bed columns of PLgel 13 μm (Olexis) with a linear MW operating range: 500 - 15,000,000 g mol^{-1} . GPC analysis was performed at 150°C using 1,2,4-trichlorobenzene as the mobile phase. The samples were prepared by dissolving the polymer (0.1 wt-%) in the mobile phase solvent in an external oven and the solutions were run without filtration. The molecular weights of the samples were referenced to linear polystyrene ($M_w = 162 - 6,000,000 \text{ g mol}^{-1}$, $K = 12.100$ and $\text{Alpha} = 0.707$) and were not corrected with K and Alpha values for the measured sample. Cyclic voltammetry was performed under moisture- and oxygen-free conditions using a 0.1 M tetra-*n*-butylammonium hexafluorophosphate in acetonitrile electrolyte solution. A standard three-electrode assembly connected to a potentiostat (model 263A, EG&G Princeton Applied Research) was used at a scanning rate of 100 mV s^{-1} . The working electrode was a $10 \text{ }\Omega/\square$ ITO coated glass substrate. The polymers were spincoated onto the ITO substrates from chloroform at 3 mg/mL and 1500 rpm to obtain thicknesses of 10-20 nm. A platinum wire in acetonitrile was used as counter electrode and the quasi-reference electrode consisted of an Ag wire in an $\text{AgNO}_3/\text{acetonitrile}$ solution (0.1 M). The measurements were calibrated with an external ferrocene/ferrocenium standard, IP and EA values were calculated considering the solvent effects as per a published procedure^[33] using Equation 1 and 2 where the workfunction of Fc/Fc^+ is taken to be -5.23 eV . The reduction half-step potential $E_{1/2}^{\text{red}}$ (vs Fc/Fc^+) is negative whereas the oxidation half-step potential $E_{1/2}^{\text{ox}}$ (vs Fc/Fc^+) is positive.

$$\text{EA} = -5.23 \text{ eV} - E_{1/2}^{\text{red}}(\text{vs Fc} / \text{Fc}^+) \quad (1)$$

$$\text{IP} = -5.23 \text{ eV} - E_{1/2}^{\text{ox}}(\text{vs Fc} / \text{Fc}^+) \quad (2)$$

Absorption measurements were carried out on a JASCO V-670 spectrophotometer. Photoluminescence measurements were carried out on a JASCO FP-8600 spectrofluorometer, excitation wavelengths were chosen at the maximum of the transition around 430 nm for all samples. Optical properties in solution were measured in chloroform at a concentration of

0.01 mg/mL and a path length of 10 mm, films were spin-coated onto glass slides from a 7 mg/mL chloroform solution at 1500 rpm. Solutions for spin-coating were prepared by dissolving the polymer in chloroform at the given concentration and stirring at 55 °C for 8 h. Thermogravimetric analysis was performed on a Netzsch STA 449 F3 Jupiter under N₂ atmosphere at a heating rate of 10 K min⁻¹. Temperature of decomposition ($T_{5\%}$) was calculated from the 5% degradation step of the respective curve. Flash-DSC measurements have been performed on a Mettler-Toledo Flash DSC 1.^[34]

GIWAXS measurements were conducted at the SAXS/WAXS beamline of the Australian Synchrotron.^[35] Samples were prepared by spincoating a polymer film onto an octyltrichlorosilane/SiO₂ modified silicon wafer from a 6 mg mL⁻¹ solution at 2000 rpm. Highly collimated 9 keV X-rays were calibrated to be at a tilt angle of 0 ± 0.01 degrees when parallel to the surface of each sample by use of a Silicon crystal analyzer. A Dectris Pilatus 1M detector collected 2D scattering patterns, including those shown in Figure 4-5. Each scattering pattern was tiled together from three 1-second images with the detector slightly moved between exposures, such that the resulting image removes gaps between the detector modules. The sample to detector distance was measured using a Silver Behenate scattering standard. Data was analysed using a modified version of the NIKA small angle scattering analysis package.^[36]

4.3.2 Device preparation and characterization

Organic thin film transistors substrates in bottom gate / bottom contact configuration were bought from Fraunhofer IPMS (OFET Gen. 4). Heavily n-doped silicon (doping at wafer surface: $n \sim 3 \times 10^{17} \text{ cm}^{-3}$) was used as substrate and gate electrode. Thermally grown silicon oxide (230 nm \pm 10 nm) was used as the gate dielectric. Gold electrodes (30 nm on 10 nm ITO as adhesion layer) were used as source and drain contacts. The channel width was 10 mm for all devices and channel lengths of 10 μm and 20 μm were used. The substrates were cleaned subsequently in acetone and 2-propanol in an ultrasonic bath for 10 minutes each. Treatment in an ozone oven at 50 °C for 20 min was followed by immersion in a 1 wt-% solution of octyltrichlorosilane in toluene at 60 °C for 60 min. After rinsing with toluene and 2-propanol the substrates were dried in a nitrogen stream and the polymer was spincoated from a 6 mg/mL chloroform solution at 2000 rpm under ambient conditions. Devices were measured in a nitrogen atmosphere using an Agilent B1500 Semiconductor Parameter Analyzer. The devices were annealed in a nitrogen atmosphere at a maximum of 0.9 ppm O₂ for 15 minutes consecutively at the temperatures given in the main text. Mobilities were calculated from the slopes in the $(I_d)^{0.5}$ - V_g plots in the saturation regime using Equation 3 where I_d is the drain current, W the channel width, L the channel length, C_i the capacitance, V_g the gate voltage and V_T the threshold voltage, respectively.

$$I_d \approx \frac{W}{2L} C_i \mu (V_g - V_T)^2 \quad (3)$$

4.3.3 Synthesis procedures for the DPP compounds.

All syntheses were conducted under argon using a double manifold schlenk line. Glasware was severely dried under high vacuum. Solvents were degassed by three freeze-pump-thaw cycles. Monomers used for polymerization were recrystallized freshly on the same day.

PDPP[T]₂-TPT. An oven dried microwave vial was loaded with DPP[T]₂{2DTd}₂Br₂ (124.4 mg, 0.110 mmol), 1,4-bis(5-(trimethylstannyl)thiophen-2-yl)benzene (62.85 mg, 0.111 mmol), tri-*o*-tolylphosphine (3.92 mg, 13 μ mol) and finally tris(dibenzylideneacetone)dipalladium(0) (3.15 mg, 3.4 μ mol). Dry and degassed chlorobenzene (3.0 mL) was added, the vial was sealed with a septum cap and subsequently purged with argon for 15 min. The mixture was stirred for 30 min at 180 °C in the microwave. After cooling to 50 °C 2-tributyltinthiophene (25 μ L, 79 μ mol) was added to the green gel using a microliter syringe. The mixture was again heated at 180 °C for 5 min in the microwave, cooled to 50 °C and finally 2-bromothiophene (30 μ L, 308 μ mol) was added. The mixture was heated to 180 °C for 5 min in the microwave. After cooling to room temperature the polymer was precipitated in 200 mL methanol and filtrated into a soxhlet thimble. The crude polymer was subjected to soxhlet extraction using acetone, hexane, dichloromethane and chloroform. The chloroform fraction was concentrated to 4 mL under reduced pressure and precipitated in 200 mL methanol. Filtration over a 0.45 μ m PTFE filter followed by drying in high vacuum afforded PDPP[T]₂-TPT as a dark purple solid (91 mg, 68%). ¹H NMR (300 MHz, TCE): δ (ppm) 5.85 (br, s), 7.69-7.37 (br, m), 4.10 (br, s, R₂N-CH₂-), 2.08 (br, s, -R₂CH-), 1.44-1.34 (br, m, -CH₂-), 0.95 (m, -CH₃).

PDPP[T]₂-TPF₂T. An oven dried microwave vial was loaded with DPP[T]₂{2DTd}₂Br₂ (148.80 mg, 0.132 mmol), (5,5'-(2,5-difluoro-1,4-phenylene)bis(thiophene-5,2-diyl))bis(trimethylstannane) (79.33 mg, 0.131 mmol), tri-*o*-tolylphosphine (5.43 mg, 18 μ mol) and finally tris(dibenzylideneacetone)dipalladium(0) (4.23 mg, 4.6 μ mol). Dry and degassed chlorobenzene (5.0 mL) was added, the vial was sealed with a septum cap and subsequently purged with argon for 15 min. The mixture was stirred for 30 min at 180 °C in the microwave. After cooling to 50 °C 2-tributyltinthiophene (25 μ L, 79 μ mol) was added to the green gel using a microliter syringe. The mixture was again heated at 180 °C for 5 min in the microwave, cooled to 50 °C and finally 2-bromothiophene (30 μ L, 308 μ mol) was added. The mixture was heated to 180 °C for 5 min in the microwave. After cooling to room temperature the polymer was precipitated in 200 mL methanol and filtrated into a soxhlet thimble. The crude polymer was subjected to soxhlet extraction using methanol, acetone, hexane, dichloromethane and chloroform. The chloroform fraction was concentrated to 4 mL

under reduced pressure and precipitated in 200 mL methanol. Filtration over a 0.45 μm PTFE filter followed by drying in high vacuum afforded PDPP[T]₂-TPF₂T as a dark purple solid (131 mg, 70%). ¹H NMR (300 MHz, TCE): δ (ppm) 8.84 (br, s), 7.40-7.24 (br, m), 4.11 (br, s, R₂N-CH₂-), 2.06 (br, s, -R₂CH-), 1.44-1.34 (br, m, -CH₂-), 0.95 (br, s, -CH₃); ¹⁹F NMR (282 MHz, TCE) δ (ppm) -117.96.

PDPP[T]₂-TPF₄T. An oven dried microwave vial was loaded with DPP[T]₂{2DTd}₂Br₂ (163.46 mg, 0.144 mmol), (5,5'-(perfluoro-1,4-phenylene)bis(thiophene-5,2-diyl))bis(trimethylstannane) (93.37 mg, 0.144 mmol), tri-*o*-tolylphosphine (5.20 mg, 17 μmol) and finally tris(dibenzylideneacetone)dipalladium(0) (3.92 mg, 4.3 μmol). Dry and degassed chlorobenzene (5 mL) was added, the vial was sealed with a septum cap and subsequently purged with argon for 15 min. The mixture was stirred for 30 min at 180 °C in the microwave. After cooling to 50 °C 2-tributyltinthiophene (25 μL , 79 μmol) was added to the green gel using a microliter syringe. The mixture was again heated at 180 °C for 5 min in the microwave, cooled to 50 °C and finally 2-bromothiophene (30 μL , 308 μmol) was added. The mixture was heated to 180 °C for 5 min in the microwave. After cooling to room temperature the polymer was precipitated in 250 mL methanol and filtrated over a 0.45 μm PTFE filter. The crude polymer was subjected to soxhlet extraction using methanol, acetone, hexane and dichloromethane. The solid remains were refluxed in 150 mL chloroform for 2 h and filtrated. The filtrate was then concentrated to 4 mL under reduced pressure and precipitated in 200 mL methanol. Filtration over a 0.45 μm PTFE filter followed by drying in high vacuum afforded PDPP[T]₂-TPF₄T as a dark purple solid (108 mg, 52%). ¹H NMR (300 MHz, TCE): δ (ppm) 8.85 (br, s), 7.71-7.15 (br, m), 4.10 (br, s, R₂N-CH₂-), 2.07 (br, s, -R₂CH-), 1.44-1.33 (br, m, -CH₂-), 0.95 (br, m, -CH₃); ¹⁹F NMR (282 MHz, TCE) δ (ppm) -139.97.

4.4 Conclusions

Diketopyrrolo[3,4-*c*]pyrrole copolymers incorporating an extended thiophene-phenylene-thiophene moiety with varying degrees of fluorination have been successfully synthesized. The concept of fluorination was evaluated in terms of alignment and solid state packing. As evident from GIWAXS, fluorination has a small influence on the alkyl spacing distance as well as the π - π stacking distance. However, the crystal coherence length can be significantly improved upon fluorination. Furthermore, we showed that upon gradual increase of fluorination and annealing the edge-on alignment of the polymer chains improves significantly, resulting in almost perfect edge-on alignment throughout the complete bulk of the film in the tetrafluorinated derivative. Whereas alignment is improved, fluorination does not necessarily lead to improved hole transport, but is a good approach to achieve ambipolar character in otherwise p-type materials. From our results we are able to draw concrete structure property

relationships and their interplay regarding the degree of fluorination on alignment and charge carrier transport.

4.5 Acknowledgements

We acknowledge financial support from DFG (SFB 840) and the Bavarian State Ministry of Education, Science and the Arts (Solar technologies go hybrid). C.J.M. thanks the Fonds der Chemischen Industrie for funding the PhD with a Kekulé scholarship and the German National Academic Foundation for other support during the PhD. Support from the Elitenetzwerk Bayern (ENB), Macromolecular Science is also kindly acknowledged. Work in Australia was supported by the Australian Research Council (grant DP13012616). This research was undertaken in part on the SAXS/WAXS beamline at the Australian Synchrotron, Victoria, Australia.^[35]

4.6 References

- [1] X. Zhang, L. J. Richter, D. M. DeLongchamp, R. J. Kline, M. R. Hammond, I. McCulloch, M. Heeney, R. S. Ashraf, J. N. Smith, T. D. Anthopoulos, B. Schroeder, Y. H. Geerts, D. A. Fischer, M. F. Toney, *J. Am. Chem. Soc.* **2011**, *133*, 15073.
- [2] Z. Yi, S. Wang, Y. Liu, *Adv. Mater.* **2015**, *27*, 3589.
- [3] Z. Chen, M. J. Lee, R. Shahid Ashraf, Y. Gu, S. Albert-Seifried, M. Meedom Nielsen, B. Schroeder, T. D. Anthopoulos, M. Heeney, I. McCulloch, H. Sirringhaus, *Adv. Mater.* **2012**, *24*, 647.
- [4] I. Kang, H. J. Yun, D. S. Chung, S. K. Kwon, Y. H. Kim, *J. Am. Chem. Soc.* **2013**, *135*, 14896.
- [5] W. Li, K. H. Hendriks, A. Furlan, W. S. Roelofs, S. C. Meskers, M. M. Wienk, R. A. Janssen, *Adv. Mater.* **2014**, *26*, 1565.
- [6] W. Li, K. H. Hendriks, A. Furlan, W. S. C. Roelofs, M. M. Wienk, R. A. J. Janssen, *J. Am. Chem. Soc.* **2013**, *135*, 18942.
- [7] Z. Yi, L. Ma, B. Chen, D. Chen, X. Chen, J. Qin, X. Zhan, Y. Liu, W. J. Ong, J. Li, *Chem. Mater.* **2013**, *25*, 4290.
- [8] M. J. Cho, J. Shin, T. R. Hong, H. A. Um, T. W. Lee, G. W. Kim, J. H. Kwon, D. H. Choi, *Polym. Chem.* **2014**, *6*, 150.
- [9] H. G. Kim, B. Kang, H. Ko, J. Lee, J. Shin, K. Cho, *Chem. Mater.* **2015**, *27*, 829.

- [10] J. D. Yuen, J. Fan, J. Seifert, B. Lim, R. Hufschmid, A. J. Heeger, F. Wudl, *J. Am. Chem. Soc.* **2011**, *133*, 20799.
- [11] N. E. Jackson, B. M. Savoie, K. L. Kohlstedt, M. Olvera de la Cruz, G. C. Schatz, L. X. Chen, M. A. Ratner, *J. Am. Chem. Soc.* **2013**, *135*, 10475.
- [12] H. Zhong, C. Z. Li, J. Carpenter, H. Ade, A. K. Jen, *J. Am. Chem. Soc.* **2015**, *137*, 7616.
- [13] J. H. Park, E. H. Jung, J. W. Jung, W. H. Jo, *Adv. Mater.* **2013**, *25*, 2583.
- [14] D. J. Crouch, P. J. Skabara, J. E. Lohr, J. J. W. McDouall, M. Heeney, I. McCulloch, D. Sparrowe, M. Shkunov, S. J. Coles, P. N. Horton, M. B. Hursthouse, *Chem. Mater.* **2005**, *17*, 6567.
- [15] D. J. Crouch, P. J. Skabara, M. Heeney, I. McCulloch, S. J. Coles, M. B. Hursthouse, *Chem. Commun.* **2005**, 1465.
- [16] P. M. Sonar, J. Chang, Z. Shi, J. Wu, J. Li, *J. Mater. Chem. C* **2015**, *3*, 2080.
- [17] A. Luzio, D. Fazzi, F. Nübling, R. Matsidik, A. Straub, H. Komber, E. Giussani, S. E. Watkins, M. Barbatti, W. Thiel, E. Gann, L. Thomsen, C. R. McNeill, M. Caironi, M. Sommer, *Chem. Mater.* **2014**, *26*, 6233.
- [18] A. de Bettencourt-Dias, A. Poloukhine, *J. Phys. Chem. B* **2006**, *110*, 25638.
- [19] D. A. Guthrie, J. D. Tovar, *Org. Lett.* **2008**, *10*, 4323.
- [20] B. G. Kim, E. J. Jeong, J. W. Chung, S. Seo, B. Koo, J. Kim, *Nat Mater* **2013**, *12*, 659.
- [21] A. K. Palai, S. P. Mishra, A. Kumar, R. Srivastava, M. N. Kamalasanan, M. Patri, *Macromol. Chem. Phys.* **2010**, *211*, 1043.
- [22] C. B. Nielsen, R. S. Ashraf, B. C. Schroeder, P. D'Angelo, S. E. Watkins, K. Song, T. D. Anthopoulos, I. McCulloch, *Chem. Commun.* **2012**, *48*, 5832.
- [23] C. J. Mueller, C. R. Singh, M. Fried, S. Huettner, M. Thelakkat, *Adv. Funct. Mater.* **2015**, *25*, 2725.
- [24] H. Bronstein, J. M. Frost, A. Hadipour, Y. Kim, C. B. Nielsen, R. S. Ashraf, B. P. Rand, S. Watkins, I. McCulloch, *Chem. Mater.* **2013**, *25*, 277.
- [25] K. H. Hendriks, W. Li, M. M. Wienk, R. A. J. Janssen, *Advanced Energy Materials* **2013**, *3*, 674.
- [26] J.-L. Bredas, *Materials Horizons* **2014**, *1*, 17.
- [27] C. B. Nielsen, M. Turbiez, I. McCulloch, *Adv. Mater.* **2012**, *25*, 1859.

- [28] L. A. Perez, P. Zalar, L. Ying, K. Schmidt, M. F. Toney, T.-Q. Nguyen, G. C. Bazan, E. J. Kramer, *Macromolecules* **2014**, *47*, 1403.
- [29] A. Facchetti, M. H. Yoon, C. L. Stern, H. E. Katz, T. J. Marks, *Angew. Chem. Int. Ed. Engl.* **2003**, *42*, 3900.
- [30] M. H. Yoon, A. Facchetti, C. E. Stern, T. J. Marks, *J. Am. Chem. Soc.* **2006**, *128*, 5792.
- [31] T. Yamao, Y. Taniguchi, K. Yamamoto, T. Miki, S. Ota, S. Hotta, M. Goto, R. Azumi, *Japanese Journal of Applied Physics* **2007**, *46*, 7478.
- [32] L. L. Chua, J. Zaumseil, J. F. Chang, E. C. Ou, P. K. Ho, H. Sirringhaus, R. H. Friend, *Nature* **2005**, *434*, 194.
- [33] K. Gräf, M. A. Rahim, S. Das, M. Thelakkat, *Dyes and Pigments* **2013**, *99*, 1101.
- [34] V. Mathot, M. Pyda, T. Pijpers, G. Vanden Poel, E. van de Kerkhof, S. van Herwaarden, F. van Herwaarden, A. Leenaers, *Thermochim. Acta* **2011**, *522*, 36.
- [35] N. M. Kirby, S. T. Mudie, A. M. Hawley, D. J. Cookson, H. D. T. Mertens, N. Cowieson, V. Samardzic-Boban, *J. Appl. Crystallogr.* **2013**, *46*, 1670.
- [36] J. Ilavsky, *J. Appl. Crystallogr.* **2012**, *45*, 324.

Supporting Information

Literature Analysis on Single Crystal Structures.....	163
Monomer Syntheses	165
Materials and methods.....	165
TPT monomer	165
TPF ₂ T monomer	167
TPF ₄ T monomer	169
DPP monomer	170
Monomer Characterization	172
NMR spectra of the monomers	172
Polymer Characterization	184
Polymer NMR.....	184
Gel Permeation Chromatography (GPC).....	187
Thermogravimetric Analysis (TGA)	188
Flash-DSC.....	189
Cyclic Voltammetry	190
GIWAXS analysis and S-Parameter calculation.....	191
Additional OFET <i>I</i> - <i>V</i> curves.....	192
Supporting References	195

Literature Analysis on Single Crystal Structures

Single crystal structures were evaluated from previous publications^[1-5] on fluorinated oligoaromatic systems which reported single crystal X-ray data that was deposited at the library of the Cambridge Crystallographic Data Centre (CCDC). We analyzed all structures in the database with the relevant thiophene-*n*-fluorophenylene-thiophene motif, where *n* = 0, 2, 4. The most crystal structures describe oligomers that are either slightly larger (i.e. with terminal groups attached) or with solubilizing sidechains, mostly a hexyl-group on the thiophene ring. The relevant dihedral angles between a thiophene ring and an adjacent *n*-fluorinated phenyl ring are therefore printed bold in Table S4-1. The exact structures of all molecules with the measured dihedral angles as bold bonds and their respective values given in red is shown in Figure S4-1 and Figure S4-2.

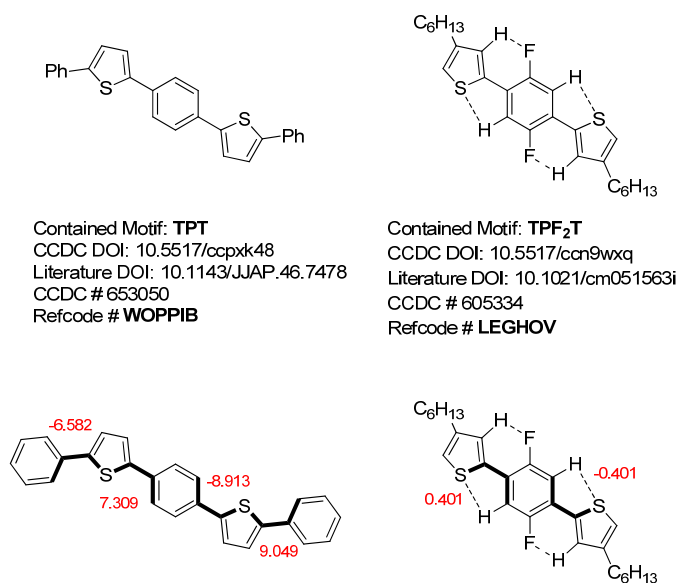


Figure S4-1. Structures with CCDC database details and the measured dihedral angles for the TPT motif (left) and the TPF₂T motif (right).

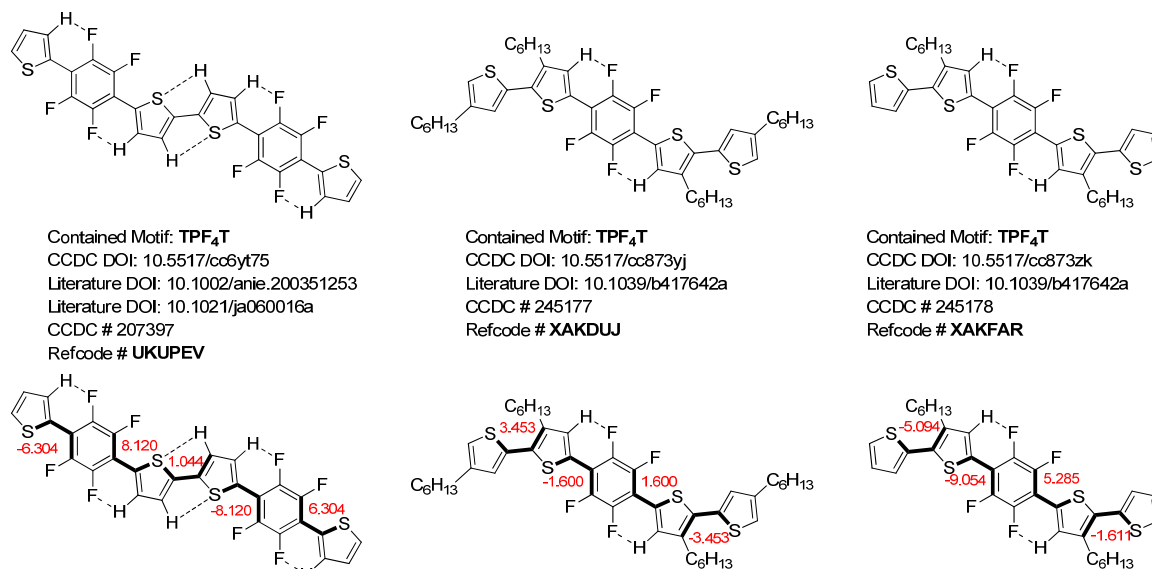


Figure S4-2. Structures with CCDC database details and the measured dihedral angles for the TPF₄T motif (right).

Table S4-1. Dihedral angles between aromatic units determined by single crystal X-ray crystallography. Bold entries describe the relevant angle between a thiophene ring and a *n*-fluorinated phenyl ring.

CCDC Refcode	structural motif contained	<i>n</i>	dihedral angle 1	dihedral angle 2	dihedral angle 3	dihedral angle 4	dihedral angle 5
WOPPIB ^[5]	TPT	0	-6.582	7.309	-8.913	9.049	
LEGHOV ^[4]	TPF ₂ T	2	0.401	-0.401			
UKUPEV ^[2-3]	TPF ₄ T	4	-6.304	8.120	1.044	-8.120	6.304
XAKDUJ ^[1]	TPF ₄ T	4	3.453	-1.600	1.600	-3.453	
XAKFAR ^[1]	TPF ₄ T	4	-5.094	9.054	5.285	-1.611	

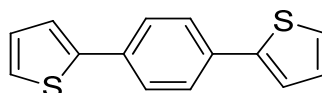
It is noteworthy that the dihedral angles decrease from roughly 8° in the unsubstituted TPT^[5] to 0.4° in the difluorinated^[4] TPF₂T and increase again upon tetrafluorination^[1-3] in TPF₄T. This might be ascribed to the unfavourable interactions of fluorine- and sulphur-lone pairs.

Monomer Syntheses

Materials and methods

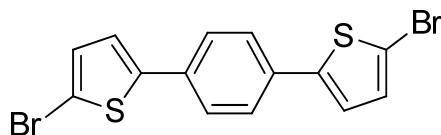
All reagents were used without further purification unless otherwise noted. Syntheses were conducted under argon using a double manifold schlenk line. Glasware was severely dried under high vacuum. Solvents were degassed by three freeze-pump-thaw cycles. ¹H NMR (300 MHz) and ¹³C NMR (75 MHz) spectra were recorded on a Bruker AC 300 spectrometer and calibrated according to the respective solvent resonance signal. ¹⁹F-NMR spectra were measured on the same spectrometer using either internal or external hexafluorobenzene as calibrant. ¹¹⁹Sn NMR were recorded on a Varian INOVA 400 spectrometer. EIMS measurements were performed on a Finnigan MAT8500 using an ionization energy of 70 eV.

TPT monomer

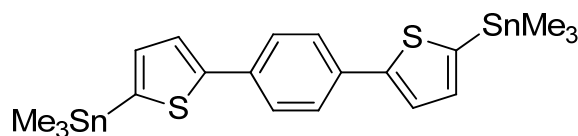


1,4-di(thiophene-2-yl)benzene (2a). In a dry 250 two neck flask 2-tributyltinthiophene (8.28 mL, 26.1 mmol) and 1,4-dibromobenzene (**1a**) (3.00 g, 12.7 mmol) were dissolved in 100 mL anhydrous toluene. The mixture was purged with argon for 15 min before tetrakis(triphenylphosphine)palladium(0) (735 mg, 636 μ mol) was added and purging with argon was continued for another 15 min. The mixture was then refluxed at 115 °C for 21 h.

The Solution was cooled to 40 °C and the solvent was removed into a liquid nitrogen trap under high vacuum to remove all volatile tin compounds. The oily residue was redissolved in 200 mL toluene and washed with water (3 x 150 mL). Finally the organic phase was washed with brine and dried over magnesium sulfate. After filtration the solvent was removed under reduced pressure. The crude yellow product was recrystallized from a mixture of hexane/ethanol/toluene (4:1.5:1). Vacuum filtration and washing with ethanol yielded 2.405 g 1,4-di(thiophene-2-yl)benzene (9.92 mmol, 78%) (**2a**) as pale yellow crystals. $^1\text{H-NMR}$ (300 MHz, CHCl_3): δ (ppm) 7.62 (s, 4 H, Ph-H), 7.34 (dd, 2 H, $J = 3.6$ Hz $J = 1.1$ Hz), 7.29 (dd, 2 H, $J = 5.1$ Hz, $J = 1.1$ Hz), 7.10 (dd, 2 H, $J = 5.1$ Hz, $J = 3.6$ Hz). EIMS (70 eV) m/z : M^+ 242 (100), 197 (20), 165 (5), 152 (5), 139 (5), 121(5).



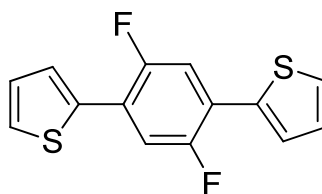
1,4-bis(5-bromothiophen-2-yl)benzene (3a). A mixture of 1,4-di(thiophene-2-yl)benzene (**2a**) (2.00 g, 8.25 mmol) and *N*-bromosuccinimide (3.67 g, 20.6 mmol) was dissolved in 183 mL anhydrous DMF. The resulting solution was stirred at 80 °C for 20 h. After addition of 600 mL water the precipitate was filtered off. The precipitate was washed with water. Recrystallization from a mixture of toluene/ethanol/chloroform (5:2:0.3) gave 2.258 g 1,4-bis(5-bromothiophen-2-yl)benzene (5.64 mmol, 68%) (**3a**) as silvery flakes. $^1\text{H-NMR}$ (300 MHz, CHCl_3): δ (ppm) 7.51 (s, 4 H, Ph-H), 7.07 (m, 2 H), 7.04 (m, 2 H). EIMS (70 eV) m/z : M^+ 400 (100), 320 (15), 277 (20), 240 (20), 195 (10), 139 (10).



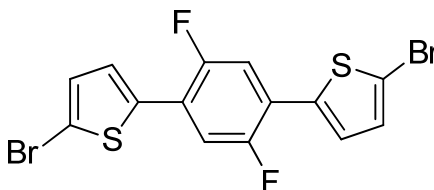
1,4-bis(5-(trimethylstannyl)thiophen-2-yl)benzene (4a). 1,4-bis(5-bromothiophen-2-yl)benzene (**3a**) (1.80 g, 4.51 mmol) was treated with 250 mL anhydrous THF in an ultrasoundbath for 1 h to afford a fine suspension of the starting material. After cooling to -78 °C *n*BuLi (2.5 M in hexane) (3.78 mL, 9.46 mmol) was added slowly. The resulting bright green suspension was stirred at -78 °C for 60 min and subsequently allowed to warm to room temperature over the course of 60 min. After cooling to -78 °C again, trimethyltin chloride (1.89 g, 9.46 mmol) in 9.5 mL anhydrous THF was added via cannula. After complete addition the suspension was allowed to warm to room temperature within 1 h. Water

(500 mL) and ethanol (250 mL) were added to precipitate the product. The precipitate was filtered off, washed with water and dried under vacuum. Recrystallization from a mixture of ethanol/toluene (10:1) gave 1.426 g 1,4-bis(5-(trimethylstannyl)thiophene-2-yl)benzene (2.51 mmol, 56%) (**4a**) as yellow-green needles. $^1\text{H-NMR}$ (300 MHz, CHCl_3): δ (ppm) 7.61 (s, 4 H, Ph-H), 7.44 (d, 2 H, $J = 3.4$ Hz), 7.17 (d, 2 H, $J = 3.4$ Hz). EIMS (70 eV) m/z : M^+ 468 (25), $[\text{M-CH}_3]^+$ 453 (100), 423 (20), 393 (10), 219 (15), 165 (15).

TPF₂T monomer

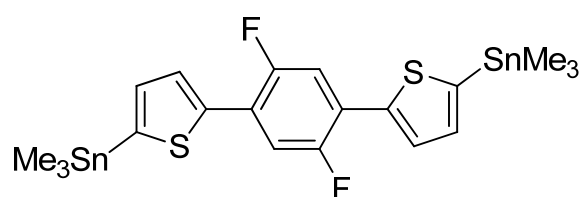


2,2'-(2,5-difluoro-1,4-phenylene)dithiophene (2b). In a dry 250 mL two-necked flask 100 mL anhydrous toluene, 2-tributyltinthiophene (4.79 mL, 15.1 mmol) and 1,4-dibromo-2,5-difluorobenzene (**1b**) (2.00 g, 7.36 mmol) were added. The mixture was purged with argon for 15 min, tetrakis(triphenylphosphine)palladium(0) (425 mg, 368 μmol) was added and purging with argon was continued for another 15 min. The mixture was then refluxed at 125 $^\circ\text{C}$ for 96 h. Water (100 mL) was added. The organic phase was separated and the aqueous phase was extracted with diethyl ether (3 x 80 mL). The combined organic phases were washed with brine and dried over magnesium sulfate. Solvents were removed under reduced pressure to obtain a fluorescent yellow solid, which was recrystallized from hexane/EtOH (1:1) to afford 1.66 g 2,2'-(2,5-difluoro-1,4-phenylene)dithiophene (5.96 mmol, 81%) (**2b**) as bright yellow crystals. $^1\text{H-NMR}$ (300 MHz, CHCl_3): δ (ppm) 7.52 (d, 2 H, $J = 3.7$ Hz), 7.45-7.39 (m, 4 H), 7.14 (dd, 2 H, $J = 5.1$ Hz, $J = 3.8$ Hz); $^{19}\text{F-NMR}$ (282.4 MHz, CHCl_3): δ (ppm) -122.39; $^{13}\text{C-NMR}$ (75.5 MHz, CHCl_3): δ (ppm) 156.62 (d, $J = 3.3$ Hz), 155.07 (d, $J = 5.4$ Hz), 153.34 (d, $J = 3.3$ Hz), 135.91, 128.04, 126.97 (t, $J = 3.2$ Hz), 126.69 (t, $J = 1.9$ Hz), 122.15, 122.00, 121.83, 115.69, 115.52, 115.44, 115.27. EIMS (70 eV) m/z : M^+ 278 (100), 246 (10), 233 (50), 220 (15), 201 (10), 188 (10), 175 (10), 139 (10).



5,5'-(2,5-difluoro-1,4-phenylene)bis(2-bromothiophene) (3b). A mixture of 2,2'-(2,5-difluoro-1,4-phenylene)dithiophene (**2b**) (1.60 g, 5.75 mmol) and *N*-bromosuccinimide

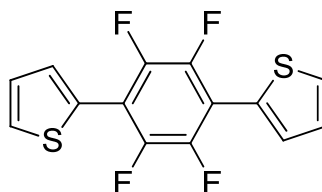
(2.56 g, 14.4 mmol) was dissolved in 100 mL anhydrous DMF. The resulting solution was stirred at 80 °C for 24 h. Toluene (200 mL) and water (200 mL) were added to the mixture. The organic layer was isolated and the aqueous layer was extracted with toluene (2 x 100 mL). The combined organic phases were washed with brine and dried over magnesium sulfate before the solvent was removed under reduced pressure. Recrystallization of the crude yellow solid from hexane/toluene (10:1) afforded 2.36 g 5,5'-(2,5-difluoro-1,4-phenylene)bis(2-bromothiophene) (5.41 mmol, 94%) (**3b**) as yellow needles. $^1\text{H-NMR}$ (300 MHz, CHCl_3): δ (ppm) 7.33 (dd, 2 H, $J = 9.2$ Hz, $J = 8.8$ Hz), 7.24 (d, 2 H, $J = 4.0$ Hz), 7.09 (d, 2 H, $J = 4.0$ Hz); $^{19}\text{F-NMR}$ (282.4 MHz, CHCl_3): δ (ppm) -121.89.



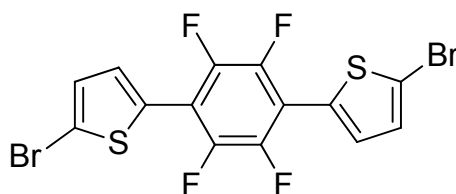
(5,5'-(2,5-difluoro-1,4-phenylene)bis(thiophene-5,2-diyl))bis(trimethylstannane)

(4b). To a solution of 5,5'-(2,5-difluoro-1,4-phenylene)bis(2-bromothiophene) (**3b**) (2.14 g, 4.90 mmol) in 200 mL anhydrous THF was added $n\text{BuLi}$ (2.5 M in hexane) (4.11 mL, 10.3 mmol) at -78 °C. The resulting bright green suspension was stirred at -78 °C for 30 min and subsequently allowed to warm to room temperature over the course of 60 min. After cooling to -78 °C again a stock solution of trimethyl tin chloride (2.24 g, 11.26 mmol) in 11.2 mL anhydrous THF was added dropwise. After complete addition the solution was stirred for 60 min at -78 °C before it was allowed to warm to room temperature and stirred for additional 2 h. Water (270 mL) was added and the mixture was extracted with diethyl ether (4 x 100 mL). The combined organic layers were then washed with brine and dried over magnesium sulfate. Solvents were removed under reduced pressure to obtain 2.921 g (5,5'-(2,5-difluoro-1,4-phenylene)bis(thiophene-5,2-diyl))bis(trimethylstannane) (4.84 mmol, 99%) (**4b**) as a bright yellow crystalline solid. Samples were recrystallized from toluene before the monomer was used in polymerizations. $^1\text{H-NMR}$ (300 MHz, CHCl_3): δ (ppm) 7.61 (d, 2 H, $J = 3.4$ Hz), 7.41 (t, 2 H, $J = 9.0$ Hz), 7.21 (d, 2 H, $J = 3.4$ Hz), 0.41 (m, 18 H, $J(^{117/119}\text{Sn-H}) = 55.3 / 57.8$ Hz, $-\text{SnMe}_3$); $^{19}\text{F-NMR}$ (282.4 MHz, CHCl_3): δ (ppm) -122.39; $^{13}\text{C-NMR}$ (75.5 MHz, CHCl_3): δ (ppm) 156.39 (d, $J = 3.1$ Hz), 153.12 (d, $J = 3.1$ Hz), 141.63, 139.89, 136.11, 127.92 (t, $J = 3.3$ Hz), 121.84 (dd, $J = 13.4$ Hz, $J = 11.7$ Hz), 115.44 (dd, $J = 18.3$ Hz, $J = 12.9$ Hz), -8.04; $^{119}\text{Sn-NMR}$ (186.5 MHz, CDCl_3): δ (ppm) -25.46 (m, $J(^{119}\text{Sn-CH}_3) = 374.3$ Hz, $J(^{119}\text{Sn-C}^1) = 483.6$ Hz). EIMS (70 eV) m/z : M^+ 604 (70), $[\text{M-CH}_3]^+$ 589 (100), 559 (35), 529 (10), 409 (10), 287 (30), 257 (15).

TPF₄T monomer

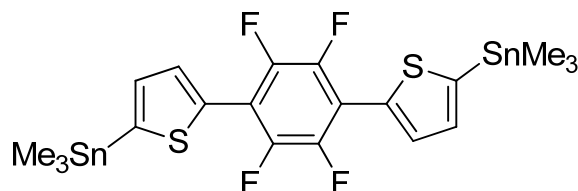


2,2'-(perfluoro-1,4-phenylene)dithiophene (2c). In a dry 250 mL two-necked flask 100 mL anhydrous toluene, 2-tributyltinthiophene (4.23 mL, 13.3 mmol) and 1,4-dibromo-2,3,5,6-tetrafluorobenzene (**1c**) (2.00 g, 6.50 mmol) were added. The mixture was purged with argon for 15 min, tetrakis(triphenylphosphine)palladium(0) (375 mg, 325 μ mol) was added and purging with argon was continued for another 15 min. The mixture was then refluxed at 130 °C for 48 h. Water (100 mL) was added. The organic phase was separated and the aqueous phase was extracted with diethyl ether (3 x 80 mL). The combined organic phases were washed with brine and dried over magnesium sulfate. Solvents were removed under reduced pressure to obtain a fluorescent yellow solid, which was recrystallized from hexane/EtOH (1:1) to afford 1.36 g 2,2'-(perfluoro-1,4-phenylene)dithiophene (4.33 mmol, 67%) (**2c**) as bright yellow crystals. ¹H-NMR (300 MHz, CHCl₃): δ (ppm) 7.68 (d, 1 H, J = 3.8 Hz), 7.57 (dd, 1 H, J = 5.2 Hz, J = 1.1 Hz), 7.21 (t, 1 H, J = 4.9 Hz); ¹⁹F-NMR (282.4 MHz, CHCl₃): δ (ppm) -144.00; ¹³C-NMR (75.5 MHz, CHCl₃): δ (ppm) 130.36 (t, J = 3.0 Hz), 128.46 (m), 127.97 (m), 127.49. EIMS (70 eV) m/z : M⁺ 314 (100), 269 (30), 256 (10), 211 (5), 157 (5), 46 (5).



5,5'-(perfluoro-1,4-phenylene)bis(2-bromothiophene) (3c). A mixture of 2,2'-(perfluoro-1,4-phenylene)dithiophene (**2c**) (1.20 g, 3.82 mmol) and *N*-bromosuccinimide (1.70 g, 9.54 mmol) was dissolved in 60 mL anhydrous DMF. The resulting solution was stirred at 80 °C for 72 h. Toluene (150 mL) and water (150 mL) were added to the mixture. The organic layer was isolated and the aqueous layer was extracted with toluene (2 x 100 mL). The combined organic phases were washed with brine and dried over magnesium sulfate before the solvent was removed under reduced pressure. Recrystallization of the crude yellow solid from hexane afforded 1.48 g 5,5'-(perfluoro-1,4-phenylene)bis(2-bromothiophene) (3.13 mmol,

82%) (**3c**) as yellow needles. $^1\text{H-NMR}$ (300 MHz, CHCl_3): δ (ppm) 7.43 (d, 1 H, $J = 4.1$ Hz), 7.16 (d, 1 H, $J = 4.1$ Hz); $^{19}\text{F-NMR}$ (282.4 MHz, CHCl_3): δ (ppm) -143.60.

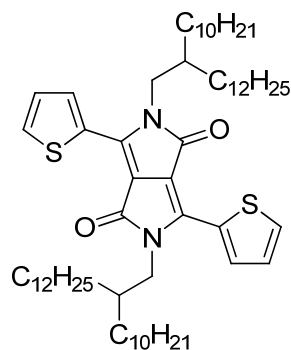


(5,5'-(perfluoro-1,4-phenylene)bis(thiophene-5,2-diyl))bis(trimethylstannane)

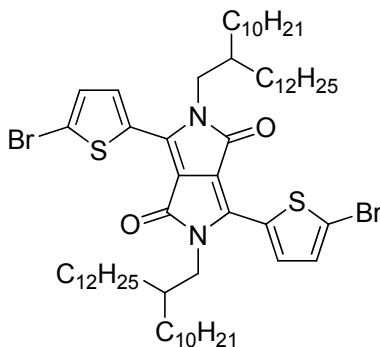
(4c). To a solution of 5,5'-(perfluoro-1,4-phenylene)bis(2-bromothiophene) (**3c**) (1.00 g, 2.11 mmol) in 260 mL anhydrous THF was added $n\text{BuLi}$ (2.5 M in hexane) (1.78 mL, 4.44 mmol) at -78°C . The resulting dark green suspension was stirred at -78°C for 30 min and subsequently allowed to warm to room temperature over the course of 60 min. After cooling to -78°C again a stock solution of trimethyl tin chloride (0.97 g, 4.86 mmol) in 5 mL anhydrous THF was added dropwise. After complete addition the solution was stirred for 60 min at -78°C before it was allowed to warm to room temperature and stirred for additional 2 h. Water (270 mL) was added and the mixture was extracted with diethyl ether (4 x 100 mL). The combined organic layers were then washed with brine and dried over magnesium sulfate. Solvents were removed under reduced pressure to obtain 1.31 g (5,5'-(perfluoro-1,4-phenylene)bis(thiophene-5,2-diyl))bis(trimethylstannane) (2.05 mmol, 97%) (**4c**) as a yellow crystalline solid. Samples were recrystallized from toluene before the monomer was used in polymerizations. $^1\text{H-NMR}$ (300 MHz, CHCl_3): δ (ppm) 7.61 (d, 1 H, $J = 3.4$ Hz), 7.41 (m, 1 H, $J = 9.0$ Hz, $J = 3.4$ Hz), 0.41 (m, 18 H, $J(^{117/119}\text{Sn-H}) = 55.3 / 57.9$ Hz, $-\text{SnMe}_3$); $^{19}\text{F-NMR}$ (282.4 MHz, CHCl_3): δ (ppm) -144.10; $^{13}\text{C-NMR}$ (75.5 MHz, CHCl_3): δ (ppm) 141.98, 135.38, 133.50, 131.12, 131.09, 131.05, 131.02, -8.00; $^{119}\text{Sn-NMR}$ (186.5 MHz, CDCl_3): δ (ppm) -24.43 (m, $J(^{119}\text{Sn-CH}_3) = 374.8$ Hz). EIMS (70 eV) m/z : M^+ 640 (55), $[\text{M-CH}_3]^+$ 625 (100), 595 (25), 565 (10), 305 (20), 275 (10), 177 (10).

DPP monomer

DPP[T]₂ was synthesized following a previously reported procedure.^[6]



DPP[T]₂{2DTd}₂. In a 500 mL three necked flask DPP[T]₂ (10.0 g, 33.3 mmol), potassium carbonate (18.4 g, 133 mmol) and 18-crown-6 (616 mg, 2.33 mmol) were suspended in 110 mL anhydrous DMF. The solution was stirred at 130 °C for 1 h before 1-bromo-2-dodecyl-tetradecane (41.7 g, 100 mmol) was added dropwise within 5 min. The reaction mixture was then stirred for 42 h at 100 °C. After cooling to room temperature and addition of 100 mL water the solution was stirred for 30 min. Solvents were removed completely under reduced pressure, the remains redissolved in chloroform washed with water. The aqueous phase was extracted with chloroform (2 x 100 mL). The combined organic phases were dried over magnesium sulfate. Solvents were removed under reduced pressure and the crude product was redissolved in 350 mL 1,4-dioxane. 1.4 mL concentrated hydrochloric was added and the mixture was stirred at 130 °C for 2 h. After cooling to room temperature the mixture was filtrated over a short aluminium oxide plug and the solvent was removed under reduced pressure. Flash chromatography (silica gel) using hexane:chloroform 1:1 as eluent and subsequent recrystallization of the product from ethanol afforded 21.58 g DPP[T]₂{2HD}₂ (22.16 mmol, 67%) as a red tacky solid. ¹H-NMR (300 MHz, CHCl₃): δ (ppm) 8.88 (d, 2H, J = 3.0 Hz), 7.62 (d, 2H, J = 4.2 Hz), 7.26 (m, 2H), 4.01 (d, 4H, J = 7.7 Hz), 1.90 (s, 2H), 1.25-1.20 (m, calc: 80H, observed: 122H), 0.87 (m, calc: 12H, observed: 17H) (Note: Alkyl-Protons in DPPs are prone to overestimation).

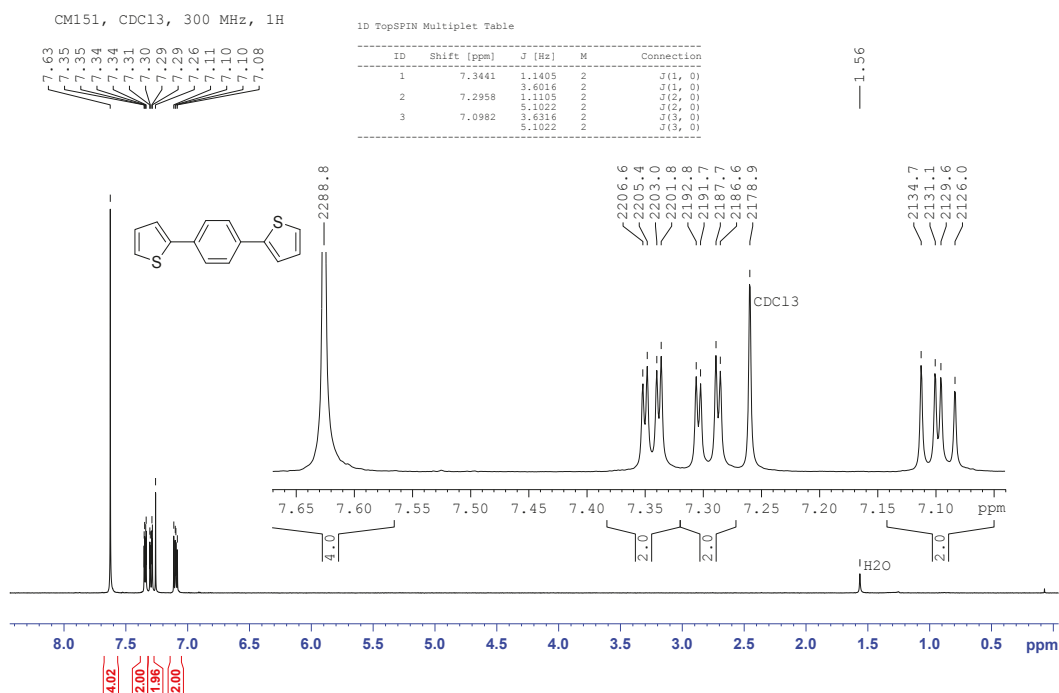


DPP[T]₂{2DTd}₂Br₂. DPP[T]₂{2DTd}₂ (10.0 g, 10.3 mmol) and *N*-bromosuccinimide (4.02 g, 22.6 mmol) were dissolved in 100 mL chloroform. The solution was purged with argon for 5 minutes and protected from light. After stirring at room temperature for 48 h the solution

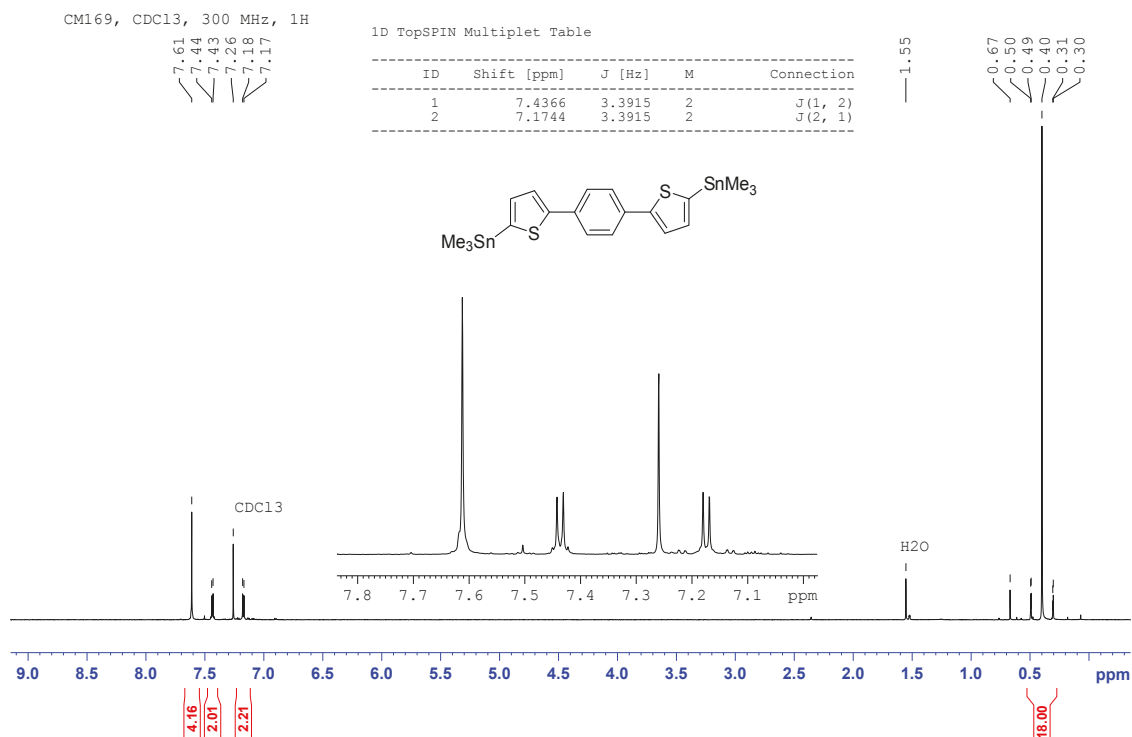
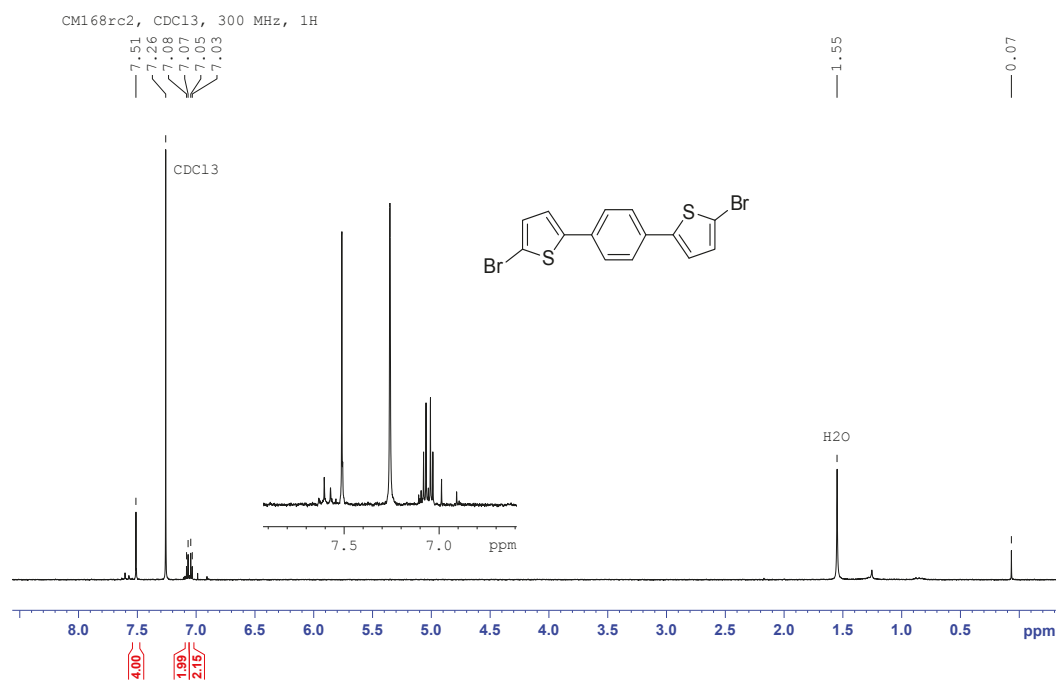
was concentrated to ca. 50 mL under reduced pressure and poured into 400 mL methanol. After waiting for 15 min without stirring the precipitate was filtered. Recrystallisation from ethanol the product still contained impurities and was subjected to flash chromatography (silica gel) using hexane/dichloromethane 3:1 as eluent. The product fractions were dried under reduced pressure and recrystallized from ethanol to yield 2.43 g DPP[T]₂{2DTd}₂Br₂ (2.15 mmol, 21%) as a red waxy solid. ¹H-NMR (300 MHz, CHCl₃): δ (ppm) 8.63 (d, 2H, J = 4.2 Hz), 7.21 (d, 2H, J = 4.2 Hz), 3.92 (d, 4H, J = 7.6 Hz), 1.87 (s, 2H), 1.21 (m, calc: 80H, observed: 87H), 0.87 (m, calc: 12H, observed: 13H) (Note: Alkyl-Protons in DPPs are prone to overestimation).

Monomer Characterization

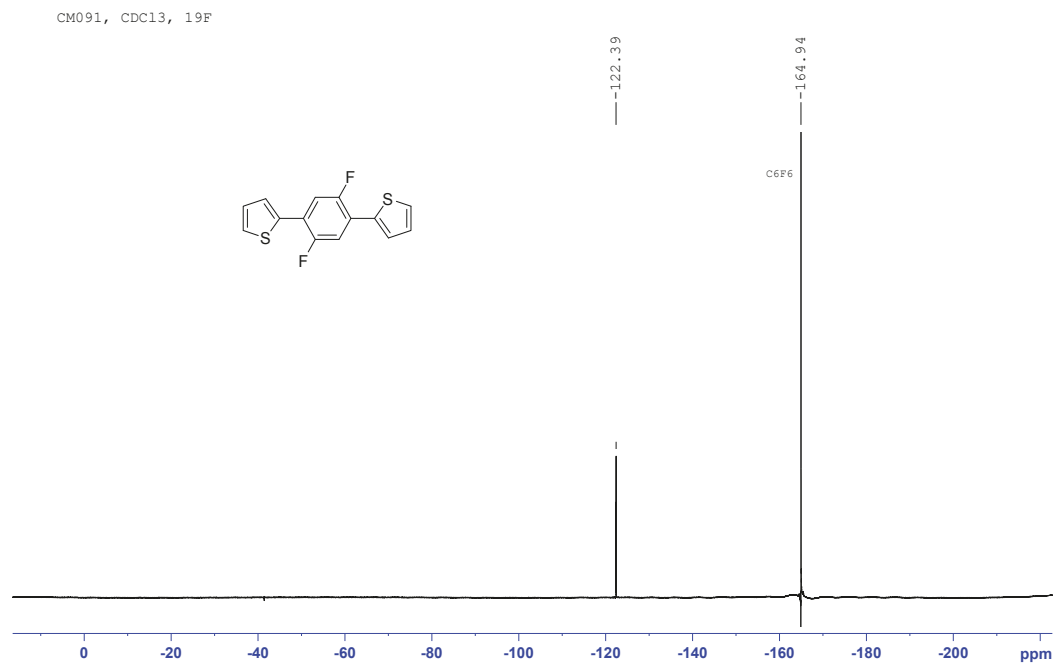
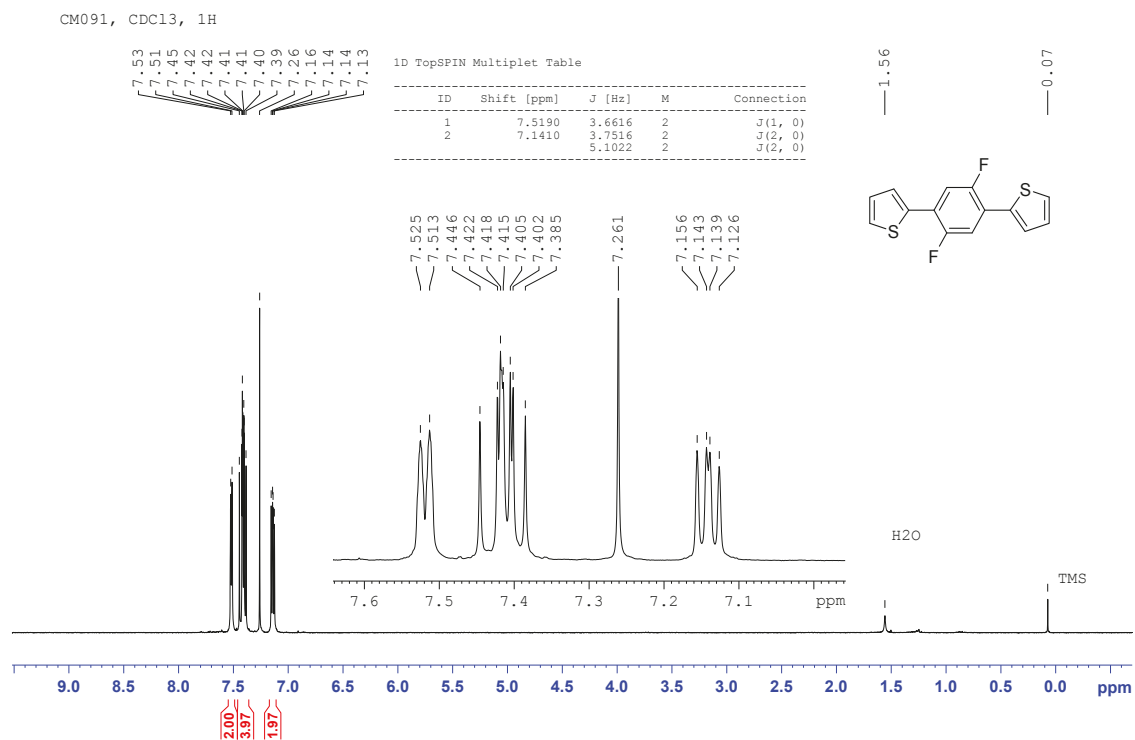
NMR spectra of the monomers



4 Influence of Fluorination in π -extended Backbone Polydiketopyrrolopyrroles on Charge Carrier Mobility and Depth-dependent Molecular Alignment

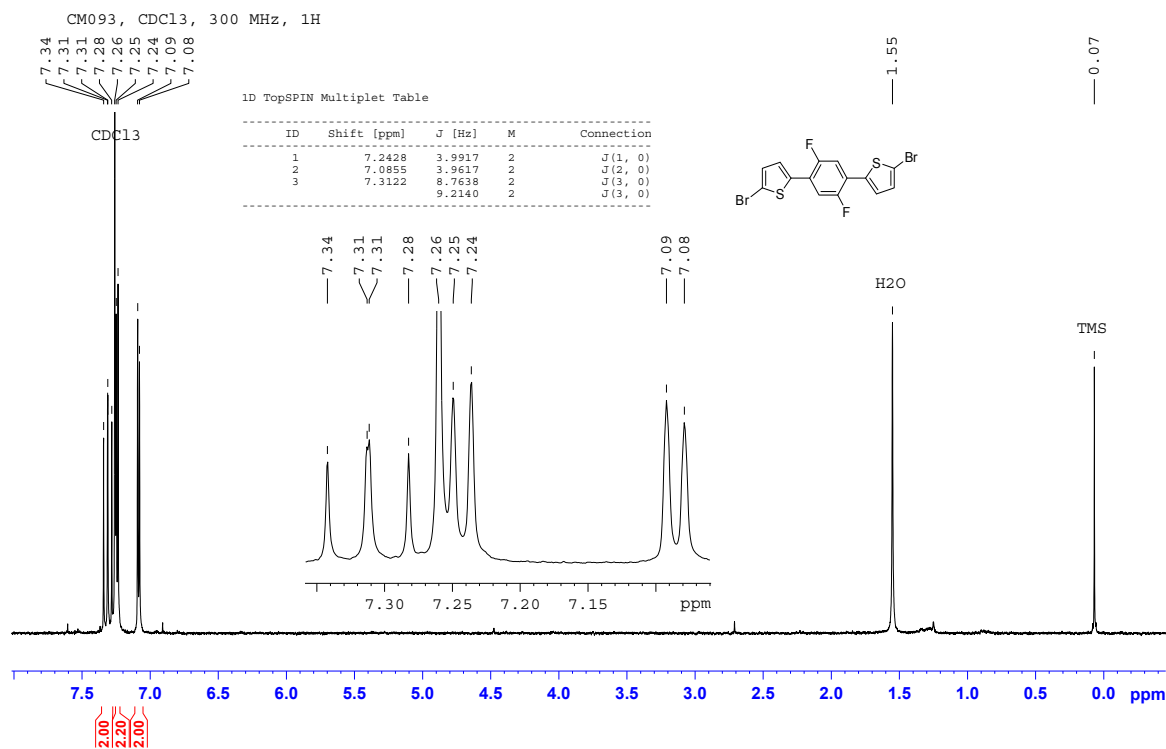
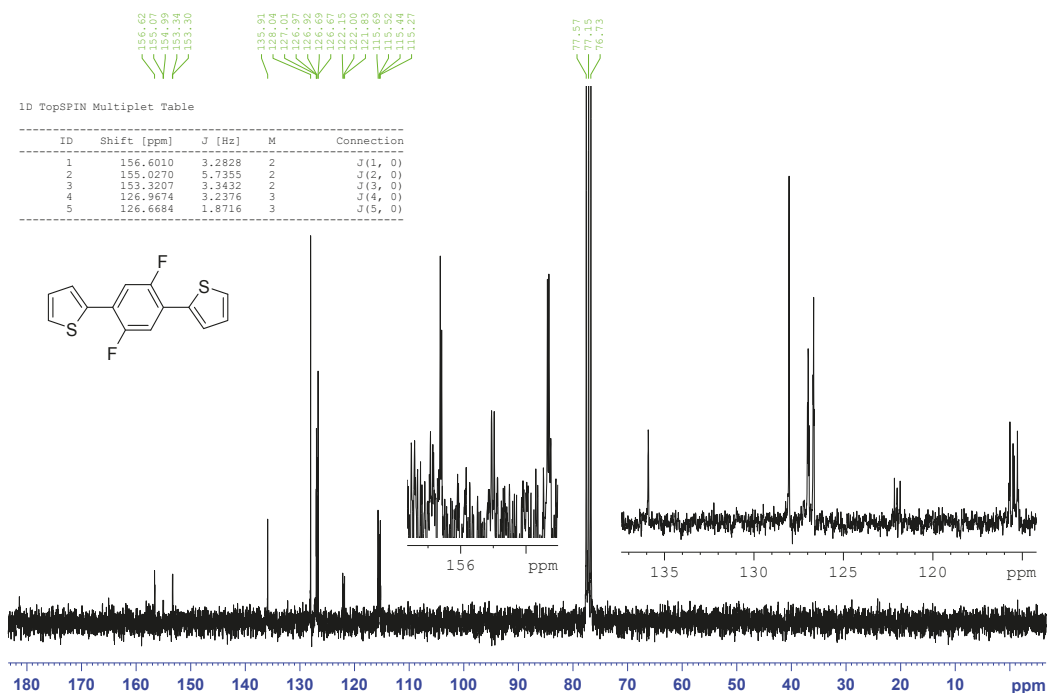


4 Influence of Fluorination in π -extended Backbone Polydiketopyrrolopyrroles on Charge Carrier Mobility and Depth-dependent Molecular Alignment



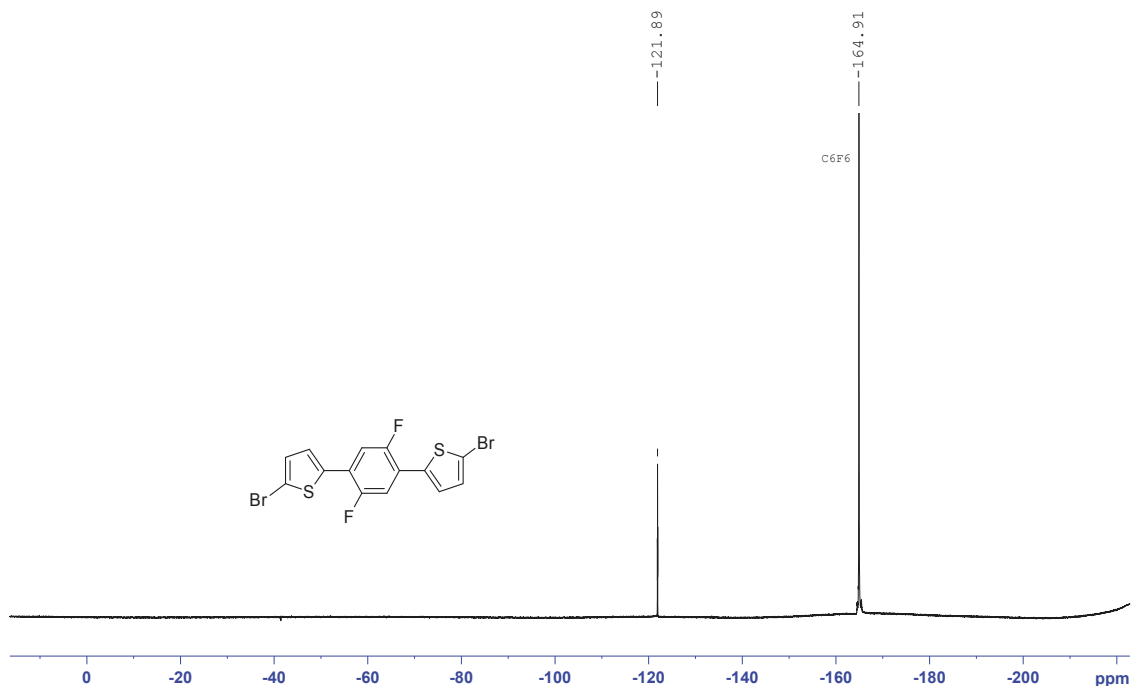
4 Influence of Fluorination in π -extended Backbone Polydiketopyrrolopyrroles on Charge Carrier Mobility and Depth-dependent Molecular Alignment

CM091, ^{13}C , CDCl₃

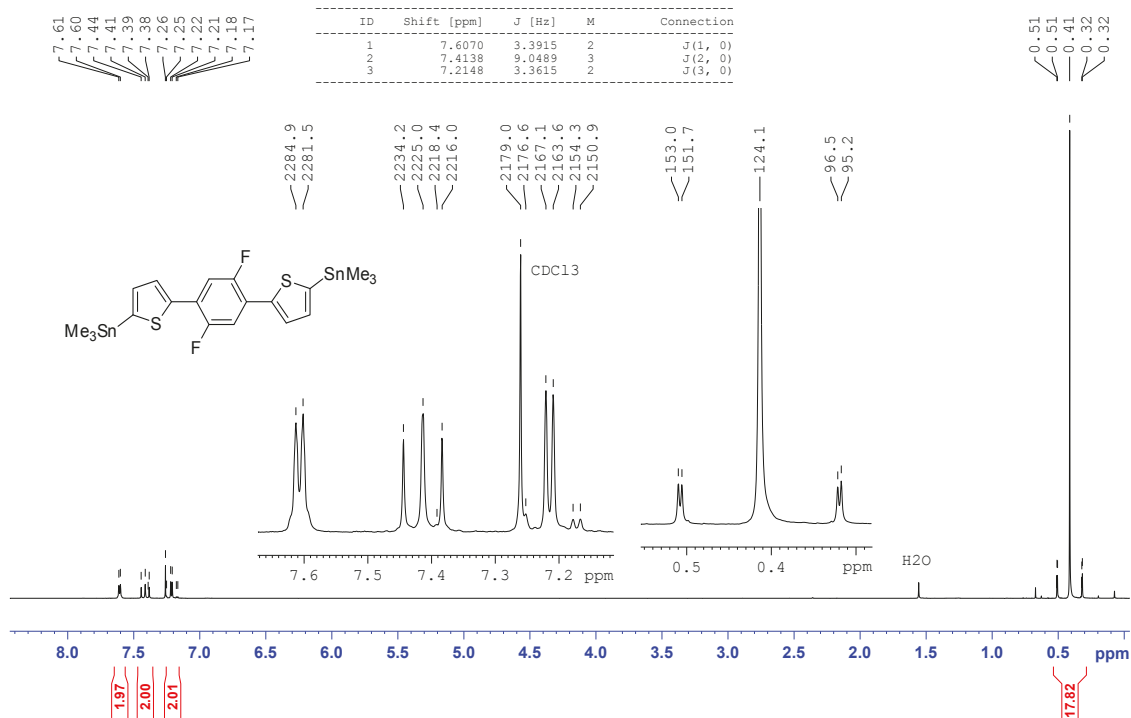


4 Influence of Fluorination in π -extended Backbone Polydiketopyrrolopyrroles on Charge Carrier Mobility and Depth-dependent Molecular Alignment

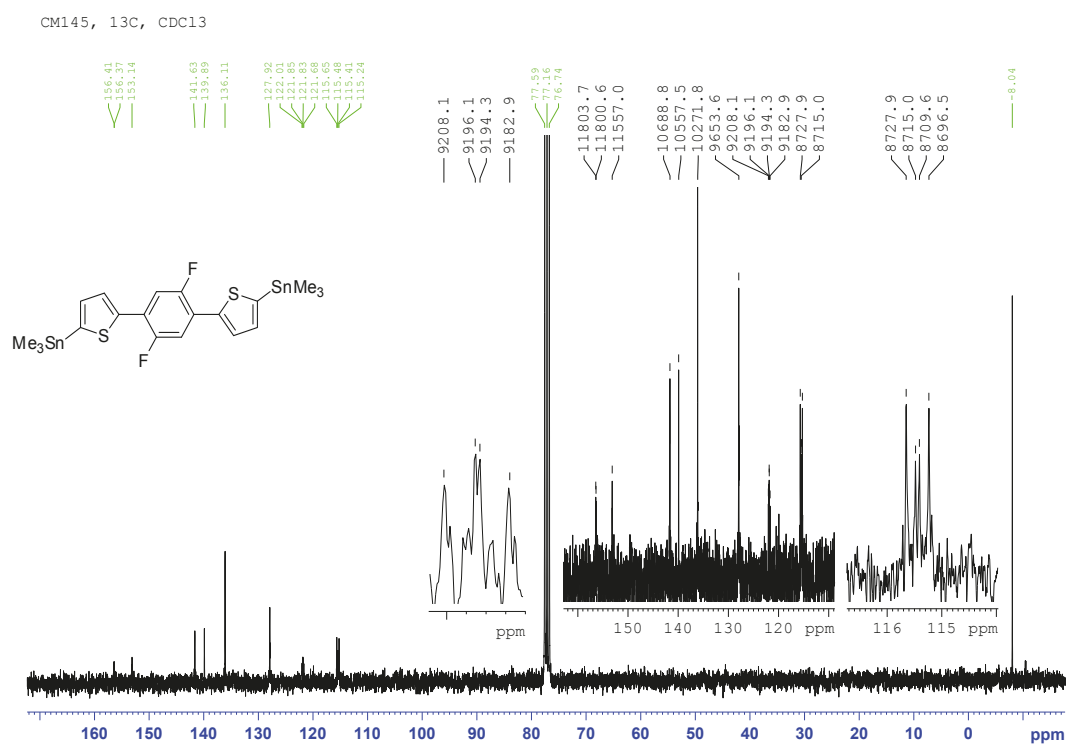
CM093, CDC13, 19F



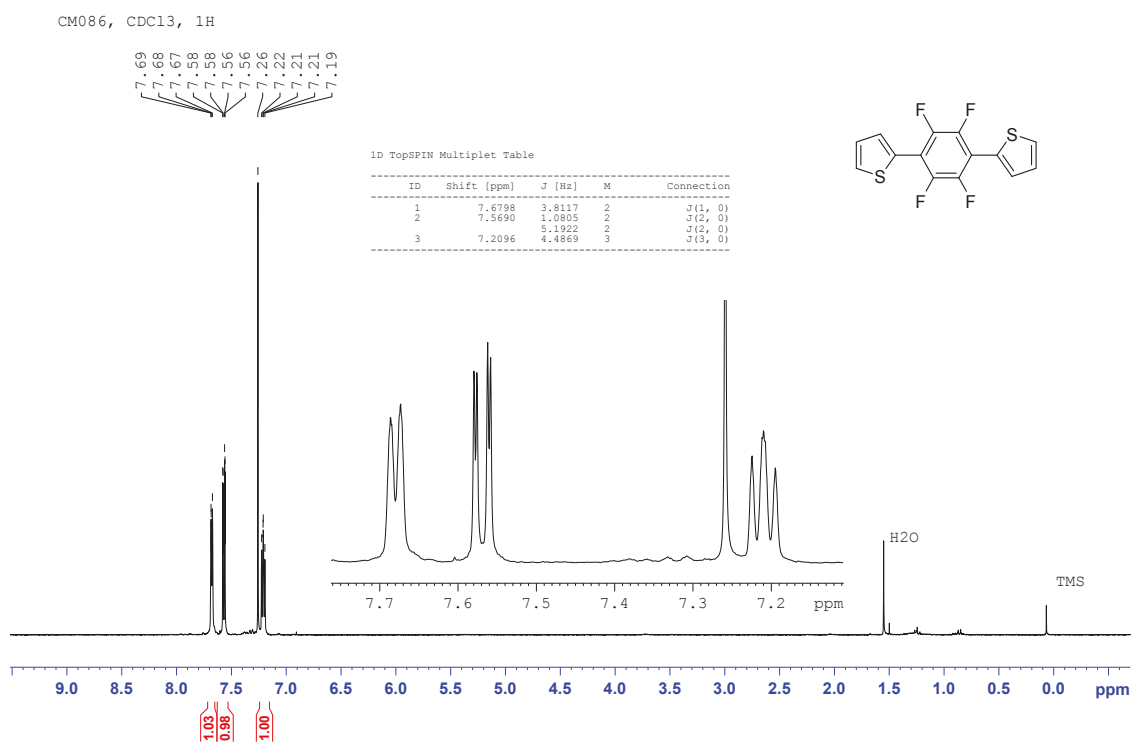
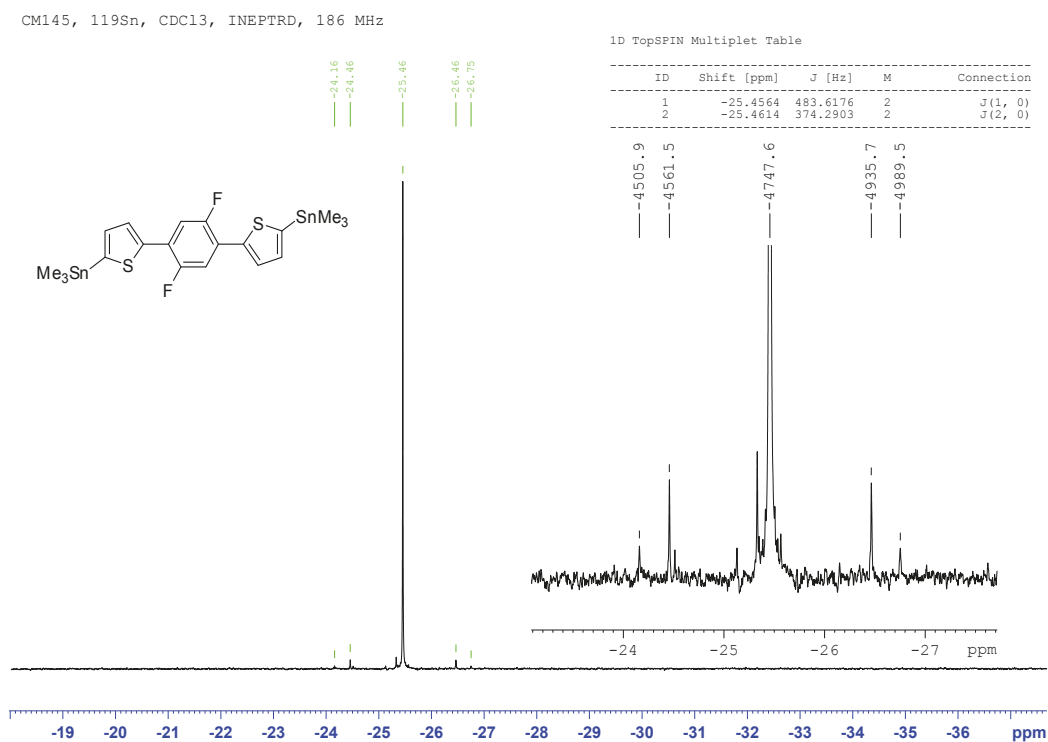
CM145, CDC13, 300 MHz, 1H 1D TopSPIN Multiplet Table



4 Influence of Fluorination in π -extended Backbone Polydiketopyrrolopyrroles on Charge Carrier Mobility and Depth-dependent Molecular Alignment

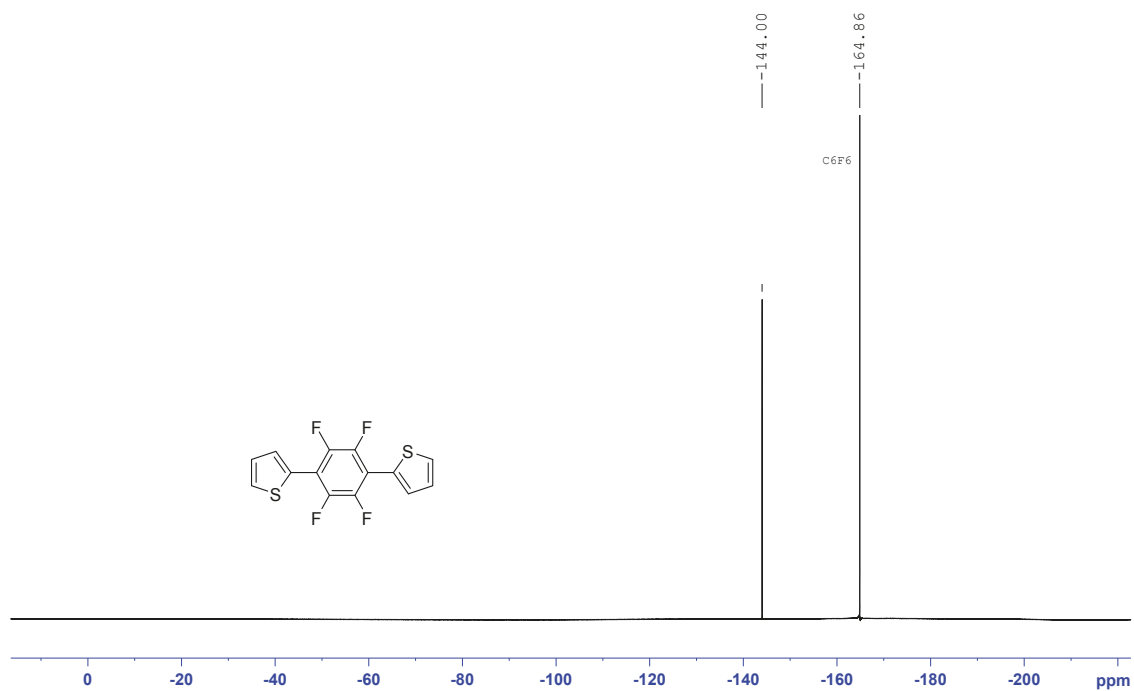


4 Influence of Fluorination in π -extended Backbone Polydiketopyrrolopyrroles on Charge Carrier Mobility and Depth-dependent Molecular Alignment

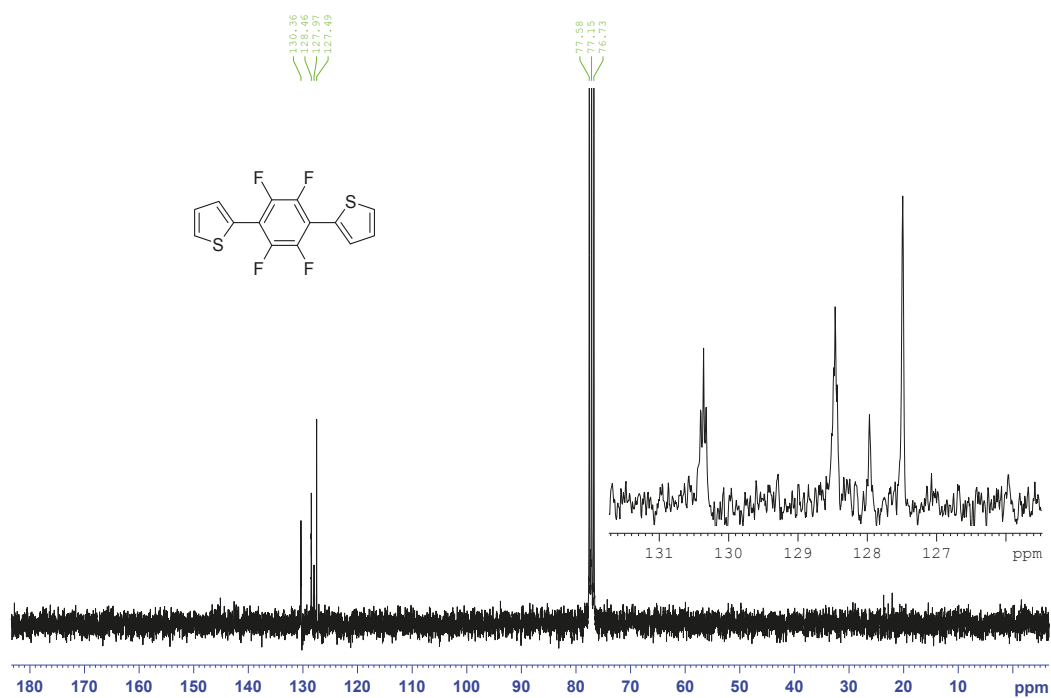


4 Influence of Fluorination in π -extended Backbone Polydiketopyrrolopyrroles on Charge Carrier Mobility and Depth-dependent Molecular Alignment

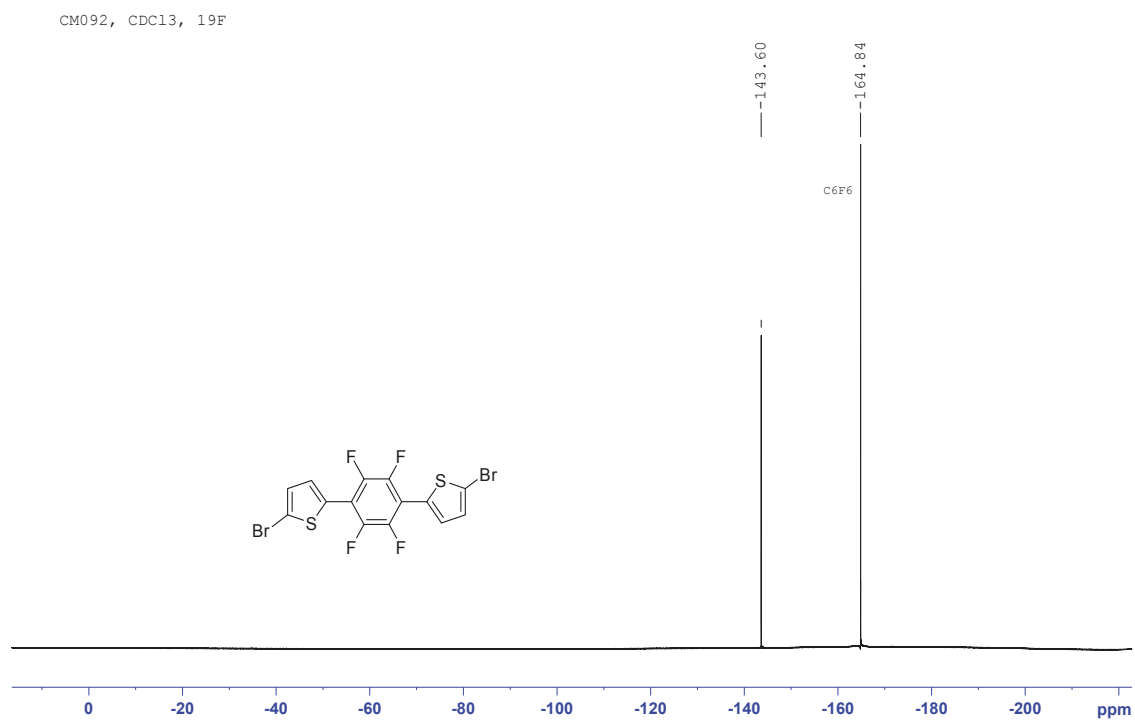
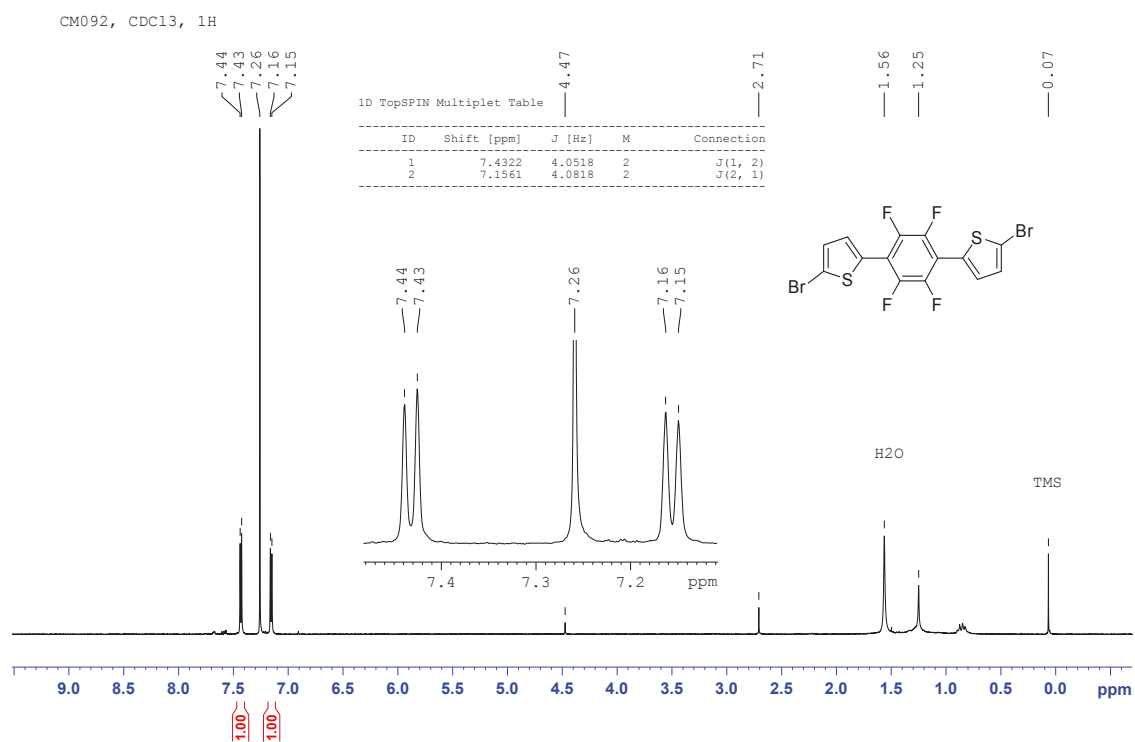
CM086, CDC13, ^{19}F



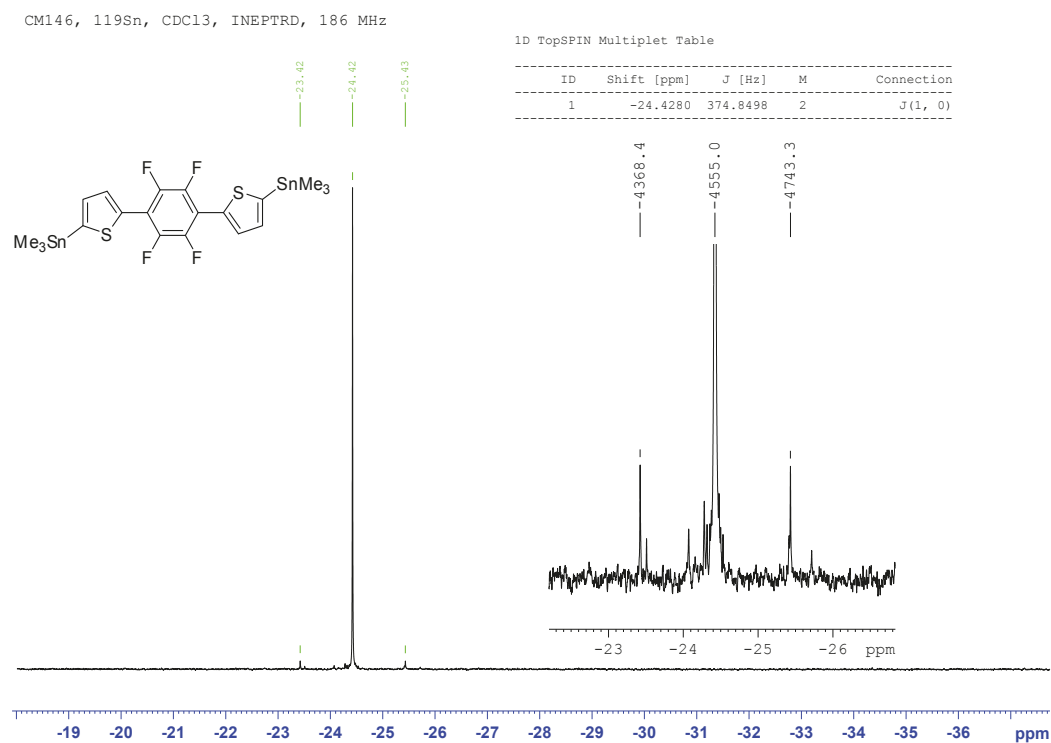
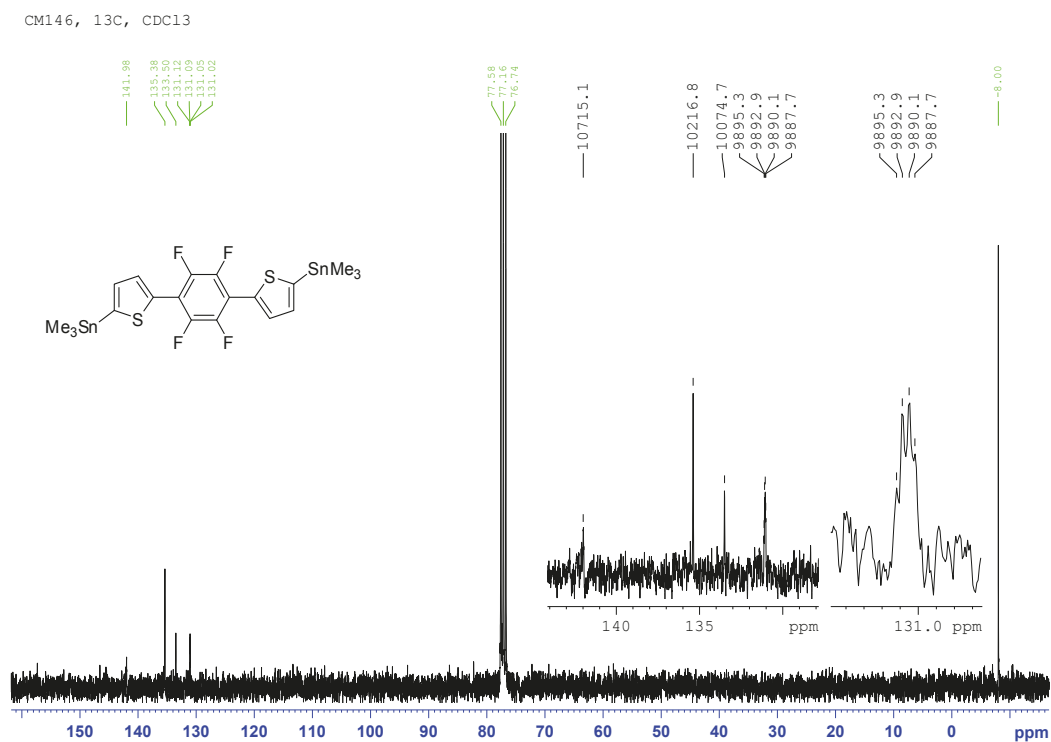
CM086, ^{13}C , CDCl_3

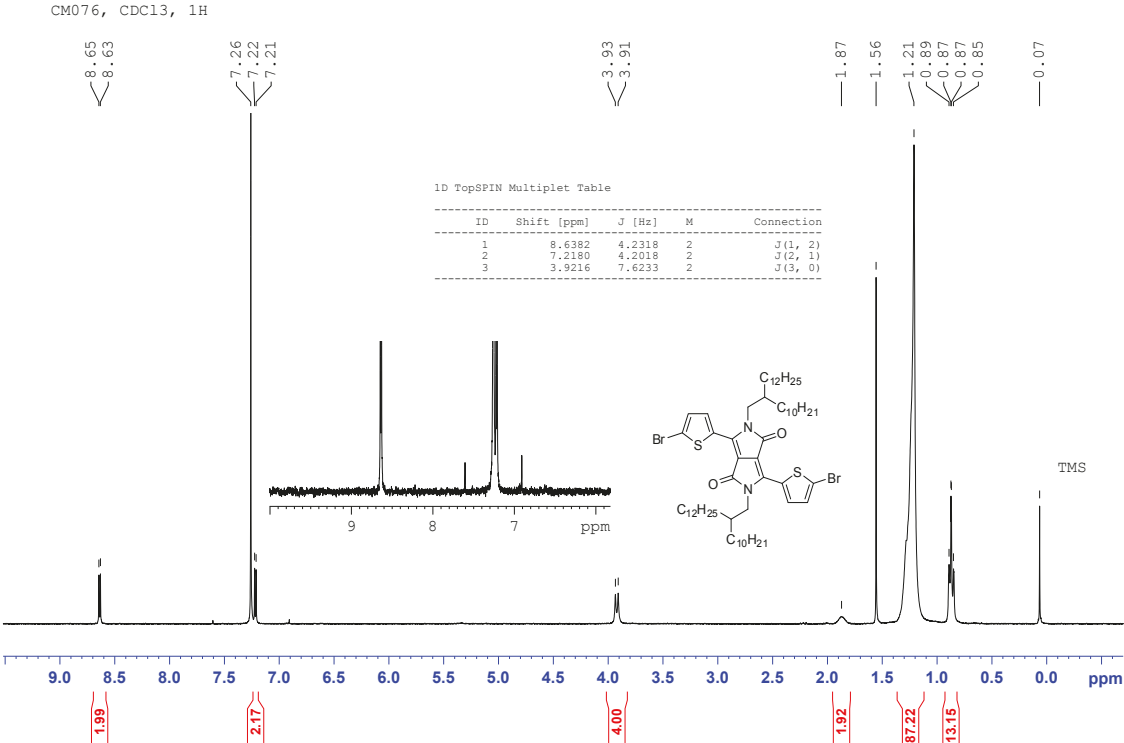
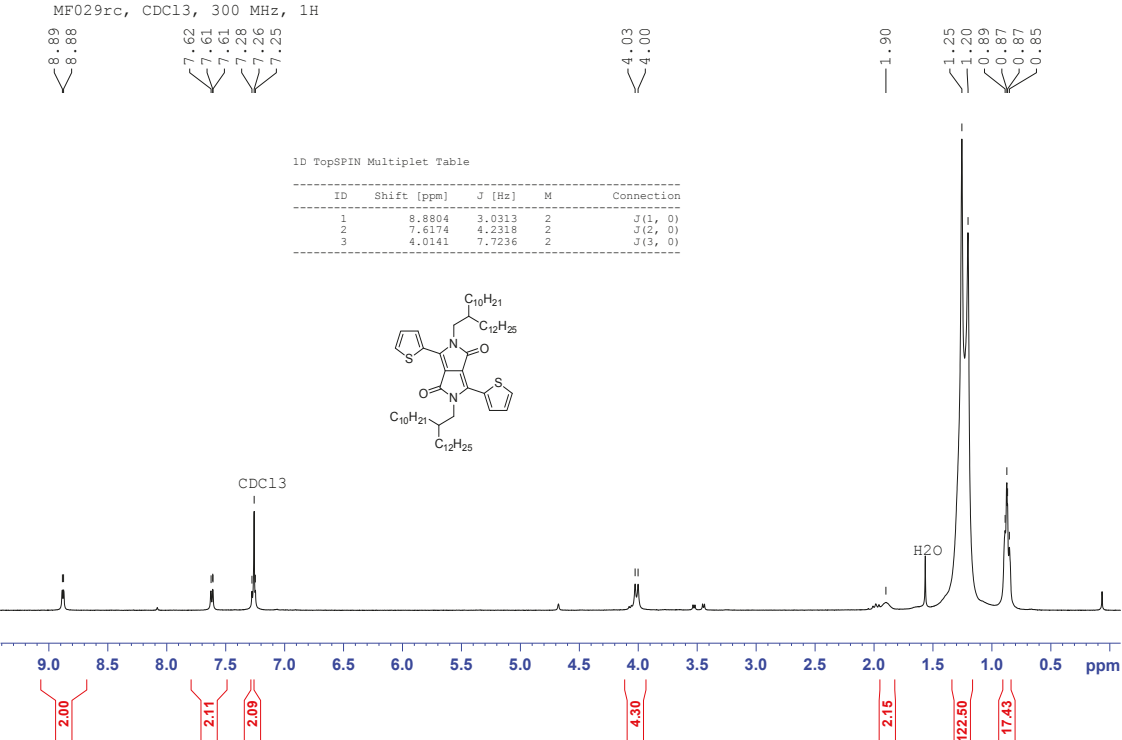


4 Influence of Fluorination in π -extended Backbone Polydiketopyrrolopyrroles on Charge Carrier Mobility and Depth-dependent Molecular Alignment



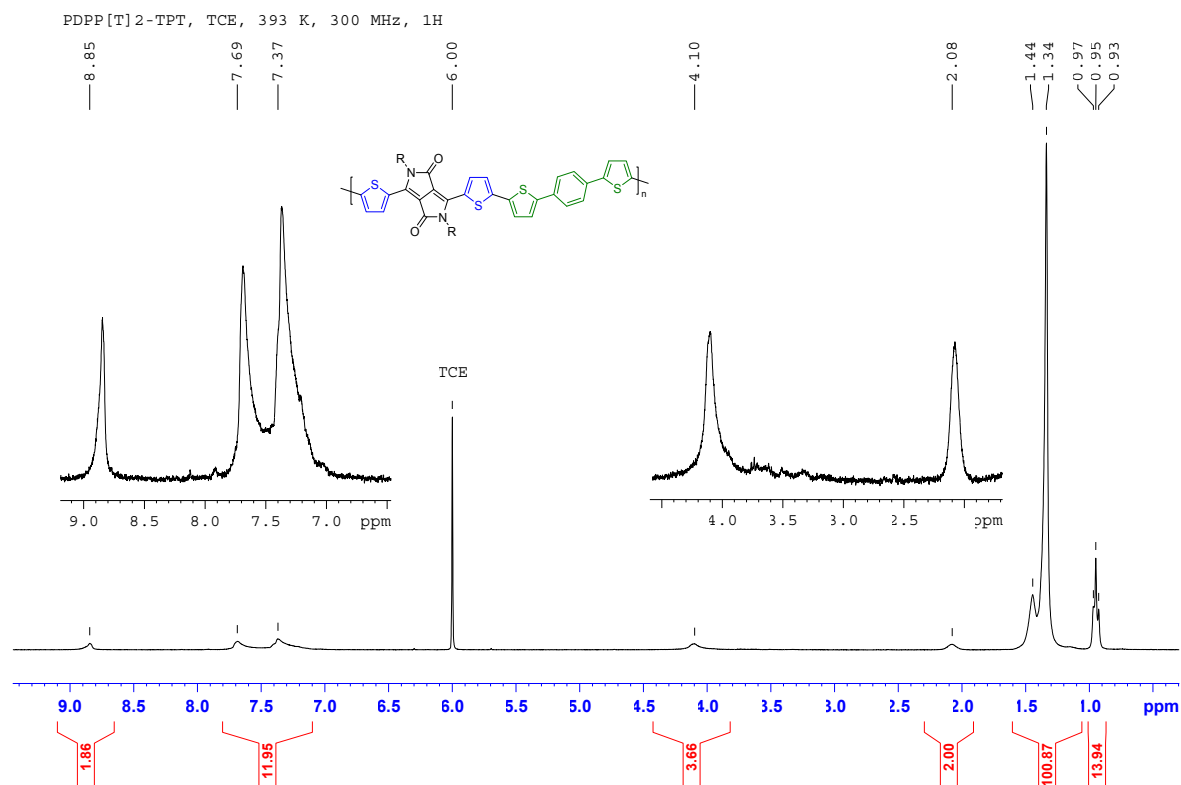
4 Influence of Fluorination in π -extended Backbone Polydiketopyrrolopyrroles on Charge Carrier Mobility and Depth-dependent Molecular Alignment



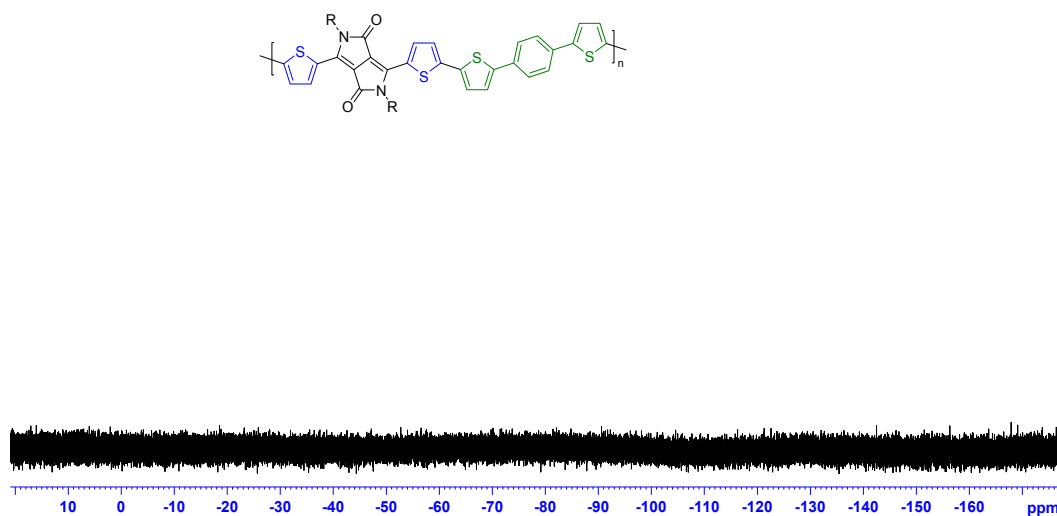


Polymer Characterization

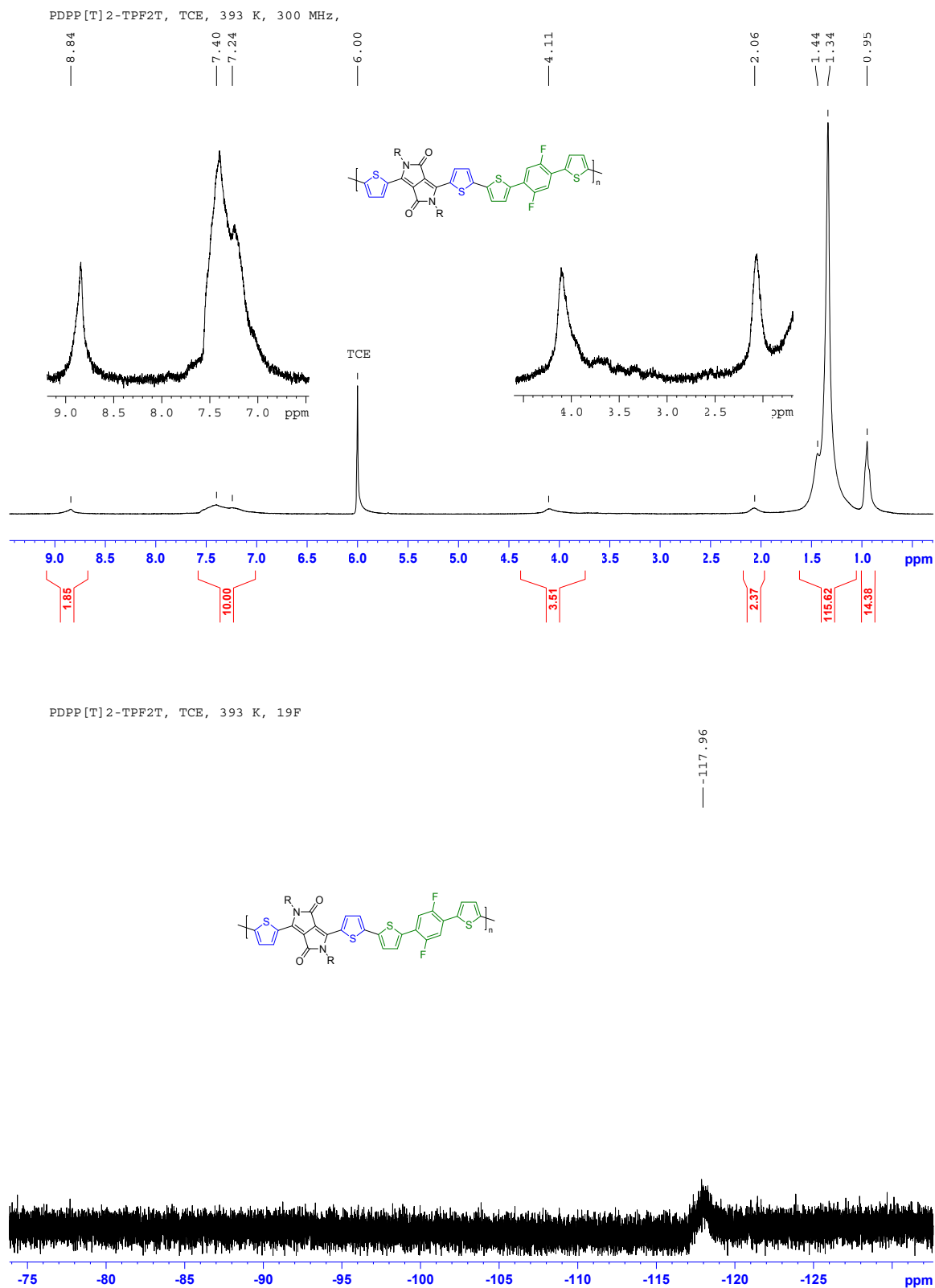
Polymer NMR



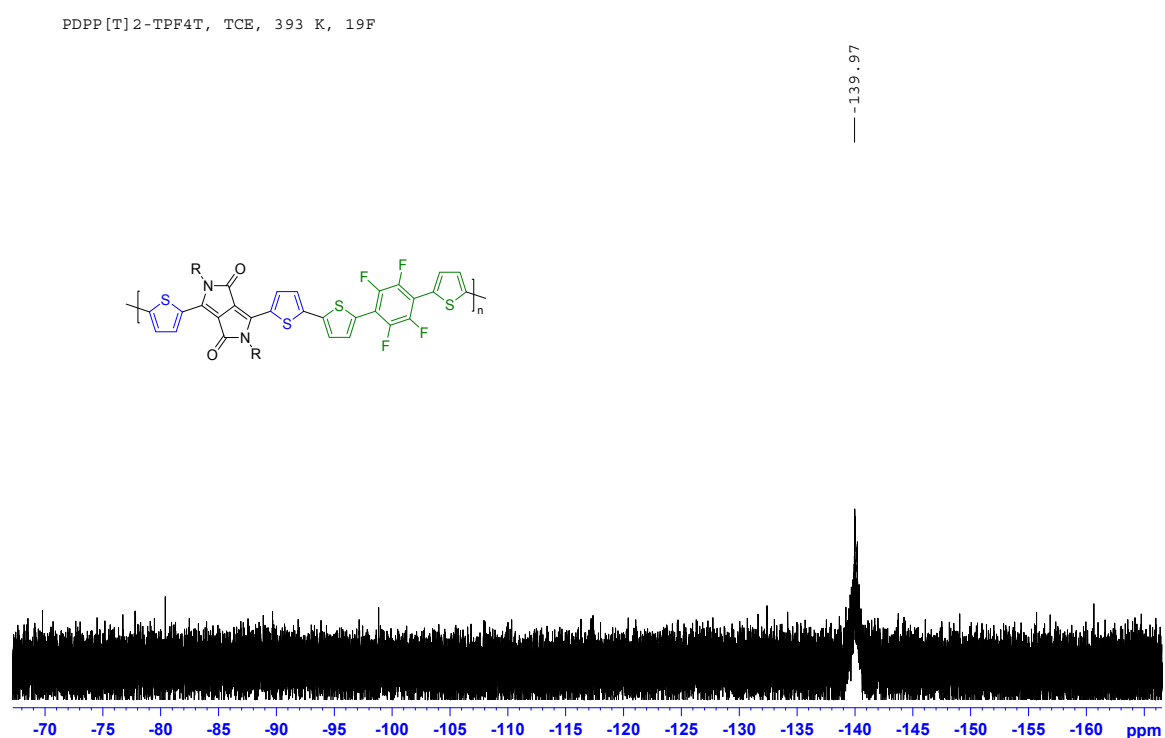
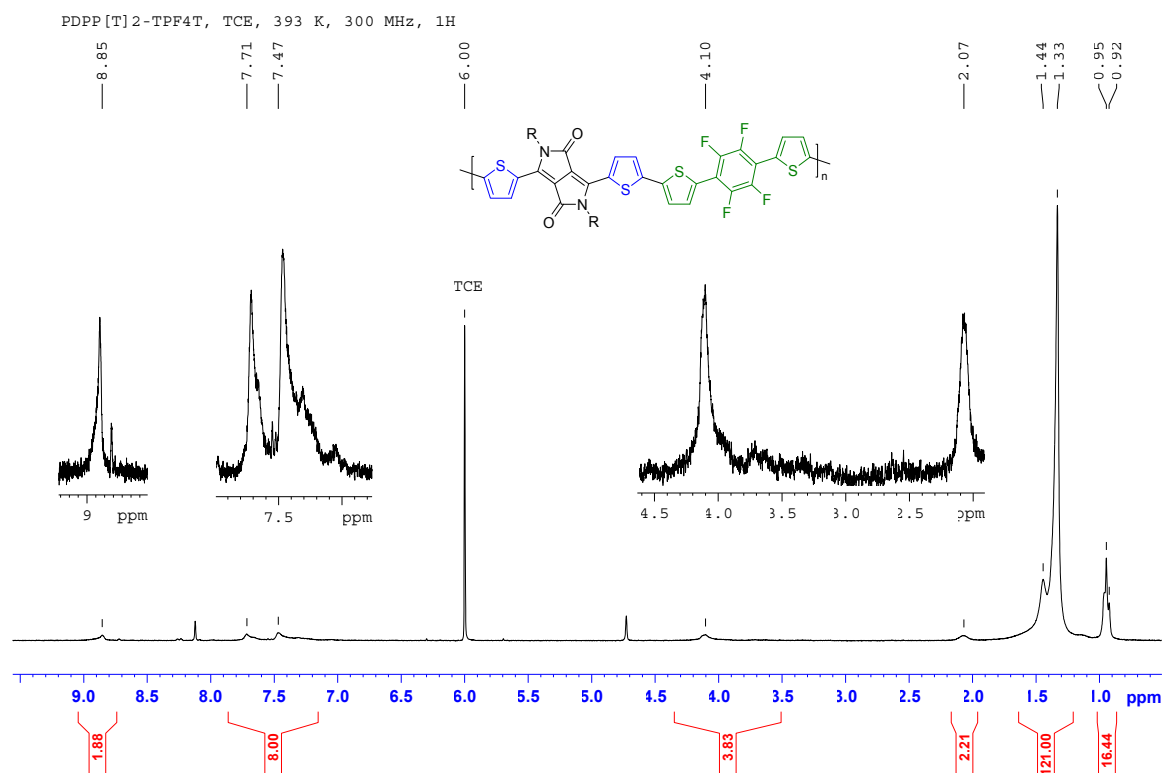
PDPP[T]2-TPT, TCE, 393 K, ^{19}F



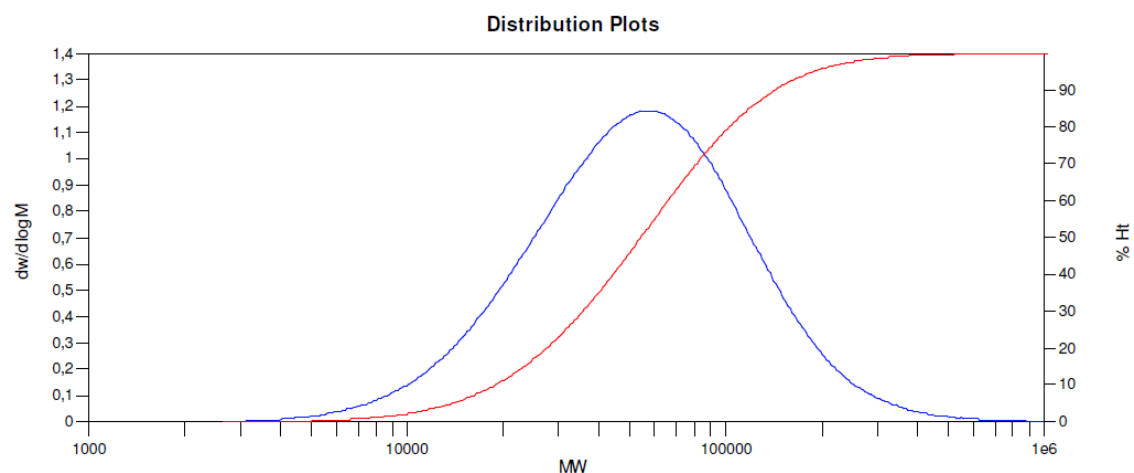
4 Influence of Fluorination in π -extended Backbone Polydiketopyrrolopyrroles on Charge Carrier Mobility and Depth-dependent Molecular Alignment



4 Influence of Fluorination in π -extended Backbone Polydiketopyrrolopyrroles on Charge Carrier Mobility and Depth-dependent Molecular Alignment



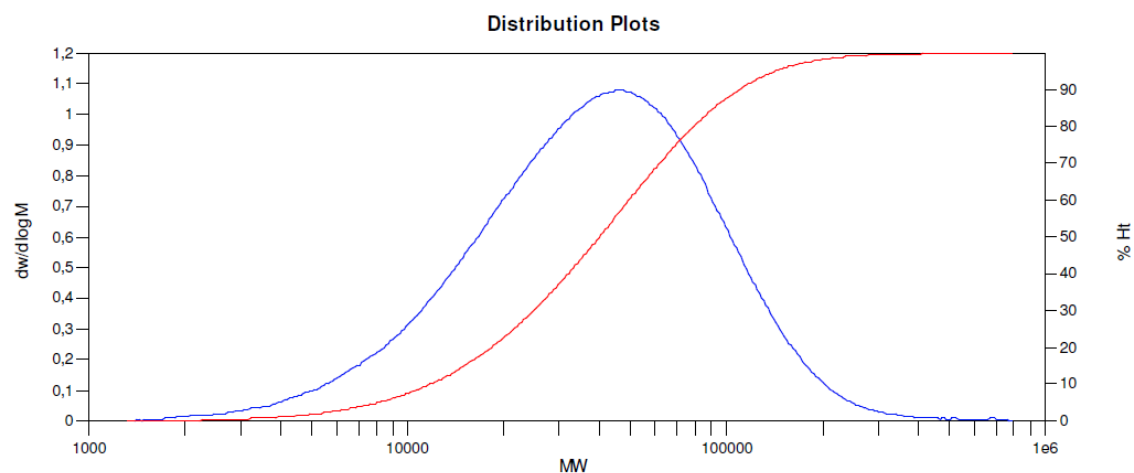
Gel Permeation Chromatography (GPC)



MW Averages

Peak No	Mp	Mn	Mw	Mz	Mz+1	Mv	PD
1	56256	38058	71357	129835	232475	65316	1.87495

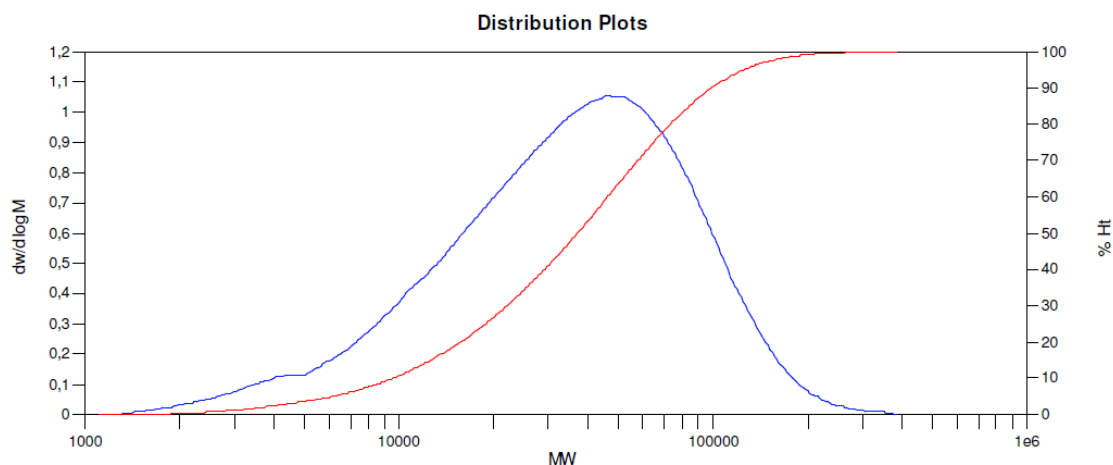
Figure S4-3: GPC trace of PDPP[T]₂-TPT.



MW Averages

Peak No	Mp	Mn	Mw	Mz	Mz+1	Mv	PD
1	44968	24498	53062	100577	189620	48105	2.16597

Figure S4-4: GPC trace of PDPP[T]₂-TPF₂T.



MW Averages

Peak No	Mp	Mn	Mw	Mz	Mz+1	Mv	PD
1	46372	20386	47232	80624	117322	43022	2.31688

Figure S4-5: GPC trace of PDPP[T]₂-TPF₄T.

Thermogravimetric Analysis (TGA)

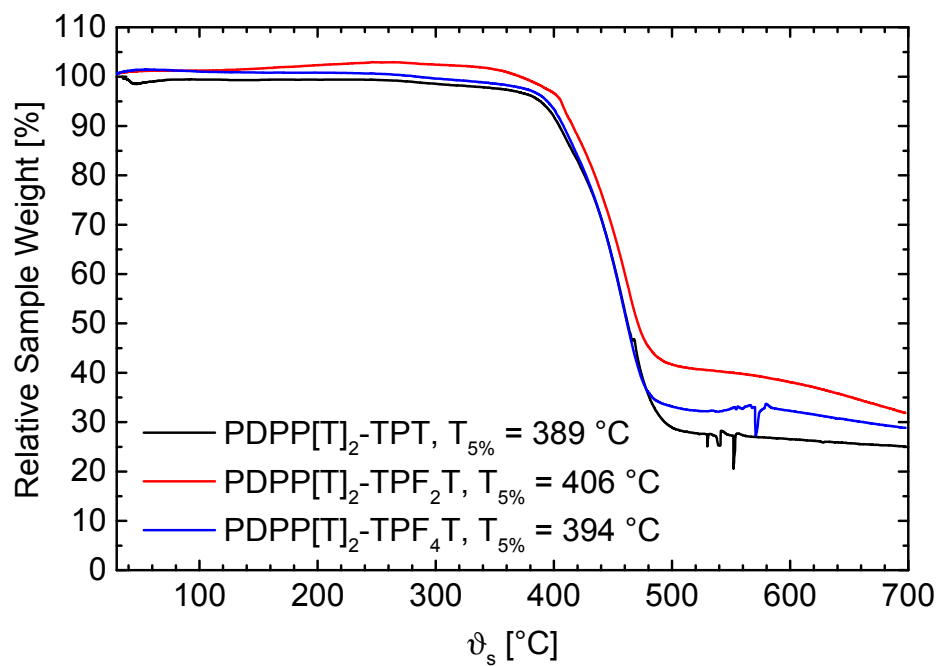


Figure S4-6. Thermogravimetric analysis of the PDPPs with the decomposition onset ($T_{5\%}$).

Flash-DSC

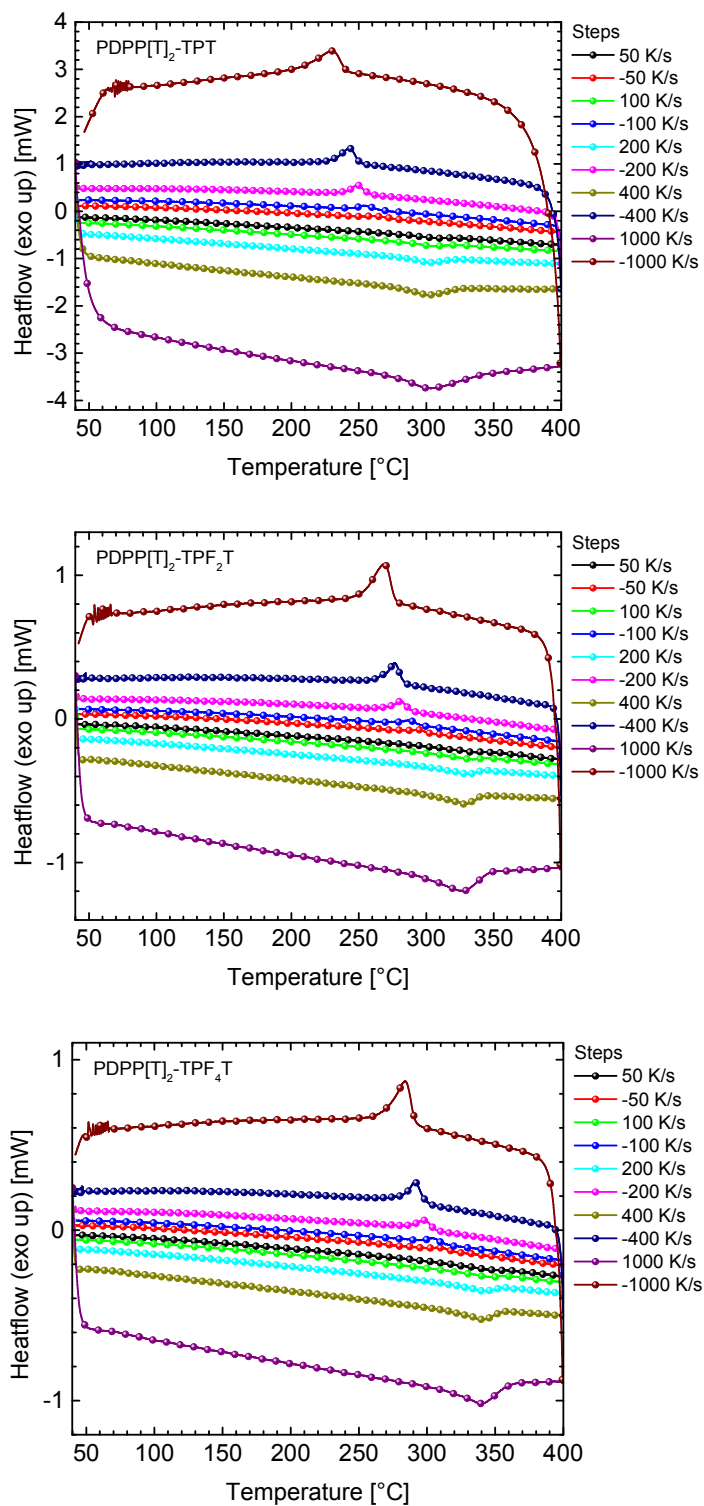


Figure S4-7. Flash-DSC curves for all three copolymers at different scan rates.

Cyclic Voltammetry

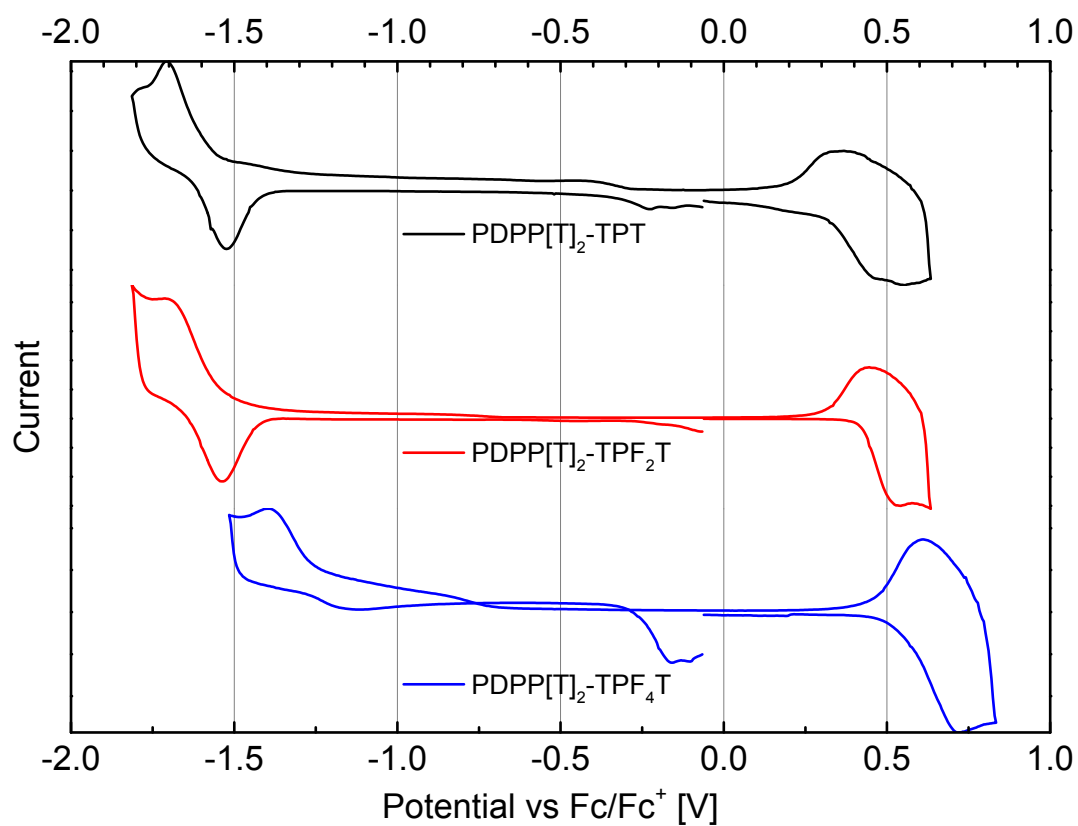


Figure S4-8: Solid state cyclic voltammograms for the DPP copolymers with a varying degree of fluorination.

GIWAXS analysis and S-Parameter calculation

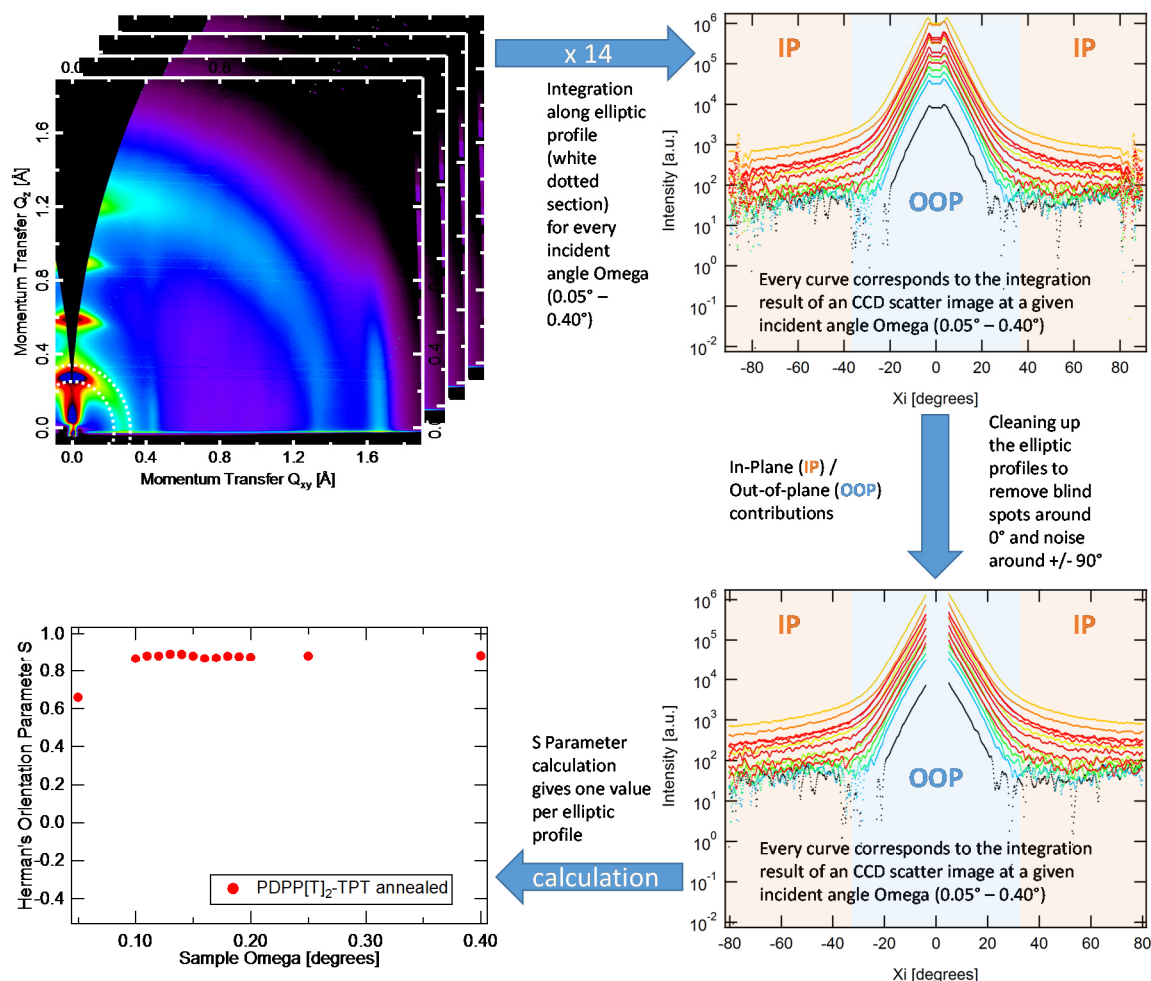


Figure S4-9. Exemplary S Parameter evaluation for PDPP[T]₂-TPT (annealed) starting from two-dimensional scatter plots. Integration of an elliptic profile along the $\langle 100 \rangle$ peak (white dotted section) results in one curve per X-ray incident angle (Sample Ω) for angles between 0.05° and 0.40°. Deleting data points in the centered range around 0° due to the geometric limitations of the grazing incidence setup and around $\pm 90^\circ$ due to noise and eventual wave guiding effects in the film at large χ_i angles. S parameters were finally calculated on a point-by-point basis using the cleaned elliptic profiles to obtain one S Parameter value per incident angle Ω .

Additional OFET I - V curves

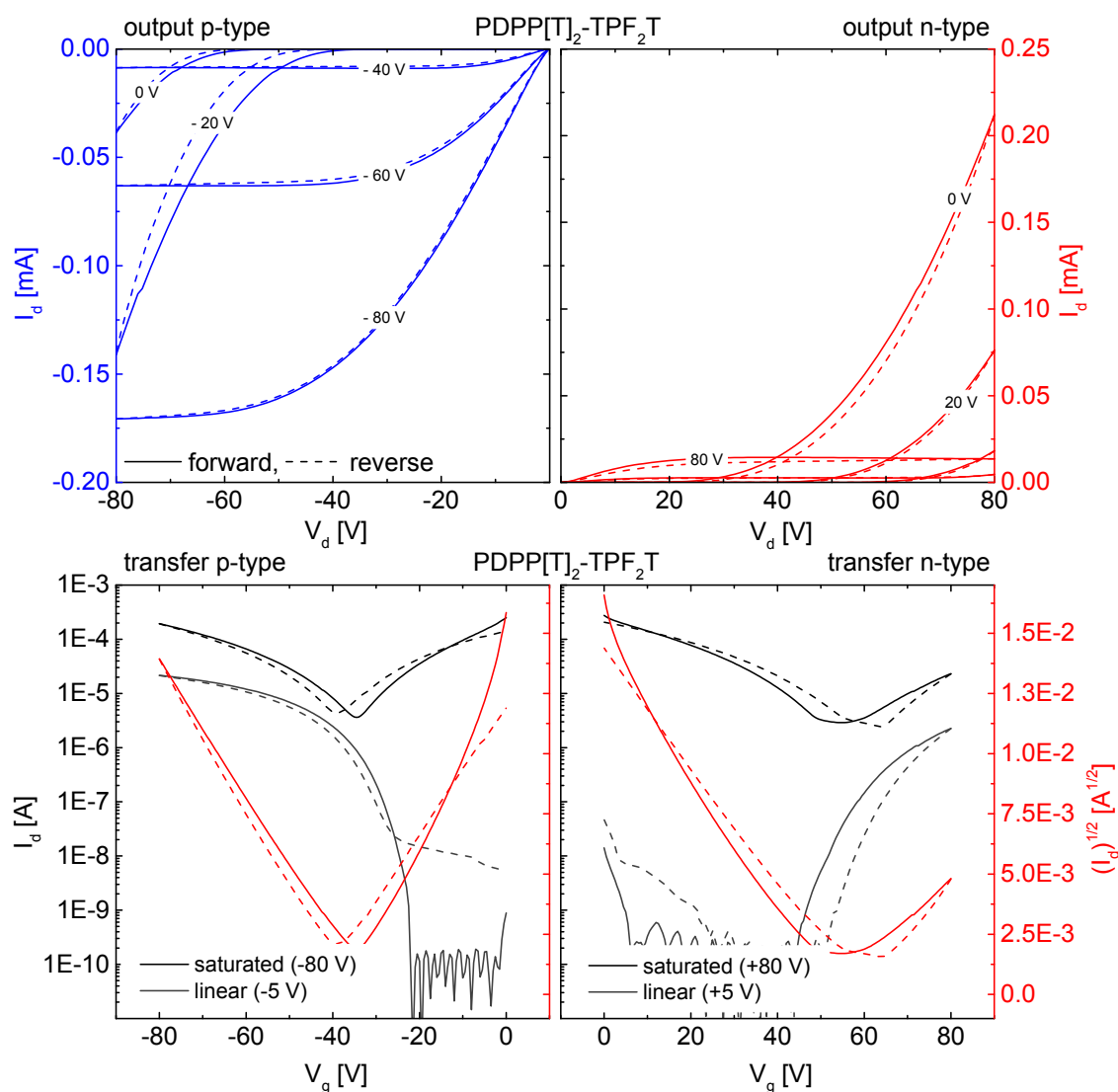


Figure S4-10. Representative OFET I - V curves in p-channel (blue output) and n-channel (red output) operation for the difluorinated PDPP[T]₂-TPF₂T after annealing at 350 °C. Solid lines represent forward scans, dashed lines the reverse scans in all graphs. In transfer curves (bottom), the black and gray plots indicate the transfer characteristics in the saturation and linear operation regime, respectively.

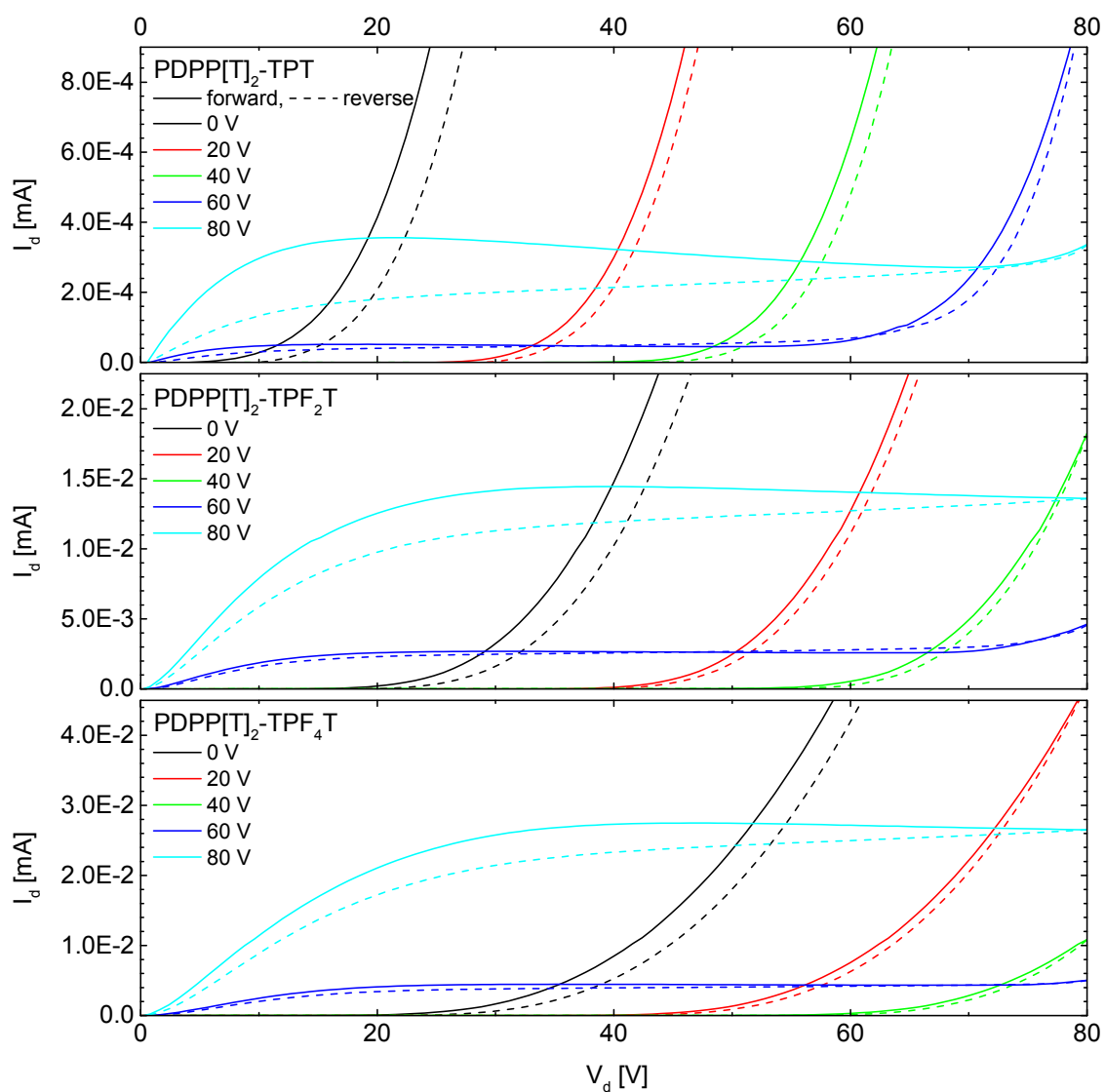


Figure S4-11. Output characteristics for the n-channel operation of OFET devices comparing all three polymers after annealing at 350 °C.

Table S4-2. OFET on/off ratios in different operation regimes. For ambipolar materials, the on/off ratio decreases in the saturation regime when high drain voltages are applied. All values were averaged over a minimum of 8 individual devices.

	On/Off ratio				Threshold Voltage	
	$I_{\text{on/off}}$	$I_{\text{on/off}}$	$I_{\text{on/off}}$	$I_{\text{on/off}}$	V_T [V]	V_T [V]
	p-type	p-type	n-type	n-type	p-type	n-type
	lin.	sat.	lin.	sat.	sat.	sat.
As cast						
PDPP[T] ₂ -TPPT	$>10^6$	$>10^6$	-	-	0 ± 2	-
PDPP[T] ₂ -TPF ₂ T	$>10^6$	$>10^5$	-	-	0 ± 3	-
PDPP[T] ₂ -TPF ₄ T	$>10^5$	$>10^3$	-	-	0 ± 5	-
Annealed 200 °C						
PDPP[T] ₂ -TPPT	$>10^6$	$>10^6$	-	-	-31 ± 10	-
PDPP[T] ₂ -TPF ₂ T	$>10^6$	$>10^6$	-	-	-25 ± 11	-
PDPP[T] ₂ -TPF ₄ T	$>10^6$	$>10^6$	-	-	-28 ± 9	-
Annealed 250 °C						
PDPP[T] ₂ -TPPT	$>10^6$	$>10^6$	-	-	-38 ± 11	-
PDPP[T] ₂ -TPF ₂ T	$>10^6$	$>10^6$	-	-	-38 ± 8	-
PDPP[T] ₂ -TPF ₄ T	$>10^6$	$>10^6$	-	-	-38 ± 8	-
Annealed 300 °C						
PDPP[T] ₂ -TPPT	$>10^6$	$>10^6$	-	-	-19 ± 7	-
PDPP[T] ₂ -TPF ₂ T	$>10^6$	$>10^6$	-	-	-32 ± 5	-
PDPP[T] ₂ -TPF ₄ T	$>10^6$	$>10^6$	-	-	-28 ± 5	-
Annealed 350 °C						
PDPP[T] ₂ -TPPT	$>10^6$	$>10^2$	$>10^5$	>4	-33 ± 4	54 ± 2
PDPP[T] ₂ -TPF ₂ T	$>10^6$	$>10^2$	$>10^5$	>8	-34 ± 6	52 ± 1
PDPP[T] ₂ -TPF ₄ T	$>10^6$	$>10^3$	$>10^5$	$>10^1$	-35 ± 4	51 ± 3

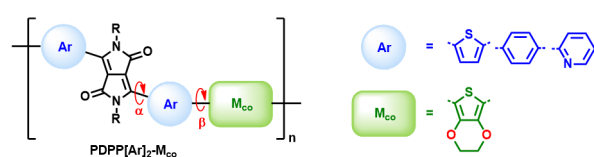
Supporting References

- [1] D. J. Crouch, P. J. Skabara, M. Heeney, I. McCulloch, S. J. Coles, M. B. Hursthouse, *Chem. Commun.* **2005**, 1465.
- [2] A. Facchetti, M. H. Yoon, C. L. Stern, H. E. Katz, T. J. Marks, *Angew. Chem. Int. Ed. Engl.* **2003**, *42*, 3900.
- [3] M. H. Yoon, A. Facchetti, C. E. Stern, T. J. Marks, *J. Am. Chem. Soc.* **2006**, *128*, 5792.
- [4] D. J. Crouch, P. J. Skabara, J. E. Lohr, J. J. W. McDouall, M. Heeney, I. McCulloch, D. Sparrowe, M. Shkunov, S. J. Coles, P. N. Horton, M. B. Hursthouse, *Chem. Mater.* **2005**, *17*, 6567.
- [5] T. Yamao, Y. Taniguchi, K. Yamamoto, T. Miki, S. Ota, S. Hotta, M. Goto, R. Azumi, *Japanese Journal of Applied Physics* **2007**, *46*, 7478.
- [6] C. J. Mueller, C. R. Singh, M. Fried, S. Huettner, M. Thelakkat, *Adv. Funct. Mater.* **2015**, *25*, 2725.

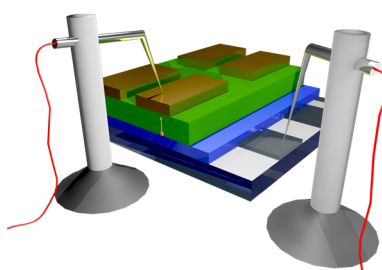
5 EDOT-Diketopyrrolopyrrole Copolymers for High Bulk Hole Mobility and Near Infrared Absorption

Christian J. Mueller, Chetan R. Singh and Mukundan Thelakkat*

Applied Functional Polymers – Macromolecular Chemistry I, University of Bayreuth, 95440
Bayreuth, Germany



**Improved bulk hole mobility
by EDOT incorporation**



Published in the *Journal of Polymer Science Part B: Polymer Physics*, **2016**, *54*, 639-648.

Reproduced with permission from Wiley VCH.

Abstract

In order to obtain novel low-bandgap materials with tailored hole-transport properties and extended absorption, electron rich 3,4-ethylenedioxythiophene is introduced as a comonomer in diketopyrrolo[3,4-*c*]pyrrole copolymers with different aryl flanking units. The polymers are characterized by absorption and photoluminescence spectroscopy, dynamic scanning calorimetry, cyclic voltammetry and X-ray diffraction. The charge transport properties of these new materials are studied carefully using an organic field effect transistor geometry where the charge carriers are transported over a narrow channel at the semiconductor/dielectric interface. These results are compared to bulk charge carrier mobilities employing space-charge limited current (SCLC) measurements, in which the charge carrier is transported through the complete film thickness of several hundred nanometers. Finally charge carrier mobilities are correlated with the electronic structure of the compounds. We find that in particular the thiophene-flanked copolymer PDPP[T]₂-EDOT is a very promising candidate for organic photovoltaics, showing an absorption response in the near infrared region with an optical bandgap of 1.15 eV and a very high bulk hole mobility of $2.9 \times 10^{-4} \text{ cm}^2\text{V}^{-1}\text{s}^{-1}$ as measured by SCLC. This value is two orders of magnitudes higher than SCLC mobilities reported for other polydiketopyrrolopyrroles and is in the range of the well-known hole transporting polymer poly(3-hexylthiophene).

5.1 Introduction

Over the last few years a variety of novel polydiketopyrrolo[3,4-*c*]pyrroles (PDPPs) has been synthesized and very successfully applied in various organic electronic devices, such as organic field effect transistors^[1] (OFET) and organic photovoltaics (OPV).^[2] Apart from π -extended systems, such as ladder-type comonomers, the exploitation of nonbonding diffusive interactions has gained interest in order to increase the backbone planarity of conjugated semiconducting polymers and to improve the delocalization length, to assist π - π -aggregation and to enhance charge transport properties of those materials.

One tool that is employed regularly is the fluorination of a subunit, such as a comonomer in order to trigger additional planarization through CH \cdots F interactions between two adjacent aromatic units. Fluorination, however, has shown to increase planarization and delocalization lengths and, furthermore, pushes the material towards an n-type semiconductor due to the

decrease of overall electron density in the polymer backbone, which originates from the large electronegativity of fluorine.

One of the most prospective applications of PDPPs is their use as a donor material in blends with fullerene as acceptor for OPV. We were therefore looking for a new solution in order to increase planarity by locking dihedral angles using diffusive heteroatom interactions without the drawback of losing electron density in the backbone.

According to a recent theoretical study by Ratner *et al.*,^[3] the CH \cdots O interactions show an even higher potential than CH \cdots F interactions. 3,4-Ethylenedioxythiophene (EDOT) represents the most accessible alkoxyated thiophene which also prevents possible sterical hindrances of the substituents with adjacent aryl units due to its constrained bicyclic geometry. Whereas EDOT was recently employed in an isoindigo polymer using direct arylation,^[4] only very few PDPPs containing EDOT are known by now. Electropolymerization of an EDOT-DPP monomer unit led to insoluble polymer films on the electrode with high electrochemical stability.^[5] A phenyl-flanked DPP-EDOT copolymer prepared by Stille polymerization was reported, but only optical properties were studied back in 2006.^[6] A more recent report briefly mentions propylenedioxythiophene derivatives in thienophene-flanked PDPPs.^[7]

Another highly demanded property of polymers for application in organic electronics is their solubility and processability from environmentally benign solvents, such as THF, toluene, xylene and tetraline. Well performing OFETs have been prepared from eco-friendly solvents by random tercopolymerization of DPPs yielding hole mobilities as high as 5 cm²V⁻¹s⁻¹.^[8]

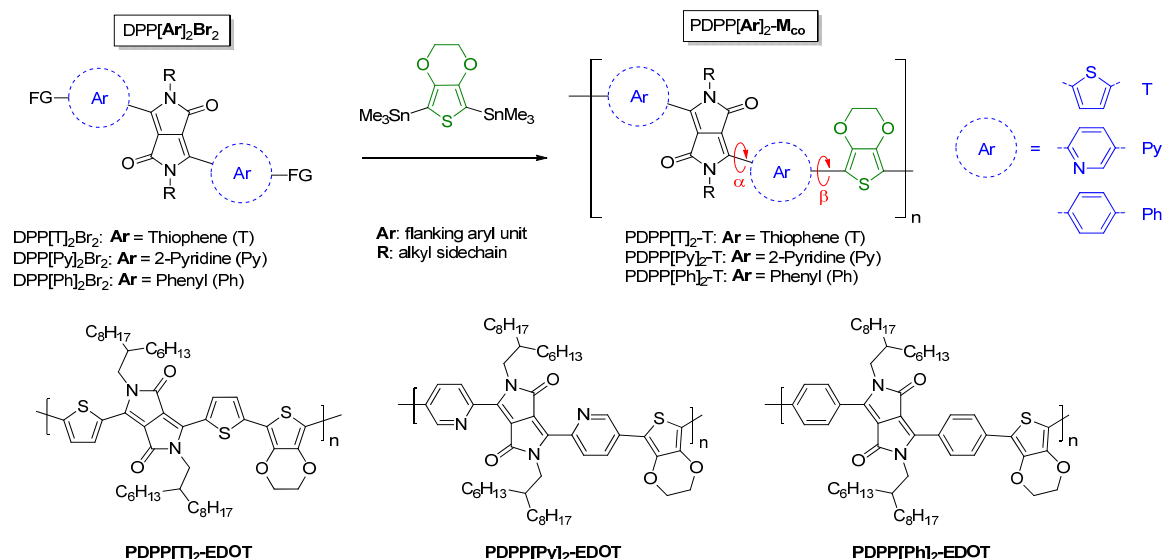
In this contribution, we report the synthesis of three novel, well defined EDOT-DPP copolymers employing different aryl flanking units on the DPP core. We show that by strategic design the hole transport of PDPPs can be tailored to suit different applications. First, our strategy involves the use of the electron rich EDOT comonomer in order to elucidate its influence on the p-type character of the materials. At the same time, this moiety provides non-covalent, diffusive interactions to the adjacent aryl units in the backbone which may improve planarization and hence delocalization as well as charge transport properties. The electron-rich EDOT units can inherently extend the absorption into the near infrared region if the planarization improves.

5.2 Results and Discussion

5.2.1 Synthesis

The nomenclature of all DPP compounds was adapted from an earlier publication.^[9] The DPP monomers were synthesized following previously reported procedures.^[9] 2,5-Bis(trimethylstannyl)-3,4-ethylenedioxy-thiophene was synthesized according to modified

literature protocols^[6] via dibromination of EDOT using NBS in a mixture of THF and acetic acid. Lithiation with *n*-butyllithium in THF and quenching with trimethyltin chloride solution gave the stannylated EDOT monomer. Experimental details on the syntheses are given in the Supporting Information. Stille polycondensations were carried out in chlorobenzene at 180 °C in sealed vials using microwave heating.^[10] All polymers were endcapped with thiophene on



Scheme 5-1. Synthesis of PDPP[Ar]₂-EDOT using Pd₂(dba)₃/P(*o*-Tol)₃ as catalytic system in chlorobenzene at 180 °C in a microwave reactor. All polymers were endcapped with 2-tributylstannylthiophene and 2-bromothiophene. Nomenclature of the compounds was adapted from a previous publication.^[9] The dihedral angles α and β are given in the polymer structure.

Table 5-1. Characteristics of the synthesized DPP polymers.

Polymer	M_n^a [kg mol ⁻¹]	M_w^a [kg mol ⁻¹]	D	DP_n^b	T_m^c [°C]	IP^d [eV]	EA^e [eV]	E_{cv}^f [eV]	E_{opt}^g [eV]
PDPP[T] ₂ -EDOT	142	377	2.7	160	361	-5.73	-3.66	2.07	1.13
PDPP[Py] ₂ -EDOT	25.7	61.2	2.4	29	290-320	-6.07	-3.74	2.33	1.59
PDPP[Ph] ₂ -EDOT	16.7	34.5	2.1	19	293	-5.89	-3.53	2.36	1.91

^aDetermined with GPC using THF/tetrabutylammoniumbromide as the eluent; ^bdegree of polymerization calculated from M_n ; ^cmelting peak values from Flash-DSC; ^dIonisation potential (HOMO), ^eelectron affinity (LUMO) and ^fband-gap determined by cyclic voltammetry in thin film; ^goptical gap determined from absorption onset in film.

both ends and are obtained in excellent yields between 80 and 95%. Gel permeation chromatography (GPC) proved to be difficult due to interactions of the EDOT-copolymers with the column material. The method we commonly use for highly aggregating PDPPs is elution with 1,2,4-trichlorobenzene at 150 °C. In this case however we observed extremely strong tailing with dispersities D between 20 and 100. Changing the eluent to chloroform improved the elution a bit, but distinct tailing towards higher molecular weights was still visible. Only after changing to THF with 0.25 wt% tetrabutylammoniumbromide as eluent the

column-analyte interactions could be suppressed sufficiently. The molecular weights and dispersities for all polymers are summarized in Table 5-1 and the individual distribution plots are given in the Supporting Information (Figure S5-3 – Figure S5-5). All polymers were obtained with high number average molecular weights M_n ranging from 142 kg mol⁻¹ in the case of PDPP[T]₂-EDOT and 17 kg mol⁻¹ for PDPP[Ph]₂-EDOT. Dispersities were in the range of 2-3 as it is common for polycondensations. Since all polymerizations were carried out under exactly the same conditions with the same degree of monomer purity for all polymers, different aggregation behavior could also explain the different molecular weights obtained for the three derivatives under the measurement conditions. Especially, the PDPP[T]₂-EDOT shows a broad eluogram and correspondingly a very high M_n . Exactly the same trend was already observed for copolymerization using thiophene and 3,4-difluorothiophene as comonomer.^[9] Interestingly, the solubility of all polymers is quite high in non-chlorinated solvents such as xylene and toluene, albeit their high molecular weights. PDPP[Py]₂-EDOT and PDPP[Ph]₂-EDOT are even soluble in tetraline and butyl acetate which makes them prospective candidates for ecofriendly processing.

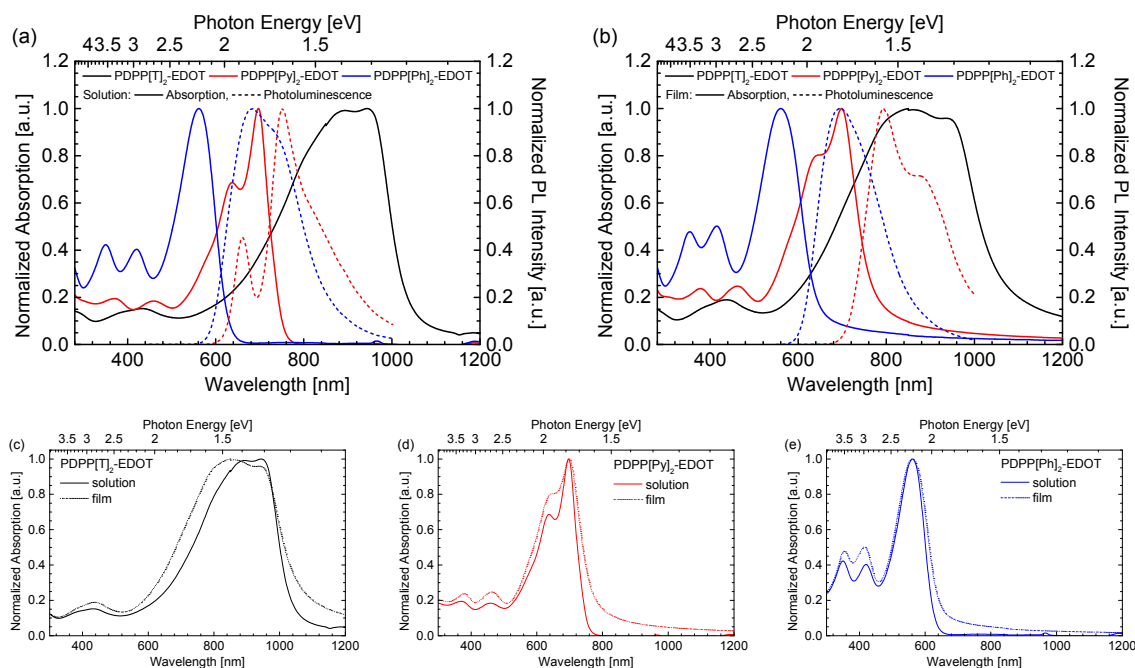


Figure 5-1. Absorption and PL spectra for the PDPP[Ar]₂-EDOT copolymers measured in (a) chloroform solution and (b) thin film. Comparison of solution and thin film spectra for the individual polymers (c-e).

5.2.2 Characterization

5.2.2.1 Optical properties

The optical absorption and photoluminescence spectra of the polymers are shown in Figure 5-1. Absorption onsets from the respective thin film spectra are summarized in Table 5-1 as optical gap E_{opt} . The most notable difference in absorption is the shift in onsets. The thiophene-

flanked PDPP[T]₂-EDOT shows a remarkably low onset energy of only 1.13 eV, corresponding to a wavelength $\lambda = 1100$ nm in the infrared region. This is not only attributed to the planar structure of the polymer backbone but also to a very strong push-pull effect of the electron rich EDOT and the electron deficient DPP core. For the pyridine-flanked PDPP[Py]₂-EDOT we observe an intermediate optical gap of 1.59 eV which is very close to the 1.6 eV that are considered as ideal optical gap for maximum performance in a single bulk heterojunction solar cell device.^[11] The phenyl-flanked PDPP[Ph]₂-EDOT shows the highest optical gap with 1.91 eV which is attributed to its low planarization due to large dihedral angles α (see Scheme 1) and hence decreased delocalization. Thus, a shift of more than 400 nm was observed for the absorption edge on moving from phenyl to thiophene flanking units. This shift is even more pronounced for the EDOT series reported here than for the thiophene series reported earlier.^[9] When comparing the individual absorption spectra in solution to those in thin film (see Figure 5-1c-e), only minor changes can be observed. PDPP[T]₂-EDOT shows a slight bathochromic shift of both onset and peak positions due to aggregation in the films. For PDPP[Py]₂-EDOT only a bathochromic shift of the onset can be observed, whereas the peak positions barely change. Finally, in PDPP[Ph]₂-EDOT both the solution and thin film spectra are almost identical, which we attribute to its poor aggregation behavior and low crystallinity as will be discussed below.

Photoluminescence (PL) measurements of all the polymers are given in Figure 5-1a,b. The emission of the thiophene-flanked PDPP[T]₂-EDOT lies in the range above $\lambda = 1000$ nm, as expected due to the $1\leftarrow 0$ transition already being very close to 1000 nm, which could not be detected in our setup. The other two polymers exhibit detectable PL (see Figure 5-1a,b). The comparison of solution and solid state emission shows distinctive changes for PDPP[Py]₂-EDOT, whereas the PDPP[Ph]₂-EDOT photoluminescence does not change considerably.

We also compare the optical properties of these three EDOT ($M_{co} = \text{EDOT}$) copolymers PDPP[Ar]₂-EDOT to our previously reported thiophene ($M_{co} = \text{T}$) copolymers PDPP[Ar]₂-T (see Supporting Information, Figure S5-6). The EDOT copolymers show a distinct red-shift in absorption for all the three aryl flanking units. The strongest effect can be observed for the thiophene flanked PDPP[T]₂- M_{co} with a bathochromic shift of 162 nm. The pyridine-flanked PDPP[Py]₂- M_{co} polymers show a red-shift of 58 nm and even the phenyl-flanked PDPP[Ph]₂- M_{co} polymers are influenced and show a bathochromic shift of 19 nm. This comparison clearly indicates that the contribution of an electron rich unit such as EDOT towards the extension of absorption is negligibly small, if the planarization is not affected.

5.2.2.2 Thermal Properties

Due to the generally very high melting points of PDPPs arising from their aggregation behavior, we used Flash-DSC measurements to avoid any degradation effects and to obtain comparative values using a single method. Heating rates from 50 to 1000 K s⁻¹ were employed

and the melting points were evaluated from the peak positions of the respective endothermic peaks. Typical heating and cooling curves are given in Figure 5-2 and all the individual DSC curves are shown in Supporting Information (Figure S5-7). The melting points T_m are summarized in Table 5-1. The flanking aryl unit largely influences the aggregation and crystallinity behavior of PDPPs^[9] and thus the thienyl-flanked PDPP[T]₂-EDOT shows the highest melting point (361 °C) and qualitatively also the largest peak areas with higher melting enthalpies than for the pyridine- and phenyl-flanked derivatives. This indicates a higher crystallinity for the thiophene-flanked derivative PDPP[T]₂-EDOT. Lower melting points of 293 °C and 290 °C-320 °C were observed for PDPP[Ph]₂-EDOT and PDPP[Py]₂-EDOT, respectively. T_m for the latter depends on the heating rate.

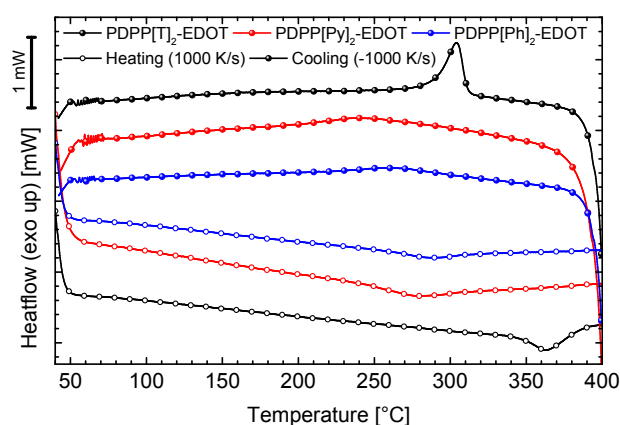


Figure 5-2. Flash-DSC curves for 1000 Ks⁻¹ heating and cooling rates. See Supporting Information Figure S5-7 for different heating and cooling rates.

5.2.2.3 Solid State Properties

The crystallinity and lamellar spacing was comparatively estimated from transmission powder XRD measurements in the small and wide angle X-ray scattering (SAXS/WAXS) region ($q = 0.016$ - 2.86 \AA^{-1}) of free standing powder samples without any thermal treatment. The diffractograms are shown in Figure 5-3 and an overview of the periodic distances d_{lam} and $d_{\pi-\pi}$ as well as the correlation lengths ζ_{lam} are given in Table 5-2. Qualitatively, the intensity of the d_{lam} peaks is decreasing from the thiophene-DPP polymers to the phenyl-DPP polymers suggesting a decreasing crystallinity when going from thiophene over pyridine to phenyl flanking units in the DPP moiety. The lamellar spacing at low q values decreases from 18.4 Å for PDPP[T]₂-EDOT to 15.9 Å for the phenyl-derivative. This can be explained by a more coplanar backbone conformation of the thiophene-flanked PDPP compared to the twisted phenyl-flanked PDPP as the backbone twist leads to a smaller inter-lamellar distance in average. On the other hand, the π - π stacking distances increase when going from thiophene (3.6 Å) over pyridine (3.7 Å) to phenyl (3.9 Å) flanking units, which can again be explained by an increasing dihedral angles in the backbone.

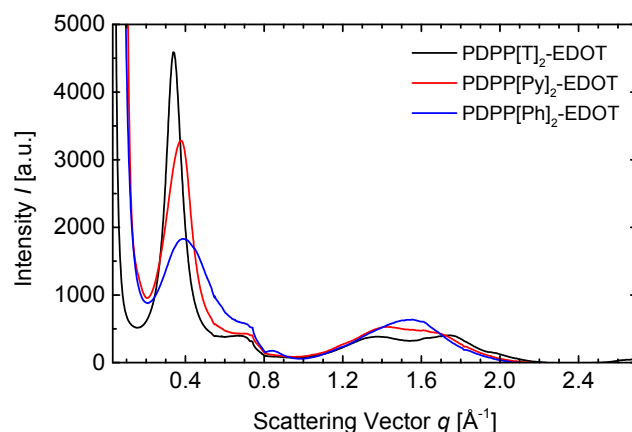


Figure 5-3. Powder SAXS/WAXS measurements of the DPP-EDOT copolymers.

Table 5-2. Periodic distances and correlation lengths for the DPP-EDOT copolymers in bulk.

Polymer	d_{lam} ^{a)} [Å]	d_{amorph} ^{b)} [Å]	$d_{\pi-\pi}$ ^{c)} [Å]	ζ_{lam} ^{d)} [Å]
PDPP[T] ₂ -EDOT	18.4	4.6	3.6	58.4
PDPP[Py] ₂ -EDOT	16.9	4.5	3.7	45.5
PDPP[Ph] ₂ -EDOT	15.9	4.2	3.9	27.6

^{a)} lamellar spacing, ^{b)} amorphous peak ^{c)} π - π spacing, ^{d)} crystal correlation length $\zeta = 2\pi/\text{FWHM}$ of the lamellar peak.

The crystal coherence length for the lamellar spacing d_{lam} is the highest for PDPP[T]₂-EDOT with 58.4 Å, decreasing to 45.5 Å for PDPP[Py]₂-EDOT and to 27.6 Å for PDPP[Ph]₂-EDOT. This suggests larger crystalline domains in the thiophene and pyridine-flanked PDPPs. A comparison of the structural data of the copolymers PDPP[Ar]₂-EDOT with previously published DPP-thiophene copolymers PDPP[Ar]₂-T is shown in the Supporting Information (Figure S5-8). The EDOT copolymers qualitatively show a slightly higher crystallinity than the thiophene copolymers. The lamellar spacing is also shifted towards slightly higher q values in the case of the EDOT copolymers, again suggesting smaller inter-lamellar distances.

5.2.2.4 Cyclic Voltammetry

The DPP-EDOT copolymers were studied using cyclic voltammetry to determine their electrochemical behavior with respect to reversibility as well as redox potentials. The individual cyclic voltammograms are shown in Figure 5-4a and the ionization potential IP as well as the electron affinity EA derived from the halfstep potentials are summarized in Table 5-1 and shown in Figure 5-4b for comparison. The fundamental gap E_{cv} increases when going from thiophene over pyridine to phenyl as flanking unit giving fundamental gaps between 2.1 eV for PDPP[T]₂-EDOT and 2.4 eV for PDPP[Ph]₂-EDOT. The fundamental gaps determined by CV are following the same trend as the optical gaps determined by absorption onset, the absolute values however are distinctively larger. This may be attributed to a large exciton

binding energy E_b .^[12] Furthermore, the redox potentials follow the expected trend with the more electron-deficient PDPP[Py]₂-EDOT having lower lying energy levels than PDPP[T]₂-EDOT. The intermediate PDPP[Ph]₂-EDOT has an *IP* in between the thiophene and the pyridine flanked PDPPs and a higher *EA* due to its weak delocalization and absence of any electron withdrawing groups such as a pyridine flanking unit.

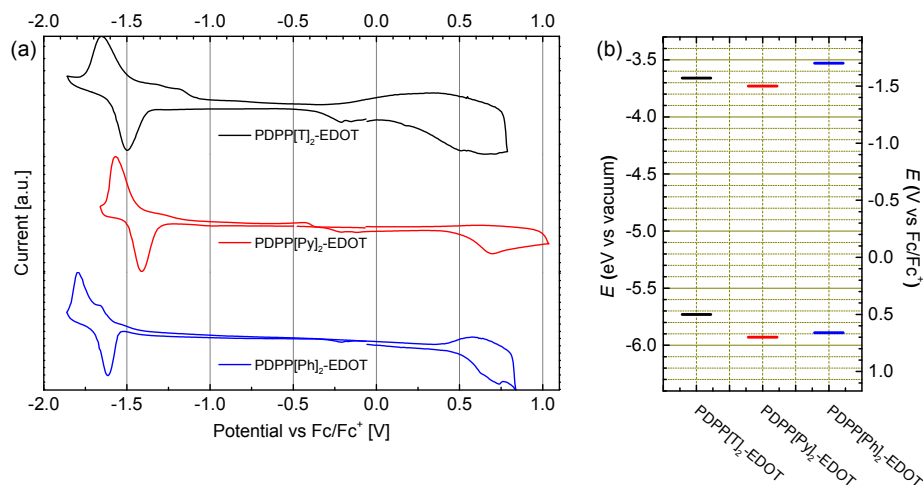


Figure 5-4. (a) Individual cyclic voltammograms for the PDPP[Ar]₂-EDOT copolymers in measured in a 0.1 m tetra-*n*-butylammonium hexafluorophosphate / acetonitrile electrolyte solution at a scan rate of 100 mV s⁻¹; (b) Energy level comparison for the EDOT DPP copolymers determined by cyclic voltammetry in thin film.

Comparing these values to previously published DPP copolymers^[9] employing a thiophene comonomer (PDPP[Ar]₂-T) instead of the EDOT comonomer used here (PDPP[Ar]₂-EDOT, for a comparison chart see Supporting Information, Figure S5-9), it is evident that especially *IP* levels are shifted to higher values in the case of the electron rich EDOT copolymers. Incorporation of EDOT leads thus to more easily oxidizable copolymers in this system.

5.2.3 Charge Transport Properties

5.2.3.1 OFET

Organic field effect transistors have been prepared employing a bottom gate / bottom contact device configuration. Charge carrier mobilities are reported for as cast films and films after thermal annealing at 250 °C for 15 min (see Table 5-3). All reported values are averaged over a set of at least 10 devices. Typical *I*-*V* curves for devices comprising PDPP[T]₂-EDOT and PDPP[Py]₂-EDOT are shown in Figure 5-5, characteristics for PDPP[Ph]₂-EDOT are given in the Supporting Information (Figure S5-10). Additional information on on/off ratios and threshold voltages is also summarized in the Supporting Information (Table S5-1). All devices showed typical p-type behavior with as cast films. The thiophene and pyridine-derivatives have an order of magnitude higher hole mobilities (10⁻³ cm²V⁻¹s⁻¹) than the phenyl derivative (10⁻⁴ cm²V⁻¹s⁻¹), which can be explained by the large dihedral twist in phenyl flanked DPP systems

that results in usually poor OFET performance.^[9] This is also in accordance with the poor crystallinity as observed in our XRD measurements. After annealing, the hole mobility in PDPP[T]₂-EDOT increased to $2.8 \times 10^{-3} \text{ cm}^2\text{V}^{-1}\text{s}^{-1}$ and the hole mobility in PDPP[Py]₂-EDOT also slightly increased to $3.7 \times 10^{-3} \text{ cm}^2\text{V}^{-1}\text{s}^{-1}$. Most interestingly, annealing introduced clear ambipolarity in the previously p-type PDPP[Py]₂-EDOT. The average electron mobility was $0.15 \text{ cm}^2\text{V}^{-1}\text{s}^{-1}$ with the best device showing a μ_e of $0.26 \text{ cm}^2\text{V}^{-1}\text{s}^{-1}$. Compared to the previously published^[9] exclusively n-type PDPP[Py]₂-T and PDPP[Py]₂-TF₂ employing thiophene and fluorothiophene comonomers, the introduction of the electron rich EDOT unit led to p-type behavior and a very balanced ambipolar device after annealing. The electron mobility remained high when compared to those n-type materials with values up to $0.26 \text{ cm}^2\text{V}^{-1}\text{s}^{-1}$.

Table 5-3. Average OFET hole (μ_h) and electron (μ_e) mobilities of PDPP[Ar]₂-EDOT copolymers in a bottom gate / bottom contact configuration for as cast and annealed films. All values were averaged over a minimum of 10 devices. Values in square brackets give the observed maximum.

Polymer	As Cast	Annealed (15 min, 250 °C)	
	μ_h [cm ² V ⁻¹ s ⁻¹]	μ_h [cm ² V ⁻¹ s ⁻¹]	μ_e [cm ² V ⁻¹ s ⁻¹]
PDPP[T] ₂ -EDOT	$(1.7 \pm 0.1) \times 10^{-3}$ [1.9×10^{-3}]	$(2.8 \pm 0.3) \times 10^{-3}$ [3.3×10^{-3}]	-
PDPP[Py] ₂ -EDOT	$(1.1 \pm 0.1) \times 10^{-3}$ [1.2×10^{-3}]	$(3.7 \pm 2.2) \times 10^{-3}$ [6.1×10^{-3}]	0.15 ± 0.06 [0.26]
PDPP[Ph] ₂ -EDOT	$(3.5 \pm 0.4) \times 10^{-4}$ [4.2×10^{-4}]	$(2.2 \pm 0.2) \times 10^{-4}$ [2.6×10^{-4}]	-

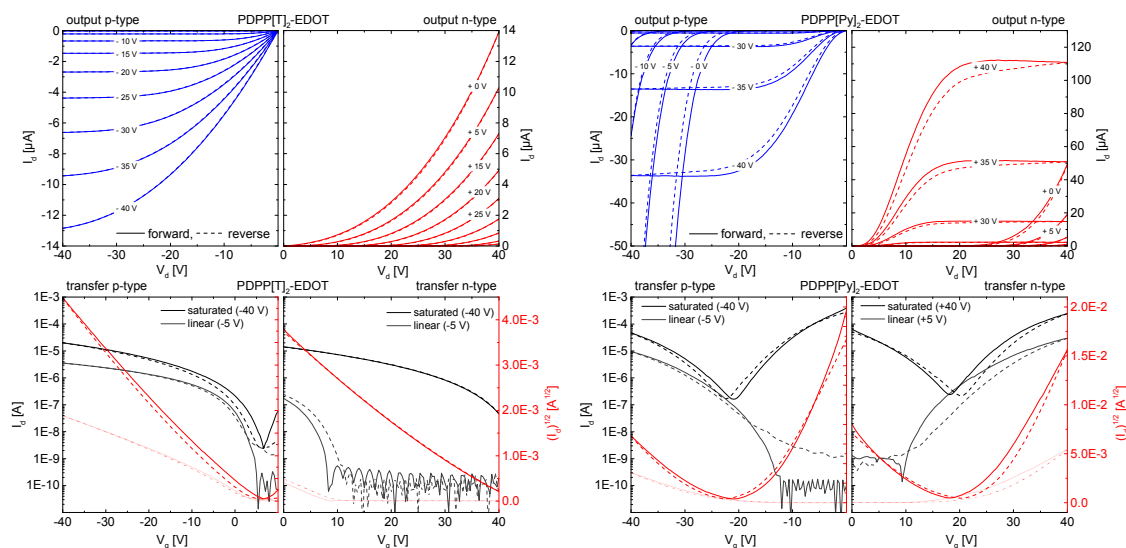


Figure 5-5. Representative OFET I - V curves in p-channel (blue output) and n-channel operation (red output) for annealed PDPP[T]₂-EDOT (left) and PDPP[Py]₂-EDOT (right). Solid lines represent forward scans, dashed lines the reverse scans in all graphs. In transfer curves (bottom), the black and grey plots indicate the transfer characteristics in the saturation and linear operation regime, respectively. The channel length was 20 μm for all devices. I - V curves for PDPP[Ph]₂-EDOT can be found in supporting information Figure S5-10.

5.2.3.2 SCLC

In contrast to SCLC measurements, the charge transport in OFET geometry is determined by a thin channel of charge at the gate/dielectric interface. Therefore the results can be heavily influenced by the interface effects, wetting issues and alignment of the polymers within the channel. In order to study the influence of the electron rich EDOT comonomer on the bulk charge transport properties, hole mobilities were determined by using the SCLC method. The measured I - V characteristics of single carrier devices were fitted with the empirical Murgatroyd formula (Equation 1).^[13]

$$J = \frac{9}{8} \epsilon_s \epsilon_0 \mu_0 \exp(0.89 \gamma \sqrt{F}) \frac{V^2}{L^3} \quad (1)$$

Here J is the current density, ϵ_s the relative permittivity of the material (~ 3.5), ϵ_0 the permittivity of vacuum, μ_0 the charge carrier mobility at zero field, γ the field dependence parameter, F the average electric field across the active layer, V the voltage across the active layer, and L the thickness of the polymer layer. Only hole-only devices were prepared as the EDOT based polymers are intended to be used as p-type materials in electronic devices. In the Murgatroyd formula two independent variables, namely the zero field mobility (μ_0) and the field dependence parameter (γ), are varied to fit the measured I - V curve. In accordance with our previous work,^[9] the hole mobility is reported as an effective mobility from all the devices at a same field, $F = 1.5 \times 10^7 \text{ Vm}^{-1}$, using the Poole–Frenkel relationship (Equation (2)):^[14]

$$\mu(F) = \mu_0 \exp(\gamma \sqrt{F}) \quad (2)$$

Reporting the charge mobility at a constant field condenses the information of two independent parameters (μ_0 and γ) to a single parameter and allows a direct charge mobility comparison across different materials.^[15]

The hole mobility value in as-cast films was checked for reproducibility and consistency by repeating the experiment for different film thicknesses. The fitted exemplary I - V curves of different PDDPs for as-cast films are shown in Figure 5-6. Double-logarithmic plots of the I - V curves are given in the supporting Information, Figure S5-11. The effective hole mobilities averaged over different film thicknesses together with the results of the annealed films are summarized in Table 5-4. A complete table listing film thicknesses and fitting parameters for all the devices can be found in the Supporting Information (Table S5-2). A plot of the film thickness versus the SCLC hole mobility is also shown in the Supporting Information (Figure S5-12).

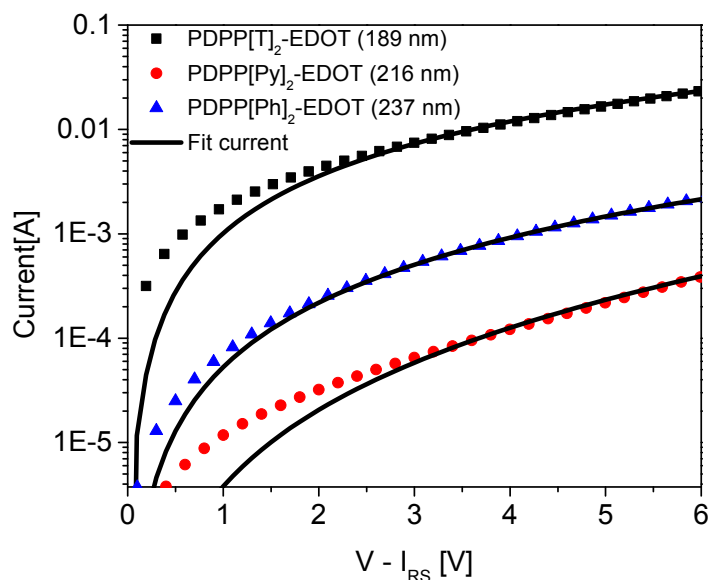


Figure 5-6. The SCLC I - V characteristics of as-cast PDDP films measured in hole-only device configuration. The solid lines represent the Murgatroyd fit with field dependent mobility. The corresponding film thicknesses are given within the parentheses. The I - V curves were corrected for the voltage drop (IR) over the contacts.

As reported in Table 5-4, the hole mobility varies significantly for the investigated set of materials. The maximum bulk hole mobility of around $3.0 \times 10^{-4} \text{ cm}^2 \text{V}^{-1} \text{s}^{-1}$ was obtained for PDPP[T]₂-EDOT followed by $4.2 \times 10^{-5} \text{ cm}^2 \text{V}^{-1} \text{s}^{-1}$ for PDPP[Ph]₂-EDOT and $2.2 \times 10^{-6} \text{ cm}^2 \text{V}^{-1} \text{s}^{-1}$ for PDPP[Py]₂-EDOT. The bulk hole mobility reported here for PDPP[T]₂-EDOT is at least one order of magnitude higher than those typically observed values for PDDP class of materials.^[9] This measured hole mobility in PDPP[T]₂-EDOT is also comparable to that of well-known P3HT polymer.^[16] It is interesting to note that the hole mobility trend measured in OFET devices is different to that obtained from SCLC devices. In SCLC measurements we see a clear correlation of electron richness and effective hole mobilities. Whereas the electron deficient pyridine-flanked PDDPs shows the poorest bulk hole mobility in the range of $10^{-6} \text{ cm}^2 \text{V}^{-1} \text{s}^{-1}$, the phenyl flanked PDPP[Ph]₂-EDOT with an intermediate electron deficiency reaches the range of $10^{-5} \text{ cm}^2 \text{V}^{-1} \text{s}^{-1}$ and ultimately the electron rich thiophene-flanked PDPP[T]₂-EDOT gives the highest bulk hole mobility of over $10^{-4} \text{ cm}^2 \text{V}^{-1} \text{s}^{-1}$. In contrast to OFET measurements, annealing at 200 °C for 15 min does not systematically influence the bulk hole mobility values. Since high temperature annealing does not improve the SCLC hole mobilities, it can be concluded that the positive effects of crystallization observed in a transistor geometry obviously do not contribute towards higher bulk charge carrier mobilities in PDPP[Ar]₂-EDOT copolymers.

Table 5-4. The average effective SCLC mobility of holes (μ_h) in as-cast PDPP films for varying film thicknesses in the range of ~200–550 nm. The charge mobility in annealed films for single film thickness is also given. The films were annealed at 200 °C for 15 min.

Polymer	As Cast	Annealed
	μ_h [cm ² V ⁻¹ s ⁻¹]	μ_h [cm ² V ⁻¹ s ⁻¹]
PDPP[T] ₂ -EDOT	$(2.9 \pm 1.0) \times 10^{-4}$	1.5×10^{-4}
PDPP[Py] ₂ -EDOT	$(2.2 \pm 1.2) \times 10^{-6}$	6.8×10^{-6}
PDPP[Ph] ₂ -EDOT	$(4.2 \pm 2.3) \times 10^{-5}$	6.3×10^{-5}

5.3 Conclusion

We have synthesized new copolymers based on EDOT and diketopyrrolo[3,4-*c*]pyrroles employing different aryl flanking units on the DPP core. We found, that especially the thiophene-flanked PDPP[T]₂-EDOT shows remarkable properties such as an ultra-low optical gap of only 1.13 eV corresponding to an optical onset in the infrared region at $\lambda = 1100$ nm. The most crystalline thiophene-flanked derivative also shows the highest planarity and the largest coherence lengths in XRD measurements. Interestingly, the OFET hole mobilities are inferior to those from PDPPs employing a simple thiophene comonomer instead of the EDOT. However, by choosing this electron rich comonomer and electron deficient pyridine flanking units on the DPP core, we were able to obtain a material showing excellent ambipolar behavior in OFET devices with electron mobilities as high as 0.26 cm²V⁻¹s⁻¹. By using the electron-rich alkoxy-substituted EDOT as a comonomer we were furthermore able to successfully improve the bulk hole mobility in the class of DPP polymers to the range of 10⁻⁴ cm²V⁻¹s⁻¹ which is about one to two orders of magnitudes higher than values previously reported for SCLC mobilities in these materials and matches the mobility observed for P3HT.

5.4 Experimental Section

Materials and methods. All reagents were used without further purification unless otherwise noted. Microwave reactions were conducted in sealed containers using a Biotage Initiator Eight+ microwave. ¹H NMR (300 MHz) spectra were recorded on a Bruker AC 300 spectrometer and calibrated according to the respective solvent resonance signal. Size exclusion chromatography was performed utilizing a Waters 510 HPLC pump and stabilized THF with 0.25 wt% TBAB (tetrabutylammoniumbromide) as eluent at a flow rate of 0.5 mL/min. 100 μ L of a solution with a concentration of approximately 1 mg/mL was injected into a column setup comprising a guard column (PSS, 5 \times 0.8 cm, SDV gel, particle size 5 μ m, pore size 100 Å) and two separation columns (Varian, 30 \times 0.8 cm, mixed C gel, particle size 5 μ m).

Polymer size distribution were monitored with a Waters 410 differential RI detector. Molecular weights were given with respect to PS-calibration. Cyclic voltammetry was performed under moisture- and oxygen-free conditions using a 0.1 m tetra-*n*-butylammonium hexafluorophosphate in acetonitrile electrolyte solution. A standard three-electrode assembly connected to a potentiostat (model 263A, EG&G Princeton Applied Research) was used at a scanning rate of 100 mV s⁻¹. The working electrode was a 10 Ω/ ITO coated glass substrate. The polymers were spincoated onto the ITO substrates from chloroform at 3 mg/mL and 1500 rpm to obtain thicknesses of 10-20 nm. A platinum wire in acetonitrile was used as counter electrode and the quasi-reference electrode consisted of an Ag wire in an AgNO₃/acetonitrile solution (0.1 m). The measurements were calibrated with an external ferrocene/ferrocenium standard, IP and EA values were calculated considering the solvent effects as per a published procedure^[17] using Equation 3 and 4 where the workfunction of Fc/Fc⁺ is taken to be -5.23 eV. The reduction half-step potential $E_{1/2}^{\text{red}}$ (vs Fc/Fc⁺) is negative whereas the oxidation half-step potential $E_{1/2}^{\text{ox}}$ (vs Fc/Fc⁺) is positive.

$$EA \approx -5.23\text{eV} - E_{1/2}^{\text{red}}(\text{vs Fc/Fc}^+) \quad (3)$$

$$IP \approx -5.23\text{eV} - E_{1/2}^{\text{ox}}(\text{vs Fc/Fc}^+) \quad (4)$$

Absorption measurements were carried out on a JASCO V-670 spectrophotometer. Photoluminescence measurements were carried out on a JASCO FP-8600 spectrofluorometer. Optical properties in solution were measured in chloroform at a concentration of 0.01 mg/mL, films were spincoated on glass slides from a 7 mg/mL chloroform solution. FlashDSC measurements were performed on a Mettler-Toledo Flash DSC 1.^[18]

OFET measurements: Organic thin film transistors substrates in bottom gate / bottom contact configuration were bought from Fraunhofer IPMS (OFET Gen. 4). Heavily n-doped silicon (doping at wafer surface: $n \sim 3 \times 10^{17} \text{ cm}^{-3}$) was used as substrate and gate electrode. Thermally grown silicon oxide (230 nm ± 10 nm) was used as the gate dielectric. Gold electrodes (30 nm on 10 nm ITO as adhesion layer) were used as source and drain contacts. The channel width was 10 mm for all devices and the channel length varied from 10 μm to 20 μm. The substrates were cleaned subsequently in acetone and 2-propanol in an ultrasonic bath for 5 minutes each. Treatment in an ozone oven at 50 °C for 20 min was followed by immersion in a 1 wt-% solution of octadecyltrichlorosilane in toluene at 60 °C for 45 min. After rinsing with toluene and 2-propanol the substrates were dried and the polymer was spincoated from a 6 mg/mL chloroform solution at 5000 rpm under ambient conditions. Devices were measured in a nitrogen atmosphere using an Agilent B1500 Semiconductor Parameter Analyzer. The devices were annealed in a nitrogen atmosphere at a maximum of 0.9 ppm O₂ at 150 °C for 15 min. Mobilities were calculated from the slopes in the $(I_d)^{0.5}$ - V_g plots in the saturation regime using

Equation 5 where I_d is the drain current, W the channel width, L the channel length, C_i the capacitance, V_g the gate voltage and V_T the threshold voltage, respectively.

$$I_d \approx \frac{W}{2L} C_i \mu (V_g - V_T)^2 \quad (5)$$

SCLC measurements: Single carrier hole-only devices in diode configuration were prepared within the layer stack of glass/ITO/PEDOT:PSS/Polymer/MoO₃/Ag. The PEDOT:PSS layer (HTL-solar) of 40 nm was spin coated onto cleaned patterned ITO glass substrates. After that, polymer solutions of concentration 10 – 20 mg/mL in chloroform were doctor bladed on top under inert conditions. Subsequently, MoO₃ (10 nm) and Ag (100 nm) were thermally evaporated to complete the device stack. The devices had an active area of 9 mm². Dark I - V measurements were made under inert environment with a Keithley 2400 source measure unit. The measured I - V from the devices were nearly symmetric around 0 V. For mobility evaluation, forward bias voltages, i.e. hole injection from PEDOT:PSS, were considered. The charge carrier mobilities were evaluated by fitting measured I - V characteristics in a voltage range from 2 to 5 V using the Murgatroyd formula.^[13] Prior to fitting, the measured I - V characteristics were corrected for the voltage drop (IR, $R = 27 \text{ } \Omega$) across contacts. The built-in voltage correction was not applied as the I - V curves were symmetrical around the 0 V.

Synthesis procedures for the DPP compounds. All syntheses were conducted under argon using a double manifold schlenk line. Glasware was severely dried under high vacuum. Solvents were degassed by three freeze-pump-thaw cycles. Monomers used for polymerization were recrystallized freshly.

PDPP[T]₂-EDOT. An oven dried microwave vial was loaded with DPP[T]₂{2HD}₂Br₂ (128.48 mg, 0.142 mmol), 2,5-bis(trimethylstannyl)-3,4-ethylenedioxythiophene (66.99 mg, 0.143 mmol), tri-*o*-tolylphosphine (5.20 mg, 17 μ mol) and finally tris(dibenzylideneacetone)dipalladium(0) (4.13 mg, 4.5 μ mol). Dry and degassed chlorobenzene (3.8 mL) was added, the vial was sealed with a septum cap and subsequently purged with argon for 15 min. The mixture was stirred for 30 min at 180 °C in the microwave. After cooling to 50 °C 2-tributyltinthiophene (25 μ L, 79 μ mol) was added to the viscous green solution using a microliter syringe. The mixture was again heated at 180 °C for 5 min in the microwave, cooled to 50 °C and finally 2-bromothiophene (30 μ L, 308 μ mol) was added. The mixture was heated to 180 °C for 10 min in the microwave. After cooling to room temperature the polymer was precipitated in 200 mL methanol and filtrated into a soxhlet thimble. The crude polymer was subjected to soxhlet extraction using acetone, hexane and dichloromethane. Solvent was removed from the dichloromethane fraction under reduced pressure and the residue was redissolved in 5 mL chloroform. Precipitation in 200 mL methanol and filtration over a

0.45 μm PTFE filter followed by drying in high vacuum afforded PDPP[T]₂-EDOT as a dark purple solid (111 mg, 88%).

PDPP[Py]₂-EDOT. An oven dried microwave vial was loaded with DPP[Py]₂{2HD}₂Br₂ (133.04 mg, 0.148 mmol), 2,5-bis(trimethylstannyl)-3,4-ethylenedioxythiophene (69.91 mg, 0.149 mmol), tri-*o*-tolylphosphine (5.41 mg, 18 μmol) and finally tris(dibenzylideneacetone)dipalladium(0) (4.05 mg, 4.4 μmol). Dry and degassed chlorobenzene (4.0 mL) was added, the vial was sealed with a septum cap and subsequently purged with argon for 15 min. The mixture was stirred for 30 min at 180 °C in the microwave. After cooling to 50 °C 2-tributyltinthiophene (25 μL , 79 μmol) was added to the blue solution using a microliter syringe. The mixture was again heated at 180 °C for 10 min in the microwave, cooled to 50 °C and finally 2-bromothiophene (30 μL , 308 μmol) was added. The mixture was heated to 180 °C for 10 min in the microwave. After cooling to room temperature the polymer was precipitated in 200 mL methanol and filtrated into a soxhlet thimble. The crude polymer was subjected to soxhlet extraction using acetone and hexane. The solvent was removed under reduced pressure from the hexane fraction and the residue was redissolved in 5 mL chloroform. precipitated in 150 mL methanol. Precipitation in 200 mL methanol and filtration over a 0.45 μm PTFE filter followed by drying in high vacuum afforded PDPP[Py]₂-EDOT as a dark purple solid (122 mg, 94%).

PDPP[Ph]₂-EDOT. An oven dried microwave vial was loaded with DPP[Ph]₂{2HD}₂Br₂ (120.83 mg, 0.135 mmol), 2,5-bis(trimethylstannyl)-3,4-ethyleneidoxxythiophene (63.22 mg, 0.135 mmol), tri-*o*-tolylphosphine (4.85 mg, 16 μmol) and finally tris(dibenzylideneacetone)dipalladium(0) (3.79 mg, 4.1 μmol). Dry and degassed chlorobenzene (3.5 mL) was added, the vial was sealed with a septum cap and subsequently purged with argon for 15 min. The mixture was stirred for 2 h at 180 °C in the microwave. After cooling to 50 °C 2-tributyltinthiophene (25 μL , 79 μmol) was added to the red solution using a microliter syringe. The mixture was again heated at 180 °C for 10 min in the microwave, cooled to 50 °C and finally 2-bromothiophene (50 μL , 516 μmol) was added. The mixture was heated to 180 °C for 10 min in the microwave. After cooling to room temperature the polymer was precipitated in 250 mL methanol and filtrated into a soxhlet thimble. The crude polymer was subjected to soxhlet extraction using methanol, acetone and hexane. The solvent was removed from the hexane fraction under reduced pressure, the solid remains were redissolved in a minimal amount of chloroform and precipitated in 250 mL methanol. The precipitate was filtrated over a 0.45 μm PTFE filter and dried in high vacuum to obtain PDPP[Ph]₂-EDOT as a dark purple solid (96 mg, 81%).

5.5 Acknowledgements

We acknowledge financial support from DFG (SFB840) and the Bavarian State Ministry of Education, Science and the Arts (Solar technologies go hybrid). C.J.M. thanks the Fonds der Chemischen Industrie for funding the PhD with a Kekulé scholarship and the German National Academic Foundation (Studienstiftung des deutschen Volkes) for additional support during the PhD. Support from the Elitenetzwerk Bayern (ENB Macromolecular Science) is also kindly acknowledged. We thank Sven Huettner for recording X-ray data at the Australian Synchrotron. Part of this research was undertaken at the SAXS/WAXS beamline at the Australian Synchrotron, Victoria, Australia.^[19]

5.6 References

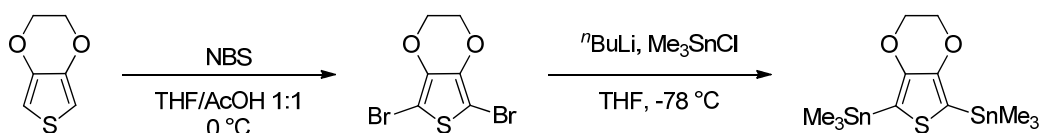
- [1] Z. Yi, S. Wang, Y. Liu, *Adv. Mater.* 2015.
- [2] W. Li, K. H. Hendriks, A. Furlan, M. M. Wienk, R. A. Janssen, *J. Am. Chem. Soc.* 2015, 137, 2231.
- [3] N. E. Jackson, B. M. Savoie, K. L. Kohlstedt, M. Olvera de la Cruz, G. C. Schatz, L. X. Chen, M. A. Ratner, *J. Am. Chem. Soc.* 2013, 135, 10475.
- [4] F. Grenier, B. R. Aïch, Y.-Y. Lai, M. Guérette, A. B. Holmes, Y. Tao, W. W. H. Wong, M. Leclerc, *Chem. Mater.* 2015, 150311140558002.
- [5] a) Y. Zhu, K. Zhang, B. Tieke, *Macromol. Chem. Phys.* 2009, 210, 431; b) K. Zhang, B. Tieke, J. C. Forgie, P. J. Skabara, *Macromol. Rapid Commun.* 2009, 30, 1834.
- [6] Y. Zhu, I. Heim, B. Tieke, *Macromol. Chem. Phys.* 2006, 207, 2206.
- [7] S. P. Mishra, A. K. Palai, M. Patri, *Synth. Met.* 2010, 160, 2422.
- [8] H. J. Yun, G. B. Lee, D. S. Chung, Y. H. Kim, S. K. Kwon, *Adv. Mater.* 2014, 26, 6612.
- [9] C. J. Mueller, C. R. Singh, M. Fried, S. Huettner, M. Thelakkat, *Adv. Funct. Mater.* 2015, 25, 2725.
- [10] C. B. Nielsen, R. S. Ashraf, B. C. Schroeder, P. D'Angelo, S. E. Watkins, K. Song, T. D. Anthopoulos, I. McCulloch, *Chem. Commun.* 2012, 48, 5832.
- [11] G. Dennler, M. C. Scharber, T. Ameri, P. Denk, K. Forberich, C. Waldauf, C. J. Brabec, *Adv. Mater.* 2008, 20, 579.
- [12] J.-L. Bredas, *Materials Horizons* 2014, 1, 17.
- [13] P. N. Murgatroyd, *Journal of Physics D - Applied Physics* 1970, 3, 151.

- [14] J. Frenkel, *Physical Review* 1938, 54, 647.
- [15] J. C. Blakesley, F. A. Castro, W. Kylberg, G. F. A. Dibb, C. Arantes, R. Valaski, M. Cremona, J. S. Kim, J.-S. Kim, *Org. Electron.* 2014, 15, 1263.
- [16] a) C. Goh, R. J. Kline, M. D. McGehee, E. N. Kadnikova, J. M. J. Fréchet, *Appl. Phys. Lett.* 2005, 86, 122110; b) C. R. Singh, G. Gupta, R. Lohwasser, S. Engmann, J. Balko, M. Thelakkat, T. Thurn-Albrecht, H. Hoppe, *J. Polym. Sci., Part B: Polym. Phys.* 2013, 51, 943.
- [17] K. Gräf, M. A. Rahim, S. Das, M. Thelakkat, *Dyes and Pigments* 2013, 99, 1101.
- [18] V. Mathot, M. Pyda, T. Pijpers, G. Vanden Poel, E. van de Kerkhof, S. van Herwaarden, F. van Herwaarden, A. Leenaers, *Thermochim. Acta* 2011, 522, 36.
- [19] N. M. Kirby, S. T. Mudie, A. M. Hawley, D. J. Cookson, H. D. T. Mertens, N. Cowieson, V. Samardzic-Boban, *J. Appl. Crystallogr.* 2013, 46, 1670.

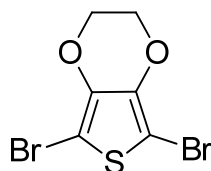
Supporting Information

EDOT monomer synthesis.....	215
Monomer Characterization	217
¹ H-NMR spectra.....	217
Polymer Characterization	218
Gel permeation chromatography	218
Additional Optical Data	219
Thermal Properties	220
Additional XRD data.....	221
Cyclic Voltammetry	222
Device Characterization.....	223
Additional OFET <i>I</i> - <i>V</i> data	223
Additional SCLC data	224
References.....	225

EDOT monomer synthesis

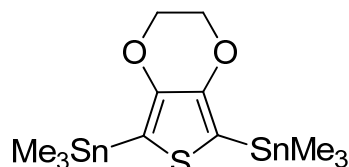


Scheme S5-1. Synthetic route for the distannyl-EDOT monomer



2,5-Dibromo-3,4-ethylenedioxythiophene (EDOTBr₂). *N*-Bromosuccinimide (7.89 g, 44.3 mmol) was dissolved in a mixture of 85 mL THF and 85 mL acetic acid. The solution was degassed by purging with argon for 10 minutes and cooled to 0 °C where 3,4-ethylenedioxythiophene (2.25 mL, 21.1 mmol) was added dropwise against an argon stream. The solution was stirred at room temperature for 4 h under exclusion of light. Water (220 mL)

was added resulting in precipitation of a silverish crystalline solid, which was isolated by filtration. The filtrate was diluted with another 300 mL water and the formed precipitate was collected again by filtration. The solids were combined and dried *in vacuo* to afford 6.25 g 2,5-dibromo-3,4-ethylenedioxythiophene (21.0 mmol, 99%) as silverish flakes. NMR and GC showed 100% purity, the product was used without further purification. Otherwise recrystallization is possible from ethanol. $^1\text{H-NMR}$ (300 MHz, CHCl_3): (ppm) 4.27 (s, 4 H).



2,5-bis(trimethylstannyl)-3,4-ethylenedioxythiophene. To a solution of 2,5-dibromo-3,4-ethylenedioxythiophene (2.77 g, 9.23 mmol) in 92 mL anhydrous THF was added *n*-butyllithium (2.5 M in hexane) (7.76 mL, 19.4 mmol) at $-78\text{ }^{\circ}\text{C}$. The resulting mixture was stirred at $-78\text{ }^{\circ}\text{C}$ for 60 min before trimethyltin chloride (3.86 g, 19.4 mmol) in 19.3 mL anhydrous THF was added via syringe. After complete addition the solution was stirred for further 10 min before it was allowed to warm to room temperature within 1 h. Water was added and the mixture was extracted with diethyl ether (3 x 50 mL). The organic layers were combined and washed with brine, dried over magnesium sulfate. After filtration solvents were removed under reduced pressure and the crude product was recrystallized from ethanol and subsequently hexane to afford 1.419 g 2,5-bis(trimethylstannyl)-3,4-ethylenedioxythiophene (3.03 mmol, 33%) as pale brown crystals. It is noteworthy that gas chromatography and NMR showed up to 5% of byproduct (mono stannylated compound) which could neither be removed by multiple recrystallization nor by sublimation at 10^{-7} mbar. $^1\text{H-NMR}$ (300 MHz, CHCl_3): (ppm) 4.15 (s, 4 H), 0.33 (s, 18 H, $-\text{SnMe}_3$).

Monomer Characterization

^1H -NMR spectra

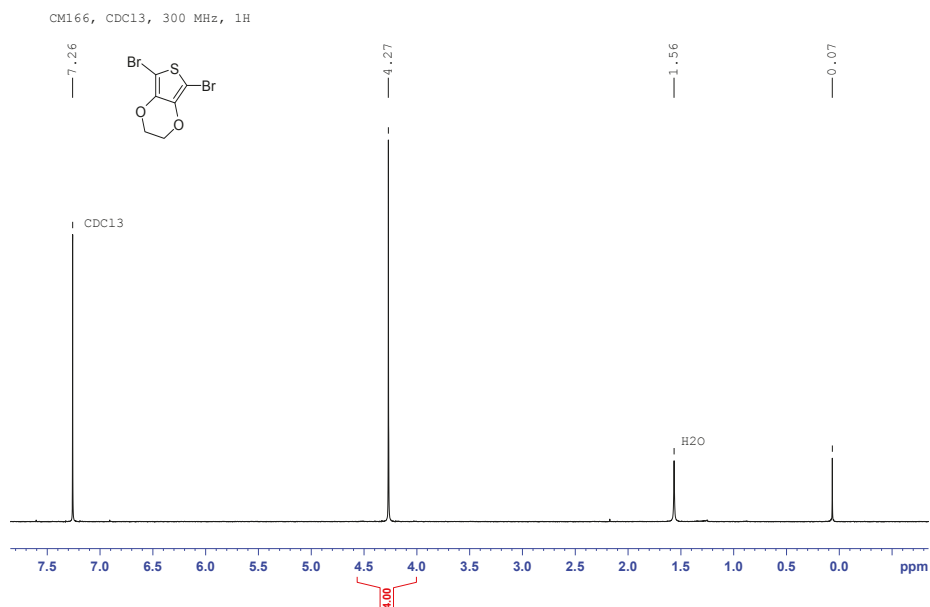


Figure S5-1. ^1H -NMR spectrum of 2,5-dibromo-3,4-ethylenedioxythiophene.

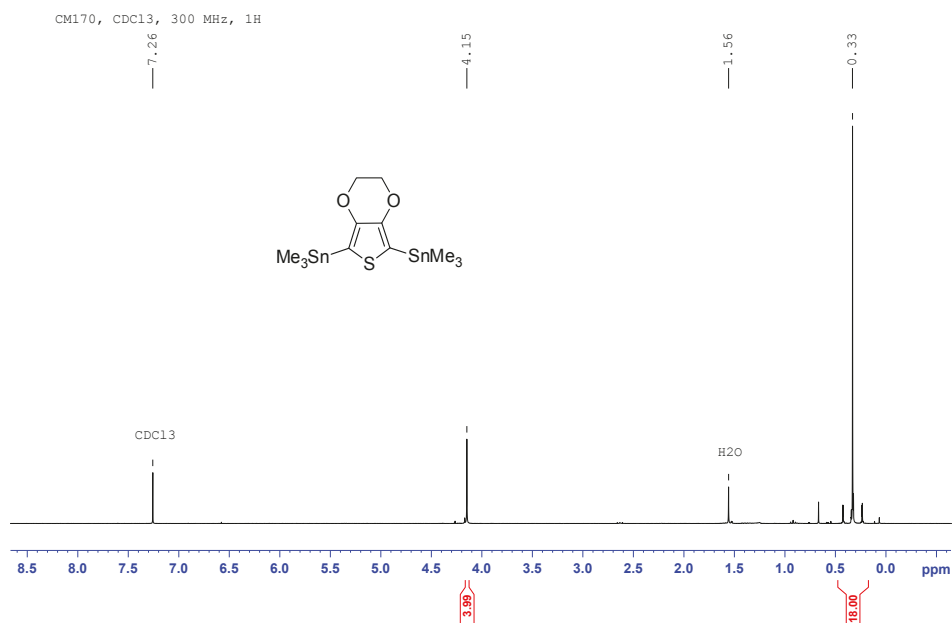


Figure S5-2. ^1H -NMR spectrum of 2,5-bis(trimethylstannyl)-3,4-ethylenedioxythiophene.

Polymer Characterization

Gel permeation chromatography

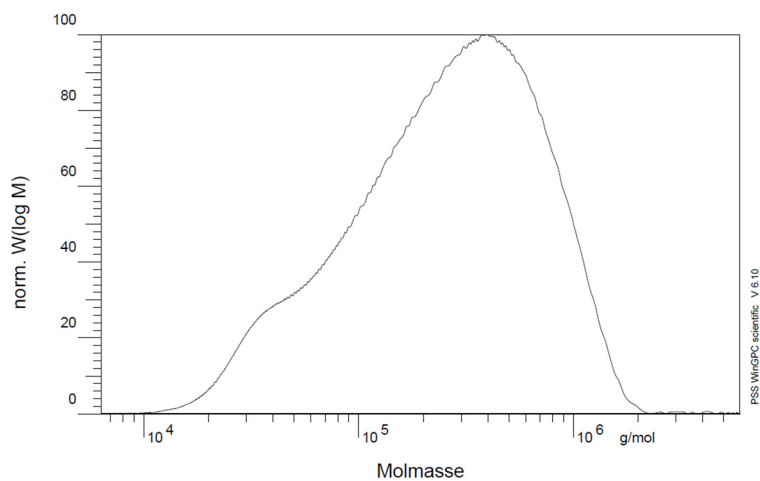


Figure S5-3. Gel permeation chromatography trace for PDPP[T]2-EDOT.

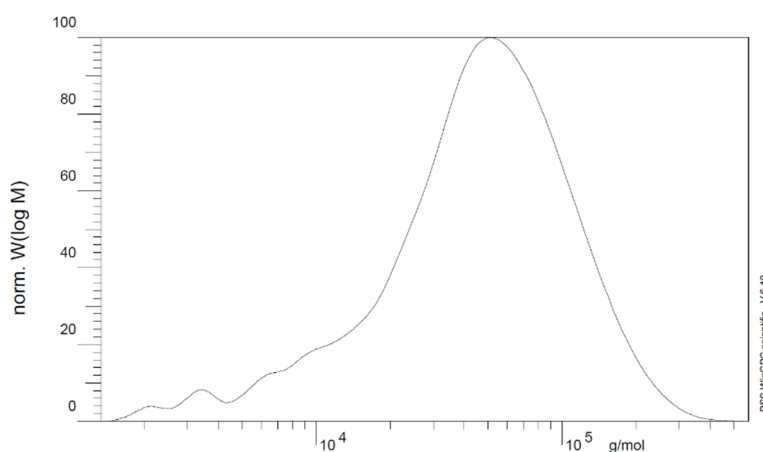


Figure S5-4. Gel permeation chromatography trace for PDPP[Py]2-EDOT.

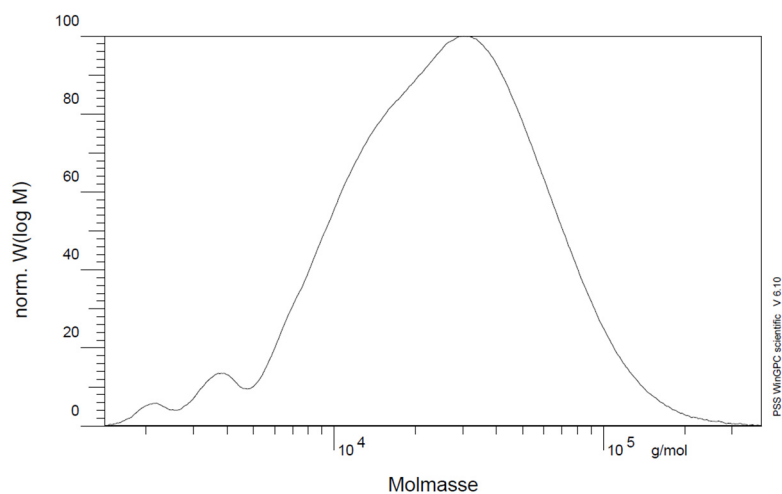


Figure S5-5. Gel permeation chromatography trace for PDPP[Ph]₂-EDOT.

Additional Optical Data

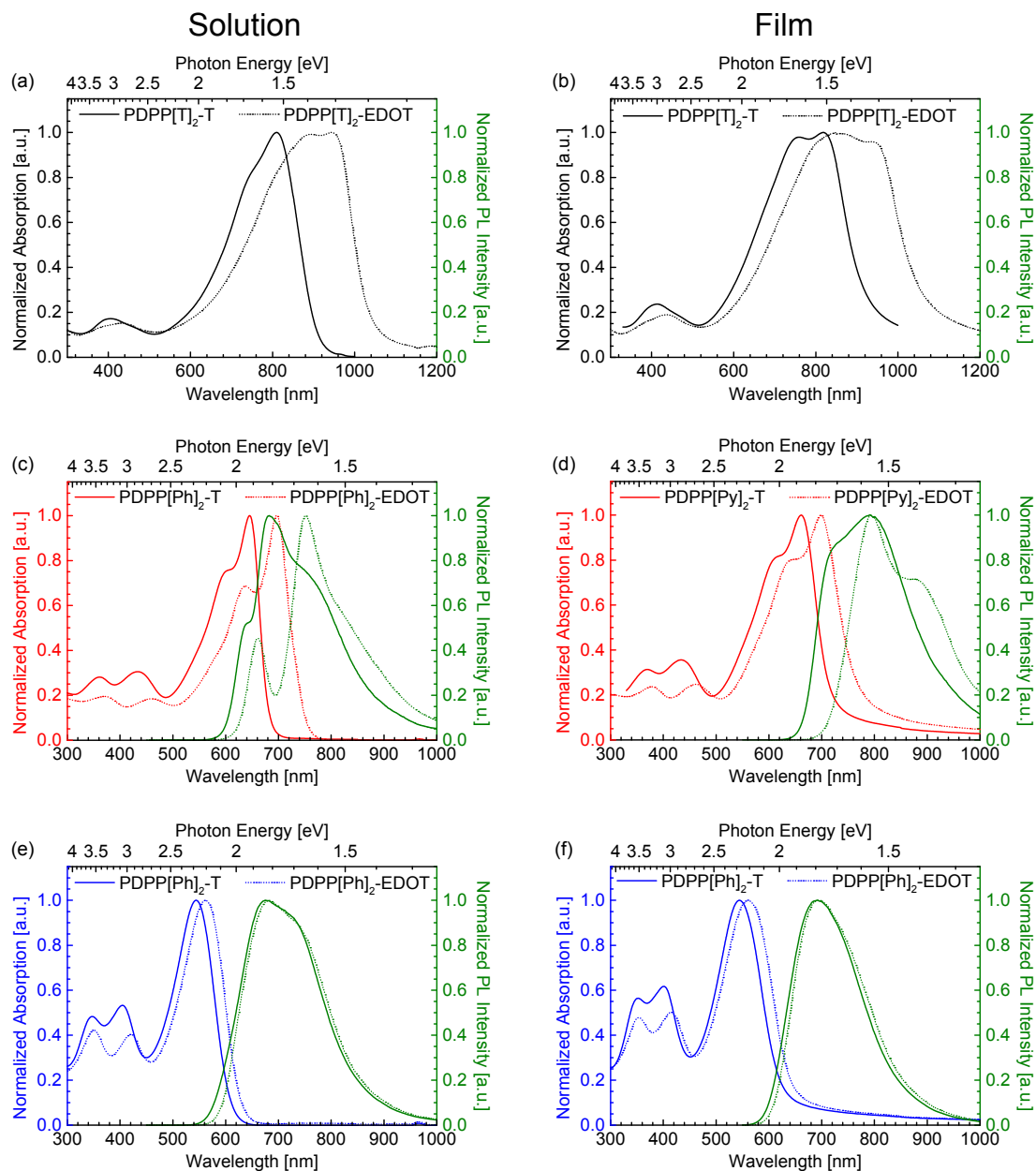


Figure S5-6. Absorption and PL spectra of the newly synthesized EDOT copolymers PDPP[Ar]₂-EDOT compared to previously published^[1] thiophene copolymers PDPP[Ar]₂-T employing different aryl flanking units Ar: Thiophene-flanked DPP (a, b), pyridine-flanked DPP (c, d) and phenyl-flanked DPP (e, f). Spectra recorded in solution on the left (a, c, e), thin film spectra on the right (b, d, f).

Thermal Properties

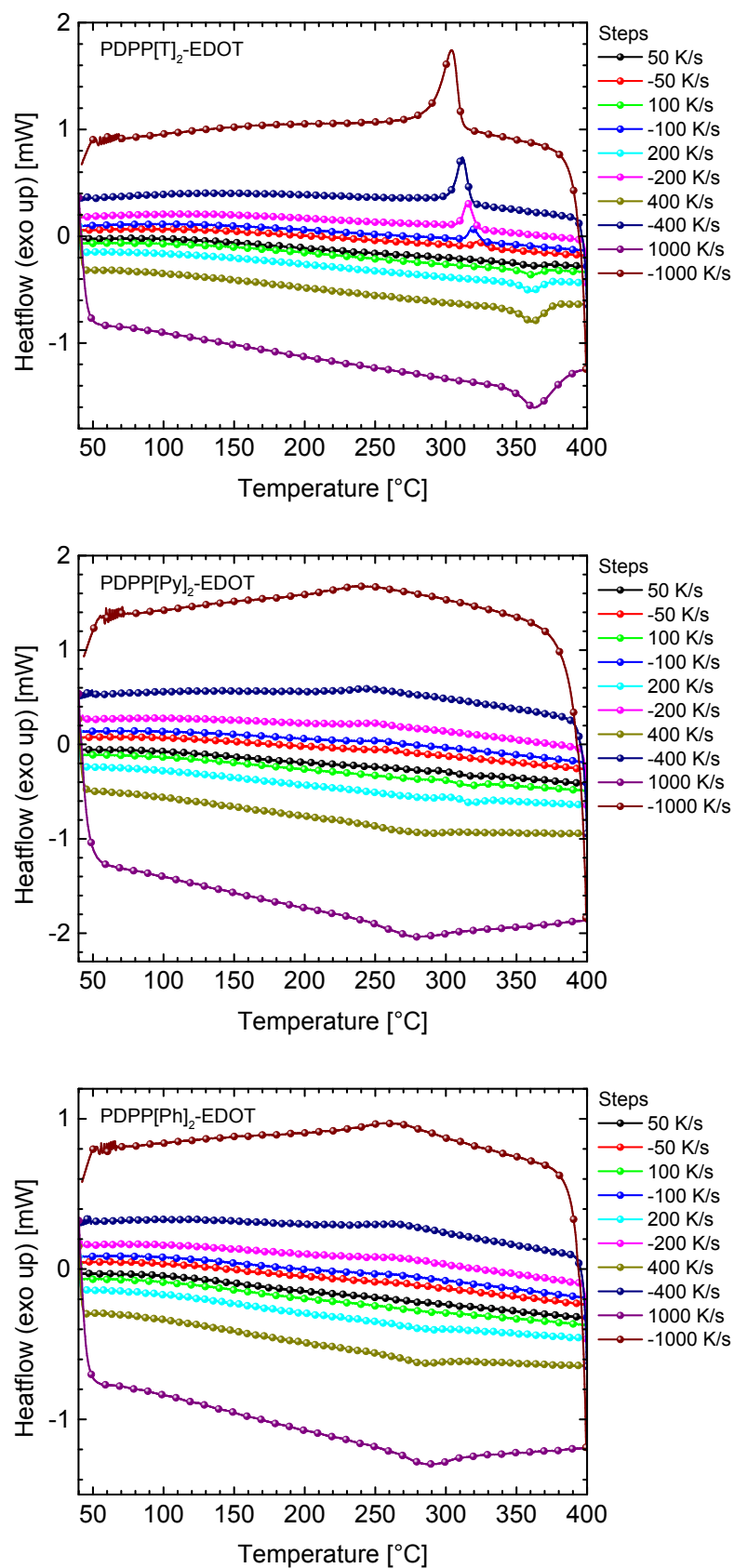


Figure S5-7. Flash-DSC curves for all three DPP-EDOT copolymers.

Additional XRD data

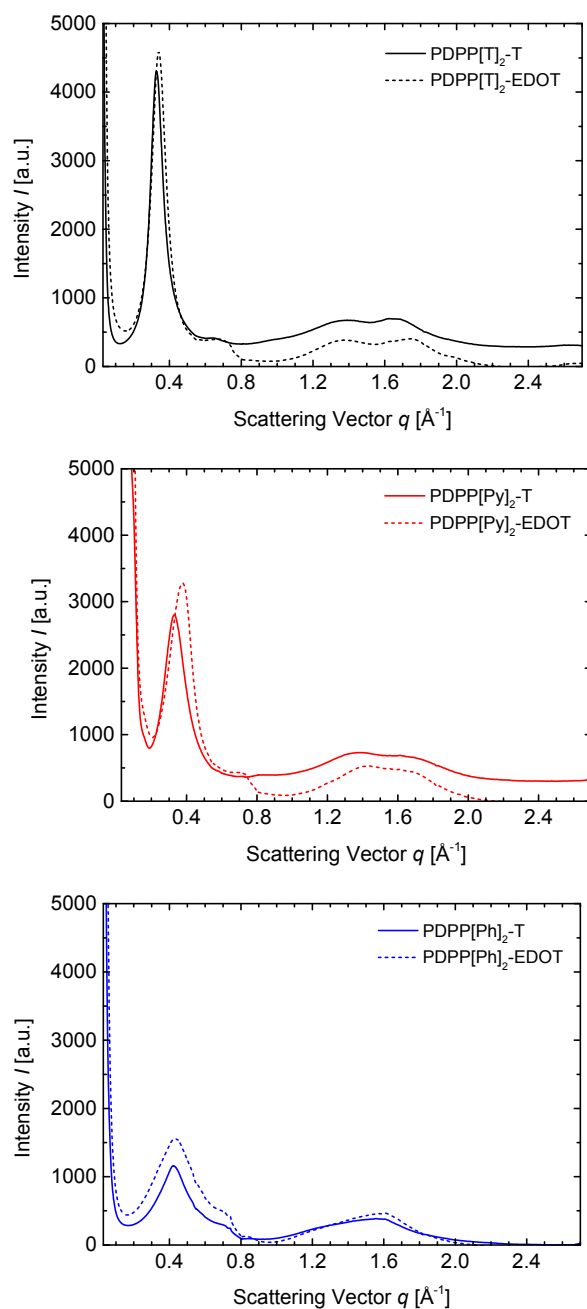


Figure S5-8. Bulk SAXS/WAXS comparison for the newly synthesized $\text{PDPP}[\text{Ar}]_2\text{-EDOT}$ employing different aryl flanking units Ar (T = Thiophene, Py = 2-pyridine, Ph = Phenyl) and the previously published^[1] thiophene-copolymers $\text{PDPP}[\text{Ar}]_2\text{-T}$.

Cyclic Voltammetry

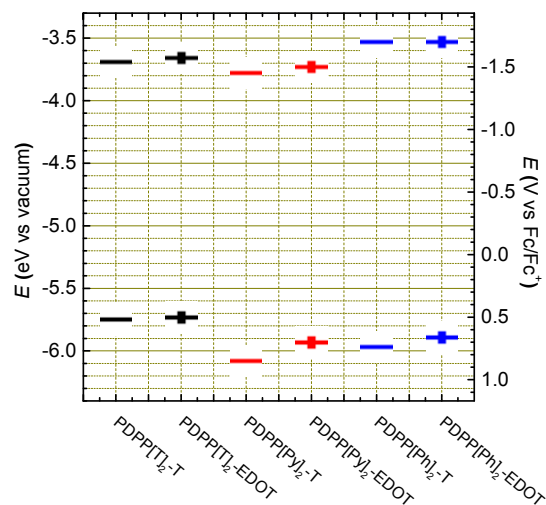


Figure S5-9. Energy level alignment for the newly synthesized EDOT copolymers PDPP[Ar]₂-EDOT compared to previously published^[1] thiophene copolymers PDPP[Ar]₂-T employing different aryl flanking units Ar. All CV data was obtained using the same experimental method, setup and analysis workflow and is therefor directly comparable.

Device Characterization

Additional OFET I - V data

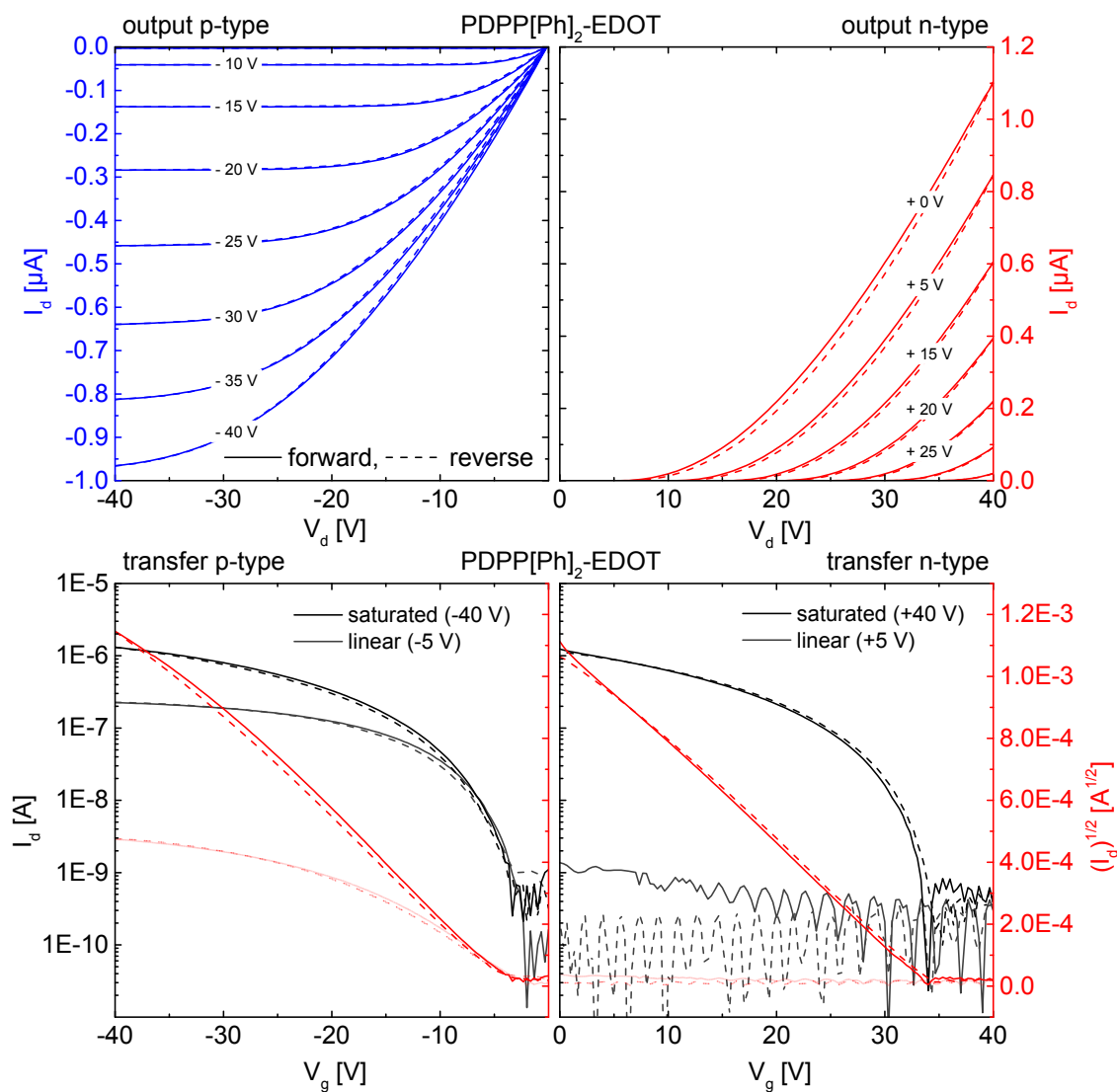


Figure S5-10. Representative OFET I - V curves in p-channel (blue output) and n-channel operation (red output) for an as-cast PDPP[Ph]₂-EDOT film. Solid lines represent forward scans, dashed lines the reverse scans in all graphs. In transfer curves (bottom), the black and grey plots indicate the transfer characteristics in the saturation and linear operation regime, respectively. The channel length was 20 μm .

Table S5-1. Listing of on/off ratios ($I_{\text{on/off}}$) and threshold voltages (V_T) for the devices prepared.

	As cast		Annealed (15 min, 250 °C)			
	p-type operation		p-type operation		n-type operation	
	$I_{\text{on/off}}$	V_T [V]	$I_{\text{on/off}}$	V_T [V]	$I_{\text{on/off}}$	V_T [V]
PDPP[T] ₂ -EDOT	6	35 ± 14	$> 10^2$	-4 ± 1		
PDPP[Py] ₂ -EDOT	80	-2 ± 1	$> 10^2$	-27 ± 2	$> 10^3$	28 ± 2
PDPP[Ph] ₂ -EDOT	$> 10^4$	-4 ± 1	$> 10^5$	-16 ± 1		

Additional SCLC data

Table S5-2. Listing of film thicknesses and fitting parameters for all the hole-only devices.

Active layer	Thickness	Fitted mobility	Fitted gamma	Mobility at 1.5×10^7 V/m
	[nm]	[$\text{cm}^2\text{V}^{-1}\text{s}^{-1}$]	[$\text{V}^{-0.5}\text{m}^{0.5}$]	[$\text{cm}^2\text{V}^{-1}\text{s}^{-1}$]
PDPP[T] ₂ -EDOT	189	3.0×10^{-4}	-1.5×10^{-4}	1.7×10^{-4}
PDPP[T] ₂ -EDOT	463	6.2×10^{-4}	-1.3×10^{-4}	3.7×10^{-4}
PDPP[T] ₂ -EDOT	521	8.4×10^{-4}	-2.5×10^{-4}	3.2×10^{-4}
PDPP[T] ₂ -EDOT + anneal	426	1.3×10^{-4}	2.2×10^{-5}	1.5×10^{-4}
PDPP[Py] ₂ -EDOT	182	3.5×10^{-7}	3.5×10^{-4}	1.4×10^{-6}
PDPP[Py] ₂ -EDOT	218	4.9×10^{-7}	3.1×10^{-4}	1.6×10^{-6}
PDPP[Py] ₂ -EDOT	216	2.8×10^{-6}	6.5×10^{-5}	3.6×10^{-6}
PDPP[Py] ₂ -EDOT + anneal	201	6.2×10^{-6}	2.3×10^{-5}	6.8×10^{-6}
PDPP[Ph] ₂ -EDOT	237	2.1×10^{-5}	4.6×10^{-5}	2.5×10^{-5}
PDPP[Ph] ₂ -EDOT	267	4.0×10^{-5}	-4.9×10^{-5}	3.3×10^{-5}
PDPP[Ph] ₂ -EDOT	405	1.9×10^{-4}	-2.7×10^{-4}	6.9×10^{-5}
PDPP[Ph] ₂ -EDOT + anneal	393	5.8×10^{-5}	2.1×10^{-5}	6.3×10^{-5}

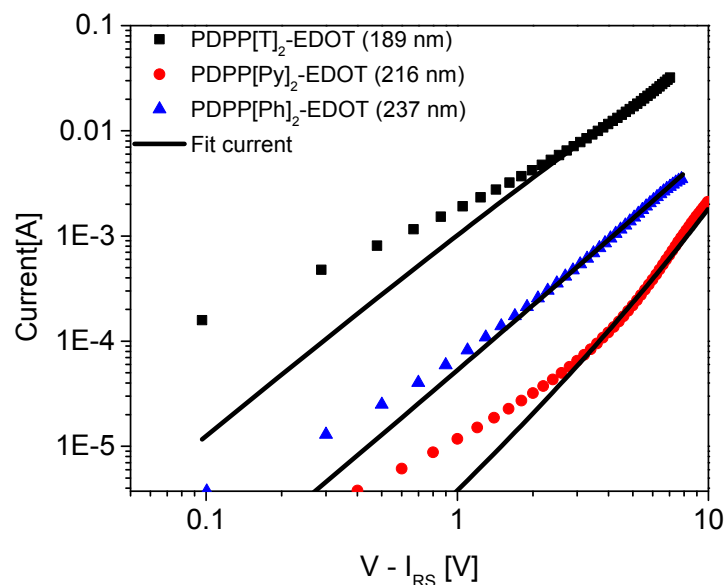


Figure S5-11. Double logarithmic plots of the SCLC I-V characteristics. The solid lines represent the SCLC fit with field dependent mobility. The corresponding film thicknesses are mentioned within the parentheses. The I-V characteristics were corrected for the voltage drop (IR) over the contacts.

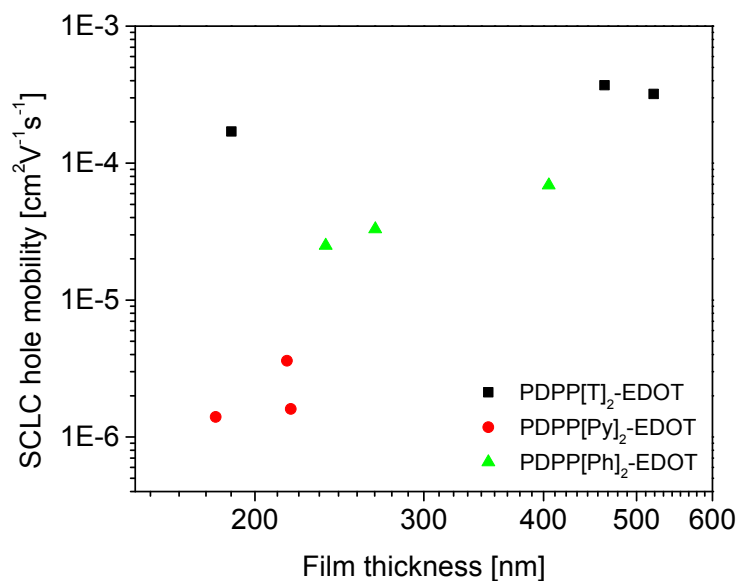


Figure S5-12. The effective SCLC charge carrier mobility of holes in different thickness as-cast PDPP films at an electric field of $1.5 \times 10^7 \text{ Vm}^{-1}$. The extracted hole mobilities were independent of the film thicknesses within the experimental error suggesting that the current response in the reported SCLC devices was not contact-limited but rather determined by the polymer films.

Supporting References

- [1] C. J. Mueller, C. R. Singh, M. Fried, S. Huettner, M. Thelakkat, Adv. Funct. Mater. 2015, 25, 2725.

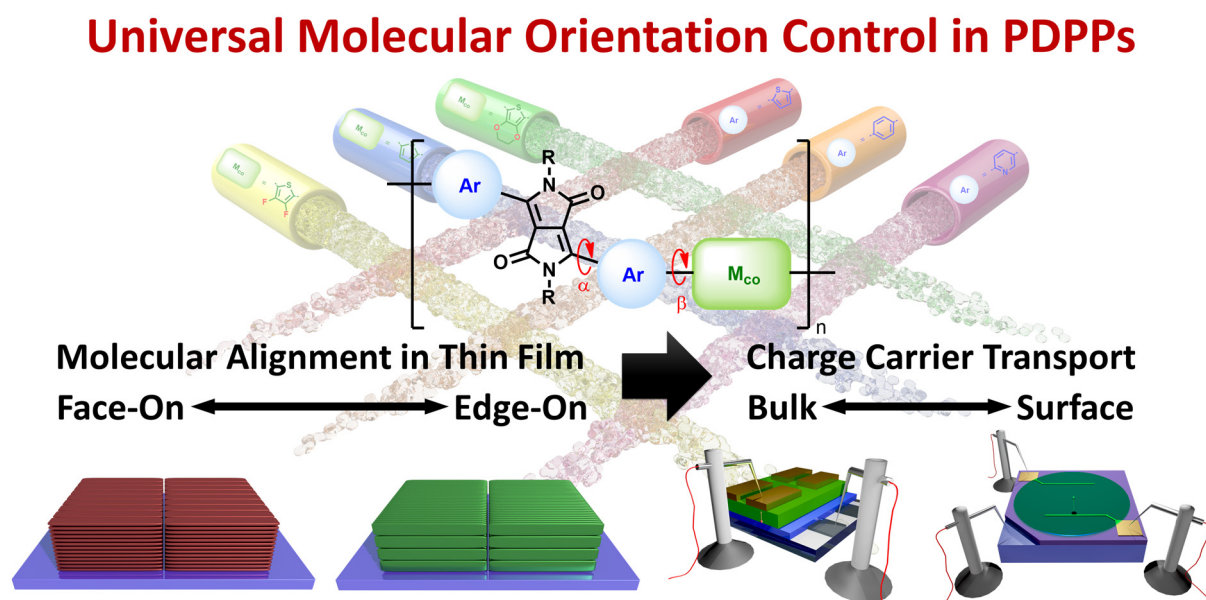
6 Universal Molecular Orientation Control in Polydiketopyrrolopyrroles

Christian J. Mueller,^a Eliot Gann,^{b,c} Chetan R. Singh,^a
Christopher R. McNeill^{c*} and Mukundan Thelakkat^{a*}

^a Applied Functional Polymers, Macromolecular Chemistry I, University of Bayreuth, 95440 Bayreuth, Germany.

^b Australian Synchrotron, 800 Blackburn Road, Clayton, VIC, 3168, Australia.

^c Department of Materials Science and Engineering, Monash University, Wellington Road, Clayton VIC, 3800, Australia.



Abstract

In thin films of semiconductor polymers, the polymer chains typically exhibit distinct orientation with respect to the substrate. The planar π -face of the backbone can orient either in edge-on or face-on manner. Especially, an edge-on alignment is favorable for transport in thin film transistors, whereas face-on alignment is considered to improve vertical transport as desired in solar cells. However, molecular orientation is among the very few parameters that usually cannot be controlled when tailoring new semiconducting polymers. Here we show that both the mode of orientation as well as the degree of alignment can be well controlled by exploiting diffusive non-covalent interactions along the backbone using polydiketopyrrolopyrroles (PDPPs) as a case study. By strategically varying the chemical structure in a systematic way, we attribute for the first time, the precise control of orientation based on chain planarization resulting from the diffusive non-covalent interactions. Our results demonstrate how orientation in thin films of semiconducting polymers can be controlled and optimized by rational design. We anticipate our findings to open the door to new high-performance organic semiconductors with the additional benefit of tailored orientation that fits the desired application.

6.1 Introduction

Since the advent of π -conjugated polymers exhibiting semiconducting properties,^[1] many different polymer systems have been synthesized and studied. One popular example is poly(3-hexylthiophene) which is certainly the most studied polymer in this regard.^[2] After decades of research, methods have been developed to precisely control many crucial parameters for the application of these polymers in organic electronic devices such as polymer solar cells.^[3] Among those parameters are intrinsic ones such as the energy levels of the frontier molecular orbitals,^[4] the band gap,^[5] the strength of optical absorption and emission^[6] as well as viscosity and solubility.^[7-9] Also solid state properties such as exciton generation^[10] and splitting into charge carriers^[11] including their transport^[2, 12] can be controlled. Ultimately, these properties are not only influenced by easily adjustable inherent properties, but also by the solid state packing of the polymers, which can neither be universally controlled nor even predicted, especially in low-bandgap polymers, which are usually copolymers prepared from arbitrarily chosen electron-rich and electron-deficient moieties. This is a considerable concern when designing new semiconducting materials for particular applications, as wrongly oriented or less ordered materials will show inferior performance even if the inherent properties of the molecular sub units are promising. Especially, a high degree of edge-on alignment is favorable for transport

in thin film transistors, whereas face-on alignment is considered to improve bulk transport in a vertical direction as desired in solar cells.^[2, 13-14] Copolymers of diketopyrrolopyrroles (PDPPs) have recently gained huge interest in the organic electronics community due to their extended absorption range,^[15] their excellent stability^[16] and their superior performance in transistors,^[17-18] integrated circuits^[19] and solar cells.^[20] PDPPs also show remarkable aggregation behavior. However, the packing of PDPPs has generally been considered on an individual basis, with no robust link between chemical structure and resulting packing.^[21]

We have chosen PDPPs as a prototype low bandgap polymer to elucidate structural features of general validity. In this contribution, we show that the orientation of polydiketopyrrolopyrroles in thin films can be well controlled by tailoring the chemical structure in a systematic manner. In particular, we demonstrate synthetic control over the mode of orientation by varying the aryl flanking unit of the DPP core, as well as the ability to lock-in and augment the degree of alignment by introducing moieties for diffusive non-covalent interactions in the monomers. Backbone planarization due to non-covalent interactions has been theoretically predicted, however experimental proof has only been indirectly provided by improved device performance. The moieties suitable for these non-covalent interactions can either be electron withdrawing fluorine atoms leading to π -electron deficient polymer systems that are well suited for n-type semiconductor applications and electron transport, or they can be alkoxy groups yielding π -electron rich polymer systems that exhibit outstanding p-type behavior and hole transport properties. Thus, a library of nine PDPPs with tailored structural changes is systematically studied using Grazing Incidence Wide Angle X-ray Scattering (GIWAXS) to obtain comprehensive information on the orientation of the polymer chains. We attribute for the first time the precise control of orientation to the diffusive interactions between the aryl units in the polymer chain. Furthermore, we correlate the consequences of the orientation for both lateral (at interface) and vertical (in bulk) charge transport by comparing the charge carrier mobilities both in field effect transistor (OFET) and space charge limited current (SCLC) devices.

6.2 Experimental Methods

The details of synthesis of the PDPPs studied here employing thiophene,3,4-difluorothiophene^[22] and 3,4-ethylenedioxythiophene (EDOT) comonomers^[23] (Figure 6-1) and their molecular weights are reported in previous publications. The molecular weights, dispersities and melting points of the polymer batches used in this study are summarized in Table S6-1 (see Supporting Information). For GIWAXS studies, samples were prepared in a similar manner as for OFET measurement, so that the alignment information and charge transport can be directly correlated to each other (see supporting information). Annealing was performed on a hotplate under inert atmosphere at similar temperatures that gave maximum

device performance in organic field effect transistors as previously reported.^[22-23] SCLC measurements were updated for all the nine copolymers supplementing with the values for the EDOT copolymers (Supporting Information Figure S6-10 and Table S6-3, Table S6-4). GIWAXS patterns were collected at the SAXS/WAXS beamline of the Australian Synchrotron^[24] in order to characterize packing behavior within the thin films.

6.3 Results and Discussion

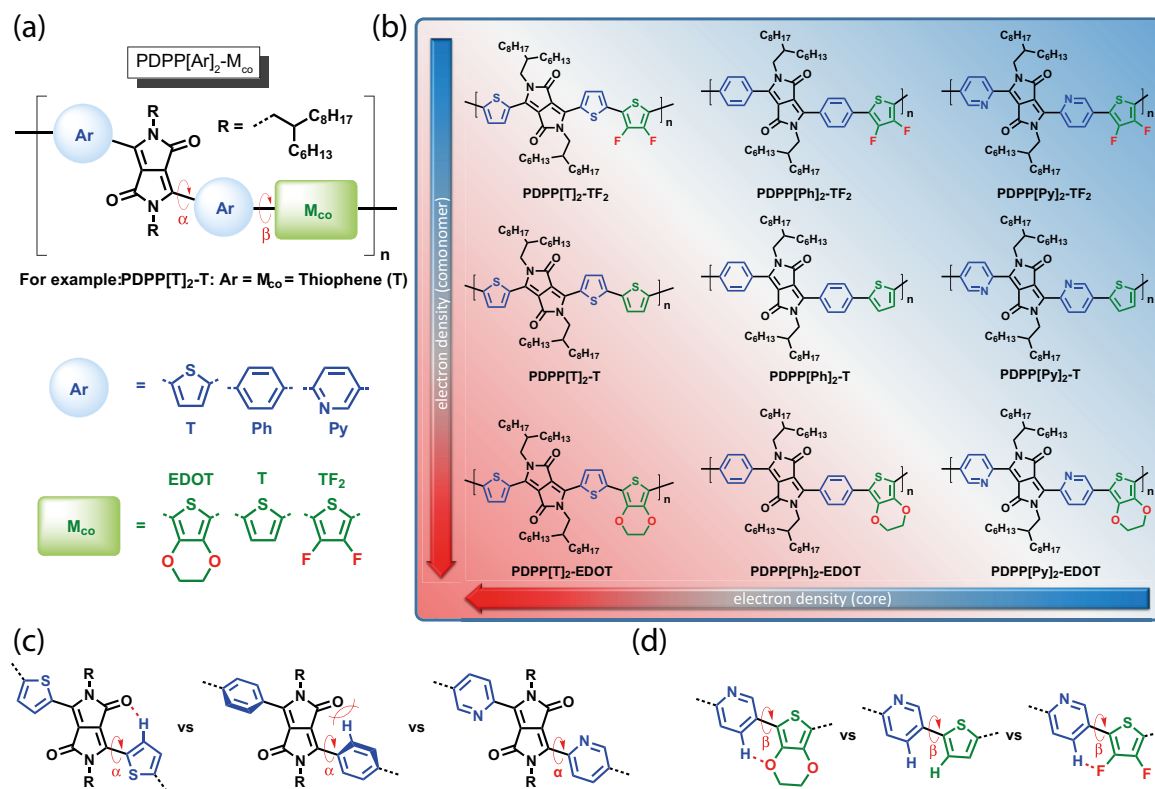


Figure 6-1. (a) Generic structure of the DPP Polymers investigated with varying aryl flanking units (Ar: in blue) and comonomers (M_{co} in green). The nomenclature used follows previously published guidelines.^[22] Ar = thiophene (T), phenyl (Ph), 2-pyridine (Py); M_{co} = 3,4-ethyldioxythiophene (EDOT), thiophene (T), 3,4-difluorothiophene (TF₂); (b) Polymer structures correlated to the increasing electron densities based on the respective DPP core (right to left) and comonomer (top to bottom). Background color correlates to high (red) or low (blue) π -electron densities. Scattering plot overviews in Figure 6-4, Figure S6-1 and Figure S6-2 show the same matrix of polymers as in here; (c) Schematic illustration of the favourable and unfavourable interactions that lead to different dihedral angles α within the DPP[Ar]₂ motif; (d) Schematic illustration of the diffusive non-covalent interactions for substituted comonomers leading to different dihedral angles β between comonomer M_{co} and the Ar unit of DPP[Ar]₂ moiety.

Polydiketopyrrolopyrroles generally comprise a bicyclic diketopyrrolopyrrole core (DPP) with solubilizing alkyl side chains (R). This core carries two identical aryl flanking units (Ar) and the resulting DPP[Ar]₂ unit is then polymerized with a comonomer (M_{co}) to obtain a copolymer, PDPP[Ar]₂-M_{co}. By this modular approach we are able to control both the dihedral angles along the polymer backbone, i.e. α defining the angle between DPP core and aryl flanking unit as well as β , defining the angle between aryl flanking unit and the comonomer.

A generic overview of the individual building blocks (Ar and M_{co}) as well as the employed nomenclature is given in Figure 6-1a.

Varying the aryl flanking unit from thiophene (T) to phenyl (Ph) to 2-pyridine (Py) gives rise to different sterical demands and different degrees of diffusive non-covalent interactions within the DPP core (Figure 6-1c).^[22] The phenyl-flanked DPPs, for example, show a large dihedral twist due to steric crowding between phenyl-hydrogens and the keto-group of the DPP core.^[22, 25] This is supported by the X-ray data of small molecules with the same structural motives as we have reviewed in a previous contribution.^[22] In the case of the five-membered thiophene ring, steric demands are smaller and the additional H···O interaction between thiophene-hydrogens and the DPP keto-group allows the lock-in of the dihedral angle and hence a planarized backbone.^[26] In the six-membered pyridine ring one hydrogen in the 2-position is missing compared to the phenyl moiety, allowing for a much more planar system compared to DPP[Ph]₂ due to decreased steric crowding. Not only do the three aryl flanking units influence the geometry of the DPP[Ar]₂ core, but also exhibit a distinct difference in their π -electron density. The comonomers employed here are based on thiophene (T) which is either unsubstituted, 3,4-difluorinated (TF₂) or 3,4-dialkoxylated (EDOT). Both the fluorine groups as well as the oxygen in the alkoxy groups allow diffusive non-covalent (H···F or H···O) interactions with hydrogen atoms of the adjacent aryl flanking units (Figure 6-1d).^[26] Additionally, the π -electron density can be controlled via substitution ranging from electron deficient in the fluorinated thiophene to electron rich in the EDOT moiety. A complete overview over all polymer structures sorted by π -electron density of the DPP core (right to left) and the comonomer (top to bottom) is given in Figure 6-1b.

When thin films of semiconducting polymers are prepared, the polymer chains can either be oriented edge-on, i.e. with the solubilizing side chains oriented perpendicular to the substrate, or face-on with the planar π -face of the backbone being in plane with the substrate. These two idealized orientations are schematically shown in Figure 6-2a, together with the GIWAXS patterns resulting from the scattering of polymers showing such a 2 dimensional order (Figure 6-2b). Edge-on orientation leads to the lamellar stacking peaks ($h00$) appearing in the out-of-plane (q_z) direction and the π - π stacking peak in the in-plane (q_{xy}) direction, whereas in a face-on oriented sample the peaks are observed in the opposed directions.

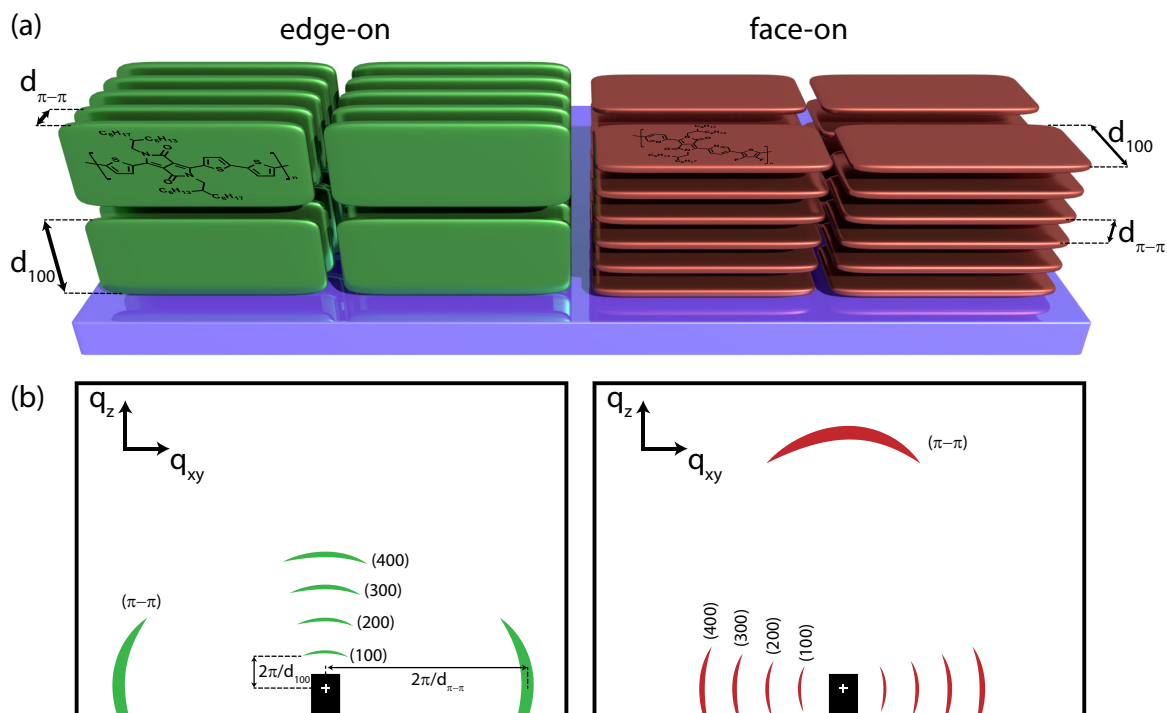


Figure 6-2. Schematic illustration for two different modes of orientation in 2D ordered polymers and their typical scattering features in GIWAXS.

Four typical examples of 2D GIWAXS patterns after thermal annealing are given in Figure 6-3 showing the varying modes of orientation. Figure 6-3a shows the scattering pattern of PDPP[T]₂-TF₂ which exhibits an edge-on orientation of the polymer backbone with liquid crystalline, i.e. 2D ordered, lamellar stacking peaks observed along Q_z (out of plane) and a π - π stacking peak observed along Q_{xy} (in plane). Figure 6-3b shows the scattering pattern of PDPP[T]₂-T that exhibits a mixture of liquid crystalline edge-on oriented and face-on oriented crystallites. The scattering pattern of PDPP[Py]₂-TF₂ (Figure 6-3c) exhibits a 3D crystalline face-on structure, with many evident mixed index peaks missing in the other samples, while PDPP[Ph]₂-T (Figure 6-3d) shows a more amorphous morphology, lacking of any preferential orientation. A complete set of 2D scattering patterns for as-cast as well as annealed films is shown in the Supporting Information (Figure S6-1 and Figure S6-2, respectively).

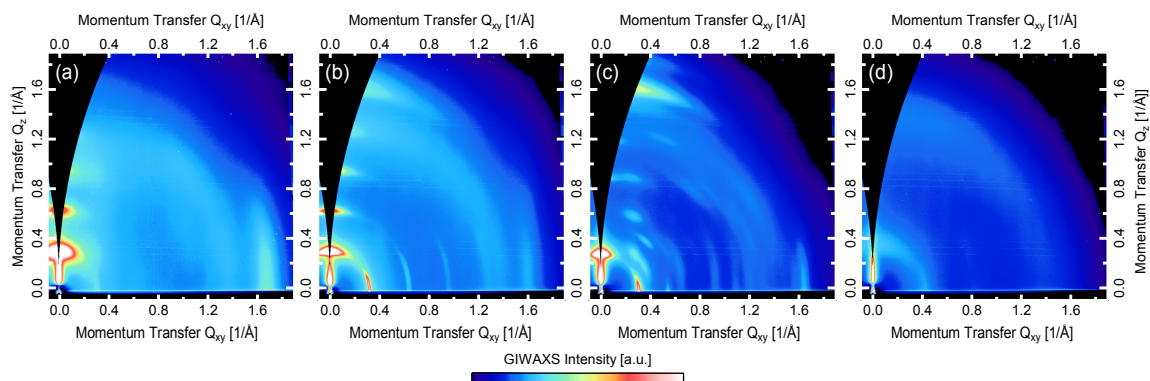


Figure 6-3. Representative 2D scattering images taken at the critical angle of a typical (a) edge-on sample (PDPP[T]₂-TF₂); (b) a typical sample showing mixed orientation with both edge-on and face-on orientation (PDPP[T]₂-T); (c) a largely face-on (indicated by the strong out-of-plane π - π peak at $\sim 1.6 \text{ \AA}^{-1}$) polymer with multiple faint mixed index peaks indicating some level of 3D crystallinity (PDPP[Py]₂-TF₂) and (d) a sample showing a lack of preferential orientation (PDPP[Ph]₂-T).

The one dimensional out-of-plane and in-plane scattering is calculated by integrating intensity within 15° sectors centered at polar angles of 0° and 90° , respectively.

In order to give a comprehensive overview over the influence of the structural moieties Ar and M_{co} on the orientation in thin films, we have compared the Herman's Orientation Parameter S for the different samples before and after annealing. S is a measure of the degree of orientation of a given scattering reflection to a direction of interest, measured as the average of the second order spherical harmonic $\langle P_2 \rangle$ within a set of scattering relative to a direction of interest.^[27-28] In this case, we take the first order alkyl stacking reflection, with the direction normal to the substrate as the axis to which we measure alignment. We calculate S by equation (1)

$$S = \frac{1}{2} \left(3 \frac{\int_0^{\frac{\pi}{2}} I(\chi) \cos^2 \chi \sin \chi d\chi}{\int_0^{\frac{\pi}{2}} I(\chi) \sin \chi d\chi} - 1 \right) \quad (1)$$

where χ is the polar angle and I is the total scattering intensity of a peak. This results in S scale from -0.5, at which the orientation of the crystallites corresponding to that peak is perfectly in-plane, through 0, at which there is no preferential orientation either in-plane or out-of-plane, to 1 when the orientation is completely out-of-plane. In the case of the first order alkyl lamella reflection, from which we calculate S in this work, $S = 1$ indicates perfect edge-on stacking and $S = -0.5$ indicates perfect face-on stacking. A detailed explanation of the data reduction to obtain S from a set of two dimensional scattering patterns recorded at different grazing incidence angles on a representative dataset is given in the Supporting Information (Figure S6-7).

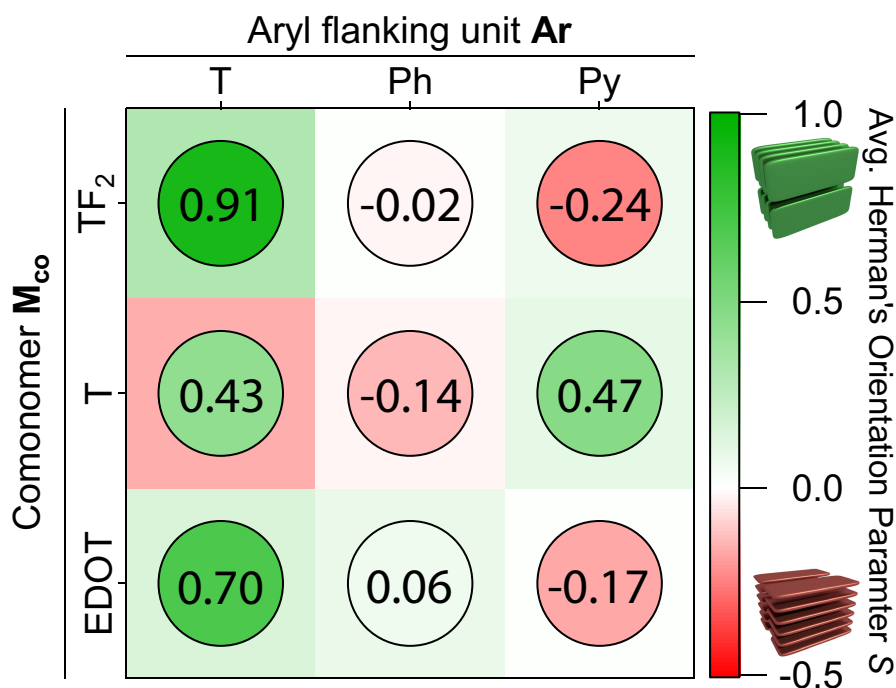


Figure 6-4. Herman's Orientation Parameter S averaged over all incident angles Ω for the as cast films (square backgrounds) and the annealed films (circle foregrounds and inset numerical values) depending on the structural parameters Ar and M_{co} . Tabulated values are given in the Supporting Information, Table S6-2.

The average S values are plotted in Figure 6-4 and in detail against the X-ray incident angle α_i to obtain representative depth-sensitive data in Figure 6-4 and in Figure S6-9 for the 9 different copolymers. Both figures employ the same matrix arrangement as used for the chemical structures shown in Figure 6-1b. First, the thiophene flanked PDPP[T]₂- M_{co} copolymers generally show a tendency towards edge-on orientation. Whereas the as cast film of the all-thiophene copolymer PDPP[T]₂-T (Figure S6-9b) shows a negligible face-on orientation ($S = -0.16$, see Table S6-2) annealing leads to a distinct edge-on orientation with an average S of 0.43. The introduction of fluorine or alkoxy moieties in the TF₂ and EDOT comonomers that enable non-covalent diffusive interactions along the polymer backbone leads to an impressive increase in S in the as-cast films (0.31 for PDPP[T]₂-TF₂, 0.15 for PDPP[T]₂-EDOT) as well as for the annealed films (0.91 for PDPP[T]₂-TF₂, 0.70 for PDPP[T]₂-EDOT) approaching unity in the case of the fluorinated comonomer (see Figure 6-4 and in Figure S6-9a-c). The degree of alignment in the PDPP[T]₂ copolymers with an inherent edge-on tendency can hence be considerably increased by providing heteroatoms such as fluorine or oxygen along the chain, which can undergo non-covalent interactions. Second, the phenyl flanked PDPP[Ph]₂- M_{co} copolymers (Figure S6-9d-f) all show a very weak alignment with S near 0 independent of thermal treatment. Only PDPP[Ph]₂-T shows a slight tendency towards face-on orientation with an average S value of -0.14. The weak alignment of the phenyl flanked copolymers can be related to their low overall crystallinity (arising from a less planar nature) as exhibited in the two dimensional scattering patterns with low intensities (Supporting Information, Figure S6-1 and Figure S6-2) which means that any preferential orientation that

might exist directly at the interface does not propagate beyond the first few layers. Third, also the pyridine-flanked PDPP[Py]₂-M_{co} copolymers show a very low degree of alignment in as cast films with S values only slightly greater than 0. Following thermal annealing the degree of alignment increases and a distinct edge-on orientation is observed for PDPP[Py]₂-T, whereas the two copolymers with moieties for non-covalent diffusive bonding, i.e. PDPP[Py]₂-TF₂ and PDPP[Py]₂-EDOT exhibit a clear face-on orientation with average S of -0.24 and -0.17, respectively. This marked difference for the PDPP[Py]₂-M_{co} systems can be explained as follows.

In the PDPP[Py]₂ copolymers that show strong 3D crystalline packing in all directions, a non-orthorhombic unit cell may make the measured S parameter misleading. Because in 3D crystalline polymers, different crystalline reflections occur at different orientations, but S is calculated relative to the out-of-plane direction in equation (1), it is only a proper measure of molecular orientation when considering a reflection corresponding to planes with preference for stacking directly out-of-plane or in-plane. Molecular orientation may be highly oriented, but this fact can be obscured when the major scattering peaks are not liquid crystalline and do not necessarily lie completely in or out of the plane of the sample. Although in this case, the precise level of alignment cannot be easily determined, the fact that the scattering patterns of the highly 3D crystalline films (Supporting Information Figure S6-1 and Figure S6-2) all exhibit a very strong and narrow out-of-plane scattering peak consistent with π - π stacking clearly supports an average face-on orientation. This is further supported by depth sensitive S calculation for different X-ray incidence angles α_i (see Figure 6-5 for M_{co} = TF₂ and Supporting Information Figure S6-9 for a complete set of data). At low incidence angles, at which only the top few nm of the polymer film contribute to the scattering signal, as well as at high incidence angles, at which a very uniform distribution of X-ray field intensity ensures all of the film contributes (see X-ray field intensity distribution in dependence of incidence angle: Supporting Information Figure S6-8), S is considerably smaller than at the critical angle. In fact, it approaches -0.4 for both, PDPP[Py]₂-TF₂ and PDPP[Py]₂-EDOT, which is close to the theoretical minimum of -0.5 and thus indicates an extremely face-on mode of orientation at the surface of those polymer films. Comparatively, the polymer films employing thiophene and phenyl aryl flanking units show a very uniform alignment over the complete film thickness, as evident from Figure 6-5 and Figure S6-9.

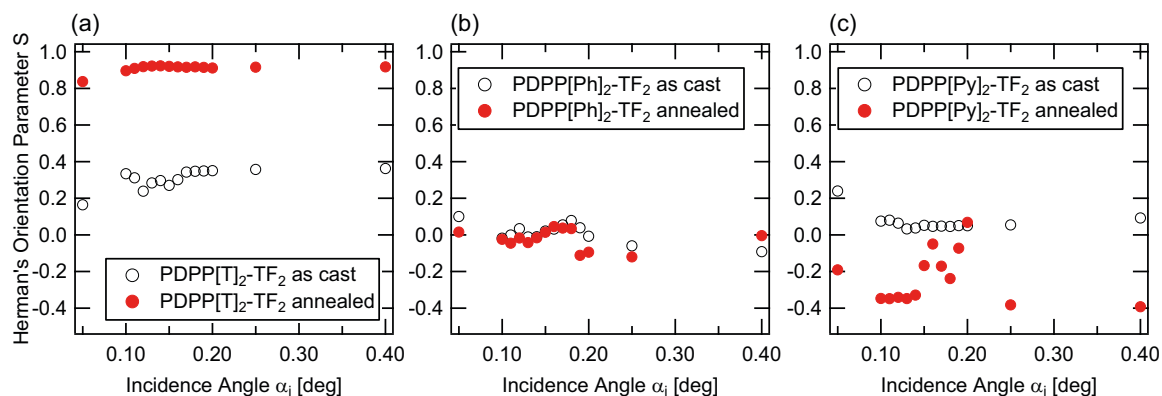


Figure 6-5. Representative depth sensitive S values for the polymers with 3,4-difluorothiophene as the comonomer and different aryl flanking units (Ar = T (a), Ar = Ph (b), Ar = Py (c)) at different grazing incidence angles α_i . Hollow black dots represent the as cast films whereas filled red dots represent the annealed samples. Depth sensitive data for the other polymers is given in the Supporting Information, Figure S6-9.

The spacing in the two main crystalline directions, i.e. lamellar (alkyl) and π - π (face-to-face) stacking for the individual polymers are visualized in Figure 6-6 and broken down for the various aryl flanking units and comonomers, both in as-cast (Figure 6-6a) and in annealed (Figure 6-6b) films. The crystalline coherence length ζ gives information about the distance over which order is maintained and is defined as $\zeta = 2\pi/\text{FWHM}$, where FWHM is the full width at half maximum of the first order lamellar stacking or π - π stacking peak, respectively. The concept of the coherence length is connected to the Scherrer equation, which connects the width of a peak to the crystal size. Although talking only of the coherence length, we leave open the possibility that decoherence along a crystalline axis may be due to disorder effects such as paracrystallinity rather than solely size effects. The values of the coherence lengths for the respective peaks are also given in Figure 6-6.

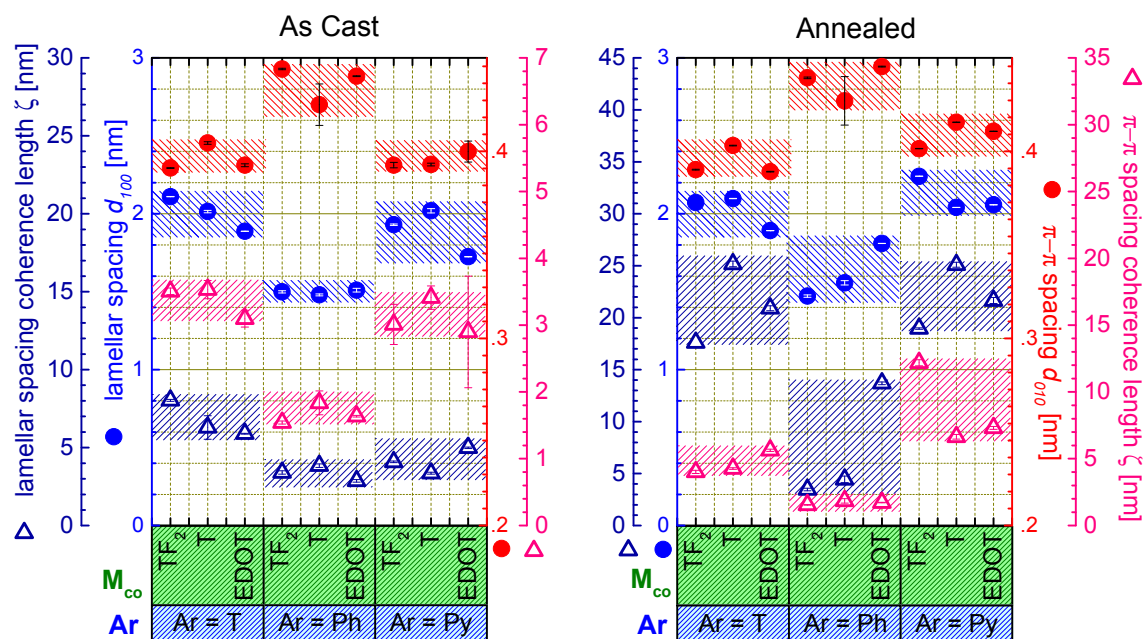


Figure 6-6. Lamellar and π - π spacing d in as cast and annealed films depending on comonomer M_{co} and aryl flanking unit Ar as well as crystal coherence lengths ζ for the respective spacings (note that the scale for the coherence lengths differs in the two graphs). Shaded areas span over the min/max values of the respective parameter. A table summarizing all numerical data can be found in Supporting Information (Table S6-2).

When the impact of structural change in the as-cast films is examined, it is obvious that the phenyl-flanked PDPP[Ph]₂ polymers behave differently than their thiophene- and pyridine-flanked derivatives, independent of the comonomer used. Generally, the aryl flanking unit has the most significant impact on the structure formation in these polymers. The packing can furthermore be fine-tuned by choosing an appropriate comonomer. The lamellar spacing is around 1.5 nm for all three PDPP[Ph]₂ polymers whereas much larger spacings of around 2.0 nm are measured for PDPP[T]₂ and PDPP[Py]₂ copolymers. This can be explained by the large dihedral twist in the phenyl-flanked polymers which is caused by steric crowding, i.e. unfavorable steric interactions between phenyl-hydrogens in the keto-group of the adjacent DPP core. Upon twisting the DPP unit by a considerable amount, polymers with a helical backbone can be formed which results in decreased lamellar stacking (see Figure 6-7).

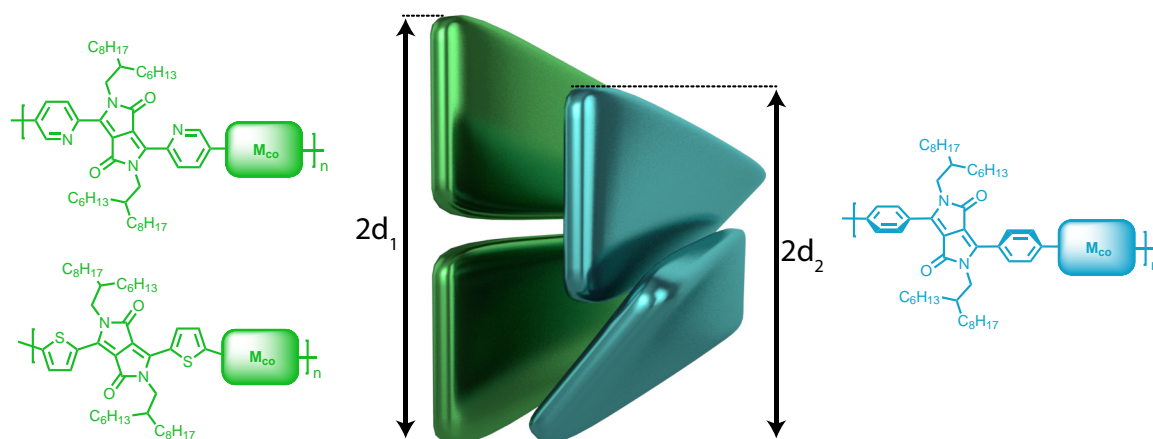


Figure 6-7. Schematic illustration of lamellar stacking in conjugated backbones exhibiting different planarities. The lamellar spacing is smaller in the case of the twisted backbone, i.e. $d_2 < d_1$, because of interlaced structures.

A similar trend can be observed in the EDOT-copolymers, where the lamellar spacings of 1.89 nm for PDPP[T]₂-EDOT and 1.72 nm for PDPP[Py]₂-EDOT are considerably decreased compared to the two other comonomer systems. As for the lamellar spacing coherence length, the thiophene-flanked PDPP[T]₂ copolymers have the largest as-cast coherence lengths averaging around 7 nm whereas the twisted PDPP[Ph]₂ polymers show the smallest values of around 3 nm which is in accordance with its rather low crystallinity as can be concluded from the relatively weaker scattering peaks (Supporting Information Figure S6-1). It is noteworthy, that upon incorporation of the fluorinated TF₂ comonomer, not only do the lamellar spacings remain large but also the coherence lengths are higher than those for with the unsubstituted thiophene comonomer indicating a higher long-range alignment upon fluorination. The twisting in the backbone has also direct consequences for the π - π packing. Thus, the twisted PDPP[Ph]₂ polymers exhibit the largest π - π spacings, around 0.44 nm. Interestingly, here the otherwise favorable fluoro- and alkoxy-functionalization of the comonomer results in a slightly increased π - π spacing, although due to the 3D crystallinity, the precise π - π spacing may be directly reflected by the peak location due to tilting within in the 3D unit-cell. Both the PDPP[T]₂ and PDPP[Py]₂ systems show small π - π spacings with average values around 0.40 nm. In the case of the thiophene-flanked PDPP[T]₂ system, the introduction of moieties for diffusive non-covalent interactions in PDPP[T]₂-TF₂ and PDPP[T]₂-EDOT leads to the smallest π - π spacings of 0.39 nm, which can be explained by enhanced backbone planarity and an increased tendency to aggregate. Likewise, the π - π stacking coherence lengths show the same trends as the lamellar coherence lengths, i.e. the phenyl-flanked polymers show very small π - π coherence lengths with values clearly below 2 nm. In contrast the crystalline PDPP[T]₂ and PDPP[Py]₂ systems show larger π - π coherence lengths with similar values averaging around 3 nm.

Upon annealing, crystallinity and alignment are considerably increased as can be directly seen (Supporting Information Figure S6-2) by the emergence of higher order lamellar ($h00$) peaks in the PDPP[T]₂ system and complex 2D scattering patterns for the PDPP[Py]₂ polymers

which point towards a well-organized three dimensional crystallinity rather than two dimensional stacking that is commonly found in conjugated polymers. The lamellar spacing of the thiophene-flanked PDPP[T]₂ polymers is hardly influenced upon annealing; only PDPP[T]₂-T shows a small increase from 2.01 nm to 2.10 nm, indicating an even more planar backbone which is now comparable to the fluorinated analog PDPP[T]₂-TF₂. Accordingly, the lamellar spacing coherence length is massively increased upon annealing in all these polymers. Interestingly, this effect is strongest for PDPP[T]₂-T with an unsubstituted thiophene comonomer, increasing from 6 nm to 25 nm. PDPP[T]₂-TF₂ and PDPP[T]₂-EDOT also show enhanced long range order with coherence lengths of 18 nm and 21 nm, respectively. In the phenyl-flanked PDPP[Ph]₂ system, PDPP[Ph]₂-T shows a moderate increase whereas the EDOT copolymer PDPP[Ph]₂-EDOT lamellar spacing increases from 1.51 nm to 1.81 nm pointing towards a considerably more planar system. This finding is supported by the immense increase in coherence length for this particular polymer, growing from 3 nm to 14 nm upon annealing. We therefore conclude that incorporation of EDOT leads to a strongly enhanced crystallinity in these otherwise twisted and largely amorphous phenyl-flanked PDPPs. In the pyridine-flanked PDPP[Py]₂ system the lamellar spacing increases in a similar fashion to the thiophene-flanked analogs with all three polymers showing values above 2.0 nm with the highest observable value being 2.24 nm for PDPP[Py]₂-TF₂ and the steepest increase for PDPP[Py]₂-EDOT going from 1.72 nm to 2.06 nm upon annealing. Likewise, lamellar coherence lengths increase significantly with the values almost identical to the coherence lengths of the thiophene-flanked analogs after annealing. Interestingly the largest coherence length of 25 nm is again with an unsubstituted thiophene comonomer (PDPP[Py]₂-T) whereas slightly lower values of 19 nm and 22 nm are observed for PDPP[Py]₂-TF₂ and PDPP[Py]₂-EDOT, respectively. Thus, the pyridyl flanked PDPPs excel in their 3D order. With respect to the π - π stacking, the spacing remains almost identical for the majority of the polymers upon annealing. Only the pyridine-based PDPP[Py]₂ system shows a slight increase for all three polymers to give an average π - π spacing of around 0.41 nm. In contrast to the π - π spacing, the respective π - π coherence lengths are significantly increased after annealing for the crystalline polymers, i.e. all polymers except the PDPP[Ph]₂ polymers where the coherence lengths remain low averaging below 2 nm. The thiophene-flanked PDPP[T]₂ system now shows π - π coherence lengths above 4 nm with a maximum for PDPP[T]₂-EDOT at 5.6 nm. The strongest enhancement is observed in the pyridine-flanked PDPP[Py]₂ system, for which the π - π coherence lengths increase from around 3 nm before annealing to 6.6 nm and 7.3 nm for PDPP[Py]₂-T and PDPP[Py]₂-EDOT, respectively. For the fluorinated PDPP[Py]₂-TF₂ we observed a superior coherence length of 12.2 nm. This outstanding increase can mostly be attributed to the exclusive face-on orientation of the PDPP[Py]₂ system and hence a stronger templating at the surfaces.

In summary, the findings based on the crystalline stacking first strongly indicate a very planar backbone in the case of PDPP[Py]₂ copolymers with lamellar spacings and lamellar coherence lengths comparable to the PDPP[T]₂ system. This behavior was predicted by theoretical calculations^[26] and was expected due to the lack of protons at the heteroatom compared to PDPP[Ph]₂, but could not until now be shown based on experimental results; Not even bulk single crystal structures of low molecular weight model compounds are available. Additionally, whereas incorporation of moieties for diffusive non-covalent interactions into the comonomer leads to improved solid state packing in as-cast films, annealing of polymers with an unsubstituted thiophene comonomer gives similar lamellar spacings and superior coherence lengths. The mode of orientation however is much more defined in the polymers comprising fluorinated or alkoxyated comonomers, as evident from the Herman's orientation parameter analyses. Furthermore, the face-on oriented PDPP[Py]₂ polymers exhibit outstanding π – π coherence lengths upon annealing which makes them very promising candidates for devices that demand charge carrier transport across the complete film thickness as in solar cells.

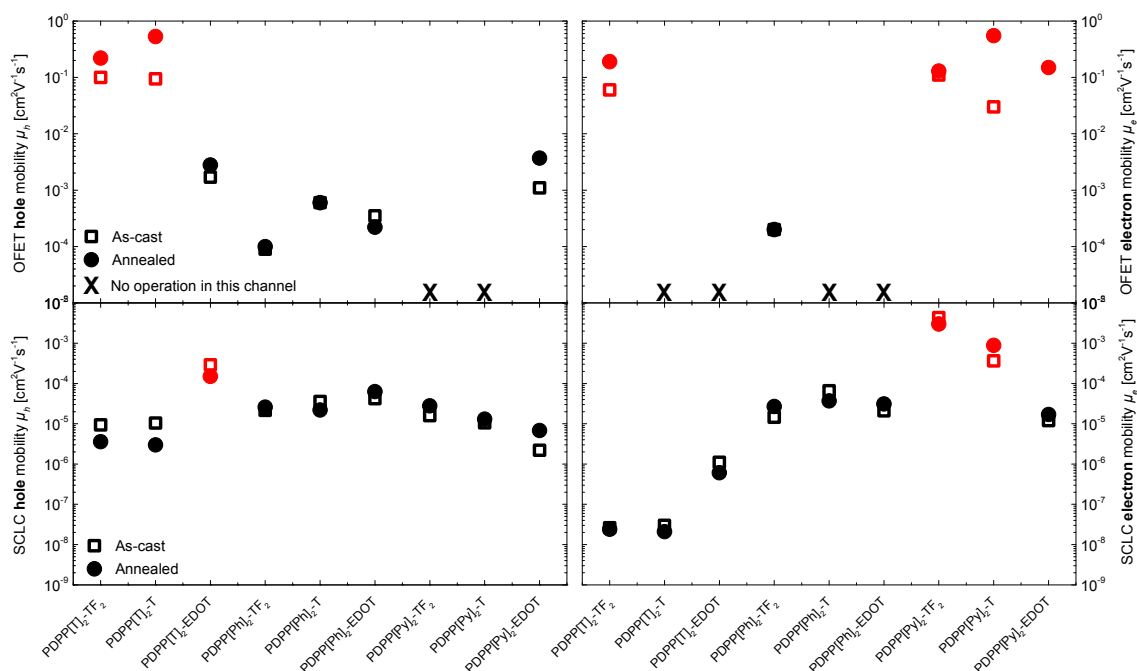


Figure 6-8. Mobility overview in both OFET and SCLC devices as published recently. The highest mobilities in each mode of operation are marked red. Materials for which no transistor operation in a particular channel (p/n, i.e. hole or electron transport) are marked with X.^[22–23]

With this structural information, we can additionally correlate and explain the reported charge transport properties (see Figure 6-8) within this class of materials.^[22–23] With regard to organic field effect transistors (OFET), the low crystallinity and even worse alignment of the phenyl-flanked PDPP[Ph]₂ copolymers explains the inferior OFET mobilities in the range of 10^{-4} $\text{cm}^2\text{V}^{-1}\text{s}^{-1}$ (Figure 6-8) that have been reported for all those polymers and the low to mediocre power conversion efficiencies in organic solar cells. In the thiophene-flanked PDPP[T]₂ system, a strong edge-on orientation, high crystallinity and small π – π spacings lead to 3–4 orders of

magnitude improvement in OFET mobility for the examples shown here; the details of which are reported elsewhere^[22-23]. This also explains the excellent mobilities in OFETs for similar PDPP systems reported in literature (up to $12\text{-}18\text{ cm}^2\text{V}^{-1}\text{s}^{-1}$)^[18, 29-30]. However, high OFET mobilities were also obtained in the face-on oriented pyridine-flanked PDPPs. As those polymers are electron deficient, they predominantly show n-channel operation, i.e. electron transport. It should be noted, that the mobility in OFET devices is mostly dictated by the alignment of the polymer in a channel only few nanometers wide which is at the semiconductor-dielectric interface, i.e. at the bottom of the polymer layer. This fact makes correlations of OFET mobilities with alignment determined by GIWAXS difficult, as GIWAXS can give information about the bulk of the film or its top surface by using X-ray incidence angles smaller than the critical angle. The alignment buried at the semiconductor-dielectric interface is not individually accessible from the top of the film in GIWAXS measurements.

Regarding bulk mobilities measured by SCLC (see also Figure S6-10, Table S6-3 and Table S6-4), the strong edge-on orientation in the PDPP[T]₂ polymers also explains their rather low bulk mobilities (e.g. $10^{-6}\text{ cm}^2\text{V}^{-1}\text{s}^{-1}$), as layers of isolating alkyl chains have to be penetrated for charge carriers to traverse from a bottom electrode to a top electrode. The less ordered phenyl-flanked PDPP[Ph]₂ copolymers show intermediate bulk charge carrier mobilities, as a poorly aligned or amorphous film of polymer still provides better transport routes in the vertical direction than a strictly edge-on oriented polymer does. In contrast, the distinct face-on orientation of pyridine-flanked PDPP[Py]₂ polymers, which is much stronger when functionalized comonomers such as difluorothiophene or EDOT are used, accounts for the high bulk mobilities of these materials as measured in SCLC devices. Thus, this explains the record bulk electron mobility of $4.3 \times 10^{-3}\text{ cm}^2\text{V}^{-1}\text{s}^{-1}$, that has been reported for the electron deficient face-on aligned material PDPP[Py]₂-TF₂.^[22]

Aside from controlled molecular orientation to suit the application of the polymer semiconductor, its intrinsic electronic requirements such as a suitable alignment of frontier molecular orbitals (HOMO/LUMO) have also be met. This can be clearly seen when comparing the trend of SCLC electron mobility to the trend of SCLC hole mobility. Concerning the electron mobility, both parameters, i.e. alignment and energy levels, go hand in hand. For electron transport, -electron deficient systems are desirable and exactly those electron deficient pyridyl-flanked PDPP[Py]₂ polymers show a favorable face-on alignment. Furthermore, the thiophene flanked PDPP[T]₂ polymers not only exhibit a much higher -electron density in the backbone, i.e. higher energy levels, but also a strong edge-on alignment which is generally unfavorable for charge carrier transport in SCLC. These two facts explain the trend of strongly increasing electron mobilities when going from thiophene flanking units through phenyl flanking units to pyridine flanking units.

In contrast, concerning the bulk hole mobilities in those polymers, the advantage of having an electron-rich system in the case of thiophene flanking units is stymied by the fact that those polymers altogether show an unfavorable edge-on orientation. Moreover, the polymers exhibiting a favorable face-on orientation, i.e. the pyridine flanked PDPP[Py]₂ polymers, have the disadvantage of being particularly electron-deficient. As a consequence, the SCLC hole mobility does not change drastically when comparing all nine polymers (Figure 6-8). Only PDPP[T]₂-EDOT stands out with a high bulk hole mobility of $2.9 \times 10^{-4} \text{ cm}^2\text{V}^{-1}\text{s}^{-1}$. This mobility can thus be mainly attributed to overwhelmingly beneficial electronic nature of the polymer despite its somewhat unfavorable overall edge-on orientation.

Depending on the π -electron density of the system and the energy levels that can also be well controlled by either fluorination or alkoxylation, excellent electron transporting or hole transporting materials are obtained.

6.4 Conclusions

By carefully examining the GIWAXS patterns of a library of 9 PDPPs with strategic variation of both the aryl flanking unit and the comonomer, we have experimentally demonstrated the influence of non-covalent diffusive bonding along the conjugated backbone of semiconducting polymers on the solid state structure. Most importantly, the mode of orientation (i.e. face-on or edge-on alignment) can be controlled by varying the aryl flanking unit whereas the degree of alignment can be enhanced by introduction of comonomers carrying moieties that allow diffusive non-covalent interactions with adjacent aryl units along the polymer backbone. Furthermore, we have shown that the pyridine-flanked PDPP[Py]₂ system is in fact as planar as the PDPP[T]₂ system as indicated by lamellar spacing distances. We therefore recommend the design of new polymers with face-on orientation as the bulk charge carrier mobilities provided by these materials make them ideal candidates for use in organic solar cells both as acceptors with improved electron transport and donors with improved hole transport. With these results in mind, we suggest the further exploitation of non-covalent diffusive bondings in semiconducting polymers. Beyond the already popular fluorination that has led to countless efficiency records in organic photovoltaics, the incorporation of alkoxy-groups is especially advocated. Incorporation of alkoxy-groups can be achieved not only through the use of common and widespread units such as EDOT, but very easily by replacing solubilizing alkyl sidechains on aromatic units with α -alkoxy-derivatives as a new lead design for the incorporation of sidechains.

6.5 Acknowledgement

We acknowledge financial support from the Bavarian State Ministry of Education, Science and the Arts (Solar technologies go hybrid). C.J.M. thanks the Fonds der Chemischen industrie for

funding the PhD with a Kekulé scholarship and the German National Academic Foundation for other support during the PhD. Support from the Elitenetzwerk Bayern (ENB), Macromolecular Science is also kindly acknowledged. C.R.M. acknowledges support from the Australian Research Council (DP130102616). This research was undertaken in part on the SAXS/WAXS beamline at the Australian Synchrotron, Victoria, Australia.^[24]

6.6 References

- [1] A. J. Heeger, *Angew. Chem. Int. Ed.* **2001**, *40*, 2591.
- [2] H. Sirringhaus, P. J. Brown, R. H. Friend, M. M. Nielsen, K. Bechgaard, B. M. W. Langeveld-Voss, A. J. H. Spiering, R. A. J. Janssen, E. W. Meijer, P. Herwig, D. M. de Leeuw, *Nature* **1999**, *401*, 685.
- [3] G. Li, R. Zhu, Y. Yang, *Nat Photon* **2012**, *6*, 153.
- [4] Z. B. Henson, K. Mullen, G. C. Bazan, *Nature Chemistry* **2012**, *4*, 699.
- [5] Y. Yang, W. Chen, L. Dou, W.-H. Chang, H.-S. Duan, B. Bob, G. Li, Y. Yang, *Nature Photonics* **2015**, *9*, 190.
- [6] L. Dou, J. You, J. Yang, C.-C. Chen, Y. He, S. Murase, T. Moriarty, K. Emery, G. Li, Y. Yang, *Nat Photon* **2012**, *6*, 180.
- [7] W. Li, K. H. Hendriks, A. Furlan, W. S. Roelofs, S. C. Meskers, M. M. Wienk, R. A. Janssen, *Adv. Mater.* **2014**, *26*, 1565.
- [8] J. J. van Franeker, G. H. Heintges, C. Schaefer, G. Portale, W. Li, M. M. Wienk, P. van der Schoot, R. A. Janssen, *J. Am. Chem. Soc.* **2015**.
- [9] J. J. van Franeker, M. Turbiez, W. Li, M. M. Wienk, R. A. Janssen, *Nat Commun* **2015**, *6*, 6229.
- [10] E. Busby, J. Xia, Q. Wu, J. Z. Low, R. Song, J. R. Miller, X. Y. Zhu, L. M. Campos, M. Y. Sfeir, *Nat Mater* **2015**, *14*, 426.
- [11] A. A. Bakulin, A. Rao, V. G. Pavelyev, P. H. M. van Loosdrecht, M. S. Pshenichnikov, D. Niedzialek, J. r. m. Cornil, D. Beljonne, R. H. Friend, *Science* **2012**, *335*, 1340.
- [12] H. Yan, Z. Chen, Y. Zheng, C. Newman, J. R. Quinn, F. Dotz, M. Kastler, A. Facchetti, *Nature* **2009**, *457*, 679.
- [13] I. McCulloch, M. Heeney, C. Bailey, K. Genevicius, I. Macdonald, M. Shkunov, D. Sparrowe, S. Tierney, R. Wagner, W. Zhang, M. L. Chabinyc, R. J. Kline, M. D. McGehee, M. F. Toney, *Nat Mater* **2006**, *5*, 328.
- [14] H. Dong, X. Fu, J. Liu, Z. Wang, W. Hu, *Adv. Mater.* **2013**, *25*, 6158.

- [15] W. Li, Y. An, M. M. Wienk, R. A. J. Janssen, *J. Mater. Chem. A* **2015**.
- [16] Y. Gao, X. Zhang, H. Tian, J. Zhang, D. Yan, Y. Geng, F. Wang, *Adv. Mater.* **2015**.
- [17] H. J. Yun, S. J. Kang, Y. Xu, S. O. Kim, Y. H. Kim, Y. Y. Noh, S. K. Kwon, *Adv. Mater.* **2014**, *26*, 7300.
- [18] I. Kang, H. J. Yun, D. S. Chung, S. K. Kwon, Y. H. Kim, *J. Am. Chem. Soc.* **2013**, *135*, 14896.
- [19] K. J. Baeg, M. Caironi, Y. Y. Noh, *Adv. Mater.* **2013**, *25*, 4210.
- [20] W. Li, W. S. Roelofs, M. Turbiez, M. M. Wienk, R. A. Janssen, *Adv. Mater.* **2014**, *26*, 3304.
- [21] X. Zhang, L. J. Richter, D. M. DeLongchamp, R. J. Kline, M. R. Hammond, I. McCulloch, M. Heeney, R. S. Ashraf, J. N. Smith, T. D. Anthopoulos, B. Schroeder, Y. H. Geerts, D. A. Fischer, M. F. Toney, *J. Am. Chem. Soc.* **2011**, *133*, 15073.
- [22] C. J. Mueller, C. R. Singh, M. Fried, S. Huettner, M. Thelakkat, *Adv. Funct. Mater.* **2015**, *25*, 2725.
- [23] C. J. Mueller, C. R. Singh, M. Thelakkat, *J. Polym. Sci., Part B: Polym. Phys.* **2016**, *54*, 639.
- [24] N. M. Kirby, S. T. Mudie, A. M. Hawley, D. J. Cookson, H. D. T. Mertens, N. Cowieson, V. Samardzic-Boban, *J. Appl. Crystallogr.* **2013**, *46*, 1670.
- [25] C. Kanimozhi, M. Naik, N. Yaacobi-Gross, E. K. Burnett, A. L. Briseno, T. D. Anthopoulos, S. Patil, *J. Phys. Chem. C* **2014**, *118*, 11536.
- [26] N. E. Jackson, B. M. Savoie, K. L. Kohlstedt, M. Olvera de la Cruz, G. C. Schatz, L. X. Chen, M. A. Ratner, *J. Am. Chem. Soc.* **2013**, *135*, 10475.
- [27] A. Prasad, R. Shroff, S. Rane, G. Beaucage, *Polymer* **2001**, *42*, 3103.
- [28] L. A. Perez, P. Zalar, L. Ying, K. Schmidt, M. F. Toney, T.-Q. Nguyen, G. C. Bazan, E. J. Kramer, *Macromolecules* **2014**, *47*, 1403.
- [29] A. R. Han, G. K. Dutta, J. Lee, H. R. Lee, S. M. Lee, H. Ahn, T. J. Shin, J. H. Oh, C. Yang, *Adv. Funct. Mater.* **2015**, *25*, 247.
- [30] J. Y. Back, H. Yu, I. Song, I. Kang, H. Ahn, T. J. Shin, S.-K. Kwon, J. H. Oh, Y.-H. Kim, *Chem. Mater.* **2015**, *27*, 1732.

Supporting Information

Materials and methods.....	245
Polymer Synthesis.....	245
OFET fabrication.....	246
SCLC device fabrication.....	246
GIWAXS.....	247
Supporting GIWAXS data.....	248
Two Dimensional Scatter Plots.....	248
Numerical data for the crystalline spacing and coherence lengths	250
Comonomer influence on out-of-plane and in-plane components	251
Annealing influence on individual polymers.....	253
S-Parameter calculation and depth sensitivity.....	255
Supporting charge carrier mobility data	257
Supporting References	259

Materials and methods

Polymer Synthesis

In general, the polymerizations were carried out for a definite time under microwave conditions and therefore the molecular weight obtained depends on the solubility of the polymers under reaction conditions. There is a slight correlation of the obtained molecular weight to the structure, with the aryl flanking unit having the most significant influence. That is, thiophene-flanked PDPPs show a bigger M_n than the pyridine-flanked PDPPs and the phenyl-flanked polymers show the lowest molecular weight. Furthermore the comonomer has an influence with the functionalized comonomers TF₂ and EDOT showing larger molecular weights than the polymers employing unfunctionalized thiophene (except in the case of PDPP[Py]₂-TF₂). This behavior was attributed to the considerable differences in crystallinity and aggregation behavior of the resulting copolymers, which influence the solubility considerably. Additionally, strongly aggregating polymers showed a distinctly higher M_n in gel permeation chromatography due to overestimation because of their rigid nature and the formation of aggregates during measurement. To the best of our knowledge, there is no report for PDPPs where polymer chain alignment is influenced by a molecular weight variation in the range used in here.

Table S6-1. Molecular characteristics of the polymers used in this study.

Polymer	T^a	M_n^b	M_w^c	\mathcal{D}^d	T_m^e
	[°C]	[kg mol ⁻¹]	[kg mol ⁻¹]		[°C]
PDPP[T] ₂ -TF ₂	200	40.8	161.9	4.0	331
PDPP[T] ₂ -T	250	34.2	107.7	3.1	290
PDPP[T] ₂ -EDOT	250	142.0	377.0	2.7	361
PDPP[Ph] ₂ -TF ₂	100	14.4	22.8	1.6	300 (LC) ^f
PDPP[Ph] ₂ -T	100	10.7	25.3	2.4	300 (LC) ^f
PDPP[Ph] ₂ -EDOT	250	16.7	34.5	2.1	293
PDPP[Py] ₂ -TF ₂	250	12.0	29.2	2.3	333
PDPP[Py] ₂ -T	250	19.6	54.0	2.8	294
PDPP[Py] ₂ -EDOT	250	25.7	61.2	2.4	290-320

^a annealing temperature; ^{b,c} Determined by gel permeation chromatography at 150 °C using 1,2,4-trichlorobenzene as the eluent; ^d Polydispersity; ^e melting temperature determined by flash dynamic scanning calorimetry, ^f LC: liquid crystalline phase (starting at ~150 °C) with clearing temperatures at ~300 °C observable in polarization microscopy, no phase transitions observable in Flash-DSC; ^{b-e} values taken from literature.^[1-2]

OFET fabrication

Silicon wafers (5 × 10 mm) to be used as substrates were ultrasonicated in acetone and 2-propanol. Following oxygen plasma cleaning for 15 min, the substrates were submerged in a 1 wt% solution of octyltrichlorosilane (OTS) in toluene at 60 °C for 60 min. The substrates were rinsed with toluene and 2-propanol subsequently and finally dried in a nitrogen stream before further use. The polymers were spin-coated onto the OTS modified silicon substrates from a 6 mg/mL chloroform solution at 2000 rpm for 60 s in ambient atmosphere. Annealing was performed on a hotplate under inert atmosphere at similar temperatures that gave maximum device performance in organic field effect transistors in previously reported work (see Table S6-1) The OFET mobilities were obtained in thin films using a bottom gate / bottom contact (BGBC) configuration as reported earlier^[1-2] and the values are just compared here to understand the consequences of orientation effects.

SCLC device fabrication

Single carrier space-charge-limited-current (SCLC) devices in diode configuration were prepared for charge carrier mobility determination of electrons within the layer stack of glass/ITO/PEDOT:PSS/Polymer/Ca/Al, for the μ_e determination of EDOT copolymers in this study, in a similar method as reported earlier for the other materials^[1-2]. For all other copolymers, the reported values are compared here in the wake of orientation studies. For

electron-only devices, a 40 nm thick layer of Zinc oxide (ZnO) was spin coated onto the patterned substrates using Sol-gel method. After depositing the bottom layers, polymer solutions (12.25 mg/mL in chloroform) were doctor bladed on top under inert conditions resulting in film thicknesses in the range of 200 to 600 nm. A set of films were also annealed in an inert atmosphere for 15 min at the temperatures given in the main text. Subsequently, the top electrode (Ca/Al) were thermally evaporated onto the polymer layers in respective devices under high vacuum. The devices had an active area of 9 mm² which is determined by the overlap of the ITO and the evaporated top electrode. Dark current-voltage I-V measurements were made under inert environment at room temperature with a Keithley 2400 source measure unit. Before these I-V measurements, the electron-only devices were exposed to 100 mW/cm² illumination for 3 min from an AM 1.5 class A solar simulator to improve the conductivity of the ZnO layer.[36] After the light treatment, the I-V from the electron-only devices were nearly symmetric around 0 V. For electron mobility evaluation, reverse bias voltages, i.e. electron injection from ZnO were considered in electron-only devices. The charge carrier mobilities were evaluated by fitting measured I-V characteristics in a voltage range from 2 to 7 V using the Murgatroyd formula. Prior to fitting, the measured I-V characteristics were corrected for the built in voltage (V_{bi}) and the voltage drop (IR) across contacts. The contact resistance was determined from a reference device without polymer layer and was found to be 27 Ω for both kind of devices. Considering the work function of the electrons and the Fermi-level pinning at contacts, the V_{bi} of 0.2 V and 0.0 V was assumed for hole-only and electron-only devices, respectively.

GIWAXS

Highly collimated 9 keV X-rays were aligned to surface of the sample by use of a Silicon crystal analyzer. The sample detector distance was calibrated using a silver behenate scattering standard. Scattering patterns were collected from 0.05° to 0.25° incidence angle (α_i) with a resolution of 0.01° to ensure collection across the critical angle of the polymer thin films and give sensitivity to both the surface and bulk packing parameters. 2D scattering patterns were converted to 1D profiles with the help of NIKA^[3]. Peaks were fitted with the use of a multipeak least squares algorithm with a logcubic background function.

Supporting GIWAXS data

Two Dimensional Scatter Plots

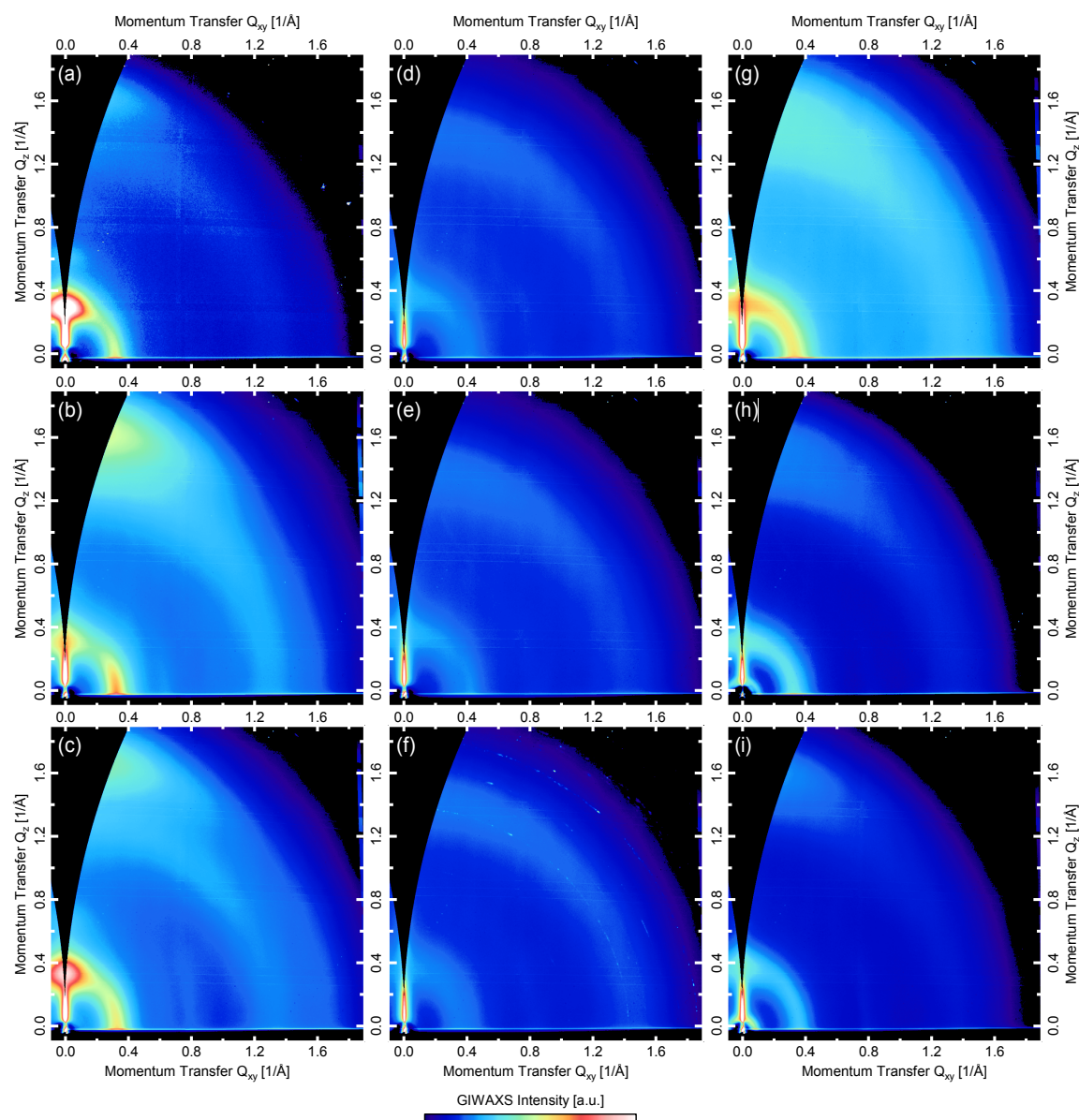


Figure S6-1. 2D GIWAXS patterns for the as cast polymer films. The order of the graphs resembles the order of polymers in Figure 2 of the main manuscript: (a) PDPP[T]₂-TF₂; (b) PDPP[T]₂-T; (c) PDPP[T]₂-EDOT; (d) PDPP[Ph]₂-TF₂; (e) PDPP[Ph]₂-T; (f) PDPP[Ph]₂-EDOT; (g) PDPP[Py]₂-TF₂; (h) PDPP[Py]₂-T; (i) PDPP[Py]₂-EDOT.

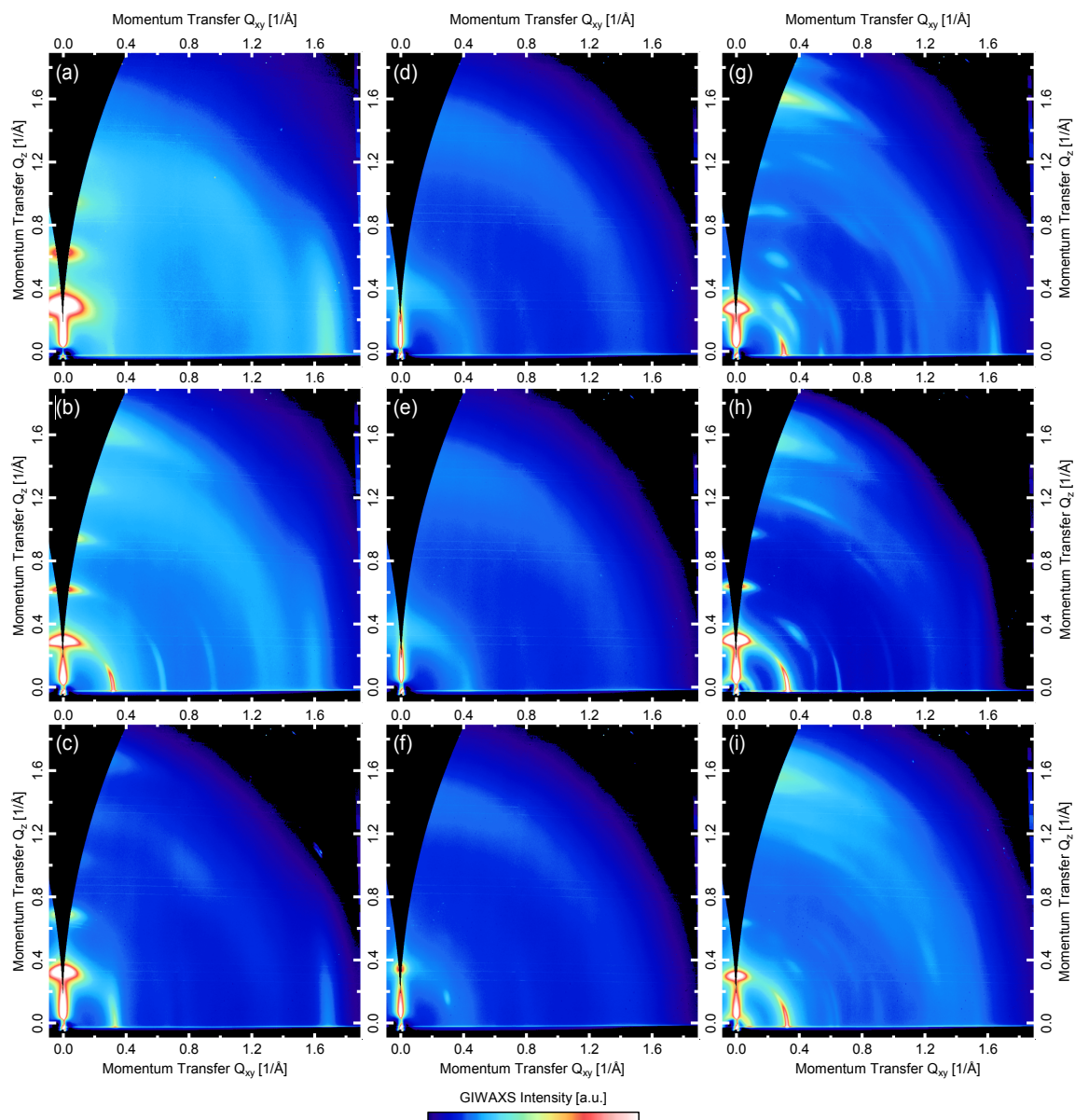


Figure S6-2. 2D GIWAXS patterns for the annealed polymer films. The order of the graphs resembles the order of polymers in Figure 2 of the main manuscript: (a) PDPP[T]₂-TF₂; (b) PDPP[T]₂-T; (c) PDPP[T]₂-EDOT; (d) PDPP[Ph]₂-TF₂; (e) PDPP[Ph]₂-T; (f) PDPP[Ph]₂-EDOT; (g) PDPP[Py]₂-TF₂; (h) PDPP[Py]₂-T; (i) PDPP[Py]₂-EDOT.

Numerical data for the crystalline spacing and coherence lengths

Table S6-2. Crystalline parameters found from the GIWAXS patterns. Annealed samples are color shaded with different colors for different aryl flanking groups.

Polymer	T^a	d_{alkyl}^b	$\zeta_{\text{alkyl}}^{c,g}$	$d_{\pi-\pi}^d$	$\zeta_{\pi-\pi}^{e,g}$	S^f
		[nm]	[nm]	[nm]	[nm]	[a.u.]
PDPP[T] ₂ -TF ₂	as cast	2.11014	8.03147	0.39113	3.5071	0.31
PDPP[T] ₂ -TF ₂	200 °C	2.07228	17.60637	0.39028	4.00908	0.91
PDPP[T] ₂ -T	as cast	2.01442	6.2944	0.40454	3.53161	-0.16
PDPP[T] ₂ -T	250 °C	2.09789	25.17786	0.40316	4.26557	0.43
PDPP[T] ₂ -EDOT	as cast	1.88766	5.89157	0.39262	3.09687	0.15
PDPP[T] ₂ -EDOT	250 °C	1.89171	20.9082	0.38918	5.63317	0.70
PDPP[Ph] ₂ -TF ₂	as cast	1.49916	3.40198	0.44404	1.54201	0.01
PDPP[Ph] ₂ -TF ₂	100 °C	1.4719	3.46934	0.43935	1.5552	-0.02
PDPP[Ph] ₂ -T	as cast	1.47976	3.84326	0.425	1.83551	-0.02
PDPP[Ph] ₂ -T	100 °C	1.55709	4.44412	0.42704	1.85066	-0.14
PDPP[Ph] ₂ -EDOT	as cast	1.51012	2.86808	0.44023	1.63669	0.08
PDPP[Ph] ₂ -EDOT	250 °C	1.80977	13.69184	0.44534	1.72287	0.06
PDPP[Py] ₂ -TF ₂	as cast	1.93018	4.0841	0.39267	3.00982	0.07
PDPP[Py] ₂ -TF ₂	250 °C	2.24053	18.9542	0.40153	12.18666	-0.24
PDPP[Py] ₂ -T	as cast	2.01967	3.35778	0.39302	3.41125	0.10
PDPP[Py] ₂ -T	250 °C	2.0406	25.0967	0.4156	6.64189	0.47
PDPP[Py] ₂ -EDOT	as cast	1.72428	4.99149	0.39995	2.89887	0.01
PDPP[Py] ₂ -EDOT	250 °C	2.05772	21.65063	0.41075	7.30869	-0.17

^a Annealing process; ^b alkyl stacking spacing; ^c alkyl stacking coherence length (determined from (100) peak in out-of-plane direction); ^d π - π stacking spacing; ^e π - π stacking coherence length (determined from 1st order π - π stacking); ^f Herman's Orientation parameter averaged over all incident angles a_i ; ^g the crystal coherence length ζ gives information about the distance over which order is maintained and is defined as $\zeta = 2\pi/\text{FWHM}$, where FWHM is the full width at half maximum of the 1st order lamellar stacking or π - π stacking peak, respectively. It is related to the Scherrer equation, which connects the width of a peak to the crystal size.

Comonomer influence on out-of-plane and in-plane components

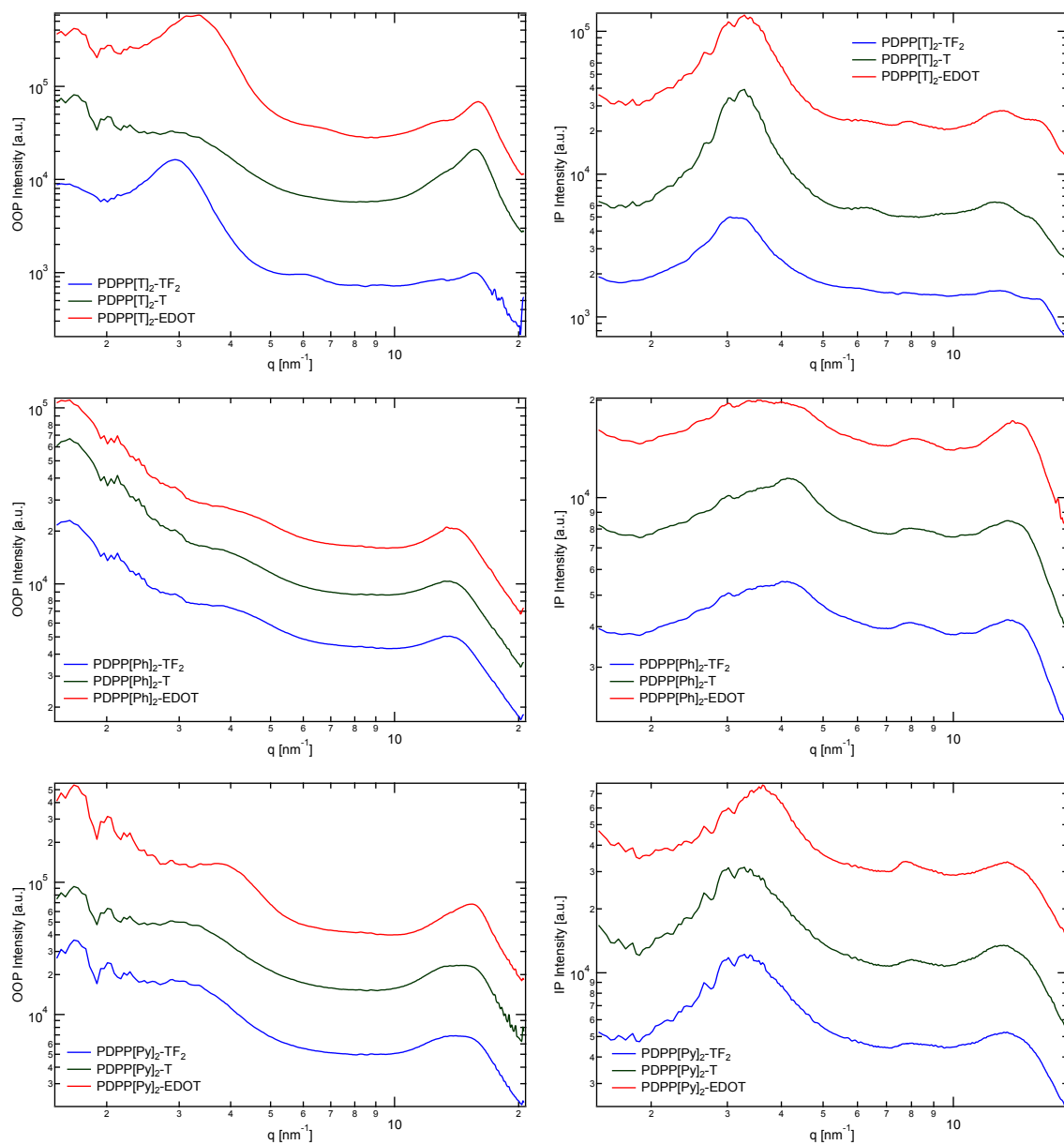


Figure S6-3. Comparison of the out-of-plane (left column) and in-plane (right column) scattering contribution for varying comonomers in as cast films.

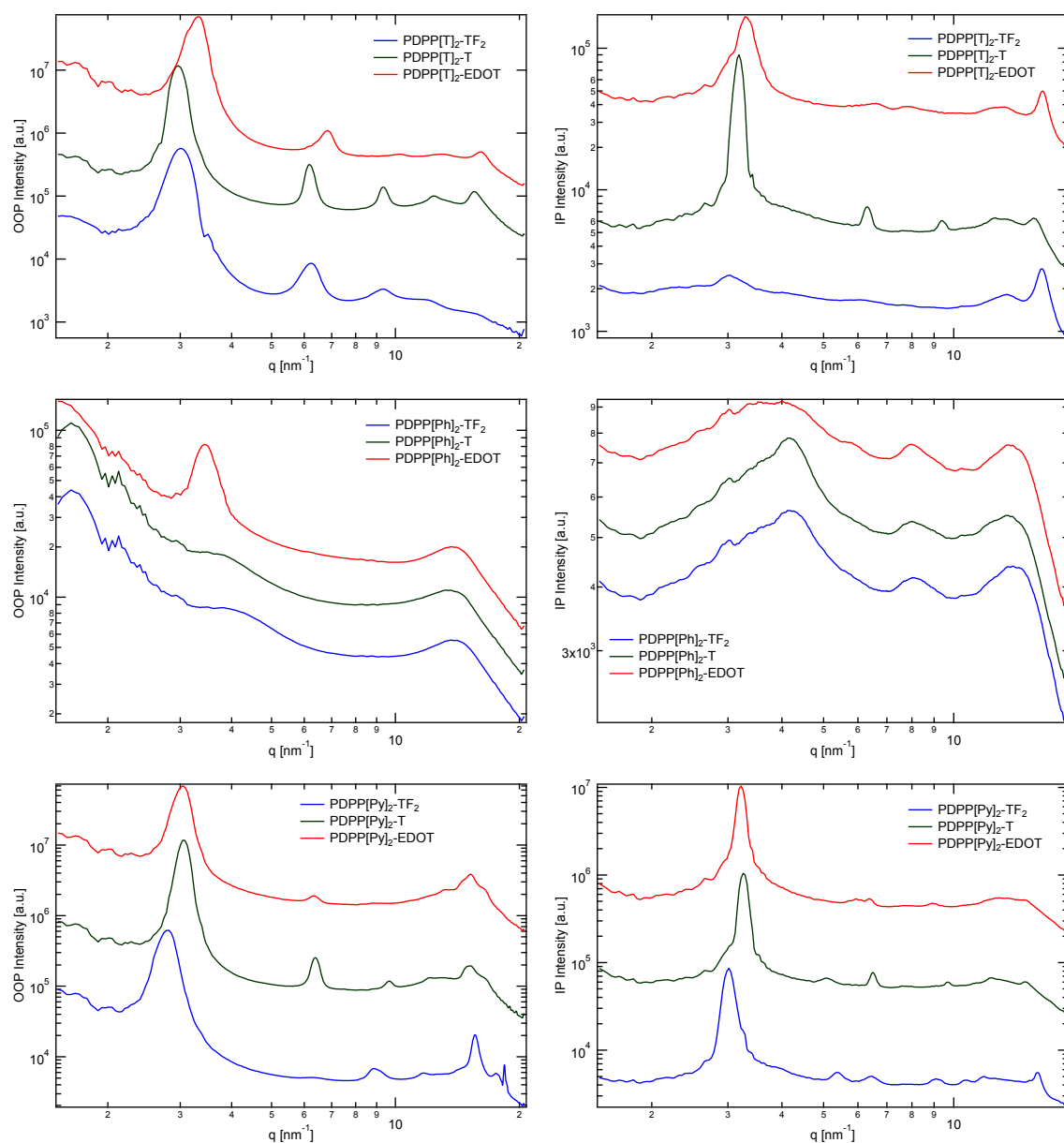


Figure S6-4. Comparison of the out-of-plane (left column) and in-plane (right column) scattering contribution for varying comonomers in annealed films.

Annealing influence on individual polymers

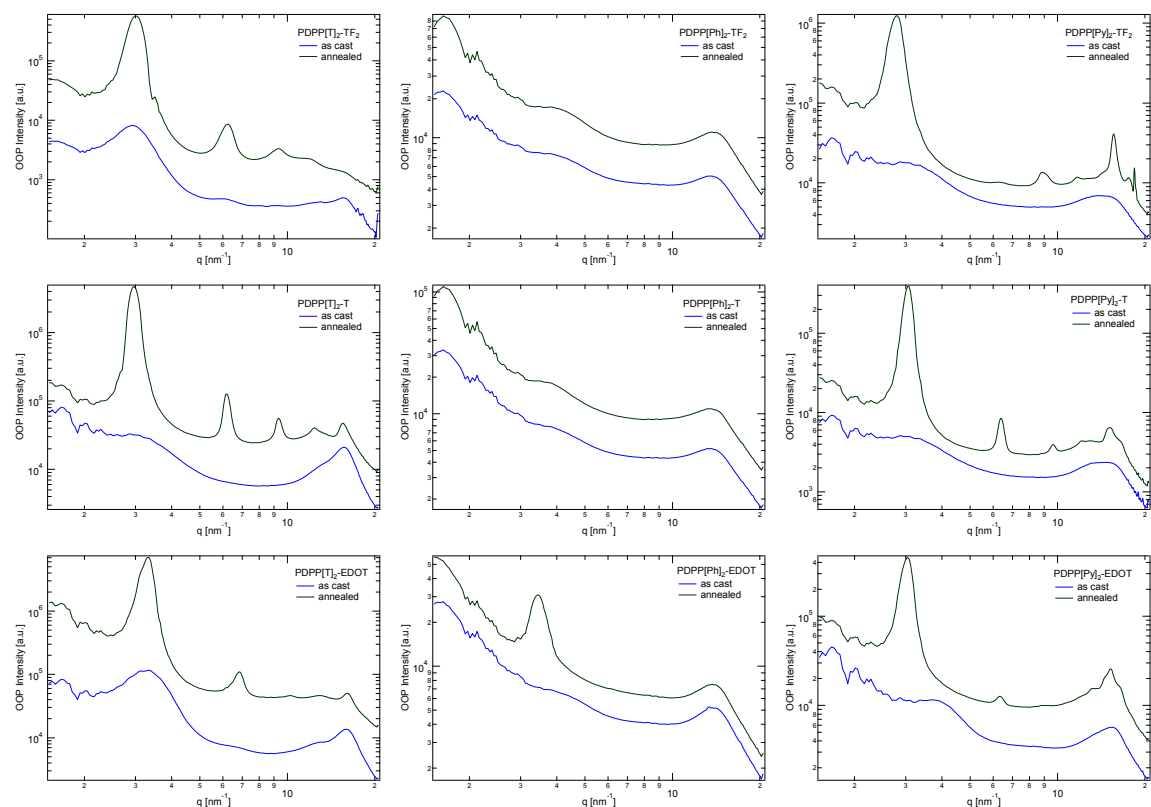


Figure S6-5. Out-of-plane scattering for the individual polymer films before (blue traces) and after (black traces) annealing. The order of the graphs resembles the order of polymers in Figure 2 of the main manuscript.

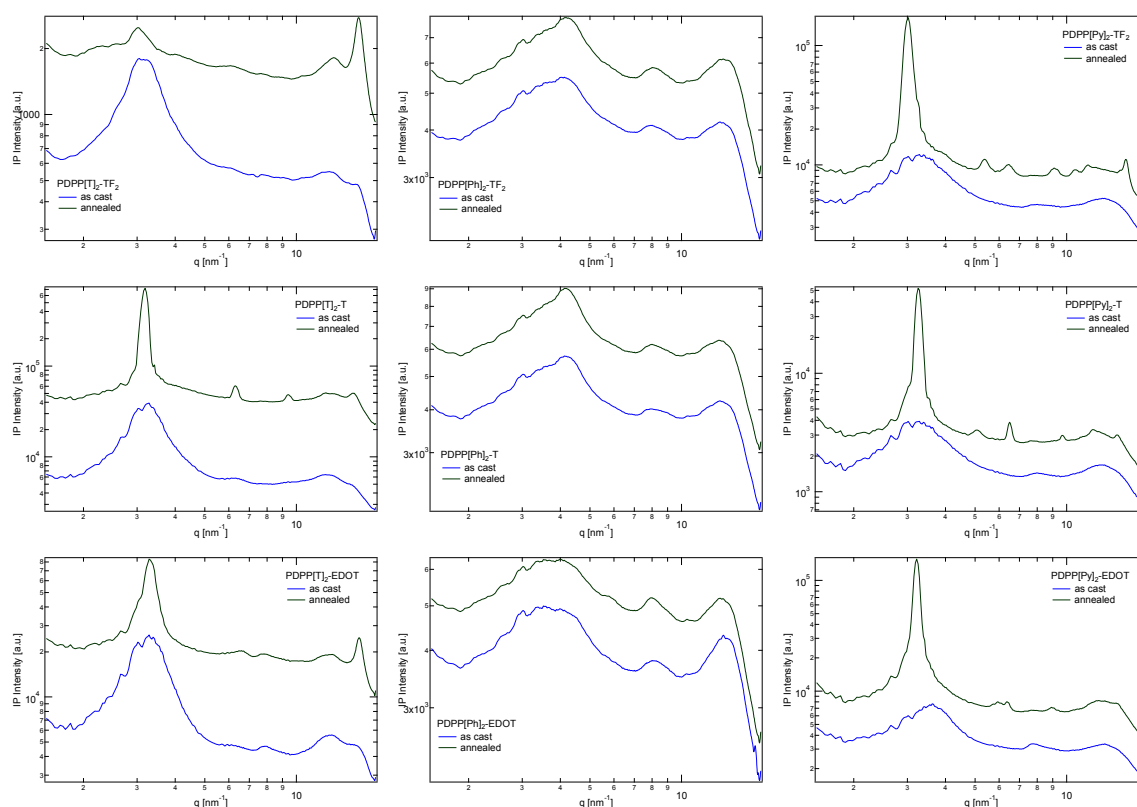


Figure S6-6. In-plane scattering for the individual polymer films before (blue traces) and after (black traces) annealing. The order of the graphs resembles the order of polymers in Figure 2 of the main manuscript.

S-Parameter calculation and depth sensitivity

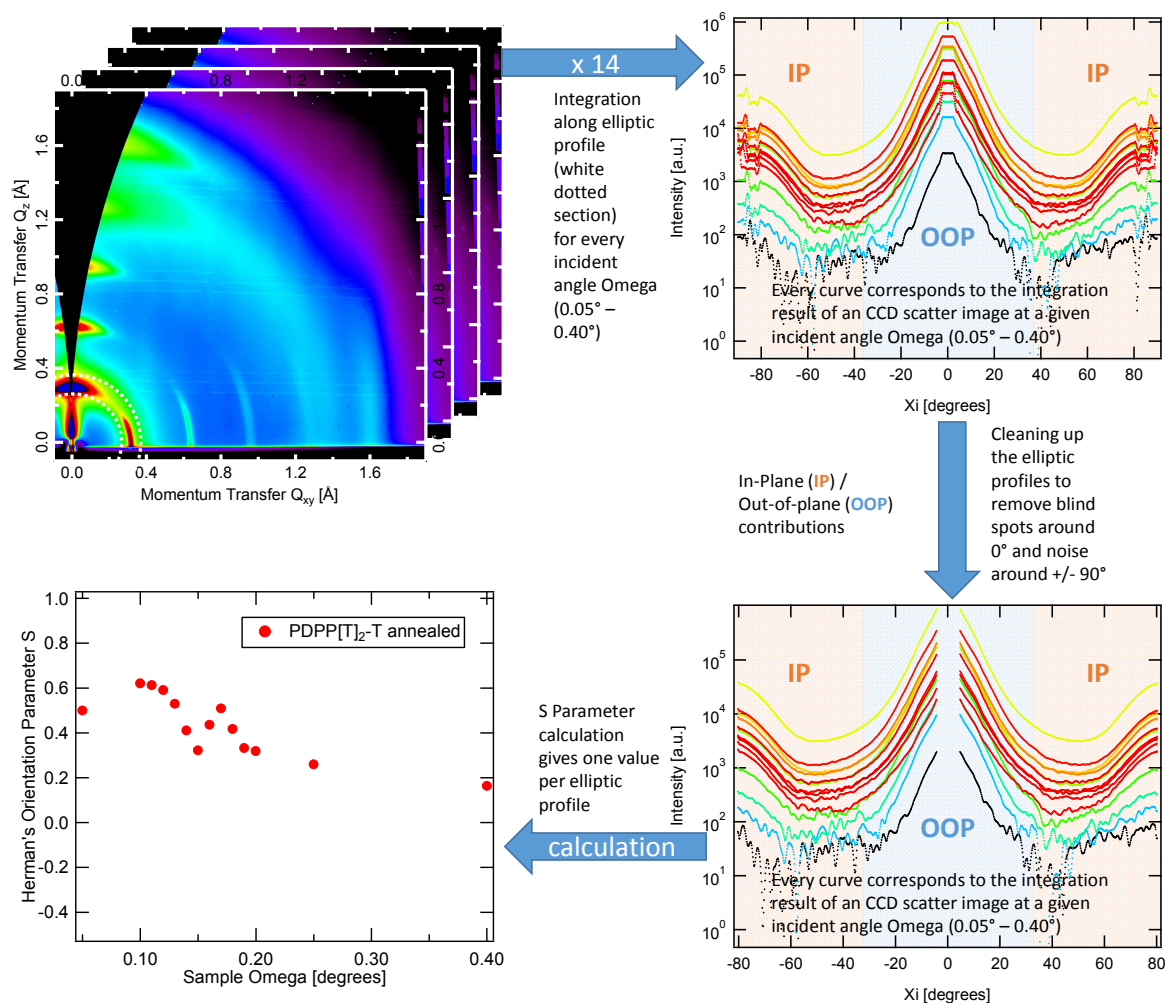


Figure S6-7. Exemplary S Parameter evaluation for PDPP[T]₂-TPT (annealed) starting from two-dimensional scatter plots. Integration of an elliptic profile along the $\langle 100 \rangle$ peak (white dotted section) results in one curve per X-ray incident angle (Sample Ω) for angles between 0.05° and 0.40°. Deleting data points in the centered range around 0° due to the geometric limitations of the grazing incidence setup and around $\pm 90^\circ$ due to noise and eventual wave guiding effects in the film at large χ_i angles. S parameters were finally calculated on a point-by-point basis using the cleaned elliptical profiles to obtain one S Parameter value per incident angle Ω .

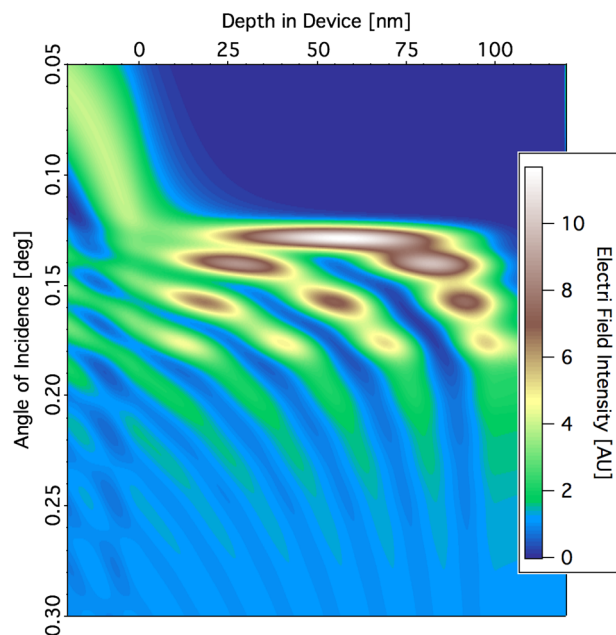


Figure S6-8. Distribution of X-ray electric field intensity (EFI) within the film thickness (depth in device) against the angle of incidence α_i .

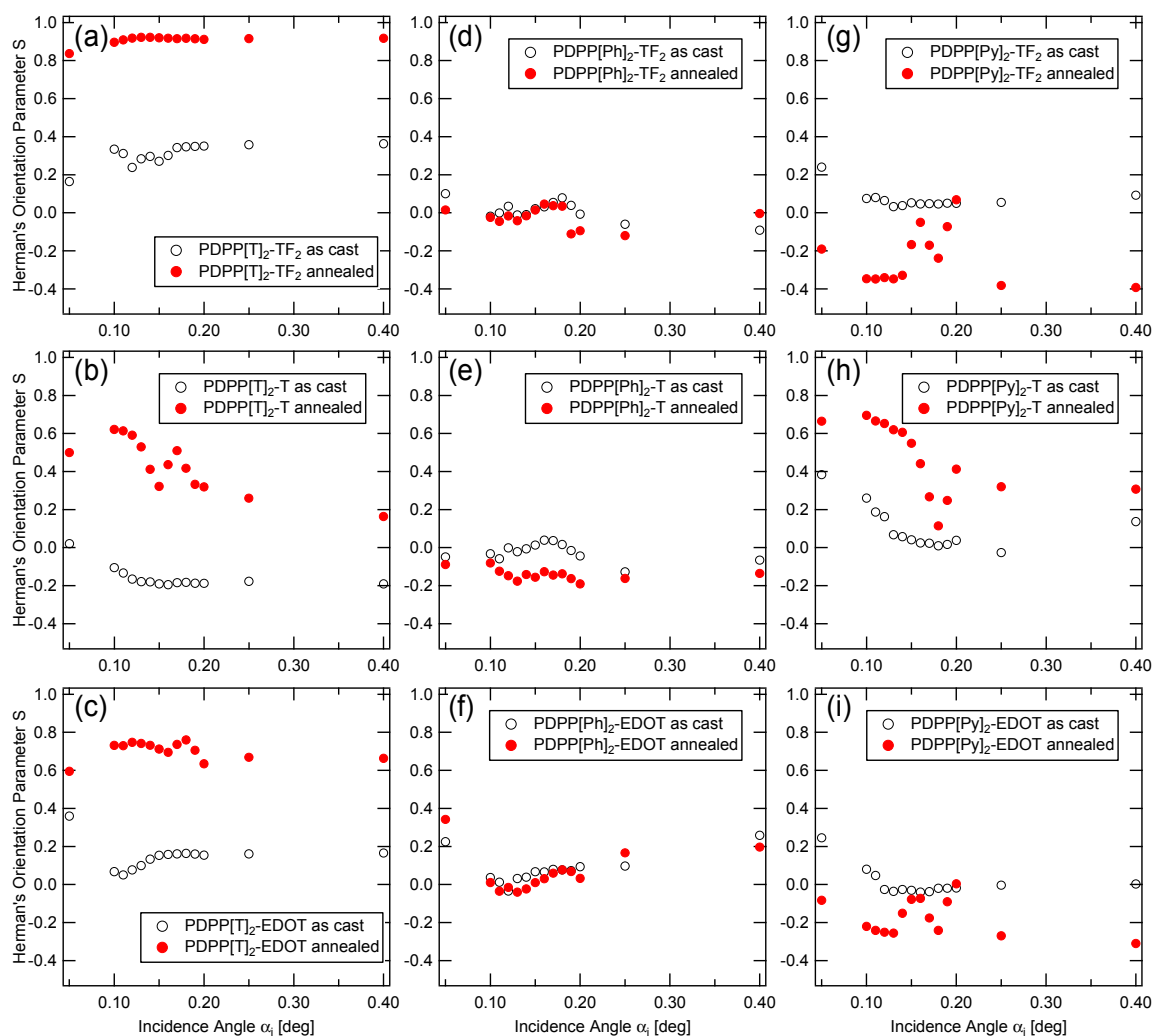


Figure S6-9. Depth sensitive S for the polymers at different grazing incidence angles α_i . Hollow black dots represent the as cast films whereas filled red dots represent the annealed samples.

Supporting charge carrier mobility data

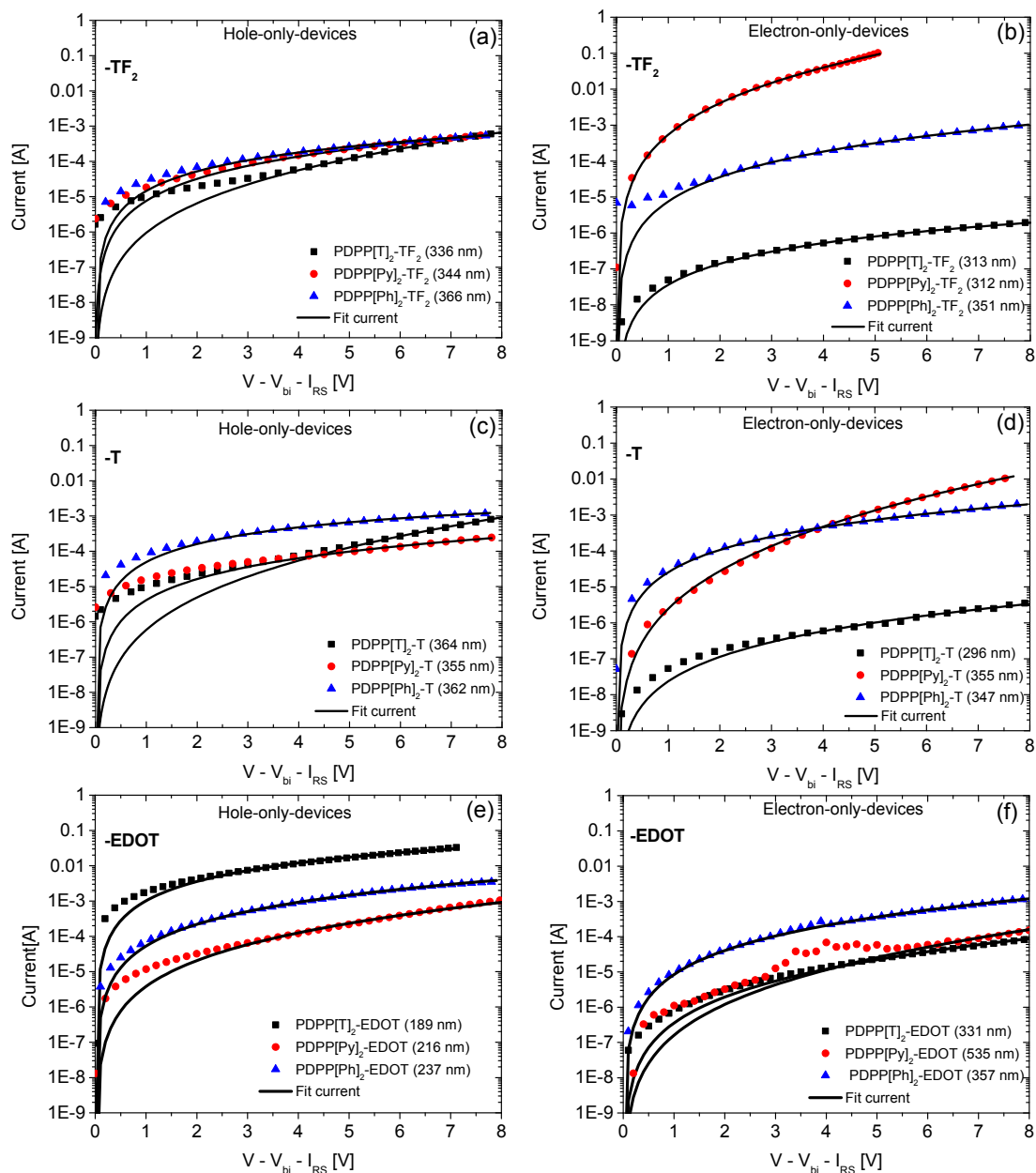


Figure S6-10. Comparison of measured SCLC semilog plots of current vs. voltage with fits for the SCLC regimes for all the nine copolymers both for hole only and electron only devices.

Table S6-3. The average effective SCLC charge carrier mobility of holes (μ_h) and electrons (μ_e) for the nine PDPPs as-cast films for varying film thicknesses. The charge mobility in annealed films for single film thickness is also given. All films were annealed at 200 °C for 15 min except for PDPP[Ph]2-TF2 and PDPP[Ph]2-T copolymers. These films were annealed at 100 °C for 15 min.

Polymer	As Cast		Annealed	
	μ_h	μ_e	μ_h	μ_e
	[cm ² V ⁻¹ s ⁻¹]	[cm ² V ⁻¹ s ⁻¹]	[cm ² V ⁻¹ s ⁻¹]	[cm ² V ⁻¹ s ⁻¹]
PDPP[T] ₂ -TF ₂	$(9.4 \pm 3.3) \times 10^{-6}$	$(2.6 \pm 1.5) \times 10^{-8}$	3.6×10^{-6}	2.4×10^{-8}
PDPP[T] ₂ -T	$(1.0 \pm 0.5) \times 10^{-5}$	$(3.0 \pm 0.9) \times 10^{-8}$	3.0×10^{-6}	2.1×10^{-8}
PDPP[T] ₂ -EDOT	$(2.9 \pm 1.0) \times 10^{-4}$	$(1.1 \pm 0.5) \times 10^{-6}$	1.5×10^{-4}	6.1×10^{-7}
PDPP[Py] ₂ -TF ₂	$(1.6 \pm 0.7) \times 10^{-5}$	$(4.3 \pm 0.1) \times 10^{-3}$	2.8×10^{-5}	3.0×10^{-3}
PDPP[Py] ₂ -T	$(1.1 \pm 0.9) \times 10^{-5}$	$(3.7 \pm 2.5) \times 10^{-4}$	1.3×10^{-5}	8.9×10^{-4}
PDPP[Py] ₂ -EDOT	$(2.2 \pm 1.2) \times 10^{-6}$	$(1.2 \pm 0.8) \times 10^{-5}$	6.8×10^{-6}	1.7×10^{-5}
PDPP[Ph] ₂ -TF ₂	$(2.2 \pm 0.1) \times 10^{-5}$	$(1.5 \pm 0.6) \times 10^{-5}$	2.6×10^{-5}	2.7×10^{-5}
PDPP[Ph] ₂ -T	$(3.6 \pm 0.2) \times 10^{-5}$	$(6.6 \pm 3.1) \times 10^{-5}$	2.2×10^{-5}	3.7×10^{-5}
PDPP[Ph] ₂ -EDOT	$(4.2 \pm 2.3) \times 10^{-5}$	$(2.1 \pm 0.6) \times 10^{-5}$	6.3×10^{-5}	3.1×10^{-5}

Table S6-4. Listing of film thicknesses and fitting parameters for the newly measured electron-only SCLC devices of EDOT copolymers.

Active layer	Thickness	Fitted mobility	Fitted gamma	Mobility at 1.5×10^7 V/m
	[nm]	[cm ² V ⁻¹ s ⁻¹]	[V ^{-0.5} m ^{0.5}]	[cm ² V ⁻¹ s ⁻¹]
PDPP[T] ₂ -EDOT	271	3.2×10^{-7}	3.9×10^{-4}	1.4×10^{-6}
PDPP[T] ₂ -EDOT	219	1.3×10^{-7}	3.6×10^{-4}	5.5×10^{-7}
PDPP[T] ₂ -EDOT	331	2.0×10^{-7}	4.8×10^{-4}	1.3×10^{-6}
PDPP[T] ₂ -EDOT + anneal	277	2.4×10^{-7}	2.4×10^{-4}	6.1×10^{-7}
PDPP[Py] ₂ -EDOT	644	1.0×10^{-8}	1.8×10^{-3}	1.1×10^{-5}
PDPP[Py] ₂ -EDOT	535	1.8×10^{-8}	1.2×10^{-3}	2.1×10^{-5}
PDPP[Py] ₂ -EDOT	159	3.2×10^{-8}	1.3×10^{-3}	5.8×10^{-6}
PDPP[Py] ₂ -EDOT + anneal	333	8.1×10^{-8}	1.4×10^{-3}	1.7×10^{-5}
PDPP[Ph] ₂ -EDOT	357	8.0×10^{-6}	2.9×10^{-4}	2.5×10^{-5}
PDPP[Ph] ₂ -EDOT	424	6.7×10^{-6}	2.3×10^{-4}	1.7×10^{-5}
PDPP[Ph] ₂ -EDOT + anneal	257	1.7×10^{-5}	1.6×10^{-4}	3.1×10^{-5}

Supporting References

- [1] C. J. Mueller, C. R. Singh, M. Fried, S. Huettner, M. Thelakkat, *Adv. Funct. Mater.* **2015**, *25*, 2725.
- [2] C. J. Mueller, C. R. Singh, M. Thelakkat, *J. Polym. Sci., Part B: Polym. Phys.* **2016**, *54*, 639.
- [3] J. Ilavsky, *J. Appl. Crystallogr.* **2012**, *45*, 324.

7 Diketopyrrolopyrroles with a Distinct Energy Level Cascade for Efficient Charge Carrier Generation in Organic Solar Cells

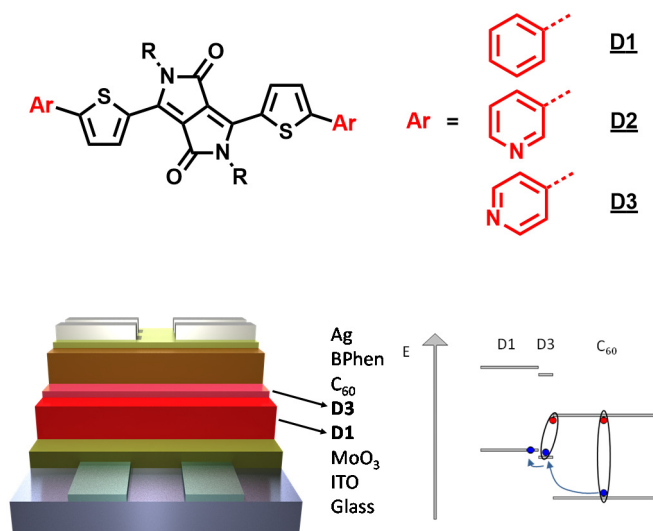
Christian J. Mueller,^a Michael Brendel,^b Pia Ruckdeschel,^a

Jens Pflaum^{b,c} and Mukundan Thelakkat^{*,a}

^a Applied Functional Polymers – Macromolecular Chemistry I, University of Bayreuth, 95440 Bayreuth, Germany

^b Experimental Physics VI, Julius-Maximilians University, Am Hubland, 97074 Würzburg, Germany

^c Bavarian Center for Applied Energy Research e.V. (ZAE Bayern), Am Galgenberg 87, 97074 Würzburg, Germany



Published in *Advanced Energy Materials*, **2015**, 5, 1500914.

Reproduced with permission from Wiley VCH.

Abstract

Three structurally different low molecular weight diketopyrrolopyrroles (DPPs) are synthesized in order to provide donors with a precise offset in their energy levels. The DPPs are characterized for optical, electrochemical and thermal properties. By changing the terminal aryl groups attached to the DPP core from phenyl over *m*-pyridine to *p*-pyridine, different solid state packing was observed in thin film studies using UV/VIS absorption spectra and X-ray diffraction. Most importantly it is shown that both, reduction as well as oxidation potentials can be precisely tuned with a gradual stepping of about 100 meV by changing the terminal groups attached to the DPP core. Exploiting this energy level modification, these materials are tested in planar cascade organic photovoltaic devices using C₆₀ as acceptor. A sub nm thick interlayer of a suitable DPP derivative is introduced to obtain a distinct energy level cascade at the donor/acceptor interface. Power conversion efficiency as well as short circuit current density are doubled with respect to the reference bilayer devices lacking the interface cascade. Spectrally resolved analysis of external quantum efficiency revealed that this enhancement can mainly be attributed to destabilization of bound charge transfer states formed in the C₆₀ layer at the interlayer interface, thus reducing geminate recombination losses.

7.1 Introduction

In the field of organic photovoltaics, for systems based on either polymers or small molecules improved light harvesting and increased power conversion efficiencies are reported.^[1] Low molecular weight systems are characterized by their monodispersity, ease of synthesis, purification and reproducibility.^[2] Electronic and photophysical properties can be more precisely tuned in low molecular weight materials and the morphologies obtained are reproducible to a large extent unlike in the case of polymers, which vary from batch to batch in their molecular weight. Therefore, also the morphology of polymer:fullerene blends, which is influenced by the long range ordering of the polymer and the viscosity of the solution is affected by batch to batch variations. Furthermore, small molecules allow for physical vapor deposition in order to obtain very well defined multilayer stacks and tandem cells.^[3-4] Diketopyrrolopyrrole (DPP) based materials are promising and well established candidates for organic electronics.^[5] Apart from their polymeric derivatives,^[6-7] also many of the small molecule DPPs have been shown to be attractive materials for application in organic field-effect transistors (OFET)^[8-10] and organic photovoltaics (OPV).^[11-14]

The key functional unit of any state of the art organic solar cell relies on a donor/acceptor heterojunction, which provides the driving force for the formation of hetero charge transfer (CT) states and their subsequent dissociation into free charge carriers. Since the introduction of this planar heterojunction structure by Tang,^[15] progress in the field of organic photovoltaics has been tremendous, partly due to improved device architecture, such as the bulk heterojunction concept or tandem solar cells.^[16] Aiming for broad spectral absorption, recently another strategy has been established successfully by the introduction of a three-layer cascade architecture, in which the frontier orbital energy levels of the interfacial layer are intermediate to those of the donor and acceptor material. By this, a remarkable power conversion efficiency of 8.4% could be achieved using a fullerene free three-layer stack.^[17] Next to increased absorption, the utilization of the cascade energy level alignment was primarily associated with the suppression of recombination losses, which is a major task for achieving high photocurrents in organic photovoltaic devices.^[18-21] The reduced recombination was attributed to a through space coupling of the energy levels of donor and acceptor molecules via the thin interfacial layer,^[19] and to a destabilization of both, excitons and the charge transfer states.^[21]

In this contribution small molecule diketopyrrolopyrrole derivatives were specially synthesized for the application in three-layer cascade photovoltaic cells. The chemical structures of these molecules D1, D2 and D3 are given in Scheme 7-1. In order to achieve a defined and gradual energy level offset in a set of DPPs without varying their structure, dipole moment and surface energy too much, we chose to vary the terminal aryl group of the DPP compounds. Phenyl and pyridine rings show a distinct difference in π -electron density, which can be further fine-tuned by changing the substitution pattern in the case of pyridine by selecting *meta*-pyridyl and *para*-pyridyl groups. Upon generic *para*-pyridine substitution of the phenyl-ring in D1, frontier energy levels are shifted by 160 meV towards lower energies in D3, as confirmed by cyclic voltammetry measurements. To our knowledge, for the first time, a donor molecule and its modified derivative were used to establish an energy level cascade in combination with the acceptor C₆₀. We verify the thickness dependent impact of the thin interfacial layer on the photovoltaic parameters of prototype D1/D3/C₆₀ OPV devices. Since the band gap remains almost unaffected upon pyridine modification in D3, we can neglect the influence of any absorption changes on device performance. The observed difference in overall device performance with respect to recombination losses and exciton diffusion can thus be attributed to the energy level alignment.

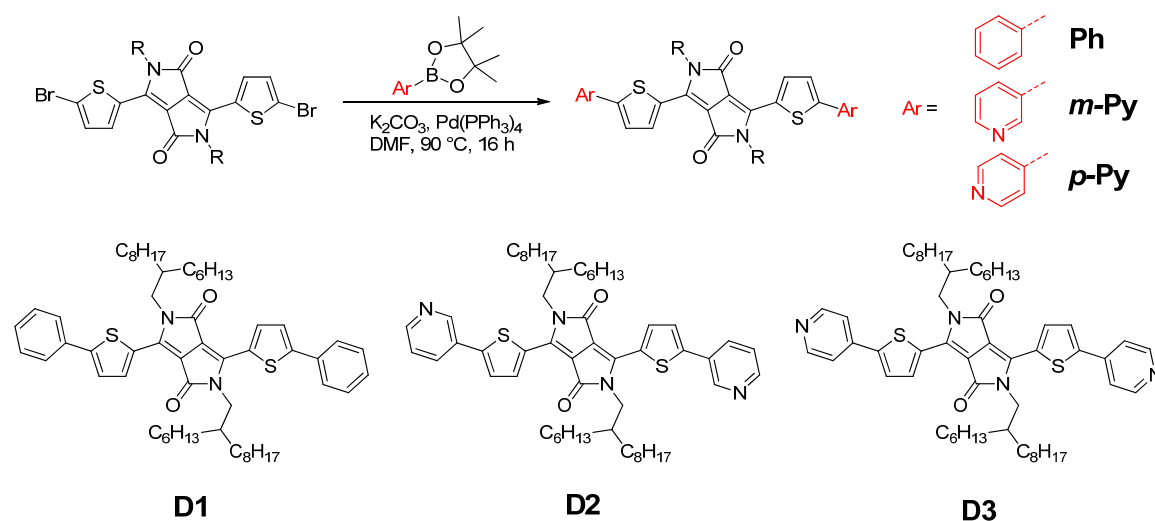
A significant increase in the short circuit current density by 80 % for a D3 interfacial layer thickness of 3 Å and 6 Å is demonstrated in comparison to the D1/C₆₀ reference devices. External quantum efficiency measurements reveal, in particular, an increased photocurrent generation yield, originating from the fullerene acceptor layer. This enhancement is attributed to the special energy level alignment, which we propose to cause energetic destabilization of

CT states at the heterojunction. Moreover, we confirm improved exciton and charge carrier transport properties across the three layer cascade structure, indicated by an enhanced fill factor in comparison to the reference cells.

7.2 Results and Discussion

7.2.1 Synthesis

The dibrominated starting material 3,6-bis(5-bibromo-2-thienyl)-2,5-dihydro-2,5-di(2-hexyldecyl)-pyrrolo[3,4c]pyrrole-1,4-dione (DPP[T]₂Br₂) was synthesized following a previously reported procedure.^[22-23] Phenyl boronic acid pinacol ester was purchased from Sigma Aldrich. The pinacol esters of 3-pyridyl boronic acid and 4-pyridyl boronic acid were synthesized from their respective boronic acids (see Supporting Information). The three DPP dyes D1-D3 were obtained by homogeneous Suzuki-Miyaura cross-coupling in DMF (see Scheme 1) in high yields of about 80%. Device grade materials were obtained after recrystallization from ethanol. For details on synthetic procedures and spectroscopic analysis see experimental section. The synthesis of D1 was previously reported as a model compound for DPP polymers by Janssen et al.^[24]



Scheme 7-1. Synthesis of the DPP dyes using Suzuki-Miyaura cross-coupling and structures of the differently terminated DPP dyes D1, D2 and D3.

7.2.2 Optical properties

Absorption spectra were recorded in toluene solution as well as in thin films (see Figure 7-1). The solution spectra have been ensured to be free from aggregation effects in a concentration series measurement. Whereas all three compounds show an almost identical spectral nature in solution, the differences in solid state spectra give rise to optical properties strongly influenced by intermolecular coupling and different solid state packing of the dyes. The optical gap as

determined from the absorption edge in solid state spectra are 1.8 eV for D1 and D2 and 1.7 eV for D3. Thus, all the three compounds absorb in the visible region. Furthermore, all three DPP derivatives exhibit a red shift in their solid state spectra, indicating the formation of J-aggregates. Especially D3 shows a large red shift of about 90 nm (90 meV).

The contributions of the individual vibronic transitions were analyzed by fitting the absorption curves in the VIS range with Gaussians. All fits are plotted in Supporting Information Figure S7-1 and the values are summarized in Table S7-1. For a comparison with the spectral photocurrent data (see Figure 6a) we refer to the absorption of the real bilayer devices presented in the Supporting Information (Figure S7-8). For a comparison of the photogenerated current in bilayer devices the absorption of the real devices are given in the Supporting Information (Figure S7-8).

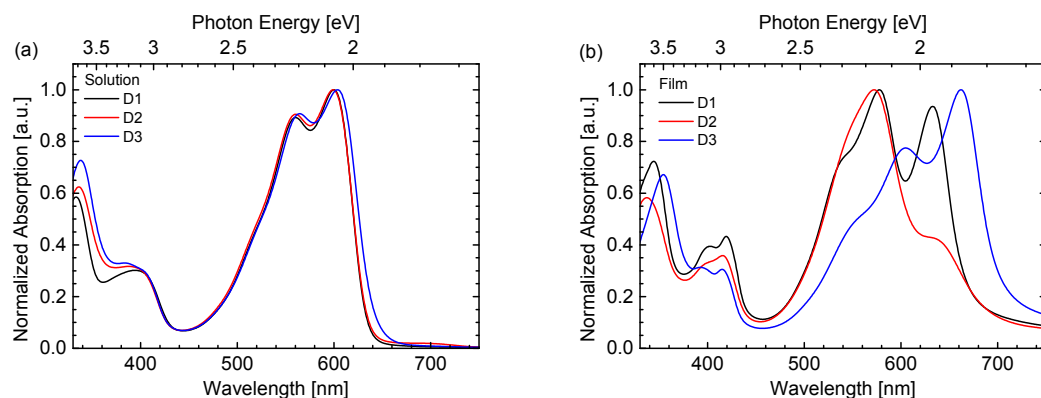


Figure 7-1. Absorption spectra in toluene solution (a) and spin-coated thin films (b) for the differently terminated DPP derivatives. Further analysis of this data is provided in the Supporting Information (see Figure S7-1 for peak fitting and Table S7-1 for individual transitions).

Comparing the wavelengths of the absorption bands $A_{2\leftarrow 0}$, $A_{1\leftarrow 0}$ and $A_{0\leftarrow 0}$ it is evident, that the phenyl- and the *m*-pyridyl-substituted dyes D1 and D2 show very similar aggregation behavior with almost identical wavelengths for all three observable transitions. The *p*-pyridine substituted D3 however shows a considerable red-shift for all transitions (Figure 7-1, Figure S7-1) when compared to D1 and D2. Hence, $A_{1\leftarrow 0}$ and $A_{0\leftarrow 0}$ are red-shifted by about 30 nm when going from D1 and D2 to D3. This may indicate the formation of a stronger J-aggregate than for D1 and D2. Comparing the $A_{1\leftarrow 0}$ and $A_{0\leftarrow 0}$ transitions, D1 shows more homogeneously distributed transitions with intensities of 0.72 and 0.76 a.u. for $A_{1\leftarrow 0}$ and $A_{0\leftarrow 0}$, respectively. Upon *m*-pyridine substitution in D2, $A_{1\leftarrow 0}$ with an intensity of 0.70 a.u. is much stronger than $A_{0\leftarrow 0}$ with an intensity of only 0.27. For the *p*-pyridine substituted D3, an inversed effect is observed with $A_{0\leftarrow 0}$ having a slightly higher intensity (0.76 a.u.) than $A_{1\leftarrow 0}$ (0.60 a.u.). The optical bandgaps derived from the absorption onset in thin films are given together with the electrochemical properties from cyclic voltammetry in Table 7-1. For a comparison of the

photogenerated current in bilayer devices the absorption of the real devices are given in the Supporting Information (Figure S7-8).

7.2.3 Thermal properties

The thermal properties of the three DPP dyes were studied using thermogravimetric analysis (TGA) to determine the thermal stability and decomposition onset. Differential scanning calorimetry (DSC) gave insights into phase transitions of these materials. Thermogravimetric curves are shown in Supporting Information Figure S7-3. The decomposition onset for D1-D3 is remarkably high at temperatures between 390-400 °C. Substitution of the terminal phenyl group with pyridine does not affect the thermal stability of these compounds and all the materials seem very suitable for processing *via* physical vapor deposition.

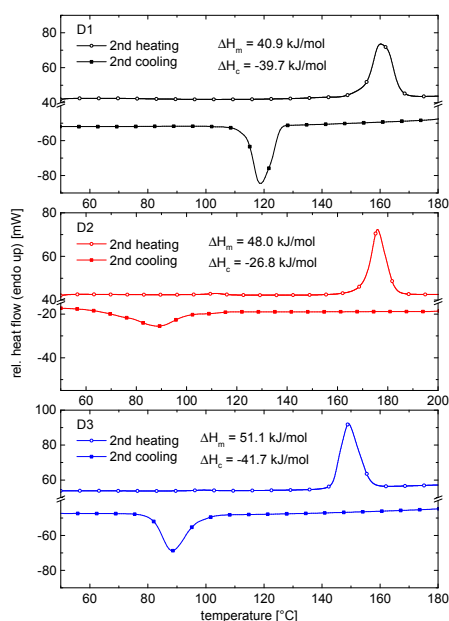


Figure 7-2. Differential Scanning Calorimetry scans for the differently terminated DPP molecules at a scan rate of 40 K min⁻¹.

Further insights into the influence of the terminal aryl unit on the solid state properties are obtained by DSC at heating and cooling rates of 40 K min⁻¹. The individual heating and cooling scans of the second cycle are shown in Figure 7-2 and the onset temperatures and enthalpies for crystallization as well as melting are summarized in Table 7-1. Evidently, the terminal substitution pattern has a large influence on the thermal bulk properties of the dyes, being more significant for the crystallization processes than for the melting processes. No liquid crystalline phase transitions could be observed in DSC measurements as well as in polarization microscopy. All samples are crystalline with very high ΔH_m values. For the pyridine-substituted derivatives D2 and D3, the melting enthalpies ΔH_m are higher than the corresponding crystallization enthalpies ΔH_c . This indicates the recrystallization to be kinetically hindered in

these materials, which is not the case for D1, where $\Delta H_m \approx \Delta H_c$. The crystal sizes in D1-D3 vary as observed by the different T_m values.

7.2.4 Electrochemical properties

The electrochemical properties of D1-D3 were studied with respect to reversibility as well as redox potentials. The individual cyclic voltammograms and a comparison of the calculated energy levels are shown in Figure 7-3, the values are listed in Table 7-1. All energy levels were calculated against a ferrocene/ferrocenium redox couple using a published procedure taking into account solvent effects.^[25] For a study of the influence of a relative offset of energy levels, these redox potentials can be very well used since the conditions of measurement and solvent polarity are the same. In general, all compounds can be oxidized and reduced reversibly. The phenyl-terminated D1 shows two reversible oxidations at 0.40 V and 0.74 V (corresponding to an IP of -5.56 eV and an IP+1 of -5.90 eV) respectively. When substituting the phenyl group by a pyridine moiety, only one reversible oxidation can be observed. The second oxidation step is still existent, but not reversible anymore (see Supporting Information Figure S7-2). Furthermore both, oxidation as well as reduction potentials are shifted towards more negative values by changing the terminal group from phenyl to pyridine. The ionization potential could hence be lowered by 80 meV when going from the phenyl-terminated D1 to the *m*-pyridyl terminated D2 and by another 80 meV for the *p*-pyridyl terminated D3. The same trend can be observed for the electron affinity with a shift of 60 meV and 100 meV, respectively. Accordingly, the electrochemical band gap E_{cv} is the same for all three dyes (2.0 eV), which is larger by about 0.2 to 0.3 eV compared to the optical gap. The trend of lower energy levels upon *m*-pyridyl and *p*-pyridyl substitution is in good agreement with values derived from density functional theory (DFT) calculations (see Supporting Information Table S7-3, Figure S7-10). The lowering of the energy levels can be explained by the change in electron density when going from a phenyl group in D1 to a more electron-deficient pyridine in D2. Furthermore, in pyridine the electron density at the *ortho* and *para* positions is lower than at the *meta* position, leading to lower energy levels in the *para*-substituted D3 compared to the *meta*-substituted D2. It is worthwhile to note, that such subtle differences in electron density can be used to fine-tune the energy levels of organic compounds by choosing the correct substitution pattern. The gradual decrease in both ionization potential (IP) and electron affinity (EA) together with a similar bandgap for these three DPP dyes allows for the design of well-defined energy level cascades in organic photovoltaic devices. In order to estimate the reduction potential of the fullerene, we measured PCBM under the same conditions in solution, as it contains the electronically active moiety of the insoluble C₆₀. Especially D3, with its energy levels lying distinctly between those of D1 and C₆₀, can be identified as a suitable interface layer for D1/C₆₀ devices (see Figure 7-3b).

Table 7-1. Properties of the DPP dyes under investigation

Compound	Cyclic Voltammetry						Thermal properties				
	$E_{1/2}^{ox\ a)}$	$IP\ a)$	$E_{1/2}^{red\ a)}$	$EA\ a)$	$E_{cv}\ b)$	$E_{opt}\ c)$	$T_{5\%}\ d)$	$T_m\ e)$	$T_c\ e)$	$\Delta H_m\ e)$	$\Delta H_c\ e)$
	[eV]	[eV]	[eV]	[eV]	[eV]	[eV]	[°C]	[°C]	[°C]	[kJ/mol]	[kJ/mol]
D1	0.40	-5.56	-1.62	-3.54	2.02	1.79	398	155	126	40.9	-39.7
D2	0.48	-5.64	-1.56	-3.60	2.04	1.77	396	171	101	48.0	-26.8
D3	0.56	-5.72	-1.46	-3.70	2.02	1.70	387	143	98	51.1	-41.7

^{a)} CV based half-step oxidation ($E_{1/2}^{ox}$) and reduction ($E_{1/2}^{red}$) potentials measured against Fc/Fc⁺ in a 0.1 M tetra-*n*-butylammonium hexafluorophosphate / dichloromethane electrolyte solution at a scan rate of 50 mV s⁻¹ and the ionization potential (IP) and electron affinity (EA) calculated therefrom; ^{b)} electrochemical gap determined by CV in solution; ^{c)} optical gap determined from absorption onset in thin film; ^{d)} 5% Degradation onset determined by thermogravimetric analysis, ^{e)} melting (T_m) and crystallization (T_c) onset temperatures and their respective enthalpies (ΔH) determined by differential scanning calorimetry.

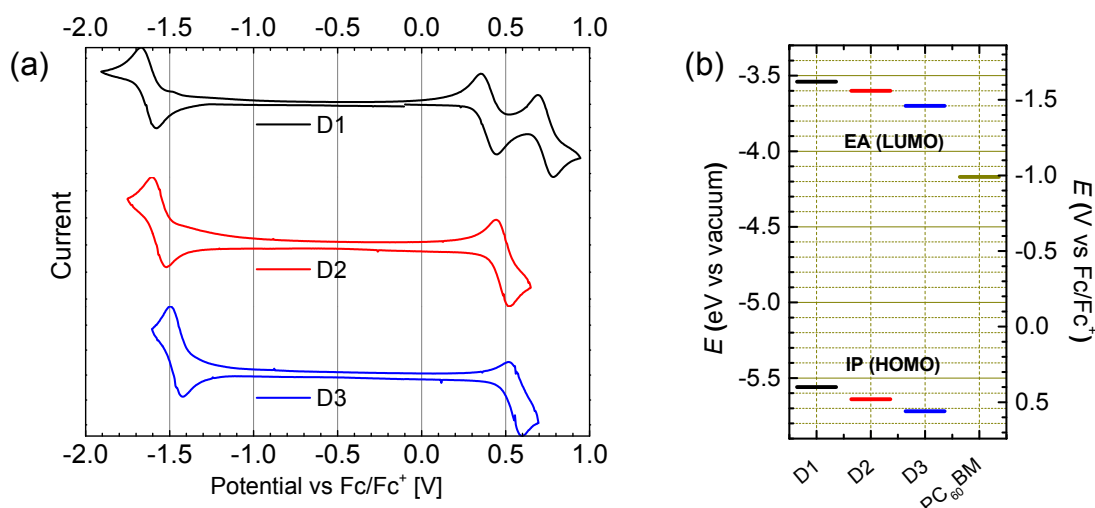


Figure 7-3. (a) Cyclic voltammograms measured in a 0.1 M tetra-*n*-butylammonium hexafluorophosphate / dichloromethane electrolyte solution at a scan rate of 50 mV s⁻¹; (b) Energy level comparison. The reduction potential of PC₆₀BM (0.99 eV), corresponding to an EA of -4.17 eV, determined using the same setup is shown for comparison.

7.3 Devices

7.3.1 $j(V)$ characterization of D1/D3/C₆₀ cascade solar cells

To gain insight into the impact of the D3 interlayer on the exciton dissociation efficiency, the $j(V)$ characteristics under AM 1.5 standard illumination intensity were measured for various D3 interlayer thicknesses in D1/D3/C₆₀ devices on ITO/MoO₃ substrates. Selected $j(V)$ characteristics are shown in Figure 7-4 and the normalized cell parameters are summarized for each D3 interlayer thickness in Figure 7-5. The normalization of the photovoltaic device

parameters was carried out with reference to the D1/C₆₀ bilayer solar cell without the energy cascade structure.

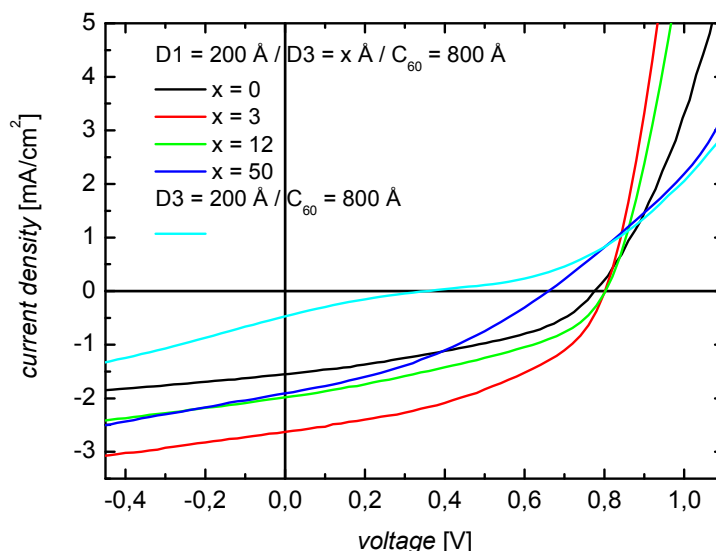


Figure 7-4. $j(V)$ characteristics of D1(200 Å)/ D3(x Å)/C₆₀(800 Å) cascade cells. Additionally, the $j(V)$ characteristics of a bilayer cell of D3/C₆₀ is displayed for comparison. A complete set of $j(V)$ and EQE curves for all the studied interface layer thicknesses are given in the Supporting Information.

We fabricated devices based on D3/C₆₀ bilayer solar cells, which are also included in Figure 7-4 to evaluate the corresponding heterojunction. The electrical characterization of D1/D2/C₆₀ cascade solar cells comprising a smaller energetic offset between the diketopyrrolopyrroles is included in the supporting information in section 7.

Considerable changes in the short circuit current densities as function of D3 interlayer thickness were detected. For interlayer thicknesses of 3 Å and 6 Å, j_{sc} is increased to 2.50 mA/cm², in comparison to D1/C₆₀ reference devices with a short circuit current density of 1.37 mA/cm². This gain corresponds to an enhancement of the short circuit current densities by 80 %. We note, that in this thickness range, no formation of a closed intermediate layer is expected, as the out-of-plane lattice spacing of D3 on ITO/MoO₃ substrates amounts to 19.3 Å (see supporting information Figure S7-5a). Upon thicker interlayers (> 6 Å) the gain in short circuit current density decreases. Nevertheless, a distinct raise of j_{sc} by 30 % to 40 % was detected for interlayer thicknesses in the range of 12 Å to 50 Å in comparison to D1/C₆₀ bilayer solar cells.

In order to judge on the effect of morphology on this increase, we investigated the solar cell stacks by X-ray diffraction measurements. Neither an effect of the respective D1/D3 layer on the texture of the top-grown C₆₀ layer, nor the formation of a crystalline C₆₀ fraction could be observed by X-ray diffraction measurements (see Supporting Information Figure S7-5a). Therefore, the thickness dependent increase of the short circuit current density is not correlated

to the structural properties of the respective C_{60} acceptor layer. Instead, we ascribe the rise in j_{sc} to a reduced geminate recombination at the D/A interface and thus, to an increased exciton dissociation yield. This assumption is corroborated by the general enhancement of the photocurrent in OPVs with D3 interlayer thicknesses of up to 25 Å, at all biases between -0.5 V and V_{oc} . We note here that a nominal contribution to the photocurrent by the D3 interlayer is present, but as will be discussed in the following section, cannot cause the observed current increase. This is further supported by the poor performance of the D3/ C_{60} devices.

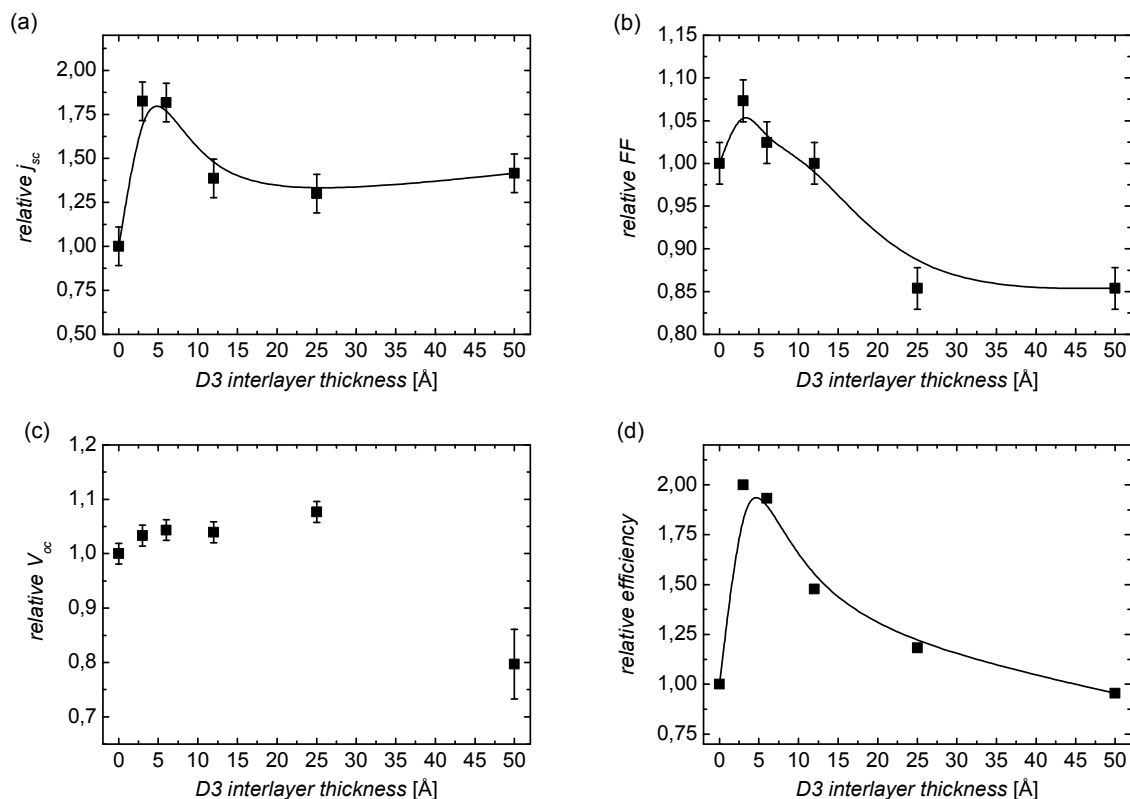


Figure 7-5. Normalized parameters of D1/D3/ C_{60} cascade solar cells with respect to D1/ C_{60} bilayer cells: (a) Short circuit current density; (b) fill factor; (c) open circuit voltage; (d) efficiency as a function of intermediate layer thickness.

As a parameter being sensitive to the macroscopic transport properties the fill factor has been analyzed. For cascade solar cells with an interlayer thickness of 3 Å the fill factor is enhanced to 44 ± 1 %, in comparison to 41 ± 1 % for the unmodified bilayer solar cells. For such thin interfacial layers the reduced recombination losses yield a better fill factor.^[26] However, upon increasing the interlayer thickness, this quantity decreases, resulting in fill factors of 35 % for 25 Å and 50 Å interlayer thicknesses. This behavior can be rationalized, considering the $j(V)$ characteristics of the D3/ C_{60} bilayer cells in Figure 7-4. As indicated by the small fill factor of only 20 % together with the occurrence of an S-shape around V_{oc} and a short circuit current density of 0.49 mA/cm², transport properties are strongly limited in these OPVs. An imbalance of charge carrier mobilities has been identified as a possible source of such S-kinks in current-voltage characteristics, because of the emergence of space charges.^[27-28] OFET measurements

on D3 thin films revealed a hole mobility of $3 \times 10^{-4} \text{ cm}^2\text{V}^{-1}\text{s}^{-1}$ constituting a decrease of an order of magnitude in comparison to D1 ($\mu_h = 5 \times 10^{-3} \text{ cm}^2\text{V}^{-1}\text{s}^{-1}$). Detailed OFET data and statistics are given in the Supporting Information (Table S7-2, Figure S7-9). Accordingly, with the insertion of a D3 interlayer there is a trade-off between improved exciton dissociation efficiency as a consequence of the gradual energetic cascade, slightly enhanced absorption and transport constraints, due to the material inherent low charge carrier mobility.^[17]

The open circuit voltage remains almost unaffected for interlayer thicknesses up to 25 Å. Only a slight monotonous increase from 0.79 V to 0.82 V is detected. Intuitively, upon increasing coverage of the D1 layer with D3, i.e. upon increasing thickness of the latter, the CT state is successively expected to be located at the D3/C₆₀ interface. The V_{oc} of an organic solar cell is related to the corresponding CT state at the D/A interface, which vice versa was shown to correlate to the energy difference between the HOMO level of the donor material and the LUMO level of the acceptor.^[29-30] As shown in Figure 7-3, the associated HOMO level of D3 is shifted by approx. 160 meV towards lower energies in comparison to D1. Thus, the slight augmentation of V_{oc} is in good agreement with our experimental results. Besides, the small gain in V_{oc} is partially attributed to reduced recombination losses, as confirmed by the enhanced photocurrents. For solar cells comprising a 50 Å interlayer, the open circuit voltage is finally reduced to 0.66 V. In this case, the formation of closed monolayers of D3 may be expected, which results in overall transport limitations, associated with the low mobility of the material. As a consequence, the $j(V)$ characteristics of D3/C₆₀ bilayer cells converge for voltages above 0.7 V, accompanied by the observed decrease in V_{oc} (see Figure 7-4).

Finally, as the figure of merit for device performance, the power conversion efficiency η was determined. Due to the distinct increase of the short circuit current densities for 3 Å and 6 Å thick D3 interlayers, the power conversion efficiency could be increased to 0.88 %, i.e. by approx. a factor of two. However, for larger interlayer thicknesses η dropped and the efficiency of cascade solar cells comprising a 50 Å D3 interlayer approximates the power conversion efficiency of D1/C₆₀ reference devices. Thus, in the established cascade OPV structures under study, there is a subtle balance between enhanced photocurrent generation yield and transport constraints.

7.3.2 External Quantum Efficiency of D1/D3/C₆₀ cascade solar cells

After highlighting the influence of the D3 interlayer insertion on the macroscopic solar cell parameters, we now focus on the origin of the photocurrent increase by analyzing the photophysical properties of the individual molecular components. Their respective contributions are correlated to the spectrally resolved photocurrents in the cascade and bilayer cells quantified by the external quantum efficiency (EQE), which is displayed in Figure 7-6a.

The *EQE* spectra resemble the device absorption spectra prepared under the same conditions (see Supporting Information Figure S7-8).

Apparently, for the D1/C₆₀ bilayer cells, both semiconductors D1 and C₆₀ contribute to the photocurrent. Between 400 and 550 nm the photocurrent generation predominantly originates from C₆₀ absorption.^[31] In this spectral range only a small absorption peak at 420 nm can be ascribed to the donor D1. In the wavelength range between 550 and 670 nm the external quantum efficiency is mainly attributed to D1 absorption, according to Figure S7-8. In agreement with these peaks, two distinct absorption peaks are apparent in the UV/VIS absorption spectra at 585 nm and 635 nm.

As a consequence of the implementation of a 3 Å D3 interlayer, the *EQE* is remarkably increased over the whole spectral absorption range. In particular, the *EQE* is strongly increased by a factor of 2.2 in the range of 400-450 nm (Figure 7-6b), where fullerene absorbs intensively. The DPP contributions in this wavelength regime are expected to be rather small and, therefore, cannot be quantified precisely.

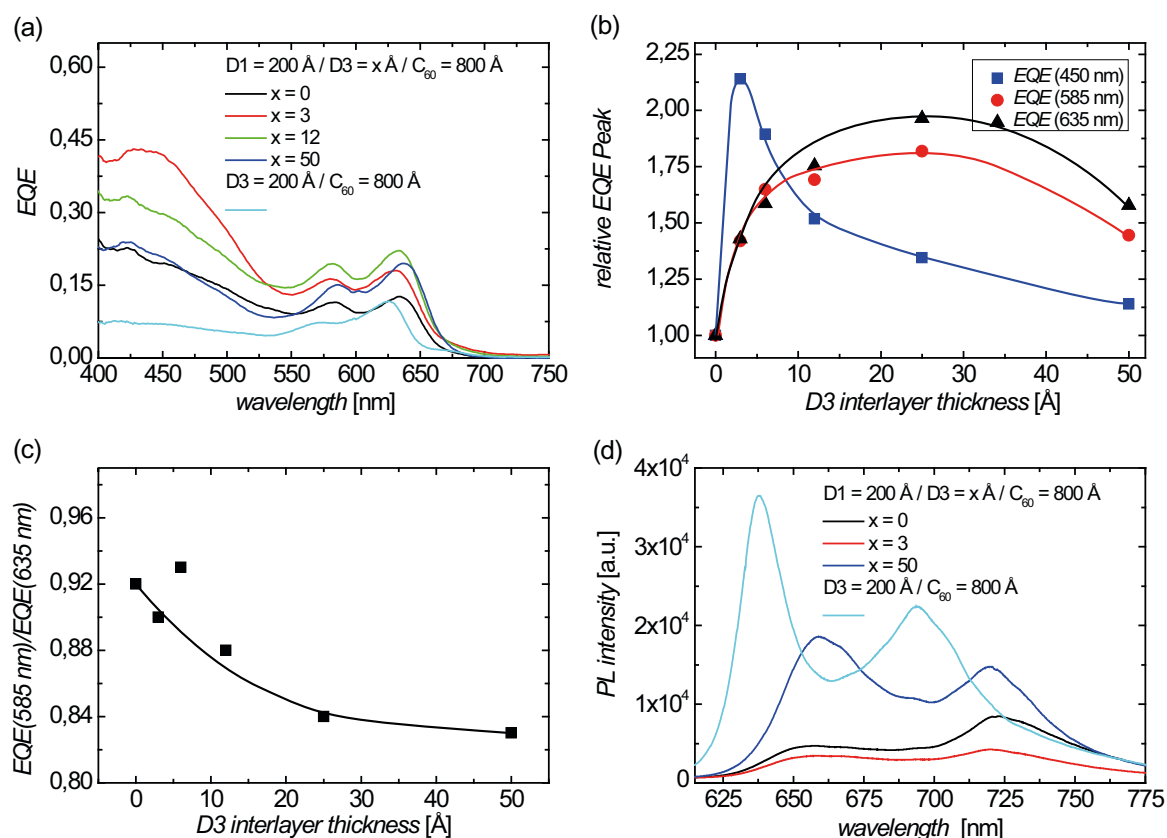


Figure 7-6. a) Selected external quantum efficiencies of cascade and bilayer solar cells. *EQE* measurements were carried out without background illumination at an average light intensity for each wavelength step of 10⁻² mW/cm² b) Relative *EQE* for cascade solar cells under study compared to the reference D1/C₆₀ bilayer device at various wavelengths. c) Ratio of *EQE* peaks at 585 nm and 635 nm. d) Spectrally resolved photoluminescence.

This gain is ascribed to the particular energy level alignment of the cascade solar cell, resulting in a reduction of geminate recombination losses at the D/A interface. The dissociation mechanism for C_{60} excitons is schematically depicted in Figure 7-7. Excitons created in the fullerene form CT excitons at the D3/ C_{60} interface. We propose the D1/D3 interface in close proximity to destabilize these bound CT states due to the favorable energy level cascade. This mechanism may be associated with a delocalization of the positive charge at the D1/D3 interface (see Figure 7-7b), effectively reducing the Coulomb binding force of CT excitons and therefore, rendering their dissociation more efficient.

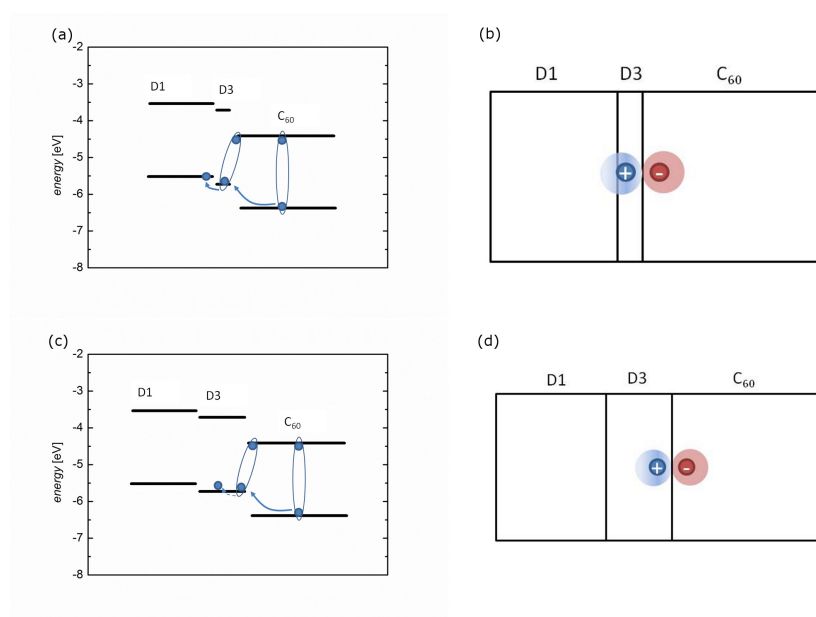


Figure 7-7. a) Energy level alignment in cascade cells with a thin interfacial layer. b) The associated hole delocalization is spread out into the D1 layer. c) Energy level alignment in cascade cells with a thick interfacial layer. d) Hole delocalization mainly restricted to the D3 interlayer. The diffuse shading in (b) and (d) indicates the charge carrier delocalization schematically.

However, with increasing interlayer thickness the C_{60} photocurrent contribution decays and, for 50 Å D3 interlayer thickness approximates the photocurrent contribution of D1/ C_{60} reference devices. Considering the root mean square roughness of 11 Å for ITO/MoO₃/D1 and the lattice spacing of 19.3 Å for D3 (see Supporting Information Figure S7-5) a closed layer may be expected for a 50 Å thick D3 interlayer. Since for such thick interlayers the second interface is spatially separated on molecular length scales, the cascade energy level alignment is limited in supporting the generation of free charge carriers, as schematically depicted in Figure 7-7c. The hole delocalization of the CT state is no longer expected to spread into the D1 layer as schematically illustrated in Figure 7-7d. Thus, upon implementation of thicker interlayers the energetics at the neat D3/ C_{60} interfaces become increasingly relevant for the dissociation of excitons created in C_{60} and therefore dominate the overall photophysical behavior of the device.

This model is corroborated by the bilayer cells based on D3/C₆₀ in Figure 7-6a. It becomes evident, that the fullerene contribution is distinctly limited in these photovoltaic devices, in comparison to the D1/C₆₀ reference cells, whereas the diketopyrrolopyrrole part is much less affected.

In the spectral range of diketopyrrolopyrrole absorption, the *EQE* is also remarkably enhanced by the incorporation of thin D3 layers, as shown in Figure 7-6b for the *EQE* maxima associated with the diketopyrrolopyrrole absorption (approx. 585 nm and 635 nm). For the D3 thicknesses under study, we detected a continuous increase of the *EQE* up to 25 Å, for which the *EQE* is approximately doubled. According to cyclic voltammetry measurements (see Figure 7-3) energy levels are shifted only by approx. 160 meV to lower energies. Therefore, we do not anticipate the formation and dissociation of CT excitons at the D1/D3 interface, since the expected energetic offset is insufficient to overcome exciton binding energies.^[32-34] However, to some extent there may be coupling between D1 and C₆₀, in particular at sites where the interlayer is not completely closed. This coupling across the interlayer may support the spatial separation of excitons, which *vice versa* reduces their Coulomb interaction. Upon further increasing the D3 thickness to 50 Å the *EQE* moderately drops, probably due to transport limitations as discussed above and due to reduced coupling between D1 and C₆₀. But nevertheless the *EQE* is higher by 50 % than for the reference cells. We note that Förster resonant energy transfer from D1 to D3 and subsequent exciton dissociation at the C₆₀ interface is a coexistent mechanism, as can be noticed in our complimentary photoluminescence (PL) measurements, since the photoluminescence spectra of D1 and the absorption spectra of D3 overlap considerably (see Figure 7-6). Moreover, the photocurrent originating from the absorption of the D3 interlayer is slightly but continuously enhanced with increasing interlayer thickness. This can be understood by considering the D3/C₆₀ bilayer cells. Apparently, the diketopyrrolopyrrole absorption peak located at higher wavelength is pronounced. Thus, upon increasing interlayer thickness in cascade solar cells, the small enhancement of the peak at 635 nm in comparison to the one located at 585 nm (see Figure 7-6c) can be attributed to the photocurrent from the D3 interlayer. The peak maximum shifts by approx. 10 nm to higher wavelengths in the cascade solar cells versus D3/C₆₀. This effect will also be elucidated in our complementary PL measurements below.

Evidently, as a function of interlayer thickness, the trend for the diketopyrrolopyrrole contribution to the *EQE* is different from that of the fullerene (see Figure 7-6b). Hence, upon increasing D3 interlayer thickness, the dissociation yield of excitons created either in the donor or the acceptor is differently affected, illustrating the subtle interplay of the interface energetics on the cell performance.

To deepen the insight into the origin of the diketopyrrolopyrrole photocurrent contribution, we conducted complementary photoluminescence measurements. Figure 7-6d shows the PL bands

of four representative solar cells. The broad photoluminescence bands between 625 and 775 nm are ascribed to the radiative decay of D1 and D3 respectively, since the photoluminescence of C_{60} is very weak, due to dipole-forbidden transitions in C_{60} . In accordance with our *EQE* measurements, a distinct quenching of the PL is detected for the implementation of a 3 Å interlayer in comparison to D1/ C_{60} reference cells, highlighting the improved exciton dissociation efficiency in the cascade structure. Bilayer solar cells based on D3 exhibit a pronounced PL with distinct peaks shifted by 20 nm to smaller wavelengths in comparison to D1/ C_{60} . The PL of a cascade solar cell comprising a 50 Å thick D3 interlayer exceeds the PL of D1/ C_{60} considerably, despite the staircase energy level alignment. However, in agreement with our *EQE* measurements the spectra in case of thick intermediate D3 interlayers still resemble those of D1/ C_{60} . This behavior may be a consequence of a morphological templating effect. Possibly, in cascade solar cells, D3 molecules adopt the underlying morphology of D1 which may change their emissive behavior due to a variation of their intermolecular coupling. Merely a small superimposed PL peak at 693 nm is present which can be associated with the peak of the D3/ C_{60} bilayer cell. Given that the PL of the cascade cell comprising a 50 Å thick D3 interlayer exceeds the PL of D1/ C_{60} reference devices and the photocurrent contribution of the diketopyrrolopyrroles is larger in the former, indicates that a Förster type resonant energy transfer from D1 to D3 takes place. This process is expected to occur since photoluminescence spectra of D1 and the absorption spectra of D3 overlap considerably. Subsequent radiative decay on D3 molecules seems to be more efficient which leads to the enhanced PL in case of the cascade cell with a 50 Å thick D3 interlayer. These data illustrate the crucial role of the cascade interface energetics which has a huge impact on macroscopic device performance.

7.4 Conclusion

Small molecule diketopyrrolopyrrole derivatives were synthesized to provide donor materials with a distinct energy level gradation. Upon pyridine substitution of the terminal phenyl-group in D1, frontier energy levels are shifted by 160 meV towards lower energies in D3. These diketopyrrolopyrroles were utilized in combination with the fullerene C_{60} to establish an energetic cascade in organic planar heterojunction solar cells comprising three photoactive layers. We investigated the thickness dependent effects of thin D3 interfacial layers on the macroscopic parameters of these cascade cells. A distinct increase of the short circuit current density by 80 % was identified for D3 layer thicknesses of 3 Å and 6 Å compared to D1/ C_{60} bilayer reference cells. *EQE* measurements reveal in particular the fullerene contribution to the photocurrent to be enhanced for these device structures. We attribute this to the distinct energy level alignment which destabilizes bound CT states at the D3/ C_{60} interface. This mechanism may be associated with hole delocalization into the adjacent D1 layer with its suited energy level alignment, reducing geminate recombination losses. The *EQE* is

continuously enhanced in the spectral range of the diketopyrrolopyrrole absorption for interlayer thicknesses of up to 25 Å. Whereas the energetic offset at the D1/D3 interface is expected to be too small for exciton dissociation, coupling between D1 and C₆₀ through the cascade and at specific sites could promote the separation of excitons. As a result of the reduced recombination losses for interlayer thicknesses of 3 Å and 6 Å the power conversion efficiency could be improved by approximately a factor of two. These results highlight the crucial role of interface energetics and morphology for the dissociation and recombination processes in organic photovoltaics and the possibilities of specifically targeting these recombination losses by the introduction of a tailored energy cascade.

7.5 Experimental Section

7.5.1 Materials and methods

All reagents were used without further purification unless otherwise noted. ¹H NMR (300 MHz) spectra were recorded on a Bruker AC 300 spectrometer and calibrated according to the respective solvent resonance signal. Absorption measurements were carried out on a JASCO V-670 spectrophotometer in toluene solutions at a concentration of 10⁻⁵ mol L⁻¹. Solid state spectra were recorded on thin films spincoated onto glass substrates from a 7 mg mL⁻¹ chloroform solution at 1500 rpm. Cyclic voltammetry was performed under moisture- and oxygen-free conditions using a 0.1 M tetra-*n*-butylammonium hexafluorophosphate in dichloromethane electrolyte solution. A standard three-electrode assembly connected to a potentiostat (model 263A, EG&G Princeton Applied Research) was used at a scanning rate of 50 mV s⁻¹. The working electrode was a 3.14 mm² platinum disk. A platinum wire in dichloromethane was used as counter electrode and the quasi-reference electrode consisted of an Ag wire in an AgNO₃/acetonitrile solution (0.1 M). The measurements were calibrated with an external ferrocene/ferrocenium standard, IP and EA values were calculated considering the solvent effects as per a published procedure.^[25] Thermogravimetric measurements were conducted on a Mettler Toledo TGA/SDTA 851e under N₂ atmosphere at a heating rate of 10 K min⁻¹. Temperature of decomposition (T_{5%}) was calculated from the 5% onset of the respective curve. Differential scanning calorimetry experiments were conducted at heating rates of 40 K min⁻¹ under N₂ atmosphere with a Perkin Elmer Diamond DSC, calibrated with indium. Melting (*T_m*) and crystallization temperatures (*T_c*) were determined from the peak onset by tangential fitting.

7.5.2 Device preparation and characterization

Organic solar cells were processed on ITO covered glass substrates. Before processing, substrates were cleaned by sonication in acetone and isopropanol for 10 minutes. The metal

oxide, organic and metal layers were deposited subsequently in-situ by thermal evaporation from Knudsen cells in a vacuum system at a base pressure of 10^{-8} mbar. For OPVs a hole transport layer consisting of molybdenum oxide (MoO_3) (Mateck) was used. The organic materials D1 and D3 and BPhen (Bathophenanthroline, Sigma-Aldrich) were used without further purification. C_{60} (Creaphys) was purified twice by thermal gradient sublimation. The silver cathode was processed through a shadow mask with a diameter of 2 mm. The OPV stacks under study comprise the following layer sequence: ITO/ MoO_3 (100 Å)/D1(200 Å)/D3(x Å)/ C_{60} (800 Å)/BPhen(100 Å)/Ag(600 Å). It should be noted, that this design was not optimized to attain highest efficiencies possible, but rather to achieve a sufficiently good device performance without shortening contacts. The solar cell parameters were measured in-situ. For measuring the $j(V)$ characteristics we used a Keithley source measurement unit 236. Illumination was carried out with a solar simulator LOT Oriel LS0306. The intensity was calibrated to 1 sun at AM1.5 (100 mW/cm^2). Spectrally resolved photoluminescence measurements were conducted using a cw laser with an excitation wavelength of 532 nm. The laser spot was focused on the respective solar cell structures with a constant excitation power density of 6 mW/cm^2 . The spectrally resolved PL emission was detected using a combination of a Pixis 100 BR eXcelon CCD camera and a SP 2500 spectrometer from Princeton Instruments. The integration time was 40 s for each sample.

To resemble the device architecture of the photovoltaic cells, morphological studies were conducted on D1(200 Å)/D3(x Å)/ C_{60} (800 Å) stacks. $\theta/2\theta$ -scans were performed with an X-ray reflectometer 3003 T/T by GE Inspection Technologies using Cu $K_{\alpha 1}$ -radiation ($\lambda = 1.54056 \text{ Å}$) with an angular resolution of 0.01 degrees.

7.5.3 Synthesis procedures for the DPP compounds

All syntheses were conducted under argon using a double manifold Schlenk line. Glassware was severely dried under high vacuum. Solvents were degassed by three freeze-pump-thaw cycles.

D1. Potassium carbonate (366 mg, 2.65 mmol), 4,4,5,5-tetramethyl-2-phenyl-1,3,2-dioxaborolan (270 mg, 1.32 mmol), $\text{DPP}[\text{T}]_2\text{Br}_2$ (300 mg, 0.33 mmol) and tetrakis(triphenylphosphine)palladium(0) (38.2 mg, 33 μmol) were suspended in 5.5 mL degassed DMF. The mixture was heated at 100°C for 72 h. After cooling to room temperature, 100 mL water and 100 mL chloroform were added. The phases were separated and the aqueous phase was extracted with chloroform (2 x 50 mL) and ethyl acetate (1 x 50 mL). The combined organic layers were dried over magnesium sulfate and the solvent was removed under reduced pressure. Column chromatography on silica gel using a hexane/chloroform 1:1 mixture afforded 244 mg D1 (0.27 mmol, 82%) as a purple solid. ^1H -NMR (300 MHz, CHCl_3): δ (ppm) 8.95 (d, 2 H, $J = 4.2 \text{ Hz}$, H-4/5), 7.70-7.67 (m, 4 H, phenyl-H), 7.47 (d, 2 H, H-4/5), 7.46-7.36 (m, 6 H, phenyl-H, H-4/5), 4.08 (d, 4 H,

$J = 7.8$ Hz, H-13), 2.05-1.92 (m, 2 H, H-14), 1.37-1.19 (m, 48 H, CH₂), 0.86-0.81 (m, 12 H, CH₃); ¹³C-NMR: δ (ppm) 161.89, 149.77, 140.05, 136.91, 133.33, 129.30, 128.96, 126.27, 124.59, 108.33, 46.41, 38.05, 32.03, 31.98, 31.45, 30.20, 29.87, 29.72, 29.45, 26.48, 22.81, 22.77, 14.26; HRMS (ESI+, [M]⁺, C₅₈H₈₀N₂O₂S₂, m/z: 900.56557 (calc), 900.56586 (observed).

D2. Potassium carbonate (366 mg, 2.65 mmol), 4,4,5,5-tetramethyl-2-phenyl-1,3,2-dioxaborolan (300 mg, 1.46 mmol), DPP[T]₂Br₂ (300 mg, 0.33 mmol) and tetrakis(triphenylphosphine)-palladium(0) (38.2 mg, 33 μ mol) were suspended in 5.5 mL degassed DMF. The mixture was heated at 100 °C for 19 h. After cooling to room temperature, 100 mL water and 100 mL chloroform were added. The phases were separated and the aqueous phase was extracted with chloroform (4 x 50 mL) and ethyl acetate (1 x 50 mL). The combined organic layers were washed with brine (1 x 100 mL), dried over magnesium sulfate and the solvent was removed under reduced pressure. Column chromatography on silica gel using a chloroform/ethyl acetate 5:1 to 0:1 gradient afforded 298 mg D2 (0.33 mmol, 100%) as a purple solid. ¹H-NMR (300 MHz, CHCl₃): δ (ppm) 8.95 (d, 2 H, $J = 1.8$ Hz, H-12), 8.93 (d, 2 H, $J = 4.2$ Hz, H-4/5), 8.60 (dd, 2 H, $J = 4.8$ Hz, $J = 1.5$ Hz, H-8/10), 7.94 (ddd, 2 H, $J = 8.03$ Hz, $J = 2.33$ Hz, $J = 1.73$ Hz, H-9), 7.53 (d, 2 H, $J = 4.2$ Hz, H-4/5), 7.41-7.32 (m, 2 H, H-8/10), 4.07 (d, 4 H, $J = 7.5$ Hz, H-13), 2.04-1.91 (m, 2 H, H-14), 1.45-1.10 (m, 48 H, CH₂), 0.91-0.87 (m, 12 H, CH₃); ¹³C-NMR: δ (ppm) 161.77, 149.77, 147.21, 145.55, 139.96, 136.71, 133.26, 130.05, 129.42, 125.60, 123.97, 108.73, 45.46, 38.04, 32.00, 31.92, 31.38, 30.16, 29.83, 29.67, 29.43, 26.42, 26.39, 22.79, 22.76, 14.25, 14.21; HRMS (ESI+, [M+H]⁺, C₅₆H₇₉N₄O₂S₂, m/z: 903.56390 (calc), 903.56499 (observed).

D3. Potassium carbonate (366 mg, 2.65 mmol), 4,4,5,5-tetramethyl-2-phenyl-1,3,2-dioxaborolan (203 mg, 0.99 mmol), DPP[T]₂Br₂ (300 mg, 0.33 mmol) and tetrakis(triphenylphosphine)-palladium(0) (38.2 mg, 33 μ mol) were suspended in 5.5 mL degassed DMF. The mixture was heated at 100 °C for 90 h. After cooling to room temperature, 100 mL water and 100 mL ethyl acetate were added. The phases were separated and the aqueous phase was extracted with chloroform (3 x 50 mL) and ethyl acetate (1 x 50 mL). The combined organic layers were dried over magnesium sulfate and the solvent was removed under reduced pressure. Column chromatography on silica gel using a chloroform/ethyl acetate 10:1 mixture afforded 205 mg D3 (0.23 mmol, 69%) as a purple solid. ¹H-NMR (300 MHz, CHCl₃): δ (ppm) 8.92 (d, 2 H, $J = 4.2$ Hz, H-4/5), 8.66 (d, 4 H, $J = 3.6$ Hz, H-9, H-11), 7.63 (d, 2 H, $J = 4.2$ Hz, H-4/5), 7.53 (d, 4 H, $J = 6.0$ Hz, H-8, H-12), 4.06 (d, 4 H, $J = 7.8$ Hz, H-13), 2.01-1.87 (m, 2 H, H-14), 1.42-1.01 (m, 48 H, CH₂), 0.91-0.76 (m, 12 H, CH₃); ¹³C-NMR: δ (ppm) 161.72, 150.27, 145.76, 140.00, 136.75, 131.17, 126.90, 120.15, 109.29, 46.47, 38.10, 32.02, 31.96, 31.41, 30.17, 29.83, 29.71, 29.44, 26.44, 22.80, 22.77, 14.25; HRMS (ESI+, [M+H]⁺, C₅₆H₇₉N₄O₂S₂, m/z: 903.56390 (calc), 903.56373 (observed).

7.6 Acknowledgement

C. J. M and M. B. contributed equally to this work. We acknowledge financial support from the Bavarian State Ministry of Education, Science and the Arts (Solar technologies go hybrid). C. J. M. thanks the Fonds der Chemischen Industrie for funding the PhD with a Kekulé scholarship and the German National Academic Foundation for other support during the PhD. Support from the Elitenetzwerk Bayern (ENB), Macromolecular Science is also kindly acknowledged. M. B. acknowledges financial support by DFG focus project SPP 1355.

7.7 References

- [1] J. Roncali, P. Leriche, P. Blanchard, *Adv. Mater.* **2014**, *26*, 3821.
- [2] B. Walker, C. Kim, T.-Q. Nguyen, *Chem. Mater.* **2011**, *23*, 470.
- [3] M. Riede, C. Uhrich, J. Widmer, R. Timmreck, D. Wynands, G. Schwartz, W.-M. Gnehr, D. Hildebrandt, A. Weiss, J. Hwang, S. Sundarraj, P. Erk, M. Pfeiffer, K. Leo, *Adv. Funct. Mater.* **2011**, *21*, 3019.
- [4] J. Meiss, T. Menke, K. Leo, C. Uhrich, W.-M. Gnehr, S. Sonntag, M. Pfeiffer, M. Riede, *Appl. Phys. Lett.* **2011**, *99*, 043301.
- [5] S. Qu, H. Tian, *Chem. Commun.* **2012**, *48*, 3039.
- [6] W. Li, K. H. Hendriks, A. Furlan, W. S. Roelofs, S. C. Meskers, M. M. Wienk, R. A. Janssen, *Adv. Mater.* **2014**, *26*, 1565.
- [7] W. Li, K. H. Hendriks, A. Furlan, M. M. Wienk, R. A. Janssen, *J. Am. Chem. Soc.* **2015**, *137*, 2231.
- [8] D. Zhang, C. Yu, Z. Liu, Y. Yang, J. Yao, Z. Cai, H. Luo, G. Zhang, *J. Mater. Chem. C* **2014**, *2*, 10101.
- [9] S. Y. Liu, W. Q. Liu, J. Q. Xu, C. C. Fan, W. F. Fu, J. Ling, J. Y. Wu, M. M. Shi, A. K. Jen, H. Z. Chen, *ACS Appl Mater Interfaces* **2014**, *6*, 6765.
- [10] W. S. Yoon, S. K. Park, I. Cho, J.-A. Oh, J. H. Kim, S. Y. Park, *Adv. Funct. Mater.* **2013**, *23*, 3519.
- [11] A. Sharenko, M. Kuik, M. F. Toney, T.-Q. Nguyen, *Adv. Funct. Mater.* **2014**, *24*, 3543.
- [12] D. Fernandez, A. Viterisi, J. W. Ryan, F. Gispert-Guirado, S. Vidal, S. Filippone, N. Martin, E. Palomares, *Nanoscale* **2014**, *6*, 5871.
- [13] J. Huang, C. Zhan, X. Zhang, Y. Zhao, Z. Lu, H. Jia, B. Jiang, J. Ye, S. Zhang, A. Tang, Y. Liu, Q. Pei, J. Yao, *ACS Appl Mater Interfaces* **2013**, *5*, 2033.

- [14] V. S. Gevaerts, E. M. Herzig, M. Kirkus, K. H. Hendriks, M. M. Wienk, J. Perlich, P. Müller-Buschbaum, R. A. J. Janssen, *Chem. Mater.* **2014**, *26*, 916.
- [15] C. W. Tang, *Appl. Phys. Lett.* **1986**, *48*, 183.
- [16] M. A. Green, K. Emery, Y. Hishikawa, W. Warta, E. D. Dunlop, *Progress in Photovoltaics: Research and Applications* **2014**, *22*, 701.
- [17] K. Cnops, B. P. Rand, D. Cheyns, B. Verreert, M. A. Empl, P. Heremans, *Nat Commun* **2014**, *5*, 3406.
- [18] G. Zhang, W. L. Li, B. Chu, L. L. Chen, F. Yan, J. Z. Zhu, Y. R. Chen, C. S. Lee, *Appl. Phys. Lett.* **2009**, *94*, 143302.
- [19] Z. K. Tan, K. Johnson, Y. Vaynzof, A. A. Bakulin, L. L. Chua, P. K. Ho, R. H. Friend, *Adv. Mater.* **2013**, *25*, 4131.
- [20] A. Barito, M. E. Sykes, D. Bilby, J. Amonoo, Y. Jin, S. E. Morris, P. F. Green, J. Kim, M. Shtein, *J. Appl. Phys.* **2013**, *113*, 203110.
- [21] T. D. Heidel, D. Hochbaum, J. M. Sussman, V. Singh, M. E. Bahlke, I. Hiromi, J. Lee, M. A. Baldo, *J. Appl. Phys.* **2011**, *109*, 104502.
- [22] A. K. Palai, S. P. Mishra, A. Kumar, R. Srivastava, M. N. Kamalasanan, M. Patri, *Macromol. Chem. Phys.* **2010**, *211*, 1043.
- [23] C. J. Mueller, C. R. Singh, M. Fried, S. Huettner, M. Thelakkat, *Adv. Funct. Mater.* **2015**, *25*, 2725.
- [24] K. H. Hendriks, W. Li, G. H. Heintges, G. W. van Pruissen, M. M. Wienk, R. A. Janssen, *J. Am. Chem. Soc.* **2014**, *136*, 11128.
- [25] K. Gräf, M. A. Rahim, S. Das, M. Thelakkat, *Dyes and Pigments* **2013**, *99*, 1101.
- [26] J. D. Servaites, M. A. Ratner, T. J. Marks, *Energy & Environmental Science* **2011**, *4*, 4410.
- [27] W. Tress, A. Petrich, M. Hummert, M. Hein, K. Leo, M. Riede, *Appl. Phys. Lett.* **2011**, *98*, 063301.
- [28] J. Wagner, M. Gruber, A. Wilke, Y. Tanaka, K. Topczak, A. Steindamm, U. Hörmann, A. Opitz, Y. Nakayama, H. Ishii, J. Pflaum, N. Koch, W. Brütting, *J. Appl. Phys.* **2012**, *111*, 054509.
- [29] K. Vandewal, K. Tvingstedt, A. Gadisa, O. Inganäs, J. V. Manca, *Physical Review B* **2010**, *81*, 125204.

- [30] U. Hörmann, J. Kraus, M. Gruber, C. Schuhmair, T. Linderl, S. Grob, S. Kapfinger, K. Klein, M. Stutzman, H. J. Krenner, W. Brütting, *Physical Review B* **2013**, *88*, 235307.
- [31] Y. Wang, J. M. Holden, A. M. Rao, P. C. Eklund, U. D. Venkateswaran, D. Eastwood, R. L. Lidberg, G. Dresselhaus, M. S. Dresselhaus, *Physical Review B* **1995**, *51*, 4547.
- [32] M. Knupfer, *Applied Physics A: Materials Science & Processing* **2003**, *77*, 623.
- [33] X. Y. Zhu, Q. Yang, M. Muntwiler, *Acc. Chem. Res.* **2009**, *42*, 1779.
- [34] M. Brendel, S. Krause, A. Steindamm, A. K. Topczak, S. Sundarraj, P. Erk, S. Höhla, N. Fruehauf, N. Koch, J. Pflaum, *Adv. Funct. Mater.* **2015**, *25*, 1565.

Supporting Information

Absorption – Peak Fitting	282
Cyclic Voltammetry	283
Thermogravimetric Analysis	284
NMR spectra of monomer compounds	284
Powder X-ray diffraction (PXRD)	287
Structural investigation by X-ray diffraction and atomic force microscopy	288
Opto-electrical characterization of D1/D2/C ₆₀ cascade solar cells	289
Organic Field Effect Transistors	291
Quantum Computational Methods	292
Supporting References	293

Absorption – Peak Fitting

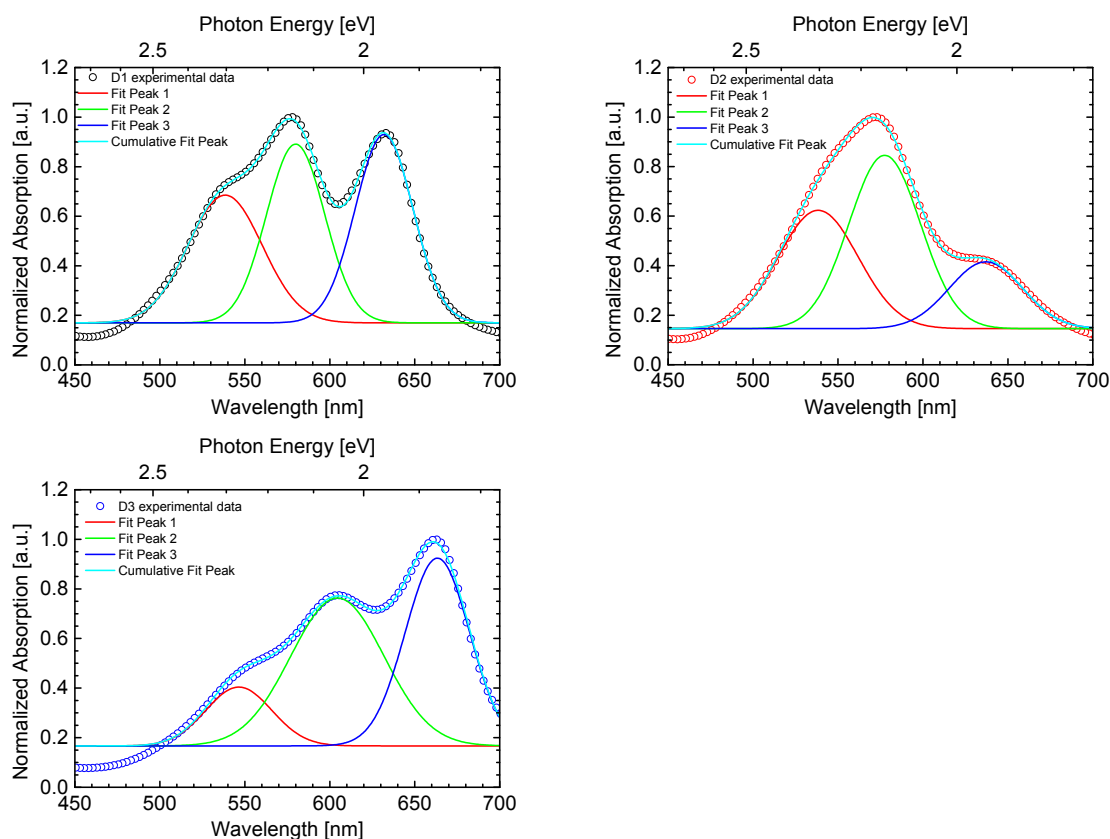


Figure S7-1. Peak fitting of the VIS absorption transitions for D1-D3.

Table S7-1. Optical transitions for D1-D3.

compound / transition	λ [nm]	area a.u.	intensity a.u.
D1			
A ₂₋₀	538.4	28.2	0.52
A ₁₋₀	579.9	31.0	0.72
A ₀₋₀	631.9	32.4	0.76
D2			
A ₂₋₀	538.3	28.2	0.48
A ₁₋₀	577.5	36.9	0.70
A ₀₋₀	637.1	14.6	0.27
D3			
A ₂₋₀	546.4	11.5	0.24
A ₁₋₀	604.5	41.1	0.60
A ₀₋₀	663.3	35.9	0.76

Cyclic Voltammetry

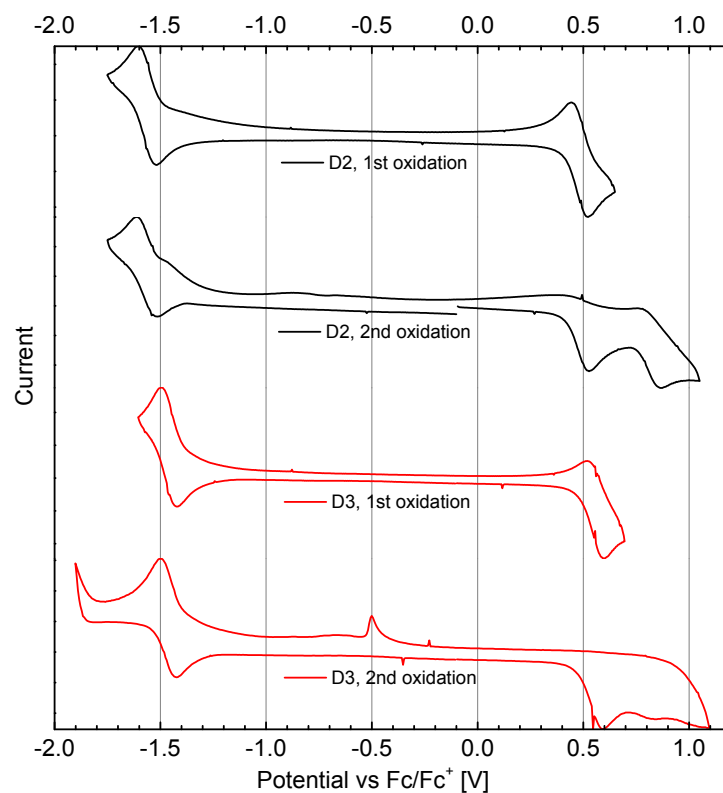


Figure S7-2. Reversible and irreversible oxidations of pyridine-capped DPP dyes D2 and D3 measured in a 0.1 M tetra-*n*-butylammonium hexafluorophosphate / dichloromethane electrolyte solution at a scan rate of 50 mV s⁻¹.

Thermogravimetric Analysis

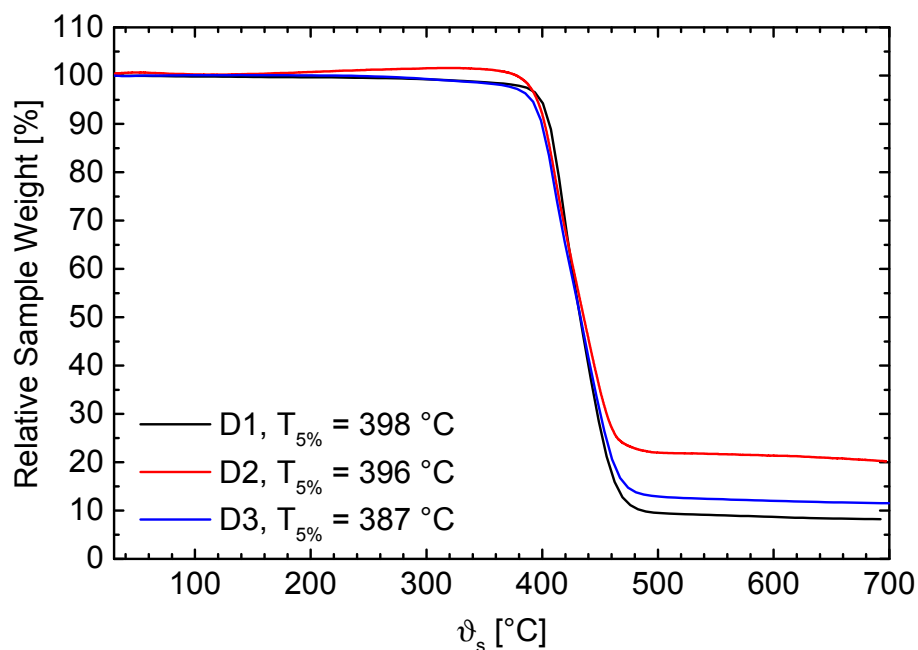
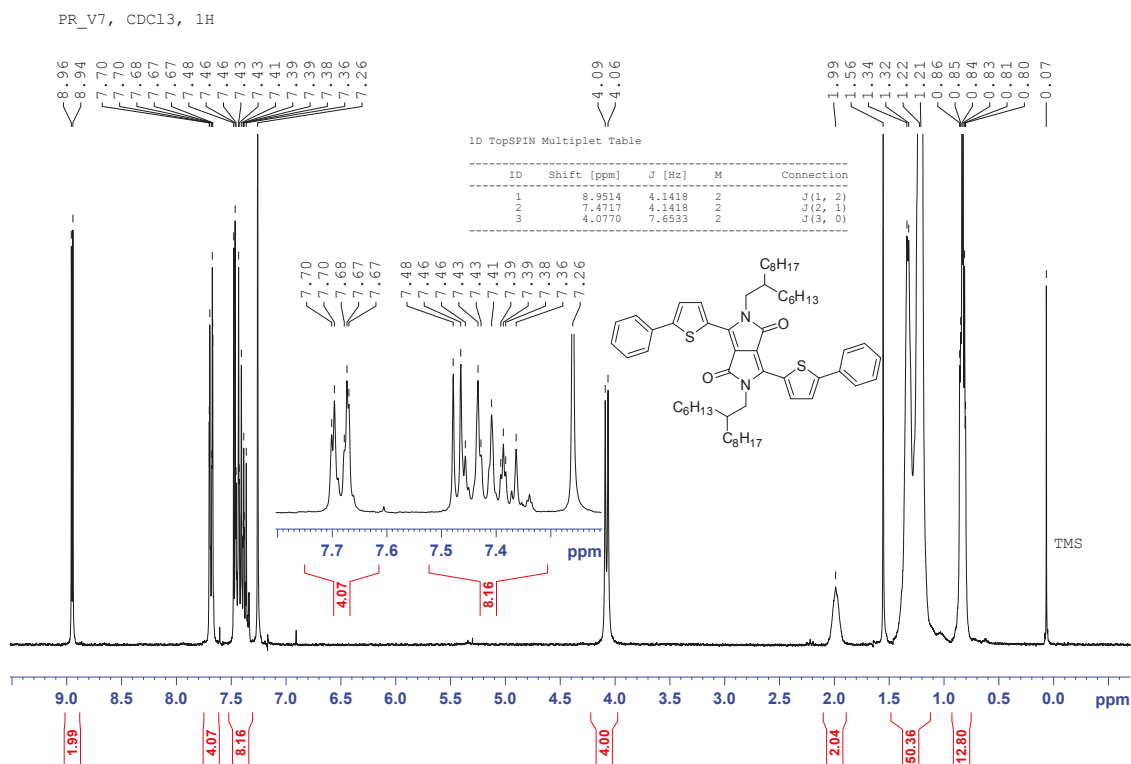


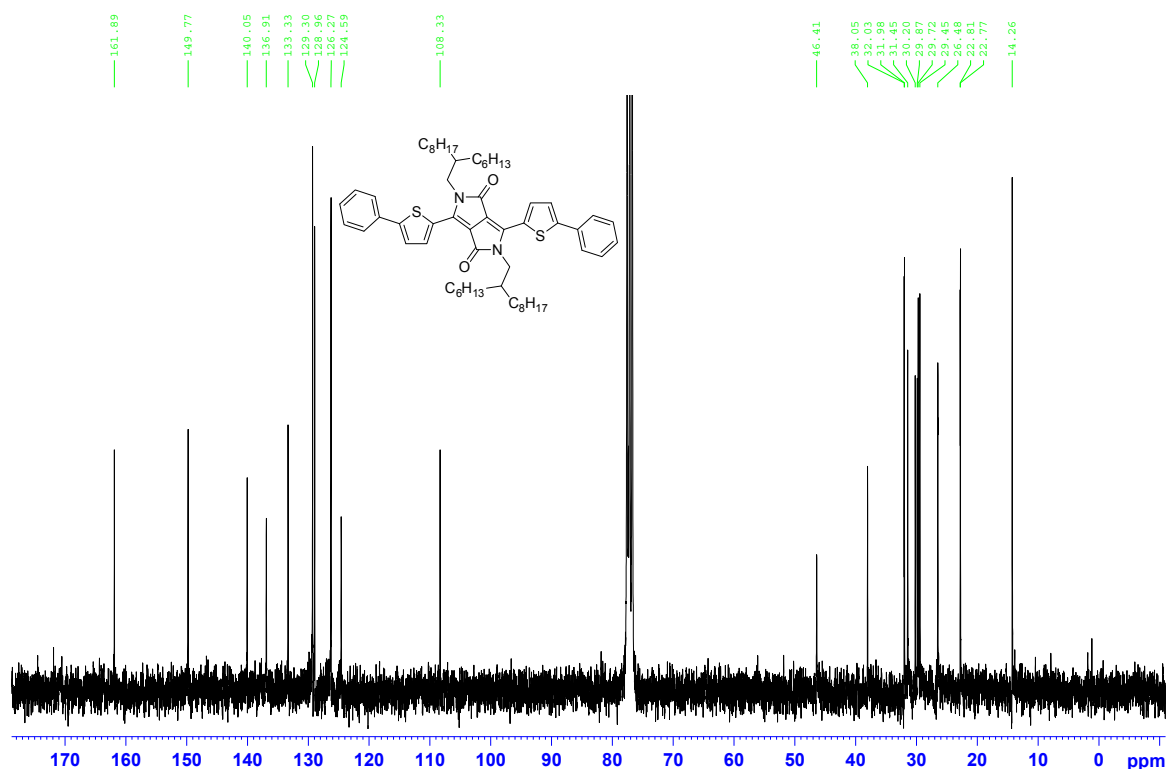
Figure S7-3. Thermogravimetric analysis for the DPP dye molecules at 10 K s^{-1} under nitrogen.

NMR spectra of monomer compounds.

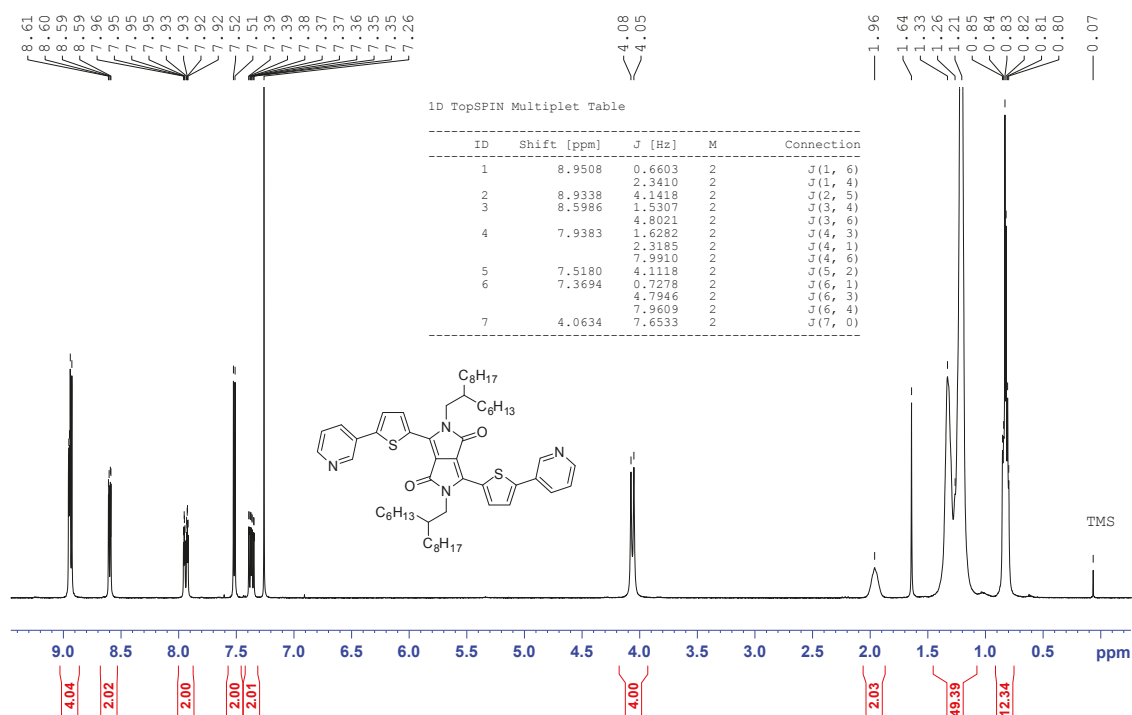


7 Diketopyrrolopyrroles with a Distinct Energy Level Cascade for Efficient Charge Carrier Generation in Organic Solar Cells

D1, ¹³C-NMR, CDCl₃

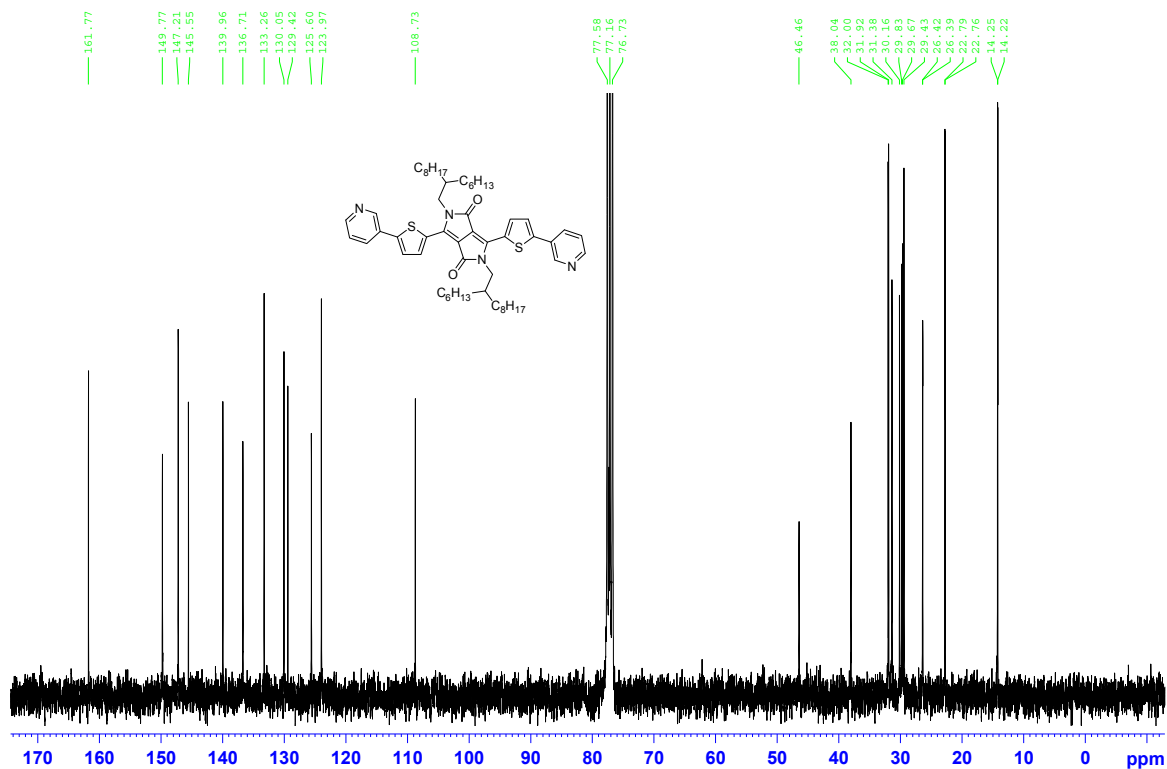


PR_V2F, CDCl₃, ¹H

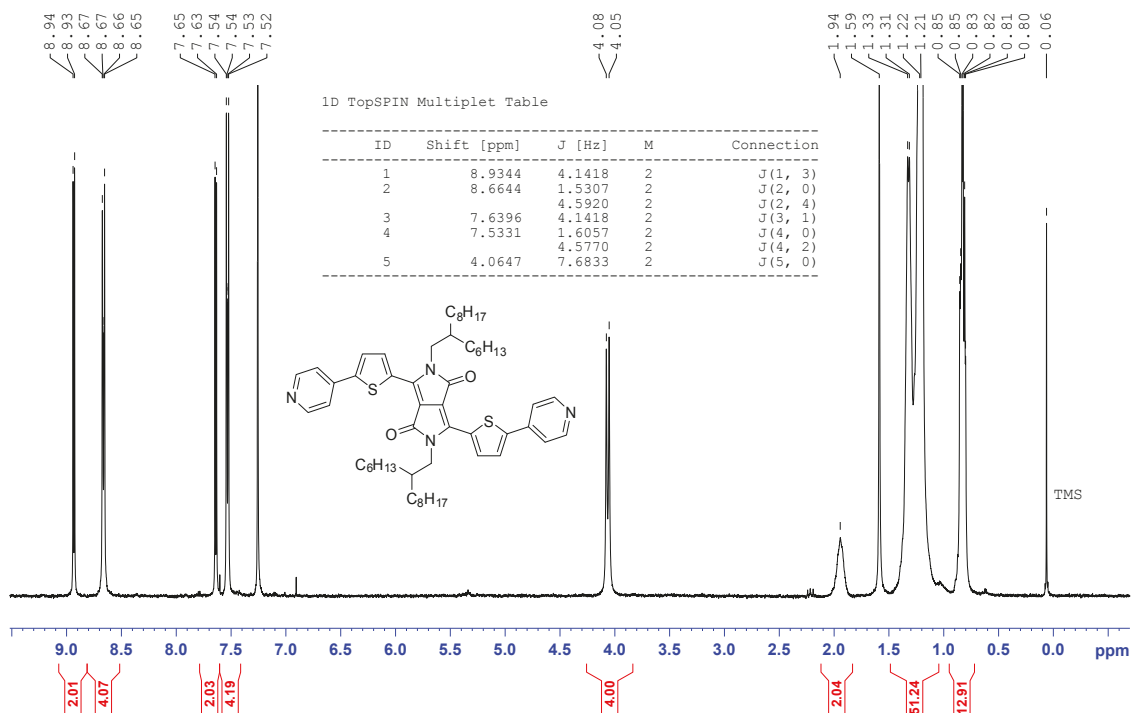


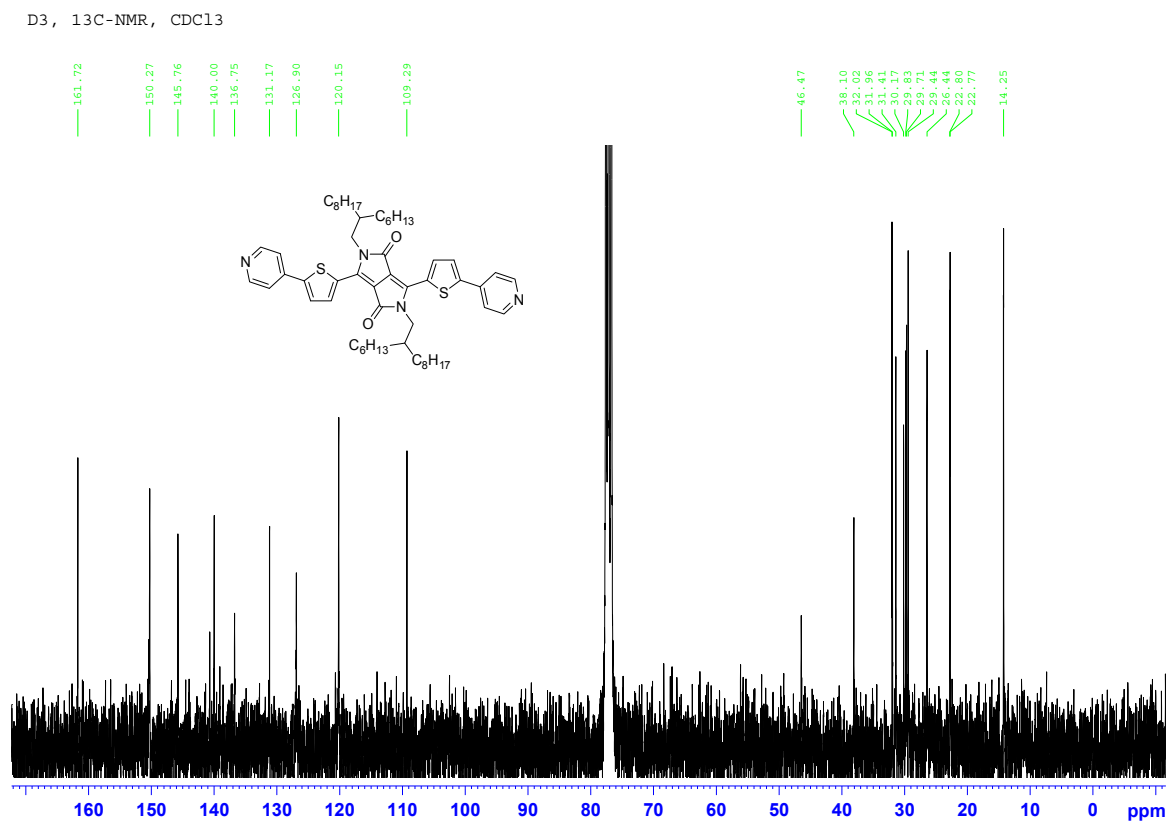
7 Diketopyrrolopyrroles with a Distinct Energy Level Cascade for Efficient Charge Carrier Generation in Organic Solar Cells

D2, ¹³C-NMR, CDCl₃



PR_V3 (DPPsmb3), CDCl₃, ¹H





Powder X-ray diffraction (PXRD)

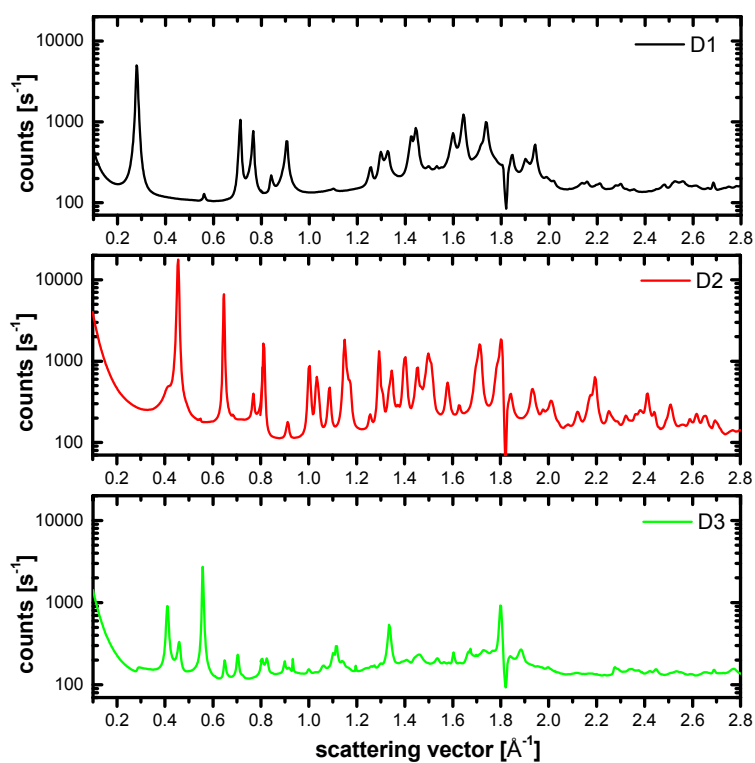


Figure S7-4. SAXS/WAXS XRD of free standing bulk films (freeze dried from solution). The negative spike at $q=1.8$ is caused by a detector changeover.

Structural investigation by X-ray diffraction and atomic force microscopy

To investigate the crystallinity and the texture of the photo-active materials, X-ray diffraction measurements were carried out in Bragg-Brentano geometry for cascade and bilayer solar cells. Figure S7-5a) shows the diffraction spectra, which refer to q_z along the surface normal and hence probe the out-of plane crystallinity. For both D1/C₆₀ and D3/C₆₀ bilayer cells a diffraction peak is observed at $q_z = 0.32 \text{ \AA}^{-1}$ which is attributed to the first order diffraction peak of the respective diketopyrrolopyrrole. These peaks correspond to a lattice spacing of 19.3 \AA . The associated peak is also existent in cascade devices, exemplarily shown in Figure S7-5a), for an interlayer thickness of 50 \AA . Since the structural motif of the molecules D1 and D3 is very similar and the growth mode on ITO/MoO₃ substrates appear to be the same, it seems intuitive that D3 adopts the molecular orientation of the underlying D1 layer in cascade solar cells.

For all bilayer cells and cascade cells under study, we did not detect the formation of a crystalline C₆₀ fraction. Thus, the thickness dependent enhancement of the observed photocurrents, as described in section 3.1 of the manuscript, cannot be ascribed to a morphological change of the respective C₆₀ layer.

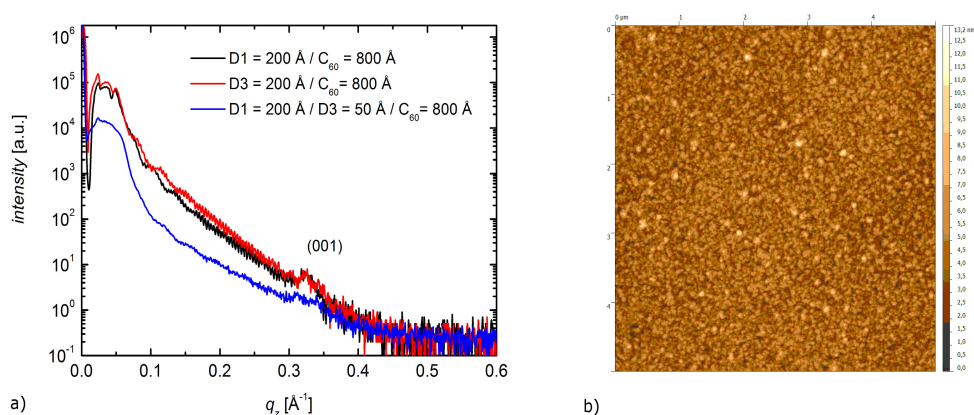


Figure S7-5. a) X-ray diffraction spectra of a cascade device with a 50 \AA thick D3 interlayer and the corresponding bilayer solar cells. b) AFM image of $5 \times 5 \text{ \mu m}^2$ ITO/MoO₃/D1 stack with $\sigma_{\text{rms}} = 11 \text{ \AA}$.

Moreover, to conclude on the coverage of the diketopyrrolopyrrole underlayer upon increasing interlayer thickness, the morphology of ITO/MoO₃/D1 thin films was investigated by atomic force microscopy. Figure S7-5b) depicts a $5 \times 5 \text{ \mu m}^2$ scan, which shows a smooth surface with a root mean square roughness (σ_{rms}) of 11 \AA . Occasionally, isolated islands are existent with a maximum height of up to 130 \AA . Considering these values in combination with the D3 lattice spacing of 19.3 \AA , the formation of an almost closed D3 interlayer seems to be justified for a thickness of 50 \AA .

Opto-electrical characterization of D1/D2/C₆₀ cascade solar cells

In section 3.2 of the manuscript the impact of the insertion of the D3 interlayer on the external quantum efficiency was illustrated. We now focus on a comparison of these devices with D1/D2/C₆₀ cascade solar cells, comprising a smaller energetic offset between the donor material and the interlayer (see Figure 2 of the manuscript). The associated *EQEs* are presented in Figure S7-6. The implementation of a 6 Å thick D2 interlayer results in a distinct increase of the *EQE* over the whole spectral absorption range, in comparison to D1/C₆₀ reference cells. Evidently, for D2 and D3 interlayer thicknesses of 6 Å, respectively, the *EQE* increase in the diketopyrrolopyrrole absorption range between 550 and 670 nm is almost identical. Thus, we attribute this enhancement to the microscopic mechanisms already-discussed in section 3.2 of the manuscript.

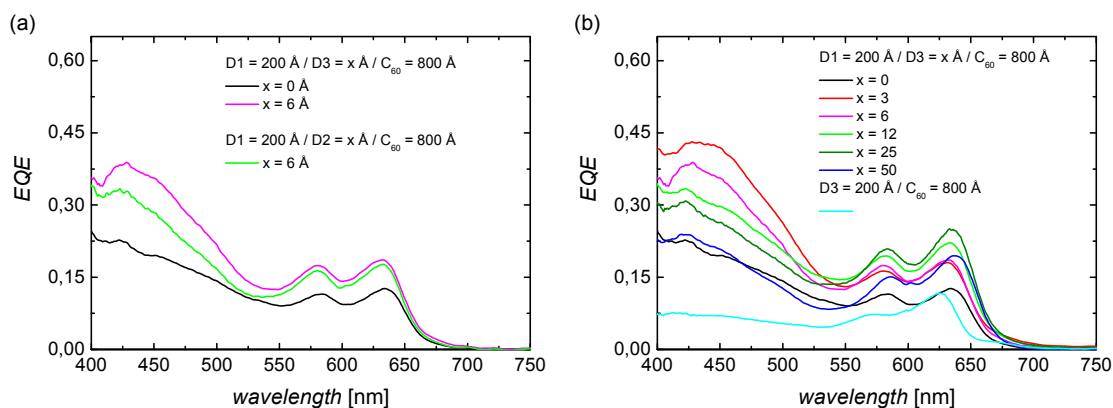


Figure S7-6. a) *EQE* of D1/D2/C₆₀ and D1/D3/C₆₀ cascade solar cells and D1/C₆₀ bilayer reference devices. b) *EQE* of all D1/D3/C₆₀ cascade devices.

In contrast, the fullerene photocurrent contribution between 400 and 550 nm varies for the different interlayer materials. In this spectral range the *EQE* of D1/D3/C₆₀ exceeds that of D1/D2/C₆₀ cascade cells markedly. This observation is ascribed to the varying energetics at the respective donor/interlayer interface. Due to the smaller energetic offset at the D1/D2 interface in comparison to the D1/D3 cascade the destabilization of bound CT states is less efficient resulting in a reduced CT dissociation yield.

This explanation is supported by the corresponding short circuit current densities obtained from the $j(V)$ characteristics which are depicted in Figure S7-7. Remarkably, apart from the difference in j_{sc} the $j(V)$ curve characteristics are very similar for D1/D2/C₆₀ and D1/D3/C₆₀ cascade cells rendering the other solar cell parameters such as V_{oc} and FF almost unaffected (see Table S2). These results illustrate the crucial role of tailoring interface energetics at the hetero-junction between photo-active materials for the optimization of cascade solar cells.

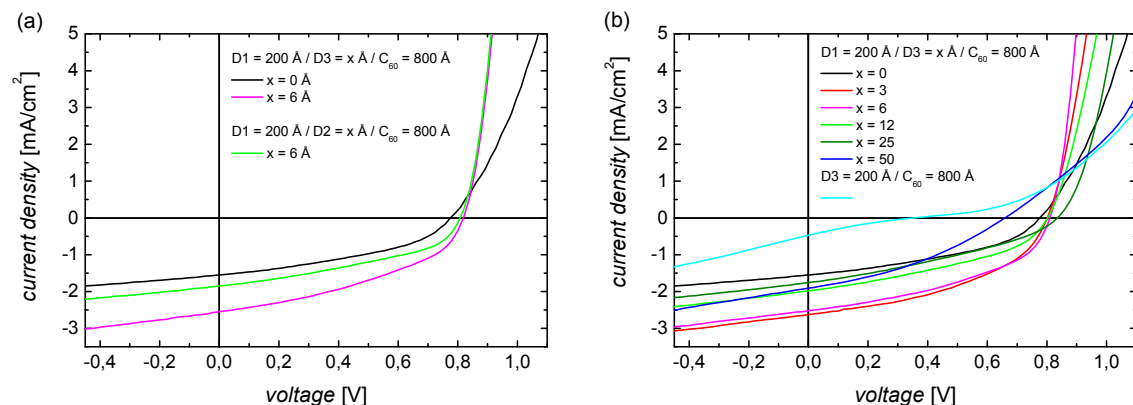


Figure S7-7. a) $j(V)$ characteristics of D1/D2/C₆₀ and D1/D3/C₆₀ cascade solar cells and, as reference, D1/C₆₀ bilayer devices. b) $j(V)$ characteristics of all D1/D3/C₆₀ cascade solar cells.

Table S7-2. Solar cell parameters for cascade cells based on different interlayer materials and D1/C₆₀ reference devices.

Solar cell	j_{sc} [mA/cm^2]	V_{oc} [V]	FF [%]	η [%]
D1 = 200 Å / C ₆₀ = 800 Å	1.37 ± 0.15	0.78 ± 0.01	41 ± 1	0.44
D1 = 200 Å / D2 = 6 Å / C ₆₀ = 800 Å	1.85 ± 0.15	0.81 ± 0.01	42 ± 1	0.60
D1 = 200 Å / D3 = 6 Å / C ₆₀ = 800 Å	2.49 ± 0.15	0.82 ± 0.01	42 ± 1	0.85

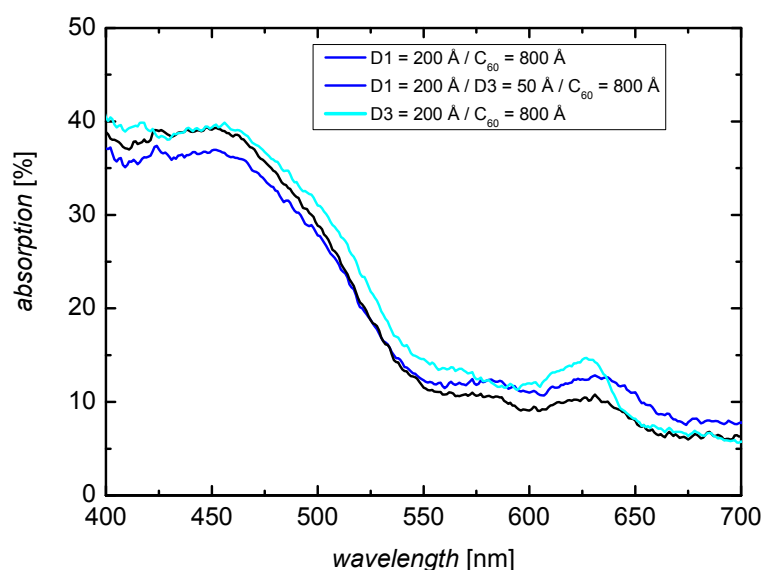


Figure S7-8. Solid state absorption spectra of the different bilayer devices with and without interface layer. Films were prepared by physical vapor deposition.

Organic Field Effect Transistors

Organic Field Effect transistors (OFET) were prepared with **D1** and **D3** as semiconductors in order to compare their respective hole mobilities.

OFET substrates in bottom gate / bottom contact configuration were purchased from Fraunhofer IPMS (OFET Gen. 4). Heavily n-doped silicon (doping at wafer surface: $n \sim 3 \times 10^{17} \text{ cm}^{-3}$) was used as substrate and gate electrode. Thermally grown silicon oxide ($230 \text{ nm} \pm 10 \text{ nm}$) was used as the gate dielectric. Gold electrodes (30 nm on 10 nm ITO as adhesion layer) were used as source and drain contacts. The channel width was 10 mm for all devices and the channel length was varied from 5 μm to 20 μm for each compound. The substrates were cleaned subsequently in acetone and 2-propanol in an ultrasonic bath for 10 minutes each. Treatment in an ozone oven at 50 $^{\circ}\text{C}$ for 20 min was followed by immersion in a 1 wt-% solution of octadecyltrichlorosilane in toluene at 60 $^{\circ}\text{C}$ for 60 min. After rinsing with toluene and 2-propanol the substrates were dried and the polymer was spincoated from a 4 mg/mL chloroform solution at 5000 rpm under ambient conditions. Devices were measured in a nitrogen atmosphere using an Agilent B1500 Semiconductor Parameter Analyzer. Mobilities were calculated from the slopes in the $(I_d)^{0.5}$ - V_g plots in the saturation regime using Equation S1 where I_d is the drain current, W the channel width, L the channel length, C_i the capacitance, V_g the gate voltage and V_T the threshold voltage, respectively.

$$I_d \approx \frac{W}{2L} C_i \mu (V_g - V_T)^2 \quad (\text{S1})$$

All values are summarized in Table S7-3 and were obtained from averages over a minimum of 8 individual devices. As a typical example, transfer and output curves of **D1** and **D3** are shown in Figure S7-9. **D1** generally performs much better with high on/off ratios and low threshold voltages. The hole mobility of **D1** was found to be more than one order of magnitude increased when compared to **D3**. Also on/off ratios are lower for **D3** and threshold voltages are considerably shifted towards lower voltages.

Table S7-3. OFET data for BGBC devices prepared from D1 and D3.

Compound	$I_{\text{on}}/I_{\text{off}}$	Hole Mobility μ_h [$\text{cm}^2\text{V}^{-1}\text{s}^{-1}$]	Threshold Voltage V_T [V]
D1	$>10^6$	$(5.14 \pm 0.67) \times 10^{-3}$	-6 ± 5
D3	$>10^3$	$(2.73 \pm 1.76) \times 10^{-4}$	-34 ± 8

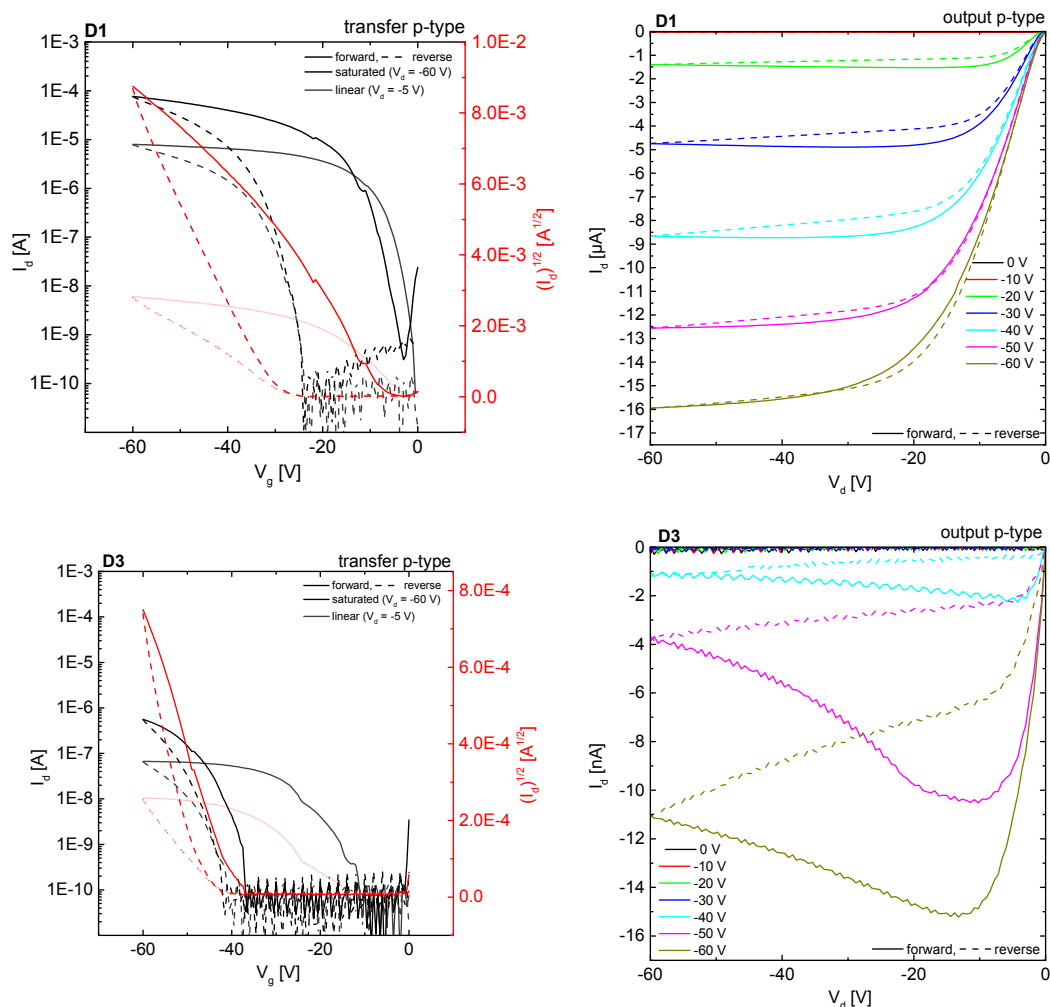


Figure S7-9. Representative OFET I - V transfer (left) and output (right) characteristics of the two DPPs D1 (top) and D3 (bottom) for a BGBC device in p-channel operation with a channel length of 10 μm . Solid lines represent forward scans, dashed lines the reverse scans in all graphs. In transfer curves (bottom), the black and grey plots indicate the transfer characteristics in the saturation and linear operation regime, respectively. Average mobilities and threshold voltages are summarized in Table S2.

Quantum Computational Methods

All calculations were carried out using the quantum chemical program system TURBOMOLE.^[1-2] Geometry optimization was performed by density functional theoretical (DFT)^[3-4] investigations using the RIDFT program^[5-6] and employing the Becke-Perdew 86 (B-P86) functional^[7-9]. Basis were of the def2-TZVP quality (triple zeta valence plus polarization).^[10] The simultaneous optimization of geometric and electronic structure was performed without symmetry restrictions, that is, in C_1 symmetry, allowing for convergence into local minima at higher symmetry. Convergence into global minima was confirmed by calculating the vibrational spectra using the AOFORCE program.^[11]

Table S7-4. Calculated energy levels and bandgap (DFT).

Compound	HOMO	LUMO	E _{g,DFT}
	[eV]	[eV]	[eV]
D1	-4.62	-3.42	1.20
D2	-4.83	-3.64	1.19
D3	-4.98	-3.81	1.17

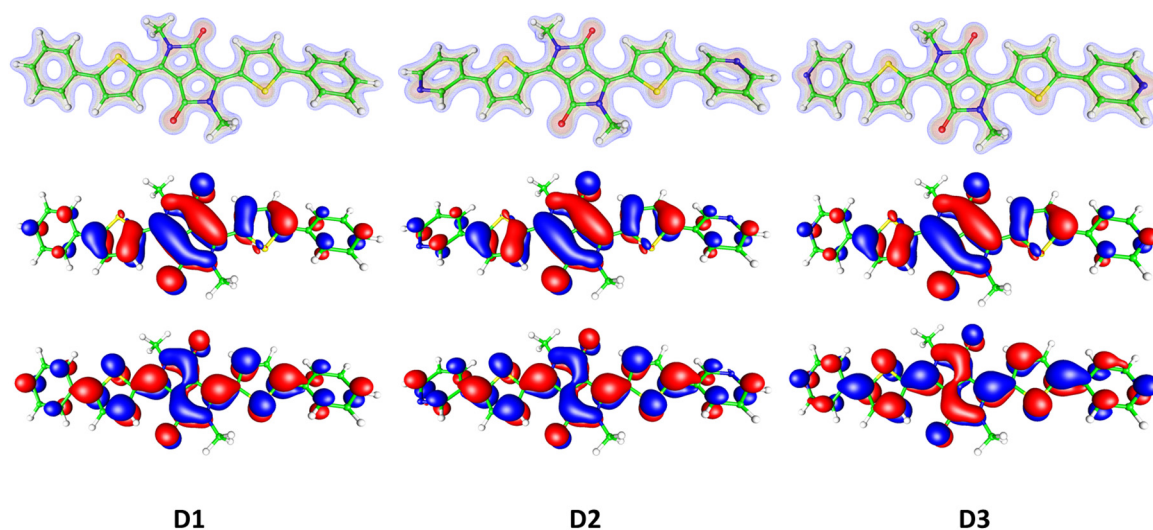


Figure S7-10. Electron density maps (top), HOMO (middle) and LUMO (bottom) of the compounds D1-D3.

Supporting References

- [1] Turbomole GmbH, Karlsruhe 2013.
- [2] R. Ahlrichs, M. Bär, M. Häser, H. Horn, C. Kölmel, *Chem. Phys. Lett.* **1989**, 162, 165.
- [3] W. Y. R. G. Parr, *Density Functional Theory of Atoms and Molecules*, Oxford University Press, New York, **1988**.
- [4] T. Ziegler, *Chem. Rev.* **1991**, 91, 651.
- [5] K. Eichkorn, O. Treutler, H. Öhm, M. Häser, R. Ahlrichs, *Chem. Phys. Lett.* **1995**, 242, 652.
- [6] K. Eichkorn, F. Weigend, O. Treutler, R. Ahlrichs, *Theoretical Chemistry Accounts: Theory, Computation, and Modeling (Theoretica Chimica Acta)* **1997**, 97, 119.
- [7] S. H. Vosko, L. Wilk, M. Nusair, *Can. J. Phys.* **1980**, 58, 1200.
- [8] A. D. Becke, *Physical Review A* **1988**, 38, 3098.

- [9] J. P. Perdew, *Physical Review B* **1986**, *33*, 8822.
- [10] F. Weigend, R. Ahlrichs, *Phys. Chem. Chem. Phys.* **2005**, *7*, 3297.
- [11] P. Deglmann, K. May, F. Furche, R. Ahlrichs, *Chem. Phys. Lett.* **2004**, *384*, 103.

8 Azido-Functionalized Thiophene as a Versatile Building Block To Cross-Link Low-Bandgap Polymers

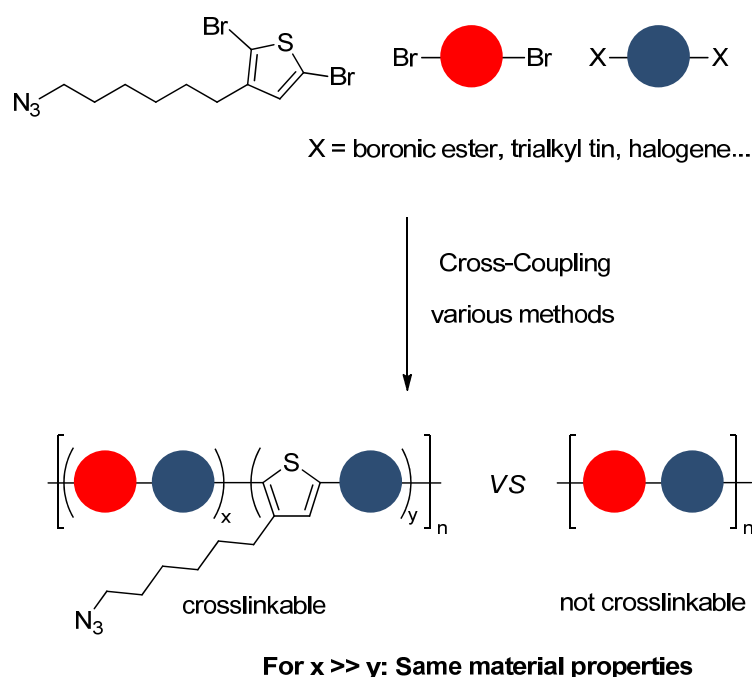
Christian J. Mueller,^a Tobias Klein,^a Eliot Gann,^{b,c}

Christopher R. McNeill^c and Mukundan Thelakkat^{*,a}

^a Applied Functional Polymers, Macromolecular Chemistry I, University of Bayreuth, 95440 Bayreuth, Germany.

^b Australian Synchrotron, 800 Blackburn Road, Clayton, VIC, 3168, Australia.

^c Department of Materials Science and Engineering, Monash University, Wellington Road, Clayton VIC, 3800, Australia.



Published in *Macromolecules*, **2016**, *49*, 3749-3760

Reprinted with permission from <http://dx.doi.org/10.1021/acs.macromol.5b02659>. Copyright 2016 American Chemical Society.

Abstract

We unveil a concept for the design of cross-linkable semiconducting polymers that is based on a modular tercopolymerization which stands out by its low synthetic effort, easy accessibility and its broad range of applications. 3-(6-Azidoethyl)thiophene was used as a comonomer in the synthesis of a variety of low-bandgap copolymers using different polymerization techniques such as Suzuki-Miyaura cross-coupling and Stille cross-coupling. We show that, when only a small amount (5-10 mol%) of azide groups is introduced into the polymers, the impact on absorption and electrochemical properties (HOMO/LUMO values) is negligible. The small amount of azide functionality is however enough to obtain polymers that can easily be cross-linked by UV illumination. Thermal stability of the solid state packing and alignment is studied in neat polymer thin films as well as in blends with [6,6]-phenyl-C₇₁-butyric acid methyl ester (PC₇₀BM) as a relevant model blend system. Solvent resistivity of these polymer films is investigated by absorption and photoluminescence measurements. It is finally shown in organic field effect transistors, that the introduction of 10% azide-functionalized monomer does not considerably influence hole transport mobility (0.20 – 0.45 cm²V⁻¹s⁻¹).

8.1 Introduction

Since the successful introduction of polymer bulk heterojunction solar cells in 1995^[1-2] tremendous progress has led to bulk heterojunction solar cell devices exceeding 10% power conversion efficiency (PCE).^[3] Aggregation and morphology control in the active layer of those bulk-heterojunction solar cells has been identified as an important key in accessing high-efficiency solar cells above 10% PCE.^[3] When moving from the research level to commercial production, morphological stability becomes indispensable not only for long lifetimes, but even for the particular processing methods. Roll-to-roll (R2R) printing with high throughput at appreciable web speeds, for example, demands fast drying of printed active layers and the morphology must therefore be stable under repeated curing conditions which are commonly above 100 °C.^[4]

Cross-linking of the polymer offers a viable route to stable morphologies as it allows for locking-in of the morphology^[5] once an optimal condition has been attained, e.g. by tuning the printing parameters or postprocessing, such as thermal or vapor annealing.^[6] Two different concepts have been shown to offer good cross-linking efficiency leading to thermally stable blends that exhibit very good PCE retention after aging the solar cells. In the first approach

semiconducting polymers can be made cross-linkable by synthetically introducing cross-linkable groups into the side chains of their respective monomers. These groups include alkyl halides, azides, oxetanes or vinylenes that can then be used for cross-linking, mostly by UV curing.^[7-13] ^[14]In the case of cross-linking using azides, highly reactive nitrenes are formed which can undergo a variety of cross-linking reactions, such as C-H insertions, C=C-cycloadditions, and other triplet reactions.^[12, 14] Taking into consideration that the new generation of donor-acceptor alternating copolymers are prepared from specifically functionalized monomers (e.g. borolanes, stannyl derivatives), this approach requires the laborious modification of one of the comonomers used, i.e. several additional synthetic steps are necessary to render a particular polymer system cross-linkable. This increases the material costs and thus impairs commercialization. The second concept relies on cross-linking using low molecular weight additives such as bisazides or dithiols.^[15-18] In this approach, non-volatile additives are introduced that might affect photophysics of charge generation as well as charge transport and extraction in the final blends. Even though each cross-linkable functional group has its advantages and disadvantages, we concentrate in our work on azides to test the generality of our novel approach for different polymerization reactions. Azides are reported to cross-link via UV illumination due to the formation of nitrenes, which can then undergo alkyl side-chain insertion reactions.^[15]

In this contribution, we unveil a third concept for cross-linking semiconducting polymers that is based on a modular tercopolymerization. We avoid the weaknesses of both above mentioned concepts; namely the synthetic effort of modifying monomers required for each particular polymer system and the dilution of electroactive materials and introduction of an at best electronically non-active cross-linking additive. Instead, we show that a simple azide-functionalized thiophene-comonomer can be used in small quantities in diverse polymerizations to give various tercopolymers with an azide content that allows efficient cross-linking but without altering any of the optical and electronical properties of the final polymers. This paves the way for effectively synthesizing various low-bandgap copolymers with inherent cross-linkability without the need of any additional synthetic steps to modify the respective electron-rich or electron-deficient monomers. A detailed analysis of structure formation and charge carrier transport is undertaken to evaluate the influence of cross-linking.

8.2 Results and Discussion

8.2.1 Synthesis

The synthetic strategy pursued in our cross-linkable tercopolymer approach is based on a versatile and common building block that can be applied to different semiconducting low bandgap polymers without having too much influence on their final properties. We hence chose

thiophene as an almost ubiquitous motif in conjugated polymers. The functional groups for polymerization were chosen to be bromines, not only in order to keep the synthesis route as short as possible, but also mostly as it can be employed in many different polymerization techniques that are commonly used to synthesize state-of-the-art low bandgap polymers, such as Stille, Suzuki, Yamamoto, Negishi, Kumada and Heck cross-coupling polymerizations. It has also been shown earlier that no strictly alternating donor-acceptor sequence is required for lowering the optical gap and random or statistical copolymerization is a viable option.^[19-20] When the azide-functionalized comonomer **5** is added in small quantities (less than 5% by weight) to AA/BB-type polycondensations, a cross-linkable tercopolymer can be obtained that exhibits repeating units y which are identical to the regular strictly alternating copolymer and a repeating unit x consisting of the azido-functionalized thiophene **5** and the comonomer carrying the complementary functional groups (Figure 8-1).

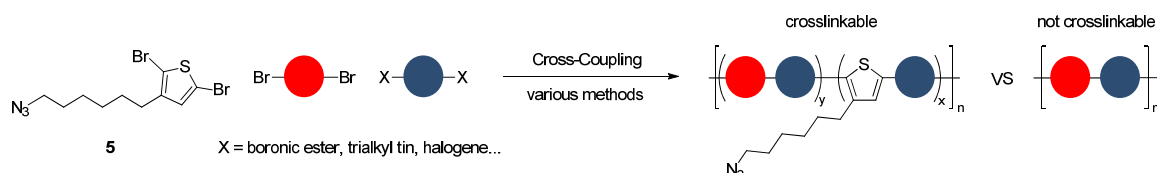


Figure 8-1. Modular concept for cross-linkable tercopolymers using 3-(6-azidohexyl)thiophene as a building block for Stille or Suzuki polycondensation.

The synthetic route of the azide-functionalized comonomer is shown in Figure 8-2. Starting from 1,6-dibromohexane we followed a previously reported route^[21] to obtain 3-(*p*-methoxyphenoxy)hexylbromide **1**. Conversion into the Grignard compound and Kumada cross-coupling using 3-bromothiophene yielded 3-(6-(4-methoxyphenoxy)hexyl)thiophene **2**. The *para*-methoxyphenyl (PMP) protecting group was then cleaved off by the use of boron tribromide and the resulting intermediate simultaneously converted to the ω -alkylhalide **3**.^[22] Dibromination using *N*-bromosuccinimide almost quantitatively gave 2,5-dibromo-3-(6-bromohexyl)thiophene **4** and finally a Finkelstein reaction using sodium azide yielded 3-(6-azidohexyl)-2,5-dibromothiophene **5** which was used as the comonomer in tercopolymerizations. We preferred this route over a previously published one^[23] in order to avoid a mixture of 2-(6-bromohexyl)thiophene and 3-(6-bromohexylthiophene) due to the “halogen shuffling” reaction after lithiation. This mixture is extremely hard to purify. The route shown here results in the desired substitution product via Grignard metathesis.

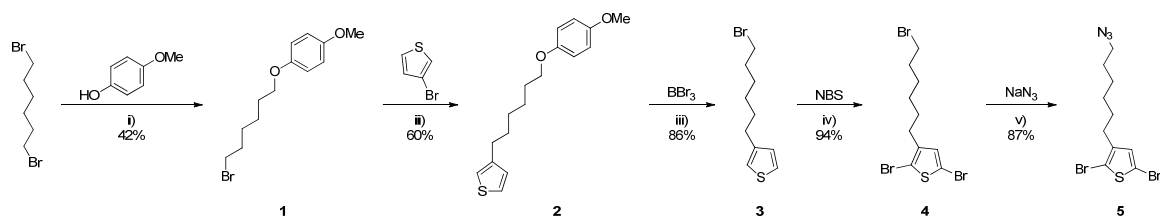


Figure 8-2. Synthesis of the azide-functionalized building block **5**; i) NaOMe, EtOH, 2 h, reflux; ii) Mg, Et₂O, Ni(dppp)Cl₂, 3 d, reflux; iii) DCM, 1.5 h, reflux; iv) THF, 24 h, rt; v) DMSO, 2 h, rt.

We chose four different polymer systems which were selected due to their promising semiconductor properties and widespread use in literature; three from the diketopyrrolopyrrole (PDPP) family and one from the carbazole-benzothiadiazole (PCDTBT) family. PDPP[T]₂-T (**P1-P4**) is a widely used and investigated low-bandgap donor for use in organic solar cells, also showing excellent field effect transistor mobilities.^[24-26] PDPP[Py]₂-T (**P5/P6**) was selected due to its remarkable n-type properties and promising bulk electron mobility.^[27] PDPP[T]₂-Ph (**P7/P8**) is another easily accessible and well-established donor polymer^[28] used in solar cells which has gained a lot of interest due to the high power conversion efficiencies (7.4%) obtained with this material.^[29] Finally we also investigate a PCDTBT system (**P9/P10**) as another widespread donor material which is not based on diketopyrrolopyrroles.^[30] Moreover, we verify the suitability of our approach for Suzuki as well as Stille polycondensations.

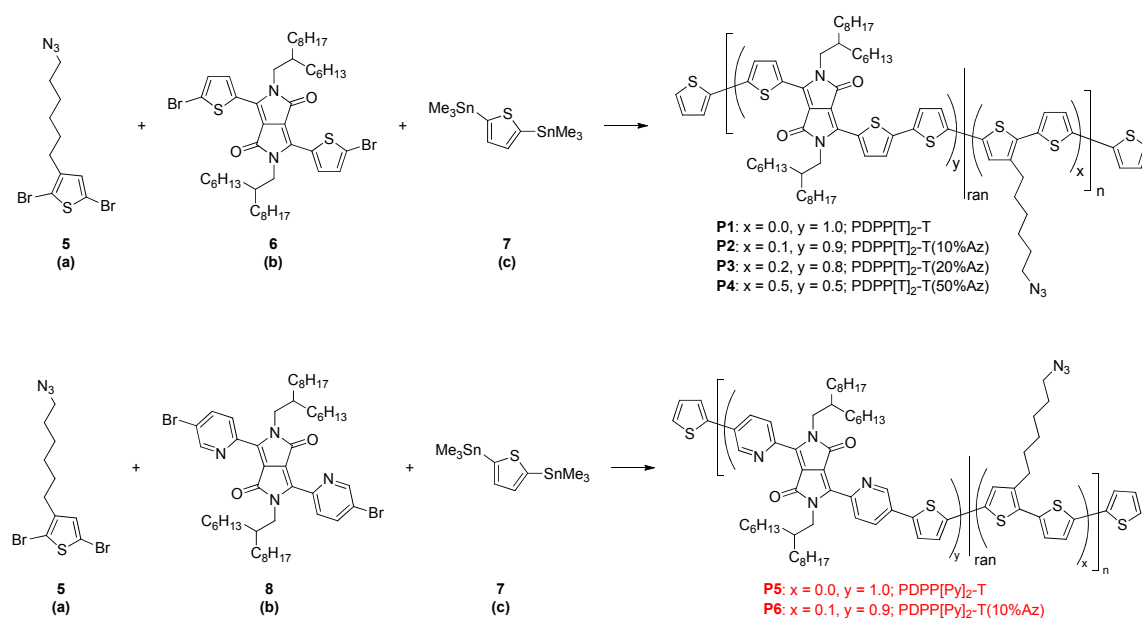


Figure 8-3. Stille polycondensations of typical hole conducting low bandgap polymers PDPP[T]₂-T (**P1-P4**) and typical electron conducting low bandgap polymers PDPP[Py]₂-T (**P5-P6**) with a varying degree of azide functionalization.

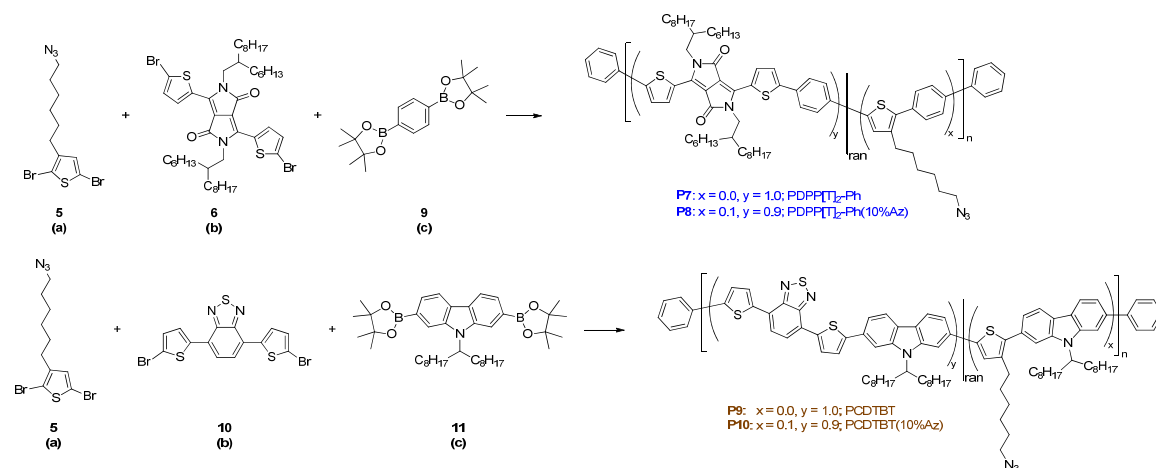


Figure 8-4. Suzuki polycondensation of a PDPP system PDPP[T]₂-Ph (**P7-P8**) and another low bandgap reference system PCDTBT (**P9-P10**) with and without azide functionalization.

For the cross-linkable PDPPs, polymerizations were performed by using either Stille polycondensation (see Figure 8-3) or Suzuki polycondensation (see Figure 8-4), whereas the cross-linkable PCDTBT was obtained via Suzuki polycondensation (Figure 8-4). All polymers were purified by repeated reprecipitations and soxhlet extractions. The removal of unreacted monomers was verified using thin layer chromatography (TLC). Feed ratios (f_a , f_b , f_c) of the three monomers **a**, **b**, **c** as well as resulting built-in ratios determined by ^1H -NMR spectroscopy are summarized in Table 8-1. The mole-fractions χ of the repeating units x and y determined by NMR are very similar to the calculated values expected from the feed ratio and are well within the error of polymer NMR spectroscopy. Detailed information on the calculation of the built-in ratio of the azido-functionalized thiophene comonomer is given in the Supporting Information (section 5.1). It also is evident from the ^1H -NMR that the azide group is suitable for the different polymerization conditions and survives in high yield under different reaction conditions by comparing the methylene protons next to the azide group (H_g) and next to the thiophene core (H_b). As given in Table S1 (see Supporting Information) the ratio is approximately 1 within the errors of polymer NMR spectroscopy. The molecular weights and the degrees of polymerization (DP) obtained from gel permeation chromatography (GPC) as well as the expected average number of azide moieties per polymer chain calculated from the feed ratio are summarized in Table 8-1. The elugrams of the individual polymers are shown in the Supporting Information. The azide-functionalized tercopolymers show similar molecular weights and degrees of polymerization compared to their nonfunctionalized reference copolymers for reasonably small degrees of azide-functionalization. Assuming full incorporation of the feed ratios of 5 to 25 mol%, the wt% of azide functionalized thiophene in the final polymers was in the range of only 2.7% to 18.5% for **P2** to **P4**.

The PDPP[T]₂-T system (**P1-P4**) has the following number average molecular weights: 36.9 kg mol⁻¹ for **P1**, 31.6 kg mol⁻¹ for **P2**, 22.2 kg mol⁻¹ for **P3** and 12.9 kg mol⁻¹ for **P4** corresponding to 0 mol%, 5 mol%, 10 mol% and 25 mol% of functionalized thiophene, respectively. The decreasing molecular weight with increasing degree of functionalization can be explained by the lower solubility of the tercopolymers with a higher x fraction due to the small alkyl chains on **5** when compared to the DPP comonomer. As all polymerizations reached the precipitation limit in pressurized chlorobenzene at 180 °C, higher molecular weights of tercopolymers with high azide-content are not accessible in this system. Moreover, the minimum degree of azide functionalization for making the polymers sufficiently insoluble was tested in the series **P1-P4** and it was found that a molar fraction of 5% content ($x=0.1$) was sufficient (*vide infra*). Therefore, only 5 mol% functionalization was carried out in further systems (**P5-P10**). The PDPP[Py]₂-T (**P5/P6**) system which was also prepared using Stille polycondensation shows very comparable molecular weights of 19.6 kg mol⁻¹ for the nonfunctionalized reference polymer **P5** and 18.3 kg mol⁻¹ for the polymer **P6** containing 10% azido-functionalized repeating units with almost identical dispersities. Concerning Suzuki

polycondensation, the PDPP[T]₂-Ph system (**P7/P8**) also shows comparable values of 27.9 kg mol⁻¹ for the nonfunctionalized **P7** and 31.6 kg mol⁻¹ for the tercopolymer **P8** containing 10% azido-functionalized repeating units. Although the dispersity is a little higher for the functionalized polymer (2.35) than for the reference (1.67), no extreme broadening or tailing can be observed in the GPC elugram, thus there is no indication for cross-linking under reaction and purification conditions. Only the functionalized PCDTBT polymer **P10** shows a considerably lower molecular weight (7.11 kg mol⁻¹) than its reference polymer **P9** (16.3 kg mol⁻¹) which is mainly attributed to two different polymerization protocols (i.e. catalyst systems) employed.

Table 8-1. Molecular characteristics of the synthesized polymers.

Polymer	f_a^a	f_b^a	$\chi_f(y)$ [$\chi_{\text{NMR}}(y)$] ^b	$\chi_f(x)$ [$\chi_{\text{NMR}}(x)$] ^b	M_n^c	M_w^d	\bar{D}^e	DP^f	$n(\text{N}_3)^g$	$wt\%(\text{N}_3)^h$
					[kg/mol]	[kg/mol]				[%]
PDPP[T]₂-T system										
P1	0.00	0.50	1.00 [1.00]	0.00 [0.00]	36.9	146	3.94	44	0	0.0
P2	0.05	0.45	0.90 [0.92]	0.10 [0.08]	31.6	254	8.03	41	4	2.7
P3	0.10	0.40	0.80 [0.85]	0.20 [0.15]	22.2	84.6	3.82	31	6	5.7
P4	0.25	0.25	0.50 [0.59]	0.50 [0.41]	12.9	27.5	2.13	23	11	18.5
PDPP[Py]₂-T system										
P5	0.00	0.50	1.00 [1.00]	0.00 [0.00]	19.6	54	2.76	24	0	0.0
P6	0.05	0.45	0.90 [0.92]	0.10 [0.08]	18.3	52.7	2.89	24	2	2.7
PDPP[T]₂-Ph system										
P7	0.00	0.50	1.00 [1.00]	0.00 [0.00]	27.9	46.5	1.67	34	0	0.0
P8	0.05	0.45	0.90 [0.92]	0.10 [0.08]	31.6	74.1	2.35	41	4	2.7
PCDTBT system										
P9	0.00	0.50	1.00 [1.00]	0.00 [0.00]	16.3	36.7	2.25	23	0	0.0
P10	0.05	0.45	0.90 [0.90]	0.10 [0.10]	7.11	15.3	2.15	10	1	3.0

^a) Feed ratio f of the respective comonomer **a** and **b** as identified in Figure 8-3 and Figure 8-4, the feed ratio of **c** f_c was kept constant at 0.50; ^b) molar fraction χ of repeating unit y and x according to feed ratio (χ_f) and calculated from ¹H-NMR (χ_{NMR}) in brackets, see Supporting Information Table S8-1 Table S8-1 for details; ^c) number average molecular weight, ^d) weight average molecular weight, ^e) dispersity, ^{c-e}) determined by gel permeation chromatography at 120 °C using 1,2,4-trichlorobenzene as the eluent; ^f) degree of polymerization estimated from M_n and the average molecular weight of the polymers repeating unit $\overline{M_{RU}}$ (for details see Supporting Information, Table S8-2); ^g) average number of azide moieties per polymer chain estimated from DP and $\chi_{RU}(x)$; ^h) weight percentage of azido functionalized thiophene in the final polymers calculated by $\chi_f(x) \times 207,29 \text{ g/mol} / \overline{M_{RU}}$ where 207,29 g/mol is the molecular weight of the azido functionalized thiophene moiety and $\overline{M_{RU}}$ is the average molecular weight of the polymer's repeating unit given in Supporting Information Table S8-2.

8.2.2 Infrared Spectroscopy

In addition to the NMR analysis the successful azide functionalization was monitored by infrared (IR) spectroscopy of thin polymer films. Comparisons of nonfunctionalized reference polymers and tercopolymers with an azide-comonomer content of 10% are shown in Figure 8-5 and Figure S8-12 (Supporting Information). A characteristic azide vibration band emerges in all functionalized copolymers at around 2100 cm^{-1} showing successful azide functionalization of the polymers.

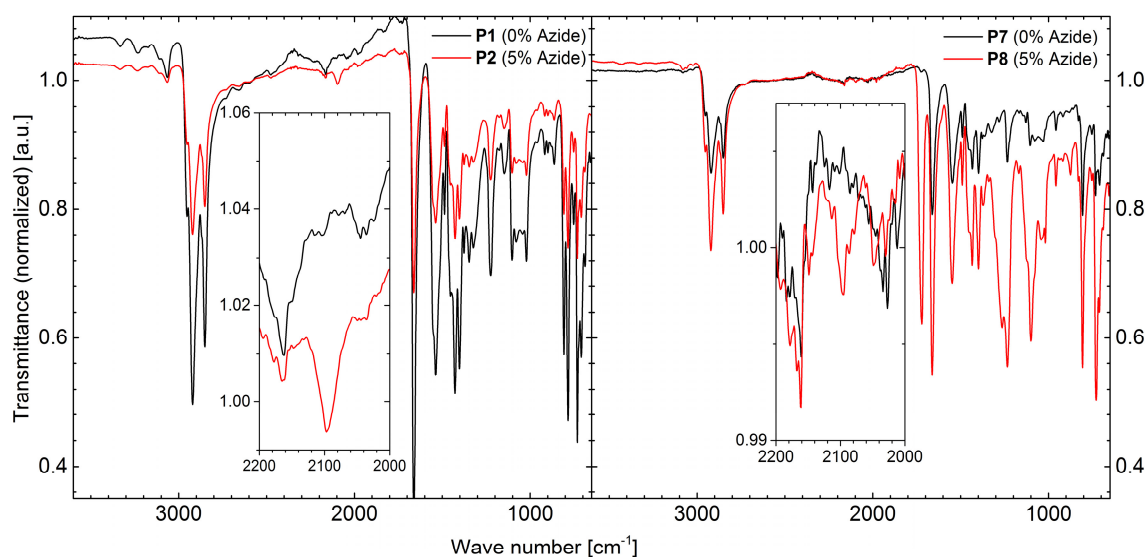


Figure 8-5. Representative infrared spectroscopy of a Stille polycondensation product (PDPP[T]₂-T system, P1/P2) and a Suzuki polycondensation product (PDPP[T]₂-Ph, P7/P8) of the tercopolymers with 5% azide repeating unit content ($x = 0.1$, red lines) and their respective nonfunctionalized reference copolymers (black lines). Insets show magnification of the characteristic azide vibration at 2100 cm^{-1} . Infrared spectra of the the polymer pairs P5/P6 and P9/P10 are given in the Supporting Information, Figure S8-12.

8.2.3 Optical Properties

The optical properties of all the polymers were investigated with respect to absorption as well as photoluminescence (PL) emission. All spectra are shown in Figure 8-6 and the individual onset wavelengths as well as optical gaps determined from solid state absorption onset are summarized in Table 8-2. The PDPP[T]₂-T (**P1-P4**) polymer system with the widest range of degree of functionalization allows to investigate the influence of the tercopolymer ratio $x:y$ on the optical properties and hence differences in the optical gap as well as aggregation properties. Whereas the spectral nature itself does not change considerably, the solution spectra (Figure 8-6a) show a small hypsochromic shift of absorption offset already at the lowest degree of functionalization with $x = 0.1$ in **P2** (5 mol% azide monomer). This shift only becomes pronounced at a functionalization ratio of $x = 0.5$ in **P4** (25 mol% azide monomer) showing an onset blue-shift of 44 nm (68 meV) and a peak shift of 86 nm (170 meV).

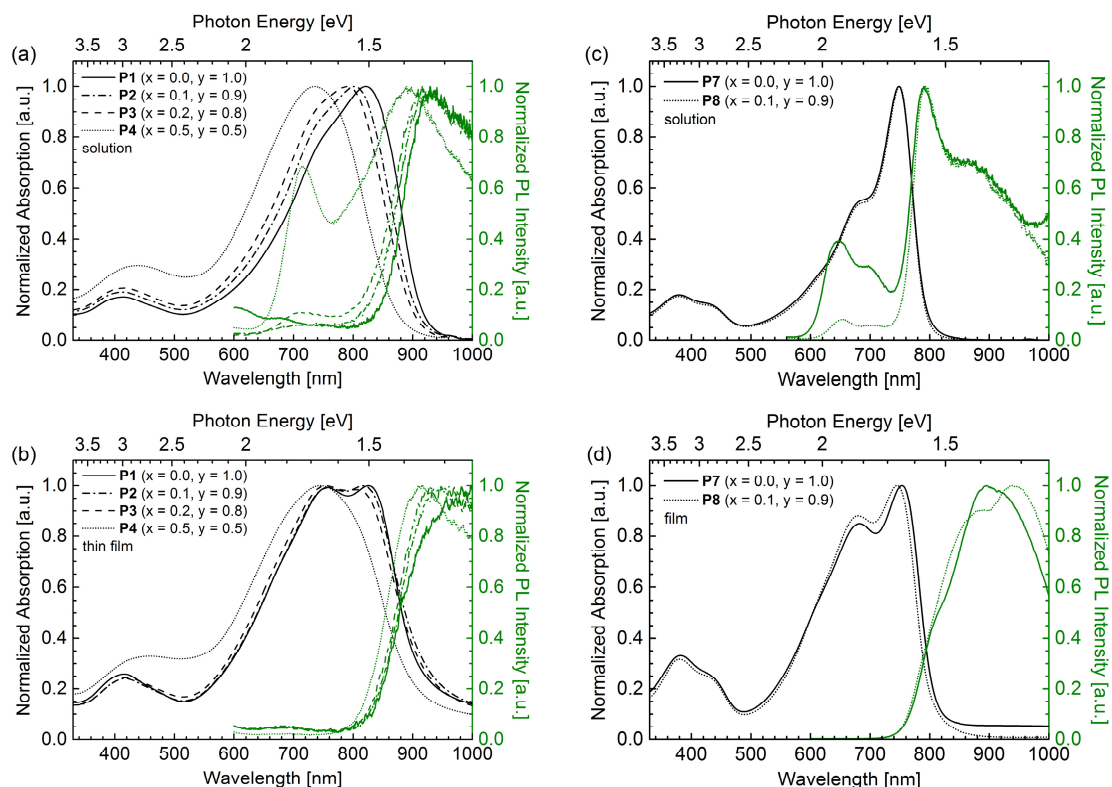


Figure 8-6. Absorption and photoluminescence spectra of cross-linkable tercopolymers compared to their respective nonfunctionalized reference polymers: PDPP[T]₂-T system **P1-P4** with varying monomer ratios in (a) solution and (b) thin film; PDPP[T]₂-Ph system **P7/P8** in (c) solution and (d) thin film. See Supporting Information Figure S8-13 for absorption and photoluminescence spectra of **P5/P6** and **P9/P10**.

For lower functionalization degrees containing 5 to 10 mol% azide monomer with $x = 0.1$ - 0.2 only a very small onset shift of 7-15 nm appears. Whereas the functionalized polymers can still be distinguished from the reference polymers in the solution absorption spectra, the solid state spectra (Figure 8-6b) taken of polymer thin films spincoated on glass are almost identical for low to moderate functionalization degrees. Only **P4** with $x = 0.5$ shows a distinct small hypsochromic onset shift which is mainly caused by the missing aggregation shoulder. **P2** and **P3** with $x = 0.1$ and $x = 0.2$, respectively, show an identical absorption spectrum compared to the unfunctionalized reference polymer **P1**. This trend is also observable in the photoluminescence of these four polymers. Only **P4** shows a distinctly different emission spectrum in solution and a small hypsochromic shift in the solid state compared to **P1-P3**. For this PDPP system it can therefore be concluded, that functionalization degrees up to $x = 0.2$ can be used without altering any solid state optical properties and that an immense amount of functionalized comonomer **5** has to be used in order to alter the optical properties considerably. It should be emphasized that the repeating unit of the PDPP[T]₂-T system comprises three thiophene moieties without addition of the functionalized comonomer **5** and that the addition of another thiophene as third comonomer only partially reduces the DPP content in the tercopolymers, which is the reason for the negligible change in optical properties.

We therefore also investigated other systems, for example the system PDPP[T]₂-Ph (**P7/P8**, Figure 8-6c,d), where the comonomer is not a thiophene but a phenyl moiety thus decreasing the overall thiophene content in the polymer repeating unit. Taking this one step further, even switching to a different DPP core in the pyridine flanked DPP copolymer system PDPP[Py]₂-T (**P5/P6**, Supporting Information Figure S8-13a,b) did not lead to a change in optical properties upon introduction of the third monomer. Finally, another low bandgap polymer system, PCDTBT (**P9/P10**, Supporting Information, Figure S8-13c,d), was shown not to be influenced by tercopolymerization with **5**. As it was found that sufficient cross-linking in the PDPP[T]₂-T system (**P1-P4**) with up to 80% retention of the polymer film (*vide infra*) is possible with as little as 5 mol% azide functionalization, we chose to pursue only this degree of functionalization for all other copolymer systems (**P5-P10**) in order to minimize the influence of chemical changes on the polymer backbone. The absorption as well as emission spectra of the functionalized tercopolymers are compared to the reference polymers in solution (Figure 8-6c,e,g) and thin film (Figure 8-6d,f,h) and it can be concluded that a functionalization degree of $x = 0.1$ has only negligible, if any, influence on the spectral response in the wide range of low-bandgap polymers investigated in this study.

8.2.4 Electrochemical Properties

For each polymer system, one functionalized polymer is compared to its unfunctionalized reference polymer. The electrochemical behavior of pairs of similar systems with and without azide functionalization (**P1/P3**, **P5/P6**, **P7/P8**, **P9/P10**) was representatively compared with respect to reversibility as well as redox potentials. The individual cyclic voltammograms are given in the Supporting Information (Figure S8-11) and the individual energy levels are listed in Table 8-2 and plotted for comparison in Figure 8-7. The energy levels were calculated from the redox potentials calibrated against the ferrocene/ferrocenium redox couple using a published procedure taking into account solvent effects.^[31] All redox potentials were obtained by cyclic voltammetry on polymer thin films with indium tin oxide (ITO) as the working electrode. Neither the reversibility, the absolute reduction and oxidation potentials nor the individual voltammograms are influenced by the introduction of the azide-functionalized comonomer. It can hence be concluded, that the electrochemical properties in thin film that are dependent on the energy levels of the materials and will not change upon functionalization in the tercopolymers compared to the reference polymers, at least for a functionalization of 5-10 mol%.

Table 8-2. Electrochemical properties of azide functionalized polymers compared to the nonfunctionalized reference polymers.

Polymer	IP^a [eV]	EA^b [eV]	E_{CV}^c [eV]	λ_{onset}^d [nm]	E_{opt}^e [eV]
PDPP[T]₂-T system					
P1	-5.75	-3.69	2.04	928	1.34
P2				938	1.32
P3	-5.69	-3.70	1.99	933	1.33
P4				911	1.36
PDPP[Py]₂-T system					
P5	-6.08	-3.78	2.30	720	1.72
P6	-6.14	-3.80	2.34	724	1.71
PDPP[T]₂-Ph system					
P7	-5.72	-3.65	2.07	812	1.53
P8	-5.77	-3.67	2.10	802	1.55
PCDTBT system					
P9	-5.75	-3.50	2.25	665	1.81
P10	-5.79	-3.52	2.27	685	1.86

^aIonisation potential (HOMO), ^belectron affinity (LUMO) and ^cband-gap determined by cyclic voltammetry in thin film; ^dabsorption onset in film and ^eoptical gap determined therefrom.

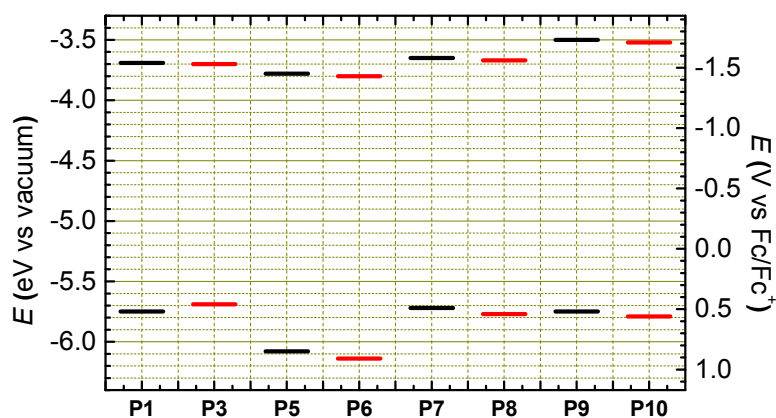


Figure 8-7. Comparison of energy levels of the polymers determined by cyclic voltammetry in thin film. Individual cyclic voltammograms are shown in Supporting Information, Figure S8-11.

8.2.5 Solvent Resistivity

In order to check the necessary degree of functionalization to obtain solvent resistivity of the polymers, thin films were cross-linked by UV (254 nm, 1780 $\mu\text{W cm}^{-2}$) exposure and then submerged in chloroform for 5 minutes followed by excessive rinsing with chloroform. The films

were dried and analyzed by means of UV/VIS absorption and photoluminescence and the peak intensities were compared to the spectra of the untreated films as obtained after spin-coating. The relative change after UV exposure and after chloroform submerging and rinsing for the polymers **P2**, **P3** and **P8** is given in Figure 8-8. Due to the shift of the absorption spectrum in case of the highly functionalized **P4** polymer (see Figure 8-6a,b), we chose to omit this polymer in solvent resistivity checks as the application of this polymer is limited by its changed semiconductor properties, even though it has the highest degree of functionalization. Neither absorption nor photoluminescence intensity changes after the films have been exposed to UV radiation, even after 20 minutes, indicating that the films are stable against UV light and that cross-linking is not negatively influencing the optical properties associated with the conjugated π -system of the polymer backbone. After rinsing the UV exposed films with chloroform, a functionalization degree of $x = 10\%$ (5 mol% azide monomer) in the PDPP[T]₂-T system (**P2**) requires a minimum UV exposure time of 10-15 minutes to obtain solvent resistant films, which retain about 80% of their initial absorption. When the functionalization degree is increased to $x = 20\%$ (10 mol% azide monomer), the films exhibit onsetting solvent resistivity even after 5 minutes of UV exposure, again retaining 80% of the absorption. A saturation in solvent resistivity can be obtained after 5-10 minutes. In the PDPP[T]₂-Ph system a functionalization degree of 5 mol% is enough to obtain full chloroform resistivity after only one minute of UV exposure. It should be noted that even when saturation in solvent resistivity is reached, the maximal obtainable absorption level was at around 80% of the initial absorption for all cases. Thus, the degree of functionalization influences mainly the onset time required for cross-linking, but for appreciable solvent resistivity 5-10 mol% functionalization is sufficient.

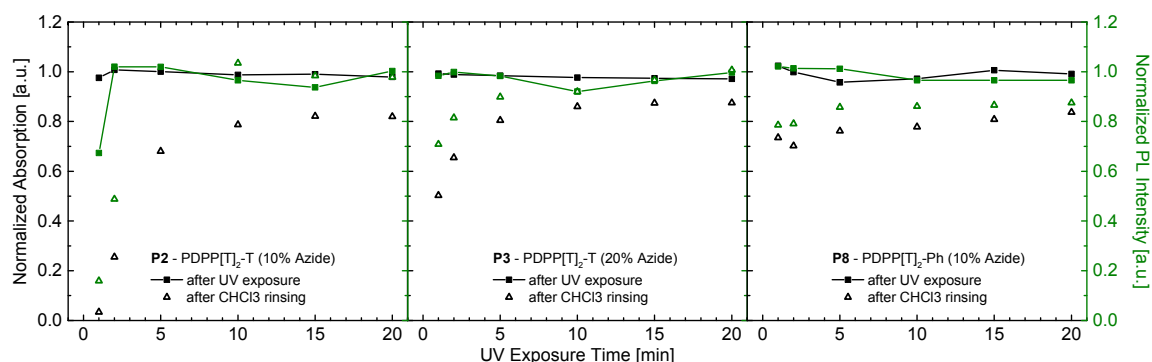


Figure 8-8. Comparison of absorption (black symbols) and photoluminescence (green symbols) for **P2**, **P3** and **P8** films after UV exposure and chloroform rinsing indicating solvent resistivity for cross-linked films.

Pictures of a typical experiment outcome is shown in Figure 8-9, showing two polymer thin films of **P3** spin-coated on a glass substrate with and without prior UV-cross-linking. Interestingly, neither **P6** (PDPP[Py]₂-T) nor **P10** (PCDTBT), both with $x = 10\%$ (5 mol% azide functionalization), could be cross-linked to a degree where resistivity against chloroform is obtained. This could be attributed to the high intrinsic solubility of those polymers. The

pyridine flanked PDPP[Py]₂-M_{co} system for example is even soluble in hexane as has been previously reported.^[27]

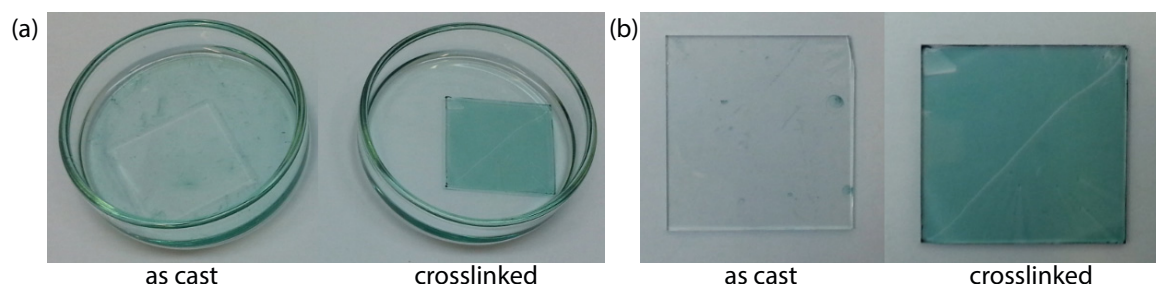


Figure 8-9. Immersion of an as-cast and cross-linked P3 thin film on glass substrates. (a) Immersion in chloroform (the green hue in the solution with the cross-linked sample is due to refraction of the green polymer thin film in the glass of the petri dish) ; (b) samples after rinsing with chloroform.

It can therefore be expected that chloroform provides enough solubility even for cross-linked systems. This also indicates that the degree of cross-linking should be tuned depending on the solubility properties of the concerned polymer system.

8.2.6 Solid State Structure

8.2.6.1 Neat polymer thin films

In order to elucidate the influence of cross-linking on the solid state structure of the polymers in thin films, i.e. crystallinity and the alignment with the substrate, we have measured grazing incidence wide angle X-ray scattering (GIWAXS) for the three different systems (**P1/P2**, **P5/P6** & **P7/P8**) comparing the unfunctionalized reference polymers to their functionalized, cross-linked tercopolymers. The individual spacing d and coherence length ζ values for the different crystalline directions (along the alkyl-stacked lamella and the π - π stacked faces) are summarized in Table 8-3. As an example, Figure 8-10 shows a comparison of unfunctionalized **P1** to the azido-functionalized **P2** (PDPP[T]₂-T system) in both as-cast as well as UV exposed and annealed films. UV exposure was performed under ambient conditions, annealing was carried out at 250 °C under inert atmosphere. Whereas in **P1** a significant increase in the degree of edge-on alignment can be observed after thermal annealing, showing up to the fourth order reflection of the alkyl-stacking peak (labeled h00) and very large coherence lengths (25.2 nm) in both the in-plane and out-of-plane direction, annealing of **P2** only leads to a moderate increase of edge-on crystallinity.

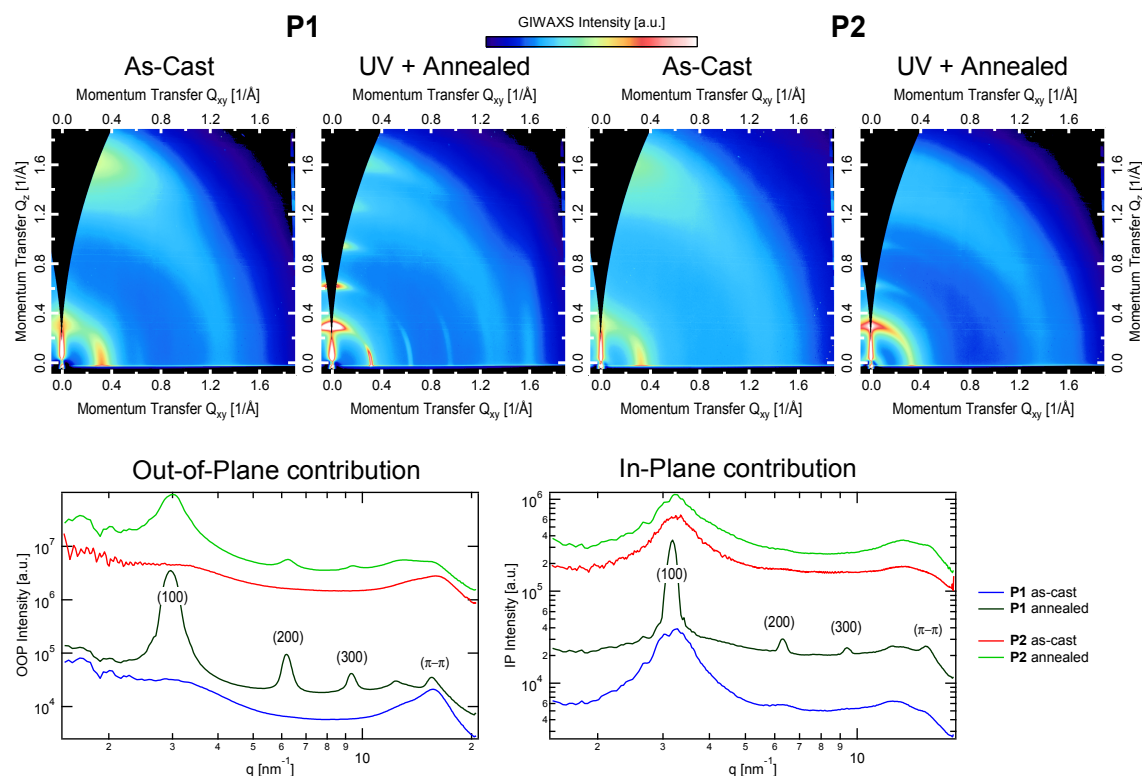


Figure 8-10. GIWAXS scatter patterns of neat unfunctionalized (**P1**) and azide-functionalized (**P2**) PDPP[T]₂-T polymer thin films. Both the reference **P1** as well as the **P2** film were exposed to UV light before thermal annealing.

While edge on crystallinity is dominant in **P1**, there is a significant population of face-on stacking with much larger coherence lengths evident by the quite sharp alkyl-stacking reflections in-plane. Comparisons for the other polymer systems (**P5/P6**, **P7/P8**) are given in the Supporting Information Figure S8-14 and Figure S8-15, respectively. Similar behavior can be observed in the pyridine flanked PDPP[Py]₂-T system when comparing unfunctionalized **P5** to functionalized **P6** (see Supporting Information Figure S8-14). **P5** shows a considerable increase in crystallinity and well-aligned films with several orders of alkyl spacing present both out-of-plane and in-plane after thermal annealing. Again, the **P6** film is somewhat influenced by annealing but to a much smaller extent, showing first order peaks and considerably smaller coherence lengths. (Table 8-3) Finally, in the PDPP[T]₂-Ph system comparing unfunctionalized **P7** to functionalized **P8** (see Supporting Information, Figure S8-15) cross-linking of **P8** has much less of an effect on both crystallinity and degree of alignment. Both polymers show a strongly enhanced crystallinity and edge-on alignment after thermal annealing, independent of the azide-content and cross-linking. In fact, **P8** shows a clearer edge-on conformation than the reference **P7** as indicated by the complete absence of the alkyl spacing peaks in the in-plane direction in **P8** after annealing. This points to face on orientation in these films being hindered by cross-linking. The backbone spacing d_{bb} and the respective backbone spacing coherence length ζ_{bb} could only be observed in **P7** after annealing and was found to be 1.53(0) nm and 10.0(5) nm, respectively.

Table 8-3. GIWAXS peak analysis of neat polymer thin films for alkyl and π - π stacking.

Polymer	T ^a	d _{alkyl} ^b [nm]	ζ _{alkyl} ^{c,f} [nm]	d _{π-π} ^d [nm]	ζ _{π-π} ^{e,f} [nm]
PDPP[T]₂-T system					
P1	as cast	1.98(4)	6.3(8)	0.401(3)	3.5(1)
P1	250 °C	2.01(4)	25.2(3)	0.402(1)	4.27(6)
P2	as cast	1.89(2)	4.5(2)	0.380(1)	3.2(2)
P2	250 °C	2.00(5)	13.5(1)	0.395(2)	4.0(3)
PDPP[Py]₂-T system					
P5	as cast	1.98(3)	3.36(7)	0.393(1)	3.4(2)
P5	250 °C	2.03(5)	25.1(2)	0.391(0)	3.9(1)
P6	as cast	1.89(0)	3.94(0)	-	-
P6	250 °C	1.98(5)	14.0(1)	0.393(0)	2.74(2)
PDPP[T]₂-Ph system					
P7	as cast	1.94(3)	8.32(3)	0.382(2)	3.3(2)
P7	250 °C	1.95(3)	16.2(1)	0.406(5)	3.43(3)
P8	as cast	1.89(4)	5.85(6)	0.402(2)	2.86(7)
P8	250 °C	1.95(2)	15.6(2)	0.412(0)	3.58(4)

^a Annealing process; ^b alkyl stacking spacing; ^c alkyl stacking coherence length (determined from (100) peak in out-of-plane direction); ^d π - π stacking spacing; ^e π - π stacking coherence length (determined from 1st order π - π stacking); ^f the crystal coherence length ζ gives information about the distance over which order is maintained and is defined as $\zeta = 2\pi/\text{FWHM}$, where FWHM is the full width at half maximum of the first order lamellar stacking or π - π stacking peak, respectively. It is related to the Scherrer equation, which connects the width of a peak to the crystal size.

8.2.6.2 Polymer : PC₇₀BM blend thin films

Since the importance of cross-linking a low band-gap polymer is usually discussed as a route to stabilize the morphology of blends with fullerene derivatives as in solar cell applications we tested the potential of our concept in similar blends as well. For this, we have selected the polymer pairs **P1/P2**, **P5/P6** and **P7/P8** and tested the cross-linking conditions. From our experience with the nonfunctionalized reference polymers **P1**, **P5** and **P7**, the Polymer:PC₇₀BM blend morphology is much more favorable for solar cell applications when DIO is used as a solvent additive. Hence, we chose to add DIO to the blends investigated in GIWAXS. Additionally, we have also performed GIWAXS measurements on polymer/fullerene blends before and after cross-linking / annealing. 2D GIWAXS patterns were taken for the as cast films as well as for films that were exposed to UV radiation followed by thermal annealing at 200 °C for 15 min in an inert atmosphere. The individual spacings d and coherence lengths ζ along the different crystalline directions (alkyl, π - π and backbone) are summarized in Table

8-4. Figure 8-11 shows the 2D scattering patterns for the PDPP[T]₂-T system comparing unfunctionalized **P1** with functionalized **P2** ($x = 0.1$) as a typical example.

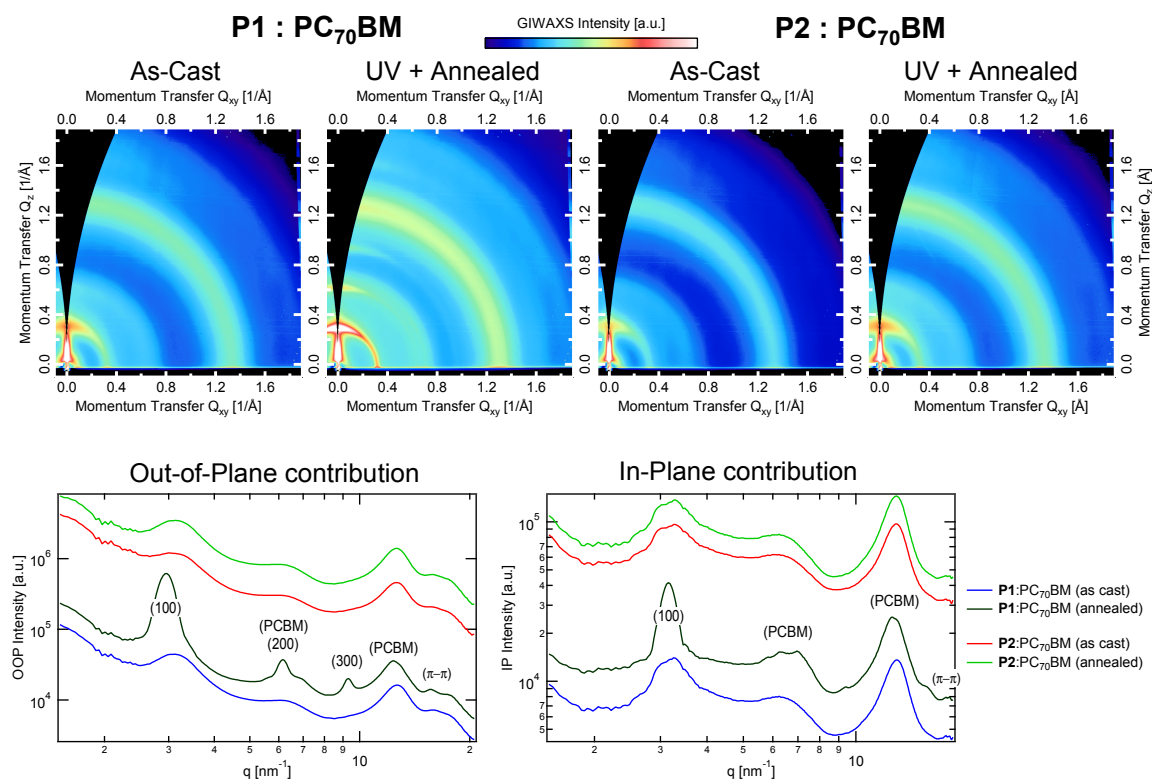


Figure 8-11. GIWAXS scatter patterns of unfunctionalized (**P1**) and azide-functionalized (**P2**) PDPP[T]₂-T polymer:PC₇₀BM blends. Both the reference **P1** as well as the **P2** film were exposed to UV light before thermal annealing. Comparisons for different polymer systems (**P5**/**P6**, **P7**/**P8**) are given in the Supporting Information Figure S8-16 and Figure S8-17, respectively.

Whereas the as-cast blend films show almost identical scattering both in in-plane as well as out-of-plane direction, upon annealing the **P1** blend shows a distinct increase in crystallinity with 2nd and 3rd order lamellar stacking peaks appearing in the out-of-plane direction. Also the in-plane scattering shows a higher intensity and a narrower peak for the 1st order lamellar stacking peak, indicating a larger crystal coherence length in the annealed sample. These annealing effects are absent in the cross-linked **P2** blend after thermal annealing, indicating a lower chain mobility which hinders improved packing upon annealing. The same effect can also be observed in the blends employing the PDPP[Py]₂-T system (see Supporting Information, Figure S8-16). Again the unfunctionalized **P5** blend shows an increasing crystallinity and exhibits distinct 2nd order peaks upon annealing which are lacking in the cross-linked and annealed **P6** blend. In fact, the scattering of the annealed **P6** blend is identical to the as-cast **P6** blend and the as-cast **P5** blend indicating successful cross-linking and chain immobilization in this system. Interestingly, the PDPP[T]₂-Ph system does not show any differences after thermal annealing in the unfunctionalized **P7** blend as well as in the tercopolymer **P8** blend having 5 mol% azide functionalization (see Supporting Information Figure S8-17).

Table 8-4. GIWAXS peak analysis of polymer : PC₇₀BM blend systems for alkyl, π - π and backbone stacking.

Blend	T ^a	d _{alkyl} ^b [nm]	ζ_{alkyl} ^{c,h} [nm]	d _{π-π} ^d [nm]	ζ_{π - $\pi}$ ^{e,h} [nm]	d _{bb} ^f [nm]	ζ_{bb} ^{g,h} [nm]
PDPP[T]₂-T system							
P1 : PCBM	as cast	1.97(3)	7.8(1)	0.380(2)	1.7(1)	1.56(1)	5.3(5)
P1 : PCBM	200 °C	2.05(4)	20.0(2)	0.358(7)	2.4(1)	1.43(1)	3.8(3)
P2 : PCBM	as cast	1.95(2)	12(1)	0.381(1)	1.6(1)	1.53(5)	3.5(6)
P2 : PCBM	200 °C	1.94(1)	7.47(9)	0.381(1)	1.6(1)	1.46(3)	3.5(6)
PDPP[T]₂-T system							
P5 : PCBM	as cast	1.89(7)	4.5(2)	0.359(1)	3.0(2)	-	-
P5 : PCBM	200 °C	2.01(6)	15.5(1)	0.389(1)	2.1(1)	-	-
P6 : PCBM	as cast	1.84(6)	6.7(6)	0.360(2)	2.9(3)	-	-
P6 : PCBM	200 °C	1.90(1)	5.06(0)	0.369(1)	1.8(1)	-	-
PDPP[T]₂-Ph system							
P7 : PCBM	as cast	1.95(3)	9.3(1)	0.393(1)	2.2(1)	1.54(1)	6(1)
P7 : PCBM	200 °C	1.95(4)	9.1(1)	0.391(1)	2.3(1)	1.50(1)	5.8(6)
P8 : PCBM	as cast	1.91(1)	7.58(8)	0.388(2)	1.6(1)	1.54(1)	5.2(7)
P8 : PCBM	200 °C	1.91(1)	7.2(1)	0.397(0)	6(1)	1.47(2)	2.9(5)

^a Annealing process; ^b alkyl stacking spacing; ^c alkyl stacking coherence length (determined from (100) peak in out-of-plane direction); ^d π - π stacking spacing; ^e π - π stacking coherence length (determined from 1st order π - π stacking); ^f backbone stacking spacing; ^g backbone stacking coherence length (determined from 1st order backbone stacking in in-plane direction); ^h the crystal coherence length ζ gives information about the distance over which order is maintained and is defined as $\zeta = 2\pi/\text{FWHM}$, where FWHM is the full width at half maximum of the 1st order lamellar stacking or π - π stacking peak, respectively. It is related to the Scherrer equation, which connects the width of a peak to the crystal size.

We want to highlight a noticeable peculiarity apart from any cross-linking questions, namely the fact that for the thiophene flanked PDPP[T]₂-T (**P1/P2**) and PDPP[T]₂-Ph (**P7/P8**) systems we consistently observe backbone stacking peaks when blended with PC₇₀BM (Table 8-4), which are not observable in the corresponding neat polymer thin films (Table 8-3), especially in **P1**, **P2** and **P8**. This is suggesting a PC₇₀BM-influenced packing in the blends.

8.2.7 Organic Field Effect Transistors

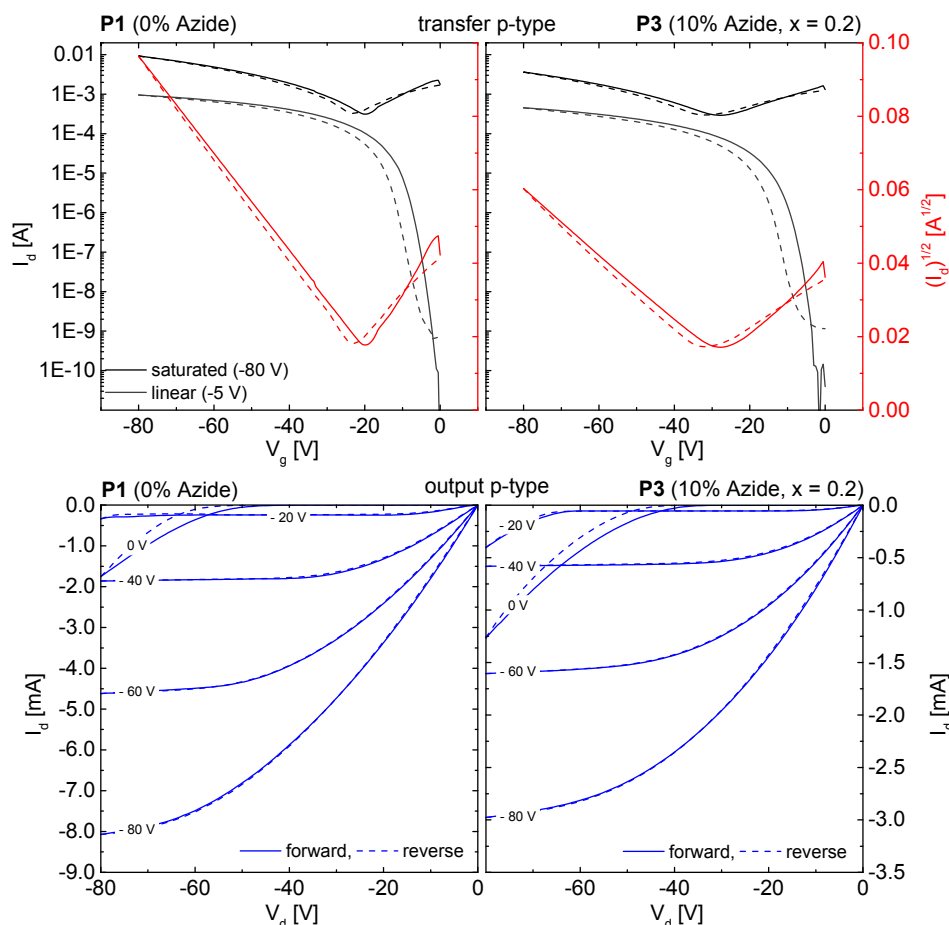


Figure 8-12. OFET p-type transfer and output I - V characteristics after annealing at 250 °C for 15 min of the nonfunctionalized strictly alternating PDPP[T] $_2$ -T **P1** and the tercopolymer containing 10% azide-functionalized repeating units **P3**. Solid and dashed lines represent the forward and reverse scans in all graphs, respectively. The voltages given in the legend of the output characteristics are the applied gate voltages.

The performance of the polymers in organic field effect transistors (OFET) was representatively investigated to study the influence of azide incorporation on the PDPP[T] $_2$ -T system using the unfunctionalized **P1** as a reference and **P3** exhibiting a functionalization degree of $x = 0.2$ (10 mol% azide monomer). OFET devices were prepared in a bottom gate/bottom contact (BGBC) configuration. In order to get a clear picture about the influence of incorporation of a third comonomer into this copolymer system, neither of the films has been exposed to UV radiation for cross-linking before characterizing the transistors. The mobility was averaged over at least three individual devices. Both polymers show an ambipolar behavior, although the p-channel is much more dominant. Transfer and output I - V characteristics for p-channel operation are shown in Figure 8-12. In the as-cast films the hole mobility was $\mu_h = 0.28 \pm 0.17$ cm 2 V $^{-1}$ s $^{-1}$ for **P1** compared to $\mu_h = 0.04 \pm 0.01$ cm 2 V $^{-1}$ s $^{-1}$ in case of the functionalized derivative **P3**. Upon annealing the mobilities increased considerably to

$\mu_h(\mathbf{P1}) = 0.45 \pm 0.02 \text{ cm}^2\text{V}^{-1}\text{s}^{-1}$ and $\mu_h(\mathbf{P3}) = 0.19 \pm 0.03 \text{ cm}^2\text{V}^{-1}\text{s}^{-1}$, respectively. Even though the final mobility of the azide-functionalized tercopolymer **P3** is a little lower than that of the reference polymer **P1** after annealing, it is important to note that mobilities in the same order of magnitude are accessible using this tercopolymerization approach and that even a moderate azide-functionalization of 10 mol% with $x = 0.2$ does obviously not drastically limit the thermal annealing options of non-UV-cross-linked films, allowing good post-processing opportunities *via* thermal annealing which is common for organic semiconducting materials. The same holds true for n-type operation. Transfer and output characteristics for n-channel operation are shown in the Supporting Information, Figure S8-18. The transistors exhibit a significant threshold voltage of 50 V and hence output in the n-channel can only be observed for gate voltages as high as 60-80 V. The electron mobilities are $\mu_e(\mathbf{P1}) = 0.14 \pm 0.01 \text{ cm}^2\text{V}^{-1}\text{s}^{-1}$ and $\mu_e(\mathbf{P3}) = 0.06 \pm 0.01 \text{ cm}^2\text{V}^{-1}\text{s}^{-1}$, respectively.

8.3 Conclusion

In conclusion we have shown a new and highly modular concept for the synthesis of photo-cross-linkable semiconducting polymers to obtain both solvent resistant films as well as thermally stable solid state packing and morphologies in thin films of neat polymers and in PC₆₀BM blends after photo-cross-linking. The synthetic effort was kept low by the universal use of a common azido-functionalized thiophene comonomer in four different copolymer systems without influencing the optical and electrochemical properties of the polymers. Successful incorporation of azide moieties in the functionalized tercopolymers was proven by infrared and NMR spectroscopy. The introduction of the additional monomer containing the azide moiety did not considerably alter the optical or electrical properties in thin films and devices as demonstrated in an organic field effect transistor for a degree of functionalization up to $x = 0.2$ (10 mol% azide monomer). We anticipate that this cross-linking approach will provide an easily accessible route towards a variety of inherently cross-linkable semiconductor polymers using a single universal cross-linkable unit without the necessity of the addition of low molecular weight cross-linking agents.

8.4 Experimental Section

8.4.1 Materials and Methods

All reagents were used without further purification unless otherwise noted. Microwave reactions were conducted in sealed containers using a Biotage Initiator Eight+ microwave. ^1H NMR (300 MHz) spectra of monomers were recorded on a Bruker AC 300 spectrometer. All polymer ^1H NMR spectra were recorded on a Varian INOVA 300 spectrometer at 393 K in 1,1,2,2-tetrachloroethane (TCE) as solvent. The ^1H spectra were referenced internally by using the

residual solvent resonances. Deuterated solvents were obtained from Deutero. Gel permeation chromatography (GPC) analysis was carried out on an Agilent (Polymer Laboratories Ltd.) PL-GPC 220 high temperature chromatographic unit equipped with DP, RI and LS (15° and 90°) detectors and three linear mixed bed columns of PLgel 13 μ m (Olexis) with a linear MW operating range: 500 - 15,000,000 g mol⁻¹. GPC analysis was performed at 150 °C using 1,2,4-trichlorobenzene as the mobile phase. The samples were prepared by dissolving the polymer (0.1 wt-%) in the mobile phase solvent in an external oven and the solutions were run without filtration. The molecular weights of the samples were referenced to linear polystyrene ($M_w = 162 - 6,000,000$ g mol⁻¹, $K = 12.100$ and $\text{Alpha} = 0.707$) and were not corrected with K and Alpha values for the measured sample. Cyclic voltammetry was performed under moisture- and oxygen-free conditions using a 0.1 M tetra-*n*-butylammonium hexafluorophosphate in acetonitrile electrolyte solution. A standard three-electrode assembly connected to a potentiostat (model 263A, EG&G Princeton Applied Research) was used at a scanning rate of 100 mV s⁻¹. The working electrode was a 10 Ω/\square ITO coated glass substrate. The polymers were spincoated onto the ITO substrates from chloroform at 3 mg/mL and 1500 rpm to obtain thicknesses of 10-20 nm. A platinum wire in acetonitrile was used as counter electrode and the quasi-reference electrode consisted of an Ag wire in an AgNO₃/acetonitrile solution (0.1 M). The measurements were calibrated with an external ferrocene/ferrocenium standard, IP and EA values were calculated considering the solvent effects as per a published procedure^[31] using Equation 1 and 2 where the workfunction of Fc/Fc⁺ is taken to be -5.23 eV. The reduction half-step potential $E_{1/2}^{red}$ (vs Fc/Fc⁺) is negative whereas the oxidation half-step potential $E_{1/2}^{ox}$ (vs Fc/Fc⁺) is positive.

$$EA \approx -5.23 \text{ eV} - E_{1/2}^{red} (\text{vs Fc/Fc}^+) \quad (19)$$

$$IP \approx -5.23 \text{ eV} - E_{1/2}^{ox} (\text{vs Fc/Fc}^+) \quad (20)$$

Absorption measurements were carried out on a JASCO V-670 spectrophotometer. Photoluminescence measurements were carried out on a JASCO FP-8600 spectrofluorometer, excitation wavelengths were chosen at the maximum of the transition around 430 nm for all samples. Optical properties in solution were measured in chloroform at a concentration of 0.01 mg/mL and a path length of 10 mm, films were spin-coated onto glass slides from a 7 mg/mL chloroform solution at 1500 rpm. Solutions for spin-coating were prepared by dissolving the polymer in chloroform at the given concentration and stirring at 55 °C for 8 h. Cross-linking by UV exposure for the resistivity experiments was performed using a benchtop UV lamp operating at 254 nm with an intensity of 1780 μ W cm⁻², cross-linking for the GIWAXS experiments was performed using a commercial system (Light Hammer 6, Fusion Systems Inc., 200-450 nm, 200 W cm⁻² on a LC6 benchtop conveyor operating at 3.5 cm/s).

8.4.2 GIWAXS

Measurements were conducted at the SAXS/WAXS beamline of the Australian Synchrotron.^[32] Neat polymer films were spincoated from chloroform onto an octyltrichlorosilane/SiO₂ modified silicon wafer from a 6 mg mL⁻¹ solution at 2000 rpm. Blend samples were prepared by spincoating polymer:PC₇₀BM blends (ratio 1:2) from chloroform at a total concentration of 18 mg/mL with 2 vol% 1,8-diiodooctane (DIO) onto an MoO₃ (15 nm) modified silicon wafer at 2000 rpm. After spin-coating the films were immediately put under ultra-high vacuum (base pressure 10⁻⁷ mbar) in order to evaporate remaining DIO. Highly collimated 9 keV X-rays were calibrated to be at a tilt angle of 0 ± 0.01 degrees when parallel to the surface of each sample by use of a Silicon crystal analyzer. A Dectris Pilatus 1M detector collected 2D scattering patterns, including those shown in Figure 8-10 and Figure 8-11. Each scattering pattern was tiled together from three 1-second images with the detector slightly moved between exposures, such that the resulting image removes gaps between the detector modules. The sample to detector distance was measured using a Silver Behenate scattering standard. Data were analysed using a modified version of the NIKA small angle scattering analysis package.^[33]

8.4.3 Organic thin film transistors.

Substrates in bottom gate / bottom contact configuration were bought from Fraunhofer IPMS (OFET Gen. 4). Heavily n-doped silicon (doping at wafer surface: n~3 x 10¹⁷ cm⁻³) was used as substrate and gate electrode. Thermally grown silicon oxide (230 nm ± 10 nm) was used as the gate dielectric. Gold electrodes (30 nm on 10 nm ITO as adhesion layer) were used as source and drain contacts. The channel width was 10 mm for all devices and channel lengths of 10 µm and 20 µm were used. The substrates were cleaned subsequently in acetone and 2-propanol in an ultrasonic bath for 10 minutes each. Treatment in an ozone oven at 50 °C for 20 min was followed by immersion in a 1 wt-% solution of octadecyltrichlorosilane in toluene at 60 °C for 60 min. After rinsing with toluene and 2-propanol the substrates were dried in a nitrogen stream and the polymer was spincoated from a 6 mg/mL chloroform solution at 2000 rpm under ambient conditions. Devices were measured in a nitrogen atmosphere using an Agilent B1500 Semiconductor Parameter Analyzer. The devices were annealed in a nitrogen atmosphere at a maximum of 0.9 ppm O₂ for 15 minutes consecutively at the temperatures given in the main text. Mobilities were calculated from the slopes in the (*I_d*)^{0.5}-*V_g* plots in the saturation regime using equation 3 where *I_d* is the drain current, *W* the channel width, *L* the channel length, *C_i* the capacitance, *V_g* the gate voltage and *V_T* the threshold voltage, respectively.

$$I_d \approx \frac{W}{2L} C_i \mu (V_g - V_T)^2 \quad (21)$$

8.5 Acknowledgement

We thank Christina Saller (Universität Bayreuth) for providing the unfunctionalized PCDTBT. We acknowledge financial support from the Bavarian State Ministry of the Environment and Consumer Protection (Umwelt NanoTech) and the Bavarian State Ministry of Education, Science and the Arts (Solar technologies go hybrid). C. J. M. thanks the Fonds der Chemischen Industrie for funding the PhD with a Kekulé scholarship. C.J.M. and T.K. kindly acknowledge scholarships from the German National Academic Foundation and support from the Elitenetzwerk Bayern (ENB), Macromolecular Science. C.R.M. acknowledges support from the Australian Research Council (DP130102616). This research was undertaken in part on the SAXS/WAXS beamline at the Australian Synchrotron, Victoria, Australia.^[32]

8.6 References

- [1] J. J. M. Halls, C. A. Walsh, N. Greenham, C. E. A. Marseglia, R. Friend, H. S. C. Moratti, A. Holmes, B, *Nature* **1995**, *376*, 498.
- [2] G. Yu, J. Gao, J. C. Hummelen, F. Wudl, A. J. Heeger, *Science* **1995**, *270*, 1789.
- [3] Y. Liu, J. Zhao, Z. Li, C. Mu, W. Ma, H. Hu, K. Jiang, H. Lin, H. Ade, H. Yan, *Nat Commun* **2014**, *5*, 5293.
- [4] M. Hösel, R. R. Søndergaard, M. Jørgensen, F. C. Krebs, *Energy Technology* **2013**, *1*, 102.
- [5] G. Griffini, J. D. Douglas, C. Piliago, T. W. Holcombe, S. Turri, J. M. Frechet, J. L. Mynar, *Adv. Mater.* **2011**, *23*, 1660.
- [6] J. W. Rumer, I. McCulloch, *Mater. Today* **2015**.
- [7] J. E. Carle, B. Andreasen, T. Tromholt, M. V. Madsen, K. Norrman, M. Jorgensen, F. C. Krebs, *J. Mater. Chem.* **2012**, *22*, 24417.
- [8] G. Wantz, L. Derue, O. Dautel, A. Rivaton, P. Hudhomme, C. Dagron-Lartigau, *Polym. Int.* **2014**, *63*, 1346.
- [9] M.-R. Chen, C.-C. Fan, T. R. Andersen, H. F. Dam, W.-F. Fu, Y.-Z. Lin, E. Bundgaard, F. C. Krebs, X.-W. Zhan, H.-Z. Chen, *Synth. Met.* **2014**, *195*, 299.
- [10] B. J. Kim, Y. Miyamoto, B. Ma, J. M. J. Fréchet, *Adv. Funct. Mater.* **2009**, *19*, 2273.
- [11] H. J. Kim, A. R. Han, C.-H. Cho, H. Kang, H.-H. Cho, M. Y. Lee, J. M. J. Fréchet, J. H. Oh, B. J. Kim, *Chem. Mater.* **2012**, *24*, 215.
- [12] C.-Y. Nam, Y. Qin, Y. S. Park, H. Hlaing, X. Lu, B. M. Ocko, C. T. Black, R. B. Grubbs, *Macromolecules* **2012**, *45*, 2338.

- [13] K. A. Murray, A. B. Holmes, S. C. Moratti, R. H. Friend, *Synth. Met.* **1996**, *76*, 161.
- [14] K. A. Murray, A. B. Holmes, S. C. Moratti, G. Rumbles, *J. Mater. Chem.* **1999**, *9*, 2109.
- [15] R. Q. Png, P. J. Chia, J. C. Tang, B. Liu, S. Sivaramakrishnan, M. Zhou, S. H. Khong, H. S. Chan, J. H. Burroughes, L. L. Chua, R. H. Friend, P. K. Ho, *Nat Mater* **2010**, *9*, 152.
- [16] B. Liu, R. Q. Png, L. H. Zhao, L. L. Chua, R. H. Friend, P. K. Ho, *Nat Commun* **2012**, *3*, 1321.
- [17] A. R. Davis, K. R. Carter, *Macromolecules* **2015**, *48*, 1711.
- [18] C. Tao, M. Aljada, P. E. Shaw, K. H. Lee, H. Cavaye, M. N. Balfour, R. J. Borthwick, M. James, P. L. Burn, I. R. Gentle, P. Meredith, *Advanced Energy Materials* **2013**, *3*, 105.
- [19] A. Neubig, M. Thelakkat, *Polymer* **2014**, *55*, 2621.
- [20] A. Karolewski, A. Neubig, M. Thelakkat, S. Kummel, *Phys. Chem. Chem. Phys.* **2013**, *15*, 20016.
- [21] P. Bäuerle, F. Würthner, S. Heid, *Angew. Chem.* **1990**, *102*, 414.
- [22] F. Buckel, P. Persson, F. Effenberger, *Synthesis* **1999**, *1999*, 953.
- [23] L. Zhai, R. L. Pilston, K. L. Zaiger, K. K. Stokes, R. D. McCullough, *Macromolecules* **2003**, *36*, 61.
- [24] J. C. Bijleveld, A. P. Zoombelt, S. G. J. Mathijssen, M. M. Wienk, M. Turbiez, D. M. de Leeuw, R. A. J. Janssen, *J. Am. Chem. Soc.* **2009**, *131*, 16616.
- [25] J. C. Bijleveld, R. A. M. Verstrijden, M. M. Wienk, R. A. J. Janssen, *J. Mater. Chem.* **2011**, *21*, 9224.
- [26] S. Venkatesan, N. Adhikari, J. Chen, E. C. Ngo, A. Dubey, D. W. Galipeau, Q. Qiao, *Nanoscale* **2014**, *6*, 1011.
- [27] C. J. Mueller, C. R. Singh, M. Fried, S. Huettner, M. Thelakkat, *Adv. Funct. Mater.* **2015**, *25*, 2725.
- [28] J. C. Bijleveld, V. S. Gevaerts, D. Di Nuzzo, M. Turbiez, S. G. J. Mathijssen, D. M. de Leeuw, M. M. Wienk, R. A. J. Janssen, *Adv. Mater.* **2010**, *22*, E242.
- [29] W. Li, K. H. Hendriks, A. Furlan, W. S. Roelofs, S. C. Meskers, M. M. Wienk, R. A. Janssen, *Adv. Mater.* **2014**, *26*, 1565.
- [30] N. Blouin, A. Michaud, M. Leclerc, *Adv. Mater.* **2007**, *19*, 2295.

- [31] K. Gräf, M. A. Rahim, S. Das, M. Thelakkat, *Dyes and Pigments* **2013**, *99*, 1101.
- [32] N. M. Kirby, S. T. Mudie, A. M. Hawley, D. J. Cookson, H. D. T. Mertens, N. Cowieson, V. Samardzic-Boban, *J. Appl. Crystallogr.* **2013**, *46*, 1670.
- [33] J. Ilavsky, *J. Appl. Crystallogr.* **2012**, *45*, 324.

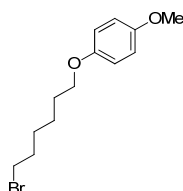
Supporting Information

Materials and Methods	319
Monomer synthesis	319
Monomer Characterization	323
Polymer syntheses	326
Polymer Characterization	332
Supporting References	349

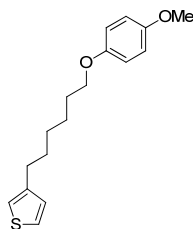
Materials and Methods

2,5-bis(trimethylstannyl)thiophene **7** was obtained from Sigma-Aldrich and recrystallized before it was used in polymerizations. 4,7-bis(5-bromo-2-yl)-2,1,3-benzothiadiazole **10** and 2,7-bis(4',4',5',5'-tetramethyl-1',3',2'-dioxaborolan-2'-yl)-N-9"-hepta-decanylcarbazole **11** were obtained from SunaTech and used as received. The reference polymers PDPP[T]₂-T **P6** and PDPP[Py]₂-T **P8** without azide functionalization were prepared as previously reported.^[1] The PCDTBT reference **P9** was synthesized following a published procedure.^[2]

Monomer synthesis

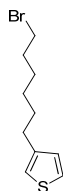


3-(*p*-Methoxyphenoxy)hexylbromide 1. In a dry 1 L flask sodium methoxide (21.76 g, 0.40 mol) was dissolved in ethanol (460 mL) and 4-methoxyphenol (40 g, 0.33 mol) was added. Finally an excess of 1,6-dibromohexane (195 mL, 1.3 mol) was added and the mixture was refluxed for 2 h. After cooling to room temperature, diethylether (250 mL) was added and the solution was washed with water. The aqueous phase was extracted with diethylether (3 x 50 mL), the combined organic layers were dried over MgSO₄, filtrated and the residual solvent was removed under reduced pressure using rotary evaporation. Unreacted 1,6-dibromohexane can be removed via distillation (60-100 °C, 5 × 10⁻³ mbar). The product was purified by distillation (140-180 °C, 5 × 10⁻³ mbar) with a heated distilling connecting tube (100 °C) to avoid solidification of the product. The product **1** was obtained as 39 g of a white crystalline solid (136 mmol, 42%).



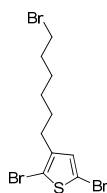
3-(6-(4-Methoxyphenoxy)hexyl)thiophene 2. In a dry 250 mL three-necked flask magnesium (1.69 g, 69.6 mmol) was provided under argon atmosphere. Anhydrous diethylether (140 mL) was poured into a dropping funnel from which 5 mL were added dropwise to the magnesium and stirred at rt. 3-(p-methoxyphenoxy)hexylbromide (20.0 g, 69.6 mmol) was transferred into a second dropping funnel, which was mounted on top of the first, and melted via a heat gun (250 °C). The molten starting material was slowly added to the residual anhydrous diethylether (135 mL) in the first dropping funnel. Afterwards approximately 20% of the diethylether solution were dropped to the suspended magnesium and the suspension stirred until the reaction started. Then the residual solution was slowly added dropwise to the reaction mixture and stirred for 16 h at rt and thereafter 3 h under reflux. In a second dry 250 mL flask Ni(dppp)Cl₂ (69.0 mg, 0.13 mmol) and 3-bromothiophene (6.0 mL, 63.3 mmol) were mixed under argon atmosphere. The Grignard-suspension in the other flask was slowly transferred via a cannula to the second flask. For this the second flask was cooled in an ice bath during the transfer. Subsequently the reaction mixture was stirred for three days under reflux in the dark. The reaction was stopped through addition of HCl (1 M, 12.5 mL, 12.5 mmol) and H₂O (70 mL). The organic phase was separated from the aqueous phase, which was then extracted with diethylether (3 x 100 mL). The combined organic phases were dried over MgSO₄, filtrated and the residual solvent was removed under reduced pressure.

The crude product was purified via vacuum distillation at 2-5 10⁻³ mbar without water cooling of the distillation apparatus and yielded 10.95 g of 3-(6-(4-methoxyphenoxy)hexyl)thiophene **2** (37.7 mmol, 60%) as white crystals.

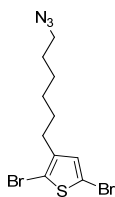


3-(6-Bromohexyl)thiophene 3. In a dry 250 mL flask 3-(6-(4-methoxyphenoxy)hexyl)thiophene (10.9 g, 37.5 mmol) was dissolved in anhydrous DCM (120 mL) under argon atmosphere at rt. Afterwards boron tribromide (3.0 mL, 31.77 mmol) and then a boron tribromide solution in DCM (1 M, 10.0 mL, 10.0 mmol) were added and the mixture stirred under reflux. The reaction was monitored via gas chromatography. After 1.5 h

the reaction was stopped through addition of saturated NH_4Cl solution (70 mL). The organic phase was separated from the aqueous phase, which was then extracted with DCM (3 x 100 mL). The combined organic phases were washed with H_2O (1 x 100 mL), saturated NaHCO_3 solution (1 x 100 mL) and again with H_2O (1 x 100 mL). The organic phase was dried over MgSO_4 , filtrated and solvents were removed under reduced pressure. The crude product was purified via column chromatography (silica gel, cyclohexane) to yield 7.98 g of 3-(6-bromohexyl)thiophene **3** (32.3 mmol, 86%) as a yellowish oil.

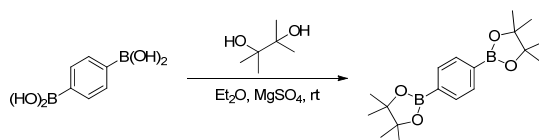


2,5-dibromo-3-(6-bromohexyl)thiophene 4. In a 250 mL flask 3-(6-bromohexyl)thiophene (7.98 g, 32.3 mmol) was dissolved in THF (40 mL) and afterwards acetic acid (40 mL) added. N-Bromsuccinimide (12.64 g, 71.0 mmol) was added in the dark and the reaction mixture stirred for 24 h at rt. The reaction was monitored via gas chromatography. The reaction was stopped through addition of H_2O (200 mL) and diluted with diethylether (100 mL). The organic phase was separated from the aqueous phase, which was then extracted with diethylether (3 x 100 mL). The combined organic phases were washed with saturated NaHCO_3 solution (70 mL), sodium hydroxide (5 w%, 50 mL) and brine (100 mL). The organic phase was dried over MgSO_4 , filtrated and solvents were removed under reduced pressure. The crude product was purified via column chromatography (silica gel, hexane). Drying in a vacuum oven yielded 12.32 g of 2,5-dibromo-3-(6-bromohexyl)thiophene **4** (30.41 mmol, 94%) as a yellowish oil.



3-(6-azidoethyl)-2,5-dibromothiophene 5. In a 100 mL flask 2,5-dibromo-3-(6-bromohexyl)thiophene (4.0 g, 9.88 mmol) was dissolved in DMSO (30 mL) and sodium azide (1.28 g, 19.8 mmol) added afterwards. The reaction mixture was stirred for 10 min at rt and sonicated for 3 min to facilitate the dissolving of sodium azide. Thereafter the reaction mixture was stirred for additional 2 h at rt. The reaction was stopped through addition of H_2O (50 mL), the organic phase was separated from the aqueous phase, which was then extracted with diethylether (3 x 50 mL). The combined organic phases were washed with brine (1 x 100 mL),

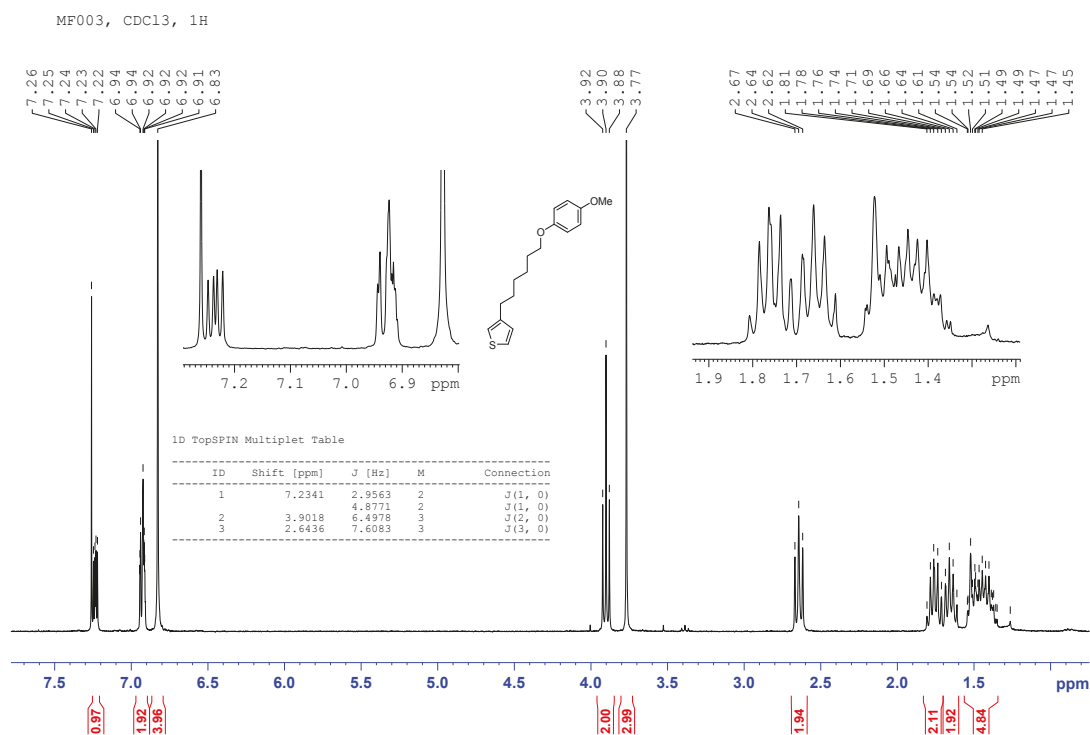
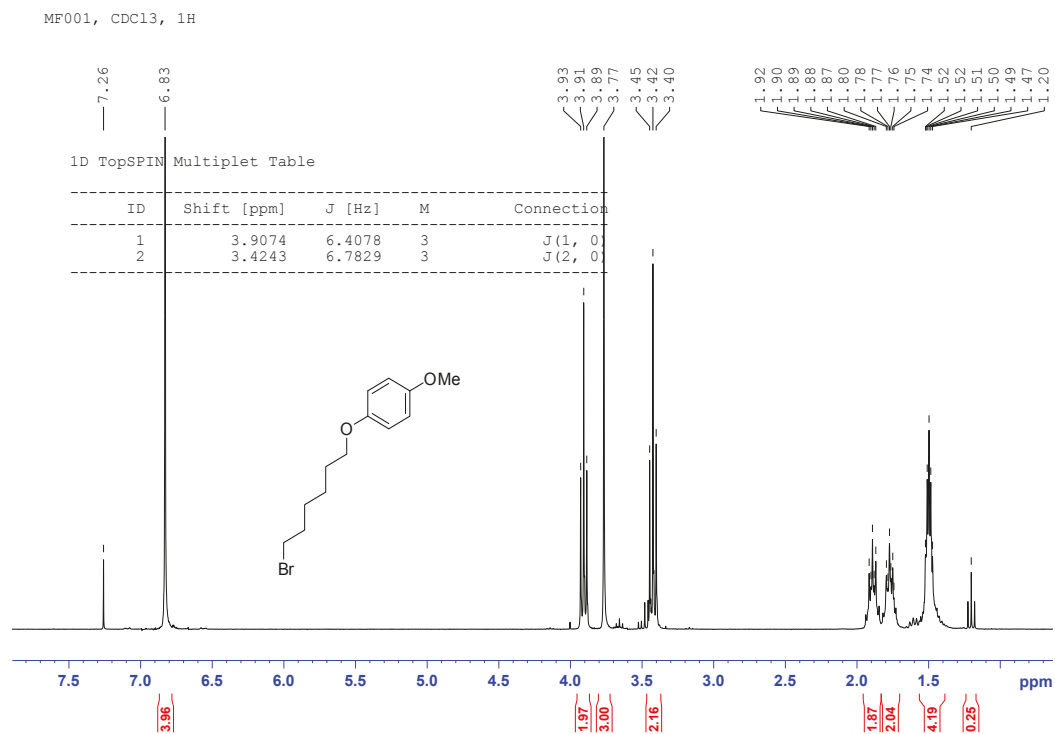
dried over MgSO_4 , filtrated and solvents were removed under high vacuum overnight. The crude product was purified via column chromatography (silica gel, cyclohexane / ethyl acetate 1:0, 10:1, 5:1, 2:1). After drying under high vacuum 3.17 g of 3-(6-azidohexyl)-2,5-dibromothiophene **5** (8.64 mmol, 87%) could be obtained as a yellowish oil.



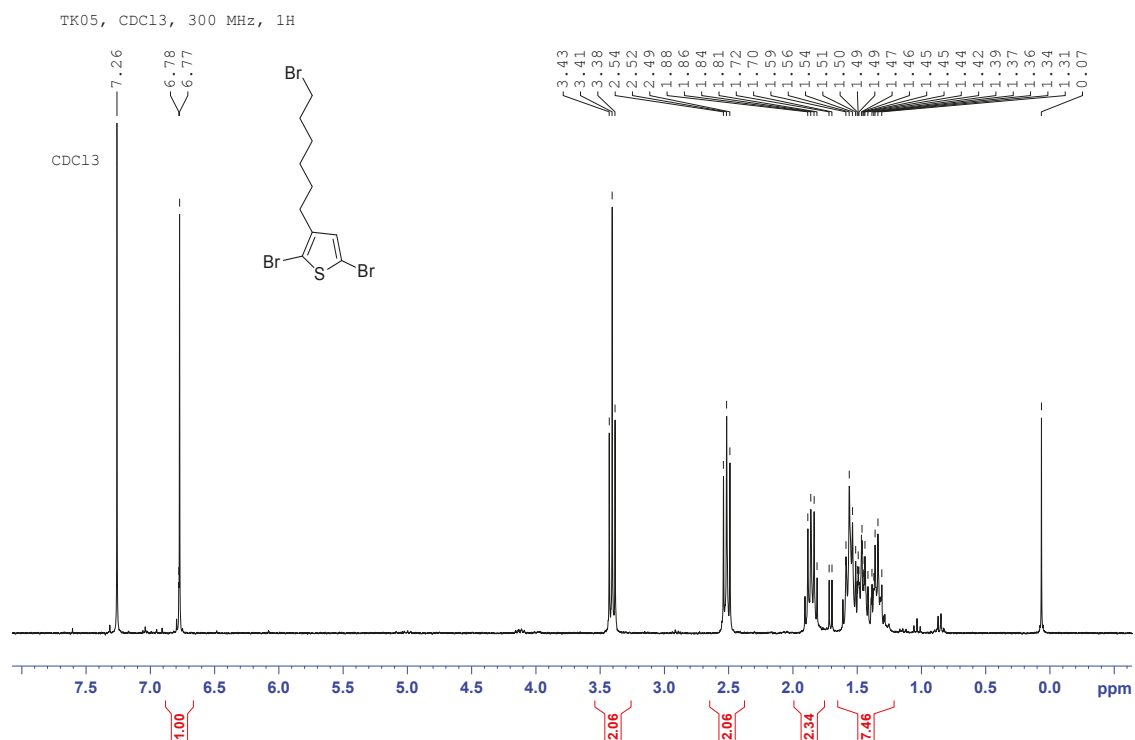
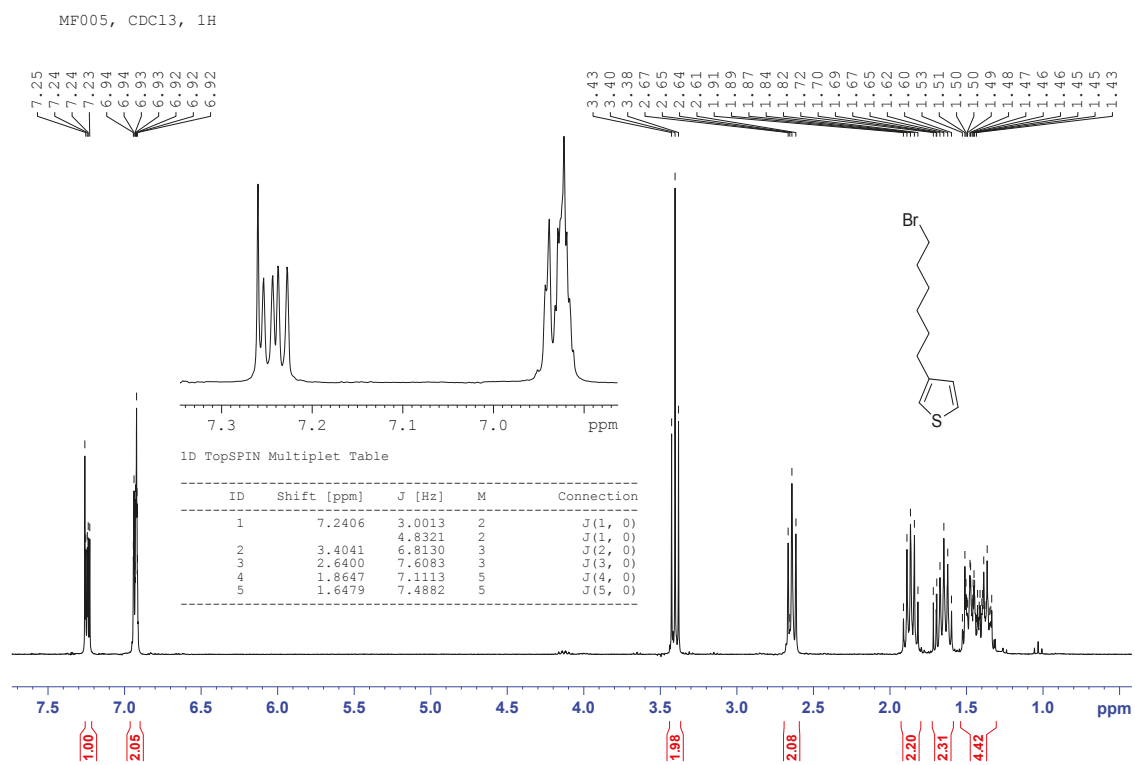
1,4-Benzenediboronic acid dipinacol ester 9. To a 250 mL three necked flask was added 1,4-phenylenediboronic acid (4.50 g, 27.1 mmol), anhydrous pinacol (7.06 g, 59.7 mmol) and dry THF (90 ml). After stirring for 5 minutes all starting materials were dissolved and anhydrous MgSO_4 (7.52 g, 62.4 mmol) was added. The flask was sealed with a rubber septum and flushed with argon. The reaction was stirred vigorously overnight at 80 °C. After cooling, the Solids were removed by filtration and washed with THF. The crude filtrate was concentrated in vacuo, redissolved in hexane/ethyl acetate 1:1 and filtered through a silica gel plug using hexane/ethyl acetate 1:1 as the eluent. Solvents were removed under reduced pressure and the residue was dried under high vacuum to yield 8.94 g of 1,4-benzenediboronic acid dipinacol ester **9** (27.1 mmol, 100%) as a white, highly crystalline solid.

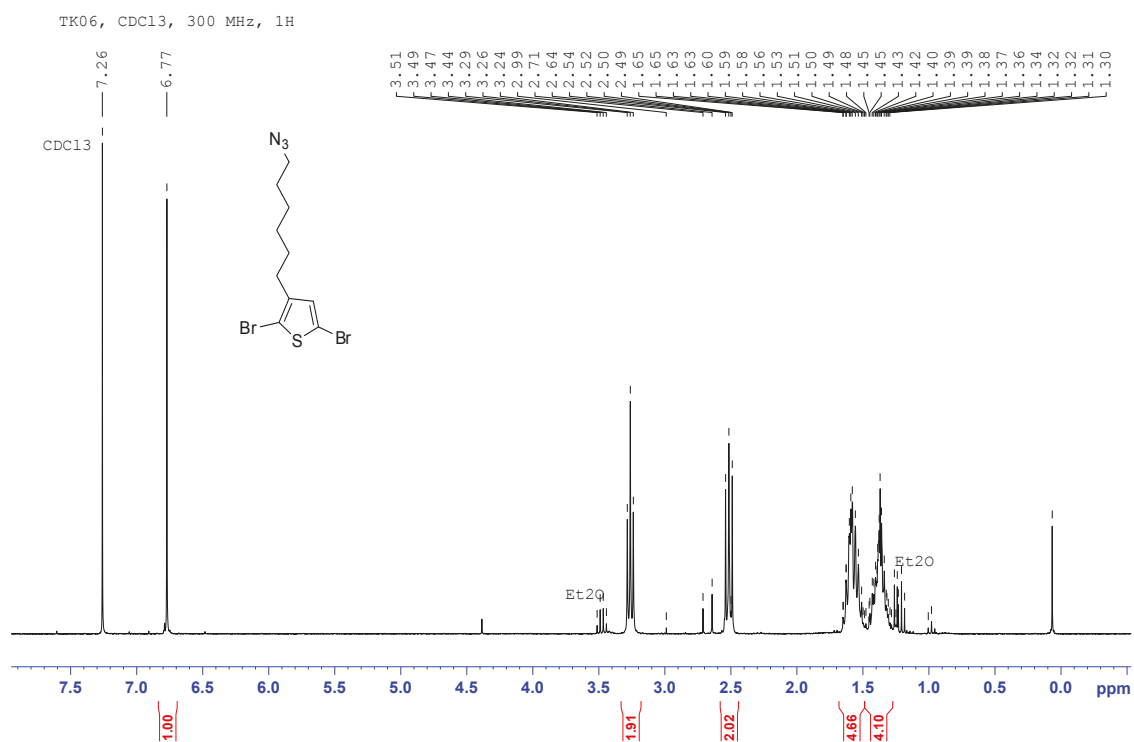
Monomer Characterization

^1H -NMR spectra of monomer compounds.

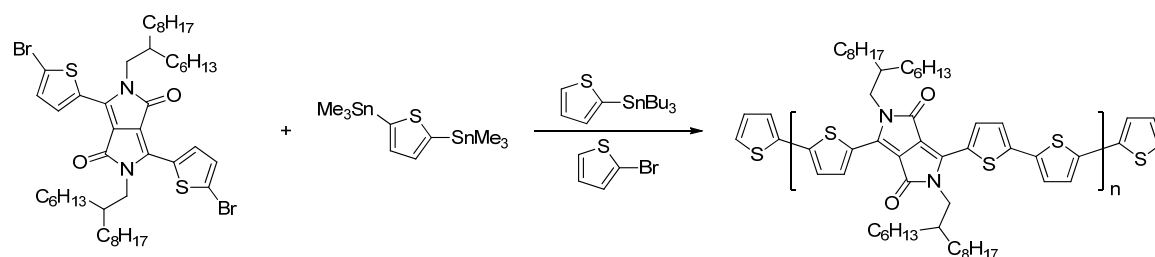


8 Azido-Functionalized Thiophene as a Versatile Building Block To Cross-Link Low-Bandgap Polymers

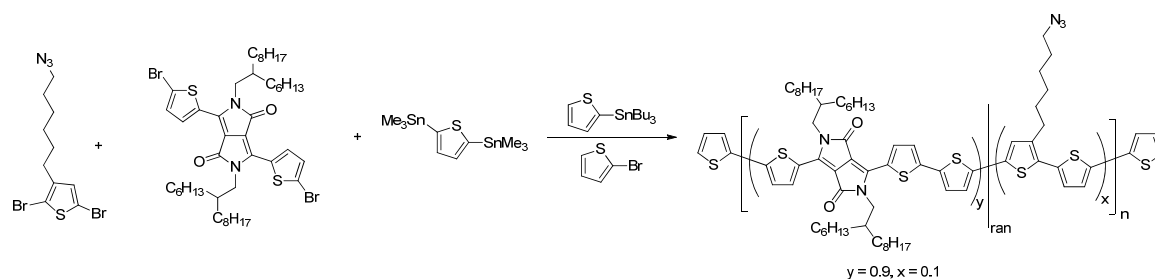




Polymer syntheses

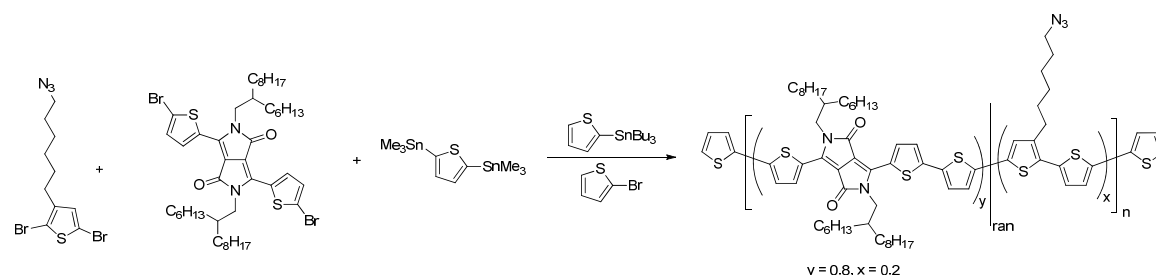


P1: PDPP[T]₂-T Similarly to an previously reported procedure,^[1] an oven dried microwave vial was loaded with DPP[T]₂{2HD}₂Br₂ (99.38 mg, 110 μmol), 2,5-bis(trimethylstannyl)thiophene (44.89 mg, 110 μmol) and tri-*o*-tolylphosphine (4.00 mg, 13 μmol). Dry and degassed chlorobenzene (2.5 mL) was added and the polymerization mixture was purged with argon for 10 min. Finally tris(dibenzylideneacetone)dipalladium(0) (3.04 mg, 3.7 μmol) was added, the vial was sealed with a septum cap and the vial atmosphere exchanged three times with argon. The mixture was stirred for 30 min at 180 °C in the microwave. After cooling to 50 °C 2-tributyltinthiophene (25 μL, 79 μmol) was added to the viscous green solution using a microliter syringe. The mixture was again heated at 180 °C for 5 min in the microwave, cooled to 50 °C and finally 2-bromothiophene (40 μL, 413 μmol) was added. The mixture was heated to 180 °C for 10 min in the microwave. After cooling to room temperature the polymer was precipitated in 250 mL methanol, filtrated over a 0.45 μm PTFE filter and dried in high vacuum. The crude polymer was subjected to soxhlet extraction using acetone, hexane and dichloromethane. The dichloromethane fraction was concentrated under reduced pressure and precipitated in 150 mL methanol. The precipitate was filtrated over a 0.45 μm PTFE filter and dried in high vacuum to obtain 85.0 mg PDPP[T]₂-T (94%) as a dark purple solid.

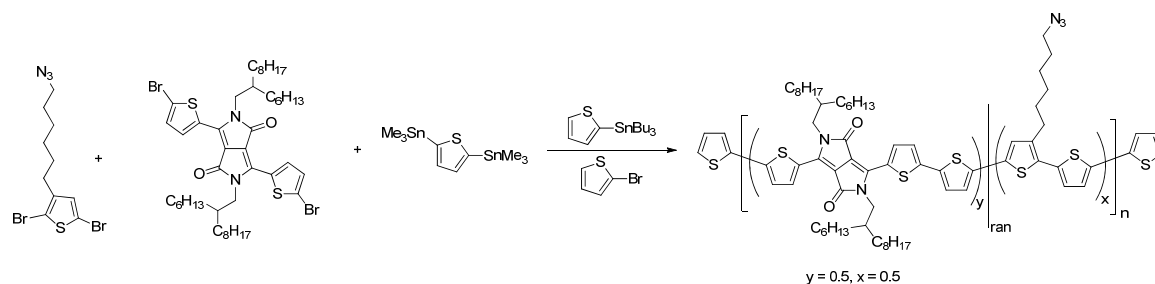


P2: PDPP[T]₂-T(5mol%Az). An oven dried microwave vial was loaded with 3-(6-azidohexyl)-2,5-dibromothiophene (5.96 mg, 16 μmol), DPP[T]₂{2HD}₂Br₂ (149.60 mg, 182 μmol), 2,5-bis(trimethylstannyl)thiophene (74.48 mg, 165 μmol) and tri-*o*-tolylphosphine (6.68 mg, 22 μmol). Dry chlorobenzene (4 mL) was added and the polymerization mixture

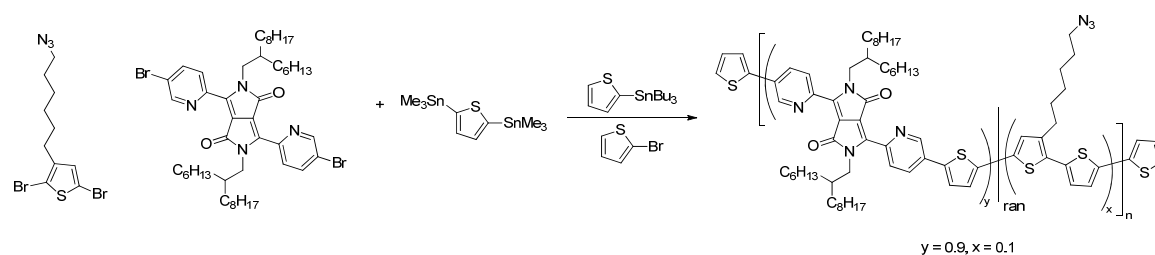
was purged with argon for 10 min. Finally tris(dibenzylideneacetone)dipalladium(0) (5.17 mg, 5.7 μmol) was added, the vial was sealed with a septum cap and the vial atmosphere exchanged three times with argon. The mixture was stirred for 30 min at 180 $^{\circ}\text{C}$ in the microwave. After cooling to 50 $^{\circ}\text{C}$ 2-tributyltinthiophene (25 μL , 79 μmol) was added to the viscous green solution using a microliter syringe. The mixture was again heated at 180 $^{\circ}\text{C}$ for 5 min in the microwave, cooled to 50 $^{\circ}\text{C}$ and finally 2-bromothiophene (40 μL , 413 μmol) was added. The mixture was heated to 180 $^{\circ}\text{C}$ for 10 min in the microwave. After cooling to room temperature the polymer was precipitated in 250 mL methanol, filtrated over a 0.45 μm PTFE filter and dried in high vacuum. The crude polymer was subjected to soxhlet extraction using acetone, hexane and dichloromethane. The dichloromethane was concentrated under reduced pressure and precipitated in 150 mL methanol. The precipitate was filtrated over a 0.45 μm PTFE filter and dried in high vacuum to obtain 132 mg PDPP[T]₂-T(10%Az) (93%) as a dark purple solid.



P3: PDPP[T]₂-T(10mol%Az). An oven dried microwave vial was loaded with 3-(6-azidohexyl)-2,5-dibromothiophene (15.04 mg, 41 μmol), DPP[T]₂{2HD}₂Br₂ (149.90 mg, 165 μmol), 2,5-bis(trimethylstannyl)thiophene (84.65 mg, 207 μmol) and tri-*o*-tolylphosphine (7.55 mg, 25 μmol). Dry chlorobenzene (4 mL) was added and the polymerization mixture was purged with argon for 10 min. Finally tris(dibenzylideneacetone)dipalladium(0) (5.85 mg, 6.4 μmol) was added, the vial was sealed with a septum cap and the vial atmosphere exchanged three times with argon. The mixture was stirred for 30 min at 180 $^{\circ}\text{C}$ in the microwave. After cooling to 50 $^{\circ}\text{C}$ 2-tributyltinthiophene (25 μL , 79 μmol) was added to the viscous green solution using a microliter syringe. The mixture was again heated at 180 $^{\circ}\text{C}$ for 5 min in the microwave, cooled to 50 $^{\circ}\text{C}$ and finally 2-bromothiophene (40 μL , 413 μmol) was added. The mixture was heated to 180 $^{\circ}\text{C}$ for 10 min in the microwave. After cooling to room temperature the polymer was precipitated in 250 mL methanol, filtrated over a 0.45 μm PTFE filter and dried in high vacuum. The crude polymer was subjected to soxhlet extraction using acetone, hexane, dichloromethane and chloroform. The dichloromethane and chloroform fractions were combined, concentrated under reduced pressure and precipitated in 150 mL methanol. The precipitate was filtrated over a 0.45 μm PTFE filter and dried in high vacuum to obtain 142 mg PDPP[T]₂-T(20%Az) (96%) as a dark purple solid.

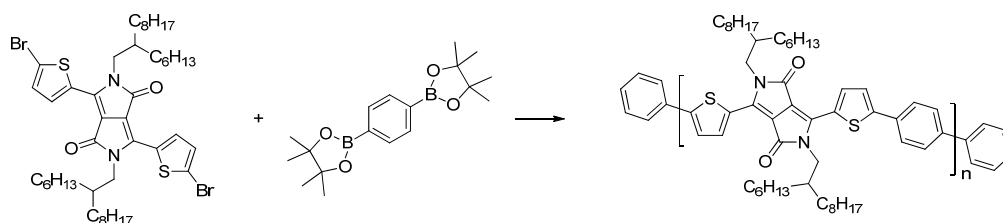


P4: PDPP[T]₂-T(25mol%Az). An oven dried microwave vial was loaded with 3-(6-azidohexyl)-2,5-dibromothiophene (48.30 mg, 132 μ mol), DPP[T]₂{2HD}₂Br₂ (120.17 mg, 132 μ mol), 2,5-bis(trimethylstannyl)thiophene (108.17 mg, 264 μ mol) and tri-*o*-tolylphosphine (9.89 mg, 33 μ mol). Dry chlorobenzene (4.8 mL) was added and the polymerization mixture was purged with argon for 10 min. Finally tris(dibenzylideneacetone)dipalladium(0) (7.71 mg, 8.4 μ mol) was added, the vial was sealed with a septum cap and the vial atmosphere exchanged three times with argon. The mixture was stirred for 30 min at 180 °C in the microwave. After cooling to 50 °C 2-tributyltinthiophene (25 μ L, 79 μ mol) was added to the viscous green solution using a microliter syringe. The mixture was again heated at 180 °C for 5 min in the microwave, cooled to 50 °C and finally 2-bromothiophene (40 μ L, 413 μ mol) was added. The mixture was heated to 180 °C for 10 min in the microwave. After cooling to room temperature the polymer was precipitated in 250 mL methanol, filtrated over a 0.45 μ m PTFE filter and dried in high vacuum. The crude polymer was subjected to soxhlet extraction using acetone, hexane and dichloromethane. The remaining precipitate was refluxed for 16 h in chloroform. The obtained solution was filtrated, concentrated under reduced pressure and precipitated in 150 mL methanol. Filtration over a 0.45 μ m PTFE filter and drying in high vacuum yielded 84 mg (57%) PDPP[T]₂-T(50%Az) as a dark purple solid.



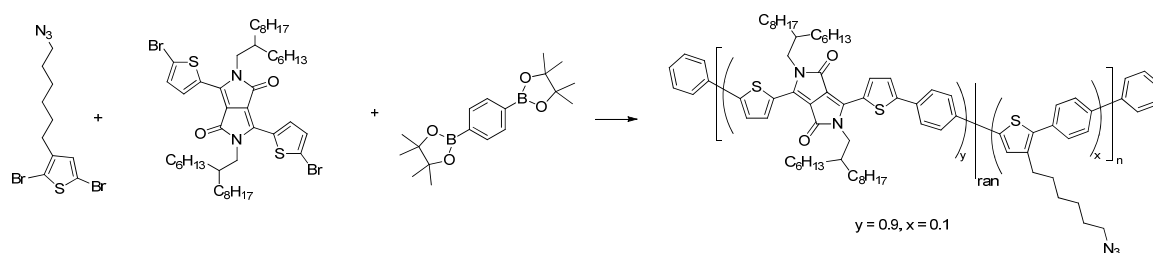
P6: PDPP[Py]₂-T(5mol%Az). An oven dried microwave vial was loaded with 3-(6-azidohexyl)-2,5-dibromothiophene (6.15 mg, 17 μ mol), DPP[Py]₂{2HD}₂Br₂ (135.03 mg, 151 μ mol), 2,5-bis(trimethylstannyl)-thiophene (68.5 mg, 167 μ mol) and tri-*o*-tolylphosphine (6.38 mg, 21 μ mol). Dry and degassed chlorobenzene (4 mL) was added and the polymerization mixture was purged with argon for 10 min. Finally tris(dibenzylideneacetone)dipalladium(0) (4.90 mg, 5.35 μ mol) was added, the vial was sealed with a septum cap and the vial atmosphere exchanged three times with argon. The mixture was stirred for 60 min at 180 °C in the

microwave. After cooling to 50 °C 2-tributyltinthiophene (25 μ L, 79 μ mol) was added to the blue solution using a microliter syringe. The mixture was again heated at 180 °C for 10 min in the microwave, cooled to 50 °C and finally 2-bromothiophene (25 μ L, 258 μ mol) was added. The mixture was heated to 180 °C for 10 min in the microwave. After cooling to room temperature the polymer was directly precipitated into methanol (200 mL). The precipitate was filtrated through a soxhlet thimble and was further purified by soxhlet extraction using methanol, acetone, hexane and chloroform. The chloroform fraction only contained 15 mg of product and was discarded. The hexane fraction was concentrated to dryness under reduced pressure and redissolved in a minimal amount of chloroform before it was precipitated in methanol (200 mL). The precipitate was filtrated over a 0.45 μ m PTFE filter and dried in high vacuum to obtain 109 mg PDPP[Py]₂-T(10%Az) (85%) as a dark purple solid.



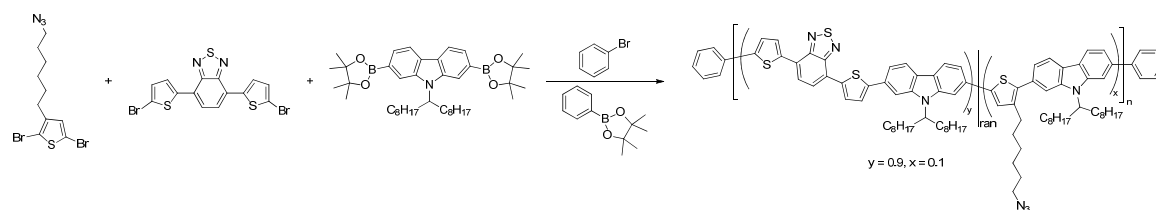
P7: PDPP[T]₂-Ph. A schlenk tube with a PTFE sealed screw cap was loaded with DPP[T]₂{2HD}₂Br₂ (551.49 mg, 608 μ mol), freshly recrystallized 1,4-benzenediboronic acid dipinacol ester (200.72 mg, 608 μ mol) and triphenylphosphine (27.13 mg, 103 μ mol). The solids were dissolved in degassed toluene (22 mL) and 4.4 mL (ratio 5:1) of an aqueous, degassed 2 M tribasic potassium phosphate solution were added. Furthermore, 3 drops of Aliquat 336 were added as a phase transfer catalyst and the mixture was purged with argon for 30 min. Pd₂(dba)₃ (23.68 mg, 26 μ mol) as added, the tube was sealed tightly and an inert atmosphere was ensured by 10 vacuum/argon cycles. The reaction mixture was protected from light and stirred at 115 °C for 18 h. The green suspension was then cooled to room temperature using an ice bath, benzenboronic acid pinacol ester (60 mg, 294 μ mol) was added and the mixture was again degassed by 5 vacuum/argon cycles. Endcapping was performed for 30 min at 115 °C and the mixture was again cooled to room temperature before bromobenzene (100 μ L, 1 mmol) was added and the mixture was finally heated to 115 °C for 2 h. After cooling to room temperature, the reaction mixture was transferred into a separating funnel using chloroform and water. The organic phase was poured into 200 mL of 25% aqueous ammonia solution and refluxed at 80 °C for 15 min in the dark. The phases were separated and the organic layer was stirred with a mixture of ethylenediaminetetraacetic acid (EDTA, 600 mg, 2 mmol) and tetrapotassium EDTA salt (900 mg, 2 mmol) for 15 min before 200 mL water were added and the mixture was stirred vigorously for 2 h in the dark. The organic phase was isolated, washed with water twice, dried over MgSO₄ and filtrated through

mineral wool. The solution was then concentrated to 20 mL and precipitated into 1.2 L of methanol. The precipitate was filtered through a glass frit, washed with methanol and dried *in vacuo* overnight. The crude polymer was further purified by soxhlet extraction using acetone, hexane and dichloromethane as solvents. The remaining solid was put into a flask and refluxed in chloroform for 1 h. The solution was filtered, concentrated under reduced pressure and precipitated into methanol (1.2 L). The precipitate was filtered through a glass frit and dried *in vacuo* for 2 h at 55 °C and at room temperature overnight to obtain 444 mg (86%) PDPP[T]₂-Ph as a purple film.



P8: PDPP[T]₂-Ph(5mol%Az). 3-(6-Azido-2,5-dibromothiophen-2-yl)propan-1-ol (6.31 mg, 17 μmol) was weighed into a snap cap vial. A schlenk tube with a PTFE sealed screw cap was loaded with DPP[T]₂{2HD}₂Br₂ (142.90 mg, 158 μmol), freshly recrystallized 1,4-benzenediboronic acid dipinacol ester (57.70 mg, 175 μmol) and triphenylphosphine (6.18 mg, 24 μmol). Degassed toluene (6 mL) was used to transfer the 3-(6-azido-2,5-dibromothiophen-2-yl)propan-1-ol into the schlenk tube and 0.6 mL (ratio 10:1) of an aqueous, degassed 2 M tribasic potassium phosphate solution were added. Furthermore, 3 drops of Aliquat 336 were added as a phase transfer catalyst and the mixture was purged with argon for 30 min. Pd₂(dba)₃ (5.27 mg, 5.8 μmol) as added, the tube was sealed tightly and an inert atmosphere was ensured by 10 vacuum/argon cycles. The reaction mixture was protected from light and stirred at 120 °C for 2 h. The green suspension was then cooled to room temperature using an ice bath, benzeneboronic acid pinacol ester (60 mg, 294 μmol) was added and the mixture was again degassed by 5 vacuum/argon cycles. Endcapping was performed for 30 min at 120 °C and the mixture was again cooled to room temperature before bromobenzene (100 μL, 1 mmol) was added and the mixture was finally heated to 120 °C for 1 h. After cooling to room temperature, the reaction mixture was transferred into a separating funnel using chloroform and water. The organic phase was poured into 70 mL of 25% aqueous ammonia solution and refluxed at 80 °C for 10 min in the dark. The phases were separated and the organic layer was stirred with a mixture of ethylenediaminetetraacetic acid (EDTA, 250 mg) and tetrapotassium EDTA salt (250 mg) for 15 min before 70 mL water were added and the mixture was stirred vigorously for 1 h in the dark. The organic phase was isolated, washed with water twice, dried over MgSO₄ and filtrated through mineral wool. The solution was then concentrated to 15 mL and precipitated into 150 mL of methanol. The precipitate

was filtered through a soxhlet thimble and was then further purified by soxhlet extraction using acetone, hexane and dichloromethane as solvents. The remaining solid was put into a flask and refluxed in chloroform overnight. The solution was filtered, concentrated under reduced pressure and precipitated into methanol (200 mL). The precipitate was filtered through a 0.45 μm PTFE filter and dried *in vacuo* at room temperature overnight to obtain 89 mg (67%) PDPP[T]₂-Ph as a purple film.



P10: PCDTBT(5mol%Az). 3-(6-Azidohexyl)-2,5-dibromothiophene (6.83 mg, 19 μmol) was weighed into a snap cap vial. A schlenk tube with a PTFE sealed screw cap was loaded with 4,7-bis(5-bromo-2-yl)-2,1,3-benzothiadiazole (77.67 mg, 170 μmol), 2,7-bis(4',4',5',5'-tetramethyl-1',3',2'-dioxaborolan-2'-yl)-N-9''-hepta-decanylcarbazole (123.7 mg, 188 μmol) and tri-*o*-tolylphosphine (6.72 mg, 22 μmol). Degassed toluene (7 mL) was used to transfer the 3-(6-azidohexyl)-2,5-dibromothiophene into the schlenk tube and 0.7 mL (ratio 10:1) of an aqueous, degassed 2 M tribasic potassium phosphate solution were added. Furthermore, 3 drops of Aliquat 336 were added as a phase transfer catalyst and the mixture was purged with argon for 30 min. $\text{Pd}_2(\text{dba})_3$ (5.13 mg, 5.6 μmol) as added, the tube was sealed tightly and an inert atmosphere was ensured by 10 vacuum/argon cycles. The reaction mixture was protected from light and stirred at 120 $^{\circ}\text{C}$ for 2 h. The red suspension and was then cooled to room temperature using an ice bath, benzenboronic acid pinacol ester (40 mg, 196 μmol) was added and the mixture was again degassed by 5 vacuum/argon cycles. Endcapping was performed for 30 min at 120 $^{\circ}\text{C}$ and the mixture was again cooled to room temperature before bromobenzene (100 μL , 1 mmol) was added and the mixture was finally heated to 120 $^{\circ}\text{C}$ for 1 h. After cooling to room temperature, the reaction mixture was transferred into a separating funnel using chloroform and water. The phases were separated and the organic layer was stirred with a mixture of ethylenediaminetetraacetic acid (EDTA, 250 mg) and tetrapotassium EDTA salt (250 mg) for 15 min before 70 mL water were added and the mixture was stirred vigorously for 1 h in the dark. The organic phase was isolated, washed with water twice, dried over MgSO_4 and filtrated through mineral wool. The solution was then concentrated to 15 mL and precipitated into 150 mL of methanol. The precipitate was filtered through a soxhlet thimble and was then further purified by soxhlet extraction using acetone, hexane, dichloromethane and chloroform as solvents. The chloroform and the dichloromethane fractions were combined, filtrated, concentrated under reduced pressure and precipitated into a methanol/water mixture (200 mL / 20 mL). The precipitate was filtered through a 0.45 μm

PTFE filter and dried *in vacuo* at room temperature overnight to obtain 56 mg (43%) PCDTBT(10%Az) as a red solid.

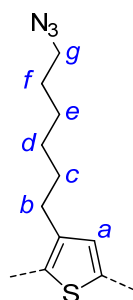
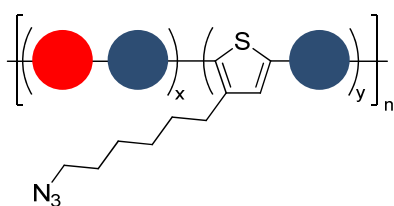
Polymer Characterization

Polymer NMR

The built-in mole fraction $\chi_{\text{NMR}}(y)$ of the 6-azido-hexyl functionalized thiophene moiety in the polymers was determined by correlating the $-CH_2N_3$ signal (H_g , 2 H) at ~ 3.35 ppm as well as the $\alpha\text{-}CH_2$ group at ~ 2.89 ppm (H_b , 2 H) to an alkyl signal of the regular sidechains (either at the DPP moiety for **P2-P8** or the carbazole moiety for **P10**). In the case of any DPP polymers the tertiary $-CH-$ signal at the sidechain branching point (at ~ 2.07 ppm, corresponds to 2 H due to two sidechains per DPP moiety) was used. For the PCDTBT system either the $-CH-$ signal at the sidechain branching point at ~ 4.77 ppm (1 H) or the $-CH_2-$ group at ~ 2.46 ppm was used. The built-in mole fractions of the two repeating units x and y were calculated as follows:

$$\chi_{\text{NMR}}(x) = \frac{H_{\text{reference}}}{H_{\text{reference}} + \frac{H_b + H_g}{2}}$$

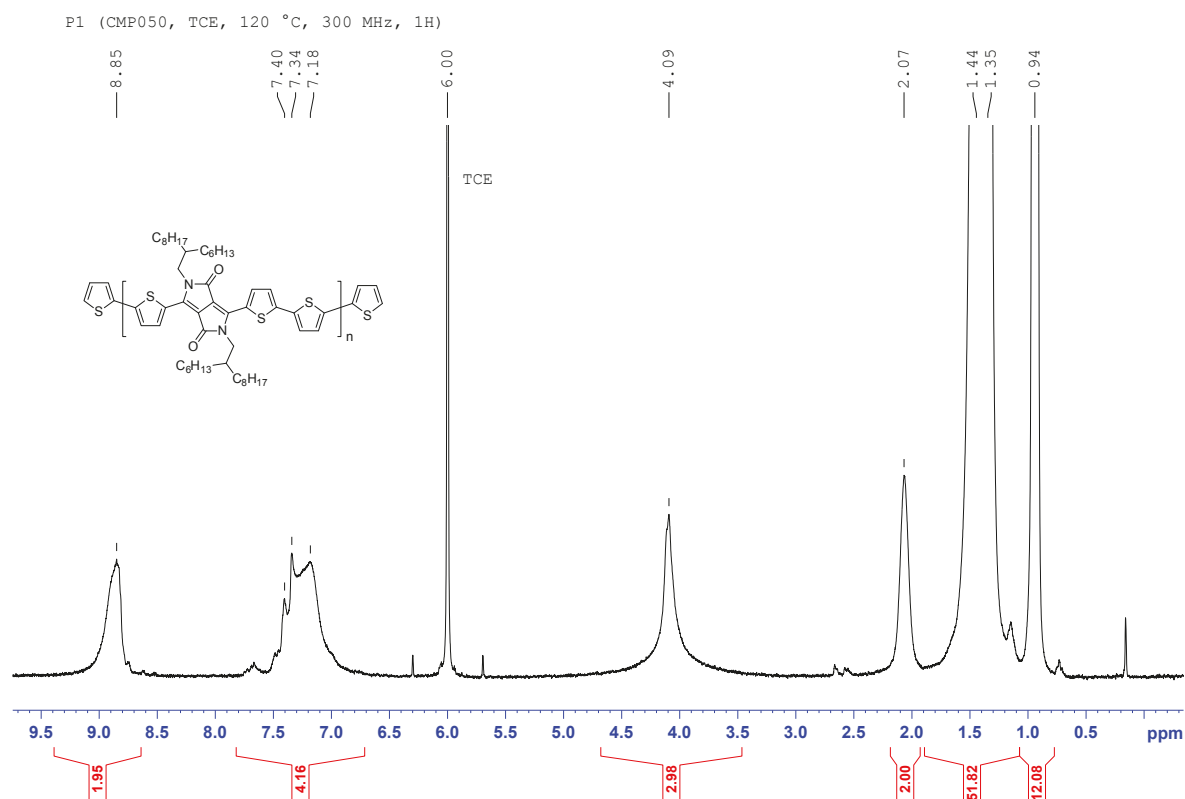
$$\chi_{\text{NMR}}(y) = \frac{\frac{H_b + H_g}{2}}{H_{\text{reference}} + \frac{H_b + H_g}{2}}$$

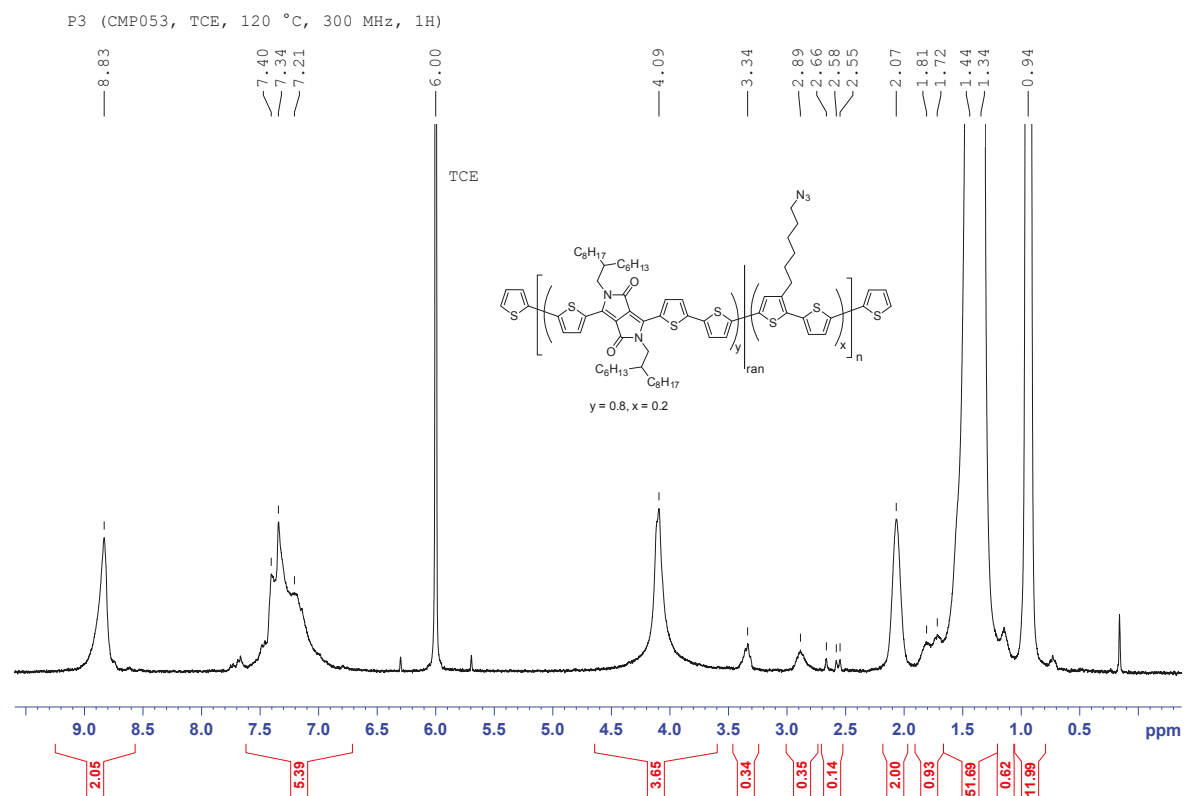
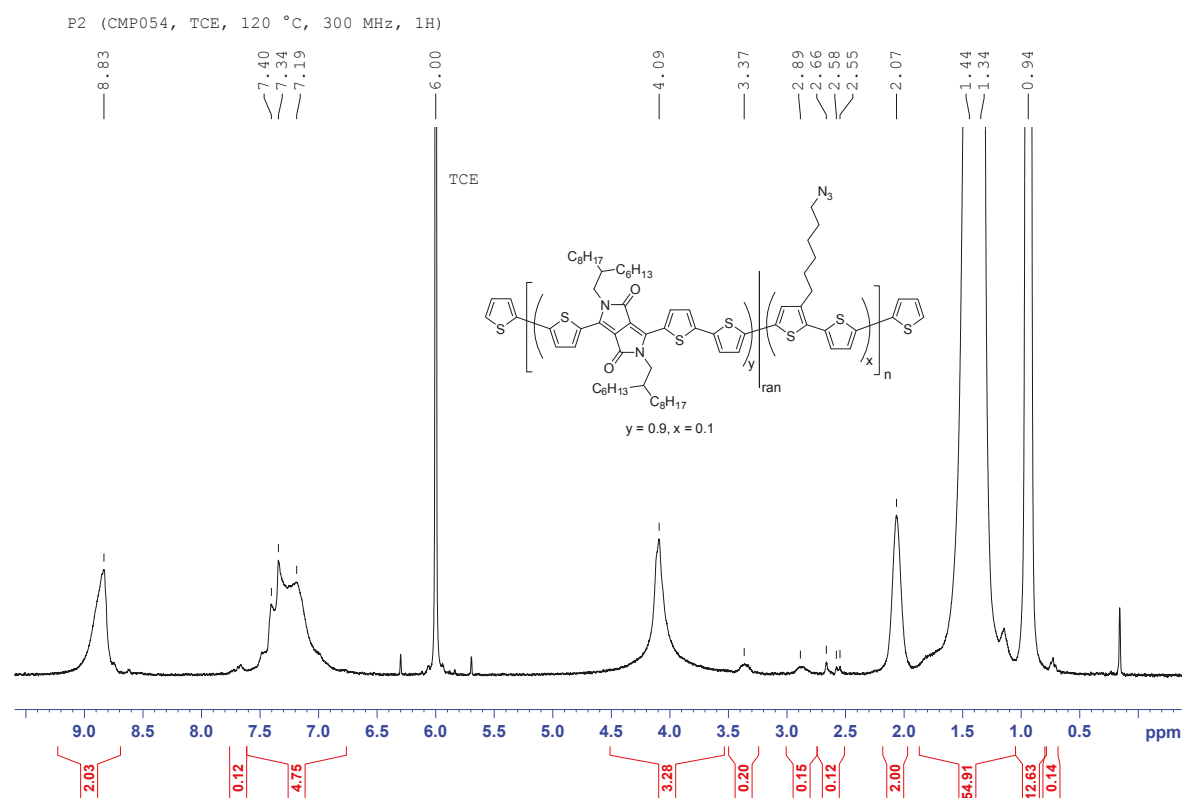


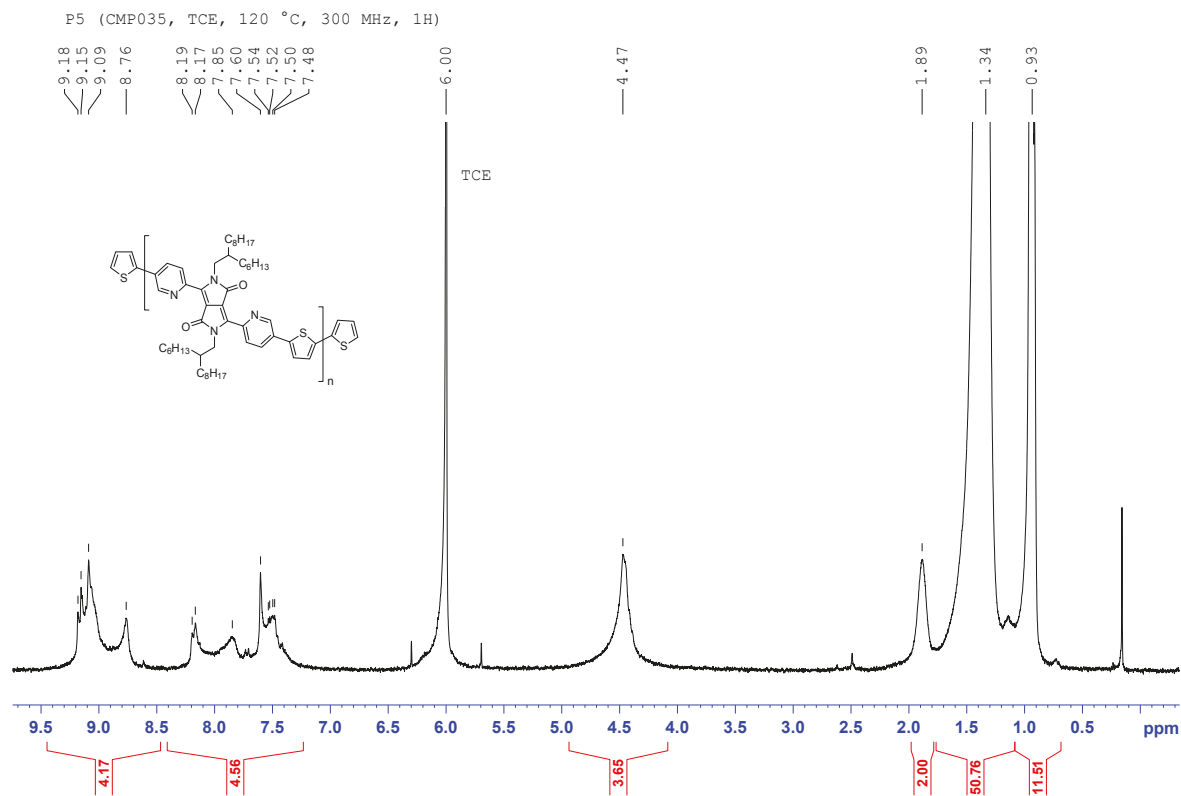
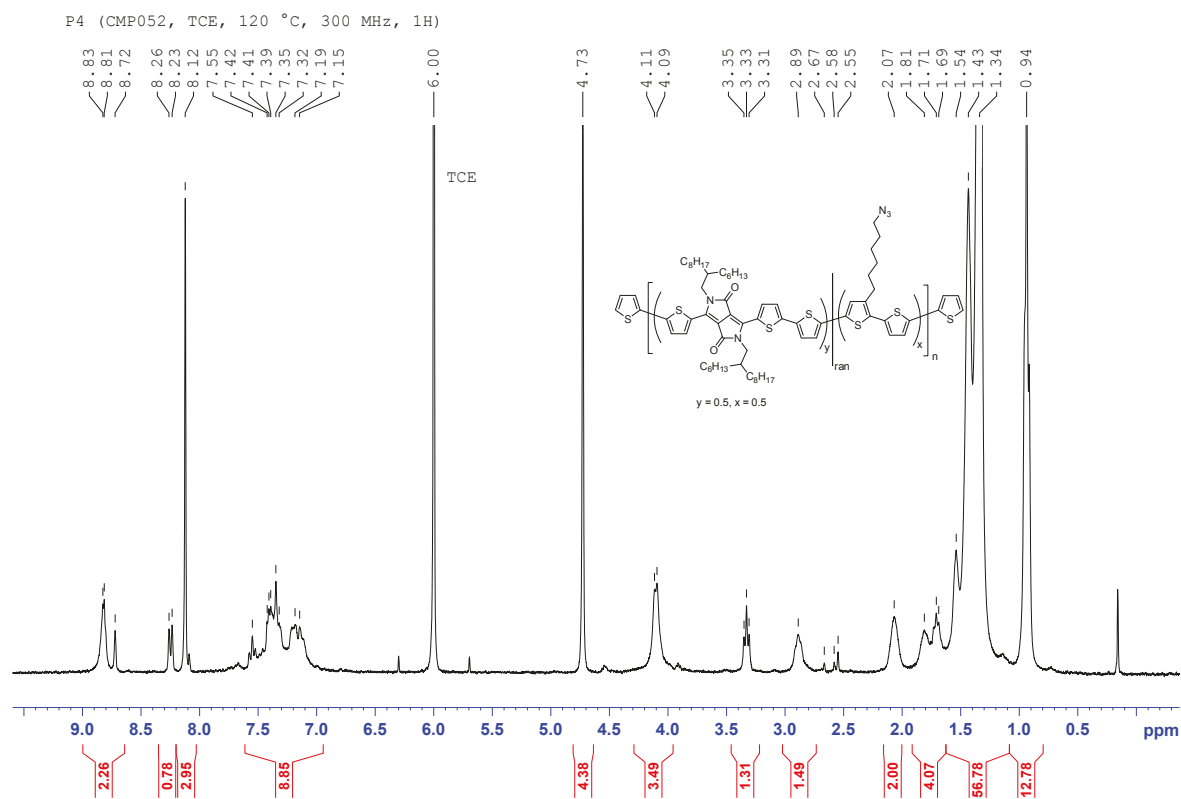
Where $H_{\text{reference}}$ is the signal of either the DPP or carbazole sidechain as described above and H_b and H_g are the signals from the azido-functionalized thiophene moiety

Table S8-1. Calculation of the built-in mole fraction of the azide-functionalized thiophene moiety by ^1H -NMR.

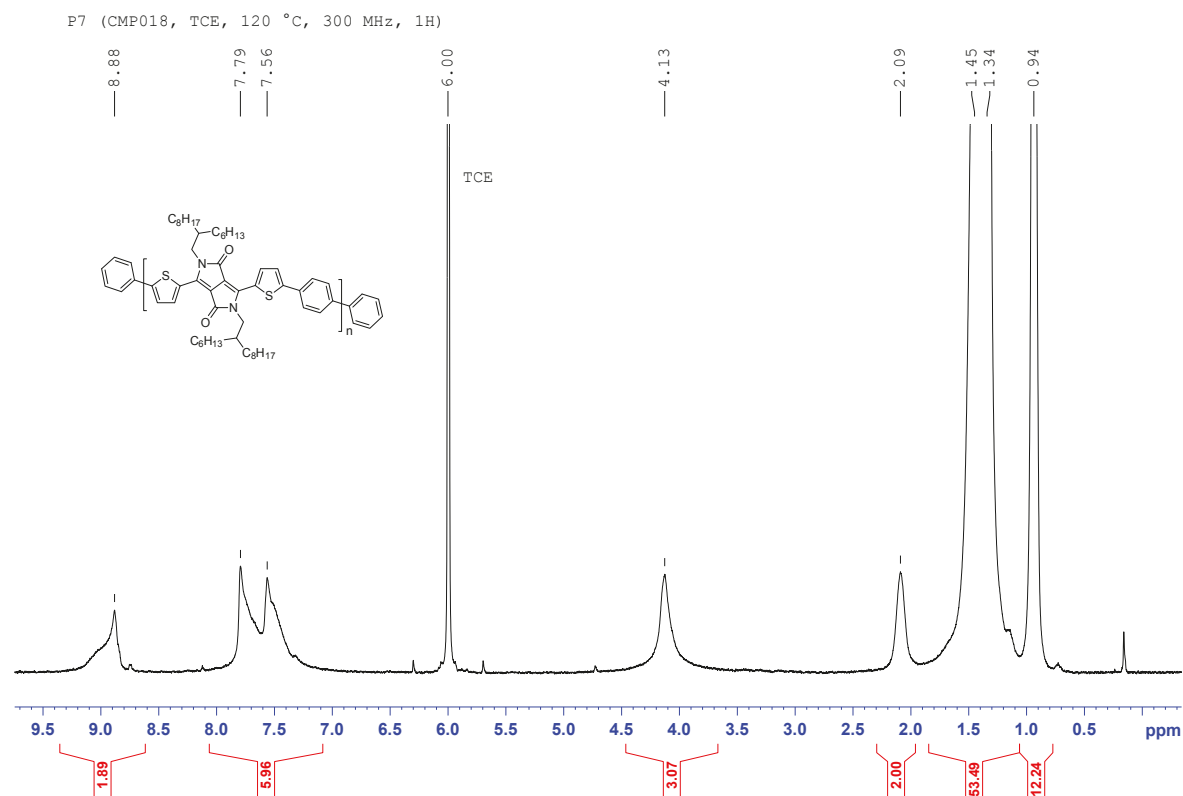
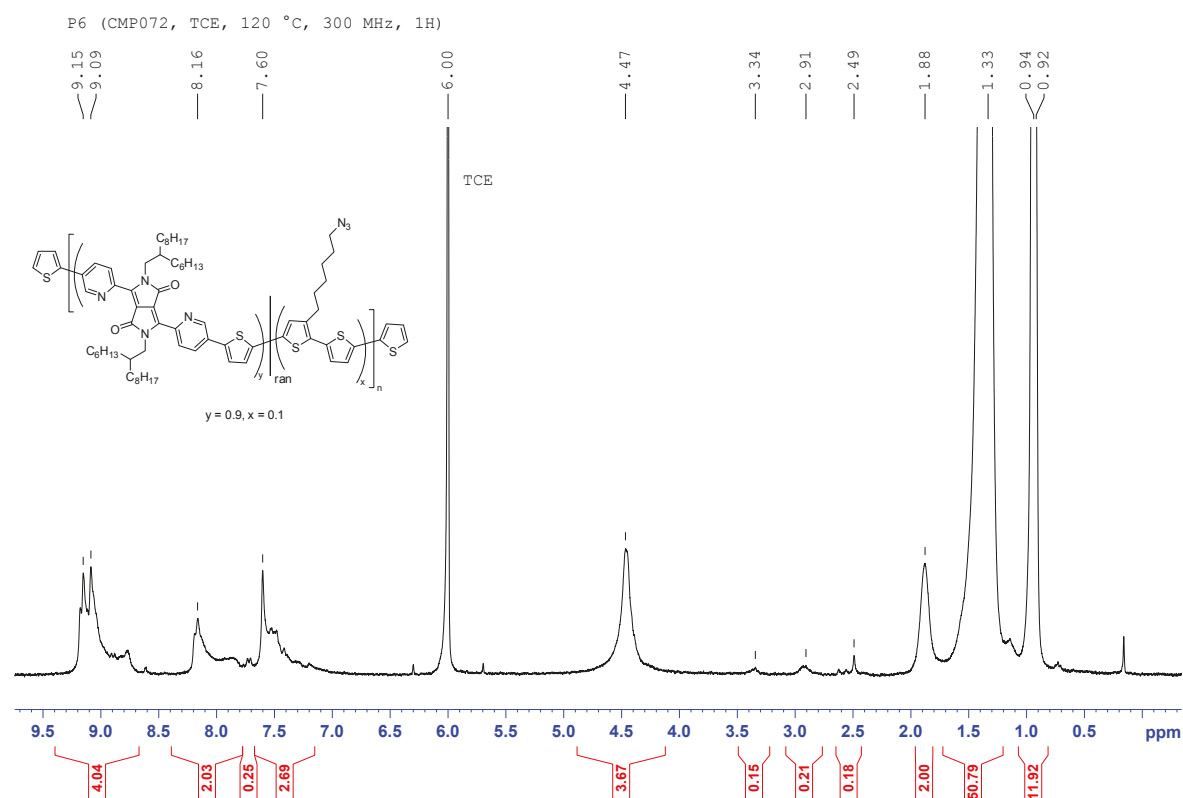
Polymer	Reference signal	H_g	H_b	$\chi^{\text{NMR}}(x)$	$\chi^{\text{NMR}}(y)$
P1	2.00	0.00	0.00	1.00	0.00
P2	2.00	0.20	0.15	0.92	0.08
P3	2.00	0.34	0.35	0.85	0.15
P4	2.00	1.31	1.49	0.59	0.41
P5	2.00	0.00	0.00	1.00	0.00
P6	2.00	0.15	0.21	0.92	0.08
P7	2.00	0.00	0.00	1.00	0.00
P8	2.00	0.17	0.17	0.92	0.08
P9	1.00	0.00	0.00	1.00	0.00
P10	1.00	0.14	0.08	0.90	0.10

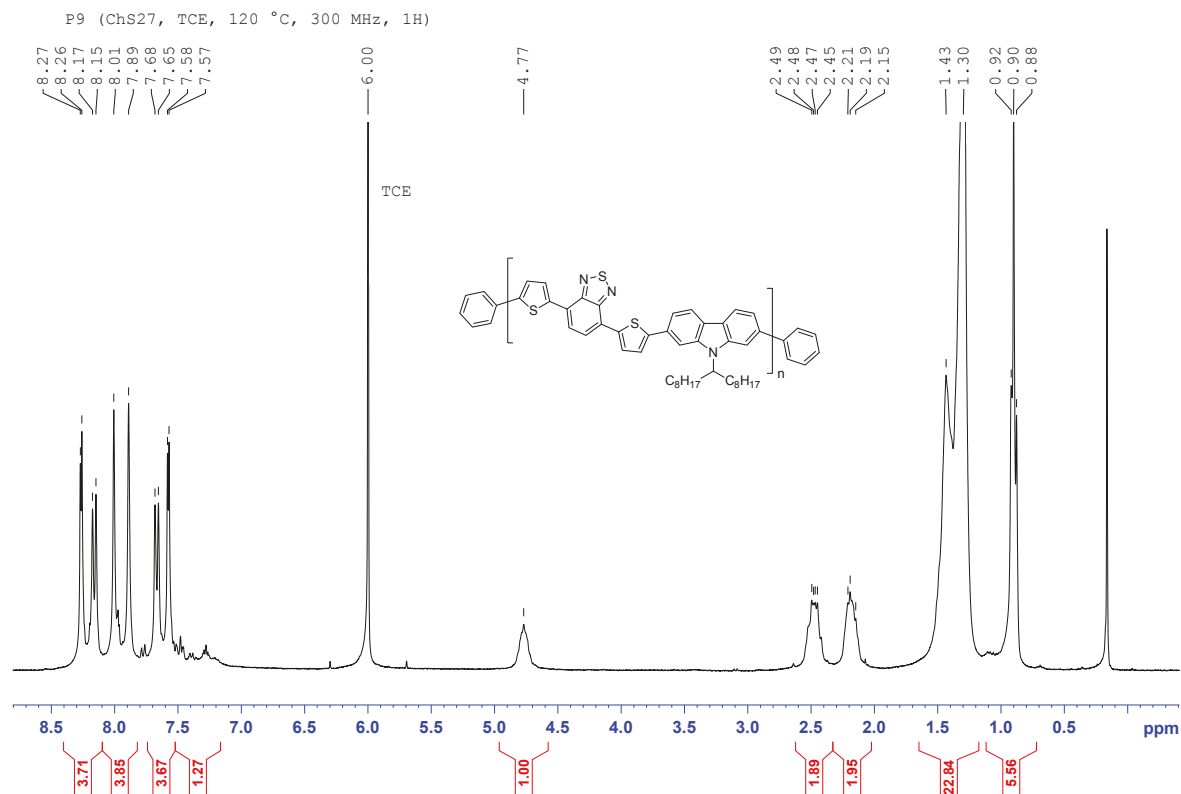
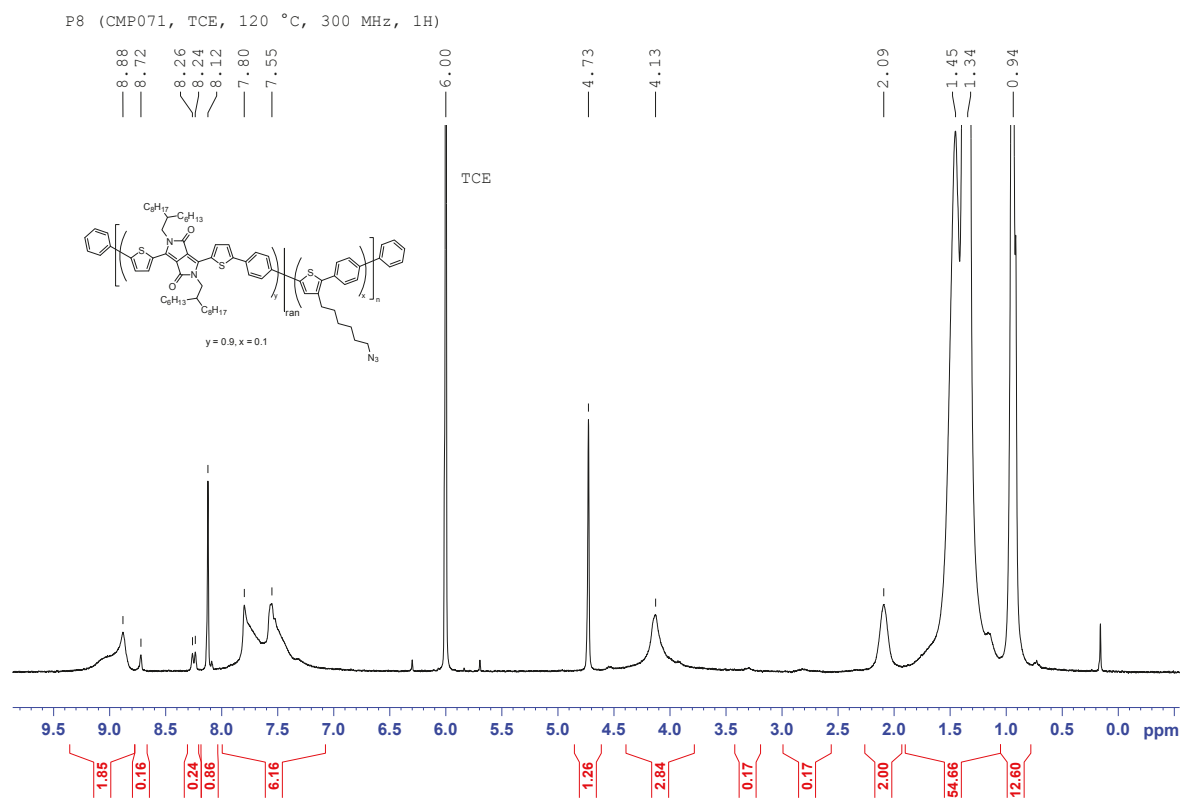




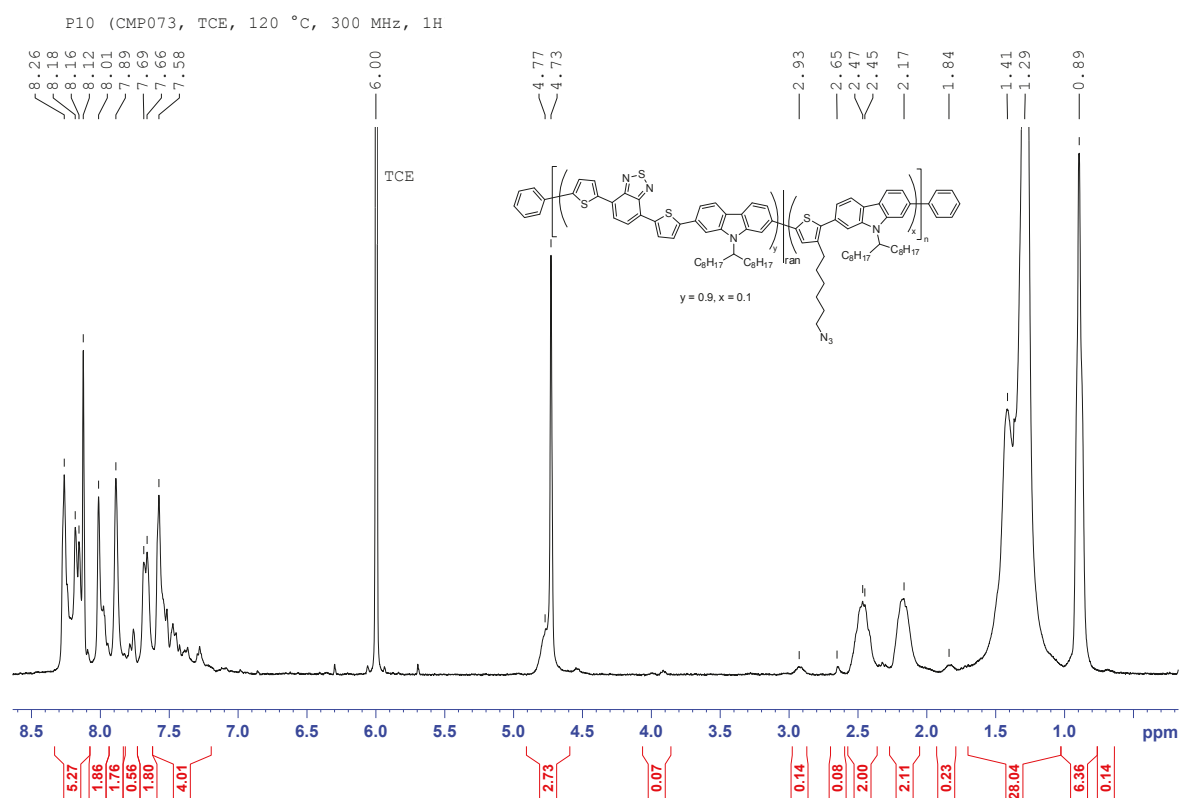


8 Azido-Functionalized Thiophene as a Versatile Building Block To Cross-Link Low-Bandgap Polymers

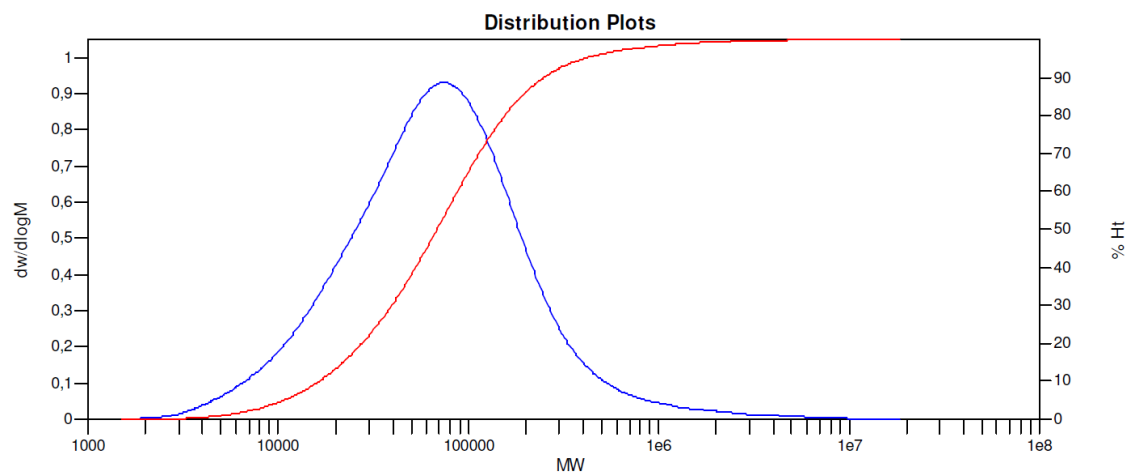




8 Azido-Functionalized Thiophene as a Versatile Building Block To Cross-Link Low-Bandgap Polymers



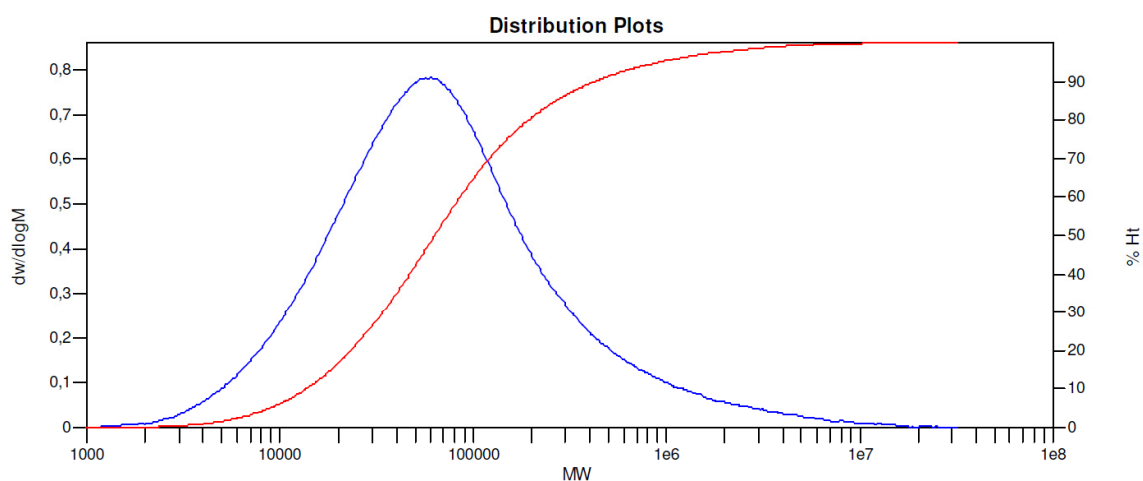
Gel Permeation Chromatography



MW Averages

Peak No	Mp	Mn	Mw	Mz	Mz+1	Mv	PD
1	74390	36932	145504	1488203	6627220	110739	3.93978

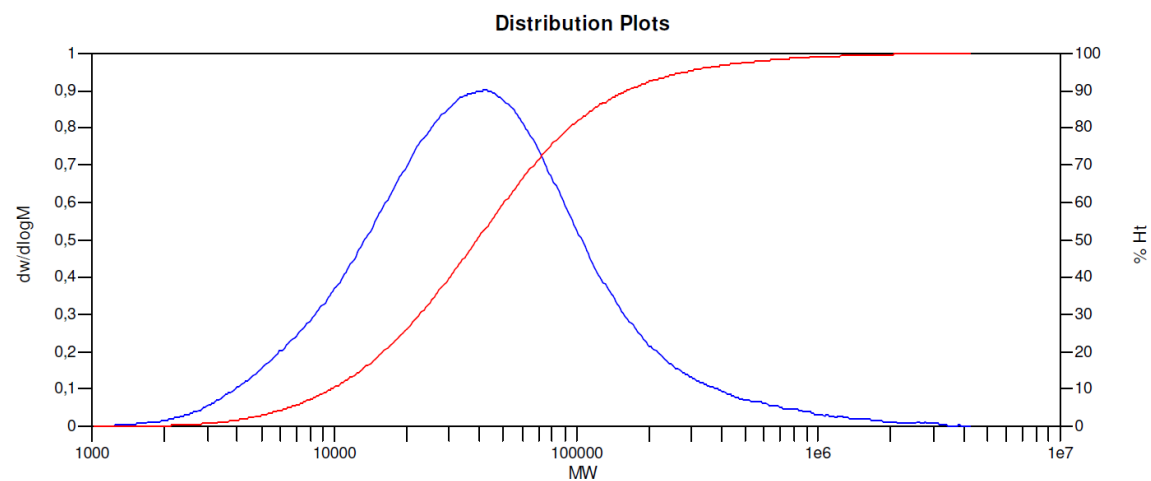
Figure S8-1. GPC molecular weight distribution of P1 PDPP[T]₂-T.



MW Averages

Peak No	Mp	Mn	Mw	Mz	Mz+1	Mv	PD
1	60552	31575	253520	3635108	10483408	163343	8.02914

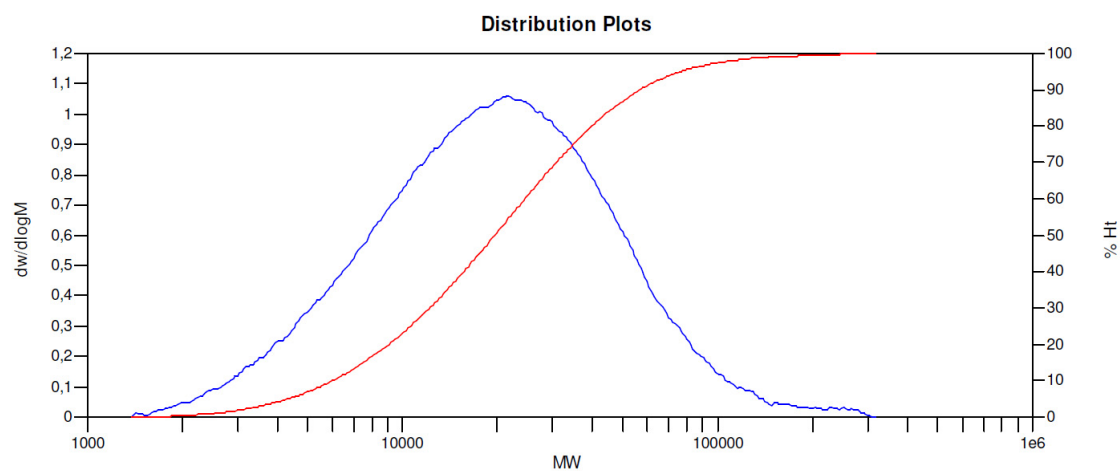
Figure S8-2. GPC molecular weight distribution of P2 PDPP[T]₂-T (10% azide content).



MW Averages

Peak No	Mp	Mn	Mw	Mz	Mz+1	Mv	PD
1	42506	22157	84630	508642	1515681	66014	3.81956

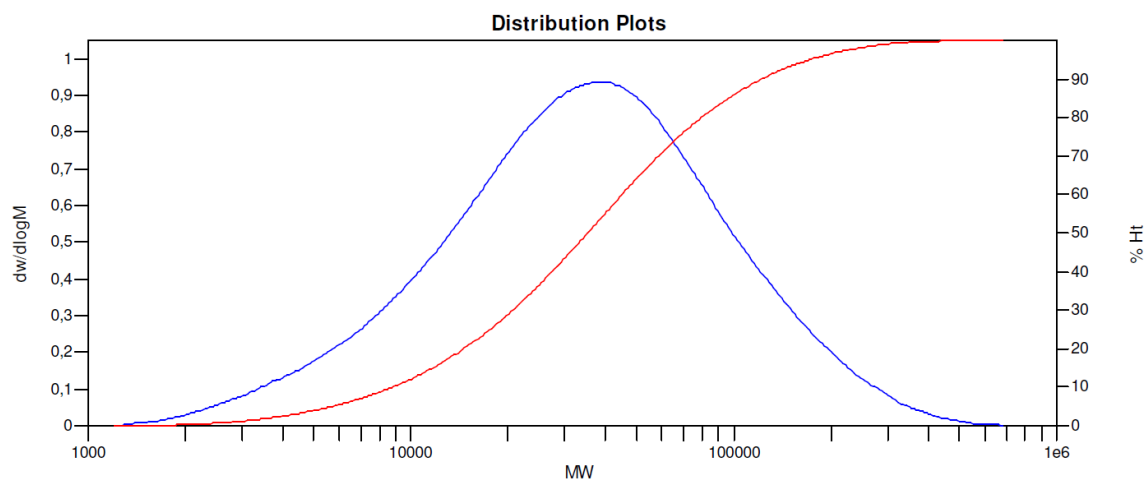
Figure S8-3. GPC molecular weight distribution of P3 PDPP[T]₂-T (20% azide content).



MW Averages

Peak No	Mp	Mn	Mw	Mz	Mz+1	Mv	PD
1	21456	12949	27537	56517	106264	24719	2.12657

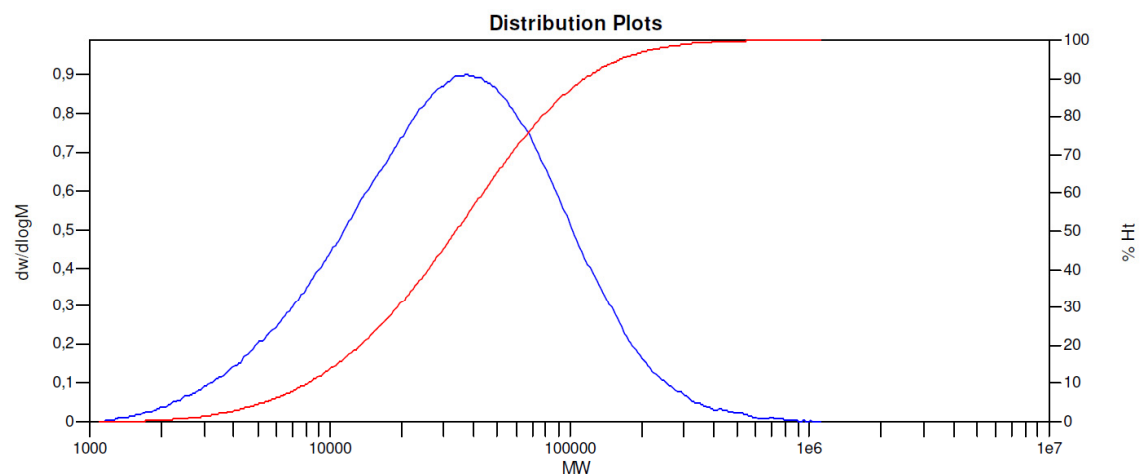
Figure S8-4. GPC molecular weight distribution of P4 PDPP[T]₂-T (50% azide content).



MW Averages

Peak No	Mp	Mn	Mw	Mz	Mz+1	Mv	PD
1	37383	19571	54028	119771	208161	47352	2.76062

Figure S8-5. GPC molecular weight distribution of P5 PDPP[Py]₂-T.^[1]



MW Averages

Peak No	Mp	Mn	Mw	Mz	Mz+1	Mv	PD
1	37730	18253	52745	130675	273036	45755	2.88966

Figure S8-6. GPC molecular weight distribution of P6 PDPP[Py]₂-T (10% azide content).

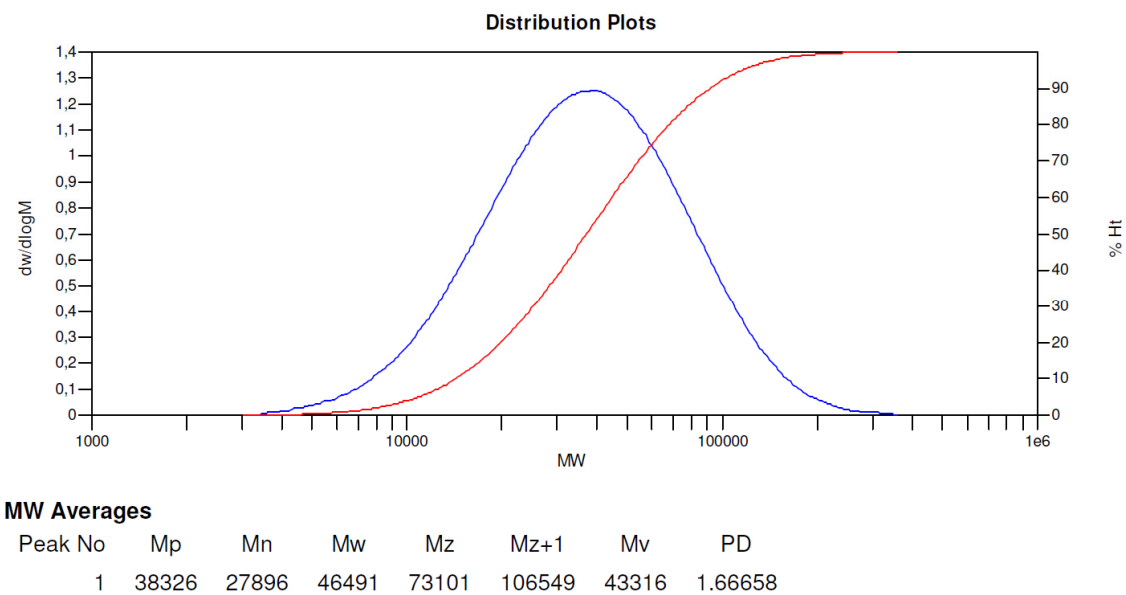


Figure S8-7. GPC molecular weight distribution of P7 PDPP[T]₂-Ph.

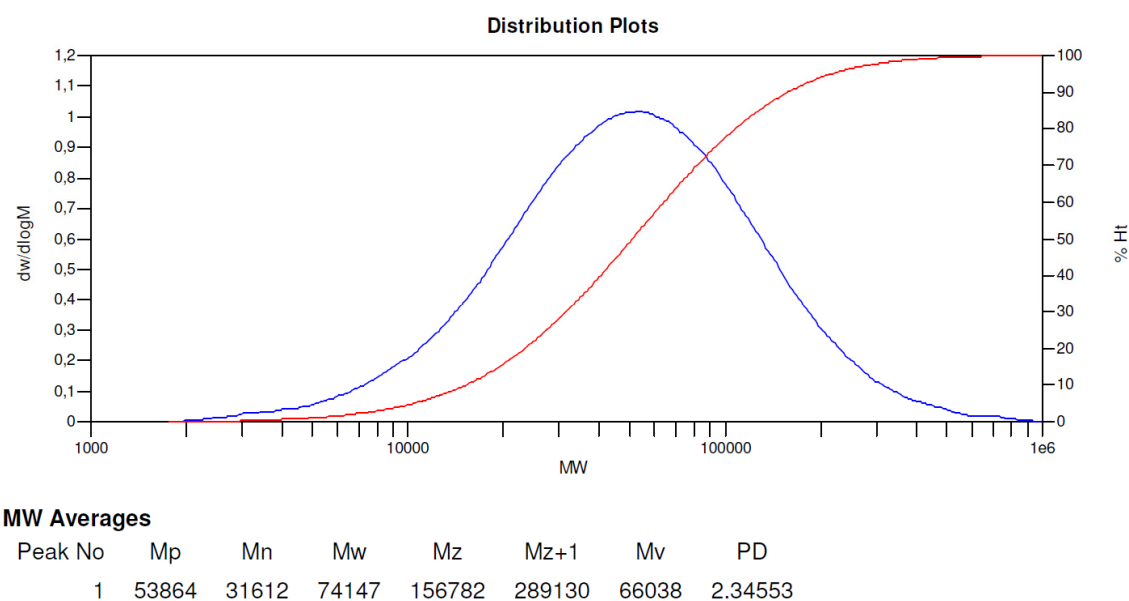


Figure S8-8. GPC molecular weight distribution of P8 PDPP[T]₂-Ph (10% azide content).

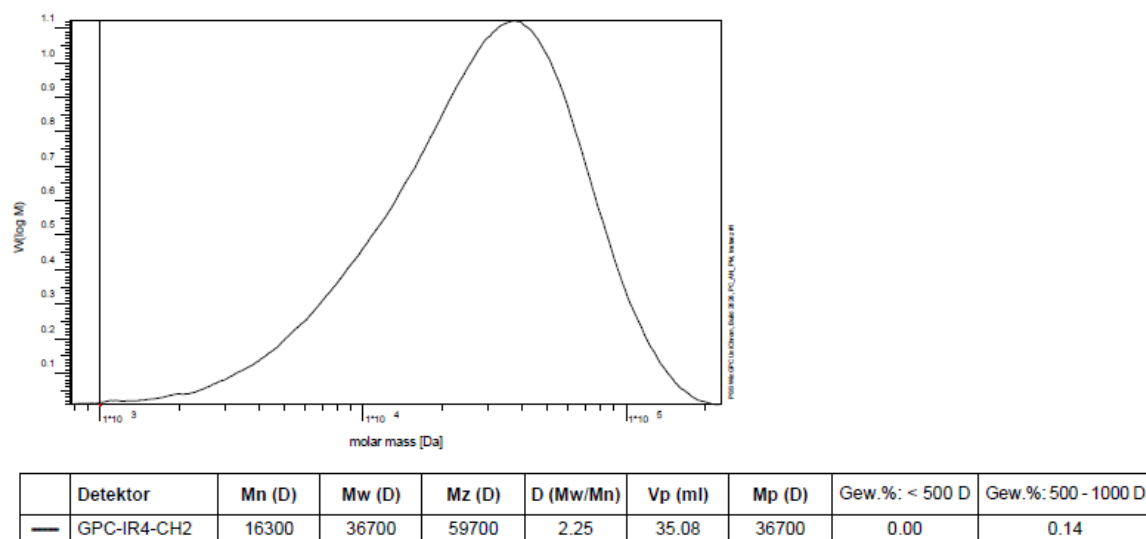
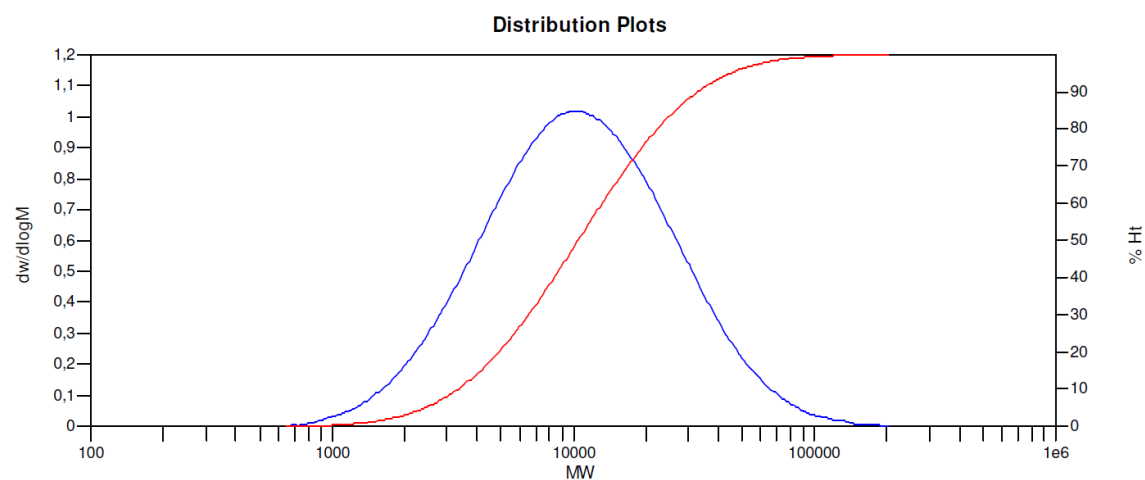


Figure S8-9. GPC molecular weight distribution of P9 PCDTBT.



MW Averages

Peak No	Mp	Mn	Mw	Mz	Mz+1	Mv	PD
1	10073	7110	15262	31113	55050	13663	2.14655

Figure S8-10. GPC molecular weight distribution of P10 PCDTBT (10% azide content).

Table S8-2. Calculation of the average molecular weight of the polymer's repeating unit and the degree of polymerization.

Polymer	$\chi_{RU}(y)^a$ [%]	$\chi_{RU}(x)^a$ [%]	$M_{RU}(y)^b$ [g/mol]	$M_{RU}(x)^b$ [g/mol]	\overline{M}_{RU}^c [g/mol]	DP^d
PDPP[T]₂-T system						
P1	100	0	831.33	290.43	831.33	44
P2	90	10	831.33	290.43	777.24	41
P3	80	20	831.33	290.43	723.15	31
P4	50	50	831.33	290.43	560.88	23
PDPP[Py]₂-T system						
P5	100	0	819.23	299.42	819.23	24
P6	90	10	819.23	299.42	767.249	24
PDPP[T]₂-Ph system						
P7	100	0	823.29	283.39	823.29	34
P8	90	10	823.29	283.39	769.3	41
PCDTBT system						
P9	100	0	702.05	610.94	702.05	23
P10	90	10	702.05	610.94	692.939	10

^{a)} molar fraction of repeating unit y and x according to feed ratio; ^{b)} molecular weight of repeating unit y and x ; ^{c)} average molecular weight of the polymer's repeating unit; ^{d)} degree of polymerization estimated from M_n and \overline{M}_{RU} .

Cyclic Voltammetry

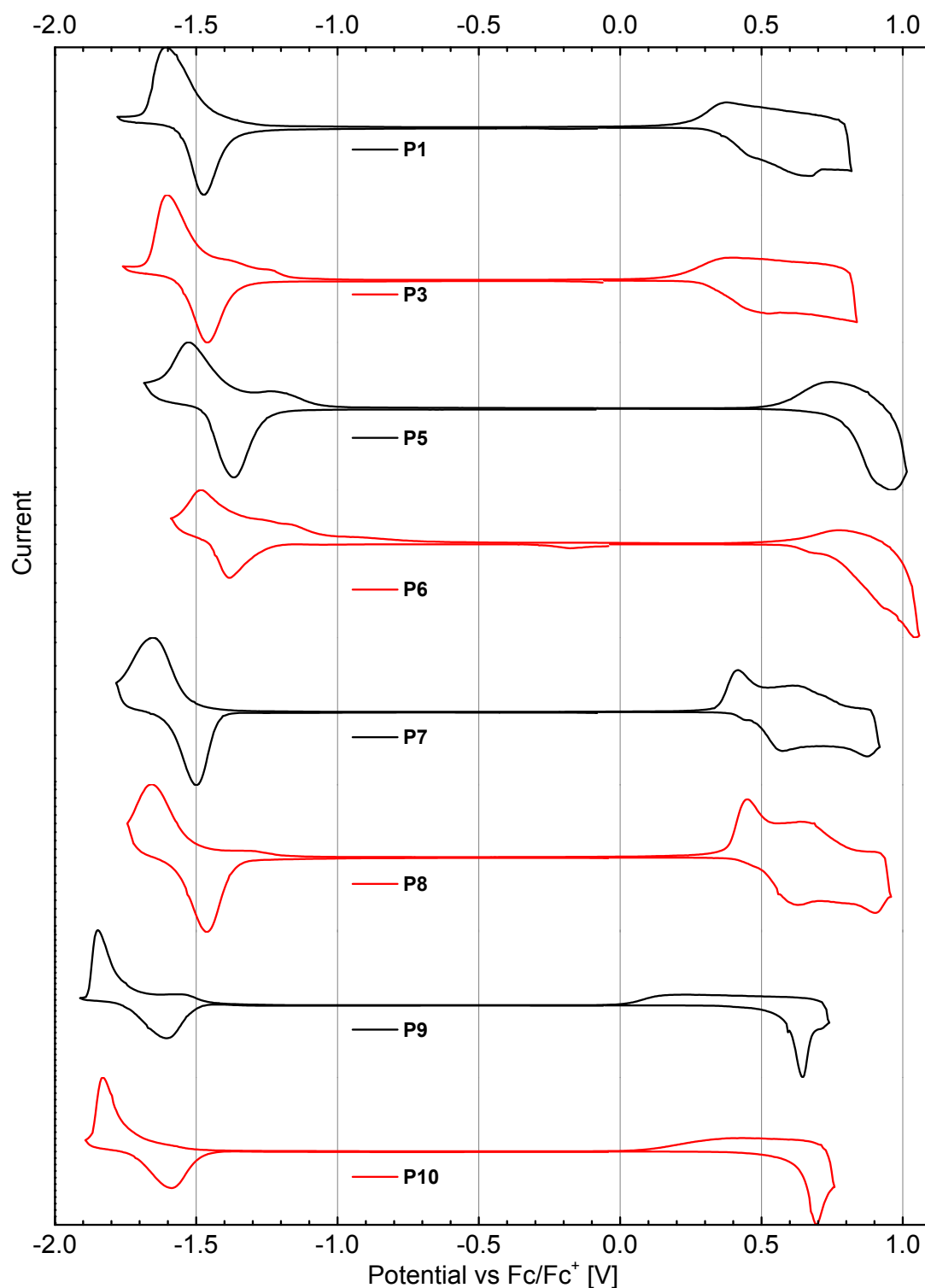


Figure S8-11. Solid state cyclic voltammetry scans using an acetonitrile / 0.1 M tetra-*n*-butylammonium hexafluorophosphate electrolyte solution at a scan rate of 100 mV s⁻¹ comparing azide functionalized tercopolymers (red lines) with their respective non-functionalized reference copolymers (black lines).

Infrared Spectroscopy

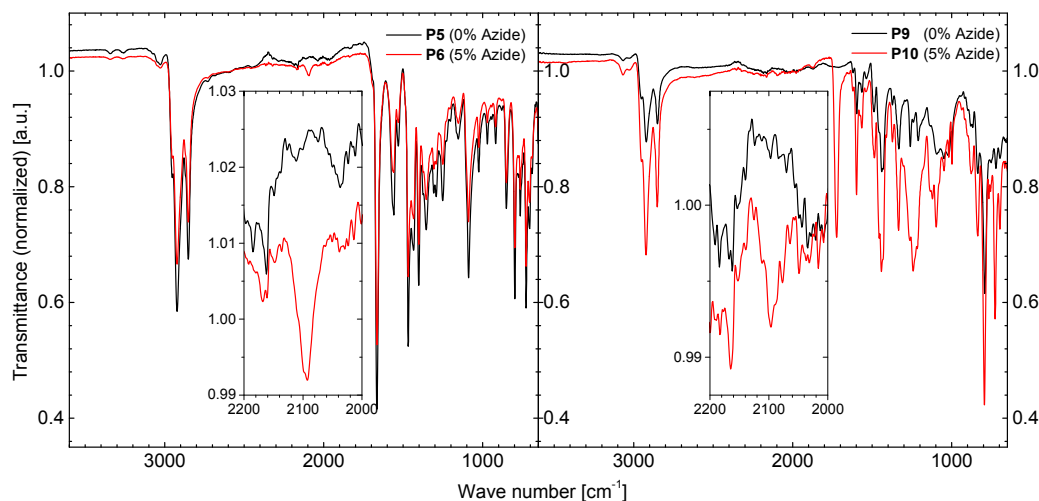


Figure S8-12. Infrared spectroscopy of the tercopolymers with 5% azide repeating unit content ($x = 0.1$, red lines) and their respective non-functionalized reference copolymers (black lines) for the PDPP[Py]₂-T system (P5/P6) and the PCDTBT system (P9/P10). Insets show magnification of the characteristic azide vibration at 2100 cm^{-1} .

Absorption and photoluminescence spectra

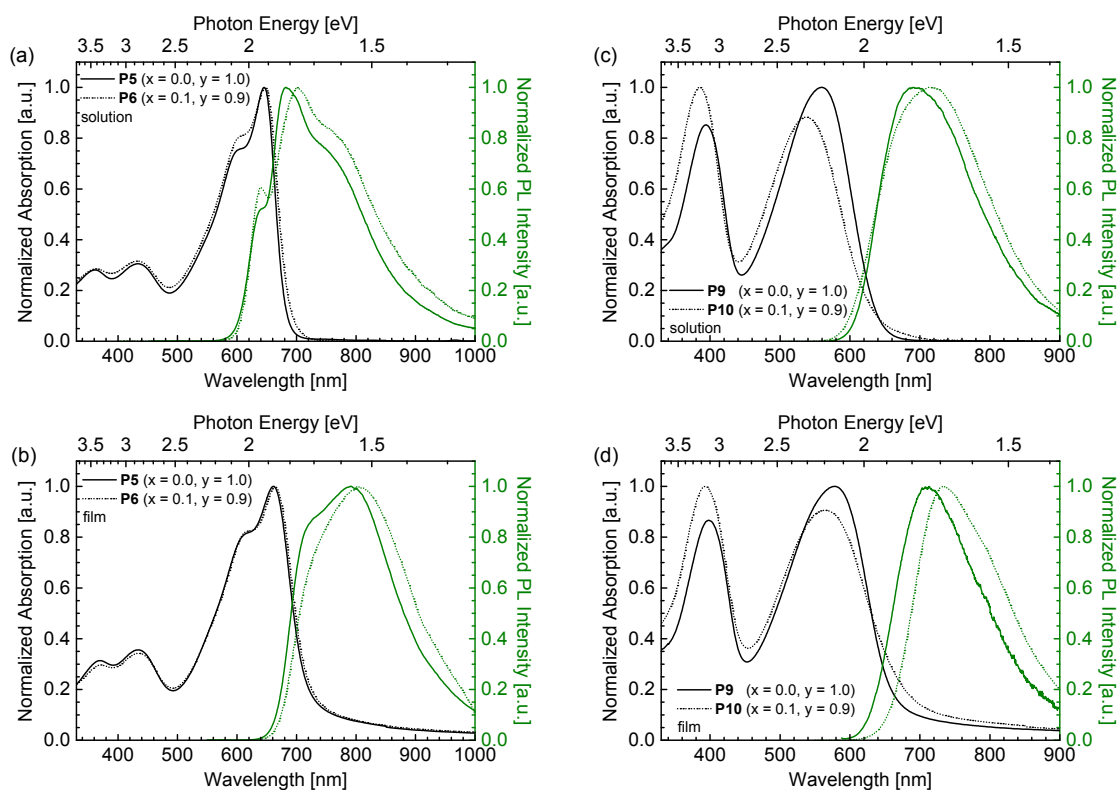


Figure S8-13. Absorption and photoluminescence spectra of crosslinkable tercopolymers compared to their respective non-functionalized reference polymers: PDPP[Py]₂-T system P5/P6 in (a) solution and (b) thin film; PCDTBT system P9/P10 in (c) solution and (d) thin film.

GIWAXS analysis of neat polymer films

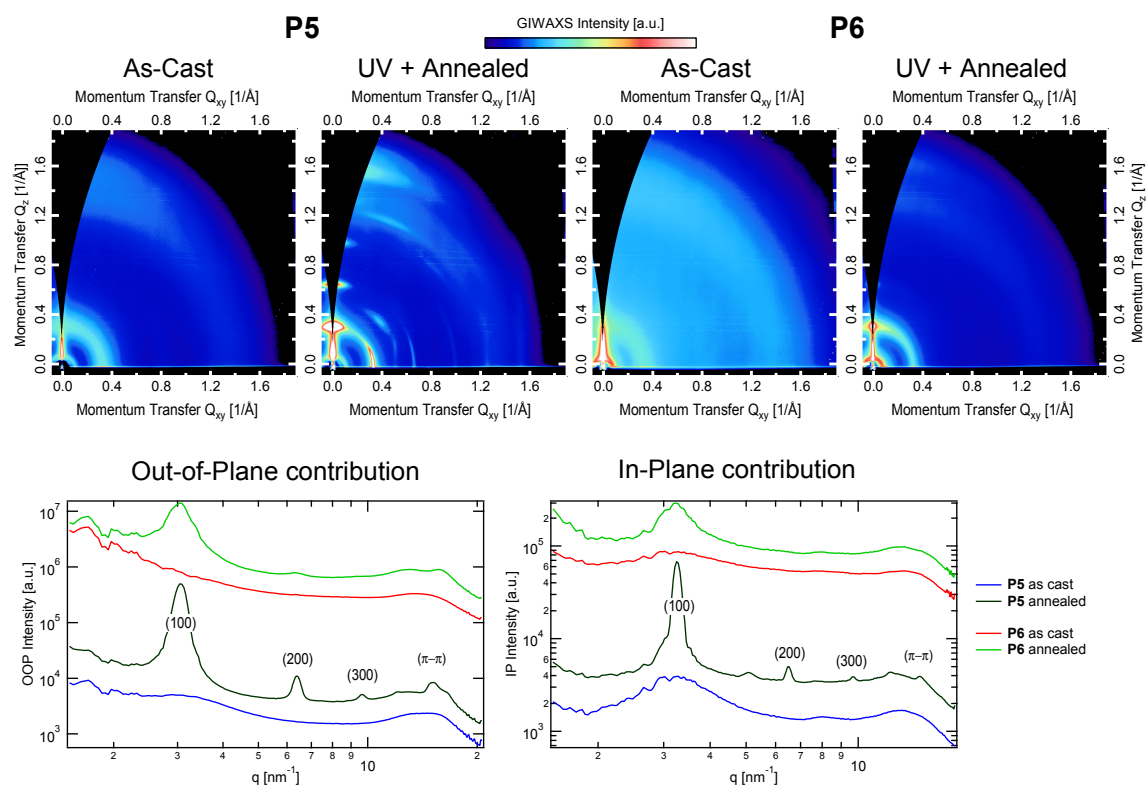


Figure S8-14. GIWAXS scatter patterns of neat unfunctionalized (P5) and azide-functionalized (P6) PDPP[Py]₂-T polymer films.

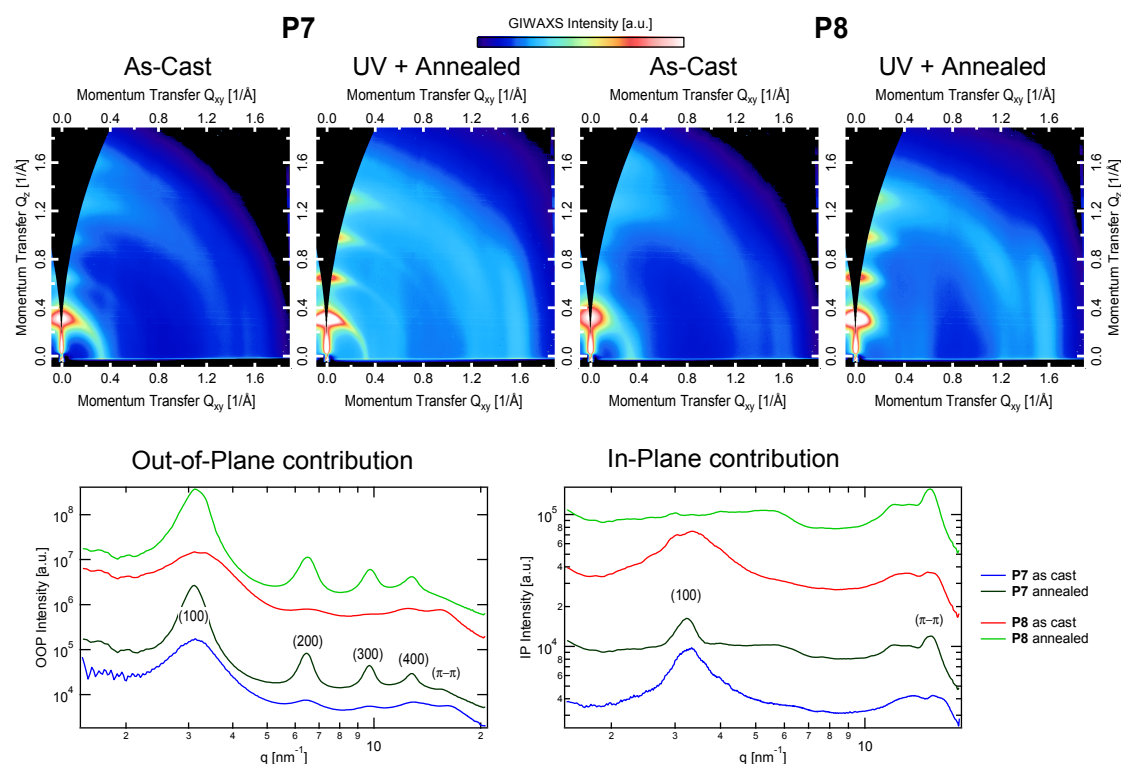


Figure S8-15. GIWAXS scatter patterns of neat unfunctionalized (P7) and azide-functionalized (P8) PDPP[T]₂-Ph polymer thin films.

GIWAXS analysis of PCBM blends

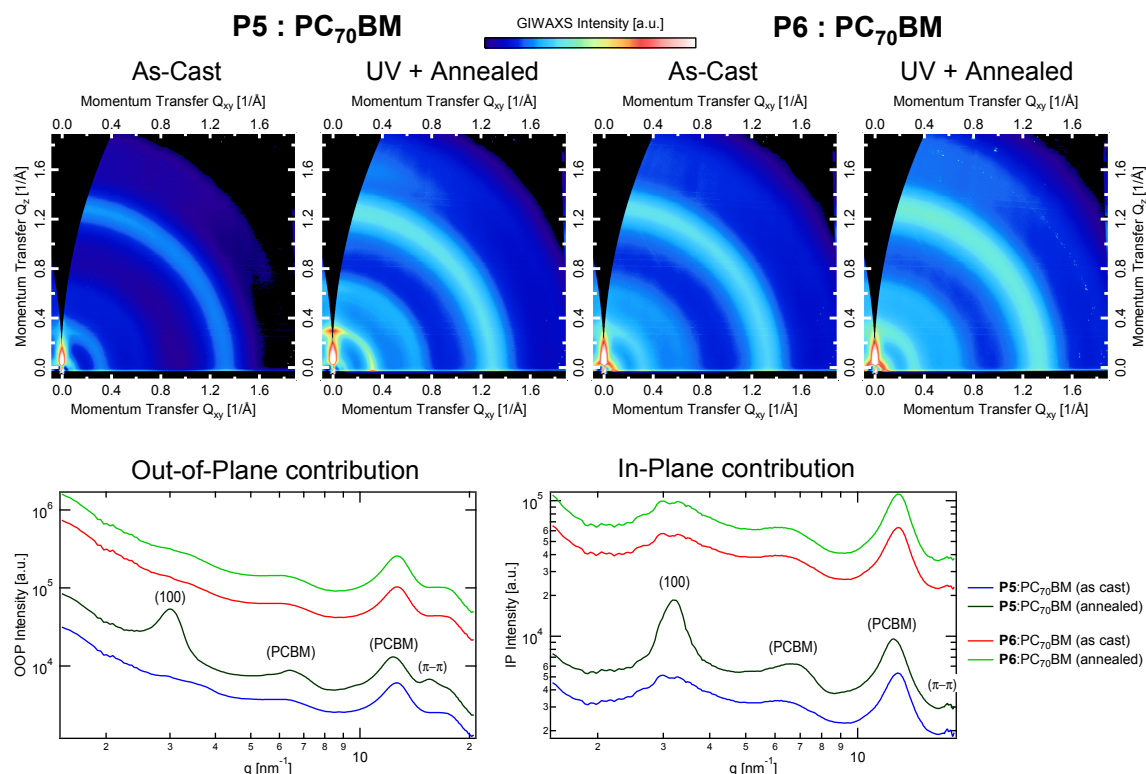


Figure S8-16. GIWAXS scatter patterns of unfunctionalized (P5) and azide-functionalized (P6) PDPP[Py]₂-T polymer:PC₇₀BM blends.

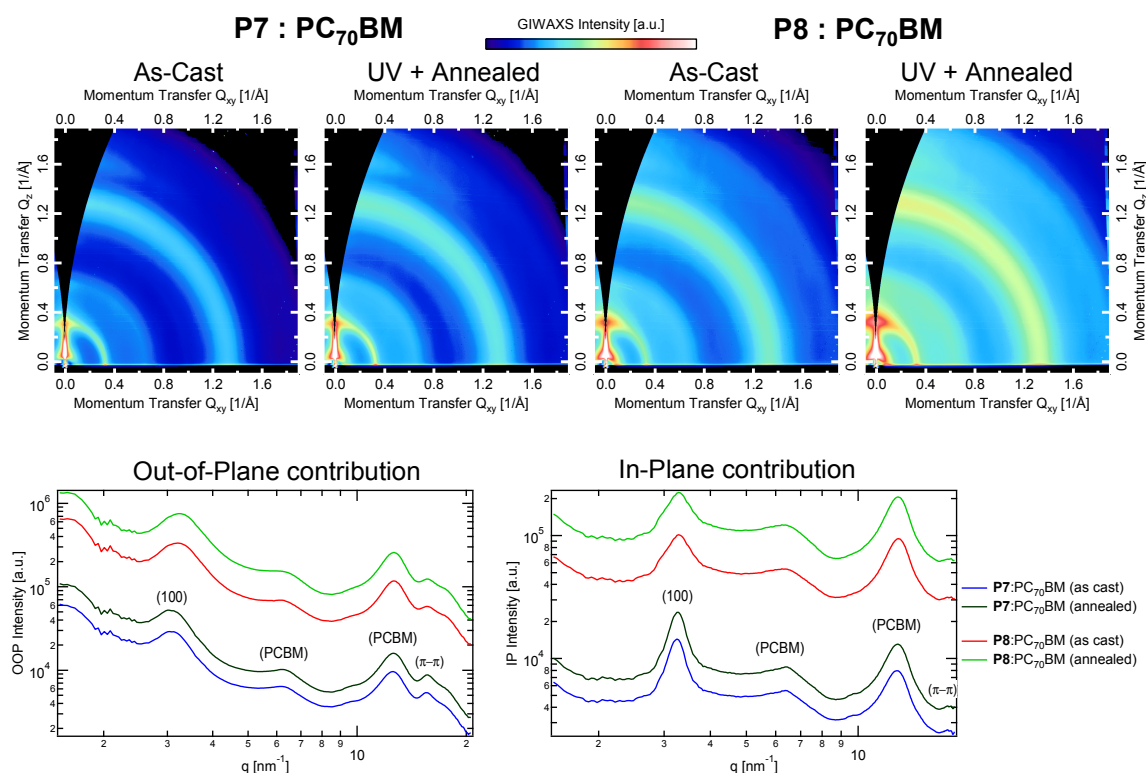


Figure S8-17. GIWAXS scatter patterns of unfunctionalized (P7) and azide-functionalized (P8) PDPP[T]₂-Ph polymer:PC₇₀BM blends.

OFET Operation in n-channel

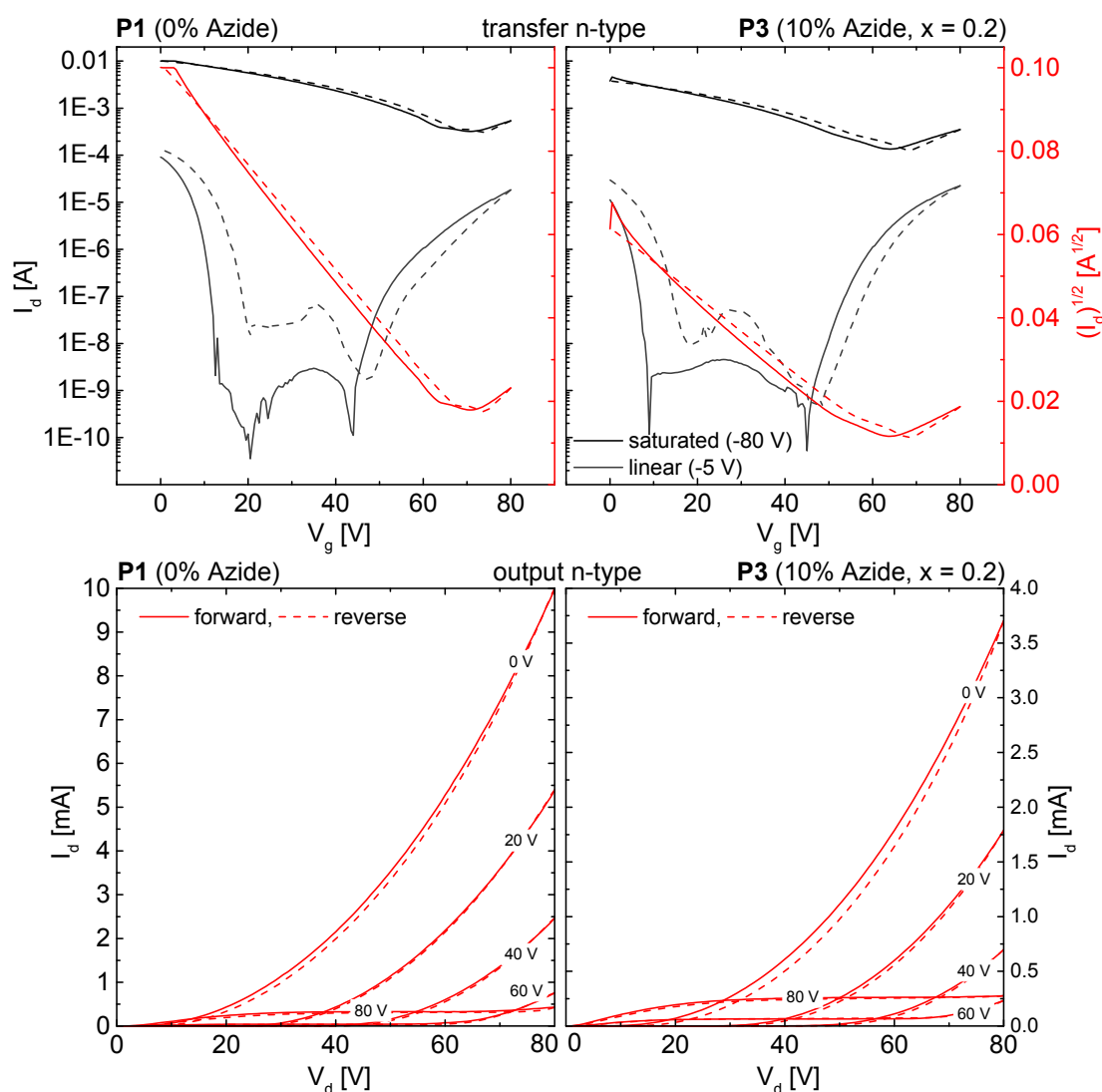


Figure S8-18. OFET n-type transfer and output I - V characteristics after annealing at 250 °C for 15 min of the non-functionalized strictly alternating PDPP[T]₂-T P1 and the tercopolymer containing 10% azide-functionalized repeating units P3. Solid and dashed lines represent the forward and reverse scans in all graphs, respectively. The voltages given in the legend of the output characteristics are the applied gate voltages.

Supporting References

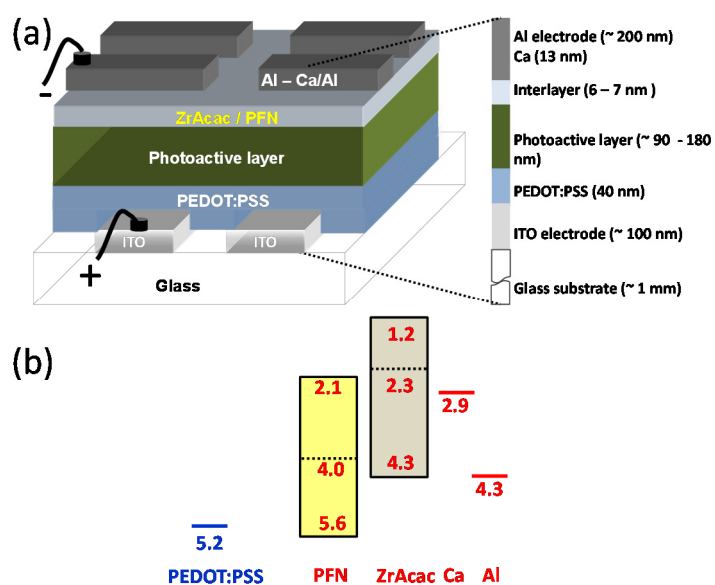
- [1] C. J. Mueller, C. R. Singh, M. Fried, S. Huettner, M. Thelakkat, *Adv. Funct. Mater.* **2015**, *25*, 2725.
- [2] N. Blouin, A. Michaud, M. Leclerc, *Adv. Mater.* **2007**, *19*, 2295.

9 Influence of Electron Extracting Interface Layers in Organic Bulk-Heterojunction Solar Cells

Chetan R. Singh, Cheng Li, Christian J. Mueller,

Sven Huettner and Mukundan Thelakkat*

Applied Functional Polymers – Macromolecular Chemistry I, University of Bayreuth, 95440
Bayreuth, Germany



Published in *Advanced Materials Interfaces*, **2016**, *3*, 1500422.

Reproduced with permission from Wiley VCH.

Abstract

The influence of different electron extracting interlayers including calcium (Ca), zirconium acetylacetonate (ZrAcac), and a polyfluorene derivative (PFN) compared to reference aluminum (Al) electrode is investigated on the performance of P3HT:PC₆₁BM and PDPP:PC₇₁BM bulk-heterojunction solar cells. The optoelectrical investigations are carried out using electroabsorption measurements for the built-in voltage (V_{bi}) determination and transfer matrix simulations for the determination of parasitic absorption in interface layers. It is shown that the solar cell performance is influenced by different parameters such as diode turn-on voltage, leakage currents, built-in voltages and parasitic absorption. The small diode turn-on voltage and high parasitic absorption in Ca contact devices limit the open circuit voltage and short circuit current, respectively. Likewise, high leakage currents using ZrAcac contact limit the fill factor in P3HT:PC₆₁BM solar cell devices. However, the PFN based devices with small parasitic absorption, smaller leakage currents and a relatively high V_{bi} show maximum performance with both material systems. This work highlights the importance of choosing the suitable interlayers in device optimization and clearly demonstrates that it is not only the low work function of an electron extracting interlayer, but also its optical properties and charge selectivity significantly influence the final solar cell performance.

9.1 Introduction

Organic photovoltaics have attracted great attention in last two decades due to their potential for the fabrication of low cost, light weight, and large-area flexible energy sources. In the past few years, extensive effort focused on synthesizing novel donor-acceptor conjugated polymers led to a steady increase in power conversion efficiencies (PCE)s. Lately, PCEs more than 10% have been reported for tandem as well as for single junction organic solar cells.^[1–4] However, in many of these highly efficient solar cells, interlayers at the interface of the photoactive layer and the charge-collecting electrodes have been introduced to optimize the device performance.^[1,3,5,6] The optoelectronic processes at the interface play a critical role in determining the efficiency for photon-to-current conversion.^[7,8] An ideal electrical contact in a solar cell requires the formation of ohmic contact with minimum resistance and it must be selective to prevent charge carriers from reaching the opposite electrodes. Therefore in normal geometry organic solar cells, low work function cathodes are desired as they are expected to form ohmic contact^[9,10] and efficiently extract photo-generated electrons due to high built-in field across the active layer.^[11–13] Thus, a low work function Ca (2.9 eV) contact has been

extensively used in literature in high performance solar cells despite being highly air-unstable. To overcome stability problems, polyelectrolyte, transition metal chelates, oxides, and salts have also been successfully introduced as electron extracting interlayers as an alternative to conventional Ca and Al cathodes.^[7,8] However it remains an open question to what extent these low work function interlayers contribute to the effective built-in voltage and enhance the solar cell performance. Furthermore there may be other secondary effects of interlayers which affect the final solar cell performance.

In this study, the influence of two efficient solution processed electron extracting interlayers, poly [(9,9-bis(3'-(N,N-dimethylamino) propyl)-2,7-fluorene)-alt-2,7-(9,9-dioctylfluorene)], (PFN),^[6,14] and zirconium acetylacetonate, (ZrAcac)^[15] along with Ca interlayer is systematically investigated in normal geometry solar cells with Al as a cathode. Figure 9-1 shows the device schematic and the energy values of the interlayers and top metal cathodes determined from UPS experiments. The polyfluorene derivative, PFN, has been successfully applied by many groups as an electron injecting and electron extracting interlayer in highly efficient polymer light-emitting devices and solar cells.^[14,16,17] It has been suggested that the improved device performance is due to improved built-in field and charge carrier mobility.^[6] The ZrAcac as an electron extracting interlayer was first introduced by Li *et al.*^[15] and later applied by Huo *et al.* in highly efficient solar cells reaching 9.7% PCE.^[5] The authors suggested that the ZrAcac interlayer acts as an optical spacer and manipulates the optical interference within the active layer leading to an improvement in performance.^[15]

In this work, the built-in fields are estimated directly by measuring the built-in voltage by electroabsorption spectroscopy. The influence of parasitic absorption in electrodes is carefully considered by calculating the internal quantum efficiencies. To keep the generality, different interlayer and cathode combinations were tested with two different and well-known bulk-heterojunction photoactive layers, P3HT:PC₆₁BM^[18] and PDPP:PC₇₁BM.^[19-21] The structure of the photoactive materials are shown in the Figure 9-2. We have purposefully selected these systems as universal prototypes in which the donor polymers differ in their bulk hole carrier mobilities. The PDPP is a derivative of diketopyrrolopyrrole (DPP) polymers endcapped with pyridine units. For DPP polymers, often the PCE has been shown to be closely linked with the molecular weight of these polymers and Janssen *et al.* have published up to 8% PCE for some of these polymers.^[19] Nevertheless, in our case the optimum donor acceptor ratios were 1:0.8 and 1:2 for P3HT:PC₆₁BM and PDPP:PC₇₁BM reference devices with top Al contact, respectively. The optimized film thicknesses were ~180 nm and ~90 nm for P3HT:PC₆₁BM and PDPP:PC₇₁BM, respectively. In the next section, the solar cell results are discussed and the results are analyzed in the light of optoelectrical investigations.

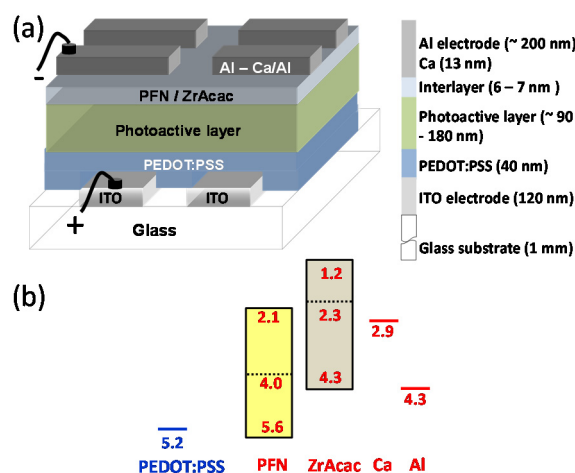


Figure 9-1. (a) Device layout of the studied polymer solar cell. (b) Energy values of interlayers obtained from UPS measurements are taken here from literature.^[8,15,22] For PEDOT:PSS, Ca and Al, the work function is depicted by a line while for PFN and ZrAcac, the Fermi level by a dashed line. The HOMO values for PFN and ZrAcac are from UPS measurements and LUMO values were estimated from the band gap. For better reading, the Fermi level of the semiconductors is discussed as work function in the text.

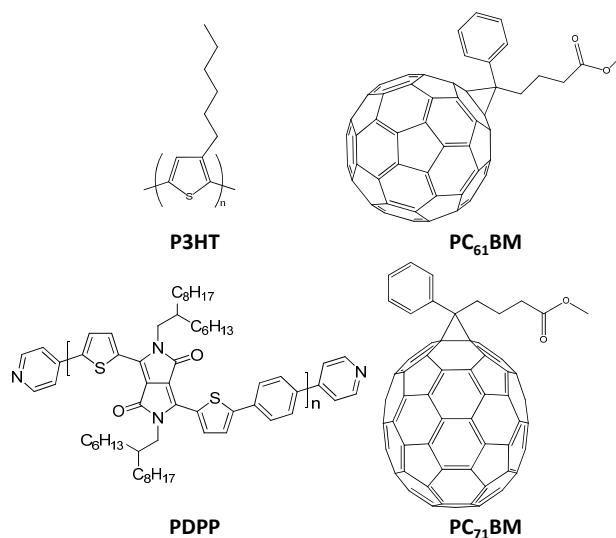


Figure 9-2. Molecular structures of the applied polymers and acceptor materials.

9.2 Results and discussion

9.2.1 Solar cell results

Figure 9-3 shows the J - V curves under illumination and in dark for P3HT:PC₆₁BM and PDPP:PC₇₁BM devices with different top contacts. The solar cell performance for each case was checked for reproducibility and consistency by repeating the experiment multiple times. Table 9-1 summarizes the best solar cell performance parameters obtained for each case. The average PCE values obtained from 8 devices are also mentioned in the table. In the case of P3HT:PC₆₁BM devices, the short circuit current, J_{sc} , was almost the same for Al, PFN/Al and

ZrAcac/Al contacts. Thus no J_{sc} increment was observed after incorporating solution processed low work function interlayers. The maximum PCE of 3.5% was observed for both reference Al and PFN/Al devices. For the case of Ca/Al contact, a reduced J_{sc} and open circuit voltage, V_{oc} , was observed in P3HT:PC₆₁BM devices. Figure 9-3(b) shows the dark current on a log-linear scale for P3HT:PC₆₁BM devices and compares the leakage currents (for eg. J at -1 V) for different top contacts. Surprisingly, high leakage currents with ZrAcac cathodes were observed in P3HT:PC₆₁BM devices, which mainly reduces the fill factor, FF, of the ZrAcac/Al devices and consequently the PCE. On P3HT:PC₆₁BM/ZrAcac/Al devices, pinholes were observed where Al made contact with the interlayer which might be the reason for the high leakage currents. Figure S9-1, in the supporting information (SI), compares the optical microscopy of the solar cell devices and pin-holes could easily be observed for the ZrAcac/Al devices.

In contrast to the P3HT:PC₆₁BM system, the PDPP:PC₇₁BM devices show a consistent improvement especially in terms of J_{sc} (8.6 mA/cm² to 10.3 mA/cm²) and FF (44% - 59%) using low work function cathodes in comparison to the reference Al devices (Figure 9-3 (c) and Table 9-1). The maximum PCE in PDPP:PC₇₁BM devices was around 4.7% for PFN/Al cathode compared to 2.6% in the Al reference devices. The leakage currents were considerably less for all the contacts, the ZrAcac/Al contact also improved all the solar cell performance parameters in contrast to the observations in P3HT:PC₆₁BM devices. In comparison to P3HT:PC₆₁BM devices, even more pronouncedly reduced V_{oc} values were obtained for PDPP:PC₇₁BM/Ca/Al devices. The reduced V_{oc} could be explained by a decreased diode turn-on voltage in Ca/Al devices. Figure 9-3 (a) and (c) show that the dark currents in the Ca/Al contact devices turn-on early which will cause an increase in the recombination of photo-generated charges with the injected charges and thus leading to the reduced V_{oc} values. It has been shown in literature that for morphologies with significant amount of fullerene at the film surface, electron transfer from a metal to active layer pins the top metal work function to the reduction potential of the fullerene molecule.^[23,24] We expect that in the case of Ca/Al contact, Ca forms an ohmic or quasi-ohmic contact which leads to increased dark injected currents. Thus, the larger influence of Ca/Al contact on the V_{oc} of the PDPP:PC₇₁BM device could be understood in the context of its larger fullerene content than in the P3HT:PC₆₁BM system.

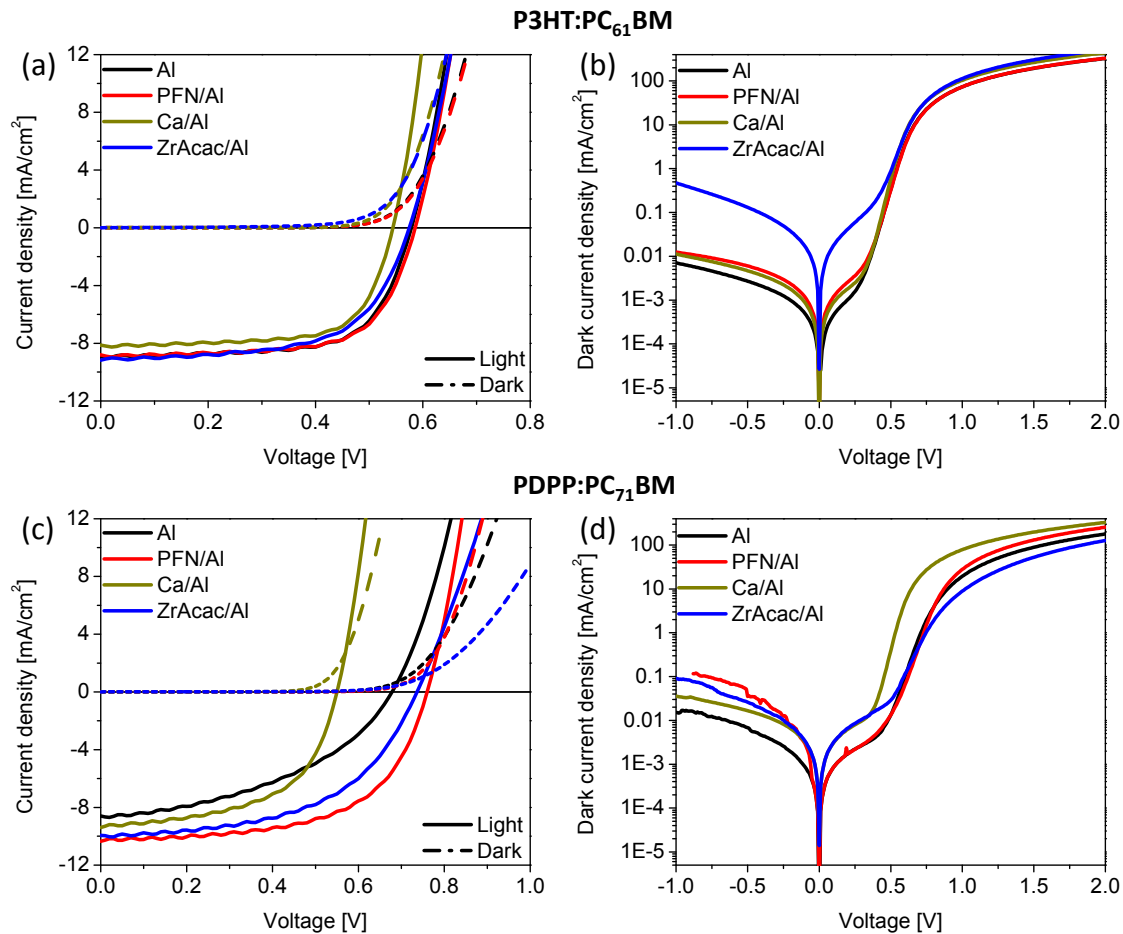


Figure 9-3. (a) and (c) are the J - V curves under illumination and in dark for the P3HT:PC₆₁BM and PDPP:PC₇₁BM solar cells, respectively. (b) and (d) are the dark J - V curves on log-linear scale of the corresponding P3HT:PC₆₁BM and PDPP:PC₇₁BM solar cells, respectively.

Table 9-1. Solar cell parameters of the P3HT:PC₆₁BM, and PDPP:PC₇₁BM devices with different top contacts measured under illumination. The average PCE values from minimum of 8 devices are mentioned in the parentheses.

Active layer	Cathode	J_{sc} [mA/cm ²]	V_{oc} [V]	FF [%]	PCE [%]
P3HT:PC ₆₁ BM	Al	8.9	0.58	68	3.5 (3.4)
	PFN/Al	8.8	0.59	67	3.5 (3.4)
	Ca/Al	8.1	0.54	70	3.1 (2.9)
	ZrAcac/Al	9.1	0.57	62	3.2 (3.1)
PDPP:PC ₇₁ BM	Al	8.6	0.68	44	2.6 (2.5)
	PFN/Al	10.3	0.76	59	4.7 (4.5)
	Ca/Al	9.4	0.55	56	2.9 (2.8)
	ZrAcac/Al	9.9	0.74	53	3.9 (3.9)

In order to understand the changes in J_{sc} and FF with different contacts, J - V curves of all the devices were measured under different light intensities. Figure 9-3 (a) and (c) show the experimental power law dependence of short circuit current on incident light intensity for P3HT:PC₆₁BM and PDPP:PC₇₁BM devices, respectively. The power exponent was 1.0 for all the P3HT:PC₆₁BM devices. Similarly, the power exponent was the same for all the PDPP:PC₇₁BM devices, but here a smaller value of 0.87 was determined. A value of power exponent much less than 1.0 for the latter suggests that significant bimolecular recombination limits the performance of PDPP:PC₇₁BM solar cells.^[25,26] The identical value of power exponent for all the top contacts also suggests that at short circuit condition, the charge transport and recombination processes remain similar in each set and they are indifferent to the different work functions of the contacts. To understand the difference between the two BHJ systems, the effective hole mobility in pristine P3HT and PDPP films were determined using the SCLC method.^[27,28] The J - V curves of single carrier hole-only SCLC devices are shown in the SI (Figure S9-2). The electron mobilities of the fullerene components are very similar.^[29] Around two orders of magnitude higher hole mobility in P3HT explains good charge transport properties and the ideal power exponent at short circuit conditions in P3HT:PC₆₁BM devices.

For understanding the device physics, it is very helpful to plot the photocurrent (J_{ph}) of a solar cell as a function of effective applied voltage (V_{eff}), where $J_{ph} = J_L - J_D$ and $V_{eff} = V_0 - V_{app}$. J_L is the light current, J_D the dark current, V_0 the compensation voltage at which the photocurrent $J_{ph} = 0$, and V_{app} the externally applied voltage.^[30] Figure S9-3 in the SI shows typical J_{ph} vs V_{eff} curves of a device for different light intensities. At an effective voltage, V_{eff} , of 0.1 V, the power exponent of photocurrent (J_{ph}) dependence on light intensity changes with the top contacts as shown in the Figure 9-4 (b) and (d). The effective voltage of 0.1 V was chosen for analysis as it represents a condition away from short circuit and near to open circuit condition and thus provides a good base to compare charge extraction processes in different cathode devices. In P3HT:PC₆₁BM devices, the power exponent increases for the low work function contacts compared to the reference Al reference device. The power exponents at $V_{eff} = 0.1$ V are 0.79, 0.81, 0.95 and 0.90 for Al, PFN, Ca and ZrAcac contacts, respectively. Remarkably the trend of the power exponent matches well with the work function values of the contacts depicted in Figure 9-1, with an exception of ZrAcac. Al with its highest work function has the least power exponent and Ca with its very low work function has the highest power exponent. ZrAcac with its lowest work function has its power exponent just below that of Ca. Likewise, a similar trend of power exponent values was observed for the PDPP:PC₇₁BM devices. The power exponents at $V_{eff} = 0.1$ V for the PDPP:PC₇₁BM devices are 0.75, 0.77, 0.81 and 0.78 for Al, PFN, Ca and ZrAcac contacts, respectively. Thus for both material systems, the maximum power exponent was observed for Ca and ZrAcac contacts suggesting reduced bimolecular recombination and better charge extraction in those devices at voltages near the open circuit condition.

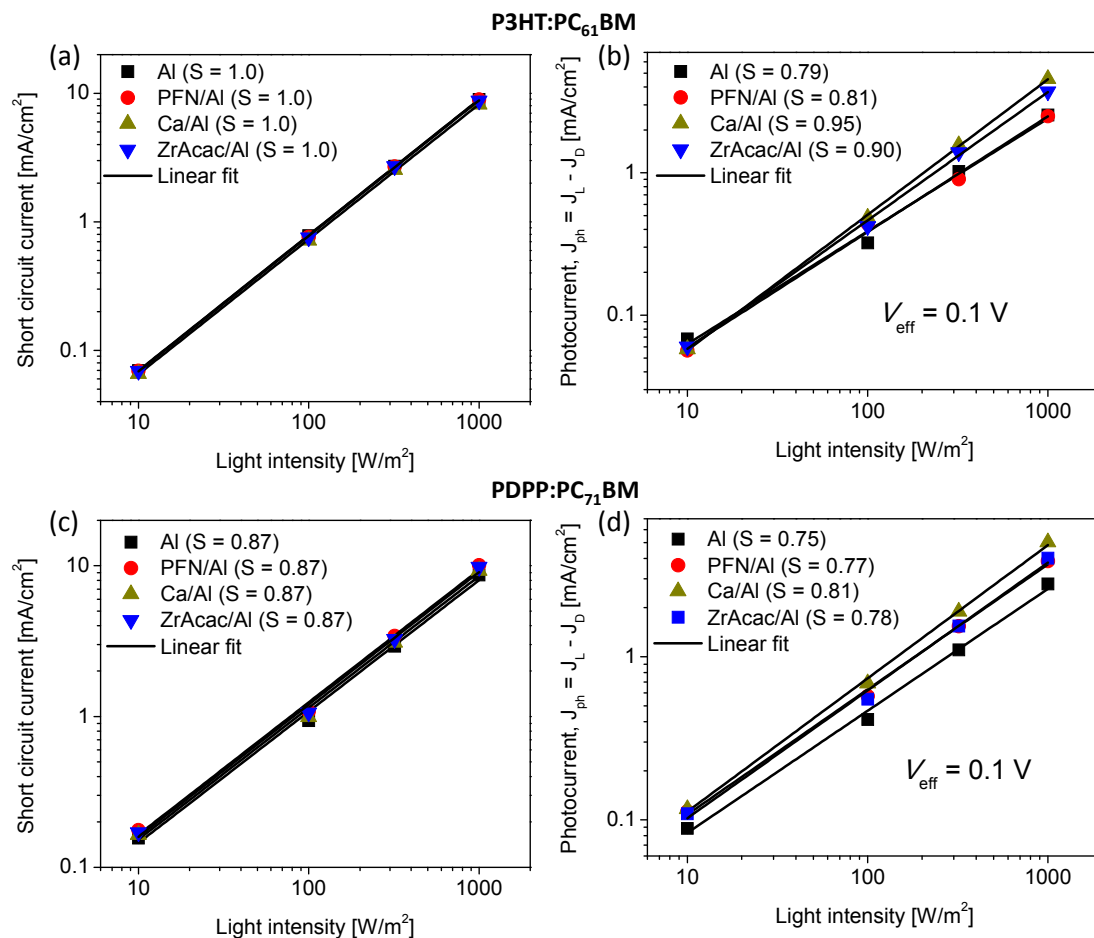


Figure 9-4. The influence of the different cathodes on the photocurrent in P3HT:PC₆₁BM and PDPP:PC₇₁BM solar cells for varying incident light intensity. (a) and (b) are the double logarithmic plot of photocurrent density as a function of the incident light intensity for P3HT:PC₆₁BM and (c) and (d) for PDPP:PC₇₁BM. The photocurrent in (a) and (c) is at the short circuit condition whereas in (b) and (d) is at effective voltage (V_{eff}) of 0.1 V. The lines represent the best power fitting.

9.2.2 Optoelectrical investigations

9.2.2.1 Electroabsorption spectroscopy

Another parameter of importance to understand the influence of different interface layers is built-in voltage (V_{bi}). According to the classical metal-insulator-metal (MIM) model, the V_{bi} in a device is attributed to the work function difference between the two metallic electrodes.^[31] However in practice, the V_{bi} cannot be easily predicted due to mechanisms at the semiconductor-interlayer/metal interfaces such as charge transfer, formation of dipoles etc.^[32] Electroabsorption (EA) measurements were carried out to directly determine the V_{bi} for different cathode interfaces in solar cells. The EA spectroscopy has been frequently applied to determine the V_{bi} in organic light emitting devices.^[33–36] EA measurements have been also carried out on organic solar cells to estimate the internal field.^[11,37,38] The detailed EA experiment has been described elsewhere in literature.^[39,40] In short, an electric-field

modulation, i.e. a superposition of DC and AC voltages, is applied to the device and the relative change in intensity of the reflective probe light, ΔR , is monitored using a silicon detector connected with a lock-in amplifier. In a device with a uniform internal field, the EA response at the fundamental frequency of the applied AC bias can be expressed as:

$$\left. \frac{\Delta R}{R} \right|_{\omega} \propto \text{Im} \chi^{(3)}(h\nu) V_0 V_{ac} \sin(\omega t) = \text{Im} \chi^{(3)}(h\nu) (V_{dc} - V_{bi}) V_{ac} \sin(\omega t) \quad (1)$$

where, $\text{Im} \chi^{(3)}(h\nu)$ is the imaginary part of the third-order of electric susceptibility, which is a function of the photon energy $h\nu$, while V_{dc} and V_{ac} are the applied external DC and AC voltages, respectively. V_0 is the internal DC voltage and V_{bi} the built-in voltage in the device. Thus according to eq (1), the V_{bi} can therefore be obtained by finding the null voltage V_{null} ($V_{null} = V_{dc} = V_{bi}$), where the EA signal reduces down to zero.

Figure 9-5(a) shows exemplary EA spectra measurements of a typical PDPP:PC₇₁BM solar cell measured at different applied DC voltages. In the reverse bias range from -2V to 0V, each EA spectrum has a characteristic first derivative shape and around two orders of magnitude less out-of-phase signal. Figure S9-4 in the SI compares the absorbance signal, its first derivative and the EA signal from a PDPP:PC₇₁BM device. Besides, the EA spectra decrease linearly with increasing voltages, suggesting that clear EA signals were measured with minimal influence from other charge modulation features.^[41] To extract V_{bi} of the PDPP:PC₇₁BM devices, the magnitude of the EA signal was measured as a function of DC bias at constant probe light of energy 1.55 eV. A linear fit to the data was performed in the reverse bias region, and the V_{bi} value was extrapolated from the intercept as shown in the Figure 9-5 (b). The extracted average V_{bi} values for all devices are given in the Table 9-2. An exemplary EA spectra of a P3HT:PC₆₁BM device is shown in the Figure S9-5 of the SI.

For both material systems, increased built-in voltage values were obtained for PFN/Al Ca/Al, and ZrAcac/Al devices in comparison to reference Al devices. The smaller value of V_{bi} for Al solar cells can be explained by considering the highest work function of Al among the studied cathodes leading to smallest difference between the anode and cathode work functions. The V_{bi} value of 1.05 V and 0.75 V obtained for P3HT:PC₆₁BM and PDPP:PC₇₁BM devices with Al contact, respectively seems to match with the difference of work function values mentioned in the Figure 9-1. However for Ca and ZrAcac cathodes, built-in voltages for both material systems were much lower than these expected from their low work functions. Guerrero *et al.* also investigated the built-in voltages of P3HT:PC₆₁BM solar cells with different top metal contacts using Mott-Schottky analysis.^[23] Although the absolute values of V_{bi} reported by Guerrero *et al.* were lower than those obtained here, they also did not observe significant increase in the built-in voltage when changing the contact from Ag to Ca. They suggested that most of the energy mismatch between the cathode and the organic layer Fermi level occur as

a voltage drop at the interface dipole layer caused by net electron transfer from the cathode to metal-semiconductor interface states. Origin of the interface states was linked with fullerene reduced molecules covering the metal contact. Thus the reduced built-in voltages observed for PDPP:PC₇₁BM in comparison to P3HT:PC₆₁BM for similar contacts could be understood as due to a similar effect, if the larger amount of fullerene loading in PDPP:PC₇₁BM blend films is taken into consideration. Also by comparing the obtained V_{bi} voltages and the lower work functions of Ca and ZrAcac, it can be safely argued that Ca/Al and ZrAcac/Al contacts would have higher voltage drop at the cathode interface than the Al and PFN/Al contacts. This higher voltage drop at the interface could assist in the charge extraction before the open circuit condition when most of the built-in voltage is cancelled by the applied voltage. On the other hand, the built-in voltage guides the charge transport as it provides the necessary force to drive the photo-generated charge carriers. Thus combining the observation of higher power exponents at an effective voltage of 0.1 V in Ca/Al and ZrAcac/Al devices (Figure 9-4 (b) and (d)) along with the possibility of higher voltage drop at the cathode interface, it can be suggested that low work function contacts mainly enhance the charge extraction at cathode interface without significantly improving the charge transport in photoactive layers.

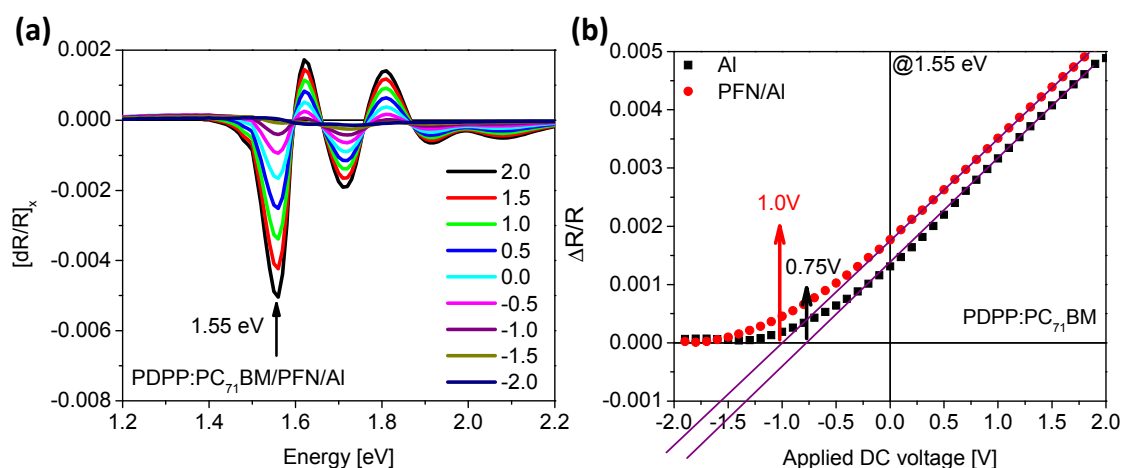


Figure 9-5. (a) Electroabsorption (EA) spectra of a ITO/PEDOT:PSS/PDPP:PC₇₁BM/PFN/Al solar cell device measured at different applied DC voltages. (b) DC dependence of EA signal of PDPP:PC₇₁BM devices with Al and PFN/Al cathodes. V_{bi} values were obtained by extrapolating the linear fit in the reverse bias region to x-axis.

Table 9-2. Built-in voltage (V_{bi}) in P3HT:PC₆₁BM and PDPP:PC₇₁BM solar cell devices obtained from electroabsorption (EA) measurements for different top cathodes and ITO/PEDOT:PSS anode. To account for sample to sample variation average values along with standard deviation taken from 4 different solar cell measurements are mentioned in the table.

Cathode	Built-in voltage (V_{bi}) [V]	
	P3HT:PC ₆₁ BM	PDPP:PC ₇₁ BM
Al	1.05 ± 0.05	0.74 ± 0.04
PFN/Al	1.11 ± 0.08	0.93 ± 0.06
Ca/Al	1.25 ± 0.10	0.86 ± 0.06
ZrAcac/Al	1.09 ± 0.20	0.99 ± 0.09

9.2.2.2 Internal quantum efficiency

In order to quantify the influence of optical interferences and parasitic absorption (PA) within the interlayers and contacts, internal quantum efficiency (IQE) was evaluated for all solar cells following a methodology suggested by McGhee *et al.*^[42]

$$IQE = \frac{EQE}{1 - R - PA} \quad (2)$$

where EQE is the external quantum efficiency and R the reflectance of a device.

The EQE and R spectra were measured on solar cell devices. Transfer matrix method was used to account optical interference and calculate the total parasitic absorption in the device stack. For this the required optical constants (n & k) of interlayers were measured using variable angle spectroscopic ellipsometry (VASE) and shown in the Figure S9-6 of the SI. For photoactive layers, $n = 2$ was assumed and k was determined using the optical density and thickness of the films deposited on glass substrate.^[42]

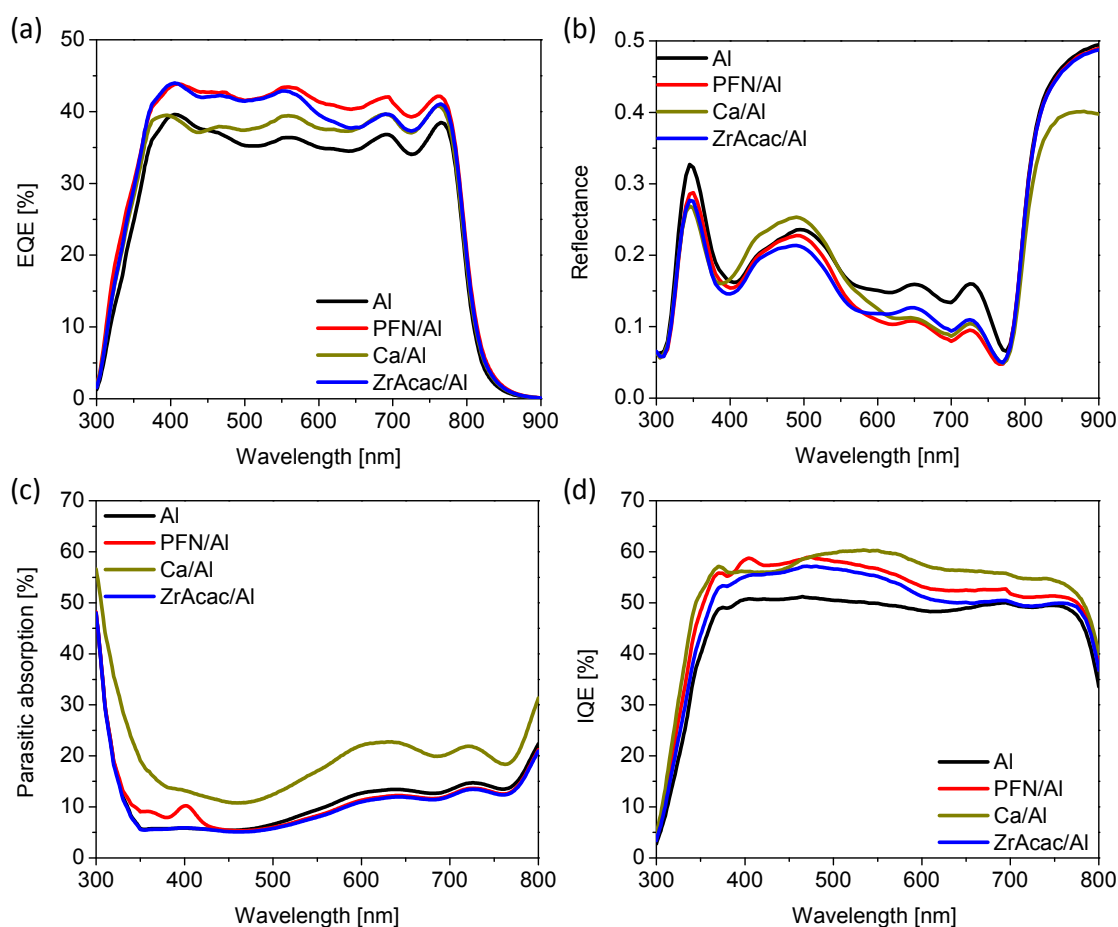


Figure 9-6. (a) Measured external quantum efficiency (EQE) and (b) reflectance (R) spectra of the PDPP:PC₇₁BM solar cells devices. (c) and (d) show the calculated parasitic absorption (PA) and IQE of the corresponding devices, respectively. The IQE of the P3HT:PC₆₁BM devices is shown in the Figure S9-5 of the SI section.

Figure 9-6 (a) shows the *EQE* spectra of PDPP:PC₇₁BM solar cells using different cathode interface layers. The corresponding spectra of P3HT:PC₆₁BM devices are shown in the Figure S9-7 (a) of the SI. In general, the values obtained by convoluting the measured *EQE* spectra with AM 1.5 sun spectrum matched well with the J_{sc} values obtained from *IV* measurements within the error limits of measurements. The reflectance spectra of devices with different interlayer do not differ significantly from each other in the main absorption region i.e. 300 nm – 800 nm (Figure 9-6 (b)). However above the light harvesting range i.e. more than 800 nm, significantly reduced reflectance signal from Ca cathode devices was observed. The simulated *PA* spectra for different devices in Figure 9-6 (c) clearly show that Ca absorbs considerable light compared to other cathode combinations in the complete visible region and limits the back reflected light available for absorption by the photoactive layer. Similar *PA* results were also obtained for P3HT:PC₆₁BM devices. It is to be noted that about 13 nm of Ca was deposited here to make sure that a closed and uniform layer of metal is formed on polymer surfaces and is within typical thickness range employed by various other research groups.^[44–46] It has also been reported by Hadipour *et al.* that the absorptive properties of the Ca buffer

layer is already present at a layer thickness of 5 nm but for enhanced electrical performance i.e. increased FF and V_{oc} , at least 10 nm of Ca is required.^[43] Thus after the influence of optical interferences and parasitic absorption were accounted for, the IQE spectrum was calculated for each case (Figure 9-6 (d)). The IQE spectra show a different picture compared to the EQE spectra. Here the Ca contact device shows the maximum IQE values followed by the PFN device. For P3HT:PC₆₁BM devices, the IQE spectra were nearly same for all the contacts except for Ca, where a bit smaller IQE values were obtained (Figure S9-7 (d)). Thus in a material system such as P3HT:PC₆₁BM, where the charge transport and bimolecular recombination do not limit the performance, incorporating low work function contacts do not have a significant influence on charge extraction processes. However in PDPP:PC₇₁BM system with less charge carrier mobilities and significant bimolecular recombination even at short circuit conditions, use of low work function metal or interlayers assist the charge extraction and improve the solar cell performance.

9.3 Conclusion

Optoelectrical investigations were carried out to investigate the influence of electron extracting layers consisting of Ca, ZrAcac, and PFN on the performance parameters of two different P3HT:PC₆₁BM and PDPP:PC₇₁BM bulk-heterojunction solar cell systems. The solar cell performance parameters were subjected to an influence by a number of device parameters such as diode turn-on voltage, leakage currents, built-in voltages and parasitic absorption. It is observed that early turn-on voltage and high parasitic absorption in Ca interlayer devices lead to low open circuit voltage and low short circuit current, respectively. In general, only a little change in the charge collection and extraction properties (J_{sc} and FF) was observed by incorporating electron extracting interlayers in P3HT:PC₆₁BM solar cells compared to the reference Al devices. In contrast, PDPP:PC₇₁BM solar cells showed a significant improvement with cathode interlayers compared to the Al reference. The different behavior of different blend systems to varying cathodes is attributed to a much better hole transport in P3HT domains in P3HT:PC₆₁BM solar cells compared to that of in PDPP domains in PDPP:PC₇₁BM cells. PDPP:PC₇₁BM solar cells were highly bimolecular recombination limited and thus were more influenced by changing electric fields across the photoactive layer. From the electro-absorption measurements, indeed an increase in the built-in voltage was observed for solar cells with electron extracting interlayers compared to the reference Al devices. However, the increase of up to 200 – 250 mV in V_{bi} for certain cathode combinations compared to Al was less compared to the theoretically possible values obtained from the metal-insulator-metal model. This suggests that most of the energy mismatch between the cathode and the organic layer Fermi level occurs as a voltage drop at the interface dipole layer. In the presented work, solar cells

with PFN interlayer worked better than with other interlayers because of small parasitic absorption, less leakage currents and relatively high built-in voltages in the former.

9.4 Experimental section

Photoactive materials and interface materials: PDPP was synthesized following a previously reported procedure using Suzuki polycondensation and was endcapped with para-pyridine. The obtained number average molecular weight was 23 kg/mol with a dispersity of 1.8.^[47] Absorption, photoluminescence and energy levels from cyclic voltammetry do not differ from a regularly phenyl-capped reference polymer. P3HT (Rieke Metals – RMI 001EE), PC₆₁BM (Solenne) and PC₇₁BM (American Dye Source) were obtained from commercial suppliers and used without any further purification. ZrAcac and PFN were purchased from Alfa Aesar and 1-Material, respectively. PEDOT:PSS (HTL solar) was purchased from CleviosTM.

Solar cell fabrication and characterization: Solar cell devices were prepared by spin coating 40 nm PEDOT:PSS onto cleaned patterned ITO glass substrates, followed by 150 °C baking for 15 min in air. Subsequently, the PEDOT:PSS modified substrates were transferred to a nitrogen-filled glove-box for photoactive layer deposition. The P3HT:PC₆₁BM layer was prepared by spin-coating (550 rpm) 80 ul of a solution containing 16.8 mg of P3HT and 13.2 mg of PC₆₁BM in 1 ml of chlorobenzene. The PDPP:PC₇₁BM layer was spin coated (2000 rpm) from 90 ul of a solution containing 6 mg PDPP, 12 mg PC₇₁BM and 20 ul of 1,8-diiodooctane in 1 ml of chloroform. The ZrAcac and PFN interlayers were deposited by spin coating respective solutions at 3000 rpm and 5000 rpm for 30 s in air, respectively. The ZrAcac solution was prepared in ethanol (0.7 mg in 1 ml) and the PFN solution in methanol (0.5 mg in 1 ml with a trace of acetic acid). The top electrodes, consisting of either Al (200 nm) or Ca (13 nm)/Al (200 nm), were deposited by vacuum evaporation at $\sim 1 \times 10^{-6}$ mbar. The P3HT:PC₆₁BM devices were post-annealed at 170°C for 5 min. *I-V* measurements were performed under inert environment with a Keithley 2400 source measure unit under 100 mW/cm² illumination from an AM 1.5 class A solar simulator. The active area of 9 mm² was defined by the overlap of black mask aperture area, the ITO and the evaporated top electrode.^[48] Light intensity variation experiment was performed under solar simulator light using a set of neutral density filters. EQE and reflectance spectra were obtained in the lock-in mode via a Bentham PVE 300 assembly unit included with an integrating sphere. The light intensity was calibrated before by a Si detector. Parasitic absorption was calculated using the transfer-matrix formalism which is available free of charge as a Matlab script at <http://mcgehee.group.stanford.edu/transfermatrix>.

SCLC measurements: Single carrier hole-only devices were prepared within the layer stack of glass/ITO/PEDOT:PSS/Polymer/Au. The PEDOT:PSS layers similar to that of in solar cells

were spin coated onto cleaned patterned ITO glass substrates. After that, polymer solutions (25 mg/mL in chloroform) were doctor bladed on top under inert conditions. Subsequently, Au (100 nm) were thermally evaporated to complete the device stack. The devices had an active area of 9 mm². Dark I - V measurements were made under inert environment with a Keithley 2400 source measure unit. For mobility evaluation, forward bias voltages, i.e. hole injection from PEDOT:PSS, were considered. The charge carrier mobilities were evaluated by fitting measured I - V characteristics in a voltage range from 2 to 5 V using the Murgatroyd formula.^[27] Prior to fitting, the measured I - V characteristics were corrected for the built in voltage ($V_{bi} = 0.2$ V) and the voltage drop (IR , $R = 27 \Omega$) across contacts.

Electroabsorption spectroscopy: The light source was an illuminator from Oriel. The light going through a monochromator (SPEX 1681B, Horiba Scientific) illuminated the devices, and was collected by a photodiode (HUV-4000B, EG&G Judson) in a reflective configuration. The AC amplitude of EA signal was monitored by a dual channel lock-in amplifier (SR 830 from Stanford Research Systems) and the DC amplitude by a digital multimeter (HP34401A). For all measurements, the ITO electrode was connected to the ground, and Al electrode was applied external voltages. The AC voltage of 1 V_{RMS} was applied while scanning the DC voltages.

Spectroscopic Ellipsometry (SE): Variable angle (45 - 75°) SE measurements were performed on films in a wavelength range from 300 nm - 800 nm using a J.A. Woollam ellipsometer, model M-2000DI, which is a rotating-compensator multichannel spectroscopic ellipsometer. The films were prepared following the aforementioned procedures except using Si/SiO₂ substrates. The acquired ellipsometric data were evaluated by the VASE32 software (J.A. Woolam). The films were measured by first determining their thickness using a Cauchy layer model in a range beyond their respective bandgap. Then the thickness was kept constant and a respective point-to-point fit was applied.

9.5 Acknowledgements

We gratefully acknowledge the financial support by the Bavarian State Ministry for Environment and Consumer Protection (UMWELTnanoTECH) and by the Bavarian State Ministry of Science, Research, and the Arts through the Collaborative Research Network “Solar Technologies go Hybrid”.

9.6 References

- [1] C.-C. Chen, W.-H. Chang, K. Yoshimura, K. Ohya, J. You, J. Gao, Z. Hong, Y. Yang, *Adv. Mater.* 2014, *26*, 5670.

- [2] J.-D. Chen, C. Cui, Y.-Q. Li, L. Zhou, Q.-D. Ou, C. Li, Y. Li, J.-X. Tang, *Adv. Mater.* 2015, *27*, 1035.
- [3] S.-H. Liao, H.-J. Jhuo, P.-N. Yeh, Y.-S. Cheng, Y.-L. Li, Y.-H. Lee, S. Sharma, S.-A. Chen, *Sci. Rep.* 2014, *4*, 6813.
- [4] H. Zhou, Y. Zhang, C.-K. Mai, S. D. Collins, G. C. Bazan, T.-Q. Nguyen, A. J. Heeger, *Adv. Mater.* 2015, *27*, 1767.
- [5] L. Huo, T. Liu, X. Sun, Y. Cai, A. J. Heeger, Y. Sun, *Adv. Mater.* 2015, *27*, 2938.
- [6] Z. He, C. Zhong, X. Huang, W.-Y. Wong, H. Wu, L. Chen, S. Su, Y. Cao, *Adv. Mater.* 2011, *23*, 4636.
- [7] F. Wang, Z. Tan, Y. Li, *Energy Environ. Sci.* 2015, *8*, 1059.
- [8] H.-L. Yip, A. K.-Y. Jen, *Energy Environ. Sci.* 2012, *5*, 5994.
- [9] V. D. Mihailetschi, Blom, P. W. M., J. C. Hummelen, M. T. Rispens, *J. Appl. Phys.* 2003, *94*, 6849.
- [10] S. Braun, W. R. Salaneck, M. Fahlman, *Adv. Mater.* 2009, *21*, 1450.
- [11] B. Liu, R.-Q. Peng, J.-K. Tan, P. K. H. Ho, *Adv. Energy Mater.* 2014, *4*, 1200972.
- [12] J. C. Blakesley, N. C. Greenham, *J. Appl. Phys.* 2009, *106*, 34507.
- [13] Ichiro Hiromitsu, Shin-ichiro Mada, Ayumi Inoue, Yuki Yoshida, and Senku Tanaka.
- [14] C. He, C. Zhong, H. Wu, R. Yang, W. Yang, F. Huang, G. C. Bazan, Y. Cao, *J. Mater. Chem.* 2010, *20*, 2617.
- [15] Z. Tan, S. Li, F. Wang, D. Qian, J. Lin, J. Hou, Y. Li, *Sci. Rep.* 2014, *4*, 4691.
- [16] H. Wu, F. Huang, Y. Mo, W. Yang, D. Wang, J. Peng, Y. Cao, *Adv. Mater.* 2004, *16*, 1826.
- [17] C. V. Hoven, A. Garcia, G. C. Bazan, T.-Q. Nguyen, *Adv. Mater.* 2008, *20*, 3793.
- [18] M. T. Dang, L. Hirsch, G. Wantz, *Adv. Mater.* 2011, *23*, 3597.
- [19] K. H. Hendriks, G. H. L. Heintges, V. S. Gevaerts, M. M. Wienk, R. A. J. Janssen, *Angew. Chem. Int. Ed.* 2013, *52*, 8341.
- [20] S. Albert-Seifried, D.-H. Ko, S. Hüttner, C. Kanimozhi, S. Patil, R. H. Friend, *Phys. Chem. Chem. Phys.* 2014, *16*, 6743.
- [21] W. Li, K. H. Hendriks, A. Furlan, Roelofs, W. S. Christian, M. M. Wienk, Janssen, René A. J., *J. Am. Chem. Soc.* 2013, *135*, 18942.

- [22] R. Xia, D.-S. Leem, T. Kirchartz, S. Spencer, C. Murphy, Z. He, H. Wu, S. Su, Y. Cao, J. S. Kim, J. C. deMello, D. D. Bradley, J. Nelson, *Adv. Energy Mater.* 2013, *3*, 718.
- [23] A. Guerrero, L. F. Marchesi, P. P. Boix, S. Ruiz-Raga, T. Ripolles-Sanchis, G. Garcia-Belmonte, J. Bisquert, *ACS Nano* 2012, *6*, 3453.
- [24] A. Guerrero, B. Döring, T. Ripolles-Sanchis, M. Aghamohammadi, E. Barrena, M. Campoy-Quiles, G. Garcia-Belmonte, *ACS Nano* 2013, *7*, 4637.
- [25] J. Nelson, *Phys. Rev. B* 2003, *67*, 155209.
- [26] S. Fabiano, Z. Chen, S. Vahedi, A. Facchetti, B. Pignataro, M. A. Loi, *J. Mater. Chem.* 2011, *21*, 5891.
- [27] P.N. Murgatroyd, *J. Phys. D: Appl. Phys.* 1970, *3*, 151.
- [28] C. J. Mueller, C. R. Singh, M. Fried, S. Huettner, M. Thelakkat, *Adv. Funct. Mater.* 2015, *25*, 2725.
- [29] P. H. Wöbkenberg, D. D. Bradley, D. Kronholm, J. C. Hummelen, de Leeuw, Dago M., M. Cölle, T. D. Anthopoulos, *Synthetic Metals* 2008, *158*, 468.
- [30] M. Lenes, M. Morana, C. J. Brabec, P. W. M. Blom, *Adv. Funct. Mater.* 2009, *19*, 1106.
- [31] T. M. Brown, R. H. Friend, I. S. Millard, D. J. Lacey, T. Butler, J. H. Burroughes, F. Cacialli, *J. Appl. Phys.* 2003, *93*, 6159.
- [32] S. van Reenen, S. Kouijzer, R. A. J. Janssen, M. M. Wienk, M. Kemerink, *Adv. Mater. Interfaces* 2014, *1*, 1400189.
- [33] P. J. Brewer, P. A. Lane, A. J. deMello, Bradley, D.D.C., J. C. deMello, *Adv. Funct. Mater.* 2004, *14*, 562.
- [34] R. J. de Vries, S. L. M. van Mensfoort, R. A. J. Janssen, R. Coehoorn, *Phys. Rev. B* 2010, *81*, 125203.
- [35] I. H. Campbell, M. D. Joswick, I. D. Parker, *Appl. Phys. Lett.* 1995, *67*, 3171.
- [36] T. M. Brown, J. S. Kim, R. H. Friend, F. Cacialli, R. Daik, W. J. Feast, *Appl. Phys. Lett.* 1999, *75*, 1679.
- [37] E. Siebert-Henze, V. G. Lyssenko, J. Fischer, M. Tietze, R. Brueckner, M. Schwarze, K. Vandewal, D. Ray, M. Riede, K. Leo, *AIP Advances* 2014, *4*, 47134.
- [38] D. J. Wehenkel, M. M. Wienk, R. A. J. Janssen, *J. Phys. Chem. C* 2013, *117*, 4374.

- [39] Z.-K. Tan, Y. Vaynzof, D. Credgington, C. Li, M. T. L. Casford, A. Sepe, S. Huettnner, M. Nikolka, F. Paulus, L. Yang, H. Sirringhaus, N. C. Greenham, R. H. Friend, *Adv. Funct. Mater.* 2014, *24*, 3051.
- [40] C. Li, D. Credgington, D.-H. Ko, Z. Rong, J. Wang, N. C. Greenham, *Phys. Chem. Chem. Phys.* 2014, *16*, 12131.
- [41] B. A. MacLeod, N. E. Horwitz, E. L. Ratcliff, J. L. Jenkins, N. R. Armstrong, A. J. Giordano, P. J. Hotchkiss, S. R. Marder, C. T. Campbell, D. S. Ginger, *J. Phys. Chem. Lett.* 2012, *3*, 1202.
- [42] G. F. Burkhard, E. T. Hoke, M. D. McGehee, *Adv. Mater.* 2010, *22*, 3293.
- [43] A. Hadipour, D. Cheyns, P. Heremans, B. P. Rand, *Adv. Energy Mater.* 2011, *1*, 930.
- [44] A. J. Morfa, A. M. Nardes, S. E. Shaheen, N. Kopidakis, van de Lagemaat, Jao, *Adv. Funct. Mater.* 2011, *21*, 2580.
- [45] X. Qiao, C. Zhao, B. Chen, L. Luan, B. Hu, *Organic Electronics* 2014, *15*, 1624.
- [46] Z. Huang, E. C. Fregoso, S. Dimitrov, P. S. Tuladhar, Y. W. Soon, H. Bronstein, I. Meager, W. Zhang, I. McCulloch, J. R. Durrant, *J. Mater. Chem. A* 2014, *2*, 19282.
- [47] J. C. Bijleveld, V. S. Gevaerts, D. D. Nuzzo, M. Turbiez, S. G. J. Mathijssen, D. M. de Leeuw, M. M. Wienk, R. A. J. Janssen, *Adv. Mater.* 2010, *22*, E242.
- [48] S. A. Gevorgyan, J. Eggert Carlé, R. Søndergaard, T. Trofod Larsen-Olsen, M. Jørgensen, F. C. Krebs, *Sol. Energy Mater. Sol. Cells* 2013, *110*, 24.

Supporting Information

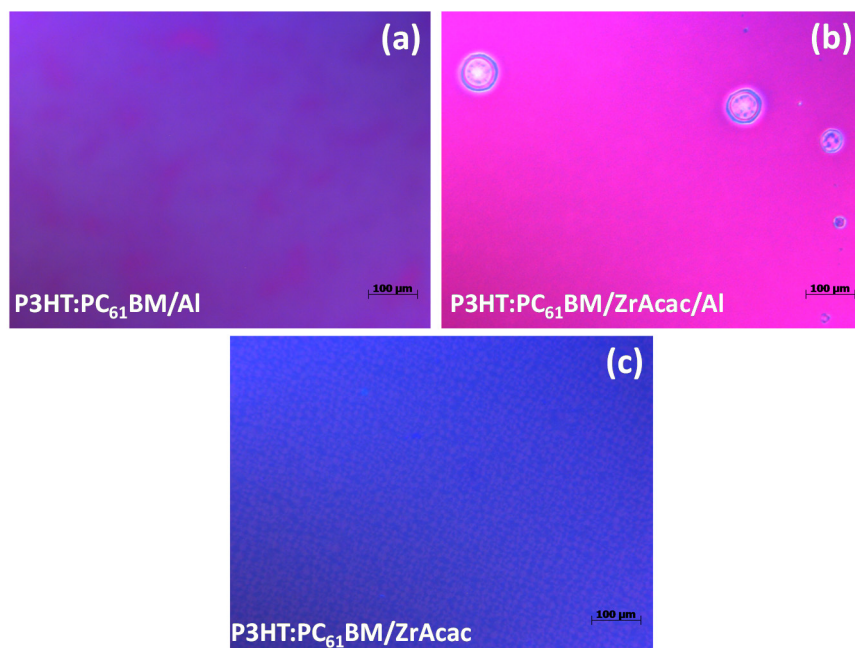


Figure S9-1. Optical microscopy of P3HT:PC₆₁BM/Al and P3HT:PC₆₁BM/ZrAcac/Al solar cells. The pictures were obtained by observing the cells through the glass substrate. Pinholes were observed on P3HT:PC₆₁BM/ZrAcac/Al devices at places where Al made contact with the ZrAcac interlayer.

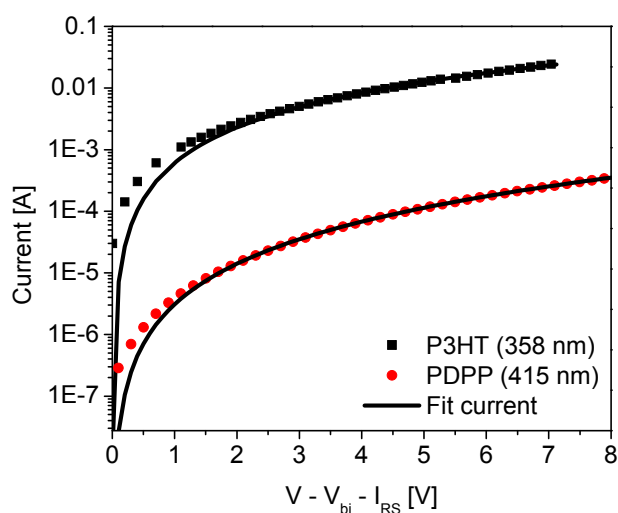


Figure S9-2. I - V characteristics of P3HT and PDPP films measured at room temperature in hole-only device configuration. The solid lines represent the SCLC fit with field dependent mobility. The corresponding film thicknesses are mentioned within the parentheses. The I - V characteristics were corrected for the built-in voltage (V_{bi}) and the voltage drop (IR) over the contacts. The effective SCLC charge carrier mobility of holes in P3HT and PDPP at an electric field of $1.5 \times 10^7 \text{ V m}^{-1}$ was $7 \times 10^{-4} \text{ cm}^2 \text{ V}^{-1} \text{ s}^{-1}$ and $1.2 \times 10^{-5} \text{ cm}^2 \text{ V}^{-1} \text{ s}^{-1}$, respectively.

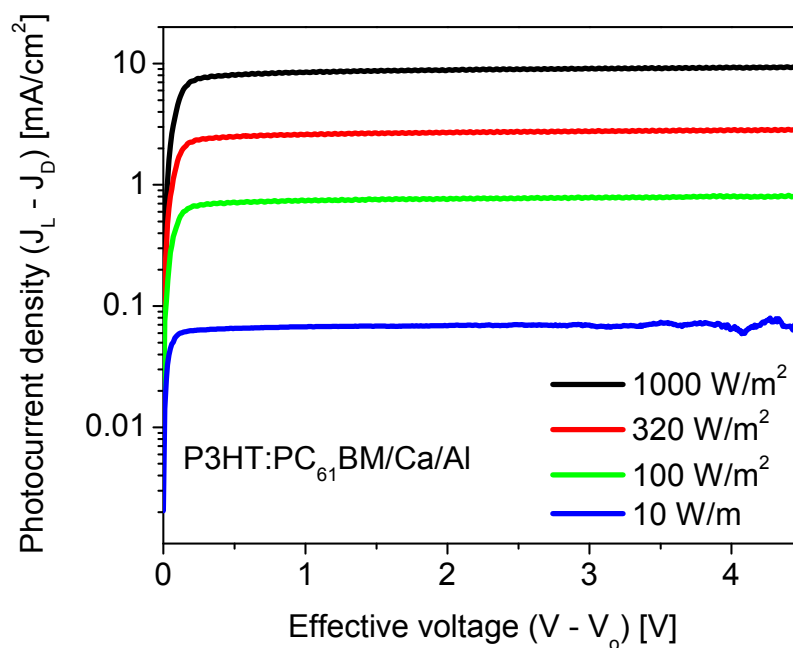


Figure S9-3. Photocurrent of a ITO/PEDOT:PSS/P3HT:PC₆₁BM/Ca/Al solar cell versus effective voltage at different intensities.

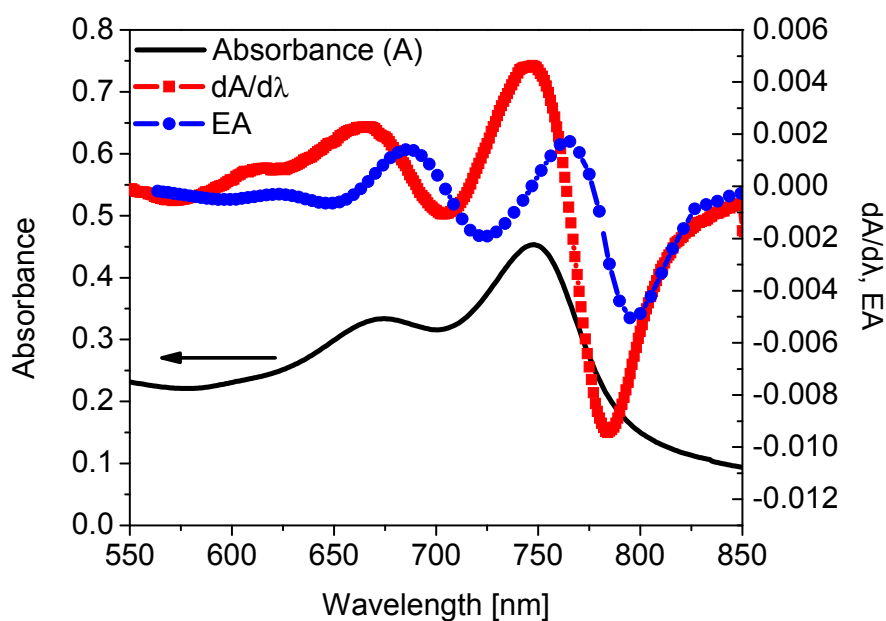


Figure S9-4. Absorbance (line) and first derivative of absorbance (square) of a PDPP:PC₇₁BM film. For comparison the EA signal (circle) of a PDPP:PC₇₁BM/PFN/Al device is also depicted. The EA signal is red-shifted and could also be due to the disorder in conjugated lengths.^[1]

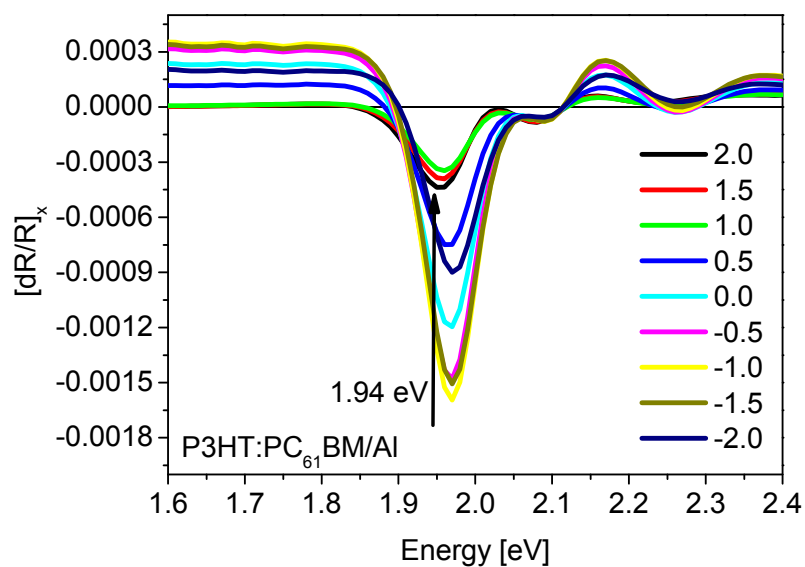


Figure S9-5. Electroabsorption (EA) spectra of a ITO/PEDOT:PSS/P3HT:PC₆₁BM/Al solar cell device measured at different applied DC voltages.

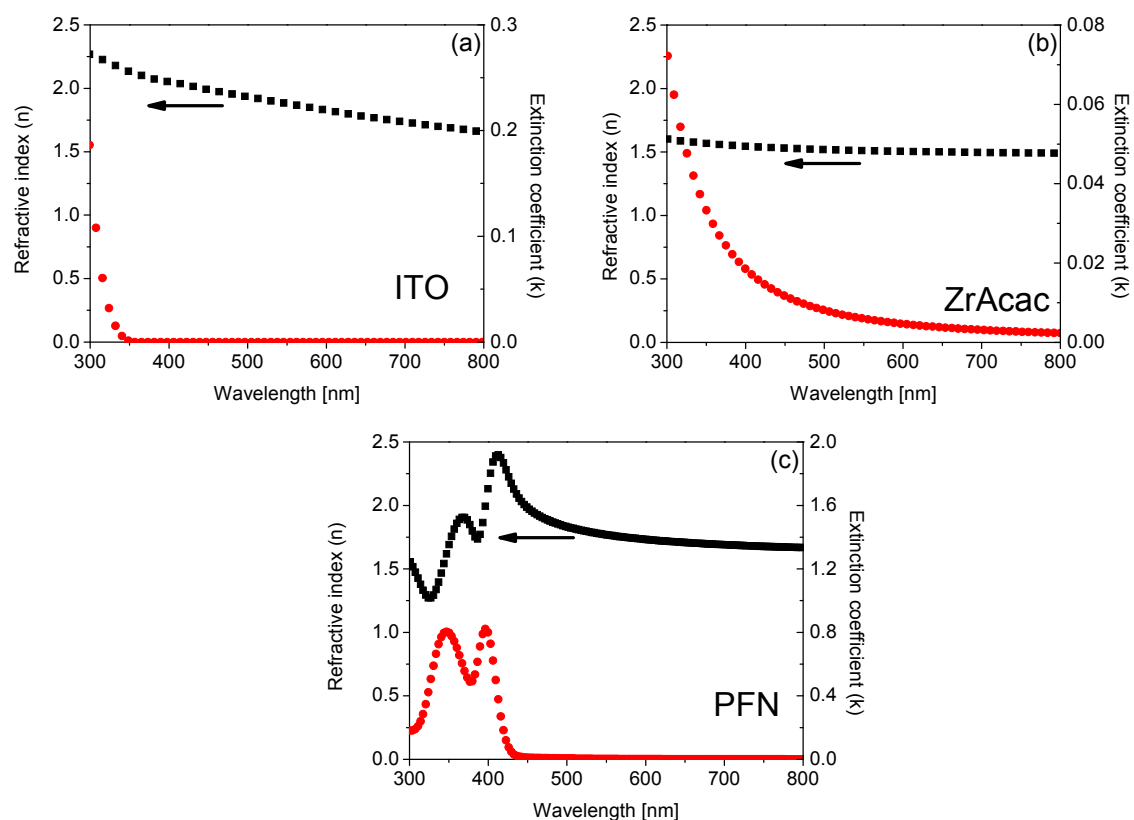


Figure S9-6. The measured refractive index (n) and extinction coefficient (k) spectra of ITO (a), ZrAcac (b) and PFN (c). The n and k values for the PEDOT:PSS, Al and Ca were taken from an open source - <http://mcgehee.group.stanford.edu/transfermatrix>.

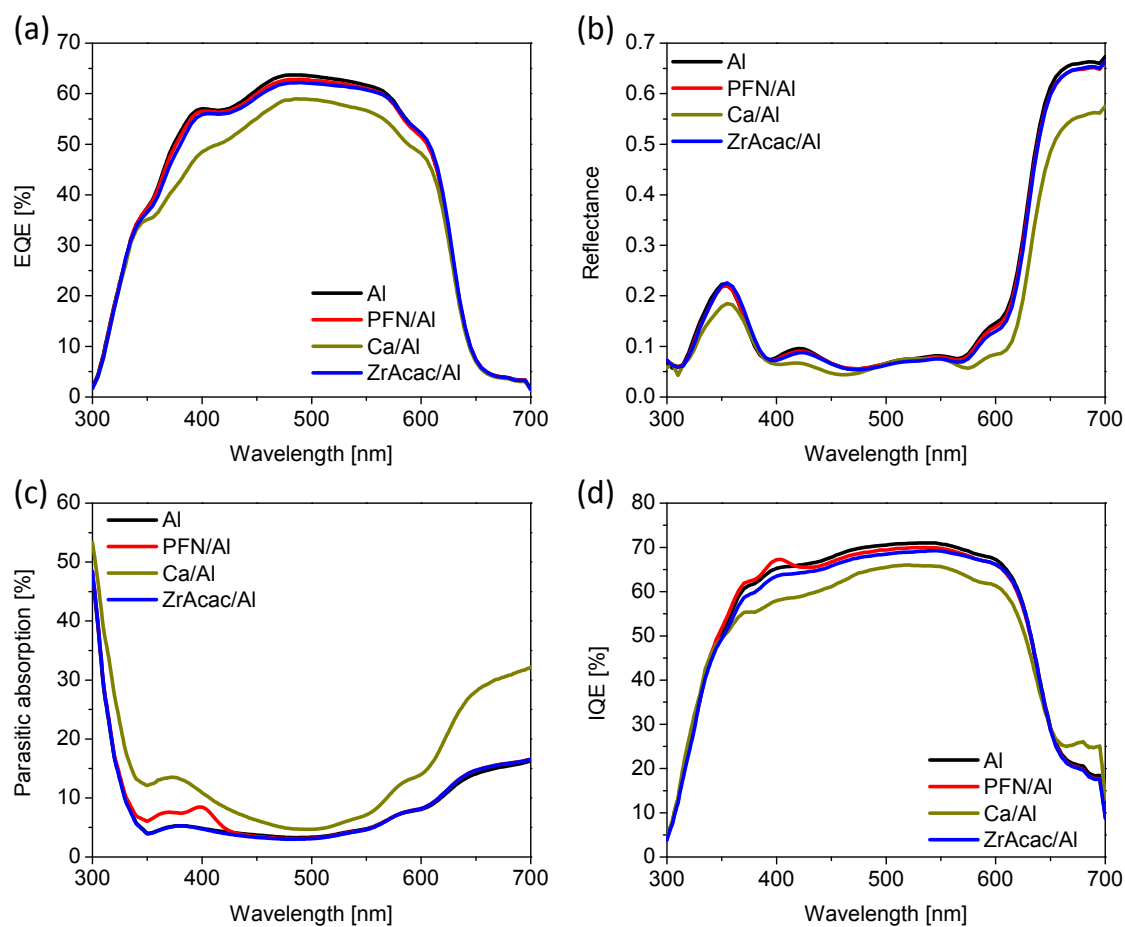


Figure S9-7. (a) Measured external quantum efficiency (EQE) and (b) reflectance (R) spectra of the P3HT:PC₆₁BM solar cells devices. (c) and (d) show the calculated parasitic absorption (PA) and internal quantum efficiency (IQE) of the corresponding devices, respectively.

Supporting References

- [1] M. Liess, S. Jeglinski, Z. V. Vardeny, M. Ozaki, K. Yoshino, Y. Ding, T. Barton, *Phys. Rev. B*. **1997**, *56*, 15712.

10 List of Publications

1. Christian J. Mueller, Chetan R. Singh, Martina Fried, Sven Huettnner and Mukundan Thelakkat:
“High Bulk Electron Mobility Diketopyrrolopyrrole Copolymers with Perfluorothiophene”
Adv. Funct. Mater. **2015**, *25*, 2725-2736.
2. Christian J. Mueller, Michael Brendel, Pia Ruckdeschel, Jens Pflaum and Mukundan Thelakkat:
“Diketopyrrolopyrroles with a Distinct Energy Level Cascade for Efficient Charge Carrier Generation in Organic Solar Cells”
Adv. Energy Mater. **2015**, *5*, 201500914.
3. Christian J. Mueller, Eliot Gann, Christopher R. McNeill and Mukundan Thelakkat:
“Influence of Fluorination in π -extended Backbone Polydiketopyrrolopyrroles on Charge Carrier Mobility and Depth-dependent Molecular Alignment”
J. Mater. Chem. C **2015**, *3*, 8916-8925.
4. Christian J. Mueller, Chetan R. Singh and Mukundan Thelakkat:
“EDOT-Diketopyrrolopyrrole Copolymers for High Bulk Hole Mobility and Near Infrared Absorption”
J. Polym. Sci., Part B: Polym. Phys. **2016**, *54*, 639-648.
5. Christian J. Mueller, Eliot Gann, Christopher R. McNeill and Mukundan Thelakkat:
“Universal Molecular Orientation Control in Polydiketopyrrolopyrroles”
Prepared for submission
6. Christian J. Mueller, Tobias Klein, Eliot Gann, Christopher R. McNeill and Mukundan Thelakkat:
“Azido-Functionalized Thiophene as a Versatile Building Block To Cross-Link Low-Bandgap Polymers”
Macromolecules, **2016**, *49*, 3749-3760.
7. Chetan R. Singh, Cheng Li, Christian J. Mueller, Sven Hüttner and Mukundan Thelakkat:
“Influence of Electron Extracting Interface Layers in Organic Bulk-Heterojunction Solar Cells”
Adv. Mater. Interfaces, **2016**, *3*, 1500422.
8. Chao Wang, Christian J. Mueller, Eliot Gann, Amelia C. Y. Liu, Mukundan Thelakkat and Christopher R. McNeill:
“EDOT-Diketopyrrolopyrrole Copolymers for Polymer Solar Cells”
J. Mater. Chem. A, **2016**, *4*, 3477-3486.
9. Eliot Gann, Christian J. Mueller, Lars Thomsen, Mukundan Thelakkat and Christopher R. McNeill:
“Angle resolved NEXAFS spectroscopy reveals alignment in DPP polymers”
Prepared for submission
10. Chao Wang, Christian J. Mueller, Eliot Gann, Amelia C. Y. Liu, Mukundan Thelakkat and Christopher R. McNeill:
“Influence of fluorination in π -extended Backbone Polydiketopyrrolopyrroles for Polymer Solar Cells”
Prepared for submission

11 List of Contributions

1. Christian J. Mueller, Chetan R. Singh, Eliot Gann, Christopher R. McNeill and Mukundan Thelakkat.
Bayreuth Polymer Symposium, September 20-22, **2015**, Bayreuth (Germany).
Poster presentation: “Conformation-Locked Semiconducting Polymers. Improved Charge Carrier Mobilities and Enhanced Thin Film Alignment”.
2. Christian J. Mueller, Chetan R. Singh, Martina Fried, Sven Hüttner and Mukundan Thelakkat.
European Polymer Congress (EPF), June 21-26, **2015**, Dresden (Germany).
Oral presentation: “High bulk electron mobility diketopyrrolopyrrole copolymers with perfluorothiophene”.
3. Christian J. Mueller, Chetan R. Singh and Mukundan Thelakkat.
Gordon Research Conference “Polymers”, June 15-19, **2015**, Amherst (USA).
Poster presentation: “High Bulk Electron Mobility Diketopyrrolopyrrole Copolymers with Perfluorothiophene”.
4. Christian J. Mueller, Chetan R. Singh and Mukundan Thelakkat.
Gordon Research Seminar “Polymers”, June 13-14, **2015**, Amherst (USA).
Poster presentation: “High Bulk Electron Mobility Diketopyrrolopyrrole Copolymers with Perfluorothiophene”.
5. Christian J. Mueller, Chetan R. Singh and Mukundan Thelakkat.
Hybrid and Organic Photovoltaics (HOPV), May 10-13, **2015**, Rome (Italy).
Poster presentation: “High Bulk Electron Mobility Diketopyrrolopyrrole Copolymers with Perfluorothiophene”.
6. Christian Müller and Mukundan Thelakkat.
FP7 project meeting (LARGECELLS), June 23-25, **2014**, Brussels (Belgium).
Poster presentation: “Low molecular weight DPP dyes for OPV – Fullerene interaction”.
7. Christian Müller and Mukundan Thelakkat.
EU-India Meeting (LARGECELLS), February 11-13, **2013**, Bangalore (India).
Oral presentation: “New Materials for LARGECELLS based on Diketopyrrolopyrroles”.

Danksagung – Acknowledgements

An dieser Stelle möchte ich mich ganz herzlich bei allen Menschen bedanken, die mich über die letzten Jahre begleitet und sehr zum Gelingen dieser Arbeit beigetragen haben.

Mein erster Dank gilt hierbei meinem Doktorvater Prof. Dr. Mukundan Thelakkat, einerseits fachlich für das Vertrauen und völlig freie Hand bei der Wahl des Themas sowie im Gestalten dieser Arbeit bei immerwährender Bereitschaft zu hilfreichen Diskussionen, aber auch für die vielen persönlichen Gespräche und Ratschläge. Herzlichen Dank auch für die Bereitstellung eines sehr großzügigen Arbeitsplatzes und die finanziellen Mittel zur Laborgestaltung nach Wunsch!

Der gesamten Gruppe des Lehrstuhls MC1 möchte ich für die Unterstützung während der letzten Jahre danken. Danke vor allem an alle Technikerinnen für den nie versiegenden Nachschub an destillierten Lösungsmitteln auch für das B6 Exil, sowie Petra und Christina für ihre zuvorkommende Art und schnelle Hilfe bei einer Vielzahl von administrativen Dingen.

Vielen Dank an die gesamte Gruppe *AFuPo*, insbesondere Tina Weller für ein äußerst angenehmes Arbeitsklima und dem Weiterführen des einen oder anderen Konzeptes. Es hat mich sehr gefreut Büro und Labor mit dir zu teilen! Besten Dank auch an Martin Huftnagel für zahlreiche wertvolle Diskussionen. Martina Fried sei für ihre großartige Unterstützung in der täglichen Laborarbeit und für das Nachziehen zahlreicher Verbindungen sowie der angenehmen Arbeitsatmosphäre während ihrer Einarbeitungszeit herzlich gedankt! Chetan Singh gilt großer Dank für zahlreiche SCLC Messungen, die zwei Kapitel dieser Arbeit deutlich aufgewertet haben. Auch all die außeruniversitären Unternehmungen, von Beachvolleyball- bis zu Kochabenden, haben diese Zeit zu etwas besonderem gemacht, an die ich immer gerne zurückdenken werde!

Ein großes Dankeschön an meine zahlreichen und fleißigen Praktikanten Janika Walcher, Pia Ruckdeschel, Thomas Gegenhuber, Jens Neubauer und Thomas Dietel sowie meinem Bacheloranden Tobias Klein.

Besten Dank auch an viele Mitarbeiter von anderen Lehrstühlen, die kurzfristig und unkompliziert Zugang zu teils ausgefallenen Analytikmethoden ermöglicht haben. Vielen Dank an Winfried Kretschmer für die Hochtemperaturanalytik (TCB-GPC, DCB-NMR), Sina Rösler (GC/MS), Ulrike Lacher (EI-MS), Sven Hüttner (Bulk XRD) und Markus Hund (AFM).

Auch zahlreiche Kooperationspartner haben direkt oder indirekt zum Gelingen dieser Arbeit beigetragen. Ein besonderer Dank gilt hierbei Michael Brendel und Jens Pflaum (Uni

Würzburg) für ihr Interesse an meinen niedermolekularen Verbindungen und ihren wertvollen Beitrag zum Kapitel 7!

Thanks to René Janssen for hosting me in Eindhoven for two weeks, and his postdoc Weiwei Li for his kind and valuable introduction to DPP polymerizations and solar cell preparation.

A huge thank you to Prof. Chris McNeill for giving me the possibility to join his research group at Monash University and for his hospitality. I am also very grateful to Dr. Eliot Gann from the McNeill group for all his support regarding the beamtime proposal, general beamline issues and his introduction not only to IGOR but also to several national parks in Victoria. A warm thanks to Chao Wang for his elaborate work on employing my polymers in solar cells. Thanks to the whole McNeill group for a really great and very productive time in Melbourne, which helped to improve this thesis considerably!

Ein riesiges Dankeschön an Frau Prof. Dr. Stefanie Dehnen, die mit ihrer engagierten Förderung ungemein zu meinem allgemeinen Verständnis der Chemie beigetragen hat. Herzlichen Dank für die Möglichkeit zur Mitarbeit in deinem Arbeitskreis und der soliden Publikationsliste, die mir im weiteren Studium immer einen großartigen Vertrauensvorsprung beschert hat!

Ein besonderer Dank geht an den Fonds der chemischen Industrie, die Studienstiftung des deutschen Volkes und das Elitenetzwerk Bayern, die mich sowohl finanziell als auch ideell erheblich unterstützt haben.

Ein großer Dank gebührt auch Prof. Jochen Roth, Mondi Benoit, Merle Neumann und allen voran Jasmin Steiner für großartige musikalische Momente, die mir nach langen Labortagen viel Abwechslung und Erfüllung geschenkt haben.

Meiner lieben Kristina danke ich für ihre großartige Unterstützung trotz all den arbeitsreichen Tagen und Nächten im Labor oder vor dem PC. Ohne dich wäre das letzte Jahr sehr hart geworden!

Der größte Dank gebührt meiner tollen Familie, meiner Mutter Brigitte, meinem Vater Klaus und meinen Schwestern Michaela und Simone, auf deren Unterstützung ich mich trotz schwerer Umstände jederzeit blind verlassen konnte. Vielen Dank für all das Vertrauen und euren Glauben. Ohne euren Rückhalt wären weder das Studium noch diese Arbeit möglich gewesen und ich wäre nicht da, wo ich heute bin.

(Eidesstattliche) Versicherungen und Erklärungen

(§ 8 S. 2 Nr. 6 PromO)

Hiermit erkläre ich mich damit einverstanden, dass die elektronische Fassung meiner Dissertation unter Wahrung meiner Urheberrechte und des Datenschutzes einer gesonderten Überprüfung hinsichtlich der eigenständigen Anfertigung der Dissertation unterzogen werden kann.

(§ 8 S. 2 Nr. 8 PromO)

Hiermit erkläre ich eidesstattlich, dass ich die Dissertation selbständig verfasst und keine anderen als die von mir angegebenen Quellen und Hilfsmittel benutzt habe.

(§ 8 S. 2 Nr. 9 PromO)

Ich habe die Dissertation nicht bereits zur Erlangung eines akademischen Grades anderweitig eingereicht und habe auch nicht bereits diese oder eine gleichartige Doktorprüfung endgültig nicht bestanden.

(§ 8 S. 2 Nr. 10 PromO)

Hiermit erkläre ich, dass ich keine Hilfe von gewerblichen Promotionsberatern bzw. -vermittlern in Anspruch genommen habe und auch künftig nicht nehmen werde.

.....

Ort, Datum, Unterschrift